197(2), 2024

COMBUSTION ENGINES

Due to the dynamic development of machine and vehicle powertrains, the "Combustion Engines" scientific journal, while retaining its historical title, currently publishes works related not only to internal combustion engines, but also other powertrains, including hybrid drives, electric drives and fuel cells.

COMBUSTION ENGINES

A Scientific Magazine

2024, 197(2)

Year LXIII

PL ISSN 2300-9896
PL eISSN 2658-1442

Publisher:
Polish Scientific Society of Combustion Engines
60-965 Poznan, pl. M. Skłodowskiej-Curie 5, Poland
tel.: +48 61 6475966, fax: +48 61 6652204
E-mail: sekretariat@ptnss.pl
WebSite: http://www.ptnss.pl
Papers available on-line: http://combustion-engines.eu

Contents

Editorial:

Institute of Combustion Engines and Powertrains
Poznan University of Technology
60-965 Poznan, Piotrowo 3 Street
tel.: +48 61 2244505, +48 61 2244502
E-mail: papers@ptnss.pl

Publisher:

Polish Scientific Society of Combustion Engines
60-965 Poznan, pl. M. Sklodowskiej-Curie 5, Poland
tel.: +48 61 6475966, fax: +48 61 6652204
E-mail: sekretariat@ptnss.pl
WebSite: http://www.ptnss.pl

Subscriptions
Send subscription requests to the Publisher's address.
Cost of a single issue PLN 100.

Preparation for print
ARS NOVA Publishing House
60-782 Poznan, ul. Grunwaldzka 17/10A

Circulation: 60 copies

Printing and binding

Zakład Poligraficzny Moś i Łuczak, sp. j.,
Poznań, ul. Piwna 1

The journal is under the patronage of the Transport Committee of the Polish Academy of Sciences

The journal is registered and listed in the Polish and international database

Papers published in the

Combustion Engines

quarterly receive 70 points as stated by the Notification of the Minister of Science dated 5 January 2024.

Declaration of the original version
The original version of the Combustion Engines journal is the printed version.

Cover
I – 6-cylinder Detroit Diesel engine – DD13 *(www.demanddetroit.com)*; background *(Nature, Natural landscape, Body of water, Sky, Reflection, Water – pl.pinterest.com)*

IV – Lamborghini LB744 V12 hybrid engine *(www.supercars.net)*

Article citation info:
Sikora M, Orliński P. Hydrotreated vegetable oil fuel within the Fit for 55 package. Combustion Engines. 2024;197(2):3-8. https://doi.org/10.19206/CE-174554

Mieczysław SIKORA
Piotr ORLIŃSKI

Combustion Engines
Polish Scientific Society of Combustion Engines

Hydrotreated vegetable oil fuel within the Fit for 55 package

ARTICLE INFO

Received: 1 June 2023
Revised: 21 September 2023
Accepted: 26 October 2023
Available online: 16 December 2023

On March 28, 2023, the EU Council adopted a regulation setting stringent carbon dioxide emission standards for new cars and vans. Under the new law, new vehicles with a 100 per cent reduction in carbon dioxide emissions will be able to be registered after 2035. The new EU legislation sets the following targets: a 55 per cent reduction in CO_2 emissions for new cars and 50 per cent for new vans between 2030 and 2034 compared to 2021 levels; a 100 per cent reduction in CO_2 emissions for both new cars and vans from 2035. This will result in only electric or hydrogen-powered cars and vans being able to be registered after 2035. The fuel omitted from the Fit for 55 packages within cars and vans is hydrotreated vegetable oil. According to the research carried out so far, it is possible to replace diesel with HVO fuel even without interference with the fuel injection control system. If an internal combustion engine is fuelled with HVO fuel instead of diesel, the greenhouse gas emissions can be reduced by up to 90 per cent. What is more, the technology for using HVO fuel has many more possibilities for reducing CO_2 emissions, if only by refining the exhaust after-treatment process. The exclusion of this fuel from the Fit for 55 package raises serious doubts about the quality of the analyses based on which HVO fuel was not included in the Fit for 55 packages.

Key words: *HVO fuel, biofuel of the second generation, Fit for 55 packages, emission of toxic exhaust gas components*

1. Introduction

Internal combustion engines are a main source of CO_2 emissions. Greenhouse gases such as CO_2 are responsible for climate change. Reducing CO_2 emissions from internal combustion engines is therefore crucial to reducing global warming and its effects, including rising temperatures, changing precipitation, melting glaciers, and rising sea levels. Given these risks from CO_2 emissions from internal combustion engines, the Council of the European Union is introducing the 'Fit for 55' package. This is a set of reforms introduced in 2021 to accelerate action to reduce greenhouse gas emissions and achieve the Paris Agreement targets [11]. From the legislature's perspective, the Fit for 55 package aims to modernize existing legislation in line with the EU's 2030 climate target, a prerequisite for the transformative changes needed in the economy to achieve climate neutrality by 2050. However, there is concern among biofuel market experts that the new legislation will ruin the internal combustion engine market. Due to EU regulations and emission standards, the automotive market will be forced to undergo a decarbonization process. The time horizon outlined by EU regulations seems very short and will force companies to implement organizational changes quickly. Unfortunately, if budgeting, purchasing, training, testing, and implementation issues are to be carried out diligently this process takes years. A great many companies with entire fleets of vehicles are now looking for solutions that quantifiably reduce the CO_2 emissions of the company's cars and at the same time do not force the company to change the composition of its fleet from combustion cars to all-electric ones. One such solution is to fuel internal combustion engines with fuels with similar physical and chemical properties to diesel. Such fuels include those derived from biomass. Vegetable oils, animal fats and waste oils can be used as raw materials for alternative fuels [14]. Such fuels include higher fatty acid methyl esters (FAME). These are fuels produced from oilseed crops such as rapeseed or soybeans by transesterification. FAME fuels have several advantages over diesel fuel such as better ignition and reduced carbon monoxide (CO), hydrocarbon (HC) and particulate matter (PM) emissions [27]. However, FAME fuel applications come with some limitations. FAME fuel can corrode storage tanks and has a higher viscosity which negatively affects fuel injection. A promising alternative to FAME may be hydrotreated vegetable oil (HVO). It is a synthetic liquid biofuel free of aromatics, oxygen and sulfur. In terms of chemical structure, it consists of straight-chain paraffinic hydrocarbons. The fuel is produced by hydrotreating vegetable oils, animal fats or waste oils [33]. Advantages of HVO fuel over FAME fuel include high heating value and cetane value, lower turbidity temperature, lower viscosity. With fewer unsaturated compounds in its chemical composition, HVO shows better oxidation stability than FAME. HVO fuel consists of straight-chain alkanes, which have a lower activation energy than the aromatic ring-shaped hydrocarbons of which diesel fuel is composed. Therefore, the ignition delay for HVO fuel is shorter than for diesel fuel. This results in an earlier onset of combustion and reduced CO, HC and PM emissions compared to diesel. This shows that hydrotreated vegetable oil can be the fuel that can allow you to professionally plan and manage the reduction of carbon footprint and toxic emissions in your fleet. The subject matter of the article is up to date, as it systematizes information on the emission of toxic exhaust components when using HVO fuel in the engine, and the article also refers to the latest legal regulations introduced by EU institutions.

2. Fit for 55

In line with a communication from the Council of the European Union on 28 March 2023, the Council adopted a regulation setting stricter CO_2 emission standards for new cars and vans. The new rules aim to reduce emissions from road transport, which accounts for the largest share of CO_2 emissions from transport [11]. They also serve to provide the right impetus for the automotive industry to move towards zero-emission mobility, while ensuring continued innovation in the sector. The new legislation sets the following targets [11]:

1. A target reduction in CO_2 emissions of 55% for new cars and 50% for new vans between 2030 and 2034 compared to 2021 levels.
2. A target of a 100% reduction in CO_2 emissions for both new cars and new vans from 2035.

The regulation amends existing legislation, last revised in 2019. Under the regulation, each manufacturer must ensure that the average CO_2 emissions of its fleet of newly registered vehicles in a given calendar year do not exceed its specific annual emissions target. If this is not the case, the manufacturer must pay a charge of €95 per gram of CO_2/km above the target per registered vehicle [31]. As a result, the newly agreed targets will ultimately make zero-emission cars cheaper than those powered by fossil fuels. The European Commission's proposal is to tighten carbon dioxide emission standards for passenger cars: by 2030 by 55 percent (compared to the status quo), and from 2035 by 100 percent. This means that in a few years it will not be possible to register a car with an internal combustion engine in the EU. This refers to newly manufactured cars. The European Commission also recommends improving the infrastructure: charging points for electric cars on main roads are to be spaced every 60 kilometers, and for hydrogen cars every 150. This could lead to a lack of profitability in the production of combustion cars. One solution that will take into account the goal of environmental protection and at the same time will not make it necessary to reorganise the operations of companies and ordinary households very quickly is to use biofuel as a substitute for diesel. Such a fuel is hydrotreated vegetable oil.

3. Review of HVO fuel properties

HVO (Hydrogenated Vegetable Oil), or hydrogenated vegetable oil, is a high-quality diesel product made entirely from renewable raw materials, i.e. vegetable oils and fat waste. HVO is a second-generation biofuel (the first was FAME or rapeseed oil methyl ester). HVO emits 90 per cent less carbon dioxide, 30 per cent less particulates and 9 per cent less nitrogen oxide, compared to regular diesel [9, 10, 25, 29]. Its production is based on vegetable waste, such as vegetable and fruit residues or even out-of-date margarine. The transport and manufacturing industries calculate that the use of pure biodiesel will help them meet the EU's stringent targets for reducing pollution and using green energy sources [5, 32, 33]. Hydrogenated vegetable oil is a high-quality product made from renewable raw materials, i.e. vegetable oils and fatty waste. According to the literature available today, it is the most environmentally friendly fuel for diesel vehicles. Companies associated with the transport industry as a whole estimate that the use of hydrotreated vegetable oil will help the entire transport industry to meet the EU's stringent pollution reduction standards. This includes meeting EU targets for the use of clean energy as widely as possible, in all sectors of the economy. It is estimated that reducing emissions of toxic exhaust components by replacing diesel with hydrotreated vegetable oil could have a real impact on improving the health of our society. The entire transportation industry knows that the cost of fuel is not the only determinant of its popularity. The price of one liter of HVO fuel is about €0.6 higher than the price of one liter of diesel fuel. However, if you look at the total costs that transport companies have to bear due to the need to meet the European Union's requirements for emissions of toxic components of exhaust gases, transport companies are showing interest in hydrotreated vegetable oil and are willing to decide to fuel their fleet of vehicles with this fuel. What's more, this also applies to manufacturing plants and factories, which are also required to report on the use of renewable energy and biofuels throughout the product manufacturing process. HVO production technology has been known for several years. Its forerunner was the Finnish station brand Neste, which launched pure biodiesel stations in Finland, Sweden and Lithuania and Latvia. Western European networks such as Total and Eni are now following in their footsteps. In Poland, ORLEN has also conducted research into HVO fuel, which has shown that HVO fuel is of similar or even higher quality than standard diesel [25, 28]. It is worth emphasizing that filling up with HVO fuel does not exclude the use of traditional diesel fuel. HVO fuel can act as a substitute fuel for diesel [2, 19, 29]. This expands the possibilities of powering internal combustion engines traditionally powered by diesel. Studies are confirming that HVO (including HVO100) is well-suited for diesel engines without any modifications [6, 22, 24]. This is why leading truck manufacturers are supporting the popularization of this fuel. Compliance with the standard for their entire fleet was recently announced by DAF and has been declared by Scania, MAN, Volvo, Mercedes-Benz, Renault Trucks or Iveco for several years. In particular, HVO fuel can be used by owners of Euro V and VI class trucks, i.e. virtually the entire Polish fleet serving international traffic, as well as the majority of vehicles in local traffic [14, 30]. Vehicles with engines meeting Euro III and IV standards can also be fueled with HVO fuel, but this requires interference with the fuel dosage control system [23].

Hydrotreated vegetable oils are mixtures of paraffin hydrocarbons. These fuels are free of any sulfur and aromatic compounds. The cetane number of Hydrotreated vegetable oils is extremely high and their other properties are comparable to fuels currently used to power compression-ignition engines. Table 1 provides a comparison of the physicochemical properties of the three fuels: HVO, FAME and diesel.

The physics-chemical properties of HVO and FAME fuels are determined by which vegetable oil they are produced from. For this reason, in Table 1 some parameters are reported in ranges.

HVO fuel can be used for powering CI engines in three options. The first alternative is to add only a small percentage of the biocomponent to the diesel fuel [28]. This is very common with ester-type biodiesel (FAME). Now, we can most often find diesel at gas stations with a 7% content of methyl ester of higher fatty acids of rapeseed oil. This amount takes into account the results of research on fuel stability and sediment formation in diesel engine power systems.

Table 1. Physical and chemical properties of the three fuels HVO, FAME, and diesel fuel [2, 6, 16, 22, 23]

Parameter	Unit	HVO	FAME	Diesel fuel
Density at 15°C	kg/m^3	780	885	835
Viscosity at 40°C	mm^2/s	2.5–3.5	4.5	3.5
Cetane number	–	60–98	52	54.6
Distillation range	°C	170–310	340–360	170–350
Cloud point	°C	−5... −25	−5	−5
Calorific value	MJ/kg	44	37.5	42.7
Calorific value	MJ/dm^3	34.2	33.1	36.4
Sulphur content	%	0	0	30
Oxygen content	%	0	10	0
Storage stability	–	good	poor	good

The second option is to blend a few tens of per cent of HVO fuel with diesel fuel [28]. This is possible with hydrotreated vegetable oils (HVO) without any deterioration in fuel quality, adverse changes in exhaust emissions and degradation in engine performance. The fuel mixture will be of good quality, as the cetane number will be increased and the aromatic content will be reduced, resulting in lower emissions of selected exhaust components and better performance during cold start.

A final, third alternative is to take advantage of HVO as a clean fuel [28]. It is being considered primarily for public transportation, generators, and trucking companies.

Based on the available literature, a comparative analysis of the elemental and chemical composition of diesel fuel, HVO fuel and a mixture of diesel fuel and HVO fuel was analyzed. The performance of this study is shown in Table 2.

Table 2. Chemical composition of diesel fuel, HVO fuel and the mixture of diesel fuel and HVO fuel [9, 13, 35]

Name	Unit	Diesel fuel	HVO	HVO-30
Diesel fuel	%	100	0	70
HVO	%	0	100	30
Coal	%	85.9	84.8	85.8
Hydrogen	%	13.5	15.2	14
C/H ratio	–	6.4	5.6	6.1
Sulphur	mg/kg	5	2.5	3
Nitrogen	mg/kg	28	1.5	20
Aromatic compounds in total	%	18.9	0.2	13.6
Water	mg/kg	20	7	18

In the next step of the study, an analysis of the physics-chemical features of diesel, HVO fuel and a blend of diesel and HVO fuel was made. The results of the comparative study are shown in Table 3.

Table 2 and Table 3 show the physical and chemical properties of HVO fuel produced from rapeseed vegetable oil.

Special focus should be placed on the different density values of HVO fuel relative to diesel and the higher cetane number value of HVO fuel compared to conventional diesel. The major benefits of HVO fuel are its high cetane number, high energy density and the freedom from oxygen in the molecule of the resulting fuel. An important advantage of HVO fuel is its cold point level, which can be as low as –25°C. This in turn renders HVO suited for use in very cold winters. Importantly, the production and use of HVO is largely climate-neutral if only renewable energy sources are used. HVO is obtained from waste cooking oils, fats and fat residues, waste fats and vegetable oil [33]. It is then converted into hydrocarbons by catalytic hydrogenation, which is the addition of hydrogen at intense heating. This, in turn, is an energy carrier and thus a potential fuel. To what extent HVO will also establish itself in the market in the long term depends primarily on how global fuel production volumes and associated availability develop. Despite significant growth in production, HVO is widely available in only a few countries in Europe.

Table 3. Physicochemical properties of diesel, HVO fuel and the mixture of diesel and HVO fuel [11, 16, 38]

Parameter	Unit	Diesel fuel	HVO	HVO-30
Density at 15°C	kg/m^3	835	780	824
Cloud point	°C	–5	–7	–6
Flash point	°C	67	98	73
Viscosity at 40°C	mm^2/s	3.5	3.1	3.2
Calorific value	MJ/kg	42.7	44	43.4
	MJ/dm^3	36.4	34.2	35.8
Cetane number	–	54.6	70	65
Boiling point	°C	363	313	358
Lubricity (HFRR)	μm	323	361	300
Heat of combustion	MJ/kg	45.98	47.28	46.34

4. Emissions of toxic components

Toxic components in the exhaust gas can make up several per cent of the volume of the exhaust gas. The emission of toxic components depends on the type of fuel and the way it is burned in the engine [1, 18]. For compression-ignition engines, the primary concern is the emission of carbon oxides, hydrocarbons, nitrogen oxides, particulates and carbon dioxide [4, 20, 28, 34]. The use of biofuel has an impact on the emission of these toxic exhaust components. Such test results are presented in Fig. 1 for three mixtures of HVO and diesel showing the percentage difference between the emissions of selected toxic components of the exhaust gas when the engine is fueled with these fuels compared to being fueled with pure diesel. Simulation studies were carried out using AVL BOOST software. AVL BOOST is software with which you can model the operating conditions of an engine and then simulate the varying operating conditions of the engine. AVL BOOST is a calculation system with real-time capability. It contains basic engine components for the greatest possible flexibility in engine design. Modelling takes place in the following stages. First, the gas stream, i.e. the gas properties, intake manifold, air filter, compressor and cylinder must be modeled. This requires the input of data such as the geometrical parameters of the engine, the timing phases, etc. The next stage is to model the heat transfer through the cylinder walls, engine cooling. This boils down to defining the heat transfer model and the combustion process model. The next step is to model the mechanical load of the engine and the engine control, and to enter the fuel data. The volume proportions of HVO fuel and diesel were chosen to compare the results with the available literature [10].

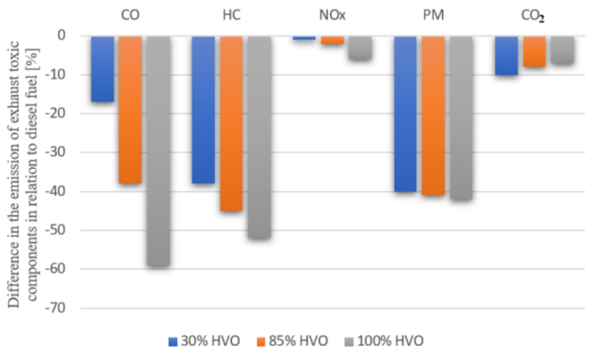

Fig. 1. Difference in emissions of toxic exhaust constituents about pure diesel

The results in Fig. 1 show that HVO biofuel significantly reduces carbon monoxide, particulate matter, and hydrocarbon emissions compared to a diesel-fueled engine. This is true for both HVO biofuel and a blend in a volume ratio of 85% HVO and 15% diesel fuel 30% HVO and 70% diesel. The emissions of nitrogen oxides when using HVO biofuel and a mixture of 15% diesel fuel and 85% HVO fuel and also 30% HVO and 70% diesel are comparable to the emissions of nitrogen oxides when using diesel. This is the main advantage of this fuel, given the comparison between HVO biofuel and FAME biofuel. The use of FAME typically increases NO_x emissions due to its elemental composition, which contains oxygen [18]. The simulation results obtained are consistent with those described by other researchers and available in the literature.

5. HVO vs. the Fit for 55 package

The transport and logistics industry is facing new challenges with the Fit for 55 packages adopted by the European Union. The new EU legislation sets the following targets [11]:

– 55 per cent reduction in CO_2 emissions for new cars and 50 per cent for new vans between 2030 and 2034 compared to 2021 levels [11]
– a 100 per cent reduction in CO_2 emissions for both new cars and vans from 2035 [11].

More precisely, such targets will force the market to replace internal combustion vehicles, with electric and hydrogen vehicles. A similar solution is to apply to heavy vehicles used in road transport, as 90% of them are to be zero-emission from 2040. However, it seems that the deadlines proposed under the Fit for 55 package are virtually unrealistic to meet! No company can make such significant changes overnight. Truck manufacturers, already have an electric truck on sale. However, the charger to charge such an electric vehicle, which will travel up to 400 km, must have a power output of 750 kW. Today, the available capacities of chargers are 20 kW, with a maximum of 50 kW. Therefore, an expansion of the electrical grid infrastructure is necessary. With hydrogen, the situation seems even more difficult. At the moment, there is not a single hydrogen-powered truck on the market for sale. Extensive research into hydrogen fuel was carried out by Lotos at one time, and it turned out that transporting this fuel was a problem. A hydrogen tanker weighs 23 tonnes and is capable of carrying about 300 kg of hydrogen at a time. It follows that hydrogen needs to be produced on-site, and hydrogen stations need to be built with small installations ready to produce this fuel on-site. Importantly, back in the second decade of the 21st century, it was estimated that with the projected increase in biodiesel demand, HVO fuel production would double on a European scale and triple globally. The entire biofuels market segment was expecting a steady increase in the share of biofuels in the fuel market and was therefore increasing its investments in this direction in order to cope with the expected increase in demand for biofuels [12]. Polish corporation PKN ORLEN is in the process of building a unit to hydrogenate vegetable oil. The investment is being built in Plock. The company estimates that it will be able to produce 300,000 tons of HVO fuel per year. The cost of this investment is estimated at €150 million. Production is scheduled to begin in 2024.

The solution to the problems described above for electric and hydrogen propulsion in heavy transport is HVO fuel, which reduces greenhouse gas emissions by 90 per cent [13]. Preliminary simulation studies carried out by the authors of this article using AVL BOOST software confirm this. A Perkins 3.4 854 E-E34TA engine equipped with a classic common rail fuel injection system was used as the test subject. As part of the simulation studies carried out by the authors, the test object was modelled by entering the geometric parameters of the engine and modelling the heat transfer process through the cylinder walls. Subsequently, the gas properties, intake manifold, air filter and HVO fuel data were modelled. Importantly, the introduction of such fuel does not require any investment in the vehicle, as the fuel simply replaces diesel. Research on this HVO fuel was conducted by ORLEN. These studies show that HVO fuel has comparable parameters to diesel. Hydrotreated vegetable oil is a very high-quality diesel fuel with an excellent cetane number level. It has a high calorific value and is free of aromatics and heteroatoms (Sulphur) and heteroatoms (Sulphur, nitrogen, or oxygen). HVO fuel is also immiscible with water and completely compatible with diesel produced from crude oil. This makes HVO fuel an excellent alternative to diesel in terms of engine performance and environmental protection [12]. It is sufficient to extend the infrastructure of a diesel filling station with the possibility of filling up with HVO fuel. Such a solution will make it possible to travel freely throughout Europe with a combustion engine fueled by HVO fuel. The exclusion of HVO fuel from the Fit for 55 packages, therefore, raises serious doubts about the quality of the experts drafting the regulation!

Conclusions

Based on a comprehensive assessment of HVO fuel and an analysis of the proposals in the Fit for 55 package, the following conclusions can be drawn:

– Under the new law, new passenger vehicles and vans will be able to be registered after 2035 with a 100% reduction in carbon dioxide emissions
– From 2040 onwards, zero-emission is to apply to 90 per cent of heavy vehicles used in road transport
– Such stringent emissions standards will result in vehicles with internal combustion engines being replaced by electric or hydrogen power

- The deadlines proposed under the Fit for 55 package are virtually unrealistic to meet
- It is possible to replace diesel with HVO fuel even without interference with the fuel injection control system
- Most of the physicochemical parameters of diesel and HVO fuel are of similar value. The exception is the density of HVO fuel, which is about 7% lower than that of diesel. Furthermore, the cetane number of HVO fuel is approx. 30% higher than the cetane number of diesel fuel. HVO fuel contains negligible amounts of aromatic compounds in contrast to diesel fuel (Table 1–3)
- HVO fuel is a solution that will simultaneously reduce emissions of toxic exhaust components while not exposing the transport market (especially heavy transport) to problems with refueling infrastructure
- The entire biofuel market segment expected a steady increase in the share of biofuels in the fuel market and therefore increased investments in this direction to meet the anticipated increase in biofuel demand
- With AVL BOOST software, the authors performed simulation studies to assess that HVO fuel can successfully replace diesel fuel. By replacing diesel with HVO fuel, similar engine performance can be achieved while reducing toxic emissions
- There are more and more voices among biofuel experts that the Fit for 55 package will revolutionize the passenger car market in Europe. In just a few years, society will no longer be able to drive cars with passenger engines. The question arises whether this does not violate civil liberties. The more so that the regulations will apply to the European market, so Europeans will pay for the transformation. This transformation would really make sense, the whole world would have to be active in this matter, including China, India and the United States
- The exclusion of HVO fuel from the Fit for 55 package raises serious doubts about the quality of the experts drafting the regulation!

The authors' achievement in this article is to systematize the knowledge on HVO fueling of internal combustion engines and to compare the results from AVL Boost with those available in the literature. The simulation studies carried out so far are the first stage of HVO fuel testing carried out by the authors of the article. In the next stage, we will carry out an empirical study of HVO fuel feeding of an internal combustion engine and its actual impact on the emission of toxic components of the exhaust gas.

Acknowledgements

The article uses the results obtained with the AVL software (available at the Faculty of Automotive and Construction Machinery Engineering of the Warsaw University of Technology under the Platinum Partnership license).

Nomenclature

AVL	simulation software in the field of internal combustion engines
FAME	fatty acid methyl esters
HVO	hydrogenated vegetable oil

Bibliography

[1] Ambat I, Srivastava V, Sillanpää M. Recent advancement in biodiesel production methodologies using various feedstock: a review. Renew Sustain Energy Rev. 2018;90:356-369. https://doi.org/10.1016/j.rser.2018.03.069

[2] Arvidsson R, Persson S, Fröling M, Svanström M. Life cycle assessment of hydrotreated vegetable oil from rape, oil palm and Jatropha. J Clean Prod 2011;19:129-137. https://doi.org/10.1016/j.jclepro.2010.02.008

[3] Bhardwaj OP, Kolbeck AF, Kkoerfer T, Honkanen M. Potential of hydrogenated vegetable oil (HVO) in future high efficiency combustion system. SAE Int J Fuels Lubr. 2013;6:157-169. https://doi.org/10.4271/2013-01-1677

[4] Bohl T, Smallbone A, Tian G, Roskilly AP. Particulate number and NO_x trade-off comparisons between HVO and mineral diesel in HD applications. Fuel. 2018;215:90-101. https://doi.org/10.1016/j.fuel.2017.11.023

[5] Bortel I, Vávra J, Takáts M. Effect of HVO fuel mixtures on emissions and performance of a passenger car size diesel engine. Renew Energy. 2019;140:680-691. https://doi.org/10.1016/j.renene.2019.03.067

[6] Chojnowski J, Nogas P. The potential of hydrotreated vegetable oil (HVO) as a high-reactive biofuel in dual-fuel power systems. Biul Wojsk Akad Tech. 2021;70:65-76. https://doi.org/10.5604/01.3001.0015.7011

[7] da Costa RBR, Roque LFA, de Souza TAZ, Coronado CJR, Pinto GM, Cintra AJA et al. Experimental assessment of renewable diesel fuels (HVO/Farnesane) and bioethanol on dual-fuel mode. Energy Convers Manag. 2022;258:115554. https://doi.org/10.1016/j.enconman.2022.115554

[8] d'Ambrosio S, Mancarella A, Manelli A. Utilization of hydrotreated vegetable oil (HVO) in a Euro 6 dual-loop EGR diesel engine: behavior as a drop-in fuel and potentialities along calibration parameter sweeps. Energies. 2022;15:7202. https://doi.org/10.3390/en15197202

[9] Dimitriadis A, Natsios I, Dimaratos A, Katsaounis D, Samaras Z, Bezergianni S et al. Evaluation of a hydrotreated vegetable oil (HVO) and effects on emissions of a passenger car diesel engine. Front Mech Eng. 2018;4. https://doi.org/10.3389/fmech.2018.00007

[10] Engman A, Gauthier Q, Hartikka T. Neste renewable diesel handbook. Neste Corp 2020;1. https://www.neste.com/sites/default/files/attachments/neste_renewable_diesel_handbook.pdf

[11] European Parliament. Revision of the Renewable Energy Directive: Fit for 55 package | Think Tank | European Parliament. Available: https://www.europarl.europa.eu/thinktank/pl/document/EPRS_BRI(2021)698781

[12] Grzelak P, Żółtowski A. Environmental assessment of the exploitation of diesel engines powered by biofuels. Combustion Engines. 2020;180:31-35. https://doi.org/10.19206/CE-2020-105

[13] Hunicz J, Krzaczek P, Gęca M, Rybak A, Mikulski M. Comparative study of combustion and emissions of diesel engine fuelled with FAME and HVO. Combustion Engines. 2021;184:72-78. https://doi.org/10.19206/CE-135066

[14] Hunicz J, Matijošius J, Rimkus A, Kilikevičius A, Kordos P, Mikulski M. Efficient hydrotreated vegetable oil combustion

under partially premixed conditions with heavy exhaust gas recirculation. Fuel. 2020;268:117350. https://doi.org/10.1016/j.fuel.2020.117350

[15] Karavalakis G, Jiang Y, Yang J, Durbin T, Nuottimäki J, Lehto K. Emissions and fuel economy evaluation from two current technology heavy-duty trucks operated on HVO and FAME blends. SAE Int J Fuels Lubr. 2016;9:177-190. https://doi.org/10.4271/2016-01-0876

[16] Ko J, Jin D, Jang W, Myung CL, Kwon S, Park S. Comparative investigation of NO_x emission characteristics from a Euro 6-compliant diesel passenger car over the NEDC and WLTC at various ambient temperatures. Appl Energy. 2017;187:652-662. https://doi.org/10.1016/j.apenergy.2016.11.105

[17] Kruczyński S, Gis W, Orliński P, Sikora M. Influence of the use of ethanol fuel on selected parameters of the gasoline engine. IOP Conf Ser Mater Sci Eng. 2018;421:042041. https://doi.org/10.1088/1757-899X/421/4/042041

[18] Kurczyński D, Wcisło G, Łagowski P. Experimental study of fuel consumption and exhaust gas composition of a diesel engine powered by biodiesel from waste of animal origin. Energies. 2021;14(12):3472. https://doi.org/10.3390/en14123472

[19] Kuronen M, Mikkonen S, Aakko P, Murtonen T. Hydrotreated vegetable oil as fuel for heavy duty diesel engines. SAE Technical Paper 2007-01-4031. 2007. https://doi.org/10.4271/2007-01-4031

[20] Murtonen T, Aakko-Saksa P, Kuronen M, Mikkonen S, Lehtoranta K. Emissions with heavy-duty diesel engines and vehicles using FAME, HVO and GTL fuels with and without DOC+POC aftertreatment. SAE Int J Fuels Lubr. 2010;2(2):147-166. https://doi.org/10.4271/2009-01-2693

[21] Parravicini M, Barro C, Boulouchos K. Experimental characterization of GTL, HVO, and OME based alternative fuels for diesel engines. Fuel. 2021;292:120177. https://doi.org/10.1016/j.fuel.2021.120177

[22] Permpool N, Gheewala SH. Environmental and energy assessment of alternative fuels for diesel in Thailand. J Clean Prod. 2017;142:1176-1182. https://doi.org/10.1016/j.jclepro.2016.08.081

[23] Pinto GM, da Costa RBR, de Souza TAZ, Rosa AJAC, Raats OO, Roque LFA et al. Experimental investigation of performance and emissions of a CI engine operating with HVO and farnesane in dual-fuel mode with natural gas and biogas. Energy. 2023;277:127648. https://doi.org/10.1016/j.energy.2023.127648

[24] Pinto GM, de Souza TAZ, da Costa RBR, Roque LFA, Frez GV, Coronado CJR. Combustion, performance and emission analyses of a CI engine operating with renewable diesel fuels (HVO/FARNESANE) under dual-fuel mode through hydrogen port injection. Int J Hydrogen Energy. 2023; 48(51):19713-19732. https://doi.org/10.1016/j.ijhydene.2023.02.020

[25] Prokopowicz A, Zaciera M, Sobczak A, Bielaczyc P, Woodburn J. The effects of neat biodiesel and biodiesel and HVO blends in diesel fuel on exhaust emissions from a light duty vehicle with a diesel engine. Environ Sci Technol. 2015;49:7473-7482. https://doi.org/10.1021/acs.est.5b00648

[26] Roque LFA, da Costa RBR, de Souza TAZ, Coronado CJR, Pinto GM, Cintra AJA et al. Experimental analysis and life cycle assessment of green diesel (HVO) in dual-fuel operation with bioethanol. J Clean Prod. 2023;389:135989. https://doi.org/10.1016/j.jclepro.2023.135989

[27] Shepel O, Matijošius J, Rimkus A, Orynycz O, Tucki K, Świć A. Combustion, ecological, and energetic indicators for mixtures of hydrotreated vegetable oil (HVO) with duck fat applied as fuel in a compression ignition engine. Energies. 2022;15:7892. https://doi.org/10.3390/en15217892

[28] Sikora M, Orliński P, Matej J. Hydro-treated vegetable oil as a potential biofuel for self-ignition engines. Transport Samochodowy. 2022;1:14-20. https://doi.org/10.5604/01.3001.0015.8709

[29] Soam S, Hillman K. Factors influencing the environmental sustainability and growth of hydrotreated vegetable oil (HVO) in Sweden. Bioresour Technol Reports. 2019;7: 100244. https://doi.org/10.1016/j.biteb.2019.100244

[30] Sonthalia A, Kumar N. Hydroprocessed vegetable oil as a fuel for transportation sector: a review. J Energy Inst. 2019; 92:1-17. https://doi.org/10.1016/j.joei.2017.10.008

[31] Stępień Z. Synthetic automotive fuels. Combustion Engines. 2023;192:78-90. https://doi.org/10.19206/CE-152526

[32] Suarez-Bertoa R, Kousoulidou M, Clairotte M, Giechaskiel B, Nuottimäki J, Sarjovaara T, Lonza L. Impact of HVO blends on modern diesel passenger cars emissions during real world operation. Fuel. 2019;235:1427-1435. https://doi.org/10.1016/j.fuel.2018.08.031

[33] Valeika G, Matijošius J, Górski K, Rimkus A, Smigins R. A study of energy and environmental parameters of a diesel engine running on hydrogenated vegetable oil (HVO) with addition of biobutanol and castor oil. Energies. 2021;14: 3939. https://doi.org/10.3390/en14133939

[34] Yang L, Franco V, Mock P, Kolke R, Zhang S, Wu Y et al. Experimental assessment of NO_x emissions from 73 Euro 6 diesel passenger cars. Environ Sci Technol. 2015;49:14409-14415. https://doi.org/10.1021/acs.est.5b04242

[35] Zeman P, Hönig V, Kotek M, Táborský J, Obergruber M, Mařík J et al. Hydrotreated vegetable oil as a fuel from waste materials. Catalysts. 2019;9. https://doi.org/10.3390/catal9040337

Mieczysław Sikora, MEng. – Faculty of Automotive and Construction Machinery Engineering, Warsaw University of Technology, Poland.
e-mail: *mieczyslaw.sikora@pw.edu.pl*

Prof. Piotr Orliński, DSc., DEng. – Faculty of Automotive and Construction Machinery Engineering, Warsaw University of Technology, Poland.
e-mail: *piotr.orlinski@pw.edu.pl*

Article citation info:
Jasiński R, Chruścielski G. Possibilities to modify the properties of the AW7075 aluminum alloy for the automotive industry. Combustion Engines. 2024;197(2):9-14. https://doi.org/10.19206/CE-170711

Robert JASIŃSKI
Grzegorz CHRUŚCIELSKI

Combustion Engines
Polish Scientific Society of Combustion Engines

Possibilities to modify the properties of the AW7075 aluminum alloy for the automotive industry

ARTICLE INFO

Received: 5 June 2023
Revised: 1 August 2023
Accepted: 5 August 2023
Available online: 11 January 2024

The paper investigated the AW7075 aluminum alloy that is used in the automotive industry. The alloy is widely used, among others, in the production of heads and engine blocks. The possibility of obtaining various properties of the alloy (material states) by appropriate heat treatment (saturation and aging) was demonstrated. The results of strength, hardness, abrasion, and fracture toughness tests of the alloy in the T73, RRA, and HTPP aging treatments, in comparison with the T651 reference state, are presented. The need to select the appropriate parameters of heat treatment in relation to the load conditions of the structural element, especially in elements with notches, was indicated. Depending on the state of the AW7075 alloy, the results prove the wide and diverse possibilities of its use and should be used consciously in the design and production processes of modern automotive drivetrain components.

Key words: *AW7075 aluminum, aging treatments, abrasion resistance, fracture toughness, cracking mechanism in the PSS*

1. Introduction

Present efforts to reduce emissions of internal combustion engines while at the same time increasing the efficiency of drive units have placed ever higher demands on the structural materials used in their production, which is of particular importance on a large-series scale and in the context of the selection of appropriate materials. It can be said that the producers of steel and aluminum-containing alloys strive for the widespread use of their materials for structural elements [22]. Apart from steel, aluminum alloys are a group of basic structural materials that, in light of the aforementioned current trends in the development of drive units, are once again gaining importance. They are used for the construction of engines and in the load-bearing components of motor vehicles, such as pistons [10], that require the use of materials with a low specific weight and a sufficiently high strength. Reducing the weight of vehicles is necessary to reduce fuel consumption and thus reduce the emission of toxic exhaust components [22].

Among the aluminum alloys, the following are most commonly used: 6061-T6, 2024-T5, and 7075-T6. Each has slightly different properties: 6061 is easy to weld and anodize and inexpensive, 2024 has greater strength and machinability, but the high copper content makes it difficult to anodize and weld. Compared to these two, 7075 has the highest strength (which, however, decreases at high temperatures) but is difficult to weld.

AW7075 aluminum alloy is used primarily in the basic T651 state, in turn ensuring maximum strength properties. This material is characterized by high strength, while at the same time maintaining good fracture toughness and corrosion resistance, despite the fact that maximum (static) strength is often achieved at the expense of both fracture toughness and stress corrosion cracking resistance [6]. Although this alloy has been used in the aerospace and automotive industries since the 1940s, work is still underway to modify its structure, mechanical properties, and resistance to intergranular corrosion through precise heat treatment [24]. Research is also conducted in the field of weldability and other methods of joining, which further expands the possibilities of using this alloy [6]. It has recently been shown that the course of metallurgical processes, including the times of soaking, solution treatment, and aging of the AW7075 alloy, affects the value of tensile strength, microstructure, and corrosion resistance. For T6-temper treatment in the pre-deformed condition, it has been proved that a short time of solution heat-treatment soaking causes a decrease of the elongation at fracture [18]. These properties are the most important with regard to the application of AW7075 in the automotive industry.

7075 aluminum is used in the production of motor vehicles for both covers and mechanism housings, as well as for heavily loaded mechanical and thermal applications: slide bearings caps, heads, connecting rods [1], and the blocks of internal combustion engines [2, 19], including engines used in motorsport [14]. Rose et al. [16] even developed a model using an aluminum composite with silicon carbide as a material for an automotive camshaft. Based on the numerical analysis, they obtained results showing that the Al-SiC composite camshafts have good strain and stress characteristics and can be a good alternative to chilled cast iron and carbon steel camshafts. Sachar et al. [21] demonstrated the suitability of aluminum alloys for the construction of cylinder block fins. The low self-weight of this material reduces the weight of the engine and increases its efficiency. Besides, it provides a better coefficient of heat removal from the engine than materials such as cast iron, copper, or magnesium.

At the same time, in the case of significant loads combined with the influence of friction, there are problems with AW7075 wear in the long term due to the load and strength of the surface layer [6]. There are also reports of fatigue damage to the tested material.

In addition, classic methods of surface finishing of engine structures, such as cylinder honing [8], require good machinability and abrasion of the material. All this makes operations modifying the AW7075 alloy, which will give it optimal properties for a given application, become very important.

The treatment that modifies the properties of the material is primarily heat treatment. For the AW7075 alloy, three aging treatments (states) other than T651 can be considered: T73 (Overaging treatment), RRA (Retrogression and Reaging), and HTPP (High-Temperature Pre-Precipitation). Each treatment is obtained by a slightly different method of solution treatment and aging (Table 1), which affects the degree of precipitate dispersion and the mechanical properties of the alloy, including fatigue strength [5, 9]. For example, it was found that the rate of fatigue cracking decreases with decreasing size of precipitates [4]. Trdan et al. [21] have also shown that the microstructure of aluminum alloys strongly affects the direction and propagation of a fatigue crack in welded joints.

However, the influence of temperature and aging time on the mechanical properties of the material is not unambiguous. Although aging at a lower temperature generally increases the effect of precipitation hardening, it turns out that for short aging times, this effect may be stronger if it takes place at higher temperatures (Fig. 1) [12, 15]. Therefore, experimental research is particularly valuable when optimizing the heat treatment process.

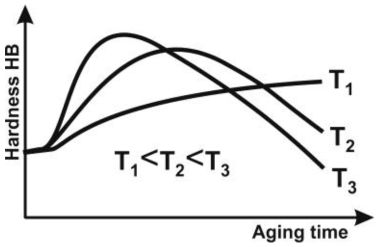

Fig. 1. The influence of temperature and aging time on the hardness of the Al-Cu alloy [12]

A large dispersion of precipitates increases the hardness, strength, and yield stress of aluminum alloys [15]. Such properties, on the one hand, have a positive effect on fatigue strength because the formation of permanent deformations in the structure is hindered (hence the use of surface work in fatigue working elements) [23]. On the other hand, however, they reduce the resistance to temporary cracking, which occurs with regard to the existing crack (notch) [7]. This paradox may be explained by the description of fracture mechanics presented in Fig. 2.

During cracking, the plastically deformed areas formed in the outer zones of the crack surface (the so-called shear lips) have the ability to stop the development of the crack, which is brittle in the inner zone. The extent of the slip lips is greater if the material is easier to be plasticized. As a result, elements made of high-strength materials have a lower fracture toughness (K_{IC} or δ_c) than those made of materials with higher plasticity (Fig. 3).

The graph shown in Fig. 3 shows another regularity: the fracture toughness decreases significantly with the increase of the thickness (B) of the fractured element. This effect must be taken into account in the design and selection of material for structural elements.

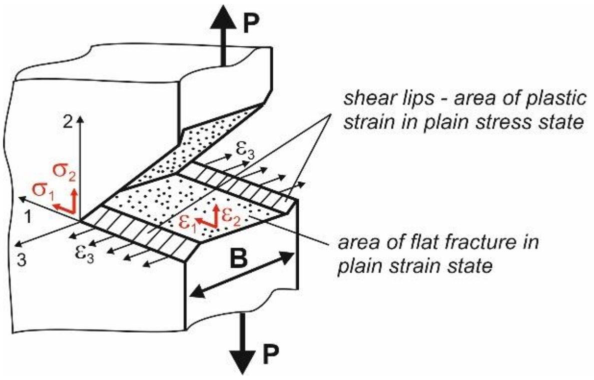

Fig. 2. Systems of strain and stress states on the fracture surface [23]

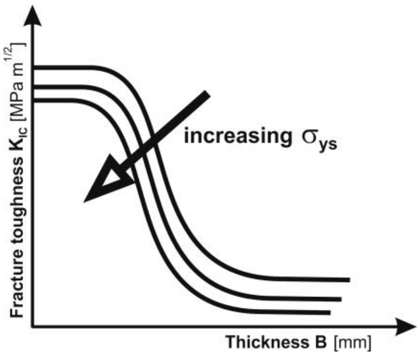

Fig. 3. The influence of yield stress on fracture toughness [15]

The presented theory was confirmed by the results of strength and the fracture toughness tests of various states of the AW 7075 material. In addition to them, hardness, microhardness, and abrasion resistance tests were also performed, which are also important in the selection of the optimal material for automotive constructions. The results of these studies are presented in the next chapter.

2. Materials and methods

The primary material for the tests was AW7075 in four states: T651, T73, RRA, and HTPP. The last three are modifications of the material properties in the basic T651 state and are most often applied in industry (Table 1) [11]. Strength tests (tensile tests), hardness tests (Brinell and Vickers methods), fracture toughness tests (CTOD tests), and abrasion wear resistance tests were carried out for the conditions mentioned above.

The static tensile tests at ambient temperature were performed on three samples from each state. Typical cylindrical, proportional test pieces were prepared with the diameter d=6 mm and the gauge length L_0 = 30 mm, which were tested in the rolling direction on an Instron 5982 testing machine with a force range of 100 kN.

The Brinell hardness test was carried out for all states on the samples intended for the CTOD test in accordance with the requirements of the standard [14] and used the ZwickRoell ZHU testing machine and a ball indenter with a diameter of 2.5 mm. The machine acted under the load of 187.5 kg applied for 15 seconds. Measurements were carried out in the central parts of the front surfaces of compact samples that did not undergo plastic deformation during the fracture toughness tests. The average values of three measurements were determined for each of the samples (macrohardness).

CTOD tests were carried out on compact samples with a thickness of B = 25 mm, which were loaded with tensile fatigue along the rolling direction (Fig. 4a) on an MTS 810 hydraulic pulsator with a range of 250 kN. The tests were conducted to ascertain the occurrence of scrap and to determine the critical value of crack opening δ_c in accordance with the requirements of the standard [20].

Microhardness was determined by the Vickers method using the Opti MMX-X7B hardness tester with a diamond indenter in the form of a square pyramid and a load of 300 g applied for 15 seconds. The measurements were carried out in the middle of the zones of occurrence of plastic deformations caused by fatigue load on the side surfaces (sections) of the samples and after the CTOD test. Mean values from three measurements were determined for each of the samples. The results obtained in this way (microhardness) were converted to the HBW scale in order to compare them with the results of hardness measurements (macrohardness).

The resistance to abrasive wear tests of the AW7075 aluminum during friction were performed on the T-07 tribotester in accordance with the requirements of GOST 23.208-79. The tests were performed under constant load conditions of F = 44 N, and alumina particles (grain size #90) as required by the standard "Bonded Abrasives (...)" (ISO 8486-2:2007) were used. The test method is described in detail in [3]. In accordance with the requirements of the standard for materials with a hardness below 400 HV, each test lasted 10 minutes, which corresponds to 600 abrasive cycles. Two samples for each of the considered AW7075 aluminum were tested. The samples had dimensions of 30×30×3 mm and were taken from the plane across the thickness of the compact samples intended for the CTOD test. Values of the abrasive wear resistance rates (K_b) were determined using the weight wear method, which involves determining the difference in the mass of the sample before and after the test of abrasion, according to the relationship:

$$K_b = \frac{Z_{ww}}{Z_{wb}}$$

where Z_{ww} – mass loss of the reference specimen [g] – the standard sample i.e. aluminum in the T651 state, Z_{wb} – mass loss of the test sample [g].

The mass loss on the actual friction path was also determined for all the samples subjected to abrasion. Sample weights were determined using Sartorius Extend laboratory scales with an accuracy of 0.0001 g.

3. Results

Table 1 summarizes the heat treatment conditions performed in order to obtain the four tested states of the AW7075 aluminum and also the results of the hardness determined in the tests.

Table 2 shows the basic strength parameters obtained in the tests. The values of $R_{p0.2}$, R_m, and δ_c for the AW7075 material in the T73, RRA, and HTPP aging treatments were referred to the properties in the T651 (reference) aging treatment. The results of the abrasion resistance and cracking resistance tests, according to the CTOD test, were also collected. They were compared, as in the case of the strength results, to the parameters of the material in the T651 aging treatment.

Table 1. Heat treatment processes applied to the AW7075 aluminum alloy and material hardness

Aging state	Applied heat treatment		Hardness	
	solution	aging	Macrohardness HBW (% value relative to T651)	Microhardness HBW (% value relative to T651)
T73	470°C, 1 h, cooling – cold water	120°C, 24 h, 160°C, 30 h	152 (90%)	169 (99%)
RRA	470°C, 1 h, cooling – cold water	120°C, 24 h, 203°C, 10 min, 130°C, 18 h	172 (102%)	180 (106%)
HTPP	470°C, 1 h, 445°C, 0.5 h, cooling – cold water	120°C, 24 h	171 (101%)	171 (101%)
T651	material as supplied: solution treated, stretch relieved and artificially aged		169 (100%)	170 (100%)

Table 2. Obtained results of the experimental tests: the strength test in relation to abrasion resistance and crack resistance according to the CTOD test

Aging state	Strength properties (along the rolling direction)		Abrasive wear resistance		Fracture toughness according to the CTOD test
	$R_{p0,2}$ [MPa] (% value relative to T651)	R_m [MPa] (% value relative to T651)	abrasion resistance coefficient K_b [–] (% value relative to T651)	weight loss due to friction [mg/m] (% value relative to T651)	δ_c [mm] (% value relative to T651)
T73	484 (89%)	543 (91%)	1.22 (122%)	1.13 (82%)	0.035 (219%)
RRA	441 (81%)	497 (83%)	1.08 (108%)	1.27 (92%)	0.047 (294%)
HTPP	508 (94%)	571 (95%)	1.00 (101%)	1.37 (99%)	0.023 (144%)
T651	542 (100%)	600 (100%)	1.00 (100%)	1.38 (100%)	0.016 (100%)

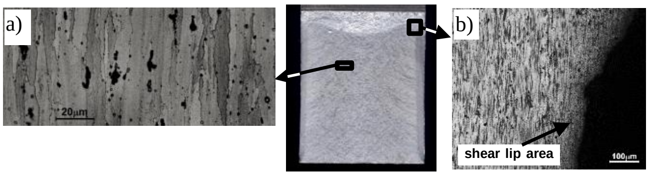

Fig. 4. Structure of the grain on the fracture surface of the AW7075-T7 compact specimen: in the middle of the flat fracture with the rolling direction indicated (a), the edge-side area with plastic strain on the shear lip (b)

4. Results analysis

The tested states of the AW7075 aluminum are characterized by very similar hardness values, with the exception of the T73 aging treatment, in which case the hardness decreased by 10% when compared to the delivery state (Table 1). However, the microhardness increases in the zone of plastic deformation and the strain hardening mechanism (noticeable in the case of RRA and HTPP aging treatments) – an increase of 11% and nearly 5%, respectively. This becomes particularly important in the case of the occurrence of material fatigue loads.

The results of the strength tests show a decrease in the value of the yield strength of each of the states of the material after heat treatment (T73, RRA, and HTPP) when compared to the T651 aging treatment (taken as the reference state). Such a modification of mechanical properties during cracking causes a greater extent of the plasticization zone in the slip lips that are formed on the edges of the crack surface. This is indicated by the greater microhardness of the material in these zones in the RRA and HTPP aging treatments (Table 2), and by the microscopic observation of the grain structure (Fig. 4b). Since the material in the slip lip zones has the ability to deform in the direction perpendicular to the direction of cracking (Fig. 2a, direction of axis 3), there is a triaxial strain state, and therefore also a plane stress state (PSN). The developing process of plastic deformation absorbs a significant part of the energy transferred to the structure by the work of external forces, which results in stopping the cracking process. This translates directly into higher fracture toughness results obtained in the CTOD tests: the best fracture toughness was shown by the material in the RRA aging treatment. It was lower for the T73 and HTPP aging treatments and the lowest in the T651 state (Table 2).

The inhibition of crack development in plastically deforming near-surface zones is also confirmed by macroscopic observations of the surface of the fatigue fractures of the compact samples, which can be seen in the photographs of the specimens (Fig. 5–6). Figure 5 shows successive stages of fatigue crack formation in the samples from the RRA, T73, and HTPP aging treatments' shear lip zone. Such an effect is clearly less visible in the T651 samples (Fig. 6).

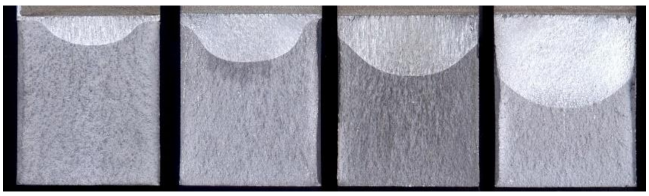

Fig. 5. Propagation of cracks in the AW-7075 material: cracks stopped by shear lips in the RRA, T73, and HTPP ageing treatment

Fig. 6. Flat cracking in the T651 treatment, where the influence of shear lips is much less visible

The determined parameters, which represent resistance to abrasive wear, clearly indicate a significant increase in wear resistance in friction conditions. This is especially the case in the T73 aging treatment, despite its reduced hardness, and also in the case of the RRA aging treatment (the value of the K_b coefficient increases by 22 and 8%, respectively, and the loss of weight by 18% and nearly 8% respectively, when compared to the generally applicable T651 aging treatment).

The obtained decrease in the yield strength and hardness values as a result of heat treatment, especially visible for the RRA state, proves the weakening of the precipitate strengthening mechanism in the AW7075 material. This is a result of the increase in the size of the second phase precipitates during annealing and aging of the material. Such precipitates, however, increase the cracking resistance of the material, stopping the development of fatigue cracking for some time [17], which can be seen in the SEM photograph shown in Fig. 7. This effect is caused by the lack of coherence between the structure of the matrix and the precipitate, as a result of which an additional strong field of internal compressive stresses is created in front of the crack tip, forcing the crack to change the propagation plane.

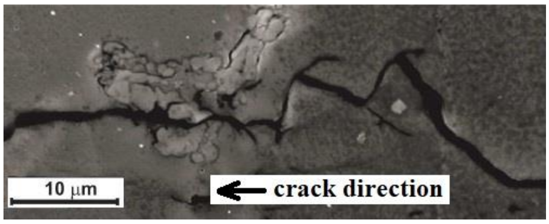

Fig. 7. Fatigue crack arrest mechanism by a second phase intermetallic precipitate in AW7075 material [17]

5. Conclusions

The results of the conducted research show that:

– the AW7075 alloy, which is a high-strength material, gains an improvement in crack resistance in notched structural elements through appropriate heat treatment, in turn resulting in greater ductility as a result of natural aging; this is indicated by the results of strength tests for the AW7075 material in the RRA and T73 aging treatments, which had the lowest yield strength $R_{p0,2}$ when compared to the reference T651 aging treatment, and the highest fracture toughness δ_c;
– the positive effect of material plasticization on fracture toughness seen in the tests applies to cases of cracking of elements with notches; a different relationship is obtained for fatigue strength, which increases with an increasing yield point of the material;

- as a result of the tests, it was found that the material in the T73 aging treatment has the best abrasion resistance;
- when using the AW7075 material for structural elements, the nature of the work and the range of loads should be taken into account. Moreover, the heat treatment (saturation and aging) should be controlled in order to obtain the desired strength properties, abrasion resistance, fatigue strength, and crack resistance.

It should be noted that the requirements for structural elements should not always prioritize maximum short-term strength, as high-strength materials have a limited and sometimes significantly lower fracture toughness. In applications where this parameter is crucial (mainly in elements with structural notches), a material with increased plastic properties should be selected at the expense of a slight reduction in strength parameters.

Detailed use of the results of this work belongs to the designers of structural elements. If they decide on the AW 7075 alloy, they should be aware that through appropriate heat treatment, the strength and resistance properties of this material can be modified to some extent. Each of the elements made of the AW 7075 alloy, examples of which are shown in Chapter 1, requires separate consideration in terms of strength requirements and hazards resulting from the presence of notches, temperature influence, dynamic loads, etc.

Continuation of the research may contribute to fuller use of the advantages of the AW7075 alloy, which is increasingly used in the automotive industry.

Nomenclature

PSS plane stress state
T73, RRA, T651, HTPP aging treatments
T73 overaging treatment
RRA retrogression and reaging
HTPP high-temperature pre-precipitation
T651 solution heat-treated, artificially aged, permanent set

Bibliography

[1] Ahmed S, Khany S, Shareef S. Design, fabrication and analysis of a connecting rod with aluminum alloys and carbon fiber. International Journal of Innovative Research in Science, Engineering and Technology. 2014;3(10):16674-16687. https://doi.org/10.15680/IJIRSET.2014.03100036

[2] Aneesh T, Pawan K, Mohan L, Krisna PH, Hotta TK, Mohantu CP et al. Exploring casting defects of AA7075 alloy in the gravity die casting simulation of an IC engine block. P I Mech Eng E-J Pro. 2022;236(4):1556-1565. https://doi.org/10.1177/09544089211073296

[3] Białobrzeska B, Kostencki P. Abrasive wear characteristics of selected low-alloy boron steels as measured in both field experiments and laboratory tests. Wear. 2015;328-329:149-159. https://doi.org/10.1016/j.wear.2015.02.003

[4] Broek D, Bowles CQ. The effect of cold deformation and ageing on fracture crack propagation and residual strength of 2024 sheet material. NLR-TR 69048 U; 1969.

[5] Chruścielski G, Korusiewicz L. The role of second phase intermetallic precipitates in fatigue fracture mechanism for aluminium alloy AW 7075. Key Eng Mat. 2013;592-593:809-812. https://doi.org/10.4028/www.scientific.net/KEM.592-593.809

[6] Czapczyk K. Research on the mechanical and tribological properties of the nanocomposite Ni-P/Si_3N_4 coating deposited by chemical reduction on the AW-7075 aluminum alloy used for machine parts. Doctoral dissertation. Poznań 2019.

[7] German J. Fundamentals of fracture mechanics. Publishing House of Cracow University of Technology. Cracow 2011.

[8] Gruszka J, Suchecki A. New methods of internal combustion engine cylinder surface forming. Combustion Engines. 2007;130(3):26-34. https://doi.org/10.19206/CE-117322

[9] Hahn CT, Simon R. A review of fatigue crack growth in high strength aluminium alloys and the revelant metallurgical factors. Eng Fract Mech. 1973;5(3):523-540. https://doi.org/10.1016/0013-7944(73)90038-6

[10] Iskra A, Babiak M, Kałużny J. The influence of applying a layer of carbon nanotubes on the piston bearing surface on friction losses, Combustion Engines. 2014;159(4):26-31. https://doi.org/10.19206/CE-116927

[11] Jin-Feng L, Zhuo-Wei P, Chao-Xing L, Zhi-Qiang J, Wen-Jing C, Zi-Qiao Z. Mechanical properties, corrosion behaviors and microstructures of 7075 aluminium alloy. T Nonferr Metal Soc. 2008;18:755-762. https://doi.org/10.1016/S1003-6326(08)60130-2

[12] Łatkowski A, Jarominek J. Metal science of non-ferrous metals. Publishing House AGH University of Krakow. Krakow 1994.

[13] Magnus Billet 6061/7075 VR38 Billet dry/wet engine block. Magnus Motorsports, Canada. https://www.magnusmotorsports.com/product/magnus-billet-6061-7075-vr38-billet-dry-wet-engine-block (accessed on 30.05.2023).

[14] Metals – Brinell hardness measurement, part 1: test method. Standard EN ISO 6506-1:2014-12. PKN; 2014.

[15] Przybyłowicz K. Metallography (in Polish). Wydawnictwa Naukowo-Techniczne. Warsaw 1996.

[16] Rose GJ, Venkatesan H, Arijit MK, Lindsay SRK, Premkumar TM, Development of automotive cam shaft using aluminium – silicon carbide composite – an effectiveness study. Mater Today-Proc. 2023;72:2108-2112. https://doi.org/10.1016/j.matpr.2022.08.220

[17] Sachar S, Parvez Y, Khurana T, Chaubey H. Heat transfer enhancement of the air-cooled engine fins through geometrical and material analysis: a review. Mater Today-Proc. 2023 (in press). https://doi.org/10.1016/j.matpr.2023.03.447

[18] Sajadifar S, Suckow T, Chandra K, Heider B, Heidazageh A, Zavasnik J at al. Assessment of the impact of process parameters on the final material properties in forming of AW 7075 employing a simulated forming process. J Manuf Process. 2023;86:336-353. https://doi.org/10.1016/j.jmapro.2022.12.056

[19] Siadkowska K, Czyż Z. Selecting a material for an aircraft diesel engine block. Combustion Engines. 2019;178(3):4-8. https://doi.org/10.19206/CE-2019-301

[20] Standard test method for crack-tip opening displacement (CTOD) fracture toughness measurement. Standard ASTM E1290-08 (E01). ASTM 2008.

[21] Trdan U, Klobcar D, Berthe L, Sturm R, Bergant Z. High-cycle fatigue enhancement of dissimilar 2017A-T451/7075-T651 Al alloy joint fabricated by a single pass FSW without

any post-processing. J Mater Res Technol. 2023;25:2333-2352. https://doi.org/10.1016/j.jmrt.2023.06.096
[22] Wieszała R. Characteristics of car structures made of aluminum alloys. Ores and non-ferrous metals recycling (in Polish). SIGMA-NOT Publishing House. 2014;59(10):497-501.
[23] Zakrzewski M, Zawadzki J. Strength of materials (in Polish). Państwowe Wydawnictwo Naukowe. Warsaw 1983.
[24] Zheng R. Mechanical properties of 7075 aluminium matrix composites reinforced by nanometric silicon carbide particulates. Master thesis. University of New South Wales Sydney 2007.

Grzegorz Chruścielski, DEng. – Department of Automotive Engineering, Wrocław University of Science and Technology, Poland.
e-mail: *grzegorz.chruscielski@pwr.edu.pl*

Robert Jasiński, DEng. – Department of Automotive Engineering, Wrocław University of Science and Technology, Poland.
e-mail: *robert.jasinski@pwr.edu.pl*

Article citation info:
Żmudka Z, Postrzednik S. Comparative analysis of theoretical cycles of independent valve control systems of the SI engine. Combustion Engines. 2024;197(2):15-21. https://doi.org/10.19206/CE-174321

Zbigniew ŻMUDKA
Stefan POSTRZEDNIK

Combustion Engines
Polish Scientific Society of Combustion Engines

Comparative analysis of theoretical cycles of independent valve control systems of the SI engine

ARTICLE INFO

Received: 26 May 2023
Revised: 22 September 2023
Accepted: 19 October 2023
Available online: 2 January 2024

The objects of the study were theoretical cycles of the load control systems and charge exchange process in the naturally aspirated SI engine, including classic, quantitative throttling control (Seiliger-Sabathe open cycle); a system with late inlet valve closing LIVC (the Atkinson-Miller open cycle); a system with early inlet valve closing EIVC; a system with early exhaust valve closing EEVC, enabling internal exhaust gas recirculation; system of fully independent valve control FIVC. The aim of using camless independent valve control algorithms is to eliminate the throttle as an control valve for load and filling control of the SI engine, while retaining quantitative load control. The research aims to select the camless valve control algorithm most beneficial in terms of energy (the highest effective efficiency) and economy (the lowest fuel consumption).

Key words: *spark ignition engine, thermodynamic cycle, charge exchange, energy efficiency, camless valve control*

1. Introduction – variable valve timing systems

In spark-ignition engines, quantitative load control is used by throttling the airflow reaching the engine. Currently, this is most often implemented by a throttle valve installed in the inlet system.

SI engines sometimes use unusual load control solutions that can regulate the engine load without using the throttle. At the turn of the 1950s and 1960s, the first patents were issued for solutions allowing to change the valve lift in internal combustion engines. The first mass-produced engine equipped with a system allowing the valve lift to be changed (or, more precisely, the disconnection of 2 of the 4 valves per cylinder at a speed 9500 rpm) was the REV (Revolution-Modulated Valve Control) system used in 1983 on the Honda CBR400RR motorcycle. In 1989, the REV system evolved into the VTEC (Variable Valve Timing and Lift Electronic Control) system, which allowed switching between two cam profiles on the camshaft. In 1992, Mitsubishi used a similar system called MIVEC (Mitsubishi Innovative Valve timing and lift Electronic Control system). At the turn of the century, more companies started to use variable valve timing (e.g. Nissan and Toyota) [6].

With advances in technology, the first solutions appeared to allow load regulation in SI engines by controlling the operation of the valve train, eliminating a throttle in the inlet system. The best known solutions are presented below.

In 2001, BMW introduced the Valvetronic system, which allows for step-less adjustment of lift and valve opening time. The solution used by BMW has an additional electromechanically operated lever between the camshaft and the rocker arm which allows adjustment of the inlet valve lift [1]. A very similar solution was used by Nissan (system VVAL – Variable Valve Event and Lift) and Toyota (Valvematic system) in 2007 [18]. A more advanced solution emerged in 2009. Fiat has developed an electro-hydraulic valve control system called MultiAir (UniAir). This solution eliminates one of the camshafts and the throttle. The inlet valves are electro-hydraulically operated and the exhaust valves are conventionally operated. This system allows the inlet valves to be opened and closed at any time and even opened several times during the suction stroke [2, 5, 7, 14]. Fiat for the first time on the Alfa Romeo MiTo has used engine with electro-hydraulic inlet valve control with "UniAir" ("Multiair") technology.

Advanced work is also being done on mechanisms where the opening and closing of valves is done by electromagnetic actuators [4, 9, 12, 17]. The latest solution is a system being developed by Freevalve AB. This technology, still in the prototype phase, eliminates camshafts and throttle valves using hydraulic and pneumatic actuators. [13].

Data presented in the literature [3, 15] demonstrate the potential for significant improvements in engine performance and fuel consumption reduction (by 20%) in the part-load range through the use of camless valve control systems. Maximum engine torque can increase by 10% and torque in the part-load range can increase by up to approximately 50%. Fuel savings in this engine operating range can be up to 20% [16].

Also noteworthy is the development of camless valve control systems for marine engines. At the beginning of the 21st century, MAN B&W launched two-stroke, low-speed, electronically controlled marine Diesel engines without a camshaft. They were marked as ME. The 7S50ME-C engine was the first ME engine. Its official presentation took place on 19.02.2003 in Denmark [10, 11].

The ME engine refers to the smart engine concept, using an electronic system to control a hydraulically driven exhaust valve, a hydraulically driven fuel injection system and an integrated engine control process. The energy to actuate both systems comes from the engine-driven hydraulic system that distributes oil at a pressure of 200 bar through a common line.

An important feature of the ME engines is the ability to optimise exhaust valve timing and fuel dosage. The main advantages of ME series engines with an electronic control system are as follows:

- liquidation of the camshaft and its drive as well as other mechanical components
- electronic control of exhaust valve opening time and fuel injection time, which leads to lower fuel consumption and better engine performance
- very low minimum engine speed, which has a decisive influence on the ship's maneuverability
- more favorable emission characteristics, lower NO_x emission and lower engine smoke at all loads.

In the development of Polish designs, the HCP D55 type engine is an example of a daring innovation solution. In the period 1961–1971, 17 engines of this type with a total of 123 cylinders were produced. [10, 11]. In the 1970s, based on this engine, the HCP plants also carried out construction and research work in the field of electronic control of marine diesel engines.

Reducing the charge exchange work, especially at partial loads, may be a design measure leading to an increase in the effective efficiency of the SI engine. This can be achieved by introducing modifications to the regulation and control systems of the charge exchange process, the essence of which is the use of independent valve control.

The objects of the study were theoretical cycles of the load control systems and charge exchange process realization of the SI engine, including:

1) classic, quantitative throttling control, using a throttle valve (Seiliger-Sabathe open cycle) [19, 21]
2) late inlet valve closing LIVC (the Atkinson-Miller open cycle) [19]
3) early inlet valve closing EIVC [19]
4) early exhaust valve closing EEVC, enabling internal EGR [20]
5) fully independent valve control FIVC that enables internal EGR and precise control of the fuel rate (general variant, which is a combination of variants 3 and 4, i.e. the systems EIVC and EEVC) [20].

In the analysis carried out, the classic control system (1) was the reference for all the other (2 to 5) studied systems for the charge exchange, using independent valve control.

This approach to the analysis was due, among other things, to the fact that the objective of independent valve control is elimination of the throttle as a load and fill control valve for the SI engine, while retaining quantitative load control. In the proposed independent valve control systems, the throttle's role in regulating the load and filling of the engine is covered by the valves controlling the entire load exchange process. The role of the intake valves is to match the amount of fresh charge delivered to the cylinder to the engine load. The task of the exhaust valves, on the other hand, is the controlled implementation of internal EGR. Eliminating the throttle through the use of independent valve control leads to a decrease in charge exchange work, an increase in the internal work of the engine and effective work, and consequently to an increase in the effective energy efficiency of the engine.

The aim of the research is an analytical study of systems of independent control of inlet and exhaust valve movement. Then, the selection of the camless valve control algorithm most beneficial in terms of energy (highest effective efficiency) and economy (lowest fuel consumption). Taking into account both aspects mentioned above, the most advantageous is the algorithm for variant 1 of the FIVC system, which has been evidenced in the following chapters.

2. Theoretical cycles of independent valve control systems – basic characteristics

2.1. System with late inlet valve closing LIVC

The theoretical Atkinson-Miller open cycle presented in Fig. 1 provides a model for the LIVC system [19].

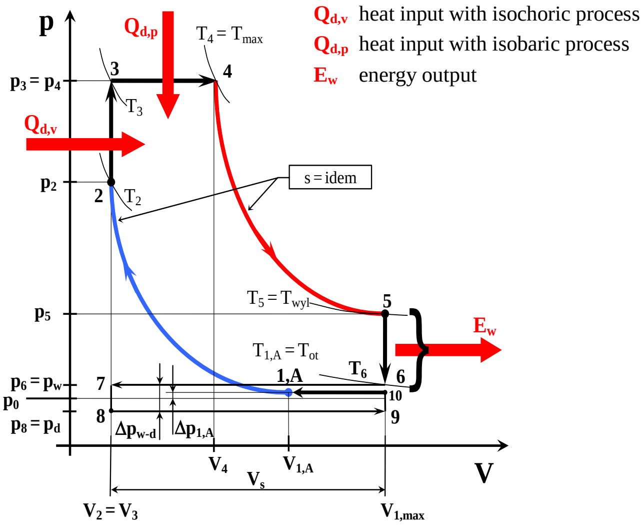

Fig. 1. System with late inlet valve closing – the open, theoretical Atkinson-Miller cycle [19]

The inlet valve closes at the volume $V_{1,A}$ and this is a load regulation parameter. This parameter can also be expressed in a relative (dimensionless) way as:

$$\varepsilon_A = \frac{V_{1,A}}{V_2}, \qquad 1 < \varepsilon_A \le \varepsilon \tag{1}$$

which can be called the isentropic compression ratio.

2.2. System with early inlet valve closing EIVC

The theoretical cycle for the EIVC system is that shown in Fig. 2 [19].

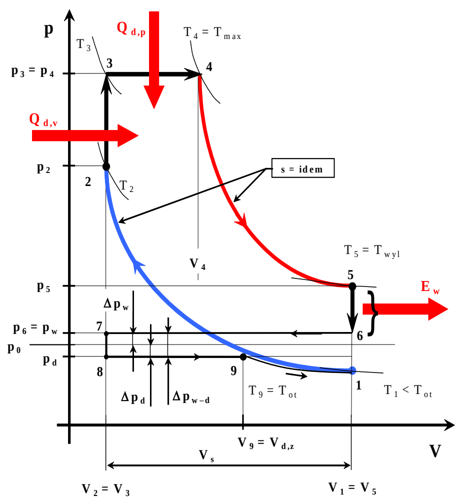

Fig. 2. The open, theoretical cycle of the system with early inlet valve closing [19]

In this case, the volume V_9 ($V_{d,z}$) of the cylinder (the moment of closing the intake valve) is a load control parameter. This parameter ε_d can also be expressed in dimensionless terms as defined by:

$$\varepsilon_d = \frac{V_{d,z}}{V_2}, \qquad 1 < \varepsilon_d \le \varepsilon \tag{2}$$

It should be mentioned here, that he expansion of gases from point "9" to point "1" leads to a lowering of temperature and as a result, to a higher specific volume of the charge.

2.3. System with early exhaust valve closing EEVC

The theoretical cycle SI engine for the EEVC is shown in Fig. 3 [20]. The load (filling) control parameter is the volume $V_{w,z}$ (V_7) of the cylinder at which the exhaust valve closes. At the same time, it is a parameter that regulates the mass of the recirculated exhaust gas m_{sr} and thus the value of the EGR rate α_r. The volume $V_{w,z}$ can be related to the minimum volume V_2 of the cylinder, thus defining the compression ratio $\varepsilon_{w,z}$ of the recirculated exhaust gas:

$$\varepsilon_{w,z} = \frac{V_{w,z}}{V_2}, \qquad 1 \le \varepsilon_{w,z} < \varepsilon \tag{3}$$

The expansion rate of the recirculated exhaust gas is also defined:

$$\varepsilon_{d,o} = \frac{V_{d,o}}{V_2} \tag{4}$$

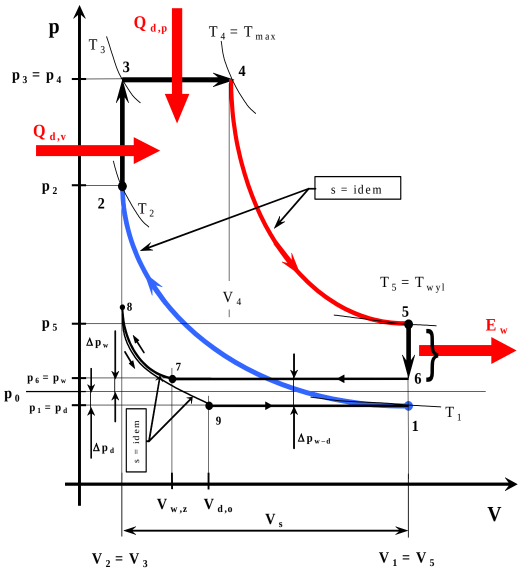

Fig. 3. Open, theoretical cycle of the system EEVC [20]

The relation between the expansion ratio $\varepsilon_{d,o}$ and compression ratio $\varepsilon_{w,z}$ of the recirculated exhaust gas is expressed by the formula:

$$\varepsilon_{d,o} = \varepsilon_{w,z}\left(\frac{p_0 + \Delta p_w}{p_0 - \Delta p_d}\right)^{\frac{1}{\kappa}} \tag{5}$$

where: p_0 – ambient pressure, Δp_d – pressure drop in inlet system, Δp_w – pressure drop in exhaust system.

It is noteworthy that the system under consideration enables, among other things, the realization of internal EGR. The EGR rate α_r is defined as:

$$\alpha_r = \frac{m_{sr}}{m_1}, \qquad 0 \le \alpha_r < 1 \tag{6}$$

where: m_{sr} – mass of a recirculated exhaust gas, m_1 – total mass of a charge.

In addition, multiplicity of the exhaust gas recirculation α_k is defined as:

$$\alpha_k = \frac{m_{sr}}{m_m}, \qquad \alpha_k > 0 \tag{7}$$

where: m_m – mass of the fresh charge.

2.4. System of fully independent valve control FIVC

The fully independent valve control system is an algorithm that combines the procedures for independent control of the inlet and exhaust valves. FIVC is achieved by combining the EIVC system [19] with the EEVC system [20]. The theoretical cycle for FIVC is presented in Fig. 4. [20].

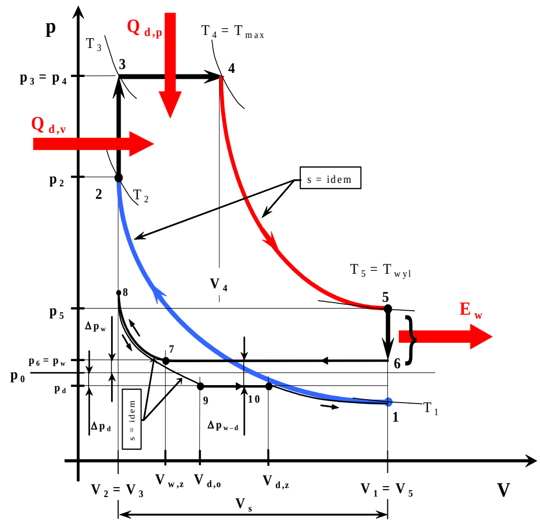

Fig. 4. Open, theoretical cycle for the system of fully independent valve control [20]

The FIVC system is implemented using two control parameters:

– $\varepsilon_{d,z}$ (2) relative cylinder volume when the intake valve is fully closed
– $\varepsilon_{w,z}$ (4) compression ratio of the recirculated exhaust gas.

3. Comparative analysis of the effectiveness of using the tested independent valve control systems

As part of the joint consideration of the studied control procedures for the internal combustion engine valves, a comparative analysis of the effectiveness of the use of the proposed systems was carried out based on the following quantities:

– load control parameters
– dose of fuel m_p
– total energy Q_d supplied to the cycle
– work of the cycle W_o

– charge exchange work W_w and relative charge exchange work μ
– theoretical open cycle efficiency η_o
– parameters of the internal EGR: α_r – recirculation rate and α_k – recirculation multiplicity (for EEVC and FIVC).

The analysis carried out assumes an excess air ratio (λ) of 1 for all systems tested, over the entire load range, including part loads, as the test object is a spark-ignition engine.

The course of the above-mentioned parameters, separately for each of the tested systems, has been presented in previous publications: LIVC in [19], EIVC in [19], EEVC in [20], FIVC in [20]. In this publication, to evaluate the effectiveness and benefits of the proposed independent valve control systems, a comparative analysis of the selected, listed above, key parameters has been carried out. In the conducted analysis, the classic throttling load control (Seiliger-Sabathe open cycle) was the reference for all other tested systems.

The values of control parameters for the tested systems, depending on the work of the cycles are compared in Fig. 5. In this figure and all others, the work of the cycles W_o is related to the maximum work $W_{o,max}$ of the theoretical Seiliger-Sabathe cycle. This approach allows to compare the tested systems with each other, and thus to assess the effectiveness and benefits of their use.

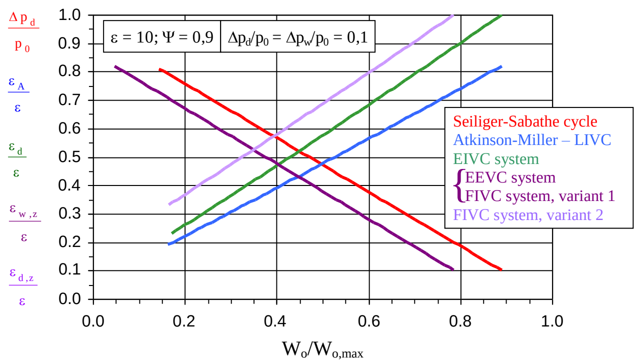

Fig. 5. Comparison of the control parameters for the analysed independent valve control systems versus work of the cycles

From the list of control parameters (Fig. 5), it can be seen that specified values of cycle work can be achieved by implementing each of the systems. This situation is observed in a wide load range. It should be emphasised that the dependence of the control parameters on circuit operation is linear for all systems, which is beneficial for regulatory reasons.

Figure 6 shows a comparison of the relative reduction of fuel doses $\Delta m_p/m_{p,SS}$ for the tested systems, in relation to the system with classic throttling control (Seiliger-Sabathe cycle).

Using each of the tested systems of independent valve control, a decrease in the fuel dose is observed in the entire range of the cycle work. Fuel consumption reduction is particularly significant in the low load range and amounts up to 4% for the EIVC system, up to 8% for variant 2 and up to 19% for variant 1 of the FIVC system. A fuel dose saving of 19% is achieved for a relative work of the cycle $W_o/W_{o,max}$ of approximately 0.18. Achieving such a reduction in fuel consumption in variant 1 may therefore not be possible due to too high value of the recirculation rate ($\alpha_r = 0.35$) at this cycle work. However, a reduction in fuel consumption in the order of 15% is realistic, as it is achieved with recirculation rates that are acceptable in operation [20].

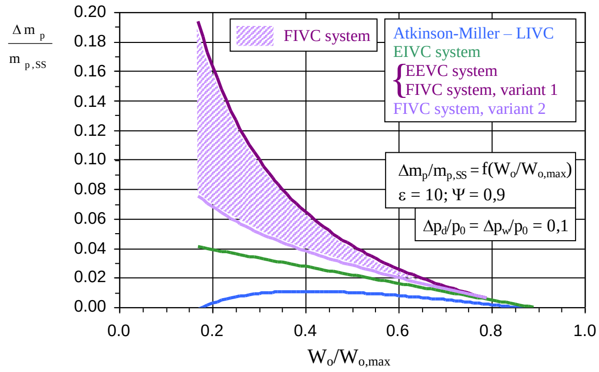

Fig. 6. Comparison of the relative reduction of the fuel doses $\Delta m_p/m_{p,SS}$ for the analysed independent valve control systems compared with the classic throttle governing system, versus work of the cycles

The observed benefits in terms of fuel consumption reduction result primarily from the fact that the charge exchange work is reduced. The charge exchange work $W_w/(p_0V_1)$ (in dimensionless terms) for the tested systems of independent valve control, depending on the achieved work of the cycles is compared in Fig. 7. Figure 8, on the other hand, shows a comparison of the index μ of relative charge exchange work, which is defined as:

$$\mu = \frac{|W_w|}{W_o} \tag{8}$$

where: W_w – charge exchange work, W_o – cycle work.

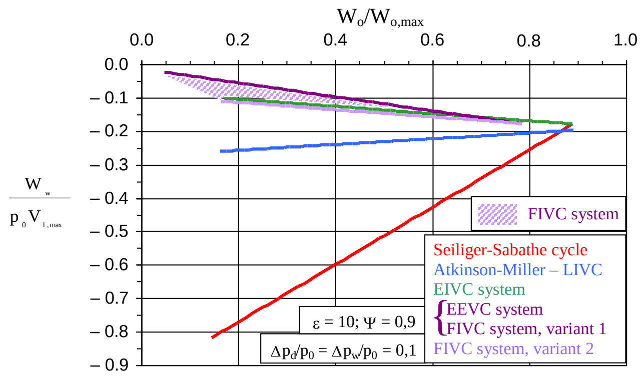

Fig. 7. Comparison of the charge exchange works $W_w/(p_0V_1)$ for the analysed independent valve control systems versus work of cycles

The works W_w of the charge exchange, as to the absolute value, for all systems of independent valve control is much smaller than the work of the charge exchange for the classic throttling control. The differences in works of charge exchange in favor of independent valve control systems are the greater, the lower the load (Fig. 7). The reduction in charge exchange work in systems of the independent valve control is primarily due to the elimination of the throttle as a load control valve for the SI engine, while retaining quantitative load control.

An advantageous feature of the EIVC, EEVC and FIVC systems is that the absolute value of the charge exchange work reduces as the value of the cycle work decreases (Fig. 7). The reverse, unfavorable situation is observed for the classical throttling control and the LIVC system, in which the absolute value of the charge exchange work increases with the decrease of the load. This increase is particularly large for the open S-S theoretical cycle and is the effect of closing the throttle, and thus increasing the resistance to the flow of fresh charge in the inlet system.

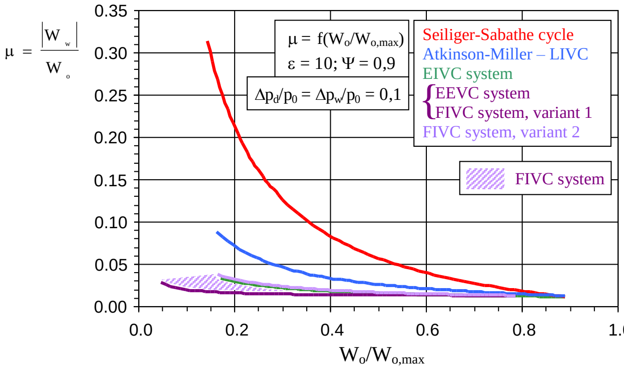

Fig. 8. Comparison of the relative charge exchange works μ for the analysed independent valve control systems versus work of the cycles

For all the tested systems of independent valve control, the relation of charge exchange work W_w to the cycle work W_o is also favorable, compared to this relation for the classical system. The parameter characterising this relationship is the index μ of the relative work of charge exchange. For the classic throttling control of load, the index μ reaches very high values, even over 30% in the range of small loads (Fig. 8.). For all variants of independent valve control, the index μ is below 10%, in the whole range of cycles work. The system of fully independent valve control, also in this case, proved to be the most beneficial, as the index μ is below 4%. Such low values for the relative work of charge exchange are precisely the result of eliminating the throttle valve from the inlet system.

From an energy point of view, the key parameter of the cycle is its efficiency, defined as follows:

$$\eta_o = \frac{W_o}{Q_d} \tag{9}$$

where: W_o – cycle work, Q_d – total energy fed into a cycle.

The efficiency η_o of the cycles for the studied charge exchange systems, depending on the cycle work achieved, is compared in Fig. 9.

The cycle efficiencies η_o of all investigated independent valve control systems are higher than the theoretical Seiliger-Sabathe cycle efficiency. The highest efficiencies are achieved by the cycle for variant 1 full independent valve control. In the low load range, the cycle efficiency η_o of variant 1 of the FIVC system is approximately 0.13 higher than the efficiency of the cycle for classic throttle control (Fig. 9). For this variant 1, a flat course of the cycle efficiency η_o is characteristic and advantageous, in the entire range of the achieved cycle work. Thus, this variant is the most suitable for controlling the load of the SI engine.

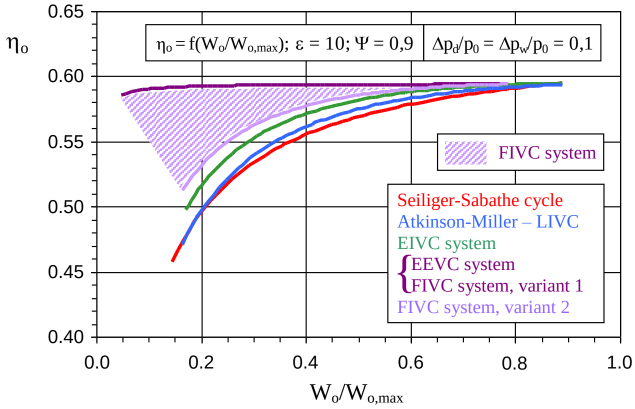

Fig. 9. Comparison of efficiencies η_o of the cycles for the analysed independent valve control systems, versus work of the cycles

4. Conclusion

Four independent valve control systems for the SI engine, presented in Chapter 3, were analysed. The reference for the evaluation of the efficiency of work acquisition, as a result of the use of independent valve control systems, is the S-S theoretical cycle, which is a model of the processes occurring in an SI engine with classic load control using a throttle.

For each system tested (except the LIVC cycle), a decrease in fuel consumption (fuel dose) is observed, with a particularly large decrease in the low load range (Fig. 6). It has been shown that the greatest (up to 15%) fuel consumption savings can be achieved using variant 1 of the FIVC system. Experimental studies of engines equipped with electromagnetic valve control systems, presented in publications, show fuel consumption savings from 7% to 19% [3, 4, 9, 12].

The charge exchange work for all proposed systems is considerably lower, especially for partial loads, than the charge exchange work for classic throttle control. For variant 1 of the FIVC system, at the smallest loads ($W_o/W_{o.max} < 0.2$), the charge exchange work is over 8 times lower than the charge exchange work for the S-S theoretical cycle. The nature of changes in the work of charge exchange is also particularly advantageous (except for the LIVC), as it, in terms of the absolute value, decreases with the decrease in the work of the cycle. The result of this desirable situation is a significant reduction in the relative work of charge exchange. For the FIVC and EEVC systems, the value of the index of the relative charge exchange work is less than 4% over the entire engine operating field. The above-mentioned beneficial effects of independent valve control systems can be best expressed by the energy efficiency of the cycles. The highest energy efficiency is achieved by the fully independent valve control system. Therefore, this variant is the most advantageous in terms of engine load regulation.

It should be emphasised that in FIVC and EEVC systems, the maximum temperature during combustion is lowered by internal EGR, with a consequent reduction in nitrogen oxide emissions. However, the main benefits investigated are related to the reduction in charge exchange work as a result of the elimination of the throttle.

Acknowledgments

This research is supported by the Ministry of Education and Science (Poland) under statutory research funds of the Faculty of Energy and Environmental Engineering of the Silesian University of Technology.

Nomenclature

EEVC	early exhaust valve closing
EIVC	early inlet valve closing
E_w	energy output
FIVC	fully independent valve control
LIVC	late inlet valve closing
m	mass
m_p	fuel dose
MIVEC	Mitsubishi innovative valve timing and lift electronic control system
p	pressure
p_d	pressure in an inlet system,
p_w	pressure in the exhaust system
Q	heat
$Q_{d,p}$	heat input with isobaric process
$Q_{d,v}$	heat input with isochoric process
REV	revolution-modulated valve control
s	entropy
SI	spark ignition
V	volume
V_s	cylinder displacement
VTEC	variable valve timing & lift electronic control
VVAL	variable valve event and lift
W	work
W_o	cycle work
W_w	charge exchange work
α_k	multiplicity of exhaust gas recirculation
α_r	exhaust gas recirculation rate
ε	compression ratio
ε_A	isentropic compression ratio for LIVC
ε_d	load control parameter for EIVC
$\varepsilon_{d,o}$	expansion rate of a recirculated exhaust gas
$\varepsilon_{w,z}$	compression ratio of a recirculated exhaust gas
η_o	cycle energy efficiency
μ	relative charge exchange work
Ψ	heat distribution number

Bibliography

[1] Benedikt K, Drexler G, Eder T, Eisenkoeldl M, Luttermann C, Schleusener M. Further development of BMW's fully-variable valve control system valvetronic. MTZ Worldw. 2005;66:10-13. https://doi.org/10.1007/BF03227780

[2] Bernard L, Ferrari A, Micelli D, Perotto A, Rinolfi R, Vattaneo F. Electro-hydraulic valve control with MultiAir technology. MTZ Worldw. 2009;70:4-10. https://doi.org/10.1007/BF03226988

[3] Chang SC. Stability analysis, routes to chaos, and quenching chaos in electromechanical valve actuators. Math Comput Simul. 2020;177:140-151. https://doi.org/10.1016/j.matcom.2020.04.021

[4] Dimitrova D, Tari M, Lanusse P, Aioun F, Moreau X. Robust control for an electromagnetic actuator for a camless engine. Mechatronics. 2019;57:109-128. https://doi.org/10.1016/j.mechatronics.2018.12.004

[5] Flierl R, Gollasch D, Knecht A. Hannibal W. Improvements to a four-cylinder gasoline engine through the fully variable valve lift and timing system UniValve. SAE Technical Paper 2006-01-0223. 2006. https://doi.org/10.4271/2006-01-0223

[6] Fujita T, Onogawa K, Kiga S, Mae Y, Akasaka Y, Tomogane K. Development of innovative variable valve event and lift (VVEL) system. SAE Technical Paper 2008-01-1349. 2008. https://doi.org/10.4271/2008-01-1349

[7] Haas M. UniAir – the first fully variable, electrohydraulic valve control system. 9th Schaeffler Symposium Book. 2010.

[8] Haas M, Rauch M. Electrohydraulic fully variable valve train system. MTZ Worldw. 2010;71:16-21. https://doi.org/10.1007/BF03227946

[9] Jiayu L, Chang S. Precise motion control of an electromagnetic valve actuator with adaptive robust compensation of combustion force. J Frankl Inst. 2019;356(4). https://doi.org/10.1016/j.jfranklin.2018.12.010

[10] Kopczyński M, Mańczak J, Przewoźny W. Evolution of two-stroke marine diesel engines design in H. Cegielski-Poznan S.A. production. Combustion Engines. 2006;126(3): 3-37. https://doi.org/10.19206/CE-117341

[11] Mańczak J, Łukomski A. Silniki okrętowe z Cegielskiego. Projektowanie i Konstrukcje Inżynierskie (in Polish). 2019; 7-8:26-31. https://www.simp-poznan.pl/file/page/141/silniki-okretowezcegielskiego5e20906b1415c853307205-5f70eef7363ce8.29991226.pdf

[12] Mianzo L, Newton S, Popovic Z. Integrated control and power electronics for an electromechanical valve actuation system. Proceedings of the IEEE/ASME. 2005:485-491. https://doi.org/10.1109/AIM.2005.1511029

[13] Möller AA. Implementing a Freevalve valve train in an automotive application. 8. VDI-Fachtagung "Ventiltrieb und Zylinderkopf 2019 – im Kontext von Euro VII und E-Mobilität". https://www.freevalve.com/insights/cam-less-valve-train-opportunities/

[14] Racewicz S, Olejnik A. Control of Fiat Multiair valve-lift system using ATmega microcontroller. Journal of KONES Powertrain and Transport. 2017;24(3):229-236. https://doi.org/10.5604/01.3001.0010.3083

[15] Reinholz BA, Reinholz L, Seethaler RJ. Optimal trajectory operation of a cogging torque assisted motor driven valve actuator for internal combustion engines. Mechatronics. 2018;51:1-7. https://doi.org/10.1016/j.mechatronics.2018.02.011

[16] Siczek KJ. Future valve train systems. Chapter 10. Tribological Processes in the Valve Train Systems with Lightweight Valves. New Research and Modelling. 2016:205-219. https://doi.org/10.1016/B978-0-08-100956-7.00020-5

[17] Yang X, Liang K. Measurement and modelling of a linear electromagnetic actuator driven camless valve train for spark ignition IC engines under full load condition. Mechatronics. 2021;77:102604. https://doi.org/10.1016/j.mechatronics.2021.102604

[18] Zheng L, Zhu G. Review of advancement in variable valve actuation of internal combustion engines. Appl Sci. 2020; 10(4):1216. https://doi.org/10.3390/app10041216

[19] Żmudka Z, Postrzednik S, Przybyła G. Throttleless control of SI engine load by fully flexible inlet valve actuation system. Combustion Engines. 2016;164(1):44-48. https://doi.org/10.19206/CE-116488

[20] Żmudka Z, Postrzednik S. Improving the effective efficiency of a spark ignition engine through the use of a fully independent valve control system. Combustion Engines. 2021; 187(4):30-35. https://doi.org/10.19206/CE-141541

Prof. Zbigniew Żmudka, DSc., DEng. – Faculty of Energy and Environmental Engineering, Silesian University of Technology, Poland.

e-mail: *zbigniew.zmudka@polsl.pl*

Prof. Stefan Postrzednik, DSc., DEng. – Faculty of Energy and Environmental Engineering, Silesian University of Technology, Poland.

e-mail: *stefan.postrzednik@polsl.pl*

Article citation info:
Chojnowski J. Analysis of the influence of substitute fuels on properties operating conditions of military hybrid drive system. Combustion Engines.2024;197(2):22-31. https:/doi.org/10.19206/CE-174553

Janusz CHOJNOWSKI

Combustion Engines
Polish Scientific Society of Combustion Engines

Analysis of the influence of substitute fuels on properties operating conditions of military hybrid drive systems

ARTICLE INFO

Received: 12 May 2023
Revised: 24 October 2023
Accepted: 26 October 2023
Available online: 10 January 2024

Despite the undoubted advantages of electric drives, the mass and volume energy density of chemical batteries makes it difficult to rely solely on cheap and green electricity in many applications such as airplanes, long-distance trains, ocean-going vessels and heavy equipment. The answer combining the advantages of EV and ICE are hybrid drives. Hybrid electric drives have also found their use in military applications thanks to, among others, the quiet operation of the system in EV mode, which may be a key advantage in some combat applications, e.g. urban areas. The range of a small hybrid vehicle extended by the use of ICE increases its operational capabilities. Hybrid systems can also use alternative hydrocarbon fuels. The aim of the work was to determine the impact of alternative fuels, potentially the most available on the modern battlefield, on the performance of the hybrid drive system of a wheeled military platform intended for operation in urban areas. The experiment showed that alternative fuels such as F-34 and Jet A-1 are compatible, but may result in increased fuel consumption, reduced energy efficiency and negative environmental impact due to higher exhaust emissions.

Key words: *hybrid drive, alternative fuels, F34, Jet A-1, military vehicle propulsion*

1. Introduction

The modern development of hybrid drive systems takes into account the need to combine conflicting requirements. On the one hand, ecological and economical requirements are growing. On the other hand, these systems are required to achieve maximum work units, long range and lightweight construction [23]. The continuous development of hybrid systems increases the complexity of their construction [16]. The internal combustion engines themselves also use very precise power and control systems to increase thermal efficiency [20]. Precision fuel systems are very sensitive to changes in fuel parameters or contamination. Modern multi-element hybrid systems, in which various forms of energy are transformed several times, are therefore very susceptible to the influence of fuel on the quality of their work [6, 9]. In connection with the above, checking the impact of the use of alternative fuels in the hybrid (electric-combustion) drive system on the operational properties of the vehicle seems to be a necessary path to check [4]. In the context of military vehicles, this task is additionally noteworthy due to the possibilities of using fuels available on the battlefield. All the possibilities of the so-called flex fuel are welcome in military applications, and the ability to use different types of fuel on the battlefield can be worth as much as a human life [13]. The article analyzes the impact of the use of 3 types of fuels that may be available during warfare in compression-ignition engines that are the "combustion part" of the hybrid propulsion system in the Light Unmanned Military Wheeled Platform (LUMWP) constructed at Military University of Technology in Warsaw as shown on Fig. 1.

The LUMWP is equipped with a series hybrid powertrain system. Figure 2 below presents a schematic diagram of a series hybrid electric-combustion drive.

Fig. 1. An isometric view of Light Unmanned Military Wheeled Platform

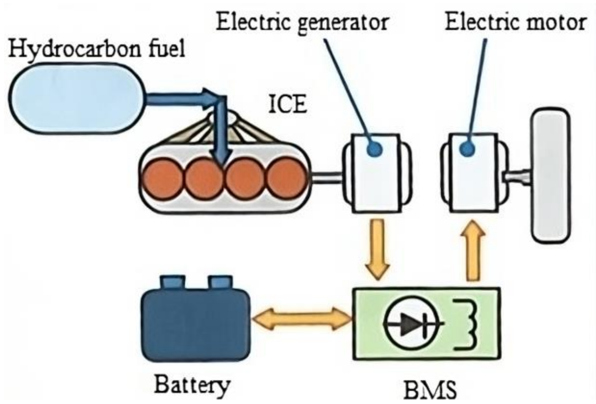

Fig. 2. Diagram of a series hybrid electric-combustion drive (based on 9)

The vehicle has electric motors built into drive modules with reducers powered by a battery charged by an electric current generator. Thus, the most important properties of electric motors are used (maximum torque at low speed, quiet operation, and the possibility of overloading), as well as the extended range of the vehicle, thanks to the possibility of recharging the battery with a combustion generator. In addition, the electric motor can work as a generator during braking, which allows for energy recovery and lower fuel consumption [16, 21]. The system with electric motors directly driving the wheels of the vehicle does not require mechanical power transmission systems (gearboxes and shafts), which allows for the reduction of the weight and size of such drive systems. Figure 3 shows a block diagram of the vehicle drive system.

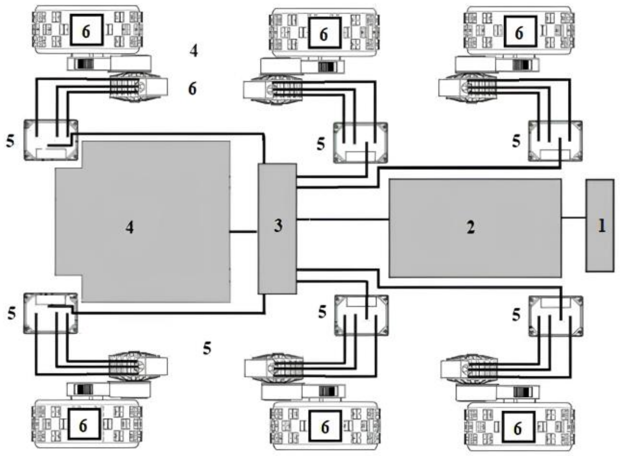

Fig. 3. Diagram of the LUMWP drive system: 1) control system, 2) electric current ICE generator, 3) distribution box, 4) battery, 5) inverters, 6) electric motors with gears and wheels [author's source]

In the further part of the article, the fuels selected for comparison, technical details of the tested propulsion system, research methods, results, and a summary with conclusions will be discussed.

2. Materials and methods

2.1. Fuels selected for comparison

The fuels selected for comparison are the crude oil fraction boiling during the refining process at a temperature of 180–350°C [19]. These are fuels widely available on any potential battlefield. F34 is a universal general-purpose fuel in NATO structures [18]. Jet A-1 is the most popular aviation fuel in the world [12]. Diesel fuel is the most popular hydrocarbon fuel in the world (dedicated to the discussed engine) [10]. Each of the fuels came from one batch and had normative parameters (important for the operation of diesel engines), which are listed in Table 1.

In general, each type of fuel has its own unique properties and is suitable for specific applications [10]. The choice of fuel depends on factors such as engine type, mode of transport, and desired performance. Analysis of the parameters of the above fuels shows a great similarity between Jet A-1 and F-34 this is also indicated in the literature [6, 10]. Replacing a compression ignition (CI) engine with diesel fuel, one should take into account the occurrence of the following problems:

– lower density, viscosity, and calorific value in relation to diesel fuel may reduce the value of the maximum useful parameters of the engine [6, 10]
– a lower cetane number may impair cold starting and increase the tendency to hard work [10, 19].

The criterion for selecting these specific fuels for testing was their potential availability in combat conditions.

Table 1. Selected normative parameters of diesel, F-34, Jet A-1 (source: fuels datasheet, [7])

	Fuel type		
Parameter	Diesel Fuel	F-34	Jet A-1
Density in 15ºC [kg/m^3]	831	804	796
Cetane number	50	45	42
Temp. ignition [ºC]	66	57	38
Viscosity at –20 ºC [mm^2/s]	2.210	3.102	3.815
Calorific value [MJ/kg]	43	42.35	42.28
CFPP [ºC]	–27	–54	–

2.2. The tested hybrid drive system

As mentioned in paragraph 1, LUMWP has a hybrid series combustion and electric drive system. Figures 4 and 5 show the actual location of the ICE and the generator on the vehicle.

Fig. 4. LUMWP without upper body and battery removed, isometric view

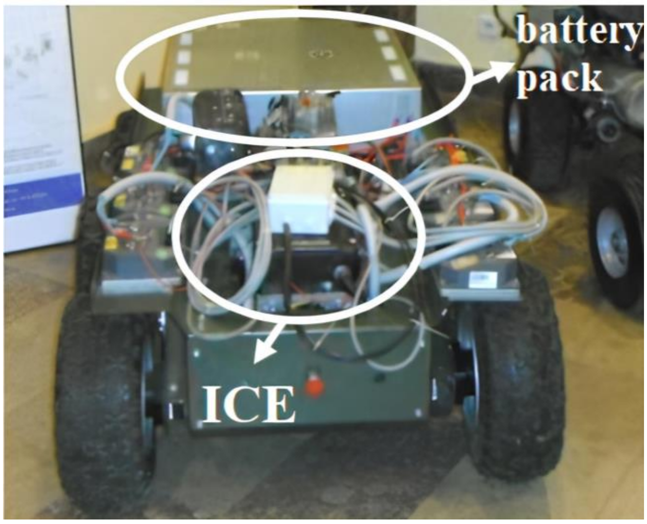

Fig. 5. LUMWP without upper body, front view

The tested hybrid drive system consists of a generating set: Yanmar L100AE diesel engine (technical information of the CI engine is shown in Table 2 below) and E1S10L KE synchronous generator (technical information of the generator is shown in Table 3 below), and a lithium-polymer electrochemical battery (technical information battery is shown in Table 3).

Table 2. Selected technical data of the Yanmar L100AE engine [source: user manual, 22]

Engine type	Yanmar L100AE
Construction	CI, air-cooled, single-cylinder
Power type	Direct injection, piston pump, mechanical injection
Stroke capacity	406 cm³
Bore x stroke	86×75 mm
Maximum power for the base fuel	6.5 kW
Crankshaft operating speed	~3000 rpm

The Yanmar L100AE engine was combined to work with a synchronous generator, the technical data of which are presented in Table 3 below.

Table 3. Technical data of the E1S10L KE generator (source: user manual, [22])

Generator type	E1S10L KE
Construction	Self-excited, synchronous
The type of electricity produced	AC, three-phase 50 Hz
Rated voltage	400 V
Rated power	7.0 kVA
Insulation class	H

The task of the generator is to charge the lithium-polymer $LiFePO_4$ battery. It consists of a stack of twelve lithium-polymer cells connected in series. Inside the battery housing is a compartment for electrical connectors, a rectifier unit, and a BMS (Battery Management System) which supervises the proper operation of all cells during battery charging and discharging [15]. This system prevents the battery from discharging to a level that could lead to irreversible damage, as well as monitors which of the battery cells is weak or damaged. The BMS system also measures cell and ambient temperatures. Inside the battery, there is a system protecting it against excessive load. Based on these data, the system assesses the condition of the cells, and in the event of a failure or overtemperature, it disconnects the battery from the output terminals. The battery is equipped with a diagnostic interface that allows to control the battery operation via a computer network. The battery parameters are presented in Table 4.

Table 4. Basic technical data of the tested lithium-polymer battery [source: user manual, provided by the battery manufacturer Wamtechnik, battery cells made by Kokam]

Rated capacity	70 Ah
Rated operating voltage	44.4 V (3.7 V/cell)
maximum charging current	70 A
Minimum discharge voltage	2.70 V/cell ±0.05 V = 32.4 V
Permissible operating temperature	–20–45°C (discharging)| 0–40°C (charging)|

The theoretical course of engine load related to charging (Fig. 6) furthermore, resulting from the operation of the generator and the battery BMS module distinguishes two stages:

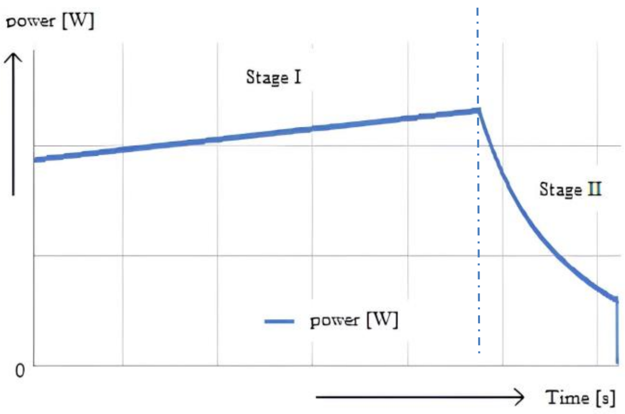

Fig. 6. Theoretical electrical loading diagram of the tested engine over time

– Stage I: the battery is charged with constant current until the appropriate cell voltage is obtained
– Stage II: BMS, after obtaining the appropriate cell voltage in the battery, maintains this voltage and reduces the current until the end of charging.

2.3. Description of the measuring station

The test stand set up to test the operational properties of the hybrid drive system powered by substitute fuels is shown in Fig. 7.

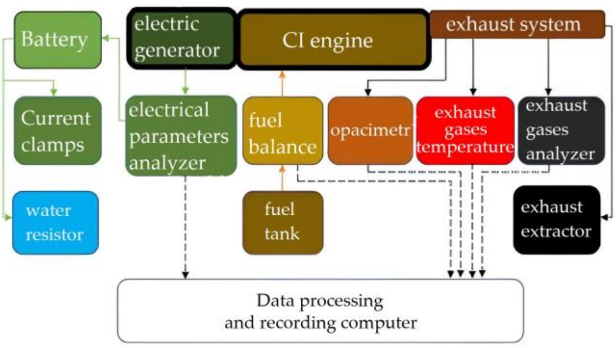

Fig. 7. Schematic layout of the research stand [author's source]

In order to analyze and record current data during the tests, the BMR trading PLA34 analyzer was used, with three voltage inputs and eight current inputs for measuring electrical parameters. The PLA34 works by continuously sampling the voltage and current inputs at 40 kHz. PLA34 is an instrument for monitoring power quality in accordance with the EN 50160 standard [5]. The analyzer was connected in series between the generator and the battery.

Fuel consumption during the tests was determined using the AVL 733S Fuel Balance fuel scale [3]. This device determines fuel consumption by means of a suitable weighing vessel connected to a bending beam with a capacitive displacement sensor. Due to the fact that the weighing vessel must be replenished for each measurement, this is a discontinuous measurement principle. The mass of the fuel consumed is thus determined gravimetrically, which means that the density need not be additionally determined. Fuel consumption can be determined with an accuracy of 0.12%. The built-in calibration unit is standard equipment and allows calibration and accuracy control according to ISO 9001 [8]. The scale saves data in the form of hourly fuel consumption G_e [3].

Exhaust gas opacity was measured using the AVL 439 OPACIMETER, which operates on the principle of light absorption [2]. The AVL 439 opacimeter measures the transparency of polluted air, in particular exhaust emissions from diesel engines. The measuring chamber with a defined measuring length and non-reflecting surface is evenly filled with exhaust gases. The light intensity loss between the light source and the receiver is measured and the exhaust gas transparency is calculated from it. The calculations are based on the Lambert-Beer law [2, 6]. The opacimeter collects exhaust gas samples from the engine exhaust manifold, where the appropriate ½ inch threaded connection is mounted.

A set of exhaust gas analyzers CEB II – 2000 was used to analyze the shares of gaseous components of exhaust gases. It is a fully automated, computer-controlled set of measuring instruments. Exhaust gases collected using a probe mounted on the exhaust manifold were pre-filtered and then flowed through the gas path to the exhaust gas dosing unit for individual analyzers. Water vapor was condensed from the exhaust gases and directed to the "cold exhaust gas analyzers" in the cooler located in the measuring cabinet with analyzers. Exhaust gases for the analyzers requiring hot exhaust gases were supplied through a heated gas path. The CO and CO_2 analyzers operated by absorbing infrared radiation. All analyzer modules are built into the gas sample conditioning cabinet. Reference gases, two concentrations of each of the measured exhaust gas components, were supplied to the analyzers [1]. The gas cylinders were placed in a rack and connected to the analyzers with teflon hoses.

The exhaust gas temperature was measured using a thermocouple. The thermocouple consists of a pair of dissimilar metals, usually in the form of wires, bonded at both ends. The thermocouple used in the tests consisted of NiCr–NiAl. The operating range of this thermocouple is 50–400 ±1°C. The thermocouple was mounted in the exhaust manifold on which the appropriate M5 threaded connection was welded. Analog data from thermocouples were converted into digital form by a computer module.

HP-605A current clamps were used during the battery discharge. With their participation, the values of the discharge current flowing through the cable connecting the battery with the water resistor were monitored.

The water resistor is a device used in the tests to discharge the electric battery of the system. It is made of elements produced from stainless steel. The resistor converts electrical energy into work in the chemical process of water hydrolysis.

The fuel tank with a capacity of 5 dm^3 was placed above the fuel scale. The fuel from the tank to the fuel scale flowed by gravity.

The tests were carried out in a closed room. In order to maintain occupational health and safety, exhaust fumes were discharged into the atmosphere outside the building using an exhaust extractor powered by an electric motor.

The control of the test stand and the recording of measurement results were carried out using a series of computers equipped with appropriate measurement and control modules and appropriate software.

2.4. Method of conducting measurements of performance properties of the tested vehicle's propulsion

Exploitation is defined as a set of purposeful organizational, technical, and economic activities of people with equipment and mutual relations between them from the moment of accepting the equipment for use in accordance with its intended purpose until its liquidation [17, 24]. In the context of the tested hybrid vehicle, the measurement of operational properties consists of examining:

- times of full charge – telling, among others, about the speed of the ability to perform tasks by the tested unmanned vehicle (the shorter, the better)
- the amount of fuel used to fully charge – talking about, for example, the frequency of refueling (the less often, the better) or the cost of its operation (the smaller the better)
- the values of the exhaust gas components – showing the level of environmental performance during the use of this vehicle (the lower the CO and CO_2 content, the better).

In order to determine these properties, tests of the hybrid system were carried out for three selected fuels. The first stage of the research was to fill the tank with the fuel used in the test. When changing fuel to another engine fuel system (filter, fuel lines), the fuel scale and the tank were previously drained. The lithium-polymer battery was discharged using a water resistor. In order to maintain the repeatability of the tests, the battery was discharged with a DC current of ~50 A. The discharge current values were monitored using current clamps. By adjusting the depth of immersion of the resistor sheets in water, the value of the current flowing from the battery was determined. The BMS battery control system disconnects the discharge circuit automatically at the appropriate cell voltage level. After discharge, the battery remained idle for at least 30 minutes in order to "relax" the cells, i.e., restore their chemical and temperature stability. At that time, the diesel engine was started in order to warm it up to the operating temperature and possibly burn out the fuel residues from the previous test.

The next stage was the preparation of the analyzers: switching on the analyzer of electrical parameters, filling the fuel scale, and calibration of the exhaust gas analyzer. When all the measuring devices were ready for work, the engine was started and the battery charging process began.

The methodology of comparing the impact of selected substitute fuels on the tested hybrid system inform about determining the load characteristics of the internal combustion engine over time. The load characteristic of the engine is the dependence of the hourly fuel consumption as a function of power. This characteristic is used to evaluate motors that are characterized by a constant rotational speed. The rotational speed of the shaft for the tested L100AE engine recommended by the manufacturer for the Diesel base fuel is 3000 rpm. Ideally, this value was set before the tests during engine operation on the base fuel. The load characteristics of the compression-ignition engine are determined during operational adjustment of the injection advance angle. The size of the dose of fuel injected into the engine is obtained by changing the position of the dose control element (i.e. the rack of the injection pump piston). At a fixed engine speed, the amount of air entering the cylinders is constant. The composition of the fuel-air mixture produced in the engine cylinders is, therefore variable. Therefore, the coefficient of excess air λ is also variable. As the amount of fuel injected increases, the combustion conditions change.

The element loading the diesel engine in the test was the generator, whose task was to carry out a full battery charging cycle. The element recording the value and change of the load over time was the analyzer of electrical parameters, which processed the measurements and calculations of all parameters and electrical values of the battery charging in real time before the battery rectifier system. Instantaneous fuel consumption values during the test were recorded by a fuel scale. Instantaneous flue gas composition values were recorded by the flue gas analyzer. The BMS disconnected the charging circuit automatically at the appropriate cell voltage level. The end of charging was a sign to turn off the internal combustion engine and end the research. The battery, as in the case of discharging after charging, remained idle for at least 30 minutes in order to "relaxation". All tests were carried out in a closed room at 20°C.

All results of parameter measurements were observed and collected throughout the experiment and during the tests for the purpose of ongoing control of the technical condition of the hybrid system and measuring instruments, and determination of the circumstances of a possible failure, and control of the implementation of subsequent phases of the research cycle. The measurement results downloaded from the analyzers were processed on a computer using the Microsoft Excel program and presented on charts.

2.5. Mathematics formulas used to develop measurement results [17]

Below are the mathematical formulas used to develop the test results:

– charging active power P_t at time t [W]:

$$P_t = (I_1 \cdot U_1 \cdot \cos\varphi_1)_t + (I_2 \cdot U_2 \cdot \cos\varphi_2)_t + (I_3 \cdot U_3 \cdot \cos\varphi_3)_t \quad (1)$$

where: I_1 – phase current 1 [A], I_2 – phase current 2 [A], I_3 – phase current 3 [A], U_1 – phase voltage 1 [V], U_2 – phase voltage 2 [V], U_3 – phase voltage 3 [V], φ_1– phase shift angle 1 [rad], φ_2– phase shift angle 2 [rad], φ_3– phase shift angle 3 [rad]

– total active charging energy E_l [W·h]:

$$E_l = \sum_t^n (P_t \cdot t) \quad (2)$$

– charging reactive power Q_t at time t [var]:

$$Q_t = (I_1 \cdot U_1 \cdot \sin\varphi_1)_t + (I_2 \cdot U_2 \cdot \sin\varphi_2)_t + (I_3 \cdot U_3 \cdot \sin\varphi_3)_t \quad (3)$$

where: I_1 – phase current 1 [A], I_2 – phase current 2 [A], I_3 – phase current 3 [A], U_1 – phase voltage 1 [V], U_2 – phase voltage 2 [V], U_3 – phase voltage 3 [V], φ_1 – phase shift angle 1 [rad], φ_2 – phase shift angle 2 [rad], φ_3 – phase shift angle 3 [rad]

– mass fuel consumption [kg]:

$$\sum_t^n (G_e \cdot t) = \text{mass fuel consumption} \quad (4)$$

where: G_e – fuel consumption [kg/h], t – time [h].

– energy produced [MJ]

$$\text{energy produced} = \frac{E_l}{1000000 \cdot 3600} \quad (5)$$

– energetic efficiency [%]:

$$\text{energetic efficiency} = \frac{\frac{\text{energy produced}}{\text{calorific value}}}{\text{mass fuel consumption}} \cdot 100\% \quad (6)$$

3. Results

This section will discuss the external charging characteristics for 3 types of fuels, common statements regarding hourly fuel consumption, Active charging power, Reactive power, and emission lists of selected exhaust gas components (including temperature and smoke). Mass fuel consumption, energy produced and overall energy efficiency are also presented.

3.1. Charging load characteristics and exhaust emission for Diesel fuel

Figure 8 below shows the characteristics of the load as a function of time performed on the diesel base fuel. The battery charging system forced a current-voltage waveform that loaded the diesel engine. The power curve of the internal combustion engine is marked in blue. The hourly fuel consumption changed analogously to the course of the power generated by the diesel engine. A full charging cycle lasted 1:29:34 hours, and 1.14 kg of diesel fuel was used to charge the battery.

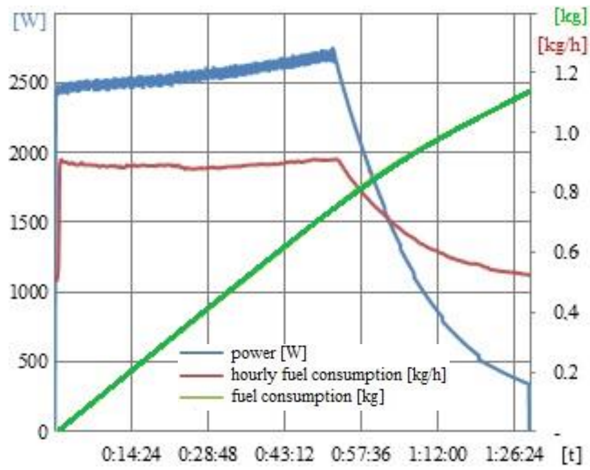

Fig. 8. Load characteristics as a function of time for diesel fuel

In Figure 9 presents the course of the percentage share of selected exhaust gas components during the performance of the load characteristics on the base fuel (diesel). The runs of the exhaust gas components change analogously to changes in the diesel engine load.

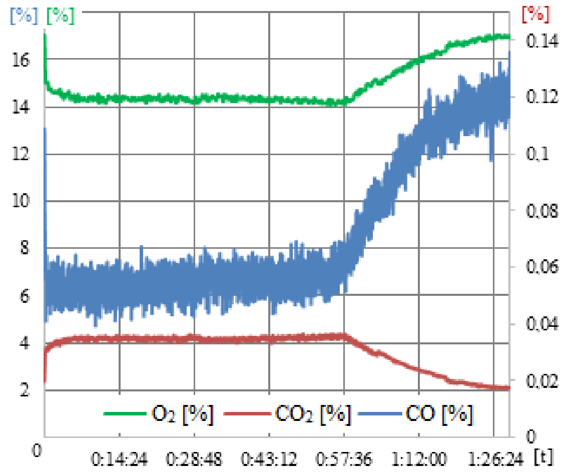

Fig. 9. Percentage share of selected exhaust gas components for diesel fuel

3.2. Charging load characteristics and exhaust emission for F-34

Figure 10 presents the load characteristics of a diesel engine made on the F-34 substitute fuel for a diesel engine being part of a serial hybrid propulsion system of an unmanned platform. During the test, the internal combustion engine maintained the rotational speed of the engine shaft at ~2850 rpm without changing the settings of the speed controller. A full charging cycle lasted 1:49:26 hour, and 1.46 kg of F-34 fuel was used to charge the battery.

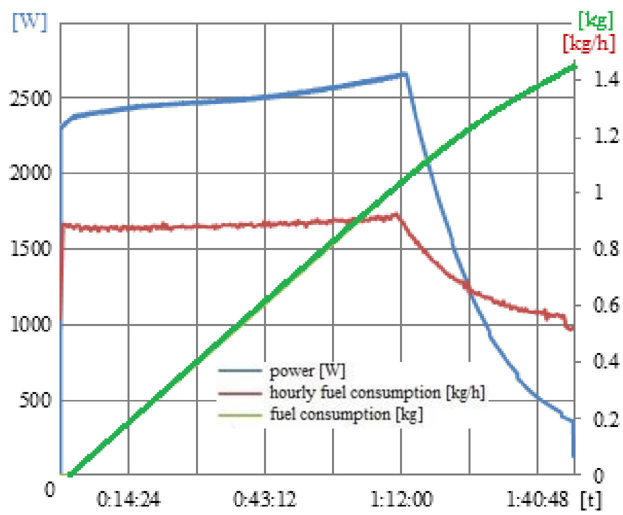

Fig. 10. Load characteristics as a function of time performed on substitute fuel F-34

Figure 11 presents the course of the percentage share of selected exhaust gas components during the performance of the load characteristics on the substitute F-34 fuel. The runs of the exhaust gas components change analogously to changes in the diesel engine load.

3.3. Charging load characteristics and exhaust emission for Jet A-1

Figure 12 shows the time load characteristics of a compression-ignition engine (part of a series hybrid drive system) made on substitute fuel, a mixture of Jet A-1 fuel. During the test, the internal combustion engine maintained the rotational speed of the engine shaft at ~2830 rpm without changing the settings of the speed controller. A full charging cycle lasted 1:52:52 hours, and 1.61 kg of Jet A-1 was used to charge the battery.

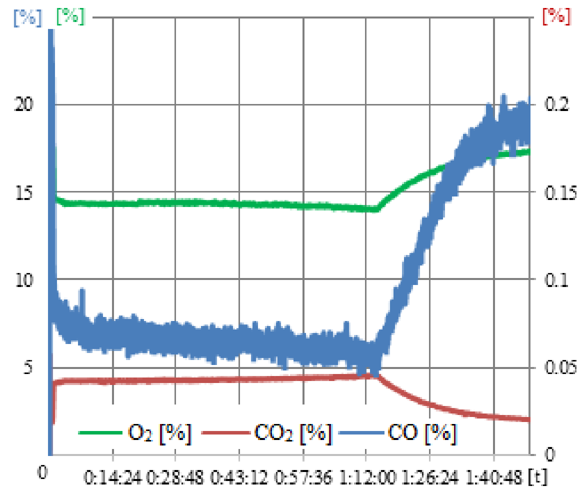

Fig. 11. Percentage of selected exhaust gas components for F-34 fuel

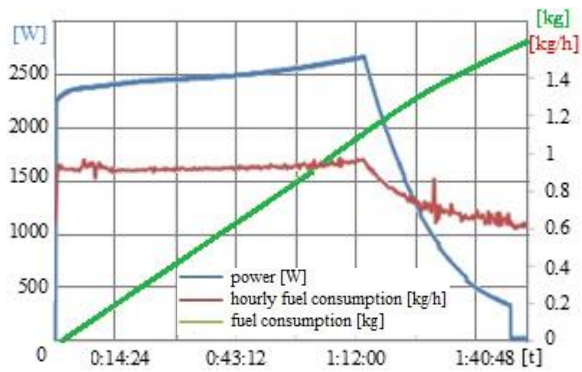

Fig. 12. Load characteristics over time performed Jet A-1

Figure 13 shows the course of the percentage share of selected exhaust gas components during the performance of the load characteristics on the substitute fuel – Jet A-1 fuel mixing. The runs of the exhaust gas components change analogously to changes in the diesel engine load.

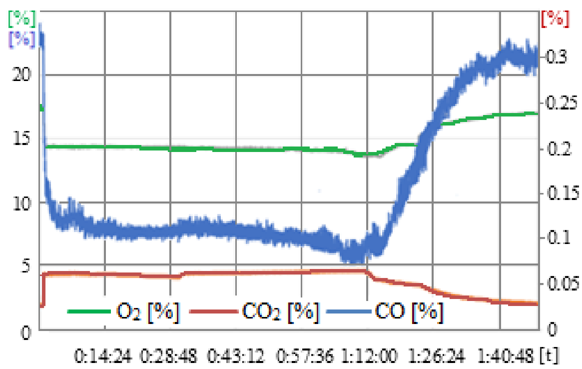

Fig. 13. Percentage of selected exhaust gas components for F-34 fuel

3.4. Common results for all tested fuels

3.4.1. Hourly fuel consumption

Due to the differences in the calorific values of fuels and the decrease in the charging power resulting from the change in engine speed on the substitute fuels, the hourly fuel consumption values differ, as shown in Fig. 14.

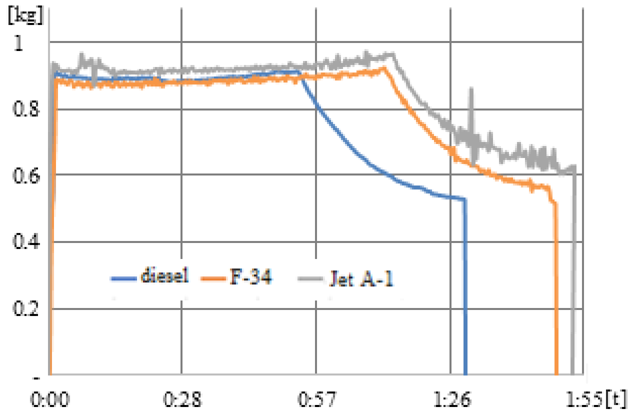

Fig. 14. Summary of hourly fuel consumption over time for diesel, F-34 and Jet A-1

3.4.2. Active charging power

Figure 15 shows the active power generated during the tests for individual fuels. Active power is the part of the power that the load takes from the source and converts it to work or heat. The differences in the power generated for the base and substitute fuels result from the difference in the rotational speed of the engine crankshaft and thus, the generator rotor. This affects the desynchronization of the generator's operation and the increase in reactive power generation. The difference between the tested substitute fuels results from the difference in calorific value

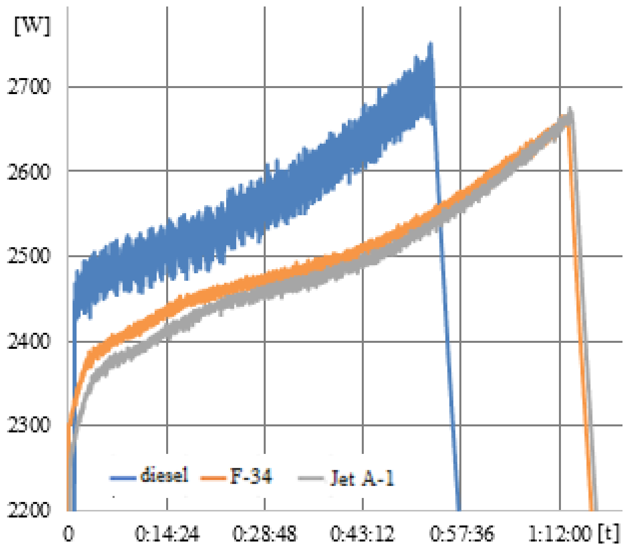

Fig. 15. List of active power over time for diesel, F-34 and Jet A-1

3.4.3. Reactive power

Reactive power in AC circuits is a quantity describing the pulsation of electric energy between the elements of the electric circuit. This oscillating energy is not converted into useful work or heat, but it is necessary for the generator to function in the hybrid system under investigation. Differences in generated reactive power have a direct impact on active power [8]. Figure 16 shows the reactive power generated during the tests for individual fuels.

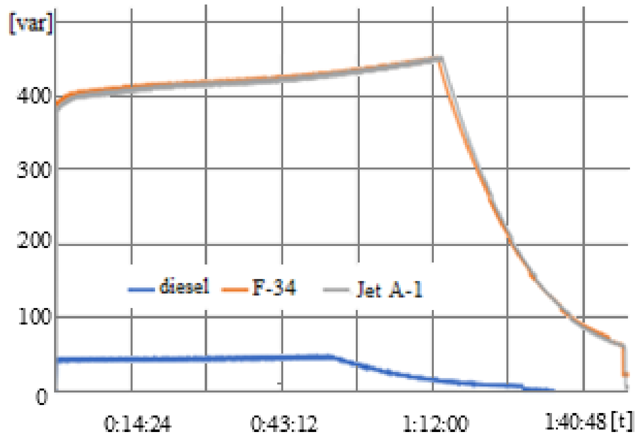

Fig. 16. Summary of reactive power over time for diesel, F-34 and Jet A-1

3.4.4. Exhaust gases composition

Carbon dioxide

Figure 17 presents the percentage share of carbon dioxide in exhaust gases for the base and tested substitute fuels. The graph shows that the carbon dioxide values oscillate in similar values for each of the tested fuels. Slightly higher contents for substitute fuels result from their incomplete combustion.

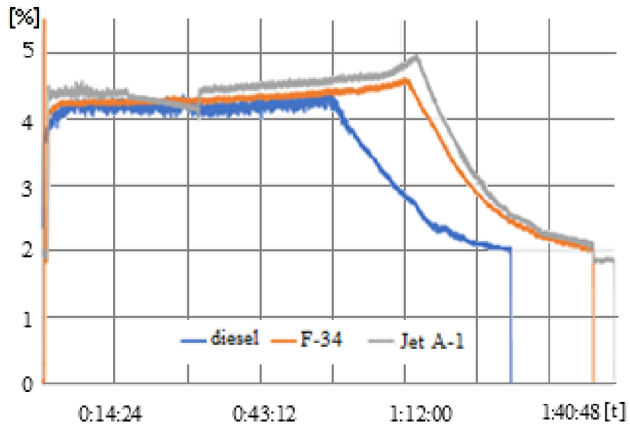

Fig. 17. A summary of the percentage of carbon dioxide in the exhaust gas composition over time for diesel, F-34 and Jet A-1

Oxygen

Figure 18 shows the percentage share of oxygen in the exhaust gas for the base fuel and the tested substitute fuels. The graph shows that the oxygen values in the exhaust gases are similar. Similar amounts of oxygen particles contained in the tested fuels are also reflected in the exhaust gas composition.

Carbon monoxide

Figure 19 presents the percentage share of carbon monoxide in exhaust gases for the base fuel and the tested substitute fuels. The chart shows that Jet A-1, due to less effective combustion (e.g. lower exhaust gas temperature) and the content of additional carbon particles in the admixture, is characterized by the highest content of carbon monoxide in exhaust gases [9].

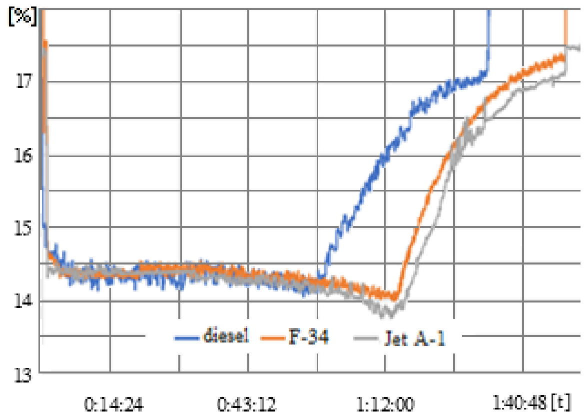

Fig. 18. Summary of the percentage of oxygen in the exhaust gas composition over time for diesel, F-34 and Jet A-1

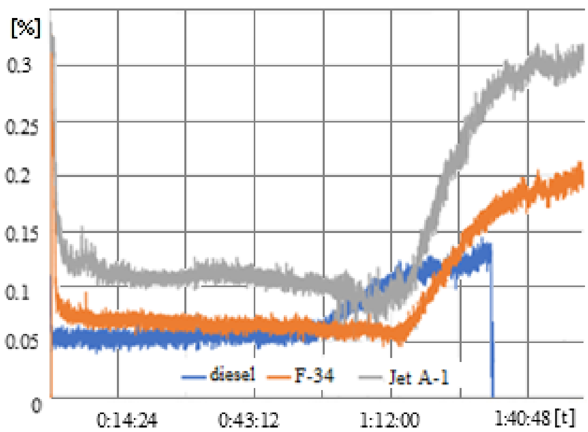

Fig. 19. Percentage of carbon dioxide in the composition of exhaust gases over time for diesel, F-34 and Jet A-1

Exhaust smoke opacity

Figure 20 presents smoke opacity for the base fuel and the tested substitute fuels. The graph shows that smoke opacity for substitute fuels is higher by about 30% throughout the charging process.

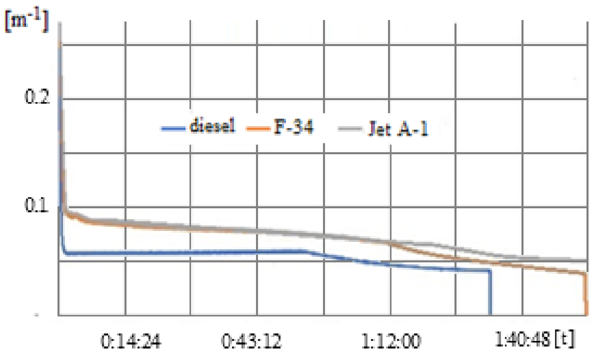

Fig. 20. Comparison of smoke opacity over time for diesel, F-34 and Jet A-1

Exhaust gases temperature

The exhaust gas temperature (Fig. 21) during the test was the highest for diesel fuel. This indicates the most efficient combustion. The exhaust temperature of the F-34 fuel is higher than that of Jet A-1, most likely due to the higher calorific value.

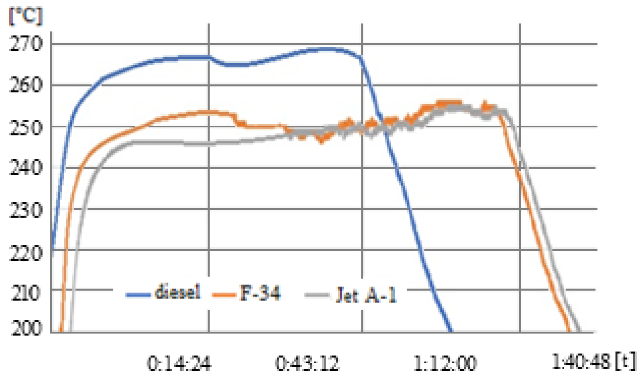

Fig. 21. Comparison of exhaust gas temperature over time for diesel, F-34 and Jet A-1

3.4.5. Mass fuel consumption

Figure 22 presents the total mass amount of fuel needed for a full charging cycle of the battery of the tested system.

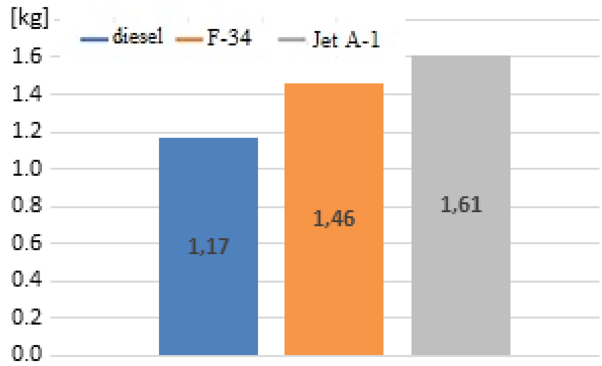

Fig. 22. Mass fuel consumption per charging cycle for diesel, F-34 and Jet A-1

3.4.6. Energy produced

Figure 23 summarizes the total amount of electricity needed to fully charge the battery during the tests for individual fuels. Different charging powers most likely affected the temporary current-voltage state of the battery cells, and thus the reaction of the BMS. Therefore, the battery charging control system disconnected the charging circuit at different values of energy produced by the generator.

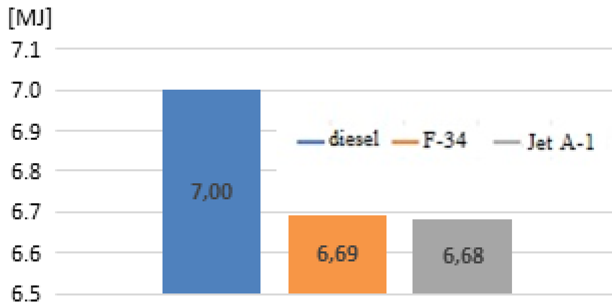

Fig. 23. Total energy produced from diesel fuel, F-34 and Jet A-1

3.4.7. Energetic efficiency

Figure 24 shows the overall efficiency of converting the energy contained in the fuel into electricity for individual fuels.

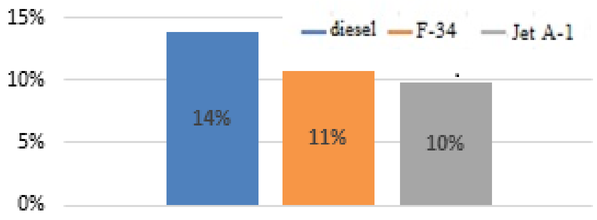

Fig. 24. Total engine energy efficiency using diesel, F-34 and Jet A-1

4. Discussion

In the tested hybrid drive system, the transition to the substitute fuels used in the test, due to the fact that the chemical composition is very similar to the base fuel, can take place at any time. The tested combustion engine can successfully use them without structural changes and fully charge the battery.

The construction of the injection system and the speed controller in the tested internal combustion engine as well as large differences in the viscosity and calorific value of the tested substitute fuels resulted in a 5–6% decrease in the rotational speed of the engine shaft. The engine speed maintenance system is not fully adapted to the use of other fuels. The rotational speeds of the generating set-in series hybrid systems are most often selected in a way that guarantees their most effective operation. The internal combustion engine operates at the point of the lowest specific combustion, and the generator at the point where the losses resulting from the generated reactive power are compensated or minimized. Changing the rotational speed has negative consequences in the form of a decrease in the energy efficiency of the entire system [15]. In terms of operational properties, this results in increased charging time (22% for F-34 and 26% for Jet A-1), increased fuel consumption (26% for F-34 and 41% for Jet A-1) and more frequent refueling. However, in ad-hoc situations, tested alternative fuels can be used. Changing the volumetric size of the injected fuel (moving the injector's control rack, or using a different speed regulator system) to a larger one would increase the efficiency of the generator. At the same time, the entire system, and recommended changing it in long-term applications of the tested substitute fuels. Literature analysis indicates that with long-term use due to the low viscosity and very good cleaning properties of the tested alternative fuels, any faults in the fuel system may be revealed [6, 12, 14]. This may exacerbate the decline in energy efficiency. Also, the lower cetane number of the tested alternative fuels may impair the cold start of the engine and increase the tendency to hard work. Due to the lower combustion temperature of substitute fuels, a greater amount of incomplete combustion products and greater opacity of exhaust gases can be observed in the exhaust gases. Both this and the very fact of the longer charging process indicate the negative effects of the use of the tested substitute fuels in the ecological context. In the propulsion system, the transition to the substitute fuels used in the test, due to the fact that the chemical composition is very similar to the base fuel, may take place at any time. The tested combustion engine can successfully use them without structural changes and fully charge the battery.

5. Summary and final conclusions

The modern development of hybrid drive systems takes into account the need to combine conflicting requirements. On the one hand, ecological requirements are growing, on the other hand, these systems are required to obtain maximum work units. The continuous development of hybrid systems increases the complexity of their construction. The internal combustion engines themselves also use very precise power and control systems to increase thermal efficiency. Precision fuel systems are very sensitive to changes in fuel parameters or contamination. Modern multi-element hybrid systems, in which various forms of energy are transformed several times, are therefore very susceptible to the influence of fuel on the quality of their work. Therefore, the use of alternative fuels in such systems should be part of the design process. The use of substitute fuels at this point may turn out to be very beneficial in the ecological context, and in the long term, their use due to the depletion of oil resources will be a necessity. The final conclusions are presented below:

– alternative fuels can be successfully used in internal combustion engines of hybrid drive
– in the tested serial hybrid propulsion system of the unmanned platform, it is possible to use F-34 fuel and Jet A-1 fuel
– if the above-mentioned fuels are used to propel the platform, one should be aware of the increased fuel consumption and the potential decrease in energy efficiency and the negative impact on the environment associated with increased exhaust emissions
– if there is an intention or need to use substitute fuels in modern multi-element hybrid systems, the possibility of using such fuels should be taken into account in the process of designing and constructing these hybrid systems. Thanks to this, they will maintain their high work efficiency.

Acknowledgements

This work was financed by Military University of Technology under research project UGB 22-833/2023.

Nomenclature

AC	alternate current	CI	compression ignition
Al	aluminium	CO	carbon oxide
BLDCM	brushless direct current motor	CO_2	carbon dioxide
BMS	battery management system	DC	direct current
Cd	cadmium	EN	European Standard
CFPP	cold filter plugging point	E_t	total active charging energy

F-34	NATO general use fuel	O	oxygen
G_e	hourly fuel consumption	PC	personal computer
I	phase current	P_t	charging active power
ICE	internal combustion engine	Q_t	charging reactive power
ISO	International Organization for Standardization	t	time
Jet A-1	type of aviation fuel	U	voltage (phase voltage)
LUMWP	light unmanned military wheeled platform	VAR	volt ampere reactive
NATO	North Atlantic Treaty Organization	λ	excess air factor
Ni	nickel	φ	current phase shift angle

Bibliography

[1] AVL CEB II – 2000 analyzer user manual.

[2] AVL. 439 Opacimeter product description. https://www.avl.com/documents/10138/885965/Download_01_AVL_439_Opacimeter_Product+Description.pdf (accessed on 27 April 2023).

[3] AVL. Product description: fuel balance. https://www.avl.com/documents/10138/2699442/Product+Description+Fuel+Balance (accessed on 22 April 2023).

[4] Barta D, Mruzek M, Kendra M, Kordos P, Krzywonos L. Using of non-conventional fuels in hybrid vehicle drives. Adv Sci Technol Res J. 2016;10:240-247. https://doi.org/10.12913/22998624/65108

[5] Elektroinstalator.com.pl. Jakość energii elektrycznej według normy PN-EN 50160. http://www.elektroinstalator.com.pl/index.php/artykuly/metrologia/2478-jakosc-energii-elektrycznej-wedlug-normy-pn-en-50160 (accessed on 24 April 2023).

[6] Heywood JB. Internal combustion engine fundamentals (2nd ed). McGraw-Hill Education 2018.

[7] Fuel data sheets obtained from the dealer – Regulation (EU) 2020/878 amending Annex II to the REACH Regulation.

[8] ISO 9001 – Quality management. https://www.iso.org/iso-9001-quality-management.html (accessed on 24 April 2023).

[9] Karczewski M, Szczęch L, Trawiński G. Motor vehicle engines (in Polish: Silniki pojazdów samochodowych). WSiP. Warsaw 2022.

[10] Kovbasenko S. Possibilities of enhancing the environmental safety of diesel vehicles using alternative fuels. J Mech Eng Transport. 2023;16:51-57. https://doi.org/10.31649/2413-4503-2022-16-2-51-57

[11] Khandelwal B. Aviation fuels (1st ed). Academic Press 2021.

[12] Legutko S. Machine operation (in Polish: Eksploatacja maszyn). Poznan University of Technology Publishing House. Poznań 2007.

[13] McDonnell K. Combat and tactical vehicles: developments and considerations for the department of defense. Military and Veteran Issues, 2nd ed. Nova Science Publishers, Inc. 2020.

[14] Merkisz J, Pielecha J. Alternative fuels and vehicle propulsion systems (in Polish: Alternatywne paliwa i układy napędowe pojazdów). Poznan University of Technology Publishing House. Poznań 2014.

[15] Merkisz J, Pielecha J. Electrical systems of hybrid vehicles (in Polish: Układy elektryczne pojazdów hybrydowych). Poznan University of Technology Publishing House. Poznań 2015.

[16] Nasoulis C, Protopapadakis G, Ntouvelos E, Gkoutzamanis V, Kalfas A. Environmental and techno-economic evaluation for hybrid-electric propulsion architectures. The Aeronautical Journal. 2023;127(1317):1904-1926. https://doi.org/10.1017/aer.2023.27

[17] National Radio Institute. Mathematics for Electronics and Electricity. 2017. USA.

[18] NATO. Logistic support agreement. https://www.nato.int/docu/logien/1997/lo-15a.htm (accessed on 24 April 2023).

[19] Schobert HH. The chemistry of hydrocarbon fuels (2nd ed.). Butterworth-Heinemann 2015.

[20] Shariz M, Gautam A, Tomar B, Gautam M, Jalil M. To Design an Optimal PV/diesel/battery hybrid energy system for Havelock Island in India. In: Rani A, Kumar B, Shrivastava V, Bansal RC (eds). Signals, machines and automation. International Conference on Signals, Machines, and Automation, Part of the Lecture Notes in Electrical Engineering book series (LNEE, 1023); 2023. https://doi.org/10.1007/978-981-99-0969-8_21

[21] Tanwar M, Tanwar P, Bhand Y, Bhand S, Jadhav K, Bhand S. Biofuels: production and properties as substitute fuels. IntechOpen 2023. https://doi.org/10.5772/intechopen.109073

[22] Yanmar. Silniki chłodzone powietrzem. https://yanmar.pl/silniki-yanmar/silniki-chlodzone-powietrzem/dsh$sajn2 (accessed on 24 April 2023).

[23] Zou Y, Li J, Hu X, Chamaillard Y. Modeling and control of hybrid propulsion system for ground vehicles. Springer Berlin, Heidelberg 2018. https://doi.org/10.1007/978-3-662-53673-5

Janusz Chojnowski, MEng. – Faculty of Mechanical Engineering, Military University of Technology in Warsaw, Poland.

e-mail: *janusz.chojnowski@wat.edu.pl*

Article citation info:
Stępień Z. Analysis of the prospects for hydrogen-fuelled internal combustion engines. Combustion Engines. 2024;197(2):32-41. https://doi.org/10.19206/CE-174794

Zbigniew STĘPIEŃ

Combustion Engines
Polish Scientific Society of Combustion Engines

Analysis of the prospects for hydrogen-fuelled internal combustion engines

ARTICLE INFO

Received: 5 October 2023
Revised: 15 October 2023
Accepted: 3 November 2023
Available online: 6 November 2023

Hydrogen, as a zero-emission fuel, makes it possible to build a piston combustion engine that can be qualified as a drive for a "Zero Emission Vehicles", in terms of CO_2 emissions. Thus, a hydrogen-powered piston combustion engine may be a future transitional technology for powertrains, especially in trucks and off-road vehicles, competitive with both electric drives and fuel cells. The article presents a multi-directional analysis of the prospects for the development and dissemination of hydrogen-powered internal combustion piston engines in motor vehicles. The current interest of the automotive industry in hydrogen-powered internal combustion engines, the current state of their development and the challenges that need to be overcome were presented. Various conditions that will determine their future in Europe were also indicated.

Key words: *piston combustion engine, hydrogen, fuel injection, combustion process, hydrogen combustion engines, exhaust emissions*

1. Introduction

Climate protection has long become a priority topic in the activities of many political groups in the world. New regulations, standards, norms and directives related to counteracting the broadly understood degradation of the natural environment are being introduced or tightened continuously. Concerns about combustion engines exacerbating climate change have become a public and political topic. Impartial assessments of the actual impact of combustion engine emissions on climate change are necessary, taking into account the enormous progress that has been made in reducing all standardized exhaust emissions from combustion piston engines (Euro 1–Euro 6; Euro 7). To achieve national and EU climate goals and meet the successively stricter regulations on reducing exhaust emissions from road and off-road vehicles, it became necessary to both significantly increase the energy efficiency of their power units and move away from fossil fuels. As part of the adopted action plan called the Green Deal, the European Union has set itself the goal of achieving net zero greenhouse gas emissions by 2050. The intermediate goal is to reduce their emissions by 55% by 2030 compared to the reference year of 1990. Therefore, the entry of EU Regulation 2019/1242 into force, the targets for reducing CO_2 emissions of the vehicle fleet by –15% by 2025 and –30% by 2030 (compared to 2019 levels) became permanent legislation for truck manufacturers in the EU. Currently, the automotive industry is looking for and developing various solutions for power units with zero or very low CO_2 emissions and at the same time reducing emissions of harmful, regulated and not yet regulated exhaust gas components. So far, a rapid development of electric drive units, an increase in interest in fuel cells and the possibility of using various alternative, pro-ecological fuels such as hydrogen, ammonia and others have all been observed. This raises the question of what role combustion engines will play in the coming decades and whether they can meet future environmental requirements through the use of alternative, non-hydrocarbon fuels [20, 22]. It is worth remembering the basic advantages of combustion engines over electric drives and fuel cells, the most important of which are: resistance to environmental conditions, including fuel and air pollution, low demand for rare earths and precious metals, and well-established development and production practices [4, 32].

Hydrogen has the potential to become a sustainable fuel of the future, to reduce global dependence on fossil fuel resources, and can also be used as an ecological fuel with zero CO_2 emissions because it does not contain carbon. Hydrogen is the most common element in the world, as an energy carrier it has the highest specific energy of 33 Wh/g and a calorific value of 120 MJ/kg. The energy per unit of mass stored in hydrogen is approximately 2.6 times greater than that of gasoline. However, hydrogen requires about four times more volume to store than gasoline when stored as a liquid, and about 19 times more volume when stored in gas form. Although hydrogen does not occur freely in nature, it can be produced using various processes, the most popular of which are steam reforming of natural gas or biomass gases, coal gasification and water electrolysis. The use of hydrogen as a fuel in vehicles powered by an internal combustion engine (H2ICE) or fuel cells (FC) is currently a promising direction for the future of the transport sector. The use of hydrogen as a fuel for piston combustion engines would make it possible to almost completely eliminate CO_2 emissions. In addition, emissions of toxic substances such as carbon monoxide (CO), hydrocarbons (HC) and particulate matter (PM) can be reduced to very low (trace) levels. This is because these emissions will only arise from the combustion of lubricating oil entering the engine's combustion chambers. The only exhaust component that may be produced in notable amount during hydrogen combustion in the engine is nitrogen oxides (NO_x). However, they can be reduced almost to zero through a properly designed exhaust aftertreatment system, without increasing secondary emissions such as N_2O and NH_3 [7, 11, 34]. Consequently, H2ICE may play the role of a transitional technology in the development of propulsion systems, especially in trucks and off-road vehicles, at least until fuel cells become technologically advanced, easy to use and fully profitable. In the medium term, a hydrogen-powered internal combustion engine may provide a competitive alternative to electric powertrains until a sufficient amount of fully renewable electricity is available. In turn, hybrid drive systems with a hydrogen combustion engine are a real alternative to electric drives and fuel cells, both from the point of view of CO_2 emission equivalent and the total cost of production and long-term use [27, 31]. In addition to advantages in terms of efficiency and driving range, this leads to attractive functional synergies and additional degrees of freedom in terms of design and operating strategies that need to be taken into account. Hydrogen can also be used as admixtures with hydrocarbon fuels or as alternative fuels such as ammonia [34]. Despite extensive work already being carried out on the use of both pure hydrogen and its mixtures with other fuels to power piston combustion engines, further actions are necessary to optimize the design changes of the piston combustion engine, in particular its fuel supply system and combustion processes allowing the full use of the properties of hydrogen. There are several manufacturers currently interested in introducing hydrogen-powered internal combustion piston engines into production that have announced their current status of work on such drive units (Table 1).

Table 1. List of manufacturers currently exploring new H2ICE technologies [13, 17, 18, 23]

Manufacturer	Status of work
JCB	Start of production announced
MAN	
PUNCH - Torino	
Toyota	
Deutz	
DAF	Ongoing development
Kawasaki	
Yamaha	
Daimler	
Cummins	
Liebherr	
MTU	
Hongqi	Research announced
Ford	
Volvo	
Scania	
Great Wall	
Caterpilar	

The article was motivated by the intention to present the current interest and plans of the automotive industry in the field of hydrogen-powered internal combustion engines, the challenges facing their further development and to analyze the prospects for using such engines in the future.

2. Advantages of H2ICE – future possibilities

The use of hydrogen as a standalone fuel or as an admixture with another fuel (e.g. hydrocarbon, synthetic or alternative) is considered possible in both SI (spark ignition) and CI (compression ignition) engines. Hydrogen as a fuel is characterized by several favorable properties enabling high efficiency of the combustion process. The most important of these properties are [31]:

– Wide range of flammability

Compared to hydrocarbon fuels, the flammability range of hydrogen is very wide, it ranges from 4 to 76% of the volume content in air [9, 21, 28] (these values are for example 1–7.6% for diesel oil, and 0.6–5.5% for gasoline). This property allows the engine to run on a very lean mixture. This, combined with the complete combustion of hydrogen, allows for greater fuel savings and optimization of the combustion process in terms of reducing NO_x emissions thanks to a lower combustion temperature. Moreover, lower heat losses through the walls of the combustion chamber make it possible to achieve higher thermal efficiency of the engine [5].

– High rate of combustion

The combustion rate of a hydrogen-air mixture is approximately seven times faster than a mixture of air and any hydrocarbon fuel. As the combustion rate increases, the actual curve of the indicator graph approaches the ideal one. This means that an increasingly higher thermodynamic efficiency can be achieved [1]. When using a stoichiometric mixture, the hydrogen engine comes closest to the ideal thermodynamic cycle, and the propagation speed of the hydrogen flame is almost an order of magnitude greater than that of the gasoline flame [19]. Making the combustion mixture more lean reduces the speed of flame propagation. The speed of flame propagation and its adiabatic temperature have a significant impact on the thermal efficiency of the engine, the stability of the combustion process and the level of emissions (especially NO_x) [9, 19, 28].

– High stoichiometric air-to-fuel ratio

The stoichiometric air-to-fuel (A/F) mass ratio for complete combustion of hydrogen in air is approximately 34.4:1, which is significantly greater than that of gasoline (14.7:1) or diesel (14.5:1) [9, 19, 28].

– Very low energy of ignition

The ignition energy of the hydrogen-air mixture is only 0.02 mJ, which is very low compared to a mixture of gasoline with air or diesel fuel with air, which both require 0.24 mJ. Such low ignition energy creates a risk of premature, uncontrolled ignition and flame returning to the engine intake duct. Such premature ignition may be initiated by particles of unburned lubricating oil in the fuel-air mixture, hot spots in the combustion chamber resulting from the formation of deposits, hot electrodes of the spark plug, etc. [13, 28].

– High auto-ignition temperature

The auto-ignition temperature of hydrogen fuel is high compared to hydrocarbon fuels (853 K compared to ~623 K for gasoline and ~520 K for diesel oil). Thus, it is difficult to ignite the hydrogen-air mixture through compression in the engine cylinder and an external ignition source is usually required. Therefore, the auto-ignition temperature is an important factor in determining the engine's compression ratio, which is related to the temperature of the compressed mixture. The possibility of increasing the compression ratio makes it possible to increase the engine thermal efficiency. On the other hand, the high auto-ignition temperature of hydrogen makes it difficult to achieve auto-ignition in a diesel engine [1, 13, 28].

– Small distance of flame quenching from the cylinder wall

The quenching distance is the shortest distance from the inner wall of the cylinder at which the flame is quenched. In the case of hydrogen, the flame-quenching distance is 0.64 mm, while for gasoline it is 2 mm. Thus, it is more difficult to extinguish a hydrogen flame compared to other fuels. This creates the possibility of hydrogen burning in narrow gaps, such as between the piston and the cylinder, or retreating into the intake channel when the intake valve is not yet fully closed [1, 13, 28].

– High diffusivity

Hydrogen is characterized by a very high diffusivity, which means that its ability to disperse in the air is much greater than that of gasoline. This is beneficial from the point of view of the combustible mixture quality in the engine, as it facilitates the rapid creation of a homogeneous mixture of fuel and air. Moreover, if hydrogen leaks, it quickly dissipates in the surrounding air. In this way, the potential hazards of hydrogen leaks can be at least partially avoided or minimized [9, 19, 28].

– High octane number (~130)

This makes hydrogen more resistant to knocking combustion even when burning in very lean mixtures.

The interest in H2ICE has been increasing in recent years due to significant progress in optimizing their power and combustion processes, which allow for a significant increase in their thermal efficiency while reducing NO_x emissions [25]. This was graphically presented (Fig. 1) by the relationships between the air-fuel ratio (AFR), mean effective pressure, thermal efficiency and NO_x emission [2, 25]. The operation of H2ICE in the stoichiometric mixture range is unfavorable because at high engine load, the onset of knocking combustion occurs at lower BMEP values, while the thermal efficiency is low and NO_x emissions are quite high due to high cylinder temperatures. With high excess air coefficients (with very lean mixtures, AFR = 2.0–2.5), high thermal efficiency and low NO_x emissions can be achieved at the same time, (Fig. 1 – area in green dashed line). However, in this range of the excess air ratio, the combustion process slows down significantly, the stability of the combustion process becomes difficult to maintain and control, and NO_x emissions increase in transient engine operating states [2, 25]. All in all, the operation of the engine in the indicated range of the excess air coefficient has more advantages than disadvantages and is currently a direction for further work in the optimization of the H2ICE combustion process [2, 10, 15, 16, 23, 25, 35].

Overall, the research and development work carried out so far has shown that the combustion process of a lean hydrogen-air mixture with the selective addition of exhaust gas recirculation (EGR) is the basis for achieving competitive operational parameters for the H2ICE. This combustion process allows obtaining high torque at low engine speeds, high specific engine power, maximum thermal efficiency and low NO_x emissions [3, 24]. The stoichiometric mixture combustion process, due to the high laminar flame speed, high isentropic exponent and high adiabatic combustion temperature, favors the formation of nitrogen oxides (NO_x) [3, 24, 25]. Moreover, hydrogen combustion is characterized by short flame quenching distances, which causes the hydrogen flame to burn close to the walls of the combustion chamber. As a consequence, heat losses increase, which in turn leads to a reduction in engine efficiency [25]. Lowering the temperature in the combustion chamber y using a leaner combustible mixture counteracts these phenomena. Lean mixture combustion requires a large amount of intake air, which necessitates the use of a high compression ratio to obtain high engine efficiency [12].

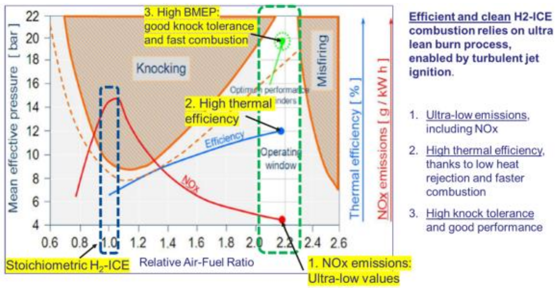

Fig. 1. Visualization of the relationships between the parameters involved in optimization of the combustion process in H2ICE [16, 17]

ICE can be divided into two groups based on the employed injection strategy: engines with indirect injection, i.e. with fuel injection into the intake manifold (PFI – port fuel injection or MPI – multi-point injection) and engines with direct injection (DI – direct injection). These two groups can be further divided into categories according to the ignition strategy [18, 36]. The divisions in question along with specific solutions were presented in Fig. 2 [18].

Injecting fuel into the intake port of each cylinder (ahead of the intake valves) has the advantage of providing a longer homogenization and mixing period for the mixture. At the same time, the turbulence generated at the intake valve ensures a high level of mixture homogeneity. In addition, lower injection pressures (~10 bar) can be used, which simplifies the injection system. However, with the transition to hydrogen fueling, problems may arise when using PFI. These include pre-ignition, knocking and flashback into the intake system due to low ignition energy and the low hydrogen flame quenching distance.

Moreover, the injected hydrogen displaces a significant amount of air from the air intake system, which significantly reduces the amount of specific power obtained and engine efficiency [32, 34]. PFI reduces the filling of the cylinder. The reduction in volumetric efficiency depends largely on the air-fuel ratio. This efficiency decreases the more the leaner the mixture becomes. At a typical relative air-fuel ratio of $\lambda = 2$, the air dose in the cylinder is reduced by approximately 20% due to the presence of hydrogen. As a result, this incentivizes a further increase in boost pressure.

Moreover, the injected hydrogen displaces a significant amount of air from the air intake system, which significantly reduces the amount of specific power obtained and engine efficiency [32, 34]. PFI reduces the filling of the cylinder. The reduction in volumetric efficiency depends largely on the air-fuel ratio. This efficiency decreases the more the leaner the mixture becomes. At a typical relative air-fuel ratio of $\lambda = 2$, the air dose in the cylinder is reduced by approximately 20% due to the presence of hydrogen. As a result, this incentivizes further increase in boost pressure.

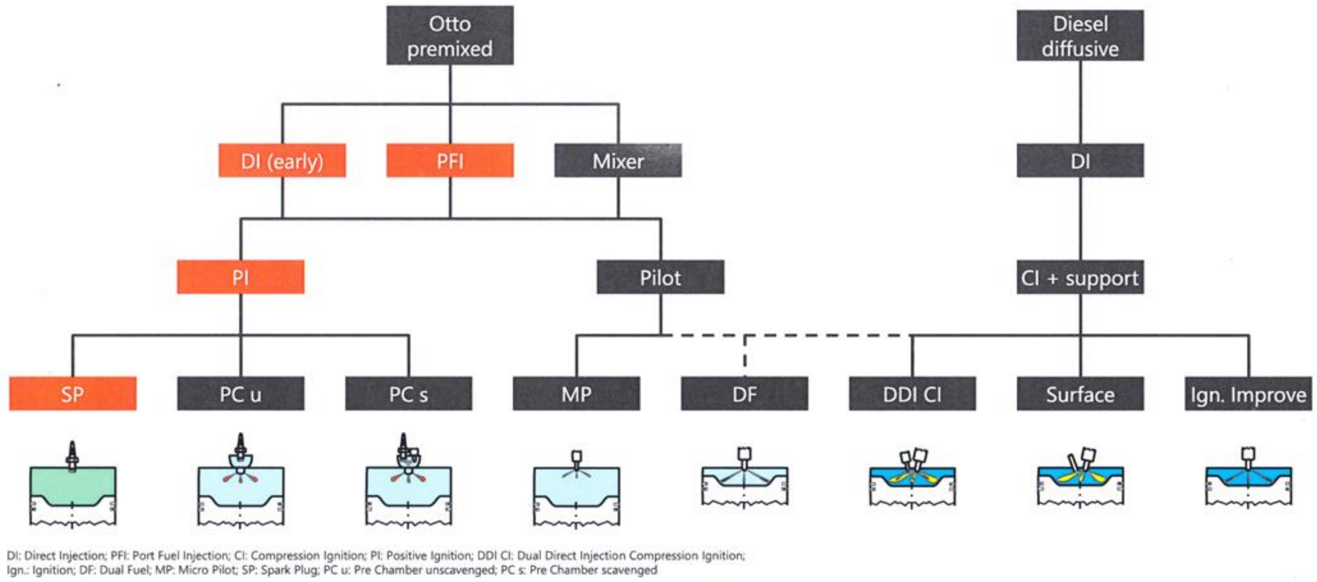

Fig. 2. Possible combustion strategies that can be employed in a H2ICE [18]

In the case of direct injection (DI) of fuel into the engine cylinder, the injection begins immediately after the intake valve closes, which should completely prevent the occurrence of dangerous phenomena such as reverse ignition due to the return of the flame from the combustion chamber into the intake channel. In addition, pre-ignition can be prevented because the exposure time of the hydrogen mixture to the so-called "hot spots" is shortened. Moreover, hydrogen is injected directly into the combustion chambers, which avoids the problems of limiting the engine's specific power due to the displacement of air by the injected hydrogen. The disadvantage of DI is the shorter time afforded to homogenize the air-fuel mixture before the start of the combustion. The probability of knocking combustion occurring increases as a consequence of this. However, direct injection enables the implementation of other combustion processes, including stratified combustion.

It is also possible to use a multiple injection strategy with controlled, variable fuel injection timing. Direct fuel injection requires a much higher injection pressure compared to indirect injection (PFI) [37].

H_2 combustion concepts in ICE can be divided into spark ignition combustion with a homogeneous pre-mixed chargé, and compression ignition combustion (Table 2). Spark ignition H2ICE using a pre-mixed homogeneous air-fuel mixture enables 100% CO_2 reduction, when ignoring trace emissions from burnt lubricating oil or SCR reagent. The main operation and performance challenges of the spark ignition H2ICE are specific power, fuel economy and transient performance. For low-pressure mixture concepts, only a moderate hydrogen injection pressure is needed and there is no need to use any additional compression systems. Thus, hydrogen can be supplied to the fuel injection system directly from the hydrogen storage pressure tanks. High-pressure mixture concepts, on the other hand, require a hydrogen injection pressure level of 250–300 bar. Therefore, an additional compression system becomes necessary to be able to utilize the maximum capacity of the hydrogen storage system [6].

In terms of low-pressure mixture concepts, multi-point fuel injection (MPI) combined with spark ignition is considered the most cost-effective solution. Good mixture formation, and therefore low NO_x emissions, partially compensate for the disadvantage of needing a higher boost pressure [14] (Table 2). In the case of MPI type indirect injection, a higher boost pressure is required if the same excess air ratio "λ" is to be maintained as in case of direct injection. Based on the concept of low-pressure mixture creation using direct injection (LP-DI) and spark ignition, the high calorific value of the created combustible mixture allows for obtaining a high BMEP. Currently, this mixture formation concept and combustion process is of greatest interest to researchers and manufacturers developing technologies related to H2ICE engines [30] (Table 2) [6, 14, 37]. To achieve the greatest specific power value, the lowest specific fuel consumption and the greatest stability in engine transient operating conditions, diffusion combustion (similar to diesel fuel) is indicated as the most appropriate (Table 2). To initiate a stable hydrogen ignition, it is beneficial to use pilot diesel fuel injection. However, to fully use the potential of the emission-free energy carrier hydrogen, it would be necessary to replace diesel fuel as the source of ignition initiation [30, 31].

To sum up, the greatest advantage of the DI fuel supply system is the increase in the efficiency of filling the combustion chambers and the reduction of work related to the pushing of the air-fuel mixture through the engine cylinders. Furthermore, with DI, higher torque can be achieved in the lower engine speed range as well as helping to avoid knock combustion and other irregularities in the process. These benefits are counterbalanced by the high technical difficulties associated with integrating the DI system in the case of H2ICE. Currently, this technology is still not fully developed yet and very expensive. The PFI system, on the other hand, is a well-known technology and ready for use in H2ICE. In this case, the components are available and very advanced, which allows the rapid development of new H2ICE engines, but with limited potential for optimization.

Table 2. Comparison of different mixture formation, ignition and combustion concepts in H2ICE [6, 14, 33]

	Homogeneous Combustion / Spark Ignited			Diffusion Combustion / Compressed Ignition		
	Multi-Point Injection (MPI)	Low&Mid Pressure Direct Injection (DI)		Multi-Point Injection (MPI)	High Pressure Direct Injection (DI)	
	Homogeneous lean pressure injection	Homogeneous lean pressure injection	Stratified lean pressure injection	Lean pre-mixed + diesel diffusion combustion	Diffusion combustion lean (Diesel –like)	Diffusion combustion lean (Diesel –like)
Mixture formation	Swirl	Swirl	Tumble	Swirl	Swirl / Tumble	Swirl / Tumble
Ignition	Spark plug			Compression ignition	Diesel pilot injection	Glow plug or spark plug (with pre-injection)
Combustion	Stoich/Lean	Lean	Lean	Stoich/Lean	Lean - Diffusive	
H_2 Injection pressure	5 – 20 bar	15 - 30 bar	40 – 100 bar	10 – 20 bar	250 – 300 bar	
Specific Power (HD engine)	< 25 kW/l	> 25 kW/l	> 25 kW/l	< 25 kW/l	~30kW/l	~30kW/l
Peak BMEP (HD engine)	< 20 bar	> 20 bar	> 20 bar	< 20 bar	> 25 bar	> 25 bar
Brake thermal efficiency	~ 40%	~ 43%	~ 43%	~ 42%	~ 47%	~ 50%
Pros	Low conversion effort	No risk of backfire	Good efficiency. Low NOx raw emission	Low conversion effort	Diesel like efficiency. Low NOx raw emission	Diesel like efficiency. Low NOx raw emission
	Easy to integrate	Robust against back-fire	Robust against back-fire	Easy to integrate	Same as KP-DI	Same as KP-DI
	Hardware available	Power density	Power density	Hardware available	Diffusive combustion possible	Diffusive combustion possible
	Low failure risk	Transient response	Transient response	Low failure risk		
			Smaller packing compared to low pressure			
			Potentially better mixture preparation			
Cons	Transient performance challenging. Risk of backfire	Conversion effort w/o benefits in terms of efficiency and power density	Dedicated cylinder head engine required	CO_2 emissions existing due to diesel	High pressure fuel supply	Very high injection pressure
CO_2 reduction compared to diesel	-100%	-100%	-100%	-30 ~-70%	-95%	-100%

The biggest disadvantage of the PFI injection system is the limited engine efficiency. Another significant disadvantage of this system is the possibility of the combustion process not taking place as intended. Therefore, the PFI system can be used in the first vehicle prototypes and then quickly enter the market as a low-cost solution [18, 30].

Achieving the intended, competitive performance of the H2ICE engine at full load with the maximum permissible NO_x emissions from the engine (< 10 g/kWh), requires a high excess air ratio (~1.9) at full load. State-of-the-art single-stage engine boost systems can meet these requirements under standard ambient and steady-state operating conditions. However, in the case of specific boundary conditions of the lean hydrogen combustion process, specific designs of the turbocharging system are required for this type of engine and its application. They can differ significantly from the existing systems in terms of complexity (Fig. 3). The combination of low exhaust gas enthalpy and high boost requirements in lean combustion concepts leads to the need for dedicated and particularly precise matching of the compressor and turbine compared to conventional engine boost systems. In addition, the turbine design must ensure a high potential for exhaust gas recirculation. To fully exploit the potential of such an H_2 combustion process, especially in direct injection concepts, it is crucial to ensure not only the appropriate design of the H_2 injection system [3], but also the engine boost system. With boost pressures required to achieve a mean effective pressure (BMEP) above 20 bar, single-stage boost systems quickly reach their limits. Therefore, more specialized boost systems are required, where some selected configurations were identified (Fig. 3) [7].

For example, the PFI H2ICE has proven that in addition to the 50% greater mass flow, a 90% higher boost pressure is required compared to a regular turbocharged petrol engine. This is something that a single-stage supercharging system cannot provide over a wide range of engine operating conditions. In this case, a two-stage boost system with a variable geometry turbocharger becomes necessary.

In the case of the H2ICE engine, trace amounts of CO, CO_2, HC and particulate matter resulting from the combustion of the engine lubricating oil, as well as urea injection in the case of an SCR catalytic converter, are expected to be found in the exhaust gases. Additionally, secondary emissions such as NH_3 and N_2O can form in the exhaust aftertreatment system itself and should be taken into account. However, NO_x emissions are the most difficult to reduce. As previously stated, this emission is strongly dependent on the excess air coefficient of the combustion mixture (so-called raw emissions), while the structure and effectiveness of the exhaust aftertreatment system depend on the composition of the exhaust gases, their temperature and mass flow rate [1]. Although exhaust gas aftertreatment systems and their components used in engines powered by conventional fuels, such as three-way catalytic converters (TWC), active and passive SCR and NO_x adsorbers, may be taken into account, in the case of engines powered by hydrogen they will not only have to be specially adapted to the composition and temperatures of hydrogen exhaust gases – but also to the required durability and operational reliability. Therefore, their design, and in particular the materials from which they are made, will have to be adapted to the different requirements of H2ICE [31].

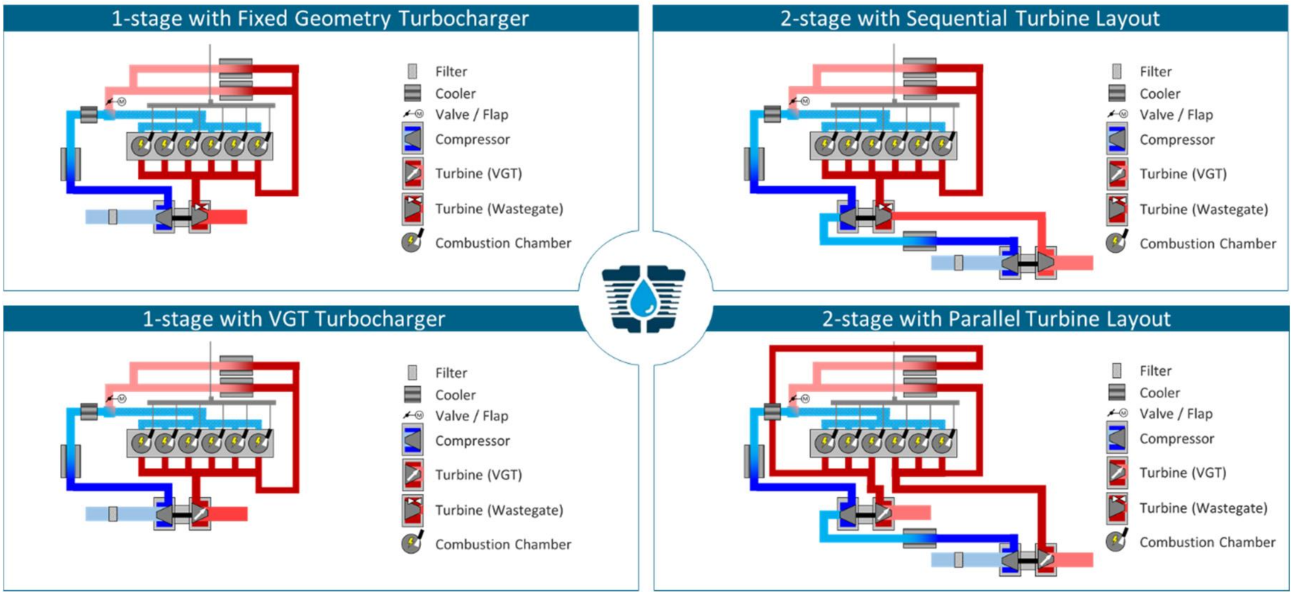

Fig. 3. Engine boost system concepts envisioned for H2ICE [7]

Figure 4 shows various concepts of exhaust gas aftertreatment systems for hydrogen-powered engines.

A different basic engine structure and a different excess air coefficient "λ" of the combusted hydrogen-air mixture were also taken into account [29, 30].

3. Disadvantages of H2ICE – challenges

A major disadvantage of H2ICE engines is their tendency to promote the formation of nitrogen oxides during combustion, especially when striving to obtain high specific power. In this case, the air-fuel ratio must be reduced to stoichiometric, leading to high NO_x emissions. A significant reduction in raw NO_x emissions, without the need to apply exhaust aftertreatment systems, requires an excess air coefficient of approximately $\lambda > 2.5$ to achieve the NO_x emissions level that would be compliant for passenger cars with the expected EU7 emission standards. This directly necessitates the use of a very high boost pressure and, consequently, engines that must be fundamentally resistant to high peak combustion pressure [30]. At the same time, the higher maximum combustion pressure, due to the laminar combustion speed being almost 6 times greater compared to liquid gasoline, causes greater mechanical stress and higher friction losses. Currently, most gasoline engines that have the structural properties to be used for H2ICE do not meet this requirement. Furthermore, very efficient and expensive turbocharging systems are needed, which must provide both sufficient air mass flow and boost pressure at low exhaust gas enthalpy levels. Otherwise, a significant reduction in engine specific power and very moderate torque levels would have to be accepted as the trade-off. Reducing boost pressure requirements can be achieved to some extent by a combination of diluting the combustible mixture with both air and external EGR. Operating the engine on a stoichiometric mixture without a combustion moderator (EGR and/or water injection) leads to irregular combustion processes [30].

The creation of NO_x reaches its peak at an excess air ratio of approximately $\lambda = 1.2$. With a leaner mixture, the combustion temperature decreases, which reduces the amount of NO_x produced. Lean combustion requires a large amount of intake air, which requires a high compression ratio to achieve the desired engine efficiency. Moreover, in this case the combustion speed decreases, which negatively affects the engine's efficiency. Hydrogen combustion is subject to anomalies such as engine knock, pre-ignition and ignited mixture backdraft. These anomalies pose problems when measuring downstream emissions because each anomaly can lead to changes in peak temperatures and emissions, making steady-state measurements challenging. An effective method of controlling combustion anomalies is to create a mixture. Direct injection (DI) after closing the intake valves can eliminate backdraft. However, the disadvantage of this method of fuel injection is the shorter homogenization time of the mixture, which means that locally areas with richer fuel content may create potential knocking combustion nodes as well as serve as sources of NO_x formation [27]. Another problem is the small quenching distance of the burning hydrogen flame from the wall, which results in increased wall heat losses, which leads to a reduction in the overall engine thermal efficiency [7].

Adapting the ICE for hydrogen fuel requires numerous changes to be made, the type and scope of which depends on the engine that is used as the basis for the hydrogen powered engine (spark ignition engine, compression ignition engine powered by diesel oil or natural gas) [6, 30, 34]. Generally, the cylinder head must usually be changed due to variable thermomechanical loads and high stresses resulting from the irregular combustion processes. These irregular processes cannot be avoided in certain H2ICE operating points. They also cause temperature and pressure fluctuations in critical areas of the engine head, such as valves or valve seats, which can lead to reduced lifespan due to fatigue. Elements of the crank system must also be adapted to the frequent occurrence of irregular combustion processes [6]. The exhaust gases of a hydrogen engine contain much more water vapor compared to the exhaust gases of an engine powered by hydrocarbon fuel. Not only exhaust gas

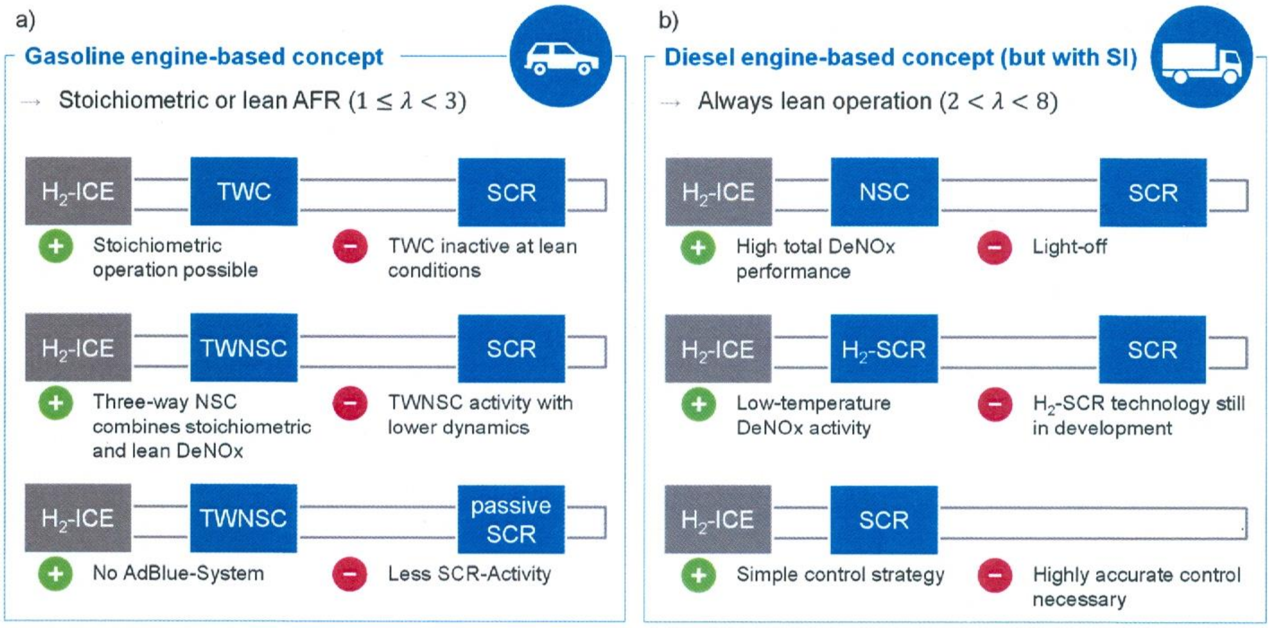

Fig. 4. Aftertreatment system layout for (a) the gasoline engine-based concept including stoichiometric operation and (b) the HD diesel engine-based concept at always lean conditions [29]

aftertreatment systems must be adapted to the increased water content in flue gases, but engine structural elements in contact with exhaust gases must also be adapter due to the higher corrosion risk [6].

Moreover, water entering the oil can accelerate the degradation processes and loss of lubricating properties. Therefore, managing the water content in the engine crankcase proves to be yet another challenge to be solved with H2ICE. It is also necessary to develop an efficient, reliable crankcase ventilation system, since a large amount of unburned hydrogen may penetrate through it, which could otherwise lead to an explosion hazard. At the same time, the piston ring assembly should minimize oil entry into the combustion chamber because, as explained earlier, oil droplets are a potential source of emissions of carbon oxides, hydrocarbons and particulates, as well as a pre-ignition source. To sum up, in recent years, great progress has been made in the development of hydrogen-powered internal combustion engines, significantly improving their performance by using direct hydrogen injection into the combustion chambers and optimizing the organization of the combustion process and turbocharging. However, the operation and popularization of internal combustion engines powered by hydrogen fuel are still associated with several challenges, especially in terms of improving reliability, which must be addressed and solved in the course of their further development. These concern maintaining low lubricating oil consumption, further optimization of hydrogen fueling processes and combustion strategy, including counteracting premature fuel ignition. Greater attention should also be paid to the harmful effects of hydrogen on metals and their alloys (hydride formation, hydrogen embrittlement, cracking caused by hydrogen leakage, and formation of hydrogen bubbles). Another challenge is the very low lubricity of hydrogen, which causes premature wear of elements that come in contact with it, such as intake valves and engine valve seat seals, injector needles and their seats (loss of airtightness), etc. Problems related to the engine lubrication system and the lubricating oil itself also require solutions. As the oil is quickly diluted with a large amount of water released from the hydrogen combustion process [30, 31].

4. Opportunities for H2ICE

Climate protection is becoming an increasingly political issue, which results in far-reaching environmental protection regulations, in particular covering economic sectors using piston combustion engines. Concerns about the impact of combustion engines on climate change have become a publicly politicized subject. Impartial assessments of the actual impact of combustion engine emissions on climate change are necessary, taking into account the enormous progress that has been made in reducing all standardized exhaust emissions from combustion piston engines (Euro 1–Euro 6; Euro 7).

In addition to the currently rapidly developed and popularized electric (battery-powered) vehicle drives and drives using fuel cells, emission-free fuels also offer great opportunities to significantly reduce CO_2 emissions. Among them, hydrogen is given wide recognition as a fuel that does not contain carbon and does not cause CO_2 emissions. Research that has already been carried out showed that H2ICE can become a drive system of the future, especially in the commercial vehicle and off-road machinery sectors, indicating that it can achieve similar levels of performance and efficiency as a modern compression-ignition engine. The criteria that a commercial vehicle must meet to qualify as (ZEV – Zero Emission Vehicles) are set out in EU Regulations 2019/1242 and 2017/2400. In the case of a heavy duty truck, which is outlined to be a vehicle powered by a non-combustion engine, or by an internal combustion engine that emits less than 1 g CO_2/kWh, following Regulation (EC) No 595/2009 and its implementing acts, or under Regulation (EC) No. 715/2007 of the European Parliament and of the Council and its implementing acts (European Parliament, 2019). According to these regulations, the only currently known combustion engine that could feasibly meet the strict EU regulations is a hydrogen-powered combustion engine. It should be remembered that in truck transport the electrification of drive systems is currently still significantly delayed compared to the vehicles of the passenger transport sector. Moreover, hydrogen as an energy carrier still has a higher storage density than batteries [26]. Hydrogen also has a much shorter refueling time than batteries, being much closer to fossil fuel refueling, which makes it more convenient to use than rechargeable batteries. Compared to a fuel cell-based drive system, H2ICE offer the following advantages: much lower purity requirements of hydrogen fuel used to power them, greater durability and longer lifespan, as well as much simpler operation and lower cost of such a drive system [11]. The hydrogen combustion engine is the next logical step in the evolution of a conventional combustion engine and is similar to it in terms of structure, operation and operating conditions. Advanced technological and design modifications, which are now possible, can change the conventional combustion engine into a H2ICE characterized by almost zero CO_2 emissions [17, 30]. Therefore, for heavy commercial vehicles for long-haul applications, H2ICE-based powertrains represent a rapid means to achieve CO_2-free mobility, especially in the short and medium term [27]. Hydrogen-powered internal combustion piston engines can be integrated with electric motors in electrified drive systems (hybrid drive systems). In addition to advantages in terms of efficiency and driving range, this leads to advantageous functional synergies and additional degrees of freedom in terms of design and operating strategies that need to be taken into account.

In 2020, the ACEA HD Expert Group on H2ICE was established and developed the necessary changes and amendments to UN R49 and UN R85 to enable the type approval of hydrogen combustion engines. ACEA experts presented the topic of OICA (Organisation Internationale des Construc-teurs d'Automobiles) in the first half of 2021. This group of experts systematically progressed their work which led to the following documents being presented at the beginning of this year:

- ECE/TRANS/WP.29/GRPE/2023/6 – Working document, joint EC/OICA proposal for a revision of R49 (07 series)
- GRPE 87 30 – Informal update document for ECE/TRANS/WP.29/GRPE/2023/6
- ECE/TRANS/WP.29/GRPE/2023/7 – Working document, OICA proposal to amend R85
- GRPE 87 16 Rev.1 – Informal update document for ECE/TRANS/WP.29/GRPE/2023/7

It is expected that further work by ACEA and OICE will soon lead to the final clarification of the regulations that will enable the full type approval of H2ICE [24].

5. Dangers for H2ICE

So far, hydrogen combustion engines have not yet entered into mass production around the world. This is primarily due to the insufficiently developed hydrogen infrastructure, which is required for all hydrogen-powered vehicles. At the same time, for the use of hydrogen in the transport sector to be sustainable it must be produced using energy from renewable sources. This requires significant development and a large increase in the rate of renewable energy production. Unfortunately, currently, the regions of the world where renewable energy – meaning primarily wind or solar – is available are not the same as the regions where this energy will be most needed [30]. Due to the still high costs of hydrogen and the small number of plants producing hydrogen, especially from renewable sources, hydrogen drive technologies are not yet competitive with conventional technologies, such as vehicles with combustion engines [35]. In practice, there are currently three main barriers that need to be overcome to the deployment of H2ICE-based powertrains in transportation to become economically and technologically viable. The first is the costs of hydrogen production and its delivery, which should be competitive with currently commonly used fuels, such as gasoline and diesel. The cost of hydrogen depends on the process/technology used for its production, the primary energy source and the adopted models of transport, storage and distribution. The second challenge is to develop a new or improved method for storing hydrogen in automotive vehicles to ensure a reasonable driving range. Thirdly, the cost of producing and operating hydrogen vehicles (H2ICE or FCV) should be reduced as a way of improving their life cycle assessment. Moreover, socio-cultural factors also play a significant role in the spread of hydrogen as a fuel in the transport system. Therefore, all information campaigns have a significant impact on the development of hydrogen technologies, especially at this early stage, to increase the awareness of people with low knowledge and have a positive impact on attitudes towards hydrogen vehicles.

The stance of the Council of the European Union, which has so far maintained their distance from this technology, will be of great importance for the development prospects and, above all, the spread of hydrogen-powered internal combustion engines. Currently, the EU is reluctant to diversify powertrains, focusing primarily on electric drives, especially in passenger cars, but not only. Currently, it is difficult to predict whether and to what extent the EU will support the development of power units based on H2ICE.

Conclusions

1. Hydrogen has the potential to become the sustainable fuel of the future, reducing global dependence on fossil fuel resources and significantly lowering automotive emissions.
2. Hydrogen, as a zero-emission fuel, can be used to make a piston combustion engine with zero emissions of CO_2.
3. H2ICE can produce trace CO, HC and particulate emissions solely from the combustion of engine lubricating oil entering the engine's combustion chambers.
4. NO_x emissions caused by H2ICE can be effectively reduced by optimizing the fuel supply and combustion systems (raw emissions) and using a dedicated exhaust aftertreatment system for H2ICE.
5. When high continuous engine power is required in low transient operating conditions, a hydrogen-powered internal combustion engine is a cost-effective approach to

CO_2-free long-distance transport, with a long service life, that relies on tested and proven technology.
6. It is possible to adapt both SI and CI engines to run on hydrogen.
7. In the medium term, a hydrogen drive system may be an alternative to electric drive systems in passenger cars until sufficient availability of fully renewable electricity is achieved.
8. H2ICE-based hybrid powertrains represent a viable alternative to electric and fuel cell drive systems to be used for light commercial vehicles in the medium to long term, both from a CO_2 equivalent and total cost of ownership perspective.
9. The advantage of H2ICE is that this technology can be brought to market relatively quickly, so it can be made available as a technology with minimal delay.
10. The operation of H2ICE presents several specific reliability challenges that will need to be addressed through further development. The already identified challenges concern maintaining low lubricating oil consumption, preventing irregularities occurring in the combustion process and ensuring the adequate durability of structural and operational elements of the engine, which can be caused by low H_2 lubricity and the so-called hydrogen embrittlement of metals.
11. The main challenge preventing the widespread use of hydrogen as fuel in automotive engine units is the limited on-board hydrogen storage technology for vehicles as well as the current scarcity of refueling stations.
12. The further development of H2ICE will require infrastructure and financial resources, which can only be achieved through a significant amount of political support, in particular from the EU.

Acknowledgements

This article was based on my own research work entitled: "Construction of a research stand with a hydrogen-powered internal combustion piston engine. Stage I: Development of assumptions for the construction of a hydrogen-powered engine stand and its power supply infrastructure; number: 1874/TE/21 (TE-5101-549/21) INiG–PIB.

Nomenclature

ACEA	European Automobile Manufacturers' Association
AFR	air fuel ratio
BMEP	brake mean effective pressure
CI	compression ignition
DI	direct injection
ECE	Europe Vehicle Certification & Solutions
EGR	exhaust gas recirculation
EU	European Union
FC	fuel cell
H2ICE	hydrogen internal combustion engine
ICE	internal combustion engine
LP-DI	low pressure direct injection
MPI	multi point injection
OICA	Organisation Internationale des Constructeurs d'Automobiles
PFI	port fuel injection
SCR	selective catalytic reduction
SI	spark ignition
TWC	three way catalyst
UN	United Nations
ZEV	zero emission vehicles

Bibliography

[1] Al-Baghdadi M. An overview of hydrogen as an alternative fuel. Encyclopedia 2020 https://doi.org/10.32545/encyclopedia202006.0003.v1 (accessed on 24.07.2023).
[2] Beatrice C. Technology review for SI ICE based powertrains with 50% brake thermal efficiency. International Workshop on Jan 21st, 2020 – Politecnico di Torino Energy Center.
[3] Bobusch B, Ebert T, Fink A, Nett O. Düse zur oszillierenden Direkteinblasung im H2-Verbrennungsmotor. MTZ Motortechnische Zeitschrift. 2021;82:42-47. https://doi.org/10.1007/s35146-021-0686-5
[4] Candelaresi D, Valente A, Iribarren D, Dufour J, Spazzafumo G. Comparative life cycle assessment of hydrogen-fuelled passenger cars. Int J Hydrogen Energ. 2021;46:35961-35973. https://doi.org/10.1016/j.ijhydene.2021.01.034
[5] Ciniviz M, Kose H. Hydrogen use in internal combustion engine. International Journal of Automotive Engineering and Technologies. 2012;1(1):1-15. https://dergipark.org.tr/tr/download/article-file/89368
[6] Dreisbach R, Arnberger A, Zukancic A, Wieser M, Kunder N, Plettenberg M et al. The Heavy-Duty Hydrogen Engine and its Realization until 2025Der Nutzfahrzeug-Wasserstoffmotor und seine Umsetzbarkeit bis 2025. 42nd International Vienna Motor Symposium. Vienna 2021.
[7] Ebert T, Leimann D, Maniezki G, Lahni T. Predictive 0D hydrogen combustion simulation. 30th Aachen Colloquium Sustainable Mobility. 2021:1131-1147.
[8] Eichlseder H, Klell M. Wasserstoff in der Fahrzeugtechnik. 2nd Edition. Vieweg+Teubner. 2010.
[9] Faizal M, Chuah LS, Lee C, Hameed A, Lee J, Shankar M. Review of hydrogen fuel for internal combustion engines. Journal of Mechanical Engineering Research and Developments (JMERD). 2019;42(3):35-46. http://doi.org/10.26480/jmerd.03.2019.35.46
[10] Golisano R, Scalabrini S, Arpaia A, Pesce F, Vassallo A, Borgia L et al. PUNCH Hydrogen Internal Combustion Engine & KERS: an Appealing Value-Proposition for Green Power Pack. 42nd International Vienna Motoren Symposium, Vienna 2021.
[11] Huth V, Virnich L, Pfortje A, Pischinger S, Sterlepper S, Wolff T et al. The hydrogen combustion engine as zero impact emission powertrain concept. 30th Aachen Colloquium Sustainable Mobility 2021:1113-1130.
[12] Jincheng L, Dingchao Q, Linghai H, Heyang M, Yingjun G, Yanfeng G et al. FAW high-efficiency zero-emission Miller cycle hydrogen internal combustion engine for carbon neu-

trality. 43rd International Vienna Motor Symposium. Vienna 2022.

[13] Kapus P, Raser B, Arnberger A, Heindl R, Egert M, Kunder N et al. High efficiency hydrogen internal combustion engine – carbon powertrain for passenger car hybrids and commercial vehicles. 43rd International Vienna Motor Symposium. Vienna 2022.

[14] Karim GA. Hydrogen as a spark ignition engine fuel. Int J Hydrogen Energ. 2003;28(5):569-577. https://doi.org/10.1016/S0360-3199(02)00150-7

[15] Klepatz K, Rottengruber H, Zeilinga S, Koch D, Prűmm W. Loss analysis of a direct-injection hydrogen combustion engine. SAE Technical Paper 2018-01-1686. 2018. https://doi.org/10.4271/2018-01-1686

[16] Koch DT, Sousa A, Bertram D. H_2-engine operation with egr achieving high power and high efficiency emission-free combustion. SAE Technical Paper 2019-01-2178. 2019. https://doi.org/10.4271/2019-01-2178

[17] Korn T, Ebert T, Vonnoe M, Tala H, Lang M. Hydrogen engines strong case – new performance benchmarks with hydrogen direct injection. 43rd International Vienna Motor Symposium. Vienna 2022.

[18] Korn T, Nobile RF, Grassinger D. Zero-emission, maximum performance – the latest generation of hydrogen combustion engines. 42nd International Vienna Motor Symposium. Vienna 2021.

[19] Kumar N. Hydrogen use in internal combustion engine. The International Journal of Advanced Culture Technology. 2015;2:87-99. https://doi.org/10.17703/IJACT.2015.3.2.87

[20] Menes M. Program initiatives of public authorities in the field of hydrogenation of the economy in a global perspective, as of the end of 2020. Combustion Engines. 2022;189(2):18-29. https://doi.org/10.19206/CE-142170

[21] Matla J. Possible applications of prechambers in hydrogen internal combustion engines. Combustion Engines. 2022;191(4):77-82. https://doi.org/10.19206/CE-148170

[22] Munshi S, Huang J. The potential for a high efficiency hydrogen engine using Westport Fuel Systems‘ commercially available HPDI fuel system. 42nd International Vienna Motor Symposium. Vienna 2021.

[23] Pauer T, Weller H, Schünemann E, Eichlseder H, Grabner P, Schaffer K. H2 ICE for future passenger cars and light commercial vehicles, 41th International Vienna Motoren Symposium. Vienna 2020.

[24] Richter K, Rost F, Schumacher M. Type approval of H_2 engines update on 87th GRPE Meeting Joint change proposals of EC&OICA for UN R49&UN R85. 87th GRPE Session 11–13 January 2023.

[25] Scalabrini S, Golisano R, Borgia L, Costa N, Fierro E, Pesce F et al. PUNCH H_2-ICE&Flybrid KERS for decarbonizing off-highway applications. 30th Aachen Colloquium Sustainable Mobility. 2021:1079-1112.

[26] Schutting E, Roiser S, Eichlseder H, Lux S, Kleiber S. Hydrogen engine exhaust aftertreatment. 43rd International Vienna Motor Symposium. Vienna 2022.

[27] Sens M, Danzer C, von Essen C, Brauer M, Wascheck R, Seebode J et al. Hydrogen powertrains in competition to fossil fuel based internal combustion engines and battery electric powertrains. 42nd International Vienna Motor Symposium. Vienna 2021.

[28] Srinivasana CB, Subramanian R. Hydrogen as a spark ignition engine fuel technical review. International Journal of Mechanical & Mechatronics Engineering IJMME-IJENS. 2014;14(05):111-117.

[29] Sterlepper S, Fischer M, Claßen J, Huth V, Pischinger S. Energies. 2021;14:8166. https://doi.org/10.3390/en14238166

[30] Stępień Z. A comprehensive overview of hydrogen-fueled internal combustion engines: achievements and future challenges. Energies. 2021;14:6504-6516. https://doi.org/10.3390/en14206504

[31] Stępień Z, Urzędowska W. Tłokowe silniki spalinowe zasilane wodorem – wyzwania. Nafta-Gaz. 2021;12:830-840. https://www.inig.pl/magazyn/nafta-gaz/Nafta-Gaz_2021-12-06.pdf

[32] Verhelst S. Recent progress in the use of hydrogen as a fuel for internal combustion engines. Int J Hydrogen Energ. 2014;39:1071-1085. https://doi.org/10.1016/j.ijhydene.2013.10.102

[33] Virnich L, Durand T, Schaub S, Ghetti S, van der Put D. Powertrain layout optimization to maximize benefits of a H_2 internal combustion engine. 43rd International Vienna Motor Symposium. Vienna 2022.

[34] Virnich L, Lindemann B, Müther M, Schaub J, Huth V, Geiger J. How to improve transient engine performance of HD hydrogen engines while maintaining lowest NO_x emissions. 42nd International Vienna Motor Symposium. Vienna 2021.

[35] Walter L, Sommermann A, Hyna D, Malischewski T, Leistner M, Hinrichsen F et al. The H_2 combustion engine – the forerunner of a zero emissions future. 42nd International Vienna Motor Symposium. Vienna 2021.

[36] Yamane K. Hydrogen fuelled ICE, successfully overcoming challenges through high pressure direct injection technologies: 40 year of Japanese hydrogen ICE research and development. SAE Technical Paper 2018-01-1145. 2018. https://doi.org/10.4271/2018-01-1145

[37] Yip HL, Srna A, Yuen ACY, Kook S, Taylor RA, Yeoh GH et al. A review of hydrogen direct injection for internal combustion engines: towards carbon-free combustion. Appl Sci. 2019;9:4842. https://doi.org/10.3390/app9224842

Prof. Zbigniew Stępień, DSc., DEng. – Performance Testing Department, Oil and Gas Institute – National Research Institute, Poland.

e-mail: *stepien@inig.pl*

Article citation info:
Skonieczna D, Szczyglak P, Lemecha M. Modelling lubricating oil wear using fuzzy logic. Combustion Engines. 2024;197(2):42-49. https://doi.org/10.19206/CE-183186

Daria SKONIECZNA
Piotr SZCZYGLAK
Magdalena LEMECHA

Combustion Engines
Polish Scientific Society of Combustion Engines

Modelling lubricating oil wear using fuzzy logic

ARTICLE INFO

Received: 28 November 2023
Revised: 11 January 2024
Accepted: 28 January 2024
Available online: 3 February 2024

The content of this article presents research on used and fresh engine oils. The aim of the experiment is to preliminarily develop a method for assessing the condition of engine oil subjected to service. A four-ball tester was used to compare the lubricating properties of the engine oil as one component of the tribosystem under laboratory conditions. The method used to determine the mashing load consisted of subjecting the kinematic node to a linearly increasing load with a build-up rate of 409 $N \cdot s^{-1}$ under operating conditions of approximately 20°C and a spindle speed of 500 rpm. The presented article is a continuation of the consideration of the lubricating properties of engine oils subjected to operation. The tests carried out made it possible to observe that fresh oils are characterised by their ability to carry higher loads in relation to oils subjected to service. This is evidenced by the obtained values of scuffing loads, which have a higher value for fresh oils (The average percentage increase in scuffing load for fresh oils was 62.23%). Comparing the friction torque characteristics with each other, it can be seen that the values of maximum friction torque are also higher for the fresh oils group. The modelling process made it possible to characterise changes in the tribological properties of the lubricating oil being used. In the future, the described model will be extended to include further input parameters (viscosity, contaminant content, fractional composition, etc.), which will allow a multi-parametric assessment of lubricating oil wear.

Key words: *engine oils, degree of wear, four ball tester, friction, scuffing load*

1. Introduction

The primary function of oil in an internal combustion engine is to protect it from wear and to slow down the depletion of its operating potential. As is well known, machines are subject to wear and tear in the process of use. This process also applies to lubricants, which are an integral part of tribosystems.

Most often, lubricating oil changes in an internal combustion engine take place when the kilometers or time resourse is exhausted [10]. Modern cars are also equipped with systems that generate messages about the need to change engine oil based on algorithms analysing driving style or signals from oil quality sensors measuring selected oil parameters or contaminant concentrations. As recent research [17] shows, the strategies used in the lube oil change process are insufficient (low precision). This can lead to a situation where engine oil degradation is so high that the oil fails to perform its key feature, resulting in reduced engine life. This is not always unambiguous, as other studies [8] show that engine oil still retains its properties despite having exhausted its entire service life. The work [7] considering used engine oils also allows us to conclude that the vehicle mileage commonly accepted as an indicator of lubricating oil change intervals is not an unambiguously reliable criterion. Due to these discrepancies, there is a need to develop a universal method for assessing the condition of engine oil to determine its ability to protect engine components.

Effective engine wear protection occurs when a permanent lubricating oil film is formed between tribological pairs. This phenomenon should occur for a wide temperature range - both after the engine has warmed up and shortly after starting at low operating environment temperatures. Engine starting at low temperatures results in increased lubricant consumption [14]. High temperatures also contribute to engine oil degradation [12]. In the temperature aspect, engine oil plays another important function, it dissipates heat. In addition to the wide range of operating temperatures at which the oil must function, a wide range of loads is also indicated in the literature. These varying operating conditions of the oil including engine start-up, idling, varying load depending on the driving mode [16] should not adversely affect the protection of the tribological nodes and the wear intensity of the friction surfaces. Another factor related to the different temperature conditions in the engine is the formation of high and low temperature sludge. This is due to the accumulation of oxidation products, which are not neutralised by the limited amount of additives improving the lubricating properties of the engine oil. The accelerated oxidation process can be influenced by overheating of the lube oil, which leads to the formation of sludge plugs that block the flow of oil and thus the distribution of oil in the engine compartment, which contributes to the aforementioned reduction in heat dissipation [20]. Another important function of engine oil is corrosion protection [13]. Its intensity is inhibited by adding inhibitors to the oil. The anti-wear additives in the oil help to prevent abrasive or adhesive wear, but also corrosion wear.

The degradation of engine oil is contributed to by phenomena such as oxidation and the depletion of additives responsible for improving lubricating properties [2]. This results in the need for more frequent oil changes to effectively protect the engine from wear. Another reason for this phenomenon is the contaminants that accumulate during the operation process. One of them is carbon black [11], which, by deteriorating tribological properties, causes an intensification of wear of the tribosystem understood as engine and lubricant. Work [5] shows that, with the process of operation, carbonaceous contaminants accumulate in the annular grooves of the engine, resulting in oil degradation. The effect of increased soot content in engine oil is to increase viscosity and also to form an abrasive substance that damages mating surfaces [19]. The formation of soot agglomerates can lead to the closing of oil distribution channels in the engine and the local occurrence of dry friction, resulting in increased wear. A second type of engine oil contamination involving metallic elements that are solid contaminants in the engine oil can pose analogous threats to the system.

Monitoring the condition of engine oil can bring benefits not only in terms of protecting mechanical systems, but also in environmental terms. This relationship exists for both the production and disposal of engine oils [9]. The possibility of extending the service life of lube oil that continues to perform its protective function has a direct impact on reducing chemical waste.

Failure to detect a defect during engine operation can lead to damage, the consequence of which may be an increased intake of engine oil, which is burned in the engine compartment causing the vehicle to fail to meet emission standards [4]. While this is insignificant in the case of a motor vehicle engine, in the case of large marine engines, the negative environmental impact is already significant and is associated with high operating costs for such a vessel.

One of the most popular lubricant testing stations is the tribotester. The test results from this tribotester make it possible to assess the quality of the engine oil under test. As the work [6] shows, if the wear trace obtained during a test run is small, it can be inferred that the lubricant has good anti-wear properties. Extending this inference, it can be concluded that the engine oil has not yet degraded and continues to protect the kinematic node. The validity of using this apparatus when considering lubricant quality is confirmed by work [1]. The high reproducibility of the testing performed with the four-ball tester ensures that the results obtained are precise.

Due to the multitude of parameters affecting the lubricating oil wear process, it is necessary to use statistical methods to show the relationships between the various parameters. Such an approach was presented in the work [3]. Its results confirmed the great potential of the application of statistical analysis in the consideration of engine oils, as well as the importance of modelling in cognitive processes in this area.

The present work is a continuation of the study [15] of motor vehicle oils. The study of the oil's physicochemical, rheological, and tribological properties has been supplemented with results obtained using a four-ball tester. An analysis of the available literature indicates that the systems used to assess engine oil degradation status are inaccurate and may have a negative impact on the environment and the operating process of an internal combustion engine. The aim of this study is to develop a method for assessing engine oil consumption. The method is based on a model using artificial intelligence algorithms (Mamdani model). The model adopted is scalable (it can be easily extended to include further parameters affecting the oil consumption rate). The coefficients in the model were determined on the basis of test results using a four-ball apparatus. The model created must be considered as a base, which will be extended based on the results of tests to be performed in the future.

2. Methodology

2.1. Object of study

Eleven engine oils obtained from passenger vehicles used in urban and extra-urban traffic were experimentally tested. The oils had five different viscosity grades (0W30, 5W20, 5W30, 5W40, 10W40). Both fresh and used lubricating oils were tested. The mileage range for the used oils was 5002 to 15,000 km. The oils were used in both compression-ignition (2 units) and spark-ignition (9 units) engines. In two cases the spark ignition engines were powered by LPG. The vehicles from which the lubricating oils came had mileages between 15,000 and 3,622,211 km. The engines lubricated by the oils had displacements in the range of 1 to 2.5 dm^3 and had power outputs of 57 to 120 kW. Detailed data on the oils tested and the vehicles in which they were used are presented in Table 1. A passive experiment was adopted during the research (users of the vehicles from which the used oil originated decided on the course of the exploitation process and the mileage at which the used oil was replaced with fresh oil).

2.2. Tribological tests

Tribological tests were carried out using a four-ball tester. The tests carried out consisted of subjecting the kinematic node to an increasing load for 18 s. The load was

Table 1. Data on operating conditions of used oil samples [15]

Engine oil				Vehicle			
#sample number	Producent	Viscosity class SAE	Oil mileage [km]	Type of fuel to power the engine	Engine capacity [dm^3]	Nominal motor power [kW]	Car mileage at oil drain [km]
1	Fanfaro	5W30	12,650	Gasoline + LPG	1.4	63	362,211
2	Mobil	5W30	14,141	Gasoline	1.6	85	91,635
3	Shell	5W30	5481	Gasoline	1.2	57	110,007
4	Total	5W40	7734	Gasoline	1.6	120	60,631
5	Fanfaro	5W30	11,452	Gasoline + LPG	1.6	63	157,473
6	Selenia	5W30	14,998	Diesel	1.6	77	101,021
7	Shell	5W30	5002	Gasoline	1.0	57	52,333
8	Mobil	10W40	6500	Gasoline	1.6	72	330,041
9	Fanfaro	5W30	5159	Diesel	2.5	88	196,427
10	Total	5W20	5126	Gasoline	1.5	110	112,927
11	Volkswagen	0W30	15,000	Gasoline	1.0	95	15,000

built up in the range 0–7200 N, with a load build-up rate of 409 N·s^{-1} throughout the run. The spindle speed was 500 rpm. The initial temperature of the test lubricant was in the range of 20–25°C. During the tests, the friction torque, the temperature in the grip of the kinematic node and the load applied to the friction node were measured. The measurements were sampled at a frequency of 50 Hz. The tests were performed in accordance with the requirements of PN-76/C-04147. Three tests runs were performed for each lubricating oil during the experiment. The result characterising each lube oil was derived from the average of the three attempt. They were subjected to an assessment as to whether there was a result with a gross error in a given set of results (Q-Dixon test).

3. Results

3.1. Results of tribological tests

Based on the experimental results, a graph of friction torque in the load domain (Fig. 1) was drawn up for each engine oil tested. Oils were designated by numbers preceded by the "#" sign. Numbers 1 to 11 were assigned to oils that had been used in the engines, while numbers 12 to 19 were assigned to corresponding fresh lubricating oils (the smaller number of fresh oils is due to the use of the same oils in more than 1 engine).

In the load range from 0 to about 1300 N for all engine oils tested, the course of the mashing torque showed almost the same increase. Changes can be observed in the range 1300–2800 N. In this range, a dynamic increase in frictional torque was recorded for all samples, but at a load of about 1790 N (red line), 2 groups of oils for which the dynamics of change differed were distinguished. In the first group, a dynamic increase in frictional torque was observed earlier, and these were oils in service, while the second group, for which a sharp increase in rubbing torque occurred later, were fresh oils. To detail this phenomenon, the scuffing load values for in-service and fresh lube oils were read from Fig. 1 and the relative differences between them were determined (Table 2 and Fig. 2). In addition, it was observed that, for fresh oils, the maximum values of the frictional torque were higher than for in-service oils and the load range in which the dynamic increase and decrease in frictional torque occurred was narrower than for the runs obtained for in-service oils.

Figure 2 shows the scuffing load values for used and fresh engine oils.

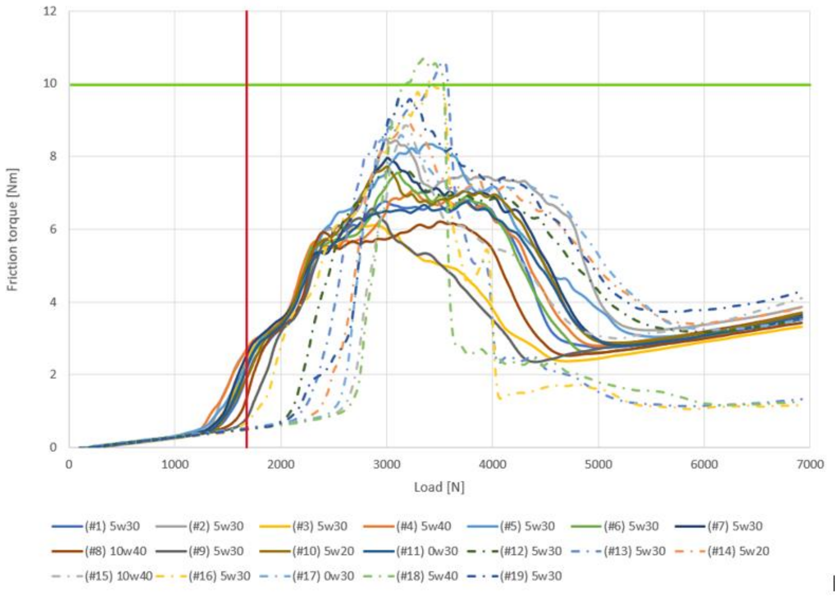

Fig. 1. Friction torque waveform in the load domain of a kinematic node

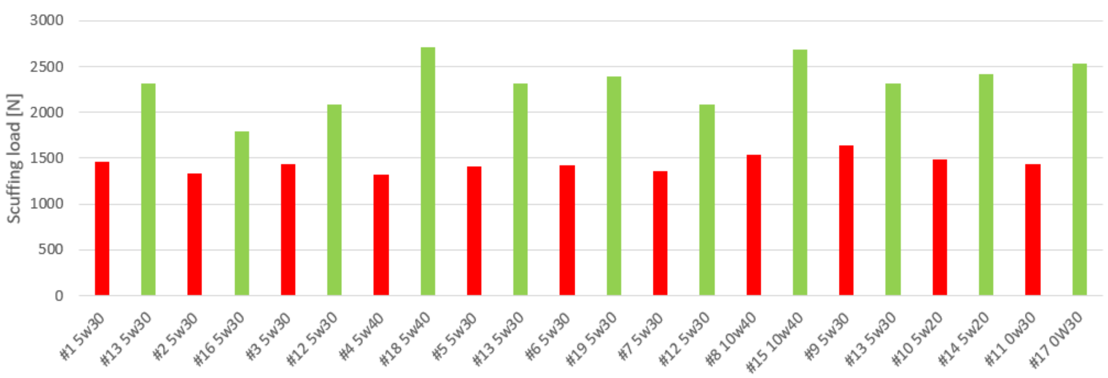

Fig. 2. Measured scuffing load values: green – fresh engine oils, red – used engine oil

Table 2. Scuffing load of engine oils

Group	Engine oil	Scuffing load [N]	Relative increase in scuffing load [%]
1 – used	#1 5W30	1467	57.94
2 – fresh	#13 5W30	2317	
1 – used	#2 5W30	1329	34.99
2 – fresh	#16 5W30	1794	
1 – used	#3 5W30	1431	45.98
2 – fresh	#12 5W30	2089	
1 – used	#4 5W40	1323	105.44
2 – fresh	#18 5W40	2718	
1 – used	#5 5W30	1407	64.68
2 – fresh	#13 5W30	2317	
1 – used	#6 5W30	1426	67.39
2 – fresh	#19 5W30	2387	
1 – used	#7 5W30	1360	53.60
2 – fresh	#12 5W30	2089	
1 – used	#8 10W40	1544	74.29
2 – fresh	#15 10W40	2691	
1 – used	#9 5W30	1641	41.19
2 – fresh	#13 5W30	2317	
1 – used	#10 5W20	1493	62.09
2 – fresh	#14 5W20	2420	
1 – used	#11 0W30	1434	76.92
2 – fresh	#17 0W30	2537	

It was observed that all of the scuffing loads for fresh oils were greater than those for in-service oils. In the case of fresh oils, the values were greater from 34.99% to as high as 105.44%. The average percentage increase in mashing load was 62.23%, and the median was 62.09%.

After statistical processing of the results obtained, an equation describing the average relationship between oil mileage and scuffing load was determined:

$$F = -0.07128 \cdot P_O + 2222.65752 \text{ [N]} \quad (1)$$

where P_O – oil mileage [km].

A green line was also plotted in Fig. 1, visualising a friction torque level of 10 Nm, above which the machine drive was switched off for safety reasons. Three of the samples tested exceeded this threshold. All of the oils tested, for which the friction torque of 10 Nm was exceeded, belonged to the group of fresh oils. It should also be noted that, during the experiment, in some cases there was a phenomenon of welding of the top ball placed in the machine spindle with the balls placed in the chuck. This phenomenon was noted in the case of three oils: #13 5W30 (in two of the three trials), #16 5W30 (in two of the three trials) and #18 5W40 (in one of the three trials). These data are the same as the samples that passed the machine's safety threshold.

It is not only the scuffing forces that change with oil mileage. Another parameter for which a similar relationship was noted is wear diameters. These were determined during ball apparatus tests in accordance with ASTM D 4172-94 and are described in [15]. The values of the wear diameters are shown in Fig. 3. In this case, an increase in wear diameter with increasing oil mileage was observed in all tests.

After statistical treatment of the data shown in Fig. 3, an equation describing the average relationship between oil mileage and wear diameter was determined:

$$D = 0.03250253 \cdot P_O + 597.67580742 \text{ [µm]} \quad (2)$$

where P_O – oil mileage [km].

4. Model for estimating oil consumption

As part of the work, a model was built to estimate oil consumption rates. When building the model, it was assumed that it must be scalable (the possibility of adding further input parameters on the basis of which the degree of wear will be determined). For this reason, it was decided to use the Mamdani model, which belongs to the group of models from the area of artificial intelligence (fuzzy logic). To build the model, data obtained during the experimental research described in Chapter 3 were used.

The input variables in the model were:
- scuffing force F [N]
- wear diameter D [µm]
- oil mileage P_O [km]

and output variables:
- wear rate Z [%].

In the first stage of model construction, linguistic variables were adopted for which their spaces (membership functions) were determined. Next, the coefficients in the membership functions were determined based on equations 1 and 2, assuming that the oil mileage according to the service life should be 15,000 km (readings of significant values from equations 1 and 2 for mileage: 3.75, 7.5, 11.25 and 15,000 km). To obtain the fuzzy consequences, the limiting equations of the coordinate of the ordinate axis were determined and the rule aggregation equation was determined. The results of this work are presented in Tables 2 and 3.

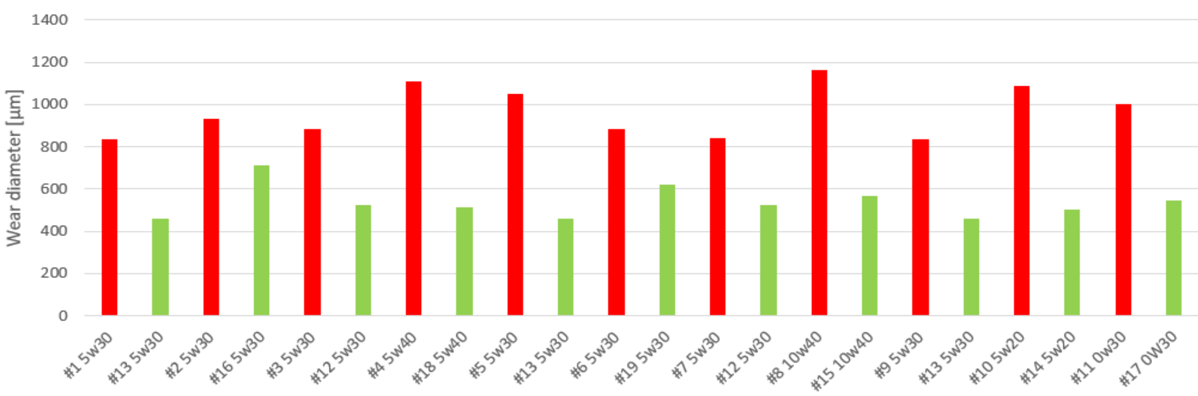

Fig. 3. Measured values of the wear diameter [14]: green – fresh oil, red –used oil

Calculations were made using the model, the results of which are shown in Fig. 4. The calculations were made for data obtained during experimental tests (engine oil runs, scuffing forces and wear diameters). Oil wear rates were determined in 3 variants (by condition, by remaining oil life, mixed model).

Analysing the calculation results shown in Fig. 4, it was found that the oil consumption rate determined from the model by condition indicates greater oil degradation for mileages up to about 11,000 km compared to the value of this parameter determined from the model by resurfacing. The relationship takes on an inverse relationship once this mileage is exceeded. This is due to the fact that the determined values of engine oil degradation by condition were based on tribological parameters. The values of these parameters are strongly influenced by the oil's rheological properties (viscosity), which change during operation. The lubricating oil's viscosity changes in the process of use. After an oil change, viscosity initially decreases and reaches a minimum after a few thousand kilometres. The viscosity then starts to increase to reach a value close to or greater than the viscosity of fresh engine oil after the resurface is exhausted. For a description of this phenomenon, see [18]. Oils with higher viscosity are more resistant to oil film rupture, which has a positive effect on the wear process in highly loaded tribological pairs.

5. Conclusion

The tribological tests carried out allow us to conclude that there is a significant difference between fresh and in-service oils. The friction torque waveforms as a function of load for fresh oils are more dynamic in a narrower load range than in the case of used oils. Significantly lower scuffing loads occurred in the group of in-service oils compared to fresh oils, indicating that fresh oils have the ability to carry higher loads and protect the mating components more effectively. As the results show, the opposite is true for maximum friction torque. It is the used lube oils subjected to the same load that show a lower friction torque value than fresh oils. For all the engine oils tested, a decrease in scuffing load and an increase in wear diameters were observed during operation. These phenomena were used in the construction of a model to estimate the degree of wear. The developed model uses artificial intelligence algorithms (fuzzy logic) and can be extended with new input parameters, which will allow it to increase its accuracy of inference after adding further parameters that will be identified in the course of future research. The presented results from the modelling process show that it is possible to determine the degree of engine oil wear based on its condition and remaining life. Thus, by comparing the calculation results, it is possible to show the differences in the dynamics of oil consumption changes according to the two strategies. In addition, the changing differences in the degree of engine oil wear according to the different strategies showed that the tribological parameters determined during oil testing do not have a linear characteristic associated with the run and are related to the rheological parameters of the oil, which include viscosity. This parameter has a non-linear characteristic during the operating process. In the first stage, it decreases, and after reaching a minimum, which occurs after a few thousand kilometres of mileage, it then begins to increase mainly due to the accumulation of wear products and contaminants in the engine oil.

The reduction in lubricating oil viscosity results in a lower oil film life and thus protection of the mating components against wear. The advantage of the represented approach is that the presented model can be successively extended with further criteria for the assessment of lubricants so that a comprehensive evaluation can be carried out. As a result of the modelling, it was found that oil consumption assessed by mileage in the range from 0 to about 50% of the assumed distance, which was 15,000 km, was higher than the consumption determined by condition. In the second mileage interval (above 50%), consumption according to condition was lower than consumption according to mileage. This demonstrates the non-linear behaviour of wear by condition. It has a degressive course. In the initial phase, lubricating oil wear has a large increase because there is a decrease in viscosity caused by changes in the fractional composition of the lubricating oil. After this period, the tribological properties stabilise and the oil wear process decelerates. Therefore, the modelling process made it possible to characterise the changes in the tribological properties of the lubricating oil being worn. In the future, the described model will be extended with further input parameters (viscosity, contaminant content, fractional composition, etc.), which will allow a multi-parametric evaluation of lubricating oil wear.

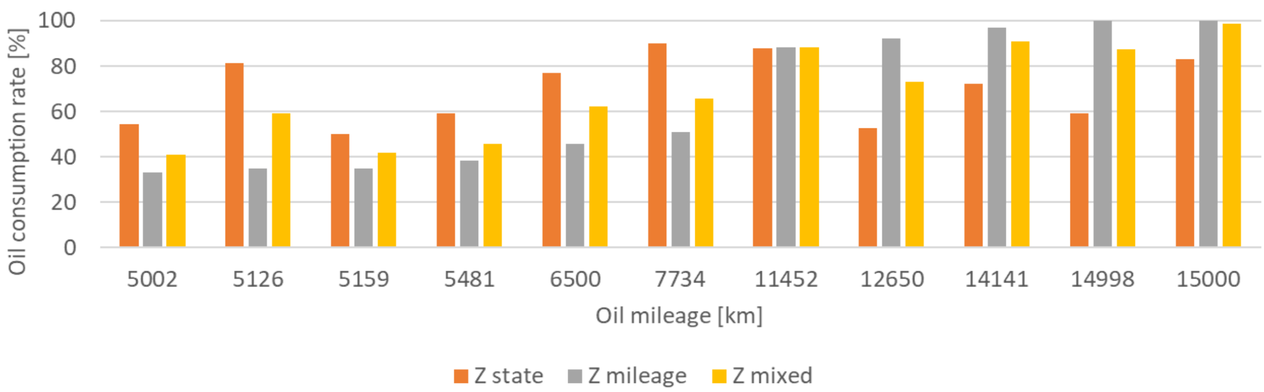

Fig. 4. Results of oil consumption calculation from the model in 3 variants (by condition, by remaining oil life, mixed model)

Table 3. Structure of the oil consumption estimation model (output variables)

Input variable	Scuffing load **F**		
Linguistic variables	High scuffing load $\boldsymbol{\mu_d(F)}$	Medium scuffing load $\boldsymbol{\mu_ś(F)}$	Low scuffing load $\boldsymbol{\mu_m(F)}$
Affiliation functions	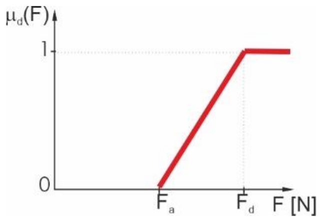	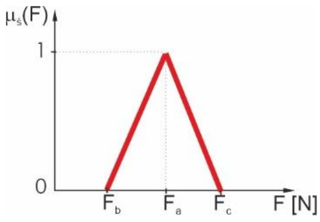	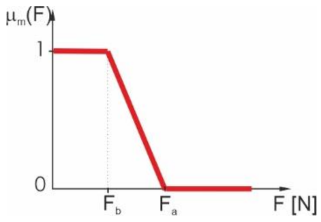
Equations	$\begin{cases} 0 \leftrightarrow F < F_a \\ \frac{F - F_a}{F_d - F_a} \leftrightarrow F \geq F_a \wedge F \leq F_d \\ 1 \leftrightarrow F > F_d \end{cases}$	$\begin{cases} 0 \leftrightarrow F < F_b \vee F > F_c \\ \frac{F - F_b}{F_a - F_b} \leftrightarrow F \geq F_b \wedge F \leq F_a \\ \frac{F_c - F}{F_c - F_a} \leftrightarrow F > F_a \wedge F \leq F_c \end{cases}$	$\begin{cases} 1 \leftrightarrow F < F_b \\ \frac{F_a - F}{F_a - F_b} \leftrightarrow F \leq F_a \wedge F \geq F_b \\ 0 \leftrightarrow F > F_a \end{cases}$
Coefficients in the equations	$\mathbf{F_a}$ = 1688 N, $\mathbf{F_b}$ = 1420 N, $\mathbf{F_c}$ = 1955 N, $\mathbf{F_d}$ = 2222 N		
Input variable	Wear diameter **D**		
Linguistic variables	Small diameter wear $\boldsymbol{\mu_m(D)}$	Medium diameter wear $\boldsymbol{\mu_ś(D)}$	Large diameter wear $\boldsymbol{\mu_d(D)}$
Affiliation functions	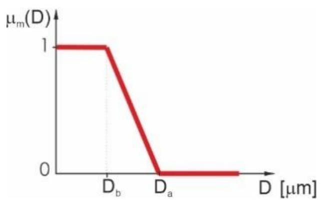	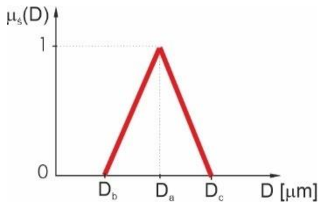	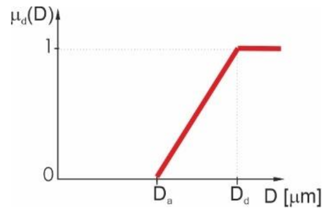
Equations	$\begin{cases} 1 \leftrightarrow D < D_b \\ \frac{D_a - D}{D_a - D_b} \leftrightarrow D \leq D_a \wedge D \geq D_b \\ 0 \leftrightarrow D > D_a \end{cases}$	$\begin{cases} 0 \leftrightarrow D < D_b \vee D > D_c \\ \frac{D - D_b}{D_a - D_b} \leftrightarrow D \geq D_b \wedge D \leq D_a \\ \frac{D_c - D}{D_c - D_a} \leftrightarrow D > D_a \wedge D \leq D_c \end{cases}$	$\begin{cases} 0 \leftrightarrow D < D_a \\ \frac{D - D_a}{D_d - D_a} \leftrightarrow D \geq D_a \wedge D \leq D_d \\ 1 \leftrightarrow D > D_d \end{cases}$
Coefficients in the equations	$\mathbf{D_a}$ = 841 μm, $\mathbf{D_b}$ = 719 μm, $\mathbf{D_c}$ = 963 μm, $\mathbf{D_d}$ = 1085 μm		
Input variable	Oil mileage $\mathbf{P_O}$		
Linguistic variables	Low engine oil mileage $\boldsymbol{\mu_m(P)}$	Average engine oil mileage $\boldsymbol{\mu_ś(P)}$	High engine oil mileage $\boldsymbol{\mu_d(P)}$
Affiliation functions	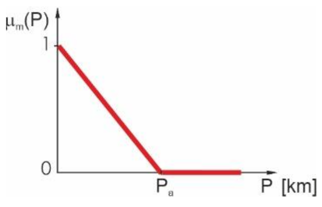	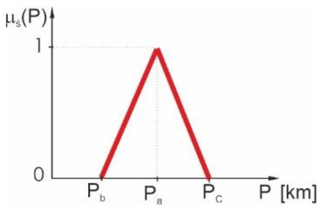	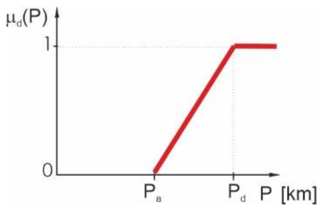
Equations	$\begin{cases} \frac{1 - P}{P_a} \leftrightarrow P \leq P_a \\ 0 \leftrightarrow P > P_a \end{cases}$	$\begin{cases} 0 \leftrightarrow P < P_b \vee P > P_c \\ \frac{P - P_b}{P_a - P_b} \leftrightarrow P \geq P_b \wedge P \leq P_a \\ \frac{P_c - P}{P_c - P_a} \leftrightarrow P > P_a \wedge P \leq P_c \end{cases}$	$\begin{cases} 0 \leftrightarrow P < P_a \\ \frac{P - P_a}{P_d - P_a} \leftrightarrow P \geq P_a \wedge P \leq P_d \\ 1 \leftrightarrow P > P_d \end{cases}$
Coefficients in the equations	$\mathbf{P_a}$ = 7500 km, $\mathbf{P_b}$ = 3750 km, $\mathbf{P_c}$ = 11250 km, $\mathbf{P_d}$ = 15000 km		

Table 4. Structure of the engine oil consumption estimation model (output variables)

Output variable	Degree of wear **Z**		
Linguistic variables	Fresh oil $\boldsymbol{\mu_ś(Z)}$	Average oil consumption $\boldsymbol{\mu_s(Z)}$	Used oil $\boldsymbol{\mu_z(Z)}$
Affiliation functions	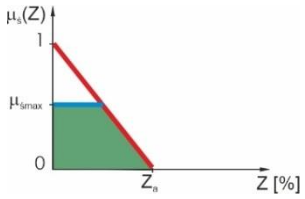	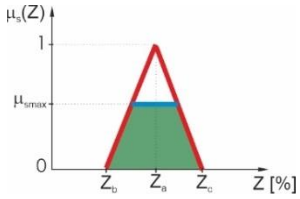	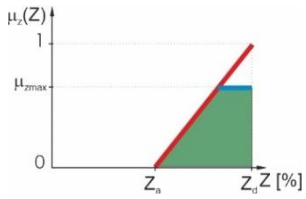
Equations	$\begin{cases} \frac{1-Z}{Z_a} \leftrightarrow Z \le Z_a \\ 0 \leftrightarrow Z > Z_a \end{cases}$	$\begin{cases} 0 \leftrightarrow Z < Z_b \vee Z > Z_c \\ \frac{Z - Z_b}{Z_a - Z_b} \leftrightarrow Z \ge Z_b \wedge Z \le Z_a \\ \frac{Z_c - Z}{Z_c - Z_a} \leftrightarrow Z > Z_a \wedge Z \le Z_c \end{cases}$	$\begin{cases} 0 \leftrightarrow Z < Z_a \\ \frac{Z - Z_a}{P_d - P_a} \leftrightarrow Z \ge Z_a \end{cases}$
Coefficients in the equations	$\mathbf{Z_a}$ = 50%, $\mathbf{Z_b}$ = 25%, $\mathbf{Z_c}$ = 75%, $\mathbf{Z_d}$ = 100%		
Limiting equation (by state)	$\mu_{śmax} = \frac{\mu_d(F) \cdot \mu_m(D)}{2}$	$\mu_{smax} = \frac{\mu_ś(F) \cdot \mu_ś(D)}{2}$	$\mu_{zmax} = \frac{\mu_m(F) \cdot \mu_d(D)}{2}$
Limiting equation (according to resource)	$\mu_{śmax} = \mu_m(P)$	$\mu_{smax} = \mu_ś(P)$	$\mu_{zmax} = \mu_d(P)$
Limiting equation (mixed)	$\mu_{śmax} = \max\left\{\frac{\mu_d(F) \cdot \mu_m(D)}{2}, \mu_m(P)\right\}$	$\mu_{smax} = \max\left\{\frac{\mu_ś(F) \cdot \mu_ś(D)}{2}, \mu_ś(P)\right\}$	$\mu_{zmax} = \max\left\{\frac{\mu_m(F) \cdot \mu_d(D)}{2}, \mu_d(P)\right\}$
Rule aggregation	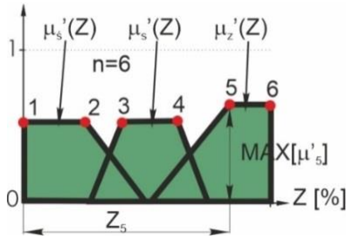	$Z = \frac{\sum_{i=1}^{n} Z_i \cdot \max[\mu_i']}{\sum_{i=1}^{n} \max[\mu_i']}$	

Nomenclature

D wear diameter
F scuffing load
P_O oil mileage
Z wear rate
Z mileage wear rate calculated with oil mileage
Z state wear rate calculated with tribological tests results
μ linguistic variables

Bibliography

[1] Al-Quraan TMA, Alfaqs F, Haddad J, Vojtov V, Voitov A, Kravtsov A et al. A methodological approach to assessing the tribological properties of lubricants using a four-ball tribometer. Lubricants. 2023;11(11):457. https://doi.org/10.3390/lubricants11110457

[2] Al Sheikh Omar A, Motamen Salehi F, Farooq U, Morina A, Neville A. Chemical and physical assessment of engine oils degradation and additive depletion by soot. Tribol Int. 2021; 160:107054. https://doi.org/10.1016/j.triboint.2021.107054

[3] Bastiampillai N. Statistical analysis and modelling of engine oil degradation. Master's Thesis Master of Science in Engineering Physics. Spring 2023.

[4] Chmielewski Z. Cylinder liner wear as a function of selected physicochemical indicators of engine oil. Combustion Engines. 2021;187(4):60-64. https://doi.org/10.19206/CE-141878

[5] Diaby M, Sablier M, Le Negrate A, El Fassi M, Bocquet J. Understanding carbonaceous deposit formation resulting from engine oil degradation. Carbon. 2009;47(2):355-366. https://doi.org/10.1016/j.carbon.2008.10.014

[6] Farhanah AN, Bahak MZ. Engine oil wear resistance. Jurnal Tribologi. 2015;4:10-20.

[7] Gołębiowski W, Zając G, Sejkorová M, Wolak A. Assessment of oil change intervals in urban buses based on the selected physicochemical properties of used engine oils. Combustion Engines. 2024;196(1):15-23. https://doi.org/10.19206/CE-169807

[8] Kozak M. A comparison of thermogravimetric characteristics of fresh and used engine oils. Combustion Engines. 2019;178(3):289-292. https://doi.org/10.19206/CE-2019-350

[9] Landowski B, Baran M. Analysis of selected results of engine oil tests. 18th International Conference Diagnostics of Machines and Vehicles. 2019;302,01010. https://doi.org/10.1051/matecconf/201930201010

[10] Moczarski J. Signaling devices resource in organization of exploitation process (in Polish). Technika Transportu Szynowego. 2015;12:2021-2025.

[11] Motamen Salehi F, Morina A, Neville A. The effect of soot and diesel contamination on wear and friction of engine oil pump. Tribol Int. 2017;115:285-296. https://doi.org/10.1016/j.triboint.2017.05.041

[12] Nagy AL, Knaup J, Zsoldos I. Investigation of used engine oil lubricating performance through oil analysis and friction and wear measurements. Acta Technica Jourinensis. 2019; 12(3):237-251. https://doi.org/10.14513/actatechjaur.v12.n3.495

[13] Nazare MI, Paleu V, Bhaumik S, Ianuş G, Olaru DN. Performances of automotive lubricants – tests on four ball machine. IOP Conf Ser Mater Sci Eng. 2018;444:022013. https://doi.org/10.1088/1757-899X/444/2/022013

[14] Sejkorová M, Hurtová I, Jilek P, Novák M, Voltr O. Study of the effect of physicochemical degradation and contamination of motor oils on their lubricity. Coatings. 2021;11(1):60. https://doi.org/10.3390/coatings11010060

[15] Skonieczna D, Vrublevskyi O, Szczyglak P. Evaluation of the antiwear properties of timely changed engine oils. Combustion Engines. 2023;195(4):116-122. https://doi.org/10.19206/CE-169137

[16] Smolиło M. Measurement of oxidation resistance of oil mixtures obtained from regeneration of used oil with naphthenic oils (in Polish). Nafta-Gaz. 2020;6:408-418. https://doi.org/10.18668/NG.2020.06.06

[17] Stępień Z. Premature degradation of lubricating oil during the service life of the positive-ignition engine. Tribology Online. 2021;16:31-37. https://doi.org/10.2474/trol.16.31

[18] Szczyglak P, Napiorkowski J, Sobiecki M. Zmiany lepkości kinematycznej olejów silnikowych w toku eksploatacji. Logistyka. 2015;4:5983-5990.

[19] Zając G, Gołębiowski W, Szczepanik M, Wolak A, Sejkorová M. Analysis of changes in soot content in engine oils under operating conditions. Lubricants. 2023;11(2):89. https://doi.org/10.3390/lubricants11020089

[20] Ziółkowska M. Influence of the soot on the gelation process of the engine oil (in Polish). Nafta-Gaz. 2019;3:178-184. https://doi.org/10.18668/NG.2019.03.06

Daria Skonieczna, MEng. – Faculty of Technical Sciences, University of Warmia and Mazury in Olsztyn, Poland.

e-mail: *daria.skonieczna@student.uwm.edu.pl*

Piotr Szczyglak, DSc., DEng. – Faculty of Technical Sciences, University of Warmia and Mazury in Olsztyn, Poland.

e-mail: *szczypio@uwm.edu.pl*

Magdalena Lemecha, DSc., DEng. – Faculty of Technical Sciences, University of Warmia and Mazury in Olsztyn, Poland.

e-mail: *magdalena.lemecha@uwm.edu.pl*

Article citation info:
Kamińska M, Szymlet N, Fuć P, Rymaniak Ł, Lijewski P, Grzeszczyk R. Analysis of harmful compounds concentrations in the exhaust behind a vehicle with compression ignition engine. Combustion Engines. 2024;197(2):50-55. https://doi.org/10.19206/CE-183184

Michalina KAMIŃSKA
Natalia SZYMLET
Paweł FUĆ
Łukasz RYMANIAK
Piotr LIJEWSKI
Rafał GRZESZCZYK

Combustion Engines
Polish Scientific Society of Combustion Engines

Analysis of harmful compounds concentrations in the exhaust behind a vehicle with compression ignition engine

ARTICLE INFO

Received: 27 June 2023
Revised: 21 November 2023
Accepted: 28 January 2024
Available online: 13 February 2024

The article presents issues related to the assessment of concentrations of harmful substances in the exhaust gas cloud behind a compression-ignition passenger vehicle. The introduction describes issues related to the impact of air pollution on the environment and on human health and life expectancy. The article presents exhaust gas dispersion tests behind the vehicle were carried out both in stationary conditions (a specially prepared laboratory stand) and in real operating conditions. PEMS testing equipment was used for this type of measurements. During the measurements, concentrations of harmful exhaust gas compounds were analyzed in relation to the distance of the measuring probe from the exhaust system. In stationary conditions, the influence of the engine speed on the dispersion of pollutants was also studied. The tests carried out show that the concentrations obtained behind a moving vehicle significantly decrease with the distance of the measuring probe, and their dispersion is much smaller in most cases than in the case of stationary tests. This is the basis for recognizing that thanks to this, it is possible to analyze the concentrations obtained and conduct tests using the emission gate.

Key words: *remote sensing system, car emission, teledetection, combustion engines, optical measurement method*

1. Introduction

The latest State of Global Air report published in 2019 states that air pollution was the fourth leading risk factor for premature death worldwide. It is estimated that it contributed to 6.67 million deaths per year, which is almost 12% of the global number (Fig. 1). The report also reports on the effects of pollution, which is the focus of the Global Burden of Disease Study (GBD). The GBD analysis estimates the burden on society in terms of the impact on years lived with the disease and the number of deaths resulting, in most cases, from long-term exposure to air pollution. The research focuses on mortality from the five chronic non-communicable diseases for which there is currently the strongest evidence – diabetes, stroke, chronic obstructive pulmonary disease, lung cancer, and coronary heart disease, and one infectious disease, lower respiratory tract infection. Nitrogen oxides and particulate matter have a particularly negative impact on human health and life. Therefore, scientists are constantly trying to find new ways to reduce them, including by using biofuels [9, 13, 15].

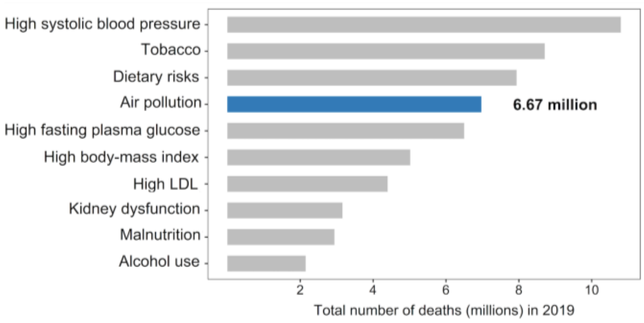

Fig. 1. Global ranking of risk factors by total deaths from all causes in 2019 [9]

One of the main threats to the environment is CO_2 emissions. About 50 billion tonnes of greenhouse gases, measured in carbon dioxide equivalents, are emitted around the world each year. The EEA (European Environment Agency) reports from 2019 state that transport is responsible for approximately one quarter of total CO_2 emissions in the European Union, of which almost 72% came from road transport, including passenger vehicles (60.6%), light commercial vehicles (11%), trucks (11%) and motorcycles (1.3%) (Fig. 2). Due to the significant impact of transport on air pollution, newer regulations are being introduced to reduce emissions of harmful exhaust gases. The main goal of the European Union is to introduce zero CO_2 emission regulations for these vehicles by 2035. However, transport is the only sector where greenhouse gas emissions have increased by 33.5% between 1990 and 2019 over the past three decades. Significant reductions in CO_2 emissions will therefore not be easy as the rate of reduction has slowed. To achieve the assumed goals and solve the health crisis related to air pollution, it is necessary to quickly take all possible actions. In highly developed countries, a number of solutions are being introduced to improve air quality, such as the creation of low-emission zones in city centers [6, 12, 14, 16, 25]. The feasibility of introducing zones of this type can be achieved by using devices for remote measurement of harmful exhaust gas compounds based on the study of the actual flow of vehicles moving within the low-emission zone. The main advantage of this type of measurements is obtaining the actual condition of vehicles driving in a given area in terms of legislative regulations and the level of wear and tear of research facilities. Remote sensing measurement makes it possible to determine the concentrations of harmful compounds from vehicles driving in low-emission zones and outside these zones. Thanks to this, it is possible to obtain information regarding the actual impact of their introduction on reducing the impact of automotive pollution on the environment [23–25].

A literature study showed that for several years in various global research centers [1, 3–5, 7, 8, 10, 11, 17, 19] work has been carried out on devices for assessing pollutant emissions both in stationary and real conditions. However, the solutions being developed are still insufficient. Due to the problem of emissions of harmful exhaust gases from motor vehicles, there is a need for further research using more developed measurement equipment.

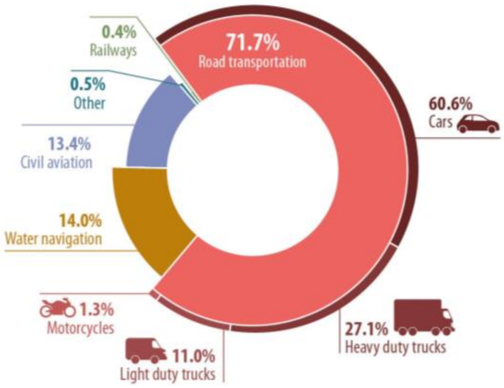

Fig. 2. Transport emission in the EU – greenhouse gas emissions breakdown by transport mode [23]

2. Research methodology

2.1. Research object

The tests were carried out using a passenger car equipped with a compression-ignition drive unit with a capacity of 1.9 dm^3 (Fig. 3, Table 1). The engine had a rated power of 110 kW at 4000 rpm and a maximum torque of 320 Nm at 2000 rpm. The vehicle was equipped with a diesel particulate filter (DPF) and was approved in accordance with the Euro 4 standard.

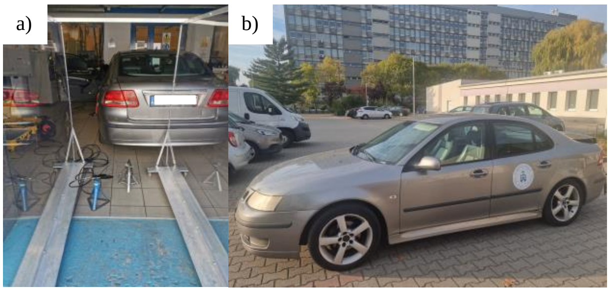

Fig. 3. Test object a) on a measuring stand, b) in real operating conditions

Table 1. Basic parameters of the research object

Parameter	Data
Year of production	2006
Fuel type	Diesel oil
Stroke capacity [dm^3]	1.9
Engine layout	R4
Power [kW]/at engine speed [rpm]	110/4000
Maximum torque [Nm]/at engine speed [rpm]	320/2000
Injection type	Common Rail
Compression ratio	18.4:1
Euro standard	Euro 4

2.2. Measuring station and research route

Tests of concentrations of harmful compounds in exhaust gases were carried out both in stationary and real conditions. Laboratory tests were carried out at a measuring station located on the campus of the Poznań University of Technology. They included measurements of concentrations of harmful compounds in the cloud of exhaust gases behind a stationary vehicle. The measurement points (Table 2) were placed at different distances and at different heights from the flue gas exhaust system. In addition, the influence of engine speed (idling, 1500 rpm, and 3000 rpm) on the obtained measurements was investigated. In the next stage, measurements were carried out in real operating conditions. The measurement route was the first communication frame of the city of Poznań, covering the very center of the city (Fig. 4). The journey covered a section of road with a length of 8.9 km.

Table 2. Basic parameters of the research object

Measurement point	Distance from the Exhaust Pipe l [cm]	Height from the Exhaust Gas System h [cm]
1	0	0
2	5	10
3	10	10
4	20	10

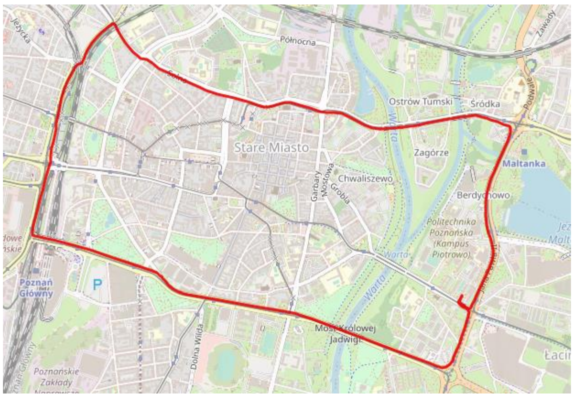

Fig. 4. Test route used [22]

2.3. Measurement equipment

The mobile Micro PEMS Axion R/S+ analyzer manufactured by Global MRV was used for the measurements (Table 3). It enables the measurement of the concentration of gaseous toxic compounds using: a non-dispersive infrared analyzer – NDIR (CO_2, CO, HC) and an electrochemical analyzer (NO). The equipment also allows testing the concentration of PM using the method based on Laser Scatter, in which the speed of particle movement is measured (taking into account the values assigned to PM_{10}) [18, 20].

Table 3. Axion R/S+ Analyzer Specifications [2]

Gas	Measurement Range	Accuracy	Resolution	Type of Measurement
HC	0–4000 ppm	±3%	1 ppm	NDIR
CO	0–10%	±3%	0.01 vol. %	NDIR
CO_2	0–16%	±4%	0.01 vol. %	NDIR
NO	0–4000 ppm	±3%	1 ppm	E-chem
O_2	0–25%	±3%	0.01 vol. %	E-chem
PM	0–300 mg/m^3	±2%	0.01 mg/m^3	Laser Scatter

3. Measurement results

Passenger vehicles with SI and CI were tested at four measurement points, differing in the distance of the measurement probe from the exhaust gas outlet system. The points were selected on the basis of previously conducted tests, which showed that the test objects should be tested directly in the exhaust system and 10 cm, 15 cm, and 20 cm behind the exhaust system. The dispersion of harmful exhaust gas compounds was determined on the basis of the last analyzed measurement point. Laboratory tests of vehicles were carried out for various rotational speeds – idle (800 rpm – SI vehicle, 850 rpm – CI vehicle), 1500 rpm, and 3000 rpm. The tests were carried out without checking the influence of load on the obtained results. The authors intend to pursue further steps in this direction. Analogous measurements were also carried out in real operating conditions on a route covering the very center of the city. These measurements were performed to confirm the possibility of conducting dispersed exhaust gas tests. These studies constitute the basis for determining the appropriateness of using the emission gate for remote sensing measurements, as well as for establishing the conditions under which such a measurement would take place.

Carbon dioxide concentrations measured stationary directly in the exhaust system were characterized by similar values – 3.58% for idling, 4.36% for 1500 rpm, and 3.67% at 3000 rpm (Fig. 5). At point 4, 20 cm away from the exhaust system, these values were between 0.39% and 0.6%. This means that the CO_2 values were similarly dispersed for all vehicle speeds. The obtained dispersion exceeded 83% for idling and 89% for rotational speeds of 1500 rpm and 3000 rpm. Measurements in real conditions for the first measurement point (3.43%) were identical to those obtained in stationary conditions. In point 4, the value of carbon dioxide was obtained at the level of 1.08%. This means that the obtained dispersion (68%) was about 20% lower than in the case of measurements on a stationary vehicle.

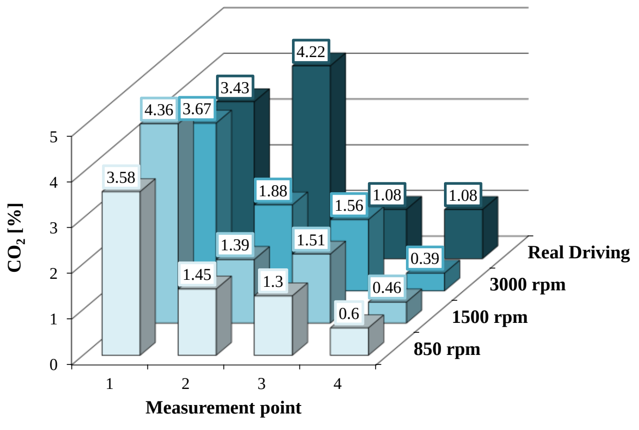

Fig. 5. Carbon dioxide concentration in relation to the measuring point and engine speed

In the case of stationary tests, the obtained CO results for the first measurement point closely depended on the engine speed. The concentration of carbon monoxide at idling was 342 ppm, for 1500 rpm 561 ppm, and for 3000 rpm – 735 ppm (Fig. 6). At the 4th measurement point, the concentration obtained for the rotational speed of 850 rpm was characterized by the lowest value, at the level of 8 ppm. For the remaining engine speeds, the following values were recorded – 122 ppm (1500 rpm) and 212 ppm (3000 rpm). The obtained dispersion for idling was therefore 97.5%, while for higher rotational speeds it was 78% and 71%, respectively. In the case of driving in real conditions, the values obtained directly from the exhaust system (550 ppm) were similar to those obtained in stationary conditions for 1500 rpm. At the farthest point from the exhaust system, 95 ppm was obtained. Thus, an exhaust gas dispersion of 83% was obtained. The achieved results were therefore only lower than those obtained at idling.

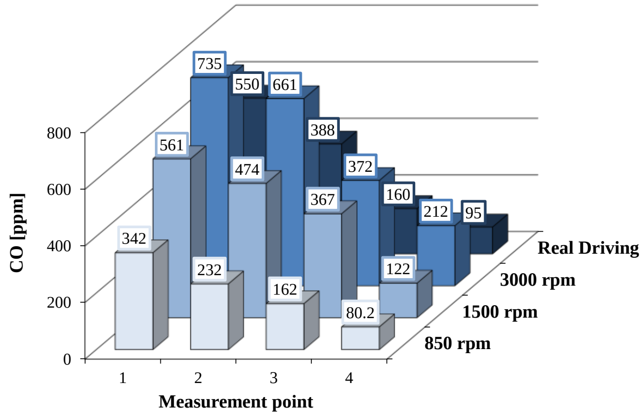

Fig. 6. Carbon monoxide concentration in relation to the measuring point and engine speed

Stationary tests of hydrocarbons for all engine speeds were similar (Fig. 7). Directly in the exhaust system, hydrocarbon concentrations ranged from 33.2 ppm to 35 ppm, while at the farthest point from 8.3 ppm to 8.6 ppm. Therefore, the HC dissipation was maintained for idling and engine speeds equal to 1500 rpm and 3000 rpm at the level of about 75%. It follows that the dispersion of this compound did not depend on the rotational speed of the vehicle. In the case of measurements in real conditions, the dispersion was at the same level (75.2%), although the concentrations obtained at the first measurement point were characterized by much higher values – 129 ppm.

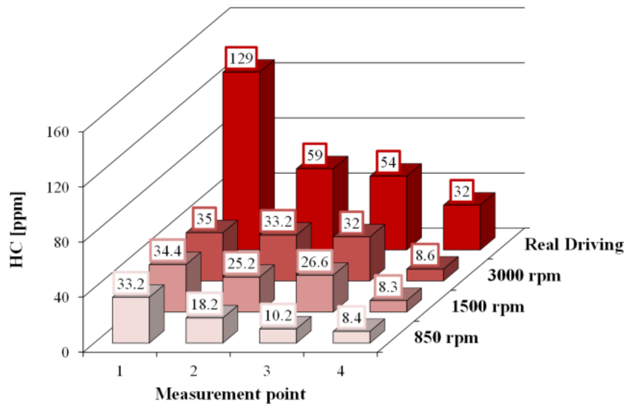

Fig. 7. Hydrocarbon concentration related to measurement point and engine speed

The concentration of nitrogen oxide also depended on the engine speed (Fig. 8). They increased in direct proportion to the rotational speed. In tests performed in laboratory conditions with the probe placed directly in the exhaust system, the following results were recorded – 96.4 ppm at idle, 144 ppm at 1500 rpm, and 229 ppm at 3000 rpm. At the furthest point, relatively similar values from 8.9 ppm to 19 ppm were recorded. The obtained dispersion for all rotational speeds was about 90%. This indicates that the dispersion of exhaust gases from the vehicle was not affected by the rotational speed of the drive unit. Measurements in real operation conditions indicate that NO dispersion obtained during the tests was much lower than in stationary conditions and amounted to 61%. At the first measurement point, a value of 154 ppm was obtained, while at the last 60 ppm.

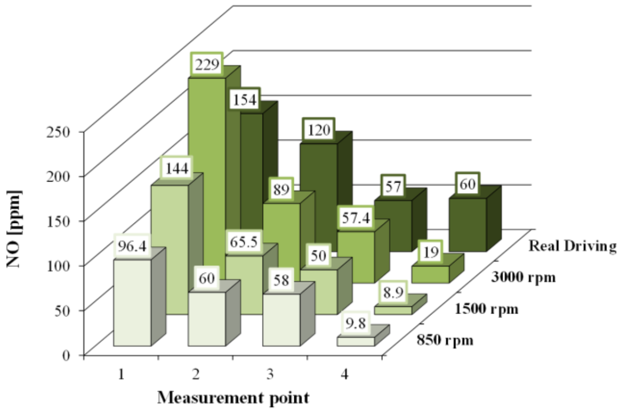

Fig. 8. Nitrogen oxide concentration related to measuring point and engine speed

The concentration of particulate matter strictly depended on the engine speed. Its increase was directly proportional to the increase in PM (Fig. 9).

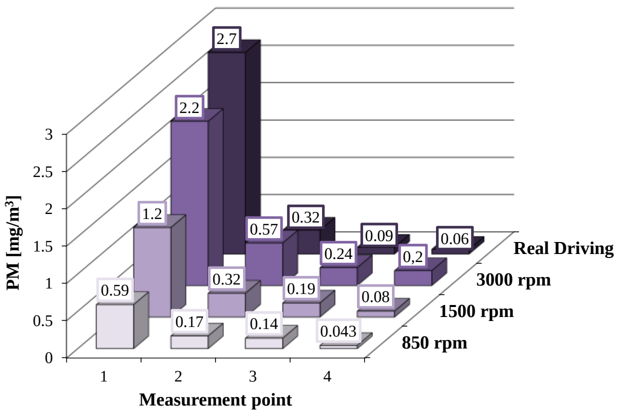

Fig. 9. Particulate matter concentration related to measurement point and engine speed

In the first point, the following results were obtained – 0.59 mg/m^3 for idling, 1.2 mg/m^3 for the rotational speed of 1500 rpm, and 2.2 mg/m^3 for 3000 rpm. These values successively decreased to 0.043 mg/m^3, 0.08 mg/m^{3,} and 0.2 mg/m^3, respectively. Thus, exhaust gas dispersion exceeding 90% was obtained at all points (92.7% – 850 rpm, 93.3% – 1500 rpm, 90.9% – 3000 rpm). Measurements in real conditions were characterized by the highest values of particulate matter concentration measured directly in the vehicle exhaust system (2.7 mg/m^3). However, at the most distant point, the result obtained was only higher than that obtained at idling and amounted to 0.06 mg/m^3. Road measurements indicate that dispersion remained at around 98%.

4. Conclusions

The conducted empirical research on the analysis of concentrations of harmful compounds in the cloud of exhaust fumes behind an object equipped with a diesel engine is part of the problem of evaluating emissions from moving vehicles. The summary of the relative dispersion of the exhaust gases behind the vehicle for both stationary and dynamic tests is presented in Table 4. As the table shows, the dispersion obtained for all stationary measurement points exceeded 90% only in a few cases. The obtained results ranged from about 70% to over 97%. The highest values were characterized by solid particles and the lowest by hydrocarbons. During real operation, the results ranged from 61% for nitrogen oxides to almost 98% for particulate matter. The dispersion values of other harmful compounds of exhaust gases ranged from about 68% to over 82%.

Table 4. Dispersion of harmful exhaust compounds

Harmful compound	Measuring point	Engine speed n [rpm]			
		850	1500	3000	Real driving
CO_2 [%]	1	3.58	4.36	3.67	3.34
	2	1.45	1.39	1.88	4.22
	3	1.3	1.51	1.56	1.08
	4	0.6	0.46	0.39	1.08
Dispersion of CO_2 [%]	1–4	83.2	89.5	89.4	67.7
CO [ppm]	1	342	561	735	550
	2	232	474	661	388
	3	162	367	372	160
	4	8	122	212	95
Dispersion of CO [%]	1–4	97.7	78.2	71.2	82.7
HC [ppm]	1	33.2	34.4	35	129
	2	18.2	25.2	33.2	59
	3	10.2	26.6	32	54
	4	8.4	8.3	8.6	32
Dispersion of HC [%]	1–4	74.7	75.9	75.4	75.2
NO [ppm]	1	96.4	144	229	154
	2	60	65.5	89	120
	3	58	50	57.4	57
	4	9.8	8.9	19	60
Dispersion of NO [%]	1–4	89.8	93.8	91.7	61
PM [mg/m^3]	1	0.59	1.25	2.2	2.7
	2	0.17	0.32	0.57	0.32
	3	0.14	0.19	0.24	0.09
	4	0.043	0.08	0.2	0.06
Dispersion of PM [%]	1–4	92.7	93.3	90.9	97.8

The results of the measurement obtained indicate that the greatest diffusion of exhaust gas is obtained at low rotational speeds in laboratory conditions. In addition, the presented summary shows that the movement of the vehicle is conducive to the assessment of concentrations behind the moving vehicle, because the obtained exhaust gas dispersion is not as large as in the case of laboratory tests (especially for low engine speeds). It is possible to analyze the obtained concentrations and conduct tests using the emission gate. The most constant conditions should be used for this, so that the dispersion remains at a similar level for each research object.

The emission gate is a modular device for quick assessment of the concentration of harmful exhaust gas compounds. It enables the identification of concentrations of harmful exhaust gases from various means of transport. The device enables individual analysis of the obtained values for each vehicle or set of vehicles moving in a given area (road in the case of road vehicles or track for rail vehicles) and time. The emission gate has extensive measurement capabilities and allows you to carry out measurements on at least several vehicles within one hour. This is undoubtedly the greatest advantage over PEMS equipment, in which the measurement of one vehicle on a precisely defined route takes at least several hours. A quick assessment of the value of harmful exhaust gases from the tested objects allows the identification of the largest emitters (worn-out, damaged and technically neglected vehicles), which may constitute the basis for eliminating them from traffic if certain standards are exceeded.

Acknowledgements

The research was funded by European Union from European Regional Development Fund through the National Centre for Research and Development (Narodowe Centrum Badań i Rozwoju) – research project within the Smart Growth Programme (contract No. POIR.04.01.02-00-0002/18).

European Funds Smart Growth | Republic of Poland | European Union European Regional Development Fund

Nomenclature

CO	carbon monoxide	l	distance
CO_2	carbon dioxide	n	engine speed
DPF	diesel particulate filter	NDIR	non dispersive infra red
h	height	NO	nitrogen oxide
HC	hydrocarbons	PM	particulate matter

Bibliography

[1] Andrews GE, Li H, Wylie JA, Zhu G, Bell M, Tate J. Influence of ambient temperature on cold-start emissions for a Euro 1 SI car using in-vehicle emissions measurement in an urban traffic jam test cycle. SAE Technical Paper 2005-01-1617. 2005. https://doi.org/10.4271/2005-01-1617

[2] AxionRS+. GlobalMRV Inc. Introducing the world's first Micro PEMS with remote monitoring capabilities. Cheektowaga 2017.

[3] Bajerlein M, Daszkiewicz P, Dobrzyński M, Rymaniak Ł, Siedlecki M. Analiza emisji zanieczyszczeń autobusu miejskiego zasilanego CNG w aspekcie procedur NTE oraz UE 582/2011. Combustion Engines. 2015;54(3):800-804.

[4] Bernard Y, German J, Muncrief R. Worldwide use of remote sensing to measure motor vehicle emissions. ICCT, 2019. https://theicct.org/publication/worldwide-use-of-remote-sensing-to-measure-motor-vehicle-emissions/

[5] Bishop GA, Burgard DA, Stedman DH. On-road remote sensing of automobile emissions in the La Brea Area: year 3, October 2003. Coordinating Research Council, Inc.: Alpharetta 2004. https://digitalcommons.du.edu/cgi/viewcontent.cgi?article=1050&context=feat_publications

[6] Ferreira F, Gomes P, Tente H, Carvalho AC, Pereira P, Monjardino J. Air quality improvements following implementation of Lisbon's Low Emission Zone. Atmos Environ. 2015;122:373-381. https://doi.org/10.1016/j.atmosenv.2015.09.064

[7] Fuć P, Lijewski P, Ziółkowski A, Siedlecki M. Trends in the type-approval regulations in terms of exhaust gas emissions for vehicles of category PC and LDV. Combustion Engines. 2015;54(3):417-424. https://bibliotekanauki.pl/articles/133307

[8] Fraser MP, Buzcu B, Yue ZW, McGaughey GR, Desai NR, Allen DT et al. Validation of source attribution using organic molecular markers for emissions of fine particles from mobile sources. Envir Sci Tech. 2003;37:3904-3909.

[9] Health Effects Institute. State of global air 2020. Special Report. 2020.

[10] Hwa MY, Hsieh CC, Wu TC, Chang LFW. Real-world vehicle emissions and VOCs profile in the Taipei tunnel located at Taiwan Taipei area. Atmos Environ. 2002;36(12):1993-2002. https://doi.org/10.1016/S1352-2310(02)00148-6

[11] Imhof D, Weingartner E, Prévôt AS, Ordonez C, Kurtenbach R, Wiesen P et al. Aerosol and NO_x emission factors and submicron particle number size distributions in two road tunnels with different traffic regimes. Atmos Chem Phys. 2006;6(8):2215-2230. https://doi.org/10.5194/acp-6-2215-2006

[12] Kelly F, Armstrong B, Atkinson R, Anderson HR, Barratt B, Beevers S et al. The London low emission zone baseline study. Research Report (Health Effects Institute). 2011; 163:3-79. https://www.healtheffects.org/system/files/Kelly-LEZ-163-IR.pdf

[13] Kozak M, Merkisz J. Oxygenated diesel fuels and their effect on PM emissions. Appl Sci. 2022;12(15):7709. https://doi.org/10.3390/app12157709

[14] Ku D, Bencekri M, Kim J, Leec S, Leed S. Review of European low emission zone policy. Chem Eng, 2020;78: 241-246. https://doi.org/10.3303/CET2078041

[15] Kurczyński D, Wcisło G, Łagowski P, Leśniak A, Kozak M, Pracuch B. Determination of the effect of the addition of second-generation biodiesel BBuE to diesel fuel on selected parameters of "B" fuels. Energies. 2023;16(19): 6999. https://doi.org/10.3390/en16196999

[16] Ma L, Graham DJ, Stettler ME. Has the ultra low emission zone in London improved air quality? Environ Res Lett. 2020;16(12):124001. https://doi.org/10.1088/1748-9326/ac30c1

[17] Merkisz J, Rymaniak Ł. Tests of urban bus specific emissions in terms of currently applicable heavy vehicles operating emission regulations. Combustion Engines. 2017;168(1): 21-26. https://doi.org/10.19206/CE-2017-103

[18] Rymaniak Ł, Kamińska M, Szymlet N, Grzeszczyk R. Analysis of harmful exhaust gas concentrations in cloud behind a vehicle with a spark ignition engine. Energies. 2021;14(6):1769. https://doi.org/10.3390/en14061769

[19] Stedman DH. Carbon monoxide amongst other chemicals. 211st American Chemical Society (ACS) National Meeting. New Orleans 1996.

[20] Warguła Ł, Kukla M, Lijewski, P, Dobrzyński M, Markiewicz F. Impact of compressed natural gas (CNG) fuel systems in small engine wood chippers on exhaust emissions and fuel consumption. Energies. 2020;13(24):6709. https://doi.org/10.3390/en13246709

[21] www.climateanalytics.org (accessed on 15 April 2023).

[22] www.gpsvisualizer.com/ (accessed on 28 February 2023).

[23] www.europarl.europa.eu (accessed on 15 April 2023).

[24] www.ourworldindata.org (accessed on 15 April 2023).

[25] www.ricardo.com (accessed on 15 April 2023).

Michalina Kamińska, MEng.– Faculty of Civil and Transport Engineering, Poznan University of Technology, Poland.
e-mail: *michalina.kaminska@put.poznan.pl*

Prof. Łukasz Rymaniak, DSc., DEng. – Faculty of Civil and Transport Engineering, Poznan University of Technology, Poland.
e-mail: *lukasz.rymaniak@put.poznan.pl*

Natalia Szymlet, DEng. – Faculty of Civil and Transport Engineering, Poznan University of Technology, Poland.
e-mail: *natalia.szymlet@put.poznan.pl*

Prof. Piotr Lijewski, DSc., DEng. – Faculty of Civil and Transport Engineering, Poznan University of Technology, Poland.
e-mail: *piotr.lijewski@put.poznan.pl*

Prof. Paweł Fuć, DSc., DEng. – Faculty of Civil and Transport Engineering, Poznan University of Technology, Poland.
e-mail: *pawel.fuc@put.poznan.pl*

Rafał Grzeszczyk, DEng. – ODIUT Automex sp. z o.o., WSB Gdańsk, Poland.
e-mail: *rafal.grzeszczyk@automex.eu*

Article citation info:
Jakliński P, Czarnigowski J, Ścisłowski K. Study of the effect of ignition crank angle and mixture composition on the performance of a spark-ignition engine fueled with ethanol. Combustion Engines. 2024;197(2):56-63. https://doi.org/10.19206/CE-174888

Piotr JAKLIŃSKI
Jacek CZARNIGOWSKI
Karol ŚCISŁOWSKI

Combustion Engines
Polish Scientific Society of Combustion Engines

Study of the effect of ignition crank angle and mixture composition on the performance of a spark-ignition engine fueled with ethanol

ARTICLE INFO

Received: 3 October 2023
Revised: 31 October 2023
Accepted: 6 November 2023
Available online: 10 January 2024

The publication presents the results of the measurements of the operating parameters of a spark-ignition engine fueled with 95-octane unleaded gasoline (ES95) and ethyl alcohol, approx. 92%. The measurements were carried out at a constant load: an engine speed of 1500 rpm and a constant pressure in the intake system – MAP = 0.45 bar. For each type of fuel, the measurements were carried out in two series for two variables. The ignition crank angle was varied in the range of 0°÷40° and the mixture composition λ in the range of 0.85–1.25. The recorded engine performance parameters included torque, intake manifold pressure, intake air temperature, exhaust gas temperature and temporal fuel consumption; and exhaust gas composition was examined in terms of carbon monoxide, hydrocarbons and nitrogen oxides. The study showed that an ethanol-fueled engine has lower average efficiency compared to a gasoline one. The highest efficiency for ethanol was obtained for rich mixtures in the range λ = 0.85–1.0 and at high ignition advance angles. The use of alcohol fuel showed a very favorable effect on the composition of exhaust gas and a significantly lower content of harmful exhaust components was demonstrated. For the same operating points, carbon monoxide content was reduced by an average of 15%, and hydrocarbons and nitrogen oxides by an average of 80%.

Key words: *ethanol, alternative fuels, alcohol fuels, emissions, biofuels*

1. Introduction

Internal combustion engines still play an important role in the economy, providing propulsion for most vehicles and agricultural or industrial machinery. However, traditional fossil fuels used to power internal combustion engines have a negative impact on the environment due to emitted harmful substances such as carbon dioxide, nitrogen oxides, hydrocarbons and other chemical compounds during combustion [5]. It is clear that it is not possible to quickly replace internal combustion engines with electric ones [19], so work and research are being conducted so that internal combustion engines could remain in use but their consumption of fossil fuels was minimized [22]. In addition to zero-carbon fuels such as hydrogen [15, 21] or its mixtures with oxygen (HHO) [9, 11, 33], reduced-carbon fuels such as gases [10] or alcohols [12, 28] are being used. These can be the primary fuel or used as an additive to the original/factory fuel [1, 3]. Such fueled internal combustion engines can reduce the CO_2 emissions of the vehicle under study [20]. Often proposed as an alternative to fossil fuels are biofuels [8, 22] which have gained great popularity in recent years due to their environmental benefits and potential to reduce transportation dependence on traditional fuel sources [14]. Therefore, one of the most important areas of research is alternative fuels that would allow the continued use of traditional internal combustion engines [24, 32]. Alcohol fuels such as ethyl alcohol, which is produced by fermenting plant biomass, are an important type of fuel produced from plant components [31]. Many publications refer to the use of alcohol fuels in internal combustion engines and their impact on the operating parameters of such engines such as vibration and the way they are measured [6, 27], noise intensity [13], energy efficiency [2] or reduction in the number of harmful exhaust components [15, 23]. Ongoing research has shown that the use of alcohol additives and alcohol as a stand-alone fuel both in spark-ignition engines [16, 25] and diesel engines [17, 30] can significantly affect the engine performance. In the case of spark-ignition engines, ethyl and methyl alcohol fuels are among the most widely studied alternative fuels due to their relatively low viscosity and high vapor pressure. Many studies focus on comparing the combustion behavior of these fuels with the properties of gasoline which is currently the most widely used fuel in this type of engine. Their effect on the performance of such engines is also investigated. Studies have also been conducted on the physical and chemical properties of alcohol fuels and their blends [14], their effect on atmospheric emissions [7, 18] and their use to increase combustion efficiency and reduce harmful gas emissions [4].

2. Test stand and test methodology

To examine the effect of fuel type on the performance of an internal combustion engine, this paper compares two types of fuel: 95-octane gasoline: ES95 and ethyl alcohol of a concentration of about 92%. Two series of measurements were carried out in which the ignition crank angle and fuel mixture composition were changed, and engine torque, fuel consumption and exhaust gas composition were recorded in each series. The purpose of the study was to compare the effects of using ethyl alcohol on selected performance parameters of a spark-ignition engine.

2.1. Engine

The study used the Lublin University of Technology's dynamometer stand with a Holden C20LE engine (Fig. 1). It is a four-stroke gasoline engine to propels cars and vans. The engine is powered by electronically controlled multipoint indirect fuel injection. The engine is equipped with a DIS ignition system and an EGR exhaust gas recirculation system. A microprocessor-based ADAM 5510 system was responsible for regulating and maintaining the engine's thermal condition. The engine's technical data is shown in Table 1.

Fig. 1. Holden C20LE engine

Table 1. Technical data of Holden C20LE engine

Type of engine	C20LE
Layout and number of cylinders	4, in-line
Cylinder diameter	86 mm
Piston stroke	86 mm
Engine displacement	1 998 cm^3
Compression ratio	8.8:1
Max power	77 kW/5200 rpm
Max torque	164 Nm/2600 rpm
Number of valves	8

2.2. Measurement equipment

The proper construction of a test bench should be preceded by a CAD design and an analysis of the robustness of the structure with a view to its safe use in scientific research [26]. The test stand was equipped with the measurement systems necessary to measure the exhaust gas composition and energy efficiency of the engine and to read basic parameters of its operation. The measuring and regulating of the engine load was done with a brake, the SAK-670 N engine brake from VEB Elbtalwerk, connected to the engine via a 5-speed gearbox and a shaft with a flexible coupling. It is an electric brake whose braking torque is controlled by direct current. The accuracy of torque measurement by the brake measuring system was 0.5 Nm. The gearbox was locked in direct gear.

Energy demand was measured using a fuel scale. Engine speed (RPM), intake manifold pressure (MAP), composition and exhaust gas temperature (CHT) were also recorded. An AMX 200 CAN programmable logic controller (PLC) was used as the engine control system. The controller allowed arbitrary changes in the ignition crank angle and injector opening time. A proprietary strain gauge fuel scale was used to measure fuel consumption. The measurement time for fuel consumption at one operating point was 60 s.

Fig. 2. Test stand with electric brake

An HGA 400 exhaust gas analyzer was used to measure the composition of the exhaust gas during the tests. The measurement range of the various components of the exhaust gas is shown in Table 2.

Table 2. Technical data of the HGA 400 exhaust gas analyzer

Component	Measuring range	Measurement accuracy
CO	0–10%	±0.06%
CO_2	0–20%	±0.5%
HC	0–20,000 ppm	±11 ppm
O_2	0–22%	±5%
NO_x	0–5000 ppm	±10%

2.3. Research methodology

The study was aimed at making comparative measurements of the performance of a spark ignition engine fueled with the original fuel – ES95 and 92% ethanol. During the measurements, the same measuring apparatus and engine supply system were used. Table 3 shows the physicochemical data of the fuels used during the study.

Table 3. Physical and chemical parameters of the fuels used [29]

Parameter	ES95	Ethanol 92%
Calorific value	42.0 MJ/kg	26.2 MJ/kg
Density	750 kg/m^3	806 kg/m^3
RON	95	110
Enthalpy of vaporization	315–350 kJ/kg	879 kJ/kg
Specific heat	2.0 kJ/kg·K	2.2 kJ/kg·K
Freezing point	–40°C	–114°C
Viscosity (20°C)	0.37–0.44 mPa·s	1.19 mPa·s

It was decided to obtain two control characteristics of the engine: the characteristics of changing the ignition advance angle and the characteristics of the mixture composition. All measurements were carried out at an engine speed of 1500 rpm, controlled with the engine brake by adjusting the load. For each measurement point, the throttle opening angle was also selected to obtain an intake manifold pressure MAP = 0.45 bar. Such an operating point was chosen because an engine operating at low speed and low load is more sensitive to changes in feed conditions, changes in mixture composition, unevenness of operation, and deterioration of the uniformity of the air-fuel mixture in the cylinder. The use of such engine operating conditions was intended to highlight the change in the performance of the internal combustion engine caused by the change in fuel. Previous series of tests have shown that under these conditions the engine will operate at the limit of stability, so all changes in parameters caused by a change in fuel, will be easily noticeable.

The first measurements were made for a variable ignition advance angle. The engine was brought to a stable operating point. The ignition crank angle was varied from 0^o to 40^o, in 10^o increments. Once the ignition crank angle was set, the stoichiometric mixture composition ($\lambda = 1$) was established by changing the opening time of the injectors. Once the engine was stabilized, the measurement started. The recording time of a single measurement point lasted 60 seconds. During this time, the fuel consumption, the exhaust gas composition and the torque were measured. When the measurement was completed, the next value of the ignition crank angle was set, the mixture composition was determined and the measurement was repeated.

The mixture composition was plotted at a fixed value of the ignition crank angle of 20^o. Once a stable operating point was established, the injection time was changed to achieve the required mixture composition in the range of $\lambda = 0.85$–1.25, with a step of 0.1. The common measuring point for both characteristics was the operating point of $\lambda =$ $= 1$, ICA = 20°. Figure 3 shows the distribution of the tested measurement points.

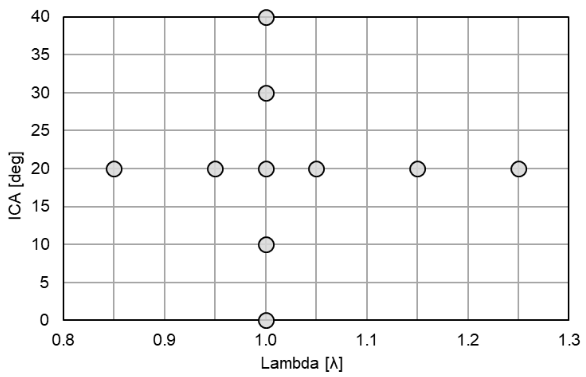

Fig. 3. Measurement points, MAP = 0.45 bar, n = 1500 rpm

3. Research results and analysis

3.1. Measurement results

From the torque measurement results, it can be concluded that when fed with lean mixtures and at a larger ignition crank angle ($\lambda > 1$; ICA > 20°), the gasoline-fueled engine had higher torque on average. In contrast, when fed with rich mixtures and at a smaller ignition crank angle ($\lambda < 1$; ICA < 20°), higher torque was generated when the engine was fed with ethanol.

For the measurement point with stoichiometric mixture and ICA = 20°, the torque values obtained were the same. The measured torque values are shown in Fig. 4.

For every measurement point except (ICA = 0°; $\lambda = 1$), the exhaust gas from ethanol combustion had a lower temperature than gasoline, by an average of 19.4℃. The highest exhaust gas temperature recorded in the tests was 655℃, while the lowest was 535℃. The measurement points are shown in Fig. 5. There is a clear tendency for the exhaust gas temperature to increase with decreasing ICA and with increasing excess air ratio λ.

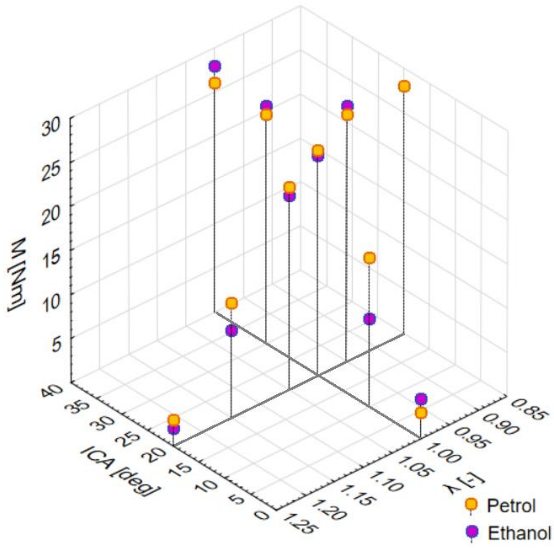

Fig. 4. Torque measurement results for gasoline and ethanol

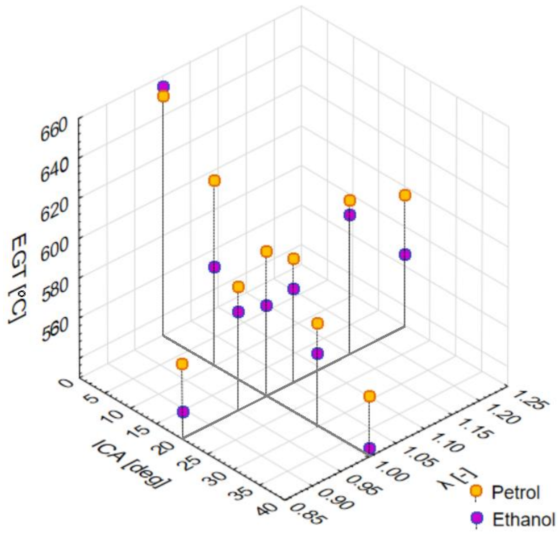

Fig. 5. Results of EGT measurements for gasoline and ethanol

The graph in Fig. 6 shows the carbon monoxide content of the exhaust gas for all measurement points. In the range of stoichiometric mixtures and lean mixtures, the carbon monoxide content of the exhaust gas oscillated between 0.12–0.53%, showing no significant differences between ethanol and gasoline. The maximum CO content was obtained for $\lambda = 0.85$ and reached 4.94% for gasoline and 3.94% for ethanol.

Figure 7 shows the hydrocarbon content of the exhaust gas during the testing of the engine fueled by ethanol and gasoline. The hydrocarbon content for ethanol was 22–78 ppm, with its average value of 41 ppm for all points, while for gasoline the range was 143–308 ppm with an average content of 209 ppm. There is a noticeable increase in the hydrocarbon content of the exhaust gas at $\lambda = 1.25$. Hydrocarbon emissions increased by 160% for ethanol (up to 78 ppm) and 76% for gasoline (up to 288 ppm). Taking into account the fact that the exhaust gas temperature decreased for this measurement point and the torque reached the lowest values, it can be concluded that this is the flammability limit of the mixture for the tested engine.

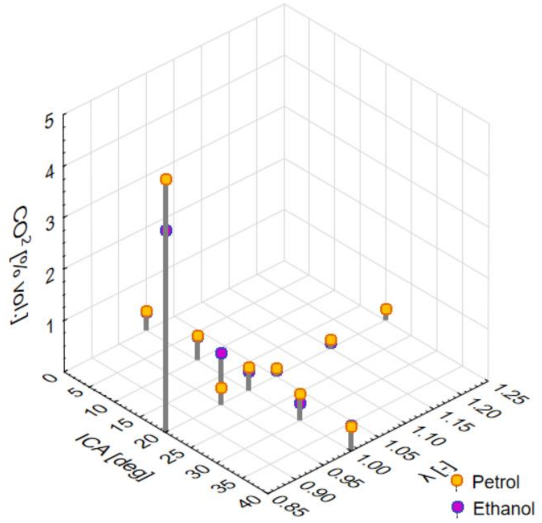

Fig. 6. Volumetric content of carbon monoxide in exhaust gases

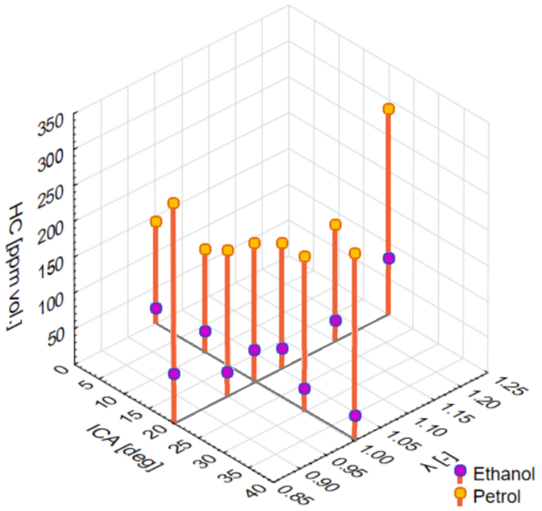

Fig. 7. Hydrocarbon content in exhaust gases

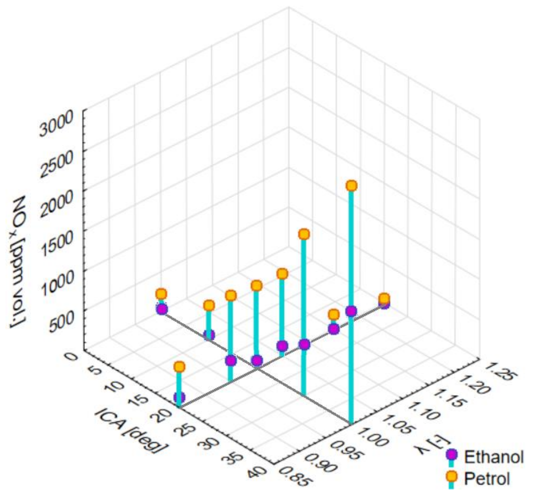

Fig. 8. Nitrogen oxides content in exhaust gases

Figure 8 shows the content of nitrogen oxides in the exhaust gas. The content of nitrogen oxides when the engine was fed with ethanol was 3–1407 ppm, with an average value of 268 ppm. For gasoline, the volumetric NO_x content was in the range of 65–2986 ppm, while the average content was 970 ppm. There was a clear increase in the exhaust gas NO_x content as the ignition advance angle increased.

The measured values of temporal fuel consumption as a function of the excess air ratio λ are shown in Fig. 9. The large difference in temporal fuel consumption for the same engine operating parameters is due to, among other things, the difference in the calorific value of the two fuels used.

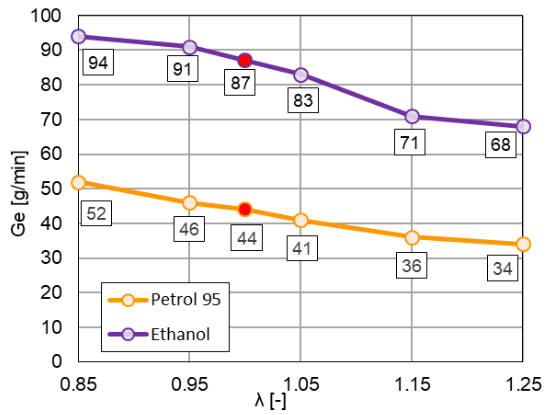

Fig. 9. Fuel consumption rate during operation with gasoline and ethanol

3.2. Results analysis

Based on the obtained data on temporal fuel consumption (Ge) and torque, the specific fuel consumption was calculated from the formula:

$$g_e = \frac{Ge}{\frac{M \cdot n}{9550}} \tag{1}$$

where: g_e – fuel consumption [g/kWh], Ge – temporal fuel consumption [g/min], M – torque [Nm], n – rotational speed – 1500 rpm.

Figure 10 and 11 shows the course of specific fuel consumption as a function of ignition crank angle and excess air ratio λ. It is noticeable that alcohol consumption is higher compared to gasoline at each recorded measurement point, which is due to, among other things, its significantly lower heating value.

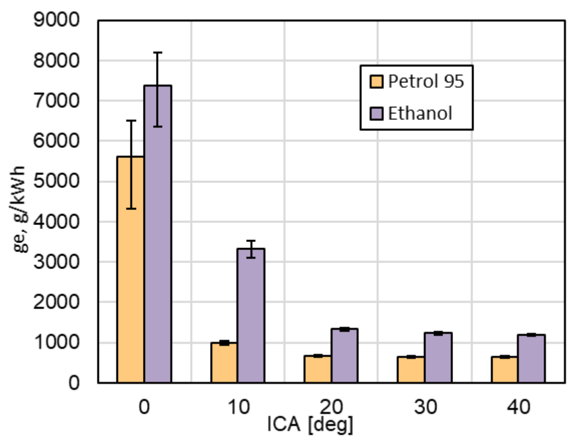

Fig. 10. The specific fuel consumption for gasoline 95 and ethanol at λ = 1.0

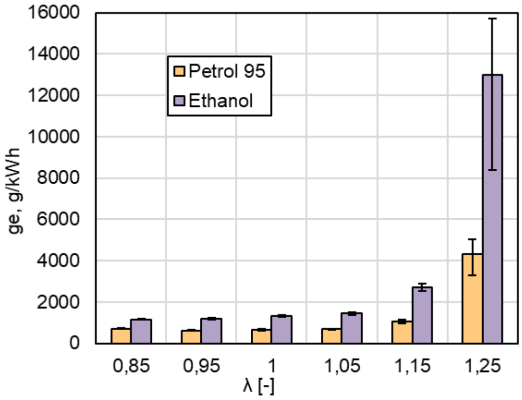

Fig. 11. Specific fuel consumption for ethanol and gasoline 95 at ICA = 20°

By determining the calorific value of gasoline in the range of 40.1–43 MJ/kg and that of ethanol – 24.03–28.31 MJ/kg, the total efficiency of the engine was determined. The highest efficiency for both fuels was obtained for ICA ranging 20–40° BTDP and for a mixture composition in the range λ = 0.85–1.05. When feeding the engine with ethanol, higher efficiency is recorded for richer mixtures. The course of engine efficiency for ethanol and gasoline fueling is shown in Fig. 12 and 13. The overall efficiency at the most favorable measurement points oscillates within 10–14%, which is a relatively small value, but this is due to the low engine load (MAP = 0.45 bar). Such an unfavorable operating condition in terms of efficiency, however, makes the differences between the two fuels become more apparent.

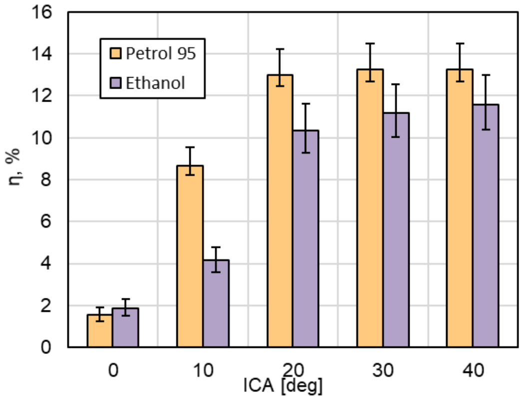

Fig. 12. Engine efficiency during fueled with gasoline 95 and ethanol at λ = 1.0

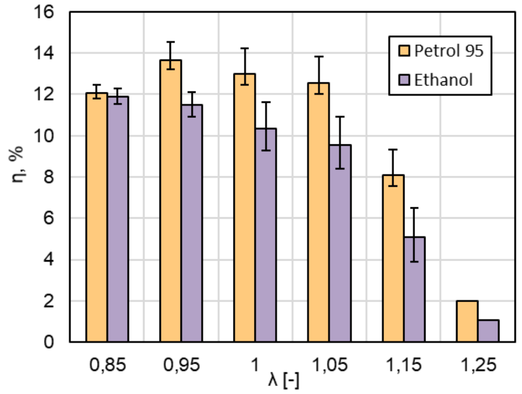

Fig. 13. Engine efficiency when fueled with gasoline 95 and ethanol at ICA = 20°

Using the neural network method prediction module in Statistica, a complete map of internal combustion engine efficiency was determined by using the neural network-based prediction method. Input data for the neural network were the efficiency values at the measurement points shown in Fig. 14 and 15, whereas output data for the algorithm were the specified missing points, identically distributed as in the experiments, for the area bounded by the parameters λ ∈ (0.85–1.25) and ICA ∈ (0–40°).

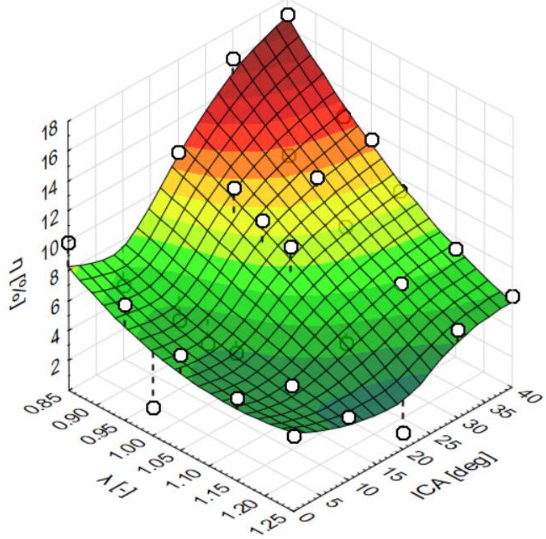

Fig. 14. Map of engine efficiency during operation fueled with ethanol, generated by predicting operating points within the range of λ ∈ (0.85–1.25) and ICA ∈ (0–40°)

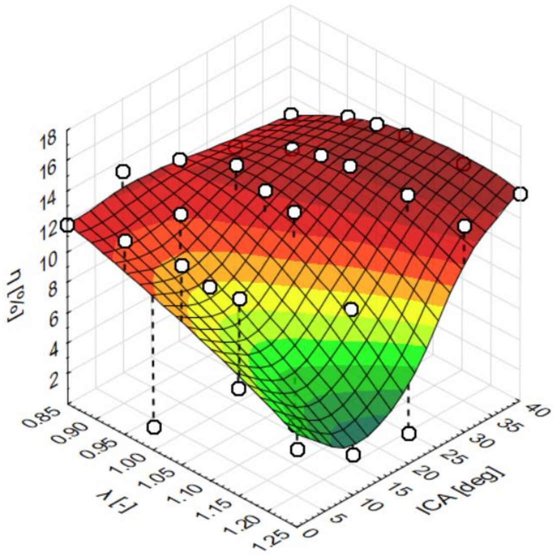

Fig. 15. Map of engine efficiency during operation fueled with gasoline 95, generated by predicting operating points within the range of λ ∈ (0.85–1.25) and ICA ∈ (0–40°)

The values determined by prediction indicate that the gasoline-fueled engine maintains its efficiency above 10% over a much wider range than the ethanol-fueled engine. The most unfavorable operating range of the engine in terms of efficiency is the operation when fed with lean mixtures (λ > 1) and at low values of ICA < 30°.

Figures 16 and 17 shows the degree of reduction in the content of harmful exhaust components after replacing gasoline with ethanol.

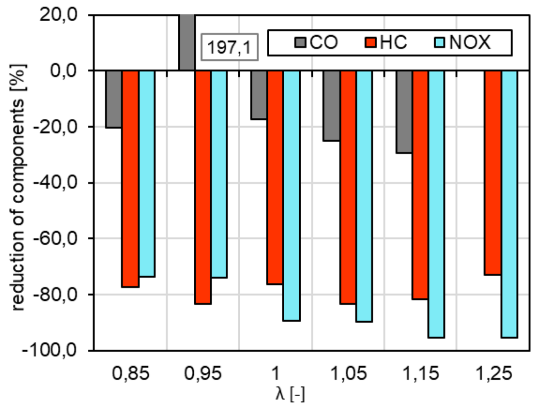

Fig. 16. Reduction of toxic emissions content after replacing gasoline with ethanol at ICA = 20°

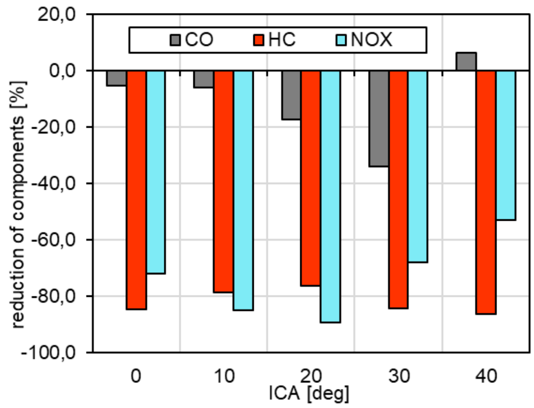

Fig. 17. Reduction of toxic emissions content after replacing gasoline with ethanol at λ = 1.0

The use of ethanol is very beneficial in terms of emission reduction. In most cases, the hydrocarbon content was reduced by approx. 75–80%. When feeding the engine with a lean mixture and at ICA = 20°, the content of nitrogen oxides was reduced by more than 90%. With increasing ICA, the degree of NO_x reduction decreases, but in the least favorable case it is: –53%. The only component of the exhaust gas for which an increase in emissions was registered at individual measurement points is CO. At the measurement point of ICA = 20° and λ = 0.95, the carbon monoxide emissions almost doubled, but with an overall content of 1.01% vol. this can be considered a measurement error. At the measurement point of ICA = 40° and λ = 1.00, ethanol showed a 6.3% increase in CO emissions relative to that of gasoline. The percentage of carbon monoxide at this point for gasoline is 0.48% vol., and for ethanol is 0.51% vol.

Knowing the parameters of the exhaust gas analyzer, it can be claimed that this difference is within the margin of a measurement error. This makes it clear that for all analyzed engine operating conditions, the use of ethanol as an alternative to gasoline allows a significant reduction in emissions.

4. Conclusions

The study showed that under the operating conditions analyzed, the SI internal combustion engine can be fueled with ethanol via the original injection system without any design changes. However, it is necessary to select the correct injection timing for the alcohol fuel. In addition, by changing the fuel from gasoline to ethanol, emissions of harmful exhaust components were reduced at all operating points. The content of carbon monoxide (CO) in the exhaust gas decreased by an average of 14.8% and the content of hydrocarbons (HC) and nitrogen oxides (NO_x) by an average of 80%. Because the heating value of gasoline is about 61% higher than that of gasoline, fuel consumption increased significantly. Temporal fuel consumption increased by 90% on average, while specific fuel consumption increased by 115%. Therefore, ethanol-fueled vehicles could have a much shorter range with the same tank capacity. At the tested operating point, the ethanol-fueled engine showed an efficiency decrease by 1.9 percentage points on average, reaching the highest values for large ICA values (20–40°) and rich mixtures λ = (0.85–0.95). The limit of operation of the tested engine, both with gasoline and alcohol fueling, is the mixture composition λ = 1.25 at which torque reached values close to zero. The study showed that the use of ethanol to power a spark-ignition internal combustion engine can provide significant emissions benefits without significantly degrading engine performance. The only modifications required to start and operate an ethanol-fueled engine are to increase the volumetric fuel flow, which can be achieved by installing higher capacity injectors or making changes to the ECU. This does not mean, however, that making such modifications will be sufficient for long-term operation of the engine on alcohol fuel. Design changes would also be needed to account for the higher temperature amplitude of the engine, the higher water content of the exhaust, or problems associated with alcohol dilution and evaporation.

Nomenclature

CO	carbon monoxide content of the exhaust gas
CO_2	carbon dioxide content of the exhaust gas
EGT	exhaust gas temperature
g_e	specific fuel consumption
Ge	timing fuel consumption
HC	hydrocarbons
ICA	ignition crank angle
M	torque
MAP	manifold absolute pressure
n	rotational speed
NO_x	content of nitrogen oxides in the exhaust gas
RON	research octane number
η	total efficiency of the internal combustion engine
λ	excess air factor in the flue gas

Bibliography

[1] Andersen VF, Anderson JE, Wallington TJ, Mueller SA, Nielsen OJ. Vapor pressures of alcohol−gasoline blends. Energ Fuel. 2010;24(6):3647-3654. https://doi.org/10.1021/ef100254w

[2] Asad U, Kumar R, Zheng M, Tjong J. Ethanol-fueled low temperature combustion: a pathway to clean and efficient diesel engine cycles. Appl Energ. 2015;157:838-850. https://doi.org/10.1016/j.apenergy.2015.01.057

[3] Balat M, Balat H. Recent trends in global production and utilization of bio-ethanol fuel. Appl Energ. 2009;86(11): 2273-2282. https://doi.org/10.1016/j.apenergy.2009.03.015

[4] Barbosa TP, Eckert JJ, Roso VR, Pujatti FJP, da Silva LAR, Horta Gutiérrez JC. Fuel saving and lower pollutants emissions using an ethanol-fueled engine in a hydraulic hybrid passengers vehicle. Energy. 2021;235:121361. https://doi.org/10.1016/j.energy.2021.121361

[5] Chandran VGR, Tang CF. The impacts of transport energy consumption, foreign direct investment and income on CO_2 emissions in ASEAN-5 economies. Renew Sust Energ Rev. 2013;24:445-453. https://doi.org/10.1016/j.rser.2013.03.054

[6] Czarnigowski J, Skiba K. The use of a low frequency vibration signal in detecting the misfire of a cylinder of an aircraft piston engine. SAE Technical Paper 2020-01-2023. 2020. https://doi.org/10.4271/2020-01-2023

[7] Czerwiński J, Comte P, Reutimann F, Mayer A. Influence of hydrous ethanol blends on particle emissions of small 2&4-stroke scooters. Part 1. Combustion Engines. 2011;144(1): 29-36. https://doi.org/10.19206/CE-117120

[8] Elfasakhany A. State of art of using biofuels in spark ignition engines. Energies. 2021;14:779. https://doi.org/10.3390/en14030779

[9] Jakliński P, Czarnigowski J. An experimental investigation of the impact of added HHO gas on automotive emissions under idle conditions. Int J Hydrogen Energ. 2020;45(23): 13119-13128. https://doi.org/10.1016/j.ijhydene.2020.02.225

[10] Jakliński P, Czarnigowski J, Wendeker M. The effect of injection start angle of vaporized LPG on SI engine operation parameters. SAE Technical Paper 2007-01-2054. 2007. https://doi.org/10.4271/2007-01-2054

[11] Kanimozhi B, Kumar G, Alsehli M, Elfasakhany A, Veeman D, Balaji S et al. Effects of oxyhydrogen on the CI engine fueled with the biodiesel blends: a performance, combustion and emission characteristics study. Int J Hydrogen Energ. 2022;47(88):37668-37676. https://doi.org/10.1016/j.ijhydene.2021.08.054

[12] Karthick C, Nanthagopal K, Ashok B, Saravanan SV. Influence of alcohol and gaseous fuels on NO_x reduction in IC engines (chapter 12). NO_x Emission Control Technologies in Stationary and Automotive Internal Combustion Engines. 2022. 347-385. https://doi.org/10.1016/B978-0-12-823955-1.00012-7

[13] Keskin A. The influence of ethanol–gasoline blends on spark ignition engine vibration characteristics and noise emissions. Energ Source Part A. 2010;32(20):1851-1860. https://doi.org/10.1080/15567030902804749

[14] Łomankiewicz D, Brodzik K, Bielaczyc P. GC-MS/FID analysis of aldehyde and hydrocarbon emissions from exhaust gases of a spark ignition engine fueled with different ethanol-gasoline blends. Combustion Engines. 2012;149(2): 30-38. https://doi.org/10.19206/CE-117038

[15] Matla J. Possible applications of prechambers in hydrogen internal combustion engines. Combustion Engines. 2022; 191(4):77-82. https://doi.org/10.19206/CE-148170

[16] Mohammed MK, Balla HH, Al-Dulaimi ZMH, Kareem ZS, Al-Zuhairy MS. Effect of ethanol-gasoline blends on SI engine performance and emissions. Case Studies in Thermal Engineering. 2021;25:100891. https://doi.org/10.1016/j.csite.2021.100891

[17] Murcak A, Haşimoğlu C, Çevik İ, Karabektaş M, Ergen G. Effects of ethanol–diesel blends to performance of a DI diesel engine for different injection timings. Fuel. 2013;109: 582-587. https://doi.org/10.1016/j.fuel.2013.03.014

[18] Pałuchowska M, Stępień Z, Żak G. The prospects for the use of ethanol as a fuel component and its potential in the reduction of exhaust emissions. Combustion Engines. 2014; 158(3):80-92. https://doi.org/10.19206/CE-116940

[19] Pereirinha PG, González M, Carrilero I, Anseán D, Alonso J, Viera JC. Main trends and challenges in road transportation electrification. Transport Research Procedia. 2018;33: 235-242. https://doi.org/10.1016/j.trpro.2018.10.096

[20] Peters JF, Burguillo M, Arranz JM. Low emission zones: Effects on alternative-fuel vehicle uptake and fleet CO_2 emissions. Transport Res D-Tr E. 2021;95:102882. https://doi.org/10.1016/j.trd.2021.102882

[21] Pietrykowski K, Majczak A, Czarnigowski J. An electronically controlled hydrogen injector for Wankel engine. Combustion Engines. 2011;1-7.

[22] Reitz RD, Ogawa H, Payri R, Fansler T, Kokjohn S, Moriyoshi Y et al. IJER editorial: The future of the internal combustion engine. Int J Engine Res. 2019;21(1):3-10. https://doi.org/10.1177/1468087419877990

[23] Saravanan P, Kumar NM, Ettappan M, Dhanagopal R, Vishnupriyan J. Effect of exhaust gas re-circulation on performance, emission and combustion characteristics of ethanol-fueled diesel engine. Case Studies in Thermal Engineering. 2020;20:100643. https://doi.org/10.1016/j.csite.2020.100643

[24] Siadkowska K, Barański G, Sochaczewski R, Wendeker M. Experimental investigation on indicated pressure and heat release for direct hydrogen injection in a dual fuel diesel engine. Adv Sci Tech. 2022;16(3):54-66. https://doi.org/10.12913/22998624/149300

[25] Stelmasiak Z, Pietras D. The evaluation of the regularity of the combustion process in the SI engine fueled with petrol and ethanol. Combustion Engines. 2017;168(1):94-99. https://doi.org/10.19206/CE-2017-11

[26] Ścisłowski K, Skiba K, Wendeker M, Kliza R, Siadkowska K, Lusiak T et al. Durability analysis of the prototype test rig for main rotors. Communications – Scientific Letters of the University of Zilina. 2022;24(2):B148-157. https://doi.org/10.26552/com.C.2022.2.B148-B157

[27] Taghizadeh-Alisaraei A, Rezaei-Asl A. The effect of added ethanol to diesel fuel on performance, vibration, combustion and knocking of a CI engine. Fuel. 2016;185:718-733. https://doi.org/10.1016/j.fuel.2016.08.041

[28] Wee J-H. Carbon dioxide emission reduction using molten carbonate fuel cell systems. Renew Sust Energ Rev. 2014; 32:178-191. https://doi.org/10.1016/j.rser.2014.01.034

[29] Yu F, Yu B. The use of ethanol–gasoline blend as a fuel in an SI engine. Renew Energ. 2004;29:1181-1191. https://doi.org/10.1016/j.renene.2003.11.012

[30] Zacharewicz M, Kniaziewicz T. Model tests of a marine diesel engine powered by a fuel-alcohol mixture. Combustion Engines. 2022;189(2):83-88. https://doi.org/10.19206/CE-143486

[31] Zangoei S, Salehnia N, Khodaparast Mashhadi M. A comparative study on the effect of alternative and fossil energy consumption on economic growth and foreign direct in-

vestment in selected countries using SUR approach. Environ Sci Pollut R. 2021;28(16):19799-19809. https://doi.org/10.1007/s11356-020-11575-5

[32] Zapata C, Nieuwenhuis P. Exploring innovation in the automotive industry: new technologies for cleaner cars. J Clean Prod. 2010;18(1):14-20. https://doi.org/10.1016/j.jclepro.2009.09.009

[33] Zhang B, Liu H. Theoretical prediction model and experimental investigation of detonation limits in combustible gaseous mixtures. Fuel. 2019;258:116132. https://doi.org/10.1016/j.fuel.2019.116132

Piotr Jakliński, DSc., DEng. – Faculty of Mechanical Engineering, Lublin University of Technology, Poland.

e-mail: *p.jaklinski@pollub.pl*

Jacek Czarnigowski, DSc., DEng. – Faculty of Mechanical Engineering, Lublin University of Technology, Poland.

e-mail: *j.czarnigowski@pollub.pl*

Karol Ścisłowski, MEng. – Faculty of Mechanical Engineering, Lublin University of Technology, Poland.

e-mail: *k.scislowski@pollub.pl*

Article citation info:
Sawczuk W, Kołodziejski S, Rilo Cañás AM. Determination of the resistance to motion of a cargo train when driving without a drive. Combustion Engines. 2024;197(2):64-70. https://doi.org/10.19206/CE-184051

Wojciech SAWCZUK
Sławomir KOŁODZIEJSKI
Armando Miguel RILO CAÑÁS

Combustion Engines
Polish Scientific Society of Combustion Engines

Determination of the resistance to motion of a cargo train when driving without a drive

ARTICLE INFO

Received: 9 August 2023
Revised: 1 February 2024
Accepted: 13 February 2024
Available online: 2 March 2024

The issue related to the motion resistance of a rail vehicle is very important for energy, environmental, and related energy consumption of the vehicle as well as vehicle performance with dynamic points. The latter aspect applies in particular to traction vehicles. The article presents several models of resistance to the movement of a freight train used by various railway authorities, for Polish and foreign rolling stock. The resistance values obtained from the models were verified against the tested freight train carrying aggregate. On the basis of the records from the locomotive recorder, linear models of speed changes over time and coasting paths (without drive) were determined. On the basis of the values obtained from the models of resistance to movement of a freight train, the paths of coasting to stop the train were determined on the basis of the UIC 544-1 card, which were related to the analyzed freight train.

Key words: *movement resistance, driving without the drive engaged, cargo train, operational tests*

1. Introduction

During the progressive movement of a rail vehicle in a gaseous medium (air), it is inseparably accompanied by resistance to motion. In the railway literature, there are many articles presenting empirical models describing the resistance to motion for both passenger and freight trains. These are the quadratic dependencies of the train speed, additionally taking into account the weight, axle load, and aerodynamic resistance while driving. Ultimately, the use of the dependence on train motion resistance is necessary for the calculation of energy consumption in the vehicle design phase as well as for the assessment of energy consumption for traction purposes. The first attempts to measure (measure) resistance to motion were carried out by Stephenson and Wood in 1818, but research in this area was only carried out by Harding and Gooch in 1840. However, these were tests conducted up to the speed of rail vehicles of about 100 km/h. It was only after 1904 that tests were carried out with vehicle speeds exceeding 200 km/h [15].

In the history of railway technology, chronologically, empirical relationships for resistance to motion were developed by Harding and Gooch in 1846, then by Clark in 1855, Barbier in 1898, Frank in 1907, Sanzin in 1908, Schmidt in 1910 in 1911, Leitzmann and von Borries in 1911, Strahl in 1913 and Sachs in 1928 [2]. The dependences on the resistance to motion are based in all cases of their creators on the equation describing the rolling resistance as a square function of speed, generally written as equation (1) [12]:

$$F_{RES} = A + B \cdot v + C \cdot v \tag{1}$$

where: F_{RES} – resistance force of the rail vehicle motion, v – speed of the rail vehicle, A, B, C – coefficients of resistance to motion.

The naming relationship (1) is the Davis equation, and its coefficients are related to the different components of resistance. The coefficient A is most often associated with the rolling resistance of the wheel on the rail, the coefficient B refers to the mechanical resistance associated with friction in the axial bearings, and the coefficient C is related to the aerodynamic resistance. In the calculations of the FRES movement resistance by various authors, special attention should be paid to the units, as they are given in N, N/t, N/kN, Ib/t. In the case of the train speed, the m/s and km/h units are interchangeable in the motion resistance equations [3, 6].

The resistance to motion of a rail vehicle or train is determined by measuring the consumption of electricity from electric traction at a constant speed. Another method that is more often used is the measurement of the run-down distance after the wagon, locomotive, or wagon train has accelerated from a given speed. Then, the measurement on a given section of the railway line with known track parameters is carried out until the wagon, locomotive, or wagon train stops. The tests related to the determination of the resistance to motion are also carried out, taking into account the aerodynamic resistance. These components of motion resistance tests are most often carried out in wind tunnels on scale models or on real objects [4, 8]. Similar works in the field of vehicle motion resistance are conducted by researchers in their works, e.g., in [9, 21], a methodology for determining motion resistance and aerodynamic resistance for electric vehicles is presented. The works [13, 14] present the movement resistances of an electric locomotive and a proposal to optimize the design of the drive system to reduce these resistances. The work [18, 22] presents the influence of the vehicle's driving route and weather conditions on the vehicle's movement resistance. Works [19, 24] determine the movement resistance of a light rail vehicle due to the wheel structure.

The article presents several models of motion resistance used by various railway authorities for Polish and foreign rolling stock to calculate the motion resistance of the tested freight train. The obtained values from the calculation of the resistance to motion were verified on the example of a selected freight train carrying aggregate. On the basis of the records from the locomotive recorder, linear models of speed changes over time and the coasting distance without the drive engaged were determined. On the basis of the values obtained from the models of resistance to movement of a freight train, the theoretical distances of the free-wheel drive were determined on the basis of the UIC 544-1 card, which were then referred to the analyzed freight train.

2. Purpose and methodology of research

The aim of the research is to verify selected models of motion resistance on the example of a freight train by determining the coasting distance of the train without drive and without the use of brakes. The test was carried out after starting up to the set speed and measuring the time and distance of driving without drive until stopping.

During the free running of the train from the set speed, the length of the path traveled by the freight train depends on such main factors as rolling resistance, aerodynamics, or load on the train with the transported load [1]. During the tests of a freight train carrying bulk materials, the coasting distance of the train without drive was determined, which was verified analytically (calculated) by determining the rolling resistance of the freight train using various models found in the railway literature. On this basis, on the example of the analyzed freight train, it was determined which of the models of motion resistance with the highest accuracy allows estimating the coasting distance without drive and without using brakes in the train during the tests.

The study was carried out on railway line 275 on the Legnica–Wrocław section. It is a standard-gauge railway line in south-western Poland with a length of 192.658 km, running through the area of the Lower Silesian and Lubuskie Voivodships, connecting Wrocław with Gubinek on the Polish-German border. A section of the railway line on the Legnica–Wrocław section with an inclination of about 0‰ was selected for the study.

3. Research object

The object of the research was a freight train consisting of a 6-axle diesel locomotive BR232 and 35 freight wagons of Eaos and Eamos 426W, 436W, and 437W coal wagons along with their variants. Figure 1 shows the view of the locomotive with the running gear, while Fig. 2 shows the composition of the loaded wagons before the tests.

Table 1. Train (composition) input before testing

No.	Name	Symbol	Value	Unit
1	Gross weight of the composition	m_{wag}	2778.8	[t]
2	Train weight	m_{poc}	2902.7	[t]
3	Train length	l_p	468	[m]
4	Number of wagons	n_{wag}	35	[pcs]
5	Train speed	v	60	[km/h]
6	Number of axles in wagons	n_o	140	[pcs]
7	Number of axles in the trainset	n_p	146	[pcs]
8	Equivalent section of the locomotive	S_{lok}	13.5	[m^2]
9	Equivalent section of wagons	S_{wag}	10	[m^2]
10	Continuous power at start	P_c	1675	[kW]
11	Pulling force at start-up	F_c	294	[kN]

All wagons were loaded with aggregate. In the loaded state, the gross weight of the trainset was 2778.7 t, with the permissible weight of 2800 t.

Fig. 1. View of the BR232 diesel locomotive – a), view of the bogie with the suspension system, power transmission and braking system – b)

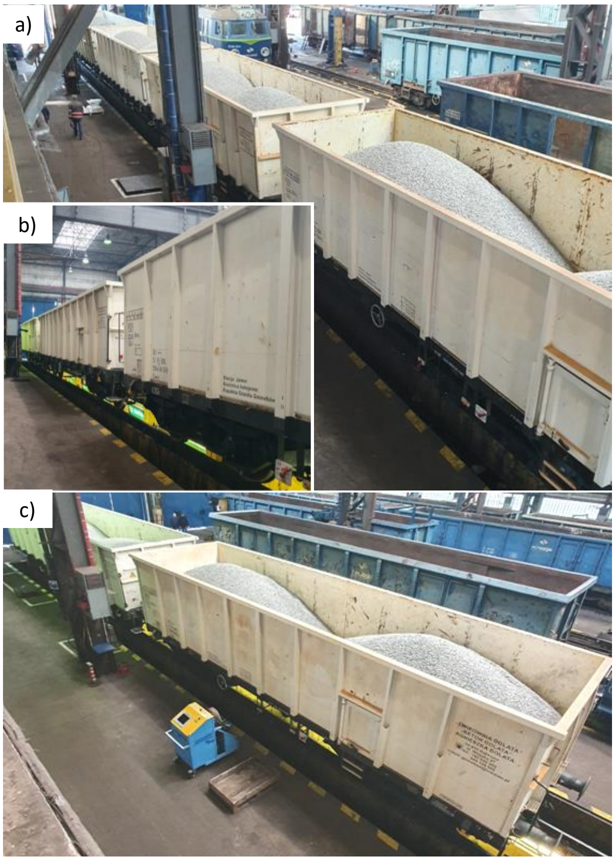

Fig. 2. View of wagons loaded with aggregate before testing

The length of the train was 468 m. Detailed data on the tested train are presented in Table 1. With these train parameters, the travel speed was set to v = 60 km/h.

4. Selected models of train motion resistance

Traffic resistance based on data from the tested freight train was determined on the basis of a number of dependencies for various railways, i.e., Polish, French, German, Czech, and Slovak [2, 3, 10]. No other models were used as for Chinese, Japanese or American railways due to the specificity of the tested train, for which the tests were carried out in the conditions of the European railway infrastructure.

Motion resistance is determined in the conditions of the Polish railway infrastructure, developed by the Railway Science and Technology Centre [3].

$$F_{res} = \left(K + 1.5\frac{v}{10}\right) \cdot m_{wag} + 150 \cdot n_o + f \cdot \left(2.5 + n_{wag}\right)\left(\frac{v}{10}\right)^2 \quad (2)$$

$$F_{res} = 77.98 \text{ kN}$$

where: F_{res} – the value of the movement resistance force in [N], K – bearing type factor, for rolling bearings K = 6.5, v – train speed in [km/h], m_{wag} – weight of wagons in [t], n_o – number of axles in the train, f – train type factor, for freight f = 8, n_{wag} – number of wagons in the train.

The resistance of the whole train, according to relation (2), is 77.98 kN, while the average resistance of one car is 2.17 kN for further calculations of the coast-down distance.

Motion resistance according to Franck's relationship [20].

$$F_{res} = 2.5 + 0.0145 \cdot \left(\frac{v^2}{10}\right) + \frac{0.54}{m_{wag}}\left(1.1 \cdot k \cdot S_{lok} + 2 + n_{wag} \cdot q\right) \cdot \left(\frac{v}{10}\right)^2 \quad (3)$$

$$F_{res} = 3.20 \ \frac{N}{kN}$$

where: F_{res} – relative value of the movement resistance force in [N/kN], k – shape coefficient of the locomotive face, for a flat front k = 1, S_{lok} – equivalent section of the locomotive in [m²] (according to Table 1), q – wagon type coefficient, for open wagons loaded with q = 0.32.

The resistance of the whole train according to relation (3) is 3.20 N/kN, which for all wagons will be 87.26 kN, while the average resistance of one wagon will then be 2.42 kN for further calculations.

Movement resistance of French rolling stock according to the UIC standard [3].

$$f_{res} = 9.81 \cdot \left(1.25 + \frac{v^2}{6300}\right) = 17.87 \ \frac{N}{t} \quad (4)$$

where: f_{res} – relative value of the movement resistance force in [N/t], v – train speed in [km/h].

The resistance of the whole train according to relation (4) is 51.87 kN, while the average resistance of one wagon will be 1.44 kN.

Train movement resistance according to Czech (ČD) and Slovak railways (ŽSR) [2].

$$f_{res} = A + B \cdot \frac{v}{100} + C \cdot \left(\frac{v}{100}\right)^2 = 2.48 \ \frac{N}{kN} \quad (5)$$

where: f_{res} – relative value of the movement resistance force in [N/kN], A – constant of the basic motion resistance force, for a train with loaded 4-axle freight wagons A = 1.4, B – motion resistance constant, for a freight train B = 0, C – drag coefficient, for a train with loaded 4-axle freight wagons C = 3.

The resistance of the whole train, according to relation (5), is 2.48 N/kN, which for all wagons will be 70.62 kN, while the average resistance of one wagon will then be 1.96 kN for further calculations of the locomotive rundown distance without the drive switched on.

Traffic resistance of freight and passenger trains according to French National Railways (SNCF) based on [11].

$$f_{res} = A + B \cdot \frac{v}{100} + C \cdot \left(\frac{v}{100}\right)^2 = 2.10 \ \frac{N}{kN} \quad (6)$$

where: f_{res} – relative value of the movement resistance force in [N/kN], A – constant of the basic motion resistance force, for a loaded freight train, A = 1.2, B – motion resistance constant, for a loaded and empty passenger and freight train, B = 0, C – drag coefficient, for a loaded freight train, C = 2.5.

The resistance of the whole train according to relation (6) is 2.10 N/kN, which for all wagons will be 59.80 kN. On the other hand, the average resistance of one wagon will then be 1.66 kN for the calculation of the coasting distance of the train without propulsion, presented in Chapter 5.

Motion resistance of an express freight train according to DB railways (based on the Strahl relationship) with rolling bearings (homogenous composition) based on [7].

$$f_{res} = 1.0 + 0.0002 \cdot v^2 = 1.72 \ \frac{N}{kN} \quad (7)$$

where: f_{res} – relative value of the movement resistance force in [N/kN], v – train speed in [km/h].

The resistance of the whole train according to relation (7) is 2.10 N/kN, which for all wagons will be 48.98 kN. The average resistance of one wagon will then be 1.36 kN.

Train motion resistance according to Strahl's relationship [11].

$$f_{res} = [2.0 + 0.1 \cdot (0.07 + C_3) \cdot v^2] \cdot g = 45.49 \ \frac{N}{t} \quad (8)$$

where: f_{res} – relative value of the movement resistance force in [N/t], C_3 – coefficient depending on the type of train, for fast and freight trains loaded (full) C_3 = 0.025, v – train speed in [m/s], g – gravitational acceleration g = 9.80665 [m/s^2].

The resistance of the whole train according to relation (8) is 45.49 N/t, which for all wagons will be 132.05 kN. The average resistance of one wagon will then be 3.67 kN.

Motion resistance of passenger trains driven by a locomotive according to German railways [7].

$$F_{res} = 3 \cdot m_{log} \cdot g + 1.59 \cdot S_{lok} \cdot v^2 + 1.5 \cdot m_{wag} \cdot g + 0.09 \cdot m_{poc} \cdot g + 0.0763 \cdot \left(n_{wag} + 2\right) \cdot S_{wag} \cdot (v + 4.17)^2 \quad (9)$$

$$F_{res} = 65301.1 \text{ N}$$

where: F_{res} – the value of the movement resistance force in [N], m_{lok} – weight of the locomotive in [t], m_{wag} – wagon weight in [t], m_{poc} – train mass in [t], S_{lok} – equivalent section of the locomotive in [m²], S_{wag} – equivalent section of wagons in [m²], v – train speed in [m/s], n_{wag} – number of wagons in the train, g – gravitational acceleration g = 9.80665 [m/s^2].

The resistance of the whole train according to relation (9) is 65.30 kN. The average resistance of one wagon will then be 1.81 kN.

Motion resistance used in French railways SNCF for wagons [23].

$$F_{res} = \left[C_1 + \frac{(3.6\cdot v)^2}{C_2}\right]\cdot m_{poc}\cdot g = 54084.9\ \mathrm{N} \qquad (10)$$

where: F_{res} – the value of the movement resistance force in [N], m_{poc} – train mass in [t], C_1, C_2 – coefficients depending on the type of train, for a heavy freight train, e.g. a coal wagon weighing 80 t, $C_1 = 1$, $C_2 = 4000$, v – train speed in [m/s].

The resistance of the whole train according to relation (10) is 54.08 kN. The average resistance of one wagon will then be 1.50 kN.

Train motion resistance according to the Italian State Railways (FS) based on [3]

$$f_{res} = A + C\cdot\left(\frac{v}{100}\right)^2 = 3.26\ \frac{\mathrm{N}}{\mathrm{kN}} \qquad (11)$$

where: f_{res} – relative value of the movement resistance force in [N/kN], A – constant of the basic motion resistance force, for a train with loaded covered freight wagons, A = 2.50 N/kN, C – motion resistance constant for a train with loaded covered freight wagons, C = 2.12 N/kN, v – train speed in [km/h].

The resistance of the whole train according to relation (11) is 3.26 N/kN, which for all wagons will be 92.92 kN. On the other hand, the average resistance of one wagon will then be 2.58 kN for the calculation of the coast-down distance, which is presented in detail in Chapter 5.

A collective list of empirical calculations of freight train motion resistance based on input data for ten models is presented in Table 2.

Table 2. The results of the calculated train motion resistances according to different models

No.	Train resistance model	Value for the train in [kN]	Value for the wagon in [kN]
1	Strahl dependencies	132.05	3.67
2	Italian State Railways (FS)	92.92	2.58
3	Franck dependencies	87.26	2.42
4	The Polish Railway developed by the Railway Science and Technology Centre	77.98	2.17
5	Czech Railways (ČD) and Slovak Railways (ŽSR)	70.62	1.96
6	German Railways for locomotive driven passenger trains	65.30	1.81
7	State Railways (SNCF) freight and passenger trains	59.80	1.66
8	French Railways (SNCF) for wagons	54.08	1.50
9	French rolling stock according to the UIC standard	51.87	1.44
10	DB Deutsche Bahn for express freight trains	48.98	1.36

The values of movement resistance, with separate details for the train and wagon, are presented in Table 2 from the highest to the lowest value. Preliminarily analyzing the data contained in Table 2, it can be unequivocally stated that the dispersion of the results of the train motion resistance according to different models (different countries) is very large. The obtained values ranged from 49 to 132 kN. This proves that despite the same marginal values of the test train being used to calculate the movement resistance, some models with extreme values (max and min) are subject to large errors. This assumes that the models in positions 5, 6 and 7 in the table have similar values and are therefore the most accurate. Verification of the calculation results with the tested test train will allow this statement to be accepted or rejected.

5. Theoretical driving distance without drive

In order to determine the distance covered by the train without drive from the set speed, the relation (12) for the braking distance from the UIC 544-1 card was used [5].

$$s = \frac{t_s}{2}\cdot v + \frac{m_{wag}\cdot v^2}{2\cdot(F_c + F_{res})} \qquad (12)$$

where: t_s – brake cylinder filling time in [s], v – braking start speed in [km/h], m_{wag} – weight of the wagon with rotating masses in [t], F_c – brake force on the circumference of the wheel, in [kN], F_{res} – rolling resistance of the wagon determined from dependence (2)–(11) in [kN].

From dependence (12), the first part related to the braking force increase time t_s, the braking start speed v and the brake force on the circumference of the wheel F_c from the second part had to be removed. Then, for all methods of train motion resistance, the coasting distance without drive to stop was determined as the product of the average weight of the wagon with rotating masses and the square of the speed, divided by twice the running resistance of the wagon [16]. Finally, the dependence (13) on the coasting of a freight train was obtained.

$$s_w = \frac{m_{wag}\cdot v^2}{2\cdot F_{res}} \qquad (13)$$

Table 3 shows the driving resistance values for individual methods and the corresponding coasting distances of the wagon to its stop. The values of the coasting distances without drive were ranked from the shortest distance with the greatest resistance to motion, to the longest distance of coasting without drive with the smallest resistance to the movement of the train.

The values of the calculated coasting distances are presented in the table from the smallest to the largest value. Analyzing the obtained and summarized results in Table 3, it is found that the values of the coasting distances without the drive are characterized by a large dispersion. The coasting distance ranges from 3 to 8 km. This is mainly due to the train movement resistance component, the values of which were also obtained with a large dispersion (Table 2). Only in the case of French railways, for three different models of train resistance, the dispersion of the results of the coasting distance was 1 km (max. 7.7 km, min. 6.7 km). The discrepancy in the values of the coasting distances results from the coefficients characterizing the freight wagon adopted for each method of driving resistance and adopted by various railway authorities. Due to the large differences in the values of the calculated coasting distances, with the same initial (boundary) conditions, it is necessary to verify the values obtained from the calculations to the test results of the test train. It will then be possible to indicate the model or group of models that most accurately determines the movement resistance of the train and freight wagon.

Table 3. List of coasting distances without drive for different methods of train motion resistance

No.	Train resistance model	Coasting distance without drive [m]
1	Strahl dependencies	3053.04
2	Italian State Railways (FS)	4338.65
3	Franck dependencies	4620.04
4	The Polish Railway developed by the Railway Science and Technology Centre	5169.96
5	Czech Railways (ČD) and Slovak Railways (ŽSR)	5708.82
6	German Railways for locomotive driven passenger trains	6173.75
7	State Railways (SNCF) freight and passenger trains	6741.85
8	French Railways (SNCF) for wagons	7454.07
9	French rolling stock according to the UIC standard	7772.96
10	DB Deutsche Bahn for express freight trains	8231.33

6. Operational tests of a cargo train

In order to verify the values of train motion resistances obtained by various methods (Table 2), the coasting distances obtained in this way without drive (Table 3) were referred to a freight train carrying aggregate. The tested train consisted of a BR232 locomotive and 35 coal wagons, which have already been described in Chapter 3. The tests were carried out on a horizontal section without inclination, the train was accelerated to a speed of 60 km/h and the coasting was started. The data of the tested train for the verification of the train motion resistance models are included in Table 1. The test was carried out at 19.00, the day was cloudy without precipitation, the air temperature was 10°C, the visibility of the air was good. From the recorder of the BR232 locomotive, the speed and time values of the locomotive were read from the moment of acceleration of the train to the speed of 60 km/h and from the moment of stopping. The measurement of the distance traveled was additionally referred to the hectometrical poles placed on the railway line every 100 m.

On the basis of the approximation of the train speed points read from the locomotive recorder over time and travel distance until stopping, the following linear function was determined.

$$\mathrm{v_w} = -0.0386 \cdot \mathrm{t_w} + 16.67 \tag{14}$$

$$\mathrm{v_w} = -0.033 \cdot s_\mathrm{w} + 16.67 \tag{15}$$

where: v_w – train speed during coasting in [m/s], t_w – rundown time of the train in [s], s_w – distance traveled by the train overrun in [m].

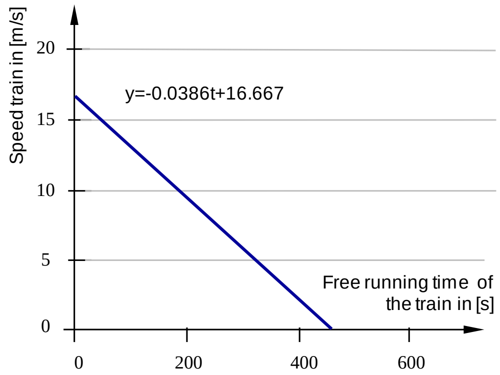

Fig. 3. Dependence of the approximated speed of the train during coasting without drive on the time of travel until stopping

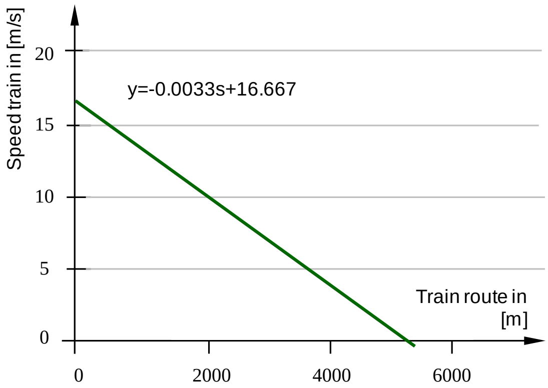

Fig. 4. Dependence of the approximated speed of the train during coasting without the drive on the distance covered until it stops

Based on data from the locomotive recorder of a freight train carrying aggregate with a total weight of 2902.7 t gross, which was accelerated to a speed of 60 km/h on a non-inclined track, the coasting distance traveled without a drive was 5050 m in 7 minutes. and 12 p.

7. Analysis of test results

The value of the coasting distance without the drive of the freight train was related to the theoretical distance determined from dependence (13). Table 4 lists again the values of the coasting distances without drive along with the relative percentage error based on the analyzed models of the motion resistance of a single freight car. The theoretical values of the coasting distances of the train without the drive switched on are listed in the order from the motion resistance model most accurately reflecting the resistance of the tested freight train to the least accurate model.

Analyzing the data contained in Table 4, it is concluded that for the analyzed case of a freight train, the most accurate method of determining the resistance to motion is the method developed for Polish railways. The relative percentage error of the calculated actual coasting distance without the drive compared to the theoretical one was 2.4%. In second place is the method resulting from the Franck dependence of the resistance of the train movement, the error of fitting the theoretical model to the real one was 8.5%. In third place is the method developed for Czech and Slovak railways with a relative percentage error of 13%.

The least accurate model of motion resistance turned out to be the DB method for German railways for express freight trains. With this method, the calculated coasting distance without the drive switched on in relation to the actual distance of the tested freight train, the error was 63%.

Table 4. Comparison of the theoretical and actual coasting distance of a freight train for different motion resistance models

No.	Train resistance model	Coasting distance without drive [m]	Difference [m]	Error [%]
1	The Polish Railway developed by the Railway Science and Technology Centre	5169.96	119.36	2.36
2	Franck dependencies	4620.04	430.56	8.52
3	Czech Railways (ČD) and Slovak Railways (ŽSR)	5708.82	658.22	13.03
4	Italian State Railways (FS)	4338.65	711.95	14.10
5	German Railways for locomotive driven passenger trains	6173.75	1123.15	22.24
6	State Railways (SNCF) freight and passenger trains	6741.85	1691.25	33.49
7	Strahl dependencies	3053.04	1997.56	39.55
8	French Railways (SNCF) for wagons	7454.07	2403.47	47.59
9	French rolling stock according to the UIC standard	7772.96	2722.36	53.90
10	DB Deutsche Bahn for express freight trains	8231.33	3180.73	62.98
The actual coasting distance of the tested train			5050.6 [m]	

Fig. 5. View of the last wagon after the tests: a) the railway inspector conducts a simplified test of the braking system operation, b) the railway inspector evaluates the technical condition of the wagon

After the tests of the coasting distance without the locomotive drive turned on, the stopped freight train was checked by the railway inspector, as shown in Fig. 5. The pressure in the main conduit was checked on the last car, and the condition of all cars (from the last to the locomotive) was visually assessed, in accordance with procedure contained in [17] and the train was dispatched to its further scheduled route.

The authors of the article are aware that the results of calculations and tests on one freight train are insufficient and tests should be carried out on a larger number of freight trains of different weights and for different coasting speeds. However, due to the extensive organizational preparation of such studies, it is complex and costly. It also requires a lot of involvement of the carrier to be willing to carry out such coasting tests during scheduled railway traffic.

8. Conclusions

On the basis of the tests carried out on a freight train and the calculations of train motion resistance, it was found that:

a) The methods of determining the coasting distance based on the weight of the train, speeds and models of driving resistance can be verified with high accuracy on the basis of operational tests of the train
b) On the example of the analyzed freight train, the most accurate method of determining the resistance of the train movement is the method for the Polish rolling stock and the method used by the Czech and Slovak railways. The relative percentage error for both methods when determining the theoretical coast-down distance and comparing it to the real driving distance without the drive was 2.4 and 8.5%, respectively
c) The literature presents a lot of models describing the train motion resistance, both for traction vehicles (locomotives) and trains. Verification of 10 models presented in the article showed that the relative percentage error is in the range of 2.4–63%
d) The high inaccuracy of matching models of motion resistance to real conditions is evidenced by the values of model coefficients and model variables. In some cases of the models, the coefficients for a freight wagon took into account only the case of covered wagons, and not, as for coal wagons, with an open roof.

Acknowledgements

The investigations were carried out within the Implementation Doctorate Program of the Ministry of Education and Science realized in the years 2021–2025.

Nomenclature

DB	Deutsche Bahn AG
ČD	České dráhy
FS	Ferrovie dello Stato Italiane
SNCF	Société nationale des chemins de fer français
UIC	Union Internationale des Chemins de fer
ŽSR	Železnice Slovenskej republiky
f_{res}	relative value of the movement resistance force
F_{res}	the value of the movement resistance force
F_c	brake force on the circumference of the wheel
m_{lok}	weight of the locomotive
m_{poc}	train mass
m_{wag}	weight of wagons
n_o	number of axles in the train
n_{wag}	number of wagons in the train
s_w	distance traveled by the train overrun
S_{lok}	equivalent section of the locomotive
S_{wag}	equivalent section of wagons
t_s	brake cylinder filling time

t_w rundown time of the train
v train speed
v_w train speed during coasting

Bibliography

[1] Anuszczyk J, Gocek A, Pacholski K, Dominikowski B. Modeling the train braking curve and analyzing the accuracy and quality of the automatic stop process. Buses Operation and Tests. 2016;12:768-774 (in Polish).
[2] Biliński J, Błażejewski M, Malczewska M, Szczepiórkowska M. Motion resistance of traction vehicles (1). TTS Research. 2019;3:34-39 (in Polish).
[3] Biliński J, Błażejewski M, Malczewska M, Szczepiórkowska M. Traffic resistance of passenger and freight trains (2). TTS Exploitation. 2019;5:39-44 (in Polish).
[4] Biliński J, Błażejewski M, Malczewska M, Szczepiórkowska M. Traffic resistance of metro trains (5). TTS Exploitation. 2020;3-4:58-59 (in Polish).
[5] Card UIC 544-1 (E) Brake – Braking Performance. 6th Edition, October 2014.
[6] Domek M. Vehicle motion resistance and minimization of rolling resistance. Drives and Controls. 2017;12:96-100 (in Polish).
[7] Garczarek A, Woźnika K, Olejniczak T, Waśkowicz R, Stachowiak D. Determination of the reactance of rail vehicles wheelsets. Rail Vehicles/Pojazdy Szynowe 2023;1-2;32-38. https://doi.org/10.53502/RAIL-168083
[8] Gąsowski W. Analysis of formulas for calculating train motion resistance. XIII Scientific Conference Rail Vehicles 1998. Scientific Papers of the Silesian University of Technology. 1998;31(1392):77-84 (in Polish).
[9] Greunen RV, Oosthuizen C. Data driven methods for finding coefficients of aerodynamic drag and rolling resistance of electric vehicles. World Electric Vehicle Journal. 2023;14(6):2-21. https://doi.org/10.3390/wevj14060134
[10] Jaworski A, Lejda K, Bilski M. Effect of driving resistances on energy demand and exhaust emission in motor vehicles. Combustion Engines. 2022;189(2):60-67. https://doi.org/10.19206/CE-142949
[11] Karwowski K. Power industry electrified transport. Publishing House of the Gdańsk University of Technology, Gdańsk 2018 (in Polish).
[12] Kwaśnikowski J. Elements of the theory of motion and rationalization of driving a train. Library of Exploitation Problems, Scientific Publishing House of the Institute for Sustainable Technologies – PIB, Radom 2013 (in Polish).
[13] Liu B, Xu X, Pan D. Influence of resistance due to locomotion mechanism configurations of a new high-speed amphibious vehicle (HSAV-II). Ocean Eng. 2023;2831:115175. https://doi.org/10.1016/j.oceaneng.2023.115175
[14] Liu B, Xu X, Pan D. Resistance reduction optimization of an amphibious transport vehicle. Ocean Eng. 2023;280:114854. https://doi.org/10.1016/j.oceaneng.2023.114854
[15] Madej J. Theory of motion of rail vehicles. Publishing House of the Warsaw University of Technology. Warsaw 2004 (in Polish).
[16] Piechowiak T. Brakes of rail vehicles. Poznań University of Technology Publishing House. Poznań 2012 (in Polish).
[17] PKP CARGO SA. Cw-1 Operation and maintenance manual for rolling stock brakes. Edition 2016 (in Polish).
[18] Schäfers L, Silber D, Savelsberg R, Pischinger S. Efficient determination of driving resistance through system identification based on driving route information and weather data. Expert Syst Appl. 2023;232(1):120755. https://doi.org/10.1016/j.eswa.2023.120755
[19] Semenov S, Mikhailov E, Kovtanets M, Sergienko O, Dižo J, Blatnický M et al. Kinematic running resistance of an urban rail vehicle undercarriage: a study of the impact of wheel design. Sci Rep. 2023;13(1):10856. https://doi.org/10.1038/s41598-023-37640-w
[20] Steimel A. Electric traction – motive power and energy supply, basics and practical experience. Oldenburg Industrieverlag. München 2008.
[21] Świeczko-Żurek B, Ronowski G, Ejsmont J. Tyre rolling resistance and its influence on fuel consumption. Combustion Engines. 2017;168(1):62-67. https://doi.org/10.19206/CE-2017-110
[22] Tomaszewski S, Medwid M, Andrzejewski M, Cerniewski M, Jakuszko W. New rail-road tractor with a combustion engine and an alternative electric drive. Combustion Engines. 2022;182(3):47-53. https://doi.org/10.19206/CE-2020-308
[23] Wende D. Fahrdynamics des Schienenverkehrs, B.G. Teubner. Wiesbaden 2003.
[24] Zhou H, Fan X, Liu Y, Lu D. Time-variant reliability analysis of simply supported PC girder bridges considering shrinkage, creep, resistance degradation and vehicle load flows. Structures. 2023;56:104885. https://doi.org/10.1016/j.istruc.2023.104885

Prof. Wojciech Sawczuk, DSc., DEng. – Faculty of Civil and Transport Engineering, Poznan University of Technology, Poznan, Poland.
e-mail: *wojciech.sawczuk@put.poznan.pl*

Sławomir Kołodziejski, MSc. – Faculty of Civil and Transport Engineering, Doctoral School of Poznan University of Technology, Poznan, Poland.
e-mail: *slawomir.kolodziejski@doctorate.put.poznan.pl*

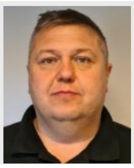

Dipl.-Ing. Armando Miguel Rilo Cañás – Faculty of Civil and Transport Engineering, Doctoral School of Poznan University of Technology, Poznan, Poland.
e-mail: *armando.rilocanas@doctorate.put.poznan.pl*

Article citation info:
Ambroszko W, Dudziński W, Walczak S. Finite Element Method analysis application in identifying the causes of brake disc failure. Combustion Engines. 2024;197(2):71-82. https://doi.org/10.19206/CE-176212

Wojciech AMBROSZKO
Włodzimierz DUDZIŃSKI
Sławomir WALCZAK

Combustion Engines
Polish Scientific Society of Combustion Engines

Finite Element Method analysis application in identifying the causes of brake disc failure

ARTICLE INFO

Received: 2 June 2023
Revised: 7 September 2023
Accepted: 1 December 2023
Available online: 11 January 2024

This article presents the results of brake disc tests aimed at identifying the causes of its failure. The first part of the article presents an analysis of the damageability of selected vehicle components, which showed that among the reported failures, the most failure was the braking system. The assessment of the brake disc worn "properly" as a result of the operation and the deformed brake disc after a very short period of operation was the subject of further analysis. The next part of the article presents issues related to the modeling of thermal loads, and then, trying to assess and search for the cause of abnormal wear of the brake system element, the use of the Finite Element Method. The results of FEM calculations for the cast iron disc confirmed the deformation of the brake disc. This phenomenon had a similar character and course in the FEM analysis as in the real object. In the final part of the article, conclusions and directions for further work were formulated.

Key words: *brake disc, deformation measurements, thermal loads, FEM numerical analysis*

1. Introduction

An important factor for car safety is an effective and reliable braking system. Vehicle manufacturers are intensively working on improving the brakes, with the main aim of improving the durability of brake system components, increasing braking efficiency and resistance to changing temperatures, and shortening the braking distance. An extremely important issue is to increase the resistance to overloads occurring, especially during intensive and long-term braking [1].

The friction brake is a mechanism in which mechanical energy is converted into thermal energy. Thermal processes inseparably accompany the operation of brakes, significantly affecting their functioning and effectiveness. Temperature has a fundamental influence on the course of tribological phenomena on friction surfaces. As the temperature increases, the coefficient of friction changes; as a rule, it initially increases slightly and, at higher temperatures, decreases significantly. This often results in the so-called "fading", i.e. a decrease in braking efficiency at elevated temperatures. In addition, the resistance of the friction pair to abrasive wear decreases. The increase in temperature combined with the phenomenon of thermal expansion causes the occurrence of stresses that are sometimes the source of micro-cracks or deformation of the surface of the brake disc or drum. Therefore, thermal deformations may also be the cause of temporary disturbances in the functioning of the braking system, related to geometric irregularities in the cooperation of friction pairs. It follows from the above that the thermal state of the brakes can significantly affect the braking efficiency, as well as the directional stability of the braked vehicle, which means that this issue is directly related to safety [1, 9].

Conducting tests of braking systems comes down to cyclical inspections at diagnostic stations, and post-exploitation tests are usually related to the observation and analysis of the causes of damage or wear of cooperating elements. Therefore, it is extremely important to develop research methods that allow for approximate mapping of the process of cooperation of friction elements, including numerical methods. Currently, many methods are used to simulate the cooperation process, starting from mapping the contact of friction elements, including the use of thermal phenomena [2, 3, 7, 12, 14, 21, 26]. As a result of vehicle operation, abnormal wear of the actuators of the braking system, in particular brake discs, often occurs. In addition to the indicated numerical methods of problem analysis, macro- and micro-structural tests of brake discs are also carried out in order to determine the causes of abnormal wear [29]. Due to the significant importance of the risk in terms of reducing, but also environmental protection, e.g. in relation to emissions released as a result of friction, in many drives around the world that actuate the braking system, including brake disc-pad friction devices brake. An example may be the works in which the authors [4, 5, 16, 23, 24] investigate the influence of various friction materials on the brake disc during operation. Included are papers [6] that cover the effects of other factors, such as moisture and corrosion, on friction functions and different brake disc materials.

In this article, trying to make an assessment and looking for the cause of abnormal wear of the brake system element, the use of numerical calculation methods was proposed.

2. Analysis of defectiveness of selected vehicle elements

On the example of service repair orders from a period of one year, an analysis of the damageability of selected vehicle components was carried out. The analysis showed that among the reported malfunctions, the most emergency was the braking system. In the analyzed period, 935 braking system repairs were carried out, compared to 3624 of all repair works. Based on the detailed analyzes and observations, a characteristic element of the braking system, i.e. the damaged brake disc, was selected for further research. This damage, which was initially identified, consisted of an axial deformation that occurred after a short period of vehicle operation. Due to the deformation of the brake disc, strong vibrations were transmitted to the steering wheel during braking, which indicated a problem and obviously affected safety. Therefore, in order to identify and attempt to determine the cause of brake disc deformation, a strength analysis was carried out using the Finite Element Method. The results of this analysis are presented in section 9.

3. Vehicle braking

The value of the kinetic energy that any moving vehicle achieves depends on the mass of the vehicle and its speed squared. The basic task of the braking system is to reduce the speed of the vehicle until it is effectively stopped and, in terms of energy, to reduce the kinetic energy of the vehicle and convert it through friction into thermal energy. This process is carried out mainly by friction forces resulting from the interaction of interacting executive elements, e.g. brake disc – brake pads or brake drum – brake shoes.

An important element during the braking process is that when the clutch is engaged, then, in addition to the weight of the vehicle, all moving parts of the engine and driveline must be braked. While during low-intensity braking, you can use engine braking (with the throttle closed), during emergency braking, the proper effect can only be obtained when the clutch is disengaged.

All forces acting on the vehicle must be transferred through the contact patch of the tires with the road surface. The maximum value of the resultant longitudinal and lateral reactions is determined by the force on the wheels and the coefficient of adhesion. Each braking system solution is designed to ensure vehicle stability during intensive braking and guarantee the shortest possible braking distance. For the optimization process, it is necessary to know what maximum braking forces for a given vehicle can be transmitted by the front and rear wheels. The answer to this question is the parabola of the ideal distribution of braking forces, which describes the distribution of maximum traction forces that can be obtained by the front and rear wheels of the vehicle during acceleration and braking. In the literature, one can find an approach that allows one to carry out dynamic simulations. They then take into account both the thermal effect on the cooperating elements and the frictional wear occurring between them [2, 3, 8]. As the authors note, dynamic simulations require significant computational effort to run a simulation with a total duration of several seconds of cooperation between the friction elements [3].

Temperature has a fundamental influence on the course of physical phenomena occurring in the components of the braking system. The increase in temperature, combined with the phenomenon of thermal expansion, may lead to the deformation of the friction surfaces of the disc or drum. This, in turn, can result in damage to the braking system components, posing a potential threat. Additionally, it determines the tribological phenomena occurring on the friction surfaces and thus affects the value of the friction coefficient. Therefore, the issues related to the transfer of heat generated in the executive elements of the vehicle braking system, i.e. the heating of the brake disc surface as a result of friction, with simultaneous convective flow of cooling air, heat radiated by the disc and the process of heat transfer to the suspension components, are so important. Boundary conditions are an important issue in this analysis. Thermal phenomena, as non-linear phenomena, increase the degree of complexity of the studied phenomenon. In the literature, apart from the analysis of deformations and the analysis of the heat flux flow between the brake disc and the brake linings, one can also find the analysis of the impact of heat flow on the elements that are part of the braking system, such as connecting bolts [19, 27]. A general review of simulation methods is presented extensively in this paper [25].

4. Boundary conditions

In heat transfer, both in steady and unsteady states, there are basically three types of boundary conditions. These phenomena have been very well described and are currently also used to describe thermal phenomena not only in the case of cooperation of friction elements but also to describe processes, e.g. energy industry simulations [10, 13, 17].

Boundary conditions of the I type occur when the heat exchange on the surface of the examined area is so intense that the surface of the object immediately assumes the temperature of the environment. This is approximately the case when the tested object has a low thermal conductivity $\lambda_{m,}$ and the heat exchange on the surface is very intense. The Biot number characterizes these properties $Bi = \alpha \cdot l/\lambda_m \rightarrow \infty$. Then, the body surface temperature $T(x,\tau)$ assumes the temperature of the environment and remains constant throughout the cooling or heating period [1, 11, 13].

$$T_{(x,\tau)}|_{x=0} = T_{ot} \tag{1}$$

Boundary conditions of the II type kind occur when the heat flux q on the heat exchange surface is constant or given by the function [12, 13]:

$$q = -\lambda_m \frac{\partial T}{\partial x} \tag{2}$$

in this case, the body temperature at the surface is unknown.

Boundary conditions of the III type kind occur most often in practice, they consist in the fact that the heat flux exchanged on the surface of the body is proportional to the temperature difference; surface of the body and the medium that surrounds the surface [12, 13]:

$$-\lambda_m \frac{\partial T}{\partial x} \Big|_{x=0} = \alpha(T_{x=0} - T_{ot}) \tag{3}$$

where: T_{ot} – ambient temperature, λ_m – thermal conductivity of the material, α – heat transfer coefficient.

Figure 1 presents a graphical interpretation of the presented boundary conditions.

The literature [1] also indicates boundary conditions of the IV type – they occur when two solid centers exchange heat through contact (Fig. 2). Conditions of this type occur in the case of cooperation of internal combustion engine elements and are used for example, in the case of modeling a cast iron insert under the first sealing ring in the piston. You can then save [12]:

$$-\lambda_1 \frac{\partial T_1}{\partial x_1} \Big|_{x=x_p} = \lambda_2 \frac{\partial T_2}{\partial x_2} \Big|_{x=x_p} \tag{4}$$

where: λ_1 – thermal conductivity of the material (1), λ_2 – thermal conductivity of the material (2).

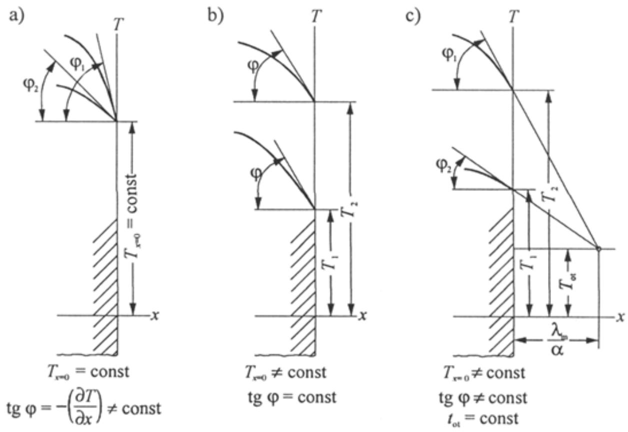

Fig. 1. Graphical interpretation of boundary conditions. Boundary conditions a) I type, b) II type, c) III type [12]

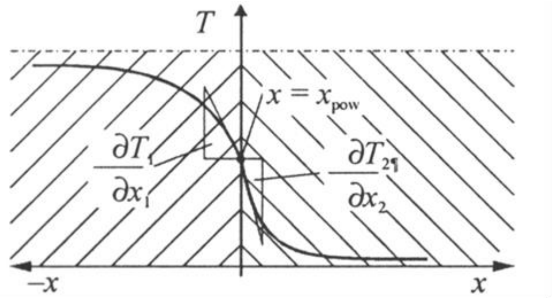

Fig. 2. Graphical interpretation of type IV boundary conditions [12]

5. Unstandable temperature

With regard to changes in the thermal state of the brakes, a single vehicle braking can be divided into two characteristic phases [26]:

– short-term, intense heat impulse
– long-term cooling phase of the brakes after braking.

The heat flux generated in the first phase of braking is many times greater than the heat flux discharged to the environment in the second phase. The first phase is characterized by large temperature gradients in the friction pairs of the brake, and this is of fundamental importance. On the other hand, the outflow of heat to the environment plays an important role in the analysis of long-term or repeated braking cycles, and in the case of single, intensive braking, it is relatively insignificant [26].

The temperature distribution in the friction elements is strictly dependent on the course of the braking process. There are three basic types of braking [26]:

– one-time (short-term until the vehicle stops)
– multiple (repeated at regular intervals)
– continuous, long-lasting (e.g. going downhill).

During single braking, a rapid increase in the temperature of the friction surface of the disc is characteristic, which reaches its maximum values on average in the temperature range 250–300ºC. In addition, large temperature gradients are observed in a thin layer of material near the surface. In disc brakes, the distribution of temperatures around the circumference of the friction surface of the brake is not uniform. During multiple braking, there is an effect of cumulating thermal loads from individual braking, as long as the time between these braking is not too long. The temperature of the friction surface shows large fluctuations in each successive braking. On the other hand, the temperature distribution on the outer surface of the cylindrical and frontal hub is characterized by a uniform increase. This is due to the resistance of heat conduction from the area of its dissipation to the hub of the disc. The most unfavorable state of brake operation is prolonged, continuous braking. In this work, the results of temperature measurements of the friction surfaces of the disc brakes of the Mercedes-Benz 300D W124 car during 21 minutes were used – descent from the Stilfer Pass (covering an average of 48 braking). After 14 minutes on the descent, the maximum temperature of the friction surface of the brake discs was set at 650ºC [26].

In addition to frictional wear, the variable temperature field in the brake disc contributes to the formation of cracks and deformations. Their source is high compressive stresses on the friction surface, caused by a large temperature gradient at the surface, which is directed outwards. Compressive stresses cannot initiate the observed cracks, but they can easily cause plastic flow of the material at elevated temperatures, which, after the thermal stresses disappear, leave tensile residual stresses on the friction surface. Tensile stresses can induce thermal cracking, either by cracking non-metallic inclusions or graphite on the surface of the material or by a low-cycle fatigue process with repeated frictional heating cycles. The unsteady temperature field combined with the phenomenon of thermal expansion causes thermal deformation of the brake disc. There are two unfavorable aspects of these deformations. The first is strong thermal stresses arising in these elements, and the second – is temporary disturbances in the functioning of the braking system. The deformation of the disc introduces an uneven distribution of normal pressures on the friction surface and, in extreme cases, a reduction in the contact area. This has the following adverse effects. Firstly, there are local, strong thermal loads on the friction surface, causing intensive, uneven wear. Secondly, there is a decrease in the effectiveness of the brakes resulting from the non-linear dependence of the friction force on the unit pressures [26].

6. Modeling of thermal conductivity in vehicle brakes

The braking process of a car is inherently unsteady, which makes the issue of unsteady heat transfer in the brakes analyzed. The fundamental problem from the point of view of the phenomena and the possibility of solving the problem is the phenomena of heat conduction in the thermal vapors of the brake. In the literature, the phenomenon of conduction, i.e. the phenomenon of heat transfer by conduction (which is very important in the case of contact of friction elements) is described in two ways. In the cylindrical coordinate description of the axial symmetry problem, the following equation (5) describes unstable heat conduction in anybody [18, 20, 21]. The second described in the most recent works is the so-called Galerkin’s method [15]. Using Galerkin's method, unsteady heat can be written in matrix form using finite elements.

$$\rho \cdot c_p \cdot \frac{\partial T}{\partial t} = \frac{1}{r} \cdot \left[\frac{\partial}{\partial r}\left(r \cdot \lambda \cdot \frac{\partial T}{\partial r}\right) + \frac{\partial}{\partial \phi}\left(\frac{1}{r} \cdot \lambda \cdot \frac{\partial T}{\partial \phi}\right) + \frac{\partial}{\partial z}\left(r \cdot \lambda \cdot \frac{\partial T}{\partial z}\right)\right] \quad (5)$$

where: ρ – density, r – radial coordinate in the cylindrical system, φ – angular coordinate in the cylindrical system, z – angular coordinate in the cylindrical system.

The density of the heat flux emitted on the friction surfaces depends on the coefficient of friction, unit pressures p and the sliding speed V.

$$q = \mu \cdot p \cdot V \quad (6)$$

The time course of the velocity V results from the course of the braking process. It is a function of the braking forces and motion resistance (air resistance, rolling resistance, hills, etc.) and also depends on the phenomena occurring at the contact point between the wheel and the road surface (wheel slip). After determining the time course of the heat flux density q emitted on the friction surfaces, its division into the brake disc and the friction lining (pad) should be taken into account. The most simplified method of analysis assumes the omission of heat penetration into the friction material due to the low thermal conductivity of this material. The material of the friction lining absorbs only a few percent of the heat released. The second method assumes that the heat is distributed to both bodies in proportions equal to their penetration coefficients [13, 26].

7. The phenomenon of friction at the interface between the brake disc and the pad

At the contact between the friction elements of the brake disc and the brake pad, a heat flux q is generated with a value that varies in time (τ), described by the relationship:

$$q(\tau) = N(\tau) \cdot \mu(\tau) \cdot v(\tau) \quad (7)$$

$$[W] = [N] \cdot [-] \cdot \left[\frac{m}{s}\right] = \left[\frac{J}{s}\right] = [W]$$

where: N(τ) – time-varying pressure of the pad on the disc; This course, in accordance with observations, looks as shown in Fig. 3.

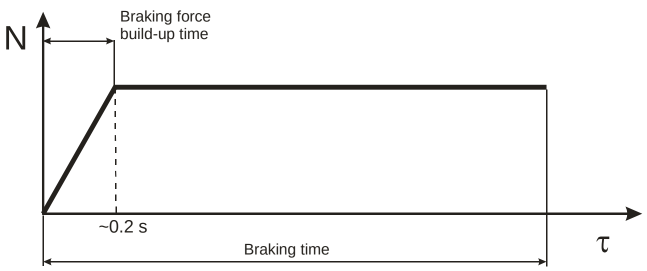

Fig. 3. The course of the pressure force on the brake pad

The pressure force is distributed over the surface of the pad and disc and depends on the contact surface area. Hence the unit pressure $q_i(\tau)$ is:

$$q_i = \frac{q(\tau)}{A} \left[\frac{W}{m^2}\right] \quad (8)$$

where: q(τ) – total heat flux at the contact surface of the block [W], A – contact area [m^2].

The pressure of the pad on the disc is uneven over the contact length along its symmetry axis and depends on the distance of the support point from the contact plane.

Another parameter on which the heat flux q(τ) depends is the friction coefficient of the pad-disc pair μ. It is assumed that it depends primarily on the speed and material that creates the friction pair. Designers are looking for composites that guarantee a constant value of the friction coefficient as a function of speed. This avoids the impact effect in the final phase of braking (sudden increase in braking force). Braking speed – it is assumed that it decreases evenly from the initial braking value to stop. Most often, a constant braking deceleration is assumed, in accordance with UNECE Regulation R13, equal to $a_h = 5.8$ m/s^2.

The potential energy of friction pairs, in accordance with the laws of physics, penetrates the surface of the disc and pad. This flux is divided in proportion to the heat transfer capacity (type II boundary conditions).

$$\frac{q_1}{q_2} = \frac{\lambda_1 \frac{\partial T_1}{\partial x_1}}{\lambda_2 \frac{\partial T_2}{\partial x_2}} \quad (9)$$

where: 1 – applies to the shield, 2 – applies to the block.

Due to the modeling of the heat transfer process, it is important how this process takes place outside the contact of friction pairs – this applies in particular to the brake disc. It is assumed that heat transfer takes place in accordance with type III boundary conditions, i.e. by convection. This process is characterized by two criterion numbers: the Bi (Biot) number and the Fo (Fourier) number. Biot number:

$$B_i = \frac{\alpha \cdot h}{\lambda} \quad (10)$$

characterizes the penetration of heat into the material, where: α – heat transfer coefficient on the surface, h – depth at which the temperature is analyzed, λ – thermal conductivity coefficient of the material. Fourier number:

$$F_o = \frac{a \cdot \tau}{h^2} \quad (11)$$

it is characterized by the equalization of temperature within the analyzed temperature field, where: a – temperature compensation coefficient (temperature conduction)

$$a = \frac{\lambda}{c \cdot \rho} \quad (12)$$

where: c – specific heat, ρ – material density, τ – time.

However, in the case of a brake disc, the thermal operating conditions change with each revolution. This can be presented as a dependence of temperature T as a function of time (τ) – Fig. 4.

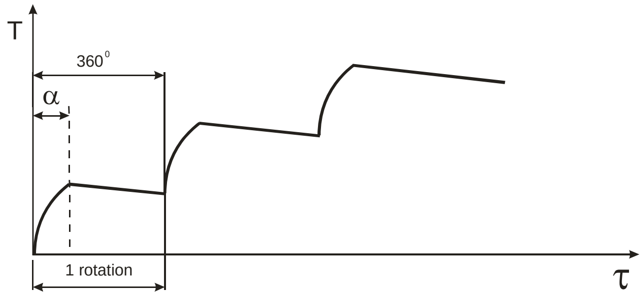

Fig. 4. The course of heating the disc point as a function of the rotation angle

8. Issues of heat exchange with the environment

The issue of heat exchange with the environment includes the process of thermal conduction in friction pairs and modeling of its boundary conditions (heat generation in brakes and heat exchange with the environment).

One of the important problems is the mathematical description of the complex, unsteady heat exchange between the brake surface and the air flowing around it. The heat flux density q exchanged with the environment by convection and by radiation is expressed by the relation [13, 26, 28]:

$$q = q_k + q_{pr} = (\alpha_k + \alpha_{pr}) \cdot (T - T_\infty) \tag{13}$$

$$\alpha = \alpha_k + \alpha_{pr} \tag{14}$$

where: q_k – heat flux density flowing to the environment by convection, q_{pr} – heat flux density exchanged with the environment by radiation, α_k – heat transfer coefficient by convection, α_{pr} – heat transfer coefficient by radiation, α – total heat transfer coefficient, T – brake surface temperature, T_∞ – ambient temperature.

It is difficult to determine the heat transfer coefficient α_k, which is a function of many variables. Its value depends on the physical properties of the air (viscosity, density, thermal conductivity, specific heat), which are functions of temperature and, to a lesser extent, air pressure. However, above all, this coefficient depends on the speed and the way the air flows around the brake (laminar, turbulent). The problem becomes more complex because due to the change in time: vehicle speed, wheel rotational speed, and brake surface temperature, there is an unsteady heat exchange in the vehicle (these values determine the value of the heat transfer coefficient). It is much simpler to determine αpr. According to the Stefan-Boltzmann law, the density of the heat flux radiated by the gray body is expressed by the relationship [13, 17, 26]:

$$q_{pr} = \varepsilon \cdot c_0 \cdot \left[\left(\frac{T}{100}\right)^4 - \left(\frac{T_\infty}{100}\right)^4\right] \tag{15}$$

Therefore, the following mathematical relationship for the heat transfer coefficient by radiation can be introduced [26]:

$$\alpha_{pr} = \varepsilon \cdot c_0 \cdot \frac{\left(\frac{T}{100}\right)^4 - \left(\frac{T_\infty}{100}\right)^4}{T - T_\infty} \tag{16}$$

where: ε – emissivity for a cast iron disc 0.29–0.30, c_0 – specific heat, T – brake surface temperature, T_∞ – ambient temperature.

At a constant ambient temperature T_∞, the coefficient α_k is proportional to the third power of the brake surface temperature. The percentage share of radiation in the overall heat exchange between the brakes and the environment is significant only at high temperatures of the friction surfaces of the discs – of the order of 400–800ºC. The phenomenon of radiation cannot be omitted in the case of long-term and cyclic braking. Heat exchange with the environment takes place mainly as a result of forced convection – cooling air flows around the brake. The dependence of α_k on temperature is relatively insignificant. For this reason, taking into account these comments, it is justified to assume a linear boundary condition of the third kind for the equation of thermal conductivity in the brake disc [23, 26, 28].

The surface of the disc heats up to high temperatures and has the largest share of the total heat transfer surface. In a disc brake, the brake pads detach the aerodynamic boundary layer, thereby significantly increasing heat transfer compared to discs where movement is caused by layer friction. The empirical coefficient αk of heat exchange with the environment by convection is presented in relation (17) [13, 26, 28]:

$$\alpha_k = \frac{0.076}{(2\pi)^{0.2}} \lambda_p \cdot r_{sr}^{0.6} \cdot \left(\frac{\omega}{\nu_p}\right)^{0.8} \tag{17}$$

where: r_{sr} – average friction radius of the brake disc [m], λ_p – thermal conductivity coefficient [W/mK], ω – angular velocity of the braked wheel [rad/s], υ_p – coefficient of kinematic viscosity of air [m^2/s].

The density of the heat flux flowing into the disc during braking q' is many times greater than the density of the flux flowing out to the environment. This means that during intensive, short-term braking, brake cooling contributes little to the energy balance. Heat flow plays an important role in the analysis of long-term or repeated braking cycles [19, 26, 27].

The analysis shows that the phenomena accompanying the braking process in a vehicle are very complex, and an attempt to model them may turn out to be complicated. In this work, the modeling of the heat exchange phenomenon was limited to the study of the behavior of the brake disc subjected to long-term exposure to high temperature. The cooling of the brake disc by flowing air was not simulated, nor was heat conduction to the suspension components taken into account. However, in the literature [7, 14, 26] one can find descriptions of the procedure for modeling heat transfer in a car brake, which include, among others, empirically determined relationships describing heat dissipation to the environment.

9. Brake disc analysis

Brake discs, like brake drums, are mounted on the wheel hubs. In most applications, discs are made of gray cast iron or cast steel. Due to the smaller surface of the friction linings, the clamping forces in the brake disc are greater than in the case of the drum. This contributes to greater heat generation and faster wear of disc brake pads in comparison to drum brake linings. When driving, air flows around the brake disc and cools it well. A distinction is made between solid and so-called disc brakes. Ventilated discs can be washed with air from the outside or inside (Fig. 5). Ventilated discs have a higher heat capacity due to their greater mass and cool down faster due to the radially arranged channels through which the air flows [9].

In the conducted tests, a ventilated brake disc was selected for the strength analysis. The damage to this disc consisted in its significant deformation, which was confirmed by axial runout measurements. For comparison, measurements of the axial runout values of a similar wheel that was properly worn were also carried out. As a result of the measurements carried out, even after such a long period of use, did not exceed the permissible axial runout value of 0.06 mm, as specified by the vehicle manufacturer. The basis for replacing this disc was only to reduce its thickness by 5 mm), which is considered normal wear resulting from the operation of the vehicle.

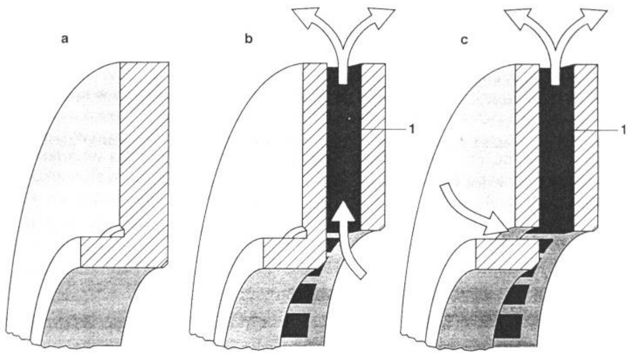

Fig. 5. Types of brake discs [2], where: a – solid brake disc, b – internally ventilated brake disc, c – externally and internally ventilated brake disc, 1 – cooling duct

9.1. External evaluation

Figure 6 shows a general view of the brake disc worn "properly" as a result of the operation, while Fig. 7 shows a deformed brake disc after a very short period of operation, which was the subject of further analysis. After the axial runout measurements and preliminary inspection, the deformed disc was cut along its diameter to examine the disc material's structure on the cross-section and to facilitate the preparation of the computational model.

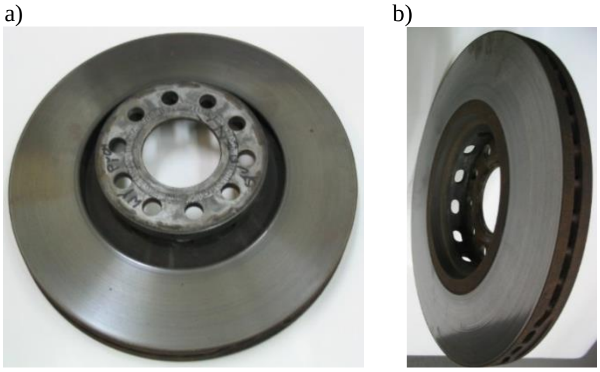

Fig. 6. Brake disc with proper exploitation wear: a) external side, b) internal side

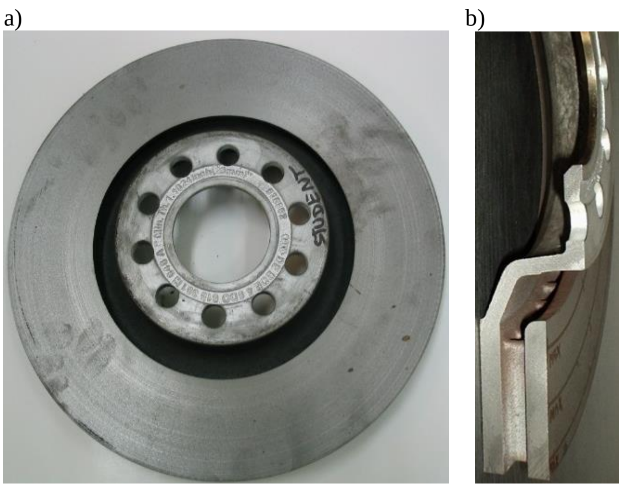

Fig. 7. Deformed brake disc: a) general view, b) cross-section of the disc

9.2. Comparative disc analysis

The main purpose of the comparative analysis of the two discs was to confirm the incorrect wear of one of them. In relation to the limit of permissible radial runout of 0.06 mm specified by the vehicle manufacturer, the disc worn as a result of normal operation did not show shape deviations on the friction surfaces. This assessment does not take into account the effect of roughness. This shield came from a similar vehicle and differed only in the use of additional ventilation channels in the vicinity of the shield mounting points. However, the geometric dimensions of both discs were the same.

The measurement of the axial runout of the brake discs was carried out using a dial indicator with an elementary division of 0.01 mm. Three measuring diameters were determined on both discs and then ten measuring points spaced every 360 degrees were determined on each diameter. Measurements were made on both sides of the disc (outer and inner sides). The measurement results obtained for a deformed disc are shown in Fig. 8, 9, and for a worn disc is correctly shown in Fig. 10 and 11.

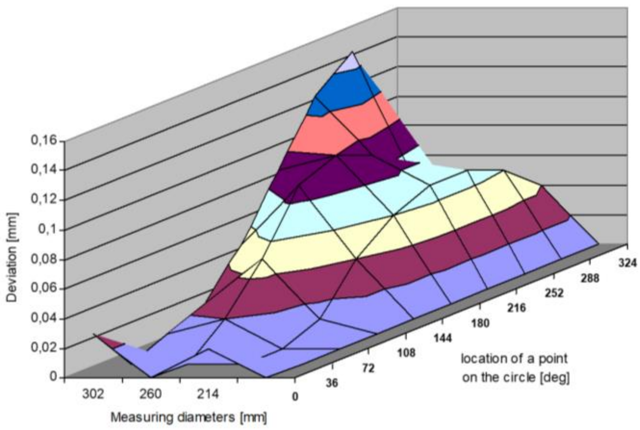

Fig. 8. Measurement results on the "deformed" surface of the brake disc. External page

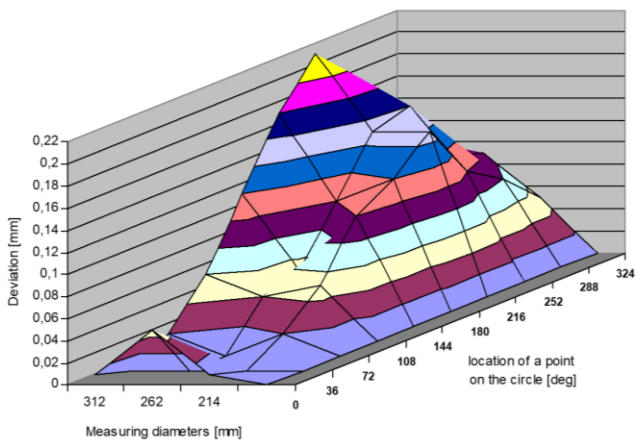

Fig. 9. Measurement results of the "deformed" brake disc surface. Inside page

As a result of the measurements, it was found that on the surface of the "deformed" brake disc, in several measurement points, the permissible values of axial runout specified by the manufacturer at 0.06 mm were almost three times exceeded. The second disc is properly worn, despite being used for 2 years at a distance of 70,000 km did not exceed the permissible deviation of the shape of the friction surfaces. Taking into account the above conclusions, further analysis was carried out using successively metallographic tests and analyses, as well as FEM calculations and strength analysis.

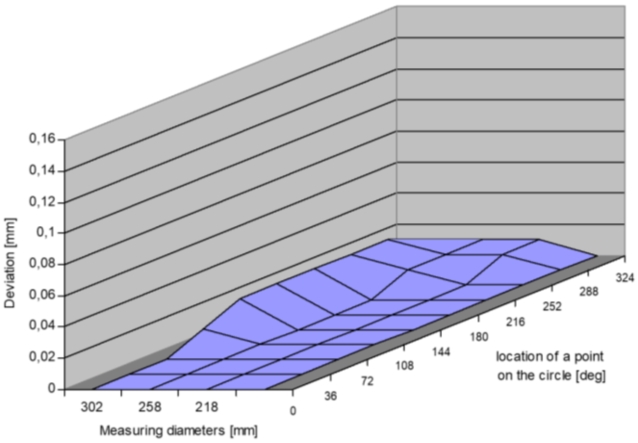

Fig. 10. Results of measurements on the surface of a properly worn brake disc, external side

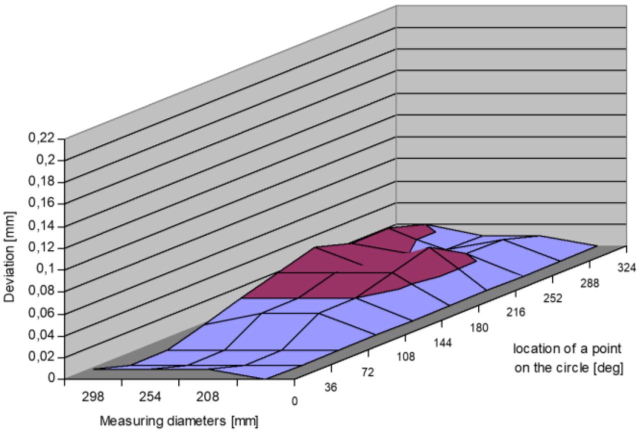

Fig. 11. Results of measurements on the surface of a properly worn brake disc inside

9.3. Shield model

The basic dimensions of the deformed brake disc are listed in Table 4.

Table 4. Basic dimensions of the brake disc

outer diameter [mm]	overall plate thickness [mm]	total height of the shield [mm]	hub hole diameter [mm]	spacing of holes for mounting screws [mm]
321	30	42	68	10 × 112

The geometric model of the analyzed brake disc and the basic technical documentation were made in the CATIA program. Figure 12 shows the view of the geometric model prepared for further analysis.

a) b)

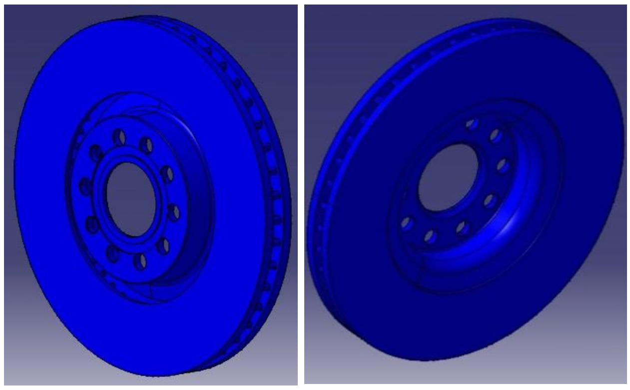

Fig. 12. Geometric model of the brake disc: a) view from the outside, b) view from the inside

10. Numerical analysis of the brake disc

In the last stage of the research, in order to identify and determine the cause of the deformation of the brake disc, a strength analysis was carried out using the Finite Element Method. For this purpose, a simulation of a long-term brake disc load under conditions of high temperature, not exceeding the temperature limit for structural changes of the disc material, was carried out. For this type of cast iron, the limit temperature is approx. 700ºC.

When starting the FEM strength analysis of the brake disc, it was expected that the calculation results would confirm the deformation of the brake disc and at least indicate the cause of such a situation. In particular, this concerned the material from which the shield was made. On the basis of metallographic tests, it was found that the disc was not "overheated", i.e. its temperature did not exceed the limit of 700ºC. Therefore, it was decided to study its behavior at a long-term temperature slightly lower – 650ºC. Due to the fact that it was not physically possible to measure temperatures in real conditions on the object, the data from the measurements included in the work [26] were used. The results of brake disc temperature measurements in the Mercedes-Benz 300D W124 car during the descent from the Stilfer Pass in the Alps were quoted. The strength analysis was carried out using the I-DEAS 10 system.

10.1. Boundary conditions

As boundary conditions in the FEM analysis of the brake disc model, input parameters such as: disc material properties (Table 5), disc heating curve (Table 6), and support conditions (Fig. 13) were adopted.

Table 5. Properties of the brake disc material [1]

	Temperature [°C]							
	20	100	200	300	400	500	600	700
Density [kg/m^3]	7100							
Conductor coefficient heat λ [W/mK]	42	60	51.9	43.3	38.6	34.6	31.1	29.9
Specific heat C_p [J/kg·K]	489	498	517	539	567	584	599	612
Expansion linear factor heat [$\times 10^{-5}$]	1.0				1.3			

On the other hand, for static calculations, i.e. stress and displacement analyses, temperatures in individual nodes, derived from thermal calculations, were additionally set (Fig. 14).

Table 6. Brake disc heating curve [26]

Time [s]	0	25	50	75	100	150
Temperature [°C]	20	62	80	104	196	242
Time [s]	200	250	300	350	400	450
Temperature [°C]	288	331	370	390	430	490
Time [s]	500	550	600	700	800	
Temperature [°C]	580	630	638	640	645	

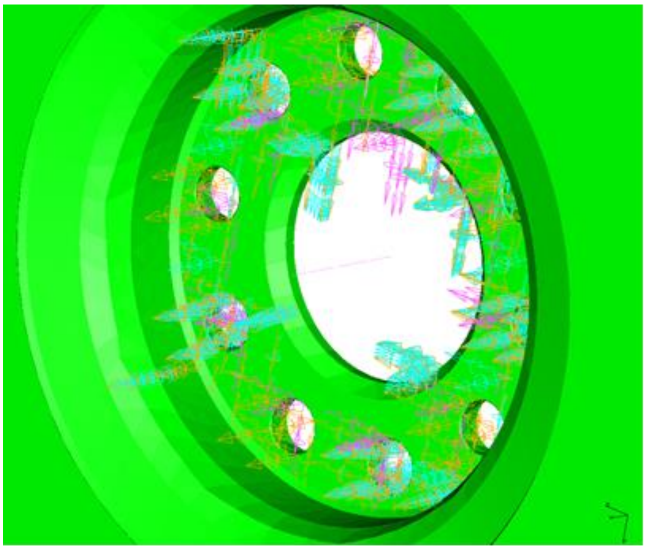

Fig. 13. Support of the brake disc model

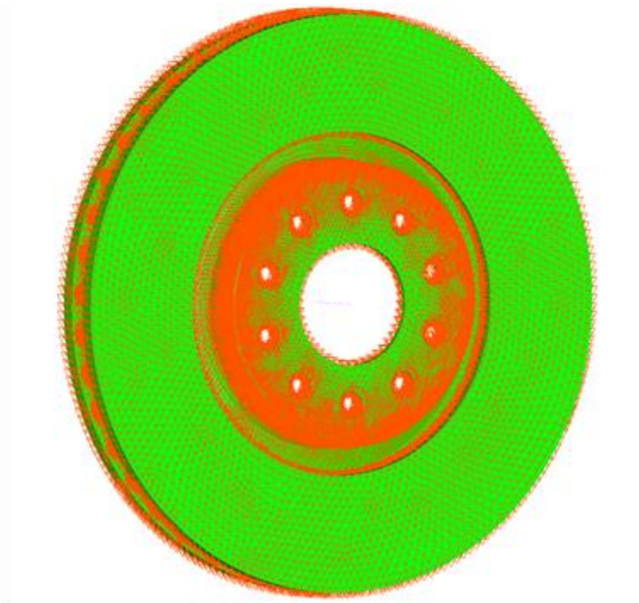

Fig. 14. Set temperatures in individual nodes of the brake disc

10.2. Calculation model

The computational model was created based on the geometrical parameters of the actual brake disc described in the previous chapters and is its faithful reflection.

For the discretization of the geometric model, higher-order volumetric elements of the TETRA 10 type, optimal for thermal analyses, were used (Fig. 15).

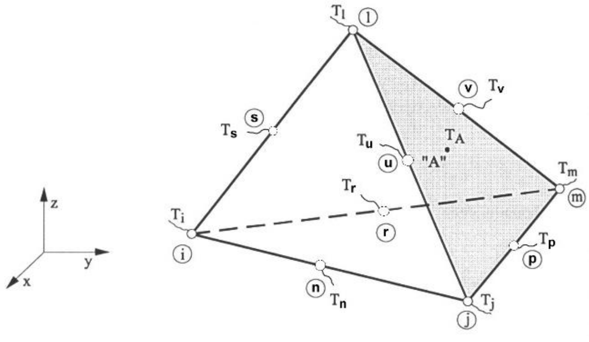

Fig. 15. TETRA 10 finite element [21]

The discrete model of the brake disc contained 68,834 SOLID finite elements and 121,325 nodes. In addition, in order to simulate the process of heat exchange with the environment, two shell grids (SHELL) were created. One necessary to set the heat flux entering the target contained 2710 finite elements. The second coating mesh, necessary to simulate heat transfer, contained 28,206 finite elements and was applied to all surfaces of the brake disc. The process of heat conduction to the disc (simulation of the disc heating process as a result of the friction of the pad-disc assembly) was caused by the temperature gradient – the heating curve. On the other hand, the disc cooling process (cooling in the "free air") was caused by free convection with the heat transfer coefficient $\alpha = 4\ W/m^2K$. As indicated in the previous chapters of the work, due to objective reasons, the analysis did not take into account the heat conduction through the disc to the suspension elements and the heat radiated by the heated disc. On the other hand, in the disc cooling process, an important simplification was that the cooling air had equal access to all surfaces of the brake disc. The direction and direction of the gravitational acceleration vector were assumed in accordance with the actual position of the brake disc mounting in the vehicle, i.e. along the X axis and directed downwards – Fig. 16. The ambient temperature was assumed to be 20°C.

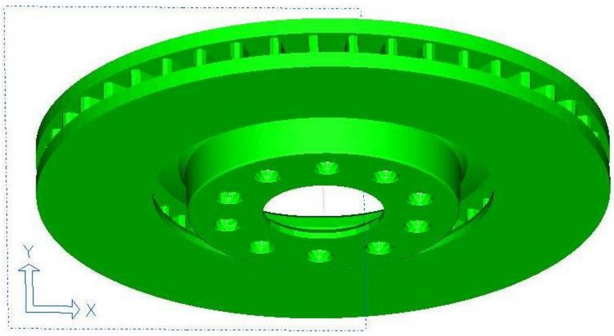

Fig. 16. Orientation of the coordinate system for the shield model

10.3. FEM calculation results

The following figures show the results of FEM calculations of the brake disc. The results include thermal analysis, i.e. the distribution of temperatures on the disc surface after successive time steps, and thus the course of "cooling down" of the brake disc cooled in "free air". The time steps have been selected so as to record clear changes in the behavior of the disc during heating and cooling. In addition, strength calculations were carried out to obtain the distribution of stresses in the disc and displacements. The measurement results are presented in Table 7 and in Fig. 19 and in Table 8, while in Fig. 18, 19 selected characteristic temperature distributions are presented, and in Fig. 20–23 displacements and stresses are presented.

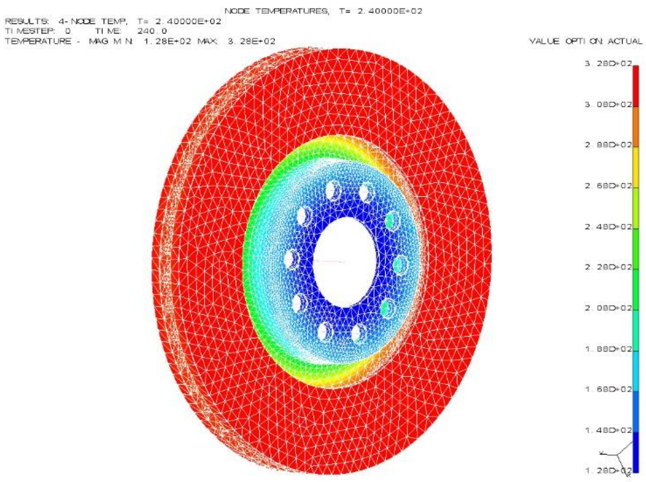

Fig. 17. Temperature distribution [ºC] after 240 s for a cast iron disc

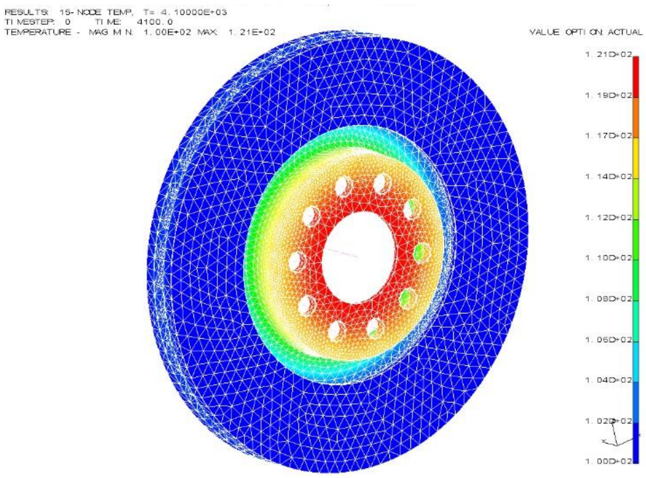

Fig. 18. Temperature distribution [ºC] after 4100 s for a cast iron disc

Table 7. Temperature values of the cast iron disc in successive time steps

Time [s]	Temperature max [ºC]
0	20
240	328
560	632
800 (end of warm-up)	644
1,500	521
2,400	368
3,600	170
4,100	121

Based on the results of the FEM calculations of the cast-iron brake disc collected in Table 8, it can be concluded that there is deformation of the brake disc. The obtained values are debatable. On the other hand, the values of maxi-

Table 8. Results from the FEM analysis for the cast-iron brake disc

Time [s]	Temperature max [ºC]	Stress max according to HMH [MPa]	Displacement [mm]
240	328	97	0.56
560	632	288 $\sigma_x = 115$ $\sigma_y = 90.2$	1.14
800 (end of warm-up)	644	420	1.16
1500	521	430	0.83
2400	368	298	0.54
3600	170	128	0.23
4100	121	85	0.14

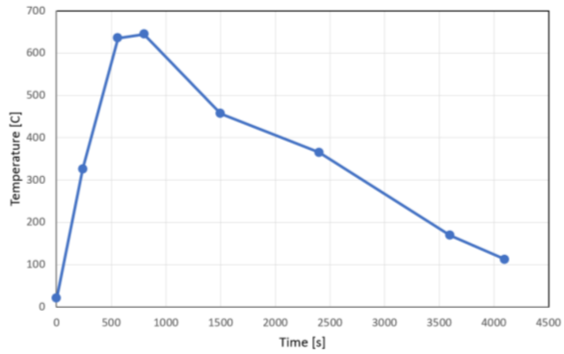

Fig. 19. Heating curve and cast iron disc

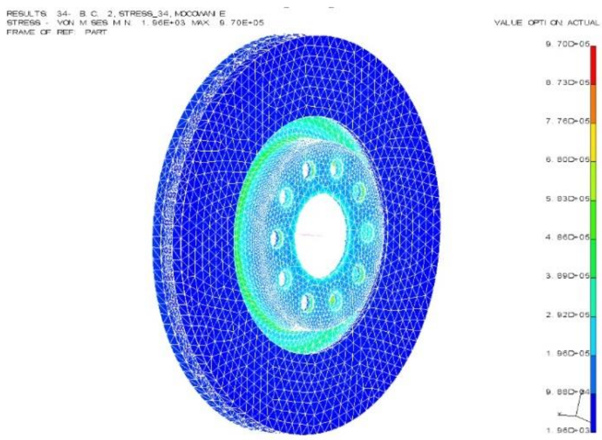

Fig. 20. Equivalent stresses [hPa] according to the HMH hypothesis for 240 s

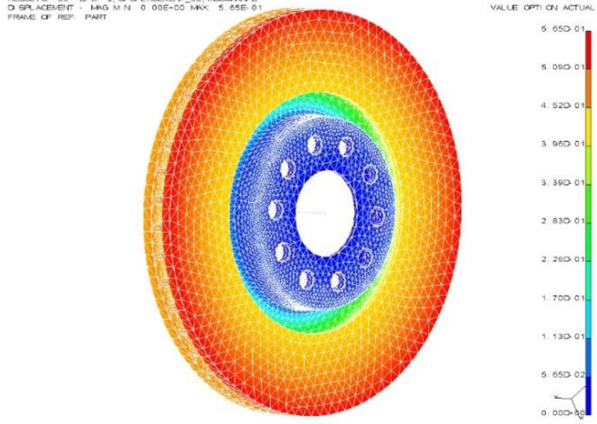

Fig. 21. Displacements [mm] after 240 s

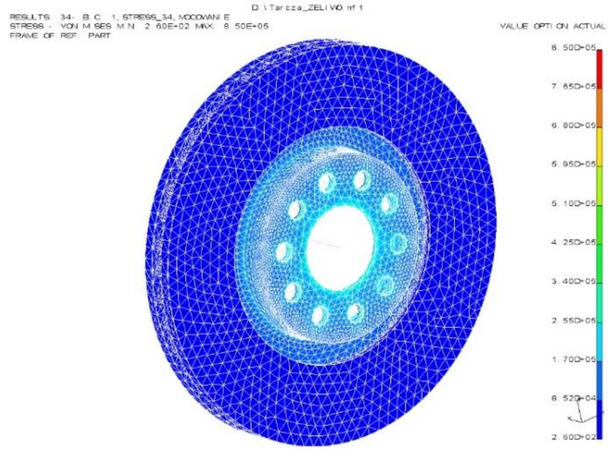

Fig. 22. Equivalent stresses [hPa] according to the HMH hypothesis for the time of 4100 s

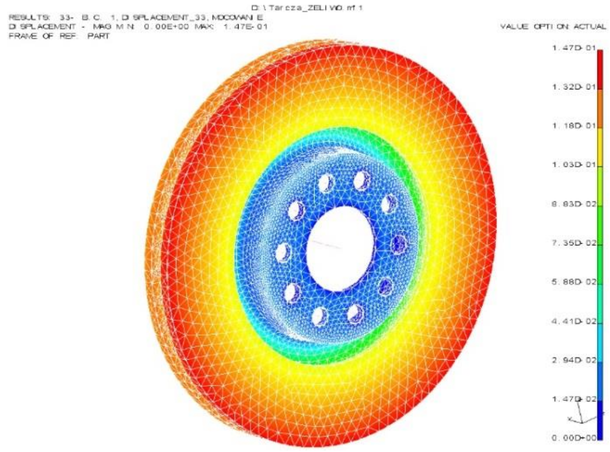

Fig. 23. Displacements [mm] after 4100 s

mum stresses in the disc at the highest temperatures and during cooling may raise concern. However, it turns out that the values of these stresses are local and after a more detailed analysis of the entire structure, it can be seen that stresses outside these places are evenly distributed, and their values are at least an order lower than the yield strength of the disc material. However, this statement can be partly explained by the "waving" of the tested brake disc, which means that in the places of stress concentration, microcracks of the material could have formed and caused "deformation" of the disc. The situation is similar with respect to displacements. The values resulting from the FEM analysis are much higher than the values measured in the real object. However, this can be explained by the fact that the heat transfer process in the car brake is much more complicated than included in the numerical model, which has been simplified and does not take into account many aspects that could affect the results of the analysis. This applies, for example, to the method of mounting the disc to the wheel hub and its additional stabilization by the brake caliper, covering a significant part of the friction surfaces of the brake disc.

11. Conclusions

The results of FEM calculations for the cast iron disc confirmed the deformation of the brake disc. This phenomenon had a similar character and course in the FEM analysis as in the real object. However, some discrepancies occur if the values of real measurements and computer simulations are taken into account. At the maximum value of the displacement during the measurements of the axial runout of the brake disc, a displacement of 0.22 mm was obtained. On the other hand, in the FEM results, the value of the maximum displacement was recorded when the disc reached the maximum temperature of 1.16 mm. It follows from the above that the differences in displacement are quite significant. However, the reason for these differences may be the simplifications of the numerical model, which were indicated in the previous chapters. The situation is similar in the case of the obtained stress results, the maximum values of which may be disturbing, as they exceed the yield point value for cast iron almost three times. However, more important than local stress concentrations – which may cause microcracks and, as a result, disc deformation – is the global stress distribution, which is acceptable and does not raise concerns. However, only on the basis of the analysis of the results of numerical calculations, it is impossible to answer the question of why the dial was bent.

12. Directions for further work

The main purpose of the work was to identify the phenomena and behavior of the brake disc and to try to reproduce them, as well as to signal the complexity of these issues.

Unfortunately, in the work, it was not possible to obtain a clear answer to the question about the direct cause of the brake disc damage. However, a good starting point for further work on these issues are the tests carried out and calculations that can be used for the test, with the use of which an attempt can be made to change the geometry of the tested brake disc and additionally use other materials.

Despite many advantages and progress in the construction of brakes other than friction brakes (e.g. electric electromagnetic brakes), friction brakes seem to be irreplaceable. Compared to other solutions, they are light, small, and cheap, hence their safe use in cars, trains, airplanes, and in various industrial devices. In the foreseeable future, no significant changes in the principles of brake operation or fundamental changes in the design features of friction elements and brake drives are to be expected. As the numerical analysis has shown, it is advisable to introduce more and more different, newer, and more specialized friction materials for linings as well as friction races of brakes. Since in friction brakes, the kinetic energy of moving vehicles or machines is converted mainly into heat, the following problems will remain valid in the further stages of development of these brakes: thermal resistance of friction materials, heat capacity and ability to dissipate heat, and thermoelastic stability of friction system elements. Other inseparable problems of almost every friction node are: stabilization of the friction coefficient, minimization of wear, and noise reduction. Therefore, the starting point for further work should be an attempt to replace the traditional material (cast iron) with another alternative material. This was initiated by carrying out FEM calculations for a composite target.

Nomenclature

c_0	specific heat [J/kgK]	V	sliding speed [m/s]
c_p	specific heat [J/kgK]	z	angular coordinate in the cylindrical system
FEM	Finite Element Method	α	heat transfer coefficient [W/m^{2}K]
HMH	Huber-Mises-Hencky	α_k	heat transfer coefficient by convection [W/m^{2}K]
p	pressure [Pa]	α_{pr}	heat transfer coefficient by radiation [W/m^{2}K]
q	heat flux density [W/m^2]	ε	emissivity for a cast iron disc [-]
q_k	heat flux density flowing [W/m^2]	λ_m	thermal conductivity of material [W/mK]
q_{pr}	heat flux density exchanged with the environment by radiation [W/m^2]	λ_p	thermal conductivity coefficient [W/mK]
		$\lambda_{1,2}$	thermal conductivity of material [W/mK]
r	radial coordinate in the cylindrical system	μ	friction coefficient [–]
r_{sr}	average friction radius of the brake disc [m]	υ_p	coefficient of kinematic viscosity of air [m^2/s]
T	brake surface temperature [K]	ρ	density [kg/m^3]
T_{ot}	ambient temperature [K]	φ	angular coordinate in the cylindrical system
T_∞	ambient temperature [K]	ω	angular velocity of the braked wheel [rad/s]

Bibliography

[1] Automotive engineer handbook. Elements and materials. WKŁ Warsaw 1990.

[2] Baranowski P, Damaziak K, Małachowski J. Brake system studies using numerical methods. Eksploat Niezawodn. 2013;15(4):337-342.

[3] Baranowski P, Damziak K, Malachowski J, Mazurkiewicz L, Kastek M, Piatkowski T et al. Experimental and numerical study of thermo-mechanical processes occurring on brake pad lining surfaces. WIT Trans Eng Sci. 2011;71(X): 15-24. https://doi.org/10.2495/SECM110021

[4] Belhocine A, Abdullah OI. Thermomechanical model for the analysis of disc brake using the finite element method in frictional contact. Multiscale Science and Engineering. 2020;2:27-41. https://doi.org/10.1007/s42493-020-00033-6

[5] Chen Y, Gao F, Fu R, Su L, Han X et al. Braking-experimental study on the relationship between friction material type and brake disc temperature. Ind Lubr Tribol. 2022; 74(8);975-984. https://doi.org/10.1108/ILT-03-2022-0107

[6] Djafri M, Bouchetara M, Busch C, Weber S. Effects of humidity and corrosion on the tribological behaviour of the brake disc materials. Wear. 2014;321:8-15. https://doi.org/10.1016/j.wear.2014.09.006

[7] Gao CH, Lin XZ. Transient temperature field analysis of a brake in a non-axisymmetric three-dimensional model. J Mater Process Tech. 2002;129:513-517. https://doi.org/10.1016/S0924-0136(02)00622-2

[8] Guru Murthy Nathi, Charyulu TN, Gowtham K, Satish Reddy P. Coupled structural/thermal analysis of disc brake. International Journal of Research in Engineering and Technology. 2012;1(4):539-553. https://doi.org/10.15623/ijret.2012.0104004

[9] Informator Techniczny Bosch. Conventional brake systems of passenger cars. 2001 Edition.

[10] Jin P, Xue Y, Chen B, Wang L. An analytical solution of temperature near nuclear waste canister under three-dimensional heat transfer condition progress in nuclear energy. Prog Nucl Energ. 2021;143:104051. https://doi.org/10.1016/j.pnucene.2021.104051

[11] Kirillov PL, Ninokata H. Heat transfer in nuclear thermal hydraulics. Thermal-hydraulics of water-cooled nuclear reactors. Woodhead Publishing. 2017:357-492. https://doi.org/10.1016/C2015-0-00235-0

[12] Kwaśniowski S, Sroka ZJ, Zabłocki W. Thermal load modeling in internal combustion engine components. Publishing House of Wrocław University of Science and Technology. Wroclaw 1999.

[13] Lu Q. A Finite Element approach for nonlinear, transient heat conduction problems with convection, radiation, or contact boundary conditions. Ann Nucl Energy. 2023;193: 110009. https://doi.org/10.1016/j.anucene.2023.110009

[14] Mackin TJ, Noe SC, Ball KJ, Bedell BC, Bim-Merle DP et al. Thermal cracking in disc brakes. Eng Fail Anal. 2002; 9(1):63-76. https://doi.org/10.1016/S1350-6307(00)00037-6

[15] Muthu Visakan M, Mahesh Kumar U, Sivadasan VK. Review on braking system in railways. International Research Journal of Engineering and Technology. 2021; 8(7):2333-2339. https://www.irjet.net/archives/V8/i7/IRJET-V8I7411.pdf

[16] Osenin YI, Krivosheya DS, Osenin YY, Chesnokov AV. Disc brake design with carbon friction material. J Frict Wear+. 2023;44:13-17. https://doi.org/10.3103/S1068366623010087

[17] Pinca-Bretotean C, Bhandari R, Sharma C, Dhakad SK, Cosmin P, Sharma AK. An investigation of thermal behavior of brake disk pad assembly with Ansys. Mater Today-Proc. 2021;47(10):2322-2328. https://doi.org/10.1016/j.matpr.2021.04.296

[18] Popescu FD, Radu SM, Andraș A, Brînaș I, Budilică DI, Popescu V. Comparative analysis of mine shaft hoisting systems brake temperature using finite element analysis (FEA). Materials. 2022;15(9):3363. https://doi.org/10.3390/ma15093363

[19] Qu J, Wang W, Wang B, Li G, Jiao B. Analysis of the axial load of bolts of wheel-mounted brake discs of high-speed trains. Eng Fail Anal. 2022;137:106250. https://doi.org/10.1016/j.engfailanal.2022.106250

[20] Riva G, Varriale F, Wahlström J. A Finite Element Analysis (FEA) approach to simulate the coefficient of friction of a brake system starting from material friction characterization. Friction. 2021;9(1):191-200. https://doi.org/10.1007/s40544-020-0397-9

[21] Rusiński E, Czmochowski J, Smolnicki T. Advanced Finite Element Method in load-bearing structures. Publishing House of Wrocław University of Science and Technology. Wroclaw 2000.

[22] Ścieszka S. Friction brakes. Material, design, and tribological aspects. Library of Maintenance Problems. Gliwice 1998.

[23] Tauviqirrahman M, Muchammad M, Setiazi T, Setiyana B, Jamari J. Analysis of the effect of ventilation hole angle and material variation on thermal behavior for car disc brakes using the finite element method. Results in Engineering.

2023;17:100844.
https://doi.org/10.1016/j.rineng.2022.100844

[24] Tripathi VK, Saini R, Joshi UK. Design and analysis of ventilated disc brake by using different materials: a review. International Journal for Research in Applied Science and Engineering Technology. 2023;11:627-631. https://doi.org/10.22214/ijraset.2023.55181

[25] Usmani D, Mohan R, Mewada CS, Goga G. A comprehensive literature review on the recent advances in braking systems technology using FEA. J Phys Conf Ser. 2023;2484. https://doi.org/10.1088/1742-6596/2484/1/012034

[26] Walczak S, Wolff A. Theoretical and experimental analysis of heat exchange in automotive brakes. Doctoral Dissertation. Warsaw University of Technology, Faculty of Automotive and Construction Machinery Engineering. Warsaw 2001.

[27] Wang Q, Wang Z, Mo J, Zhang L. Nonlinear behaviors of the disc brake system under the effect of wheel−rail adhesion. Tribol Int. 2022;165:107263. https://doi.org/10.1016/j.triboint.2021.107263

[28] Yin J, Lu C, Mo J. Comprehensive modeling strategy for thermomechanical tribological behavior analysis of railway vehicle disc brake system. Friction. 2024;12:74-94. https://doi.org/10.1007/s40544-023-0735-9

[29] Zemlik M, Dziubek M, Pyka D., Konat Ł, Grygier D. Case study of accelerated wear of brake discs made of grey cast iron characterized by increased thermal stability. Combustion Engines. 2022;190(3):45-49. https://doi.org/10.19206/CE-146698

Prof. Wojciech Ambroszko, DEng. – Faculty of Mechanical Engineering, Wroclaw University of Science and Technology, Poland.
e-mail: *wojciech.ambroszko@pwr.edu.pl*

Prof. Włodzimierz Dudziński, DSc., DEng. – Collegium Witelona Legnica, Poland.
e-mail: *wlodzimierz.dudzinski@pwr.edu.pl*

Sławomir Walczak, MEng. – Graduate student, Wroclaw University of Science and Technology, Poland.
e-mail: *slawomir.walczak.oca@outlook.com*

Article citation info:
Wróblewski P, Świątek P, Kachel S, Zyska T. Development and research of a hybrid power unit for ultralight aircraft: an innovative approach to energy efficiency and operational flexibility. Combustion Engines. 2024;197(2):83-96. https://doi.org/10.19206/CE-174721

Piotr WRÓBLEWSKI
Piotr ŚWIĄTEK
Stanisław KACHEL
Tomasz ZYSKA

Combustion Engines
Polish Scientific Society of Combustion Engines

Development and research of a hybrid power unit for ultralight aircraft: an innovative approach to energy efficiency and operational flexibility

ARTICLE INFO

Received: 6 June 2023
Revised: 29 October 2023
Accepted: 1 November 2023
Available online: 9 December 2023

This scientific article presents an innovative concept of a hybrid power unit designed for ultralight aircraft, with the aim of improving energy efficiency and operational flexibility. As part of the development of the system, the construction of the combustion unit and the electric motor / generator, which are the key elements of this solution, was described. The advanced internal combustion engine controller and the bi-directional energy conversion converter have been developed and built to enable optimal cooperation of both energy sources. In order to carry out experimental research on the developed system, a special test stand was built on which a prototype drive unit was mounted. The results of the research include preliminary performance characteristics of the prototype drive unit and an analysis of the achievements that indicate the potential benefits of using such a hybrid drive unit. The article also summarizes the conclusions and recommendations for further work on improving this innovative solution.

Key words: *hybrid drive, electric motor, combustion engine, transmission, energy optimization*

1. Introduction – development of the concept of hybrid and electric aircraft propulsion

Over the past decade, innovative ideas for fully or partly electrically powered aircraft have sparked discussions in the general community as well as intense media coverage. As a result, a significant number of start-up companies have been created that seek to commercialize electric and hybrid propulsion technologies for aircraft (Electric Propulsion, EP). Rapid developments in this area can also be observed in the technical literature. In the years 2006–2009, there was an average of one article per year on the design and analysis of electric and hybrid aircraft, while from 2015 the number of these articles increased to nearly twenty per year [9].

The main factor driving public interest in the electrification of aviation is the desire to reduce the negative impact on the environment. NASA's Subsonic Fixed Wing program has set ambitious targets for energy consumption, nitrogen oxide (NO_x) emissions and noise for three generations of aircraft to enter service by the 2030s [4]. In 2013, after a series of studies on conceptual design conducted by industry and academia, these goals were updated [9]. The most aggressive performance targets are for the "N+3" generation, which is expected to be operational in the mid-2030s. These include noise reduction at the level of –55 dB at the airport border, reduction of NO_x emissions by 75% and reduction of fuel consumption by 70% compared to the technology from 2006 [9].

The International Civil Aviation Organization (ICAO) has established noise and NO_x certification standards in 2020 [13] and a voluntary carbon offset program to keep carbon emissions at 2020 levels [2]. NASA-funded research results (discussed in Chapter 3) show that electrification can improve carbon, noise and NO_x performance, enabling the civil aviation fleet to meet its N+3 targets [2].

Electric vertical take-off and landing (e-VTOL) operational concepts have been promulgated by a number of start-ups and mature enterprises around the globe, such as Volo-Copter, Ehang, Zee Aero, Joby Aviation and Airbus. The tech giant and transportation company Uber, in its white paper "Elevate" published in 2016, argued that there is a significant market for point-to-point urban air mobility that could drive action in this new segment [18, 20, 21]. Due to noise and cost, proponents of e-VTOL argue that traditional helicopters are not the right architecture for this type of application. This review focuses on fixed-wing aircraft, leaving the booming e-VTOL segment to other market analysts.

The extensive literature in the field of EP fixed wing aircraft offers numerous review articles that provide a partial overview of the area. A particularly extensive and understandable, though not technical, summary of aviation electrification from a business perspective is presented in papers [10, 18] presenting an overview of EP architectures and some basic sensitivity analyzes based on the Breguet equation. In turn, in [1], he focuses on the practical aspects of conceptual design of hybrid passenger aircraft using low-order and graphical dimensioning methods. However, there is no discussion of higher-fidelity optimization tools or a comprehensive overview of design studies and demonstration programs.

Several other reviews include aircraft EP as a side topic in the context of another main issue [8] and [15] mainly distributed propulsion with extended coverage of EP. Papers [7, 17] present an excellent overview of more electric aircraft systems, which includes the aspect of aircraft propulsion and design solutions.

One of the most promising trends in the construction of hybrid and electric engines for ultralight aircraft is the development and implementation of battery technology with higher energy density. Improving the energy density of batteries will significantly increase the range and flight time of ultralight electric aircraft. Higher energy-density batteries also have the potential to increase the overall efficiency of hybrid engines by allowing for greater use of electricity versus fossil fuel.

Another major trend is the development of more efficient energy management systems for hybrid and electric motors. These systems, which control how and when energy is delivered to the engine, can significantly improve the aircraft's energy efficiency. They are particularly relevant for hybrid aircraft that have to balance the use of electricity and fossil fuel. Finally, companies and research institutes around the world are working on new technologies and materials that can make electric motors more efficient. For example, innovations in the field of superconducting materials could lead to electric motors with higher efficiency and lower weight.

It seems that the future of ultralight hybrid and electric aircraft is certain. With the continuous development of battery technology, energy management systems and electric motors, we can expect these aircraft to become more efficient, sustainable and accessible to a wider range of users. This represents great opportunities for the aviation sector as well as environmental benefits.

Recent years have been full of dynamic discussions of scientists and engineers from universities and the aviation sector on research into aircraft powered entirely or partially by electricity. The constantly growing need to create more and more efficient and environmentally friendly aircraft leads to broadening technological horizons and attempts to implement previously unattainable concepts. Combustion engines play a dominant role in aircraft propulsion. They use fossil fuels with a high energy density, which is an undeniable advantage for the aviation industry. Unfortunately, they are also a significant source of pollution – burning fossil fuels leads to the emission of carbon dioxide, the main gas responsible for the global warming process [9].

According to data from the Air Transport Action Group (ATAG), 2% of carbon dioxide emissions generated by human activities come from aviation, and this number seems to be increasing year by year with the increasing number of aircraft [19]. In response to this trend, the International Civil Aviation Organization (ICAO) formulates strategies, updates emission standards and recommended practices, while conducting extensive outreach activities [11].

In addition to the issue of pollutant emissions, an important aspect is the limited availability of fossil fuels in the world. Aviation is estimated to account for around 2% of the world's total fuel consumption. It is not known how much more of these resources will remain available in the future, and the price of fossil fuels is definitely going up due to the growing global demand for energy.

In connection with all this, the search for alternative forms of propulsion becomes essential. Hybrid drives seem to be the perfect solution here. Batteries can be used as a source of energy instead of traditional fuels. Nevertheless, their use brings with it a number of challenges, such as the issue of weight on board an aircraft or the problem of recycling used batteries. However, the increasing intensity of research into battery technology gives hope for more frequent use of this energy source in aviation. It is worth remembering about a significant challenge related to international aviation regulations, which require a minimum level of safety to be guaranteed in the context of the use of batteries [5].

Compared to electric motors, internal combustion engines have a lower efficiency and power-to-weight ratio. That is why it is proposed to use hybrid systems that would be able to balance the benefits of both types of engines, thus improving performance. Hybrid propulsion systems have a number of potential advantages, such as lower fuel costs, less vibration, reduction of pollution and noise reduction, for example. Developing an all-electric powertrain that balances all these factors is a challenging task. This is necessary because it is critical to improving the physical limits of these propulsion solutions.

2. The potential of hybrid engines designed to propel ultralight aircraft

2.1. Development of hybrid engines in the world

In the cited study, a theoretical analysis of various design solutions for hybrid propulsion systems used in aircraft was carried out. This study focused on several design examples that are used in various aircraft designs. One of these examples is the Alatus single-seat ultralight aircraft, which has been equipped with a parallel hybrid propulsion system. This aircraft was developed at the University of Cambridge in 2010. The Alatus hybrid demonstrator consists of a 2.8 kW four-stroke internal combustion engine that is mechanically coupled to a 12 kW brushless electric motor. The electric motor is powered by lithium-polymer (Li-Po) batteries with a capacity of 2.3 kWh [8].

Another interesting example is the Garmex Soul airframe, which is also equipped with a parallel hybrid drive. This aircraft is manufactured by Garmex in the Czech Republic and was originally powered by a 200cc Bailey V engine with up to 15 kW power. However, to hybridize the powertrain, the Bailey motor was replaced with a 7.5 kW@7000 rpm Honda GX160 motor coupled to a 12 kW JM1 brushless DC motor that can also act as a generator to recharge the battery. Unlike Alatus, Garmex Soul has the ability to recharge the batteries during the flight and uses an electric motor to increase or maintain the torque on the drive shaft during altitude increase or take-off [6].

Simulation tests and checking the results of hybridization of the Garmex Soul airframe showed that the hybridization of the drive system can lead to fuel savings of up to 50% with a 60% hybridization degree. The greater the degree of hybridization, the greater the fuel savings, however, due to the limited energy density in the batteries, greater efficiency may be associated with a reduction in the range of the aircraft [3].

In addition, the works of T. Donateo on the hybridization of the Pro Mecc Freccia ultralight aircraft equipped with the Rotax 912 ULS engine (nominal power 73.5 kW at 5800 rpm) and a 3-blade propeller with a fixed pitch and a diameter of 1.75 m are aimed at improved safety. As part of this work, a hybrid drive system with a series-parallel architecture was proposed, which is based on automotive components. It consists of two electric motors, a scaled down Wankel motor and nickel metal hydride batteries [14, 15].

The purpose of the mentioned studies was to design the aircraft in such a way as to improve the safety of its use. The propulsion system based on automotive components enabled the use of an energy management strategy whose task is to control the state of charge of the battery and the operating point of the engine in order to minimize fuel consumption. The original configuration, consisting of a piston engine combined with a fixed-pitch propeller, was compared with a new hybrid propulsion system. Despite the higher take-off weight and lower maximum efficiency of the Wankel engine, the new configuration allowed to reduce fuel consumption by about 20%. The series-parallel hybrid architecture, together with the developed energy management strategy, behaves like a parallel hybrid during take-off and climb, thus ensuring high performance. During a normal operational voyage, the system operates as a continuously variable transmission system, with the battery being discharged and recharged cyclically. IN In the event of an engine failure, the hybrid system operates as an all-electric system and can bring the aircraft to a safe landing.

Hybrid aircraft, which use both combustion engines and electric propulsion, are currently an area of intense research and development in the field of aviation. The power source for the electrical systems in these aircraft are batteries, which play a key role in ensuring reliable and efficient operation of the system. This article focuses on the issues related to the use of electric batteries in hybrid aircraft, analyzing both the challenges and prospects associated with this technology.

One of the main challenges with electric batteries is their energy density, which is the amount of energy that can be stored per unit of weight. For aircraft where mass is critical to performance and range, it is essential to achieve the highest possible energy density to provide enough energy with the lowest possible battery mass.

Hybrid aircraft often require multiple battery charging and discharging cycles in a single flight. This puts additional demands on battery life and performance as they must be able to efficiently handle these cycles without significant performance degradation.

Electric batteries, especially high-capacity batteries, must meet stringent safety requirements to avoid the risks of overheating, short circuits and leakage. In the case of aircraft, safety is an absolute priority, so the design and management of batteries must take into account high safety standards, including monitoring, cooling and security systems.

Currently available battery technologies such as lithium-ion (Li-Ion) and lithium-polymer (Li-Po) form the basis for most hybrid aircraft. However, intensive research into new battery materials and designs is aimed at improving energy density, durability and safety, opening the way to more advanced battery technologies such as solid-state batteries and high-capacity batteries.

Effective energy management in hybrid aircraft, including optimal battery charging and discharging, is a key element in achieving high efficiency and range extension. The development of advanced energy management algorithms and integration with control and monitoring systems enable optimal use of available energy.

The development of hybrid aircraft is also associated with the need to develop an appropriate battery charging infrastructure. The development of effective and efficient charging stations, both at airports and elsewhere, is essential to ensure fast and reliable charging of aircraft batteries.

2.2. Development of hybrid aircraft engines in Poland

In Poland, as well as around the world, the motivation to conduct research on the hybrid propulsion system of ultralight aircraft is the need to increase energy efficiency and reduce emissions of harmful substances into the atmosphere. Ultralight aircraft, such as paragliders and gliders, are gaining in popularity due to their low cost and simplicity of construction. In the context of air transport, hybrid propulsion systems can be an effective alternative to internal combustion engines, enabling the increase of energy efficiency and reduction of operating costs of ultralight aircraft.

On the Polish aviation market, which is one of the fastest growing in Europe, the introduction of hybrid propulsion systems could significantly contribute to the development of the sector by increasing its attractiveness for users. Research on the hybrid propulsion system of ultralight aircraft is an important step towards the sustainable development of air transport and the improvement of air quality, not only on a Polish but also global scale. Their results may be used in the future to develop new, more ecological and effective propulsion solutions for ultralight aircraft.

One of the important aspects of this research is the presentation of the concept of operation and loads occurring in hybrid propulsion systems used in aviation. This will allow for a better understanding of the mechanisms of operation of these systems and assessment of their strength and reliability. In the context of Poland, such research can contribute to increasing the safety and efficiency of aviation in the country, for the benefit of passengers, air operators and the environment. In addition, an important aspect of research on hybrid drive systems is the analysis of structural relationships between the drive train assembly and the assembly of the main mechanism of the internal combustion engine. This is to better understand the impact of these components on the performance of the entire powertrain. Studying the ratio of electric and combustion drive is an important issue that often poses a challenge in the design of a hybrid drive. In the context of the Polish market, due to its dynamic development and innovation, such research can contribute to the development of new technologies and solutions that can be used in various sectors of the economy, not only in aviation.

According to many experts, the development of hybrid technologies is of key importance for the future of aviation in Poland and in the world. The aviation industry, both domestic and global, faces many challenges, including reducing CO_2 emissions, increasing energy efficiency and reducing noise. Research on hybrid propulsion systems, such as those carried out in Poland, can contribute to solving these problems and enable further development of aviation in a sustainable and ecologically responsible manner.

The conducted research works are ultimately aimed at presenting the proprietary hybrid engine design – a pioneering achievement that is a combination of many years of science, technological innovation and ecological awareness. This ambitious task includes the development of a prototype that, in addition to having the advantages of electric and internal combustion engines, will also be characterized by high durability, reliability and optimal performance parameters.

In the context of the specificity of hybrid structures, the goal is to ensure a balance between energy efficiency and power, taking into account aspects such as weight, cost and environmental impact. The main performance parameters that are taken into account are range, speed, energy consumption, as well as ease of use and maintenance.

Longevity is a key factor in aviation, and the design of a hybrid engine must take this aspect into account. Therefore, durability and reliability are integral elements of the design process. For example, engine components such as batteries and drive trains must be designed to withstand harsh operating conditions such as temperature changes, heavy loads and operating in a variety of weather conditions.

All these aspects, from environmental benefits to practical efficiency and durability, must be integrated into the final hybrid engine design to be presented as a result of this research. The goal is for this engine to be not only an innovative technological solution, but also a viable, practical alternative to traditional internal combustion engines, contributing to the sustainable development of aviation.

Hybrid aviation engines have many advantages that may contribute to their growing popularity in the aviation industry. Here are a few of them:

1. Reducing CO_2 emissions: Hybrid aircraft engines emit less carbon dioxide (CO_2) compared to traditional internal combustion engines. This emission reduction is key to reducing aviation's impact on climate change.
2. Energy Efficiency: Hybrid engines are typically more energy efficient than internal combustion engines. Thanks to the use of batteries and electric motors, they can use the energy recovered during processes such as braking.
3. Noise reduction: Hybrid engines are typically quieter compared to internal combustion engines. This aspect is particularly important in the context of urban aviation and the increasing pressure to reduce aircraft noise.
4. Fuel economy: Due to their higher energy efficiency, hybrid engines can provide fuel economy compared to traditional internal combustion engines.
5. Greater Reliability: Hybrid propulsion systems can improve aircraft reliability because the failure of one system (electric or combustion) does not result in a complete loss of power.
6. Lower cost of ownership: While the initial cost of investing in hybrid technology may be higher, long-term operating costs can be lower due to fuel savings and the ability to charge the battery with renewable energy.
7. Flexibility: Hybrid engines offer greater flexibility, allowing you to choose between electric or combustion propulsion depending on flight conditions and operational requirements. For example, an aircraft may use electric propulsion during take-off and landing to minimize noise and emissions, then switch to internal combustion when flying at higher altitudes.
8. Renewable energy support: Hybrid engines can support aviation's transition to renewable energy because the batteries can be charged with energy from renewable sources such as wind or solar power.
9. Smaller air pollution: In addition to reducing CO_2 emissions, hybrid aircraft engines can also reduce emissions of other harmful substances, such as nitrogen oxides and particulate matter, which are often emitted by traditional internal combustion engines.
10. Innovation: Hybrid technology is part of the future of aviation. Investing in this technology means investing in innovation, which can bring benefits in the form of new business opportunities and competitive advantage.
11. Potential Economic Benefits: Greater fuel efficiency, lower running costs and potential savings from emission regulations can bring economic benefits to airlines and other aviation operators that invest in hybrid technology.

3. Designing a prototype hybrid aircraft engine

3.1. Concept and theoretical assumptions

A deep analysis of design solutions used in hybrid propulsion systems of ultralight aircraft is a key aspect of the design and development process of these advanced systems. A thorough understanding of the design, mechanisms and functionality of these innovative propulsion systems is essential to determine the most effective and efficient technological solutions, which enables the development of precise design strategies.

Design analysis of hybrid powertrains allows the assessment of the impact of various design parameters on the overall efficiency and effectiveness of these systems. This gives engineers the ability to construct propulsion systems that are most suitable for specific operating conditions and optimize resource utilization. This understanding is fundamental to making strategic design decisions that can affect the efficiency, reliability and durability of these systems.

Engineers must consider a number of important factors when designing their own hybrid engine designs for ultralight aircraft, including but not limited to:

- The method of integrating the motors with the shaft of the drive system.
- Type of internal combustion engine and electric motor used in the hybrid drive system. Different types of engines can have significant differences in power, size, weight, efficiency and other key parameters.
- A type of transmission that connects an internal combustion engine and an electric motor. Different types of gears may have different characteristics such as gear ratio, weight, strength, etc.
- The power source of the hybrid propulsion system, i.e. aviation fuel or electricity from batteries. Each of these solutions has its own unique advantages and limitations.
- Type and construction of batteries used to power the electric motor.
- Power and efficiency of combustion and electric engines and their impact on aircraft performance and fuel consumption.

- Design and dimensions of engines and gears and their impact on the weight of the entire drive system.
- The level of noise and exhaust emissions generated by the hybrid drive system and the possibility of using a hybrid drive system in changing weather conditions.
- Costs related to the purchase, operation and maintenance of the hybrid drive system and their impact on the economic viability of this solution.
- Reliability and durability of the drive system and its ease of use and maintenance.

The series hybrid architecture of the powertrain is where only the electric motor is mechanically connected to drive devices such as fans. In this system, the internal combustion engine drives an electric generator, which in turn supplies power to the electric motor or charges the batteries using an advanced power management and distribution system. During phases of flight where relatively little propulsion effort is required (e.g. cruise phase), the energy converted by the generator can be used to charge the batteries, which increases the overall efficiency of the system.

Although the presence of additional electrical components in the powertrain architecture slightly reduces transmission efficiency, the overall improvement in powertrain efficiency is due to the ability to optimize the efficiency of the internal combustion engine and electric motor independently. Although the weight of the propulsion system may increase due to the additional electrical components, the potential increase in overall flight efficiency may offset these negative effects. As a result, properly balancing these various factors can lead to significant improvements in overall energy efficiency.

A key advantage of the series hybrid architecture is that the internal combustion engine is not mechanically coupled to the fan or propeller. This means it can run continuously at its optimum operating point, increasing its reliability and reducing maintenance requirements. The simplicity of the concept also leads to easy control of the propulsion, which enables a purely electric mode and the ability to recharge the battery in flight. However, there are some limitations, such as the fact that the electric motor must be able to deliver all the driving power, which can lead to weight gain. In addition, the efficiency of the system may be reduced due to the need for energy conversion. The series configuration is particularly suitable for designs requiring high torque and low speed, but may be less efficient compared to the parallel configuration. It is also important to take into account that it requires larger batteries and electrical devices, which leads to an increase in weight and volume of the entire drive system.

The complexity of these various factors underscores the complexity of the problem and shows how many different aspects must be considered when designing and analyzing hybrid propulsion systems for ultralight aircraft. These complex systems require a thorough understanding of the principles of engineering, life sciences, technology and economics. Achieving the optimal balance between these various factors is key to designing efficient, reliable and economically viable hybrid powertrains.

A thorough analysis of the design solutions used in hybrid drive systems is crucial not only to evaluate existing systems, but also to identify areas that can be improved, and even to create new innovative solutions. This process of analysis and innovation is essential for the continued development of hybrid powertrain technologies that have the potential to deliver significant benefits to the aerospace industry, including improved efficiency, reduced emissions, and overall improved energy efficiency.

Modern hybrid engines used in aircraft combine the energy efficiency of internal combustion engines with the flexibility and efficiency of electric motors. The use of such a configuration translates into a number of advantages, among which the increase in flight safety is particularly important. From the point of view of safety, the main advantage of hybrid systems is drive redundancy. In the event of failure of one of the engines (combustion or electric), the other can take over the driving role, ensuring continued control of the aircraft. This is especially important in emergency situations, when quick reaction and adaptation to new conditions can ensure a safe landing.

In addition, the electric motors, which are an integral part of the hybrid system, have excellent torque available from the start, which translates into quick start-up and response to changing flight conditions. Compared to internal combustion engines, electric motors are inherently more reliable and require less maintenance. Their design simplicity, no moving parts and no need for lubrication or cooling translates into a lower risk of failure.

In an energy context, however, the use of decoupling systems or additional gears may be more advantageous. This is for several reasons.

Decoupling the engine from the crankshaft allows the combustion engine and the electric motor to run independently of each other. The internal combustion engine can therefore be set to its most efficient operating point, which in turn reduces fuel consumption and emissions.

Additional gearing, while adding additional weight and complexity to the system, can help improve the overall efficiency of the drivetrain. They allow for a more precise adjustment of the rotational speed of the engines to the requirements of the different phases of flight, which in turn can lead to better energy efficiency.

The choice between these two configurations depends on the specific application and requirements. However, it is important to remember that safety and energy efficiency are not the only factors determining the final choice of drive configuration. Other important factors include the cost, weight and dimensions of the propulsion system, ease of operation and maintenance, and a number of other aircraft-specific parameters and limitations.

While electrically bonded hybrid systems provide greater reliability and redundancy, they can introduce additional complexities to the propulsion system, such as the need to manage power between the two propulsion sources, and the need to install and maintain additional components such as controllers and battery management systems. They can also introduce additional thermal and mechanical stresses on the internal combustion engine, which can affect its durability and performance.

Crankshaft decoupling systems or additional gearing, while they can provide better energy efficiency, can also introduce additional design and technological complexity. They may require additional mechanical components, such as clutches or gears, which can affect the weight, size and complexity of the drivetrain. In addition, they can also introduce additional mechanical stresses to the motors and other drivetrain components, which can affect their durability and performance.

Whichever drive configuration you choose, it's important to thoroughly understand all aspects of drive operation, such as motor performance, energy management, durability and reliability, and the costs and benefits of their use. Only then will you be able to make the right choice that best suits the specific requirements and constraints of your application. Therefore, further research and development of hybrid technology is crucial to further improve their efficiency, durability and safety, as well as to expand the range of their potential applications.

3.2. Internal combustion engines used for the hybrid system

The research engine, which is the subject of our description, is intended for use in hybrid systems. Optimizing its weight is crucial for use in ULM aircraft that do not exceed 120 kg. The research facility is a compact internal combustion engine whose weight does not exceed 35 kg, and yet it is capable of generating a maximum power of up to 42 kW.

As part of our research, this engine will be tested in two variants of the cooling system – liquid and air. Comparing the results from both of these versions will allow for an accurate assessment of the impact of the cooling method on engine performance and durability. The power technology of the internal combustion engine is based on multi-point fuel injection over the intake valve (MPI). This advanced fuel injection system, electronically controlled by a dedicated ECU, provides precise fuel dosing, resulting in increased engine efficiency and lower fuel consumption. Moreover, we plan to use innovative solutions to further increase the mechanical efficiency of the entire drive. One of them is the use of ceramic coating technology on selected components of the internal combustion engine. Ceramic coatings, due to their unique tribological properties, can significantly reduce friction in the motor, which translates into higher efficiency and longer life. Plus, we're going to use innovative technologies of casting molds made in 3D printing technology. This technology, although not yet widely used in the production of engines in the world, allows for the quick and effective creation of complex molds that can significantly improve the quality and efficiency of the production process. The importance of these innovative solutions in the tested engine is invaluable – they are intended not only to increase the efficiency and durability of the engine, but also to reduce its environmental impact by reducing exhaust emissions.

Engine model: 40i

The 40i engine parameters are presented in Table 1. The displacement of 627 cm^3, which has a major impact on its efficiency. The compression ratio is 8.5, which allows for efficient fuel combustion. The maximum power of the engine is 25.74 kW, generated at a rotational speed of 4640 rpm. At lower revs, 3630 rpm, the engine generates a continuous power of 22.06 kW. Torque is 58.3 Nm, generated at 3630 rpm, which guarantees strong acceleration and good performance at low and medium revs.

Table 1. 40i engine parameters

Parameter	Unit	Value
Displacement	cm^3	627
Bore	mm	75,5
Stroke	mm	70,0
Compression ratio	–	8,5
Maximum power at rotation speed	kW	25.74 at 4640 rpm
Continuous power at rotation speed	kW	22.06 at 3630 rpm
Torque at rotation speed	Nm	58.3 at 3630 rpm
Weight	kg	33.2

The engine weighs 33.2 kg (without fluids, fuel pump, fan and shrouds, with oil filter, starter motor and alternator fitted), which allows it to be used in light aircraft units. The propeller is driven by an indirect toothed gear, and the direction of rotation of the propeller is left-hand rotation. The fuel system is based on multi-point fuel injection with electronic control, and the ignition system is also electronically controlled. Engine control is carried out by the ECU EMU Classic model.

The engine has a working range from 950 (±50) rpm in idle (warm engine), to a maximum of 4700 rpm. The operating speed of the engine is 2200–4000 rpm, and the reducer ratio is 1.77. Propeller rotation at maximum engine speed is 2655 rpm. Among the pressures, it is worth noting the minimum operating oil pressure – 28 PSI = 1.9 bar (at 2000 rpm and 70°C oil temperature), and the maximum operating oil pressure is 65.3 PSI = 4.5 bar. Average operating oil pressure is 43.5 PSI = 3.0 bar.

The fuel recommended for use with this engine is car petrol with LO 98, and the oil – for ambient temperatures from 0 to +35°C – 5W-50 synthetic oil.

The Model 40i engine is designed for a variety of operating pressures and temperatures. The maximum oil pressure can be as high as 90 PSI or 6.2 bar, but only when the engine is cold. The fuel pressure should be between 2.8 and 3.2 bar. Nominal compression pressure ranges from 114 to 142 PSI, which translates to 8.9–10.8 bar.

In the temperature range, the minimum temperature for CLT start is 71°C. The maximum oil temperature is 135°C, and the through-flow oil temperature should oscillate between 110–120°C. The temperature of the CLT cruising head ranges from 100 to 137°C. The EGT exhaust gas temperature ranges from 680 to 750°C and the maximum EGT exhaust gas temperature is 850°C. In addition, the model 40i engine has limits in the form of a mass moment of inertia of the propeller, which should not exceed 930 $kg \cdot cm^2$. These detailed technical and operational parameters make the 40i engine a high-performance unit capable of operating in a wide range of operating conditions.

In the process of designing and testing the hybrid system, three engine concepts were originally considered. Each of them differed in cylinder configuration, which affected various aspects such as performance, balance and size.

The first concept is an in-line four-cylinder engine (Fig. 1). This arrangement, in which all cylinders are placed in one line, is well known for its simplicity and efficiency. It is also relatively easy to manufacture and maintain, which makes it attractive from a cost perspective. The measurement capabilities of this stand are shown in Fig. 2.

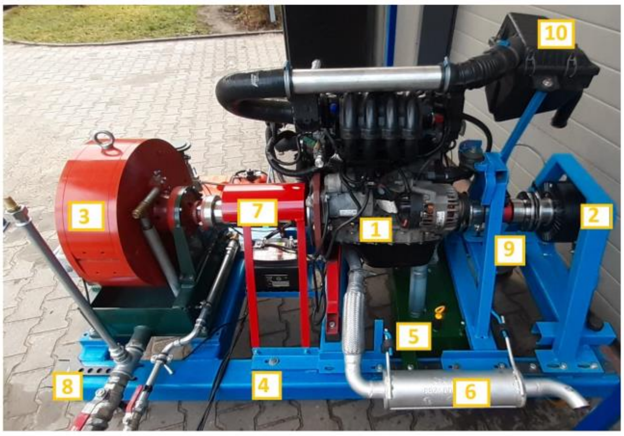

Fig. 1. View of the stand in a hybrid combination with a 4-cylinder in-line engine: 1 – 4-cylinder IC engine, 2 – EMRAX electric motor, 3 – water-cooled Eddy current brake, 4 – test stand main frame, 5 – engine oil tank, 6 – exhaust system, 7 – drive shaft between ICE and brake, 8 – cooling system connections, 9 – drive shaft between ICE and EMRAX with torque sensor, 10 – ICE intake air filter

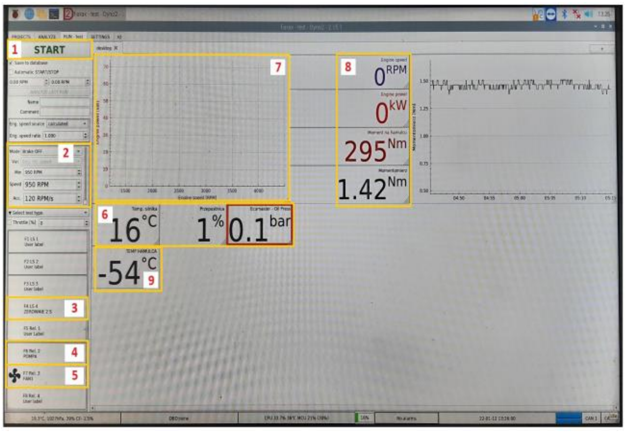

Fig. 2. Performance parameters of the hybrid set analyzed on the test stand: 1 – measurement start button, 2 – measurement mode selection, 3 – torque sensor setting to zero, 4 – water pump start button, 5 – cooling tower fan start button, 6 – ICE working parameters (temperature, throttle opening, oil pressure), 7 – characteristics chart, 8 – brake and torque sensor operating parameters, 9 – brake coolant temperature

The second concept is a two-cylinder boxer engine. In this arrangement, the two cylinders are placed on opposite sides of the crankshaft, creating a boxing-glove shape. These motors are known for their balance and smoothness, resulting in less vibration and noise. In addition, the low center of gravity of this type of engine can contribute to better vehicle stability.

The third concept is a V-twin engine. In this arrangement, the two cylinders are arranged in a "V" shape. This type of engine is often used in high-performance vehicles because it allows for a compact design while maintaining high power. The view of the dynamometer with the hybrid set for the two-cylinder V engine is shown in Fig. 3–5.

All three concepts were studied in terms of their potential use in a hybrid system, taking into account aspects such as performance, weight, size, cost and ease of use. The choice of the final concept was the result of careful consideration of these various factors.

Fig. 3. View of the connection system for 2 motors

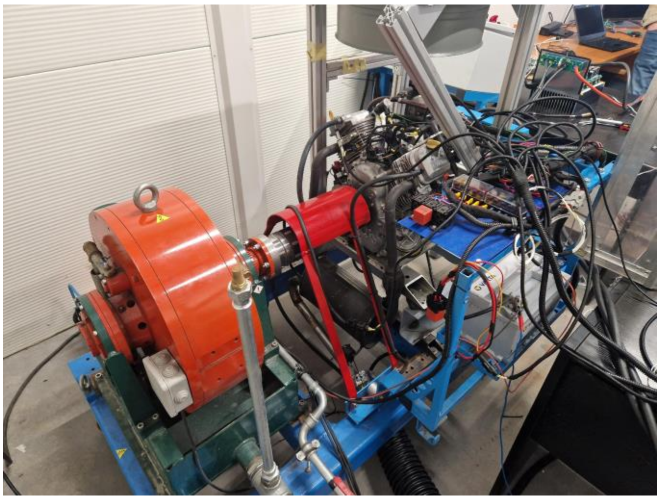

Fig. 4. View of the engine brake and drive set

The EMX-100/10000 brake was used in the tests. This brake is highly technical and is capable of absorbing a maximum power of up to 100 kW. It can achieve this at a maximum rotational speed of 10,000 revolutions per minute. From a mechanical point of view, the EMX-100/10000 is capable of generating a maximum torque of up to 240 Nm. From the design point of view, the brake has a weight of 250 kg, which proves its solid and durable construction. The direction of rotation of this brake is freewheeling, which adds flexibility to a variety of applications. However, it should be noted that the EMX-100/10000 requires a certain amount of water to function properly. The water requirement is 2.5 m^3/h and the water pressure should be between 0.75 and 1.25 bar. The temperature of the water that is fed to the brake should be more than 30ºC for optimal performance. Finally, it is worth noting that the measuring arm length of this brake model is 0.370 meters. These precise measurements are essential to guarantee the highest quality of operation and performance.

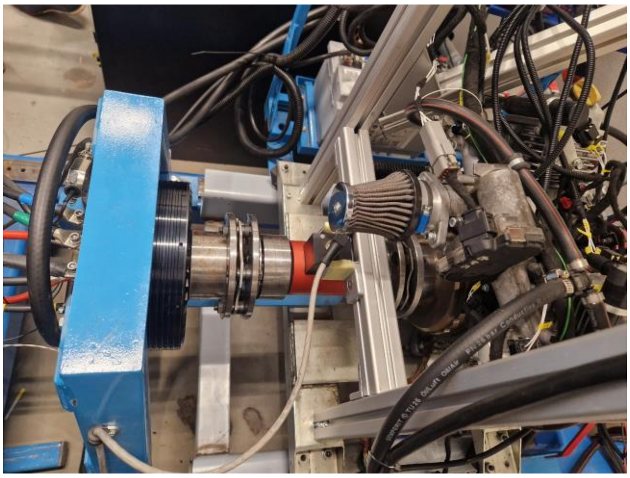

Fig. 5. View of a used electric motor and its connection

The dynamometer controller plays a key role in supervising and controlling the dynamometer operation (Fig. 6–7).

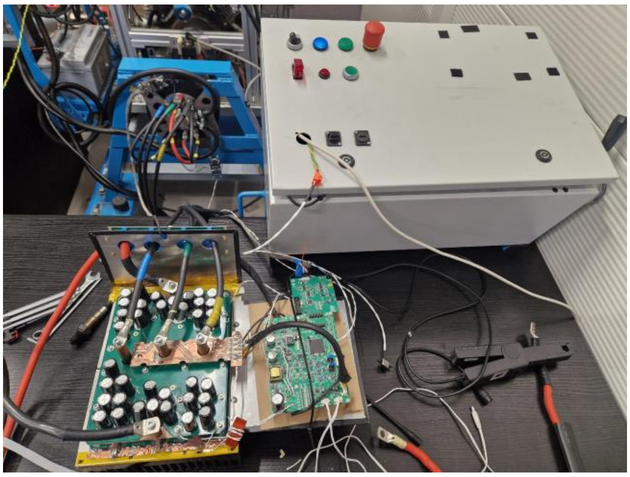

Fig. 6. Control and measurement system assembly – hybrid assembly dynamometer

Its operation covers a wide range of functions that allow effective and precise testing and diagnostic processes. The most important functions performed by the dynamometer controller are: Reading the dynamometer operating parameters and data from additional sensors. This allows continuous monitoring of the device status and current operating conditions. Generating a signal controlling the brakes of the load dynamometer. Thanks to this, the controller has a direct impact on the braking process. Control of dyno-associated accessories, such as fans. This allows to optimize the working conditions of the dynamometer and ensures proper cooling of the devices. Saving data and their subsequent analysis.

Fig. 7. Control and measurement system assembly – electric motor

Thanks to this, it is possible to track the history of the dynamometer's work, as well as identify possible problems and trends. Possibility of extending the functionality via CAN-BUS. This gives the possibility of integration controller with other systems and devices. In terms of input/output interfaces, the dynamometer controller is equipped with many connectors and ports that enable various forms of communication. Among them are Wifi, Bluetooth 5.0, Gigabit Ethernet, USB and microHDMI ports, mini jack audio connector and environmental sensor. An important element are also CAN-BUS 2.0B interfaces, various power outputs, analog outputs, PWM outputs, relay outputs, as well as inputs for speed and engine speed sensors and inputs for signals from strain gauges, general purpose analog inputs, thermocouple inputs and inputs for control buttons.

3.3. The electric motor used in the prototype

The EMRAX 208 electric motor is an advanced device used in hybrid systems. It is characterized by compact dimensions with a diameter of 208 mm and a length of 85 mm. The engine weighs between 9.4 and 10.3 kg and can be cooled by air, water or a combination of both. The motor peak power is 86 kW and the continuous power is 56 kW. The motor generates a peak torque of 150 Nm and a continuous torque of 90 Nm. Its maximum rotation speed is 7000 rpm, and the operating voltage can be from 50 to 580 V. The high efficiency of the EMRAX 208 motor reaches up to 96% (Fig. 8).

This motor is equipped with a position sensor, which can be either a resolver or an encoder, which enables precise monitoring of the position of the rotor. The EMRAX 208 electric motor offers significant power and torque while maintaining compact dimensions. Its high energy efficiency and a choice of different cooling methods make it a versatile solution for applications in hybrid systems.

So far, a number of significant activities have been carried out to develop and improve the hybrid drive. One of the key areas of work was the construction of the converter, which was based on the latest semiconductor switching elements and soft switching technology with increasing the operating frequency. The use of these advanced solutions allowed to reduce the weight of the converter and ensure high efficiency of energy conversion.

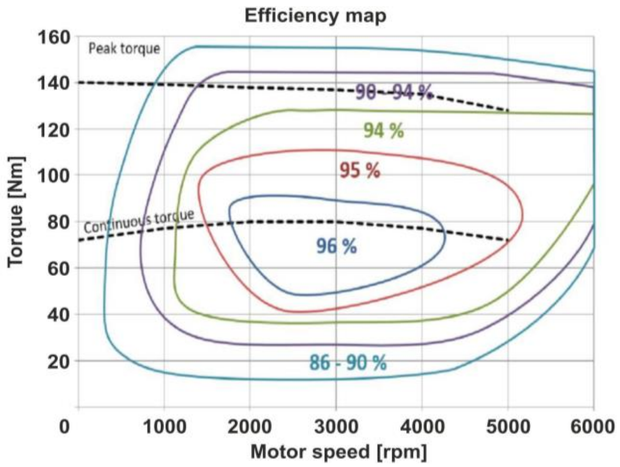

Fig. 8. Torque and speed motor characteristics – EMRAX 208

The control system uses the most modern DSP signal processors, which enable fast data processing and precise control. Active interference filtering systems and adaptive filtering algorithms have also been introduced, which significantly improve the quality of control signals. This allowed the implementation of complex vector control algorithms with a sinusoidal output current waveform, which in turn enables effective engine operation in a wide range of power and rotational speeds.

As part of the construction of the inverter, modern switching elements in SiC (silicon carbide) or GaN (threaded jelly) technologies were used, which replaced the previously used IGBT or MOSFET transistors. Soft switching technology was also used along with increasing the operating frequency of the inverter system. The latest generation DSP signal processors were used, which are responsible for real-time engine control algorithms. Back-EMF voltage measurement systems with a wide range and high measurement dynamics as well as active interference filtration systems and adaptive filtering algorithms have also been developed.

The control of the hybrid drive is based on a central supervisory system that coordinates the operation of the combustion and electric parts. Thanks to dedicated methods and algorithms for synchronization and power distribution, it is possible to achieve redundant operation of internal combustion and electric motors. This solution allows to increase flight safety, and also allows the drive to be adapted to various functionalities by changing the software. In the case of aircraft, it is possible to individually adjust the drive to the aerodynamic characteristics of the aircraft. The activities carried out are aimed at ensuring not only the efficient and effective operation of the hybrid drive, but also increasing its reliability and safety. The redundancy of the combustion and electric motors and the possibility of dynamic power sharing between them gives greater confidence that the drive will continue to function in the event of a failure of one of the parts. Additionally, an introduction dedicated synchronization methods allows for smooth and harmonious interaction of both motors, minimizing energy losses and optimizing their efficiency.

In the context of aircraft, adapting the hybrid drive to individual aerodynamic characteristics is extremely important. Thanks to the possibility of changing the software, it is possible to adapt the operating parameters of the engines and the way they are controlled to a specific vessel, ensuring optimal performance and efficiency. This, in turn, contributes to increasing the economic efficiency of the flight and reducing emissions. Conclusions from the conducted activities indicate significant progress in the field of hybrid drives. The use of advanced technologies and innovative solutions allows for the creation of high-efficiency electric motors. Optimization of both the construction of the converter and the controller enables effective management of the hybrid drive, increasing its reliability, safety and functionality.

It should be emphasized that the developed methods and solutions are a significant contribution to the development of hybrid drive technology, both in the context of aviation and other fields of transport. Their use allows for the effective use of various energy sources, reduction of pollutant emissions and achievement of better operating parameters. Further research and development in this area has the potential to lead to a revolution in propulsion, contributing to more sustainable and efficient transport.

3.4. Control system for the prototype engine and test stand

The main converter is a bi-directional converter that allows energy to flow to and from the batteries. The converter also determines the operating state of the internal combustion engine. This solution requires a specific design of the electronic controller of the internal combustion engine. Due to the generally accepted standards for aviation, the internal combustion engine controller was built as two independent units. The first unit is responsible for the value of the fuel injection parameter, and the second for the parameterization of the ignition sequence.

All three controllers – the main converter, the injection controller and the ignition controller are connected by a common CAN bus. Finally, a two-controller concept was adopted to control the hybrid drive system.

Injection electronic control unit

The electronic unit controlling the operation of the internal combustion engine is designed to generate the appropriate impulses to stimulate the injectors on the basis of strictly specific input signals. The inputs for such a signal are:
1) RPM – hall effect engine speed sensor, informing at the same time about the location of the first cylinder TDC
2) TPS – potentiometric throttle position sensor, indicating the "intent" of the pilot
3) MAP – air pressure sensor in the intake pipes
4) MAT – air temperature sensor in the intake pipes
5) FPT – fuel temperature and pressure sensor, in the fuel manifold.

Based on signals from the above sensors the dose of fuel applicable in the next one is determined.

The experimental injection control unit is based on the Texas Instruments RM48L540DPGETR DSP processor (Fig. 9). The injection sequence is built on the basis of input signals from the sensors. The injectors are controlled by current keys made in MOSFET technology. The injection control algorithm takes into account both the static states of engine operation – needed to determine the characteristic ones operating points and testing the possibility of replacing the generated mechanical power with electric power generated by the electric part of the hybrid unit. The injection controller PCB is shown below.

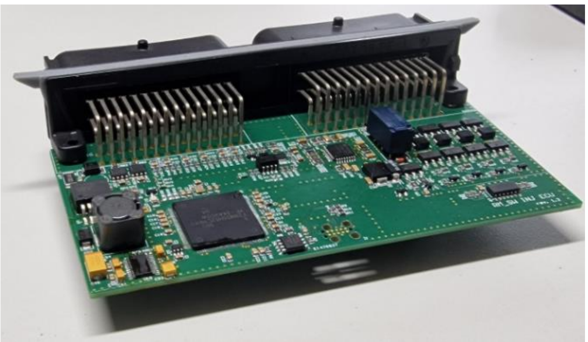

Fig. 9. Injection ECU – PCB view

Sample measurements of the generated sequence are shown below (Fig. 10). The yellow line shows the pulses coming from the rotation sensor. The orange line and the red line represent injector control for the first and second cylinders, respectively. Later in the post-start waveform, a phase shift sequence is observed for both cylinders.

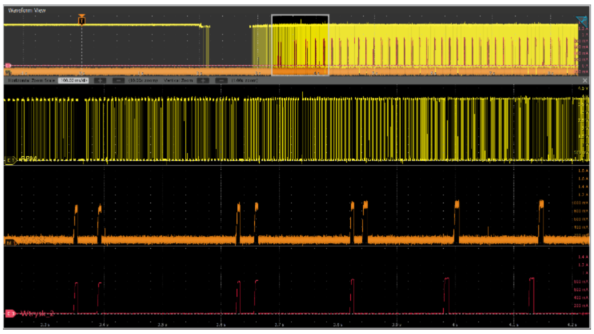

Fig. 10. An example of a sequence of injection pulses The first two pulses after the rotational speed occur are caused by fuel injection and facilitating engine start-up

The first two pulses after the onset of rotational speed are caused by the fuel injection and engine start facilitation. Later in the post-start waveform, a phase shift sequence is observed for both cylinders.

The ignition coil control sequences are shown below (Fig. 11).

The waveform from the rpm sensor is marked with a yellow line. The orange and red lines show the ramming of the ignition coils.

The angular displacement between both cylinders of the controlled internal combustion engine is clearly visible. The duration of the control pulse depends on the supply voltage and the falling edge causes a physical spark in the engine cylinder.

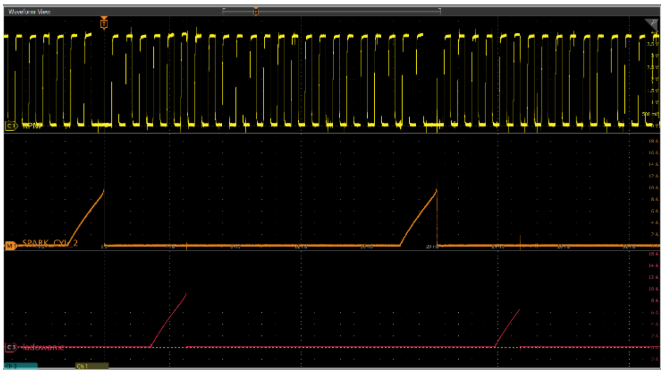

Fig. 11. Circuit layout sequence

4. Preliminary research results and discussion

As a result of the tests carried out on the combustion engine dynamometer and the comparison of the measurement results with the electric and combustion drive, it was found that there is no significant wear of the main engine components and engine timing. These studies allowed for a thorough examination of the resistance to motion of the hybrid set depending on the rotational speed of the internal combustion engine.

The results showed that after connecting the electric motor to the hybrid set, the resistance to motion increased by 8 to 17%, depending on the rotational speed of the internal combustion engine. Additional drag is also dependent on the angular velocity of the propeller and aerodynamic drag, and its value ranges from 5 to 23% (Fig. 12).

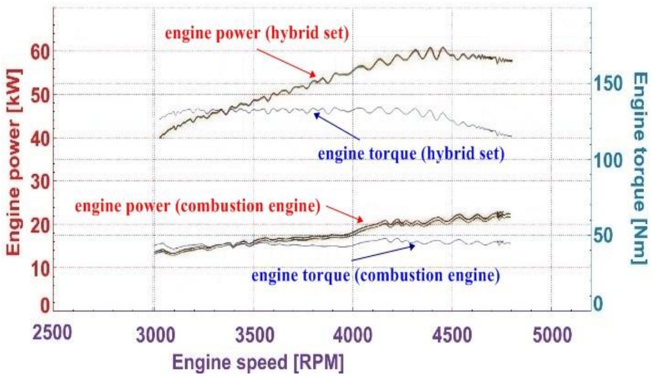

Fig. 12. Course of power and torque of the internal combustion engine and hybrid drive: torque [Nm], useful power [kW]

The resistance to movement of the combustion engine and electric motor drive set was calculated according to a specific scheme. Measurement of the engine torque in the full range of its rotational speed at the oil temperature of 90°C and 110°C. These data allowed to determine the characteristics of the moment of resistance to the movement of the internal combustion engine. A high-class torque meter placed between the internal combustion engine and the electric drive motor was used for the tests. The rotational speed of the internal combustion engine was regulated by means of the rotational speed of the electric motor controlled by the inverter. The measurement was performed at a constant oil temperature for a given rotational speed. The measurement was carried out every 250 rpm. In order to determine changes in the resistance to motion of the electric motor of the hybrid set, an electric motor was connected to the internal combustion engine. Then the measurement was carried out in a similar way as for the internal combustion engine. In the case of determining the resistance to motion of the hybrid set with the propeller connected, the author's dynamometer was used an aircraft engine from Świątek. In this case, changes in the torque of the internal combustion engine and electric motor in relation to this set with the motor connected were determined. The percentages given are ranges for the resistance moment variation of the assembly in these configurations.

These results indicate a significant impact of the electric drive on the resistance to motion of the entire hybrid system. However, it is worth noting that these values are acceptable and do not adversely affect the performance of the hybrid assembly. In addition, the increase in drag is related to additional factors, such as the angular velocity of the propeller and aerodynamic drag, which are natural factors that occur during the flight of an airplane.

A hybrid system in which an electric motor works in conjunction with an internal combustion engine can be an effective solution for hybrid aircraft, enabling significant reductions in fuel consumption and emissions. However, further research is worthwhile to further determine the effect of drag on the efficiency and range of such hybrid aircraft.

The increase in engine motion resistance in the case of a hybrid set results from several factors. First of all, connecting the electric motor to the combustion system introduces additional mechanical elements, such as gears, clutches or other elements connecting the motors. These elements introduce some energy losses due to friction, which leads to an increase in the resistance to motion.

In addition, the electric motor can affect the operation of the internal combustion engine by changing the load characteristics. For example, during hybrid drive operation, the internal combustion engine may be loaded to a greater extent to provide adequate power for the operation of the electric motor, or vice versa, when the electric motor assists the internal combustion engine. This extra load can lead to an increase in the motor's resistance to motion. In addition, the increase in the resistance to motion may also be related to the dynamic effects of the electric motor, such as the moment of inertia of the rotor, aerodynamic drag of the propeller or the influence of electronic control on the operation of the motor. These factors can cause additional energy losses and increase the resistance to motion in the hybrid assembly.

A conventional internal combustion engine, when loaded with a propeller, has a net power of 23 kW at 4750 revolutions per minute (rpm), reaching a maximum torque of approximately 48 Nm. On the other hand, the newly proposed hybrid drive system, combining an internal combustion engine and an electric motor, shows much better parameters. The useful power of the system is 61 kW at 4400 rpm, and the maximum torque is as much as 135 Nm, available over a wide speed range, from 3100 to 4400 rpm. Such a significant improvement in parameters allows for greater operational flexibility of the powertrain. The spread of the rotational speed is wider, which allows better adaptation to the variable speed of the propeller. In addition, it maintains high torque over a wide range of engine speeds, which is particularly advantageous in a variety of flight conditions. The use of a hybrid drive system, as the above data shows, brings decisive benefits in in the context of energy efficiency and operational flexibility. This confirms the innovativeness of the propulsion unit proposed in this work and indicates its potential in further research and development of ultralight aircraft technology.

The parameters of the electric motor play an important role in the case of its independent operation and in combination with an internal combustion engine. In both cases, the electric motor must overcome the additional resistance to the movement of the main engine mechanism and the propeller drive, which generates friction losses and affects the efficiency of the entire system.

When operating an electric motor in a hybrid set, key parameters such as inverter temperature (hb_{temp_C}), electric motor current ($iq_{\_A}$) and inverter input power ($power_{\_P}$) have a significant impact on its efficiency. When transferring energy from the battery to the electric motor, the current ($battery_{Current\_A}$) and battery voltage ($battery_{Voltage\_V}$) play an important role in ensuring adequate power and efficiency.

In addition, the rotational speed of the motor ($speed_{\_rpm}$) is a key parameter that affects the efficiency of the electric motor and the resistance to movement it must overcome. The higher the rotational speed, the greater the resistance to movement and the greater the friction losses. It is worth noting that the efficiency of the electric motor in the hybrid set may be reduced due to the additional load and energy losses resulting from overcoming the resistance to the movement of the main engine mechanism and the propeller drive. Therefore, it is important to properly adjust the parameters of the electric motor and optimize the control in order to minimize these losses and ensure the highest efficiency of the hybrid system.

In Fig. 13, an increase in the power of the electric motor can be observed during the simulated take-off of the aircraft. According to this drawing, the maximum power with an average load of the propeller system and the internal combustion engine for the electric motor is from 40 to 43 kW. The power change is caused by the change in the engine speed in the hybrid set with the simultaneous application of a medium load with the propeller connected. The test was carried out on a dynamometer. This is a very large increase in power, which is particularly important for quickly gaining altitude, but also for safety. The voltage drop on the hybrid set battery in this period is shown in Fig. 14. Figure 13 shows a graph of electric motor power in the full range of rotational speed. The results indicate the possibility of obtaining maximum power by the electric motor. The impact of the use of a hybrid propulsion system of an ultralight aircraft mainly influenced the increase in the torque and power of the propulsion system. The electric motor allows to increase the power and torque in key moments of the aircraft's operation, i.e. the period of take-off, landing and possible aerobatic maneuvers adapted to the structural strength of the aircraft. This system primarily improves the take-off conditions of the aircraft and provides protection in the event of a combustion engine failure. This set, together with the assumed capacity of the batteries, allows for a safe flight of the aircraft for several minutes only with the use of an electric motor. This allows you to avoid a plane crash and safely land a damaged aircraft without internal combustion engine. It is a fairly simple concept in the connection system of the internal combustion engine and the electric motor, which guarantees increased safety and a lower probability of drivetrain failure.

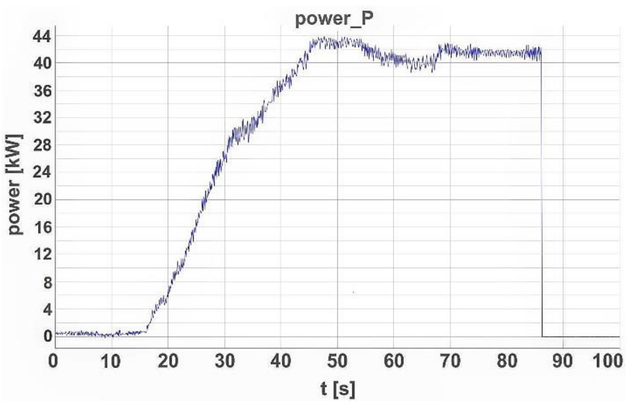

Fig. 13. Change of electric motor power in series connection with medium propeller load

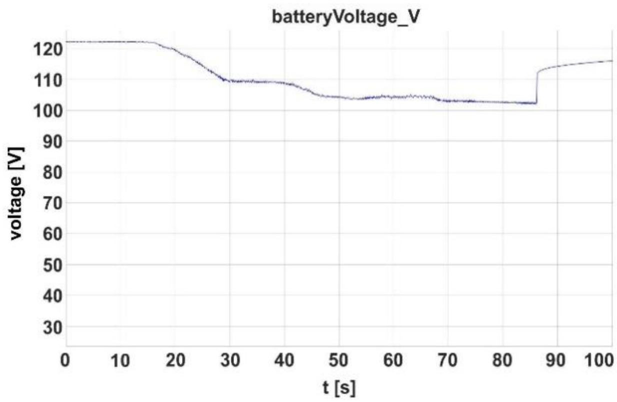

Fig. 14. Voltage drop on the battery cells of the hybrid set

Figure 15 shows the increase in the current value of the battery cells. The maximum value is 410 A. This value does not damage the battery and is a safe value. The current value analogously corresponds to the power increase of the electric motor.

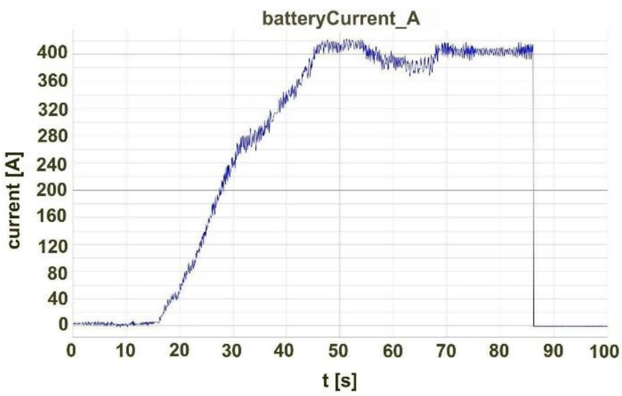

Fig. 15. Change of the current in the battery cells during the period of increasing the power of the electric motor

Similarly, Fig. 16 shows the change in the current value of the electric motor. This is an acceptable value and does not constitute a basis for damage to the electric motor during a sudden increase in the power demand of the hybrid set.

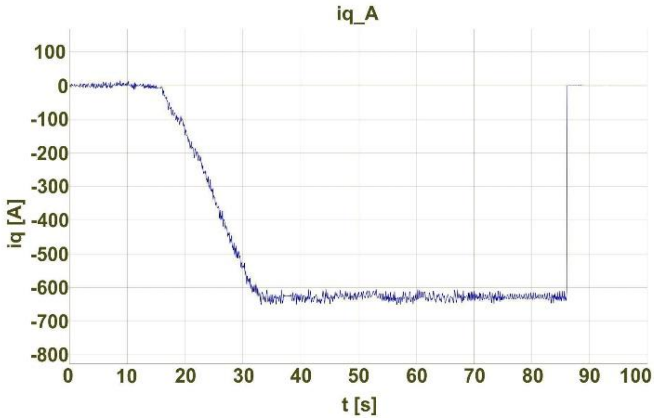

Fig. 16. Change of the current value in the electric motor

The rotational speed of the electric motor is shown in Fig. 17. The average usable range of the rotational speed of the motor shaft is in the range from 2850 to 4800 rpm. The electric motor can have different power ranges depending on the rotational speed. Appropriate adjustment of the rotational speed to the required power allows you to achieve the optimal combination of efficiency and vehicle performance.

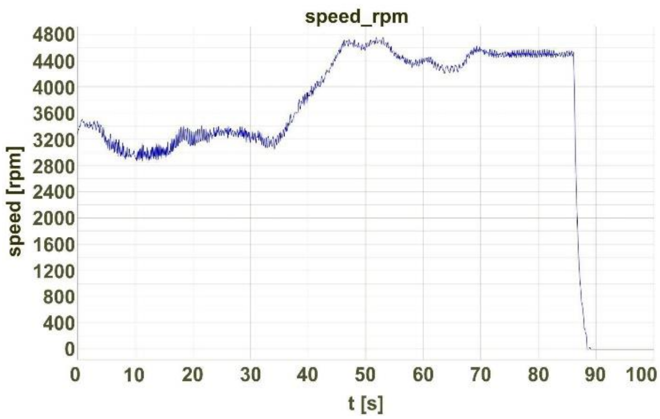

Fig. 17. The rotational speed of the electric motor for given operating conditions

For example, when accelerating or climbing hills, the high rpm of the electric motor can deliver more power, resulting in better performance. The rotational speed of an electric motor affects its energy efficiency. Electric motors are most efficient within a certain speed range, known as the optimum operating point. By operating near this point, the motor uses less electricity per unit of work done. The rotational speed of the electric motor also affects the torque it generates. Torque is the force that causes the drive shaft to rotate. In a hybrid system, the electric motor often supports the internal combustion engine. When accelerating a vehicle, the electric motor can deliver more torque than the combustion engine at low revs, allowing for quicker and smoother acceleration.

Figure 18 shows the waveform of the inverter temperature at the moment of engine load in terms of its rotational speed and the achieved power. The temperature value in this period reached a maximum level of about 46°C. Then, when the engine was turned off, the temperature decreased rapidly. This proves that during the motor overload period, in order to achieve the appropriate power, there is no need to use additional cooling measures for the inverter, and there is no risk of its overheating.

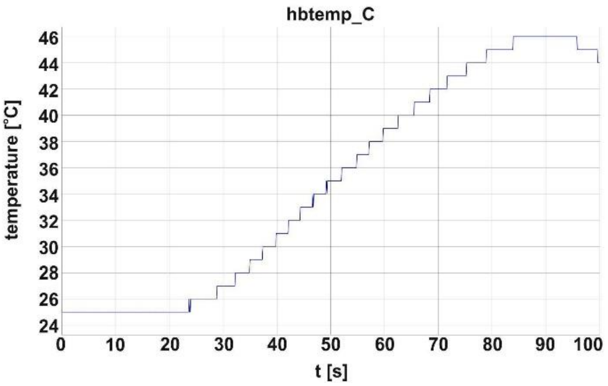

Fig. 18. The course of the inverter temperature at the time of electric motor operation

5. Summary

The work focuses on the design and research of an innovative propulsion unit for ultralight aircraft. It introduces a new approach to energy efficiency and operational flexibility, defined by a hybrid system that combines an internal combustion engine and an electric motor/generator. Key elements of this innovation include an advanced internal combustion engine controller and a bi-directional energy conversion converter, allowing the two energy sources to work together optimally. In addition, a special test stand was developed and built to carry out tests on the prototype of the drive unit.

The results of these tests, in the form of initial prototype performance characteristics and performance analysis, suggest the potential benefits of using such a hybrid drive unit.

The work also contains conclusions and recommendations for further work on improving this innovative technology. All this, combined, makes the presented work a significant step forward in the field of energy efficiency and operational flexibility of ultralight aircraft, and thus shows a significant degree of innovation.

The most important conclusions from the work are:

- The use of a hybrid propulsion system in accordance with the proposed design allows for achieving excellent operational parameters, increasing power and torque during take-off of the aircraft. This not only improves flight performance but also increases safety.
- The maximum value is 410 A. This value does not damage the battery and is a safe value. The results showed that after connecting the electric motor to the hybrid set, the resistance to motion increased from 8 to 17%, depending on the rotational speed of the internal combustion engine. Percentage differences in motion resistance result from changes in the rotational speed of the internal combustion engine shaft. To a large extent, the value of the resistance depends on the resistance of the electric motor and the internal combustion engine. In the case of an internal combustion engine, the resistance to motion depends on the lubrication parameters, and in the case of an electric motor, on the resistance of its bearings. Additional drag is also dependent on the angular velocity of the propeller and aerodynamic drag, and its value ranges from 5 to 23%. Aerodynamic drag was adopted on the basis of data from aircraft flight parameters for a given flight speed. This is also due to the angle of inclination of the propeller blades. It is assumed that a given airspeed is obtained for given engine speeds. This, in turn, can be compared in a general way to the aerodynamic drag calculated theoretically.
- The electric motor reaches its maximum power during the tests from 40 to 43 kW, in the range from 2850 to 4800 rpm, with the maximum temperature of the inverter not exceeding 46°C.
- In the classic system, the internal combustion engine alone, when loaded with the propeller, achieved a useful power of about 23 kW at 4750 rpm, the maximum torque is about 50 Nm. In the hybrid connection, the net power of the set is 61 kW at 4400 rpm, the maximum torque is approximately 135 Nm over a wide range from 3100 to 4400 rpm. As a result, the hybrid set has a wider range of useful rotational speeds and is easier to adapt to the variable speed of the propeller. This gives the propeller greater flexibility while maintaining high torque in a wide range of rotational speed of the drive set.
- The implementation of the energy control system enabled effective management of both the combustion engine and the electric motor, which resulted in optimal use of the available power. This innovation can lead to significant fuel savings and overall propulsion efficiency over a wide range of operating conditions.

Acknowledgment

This work was financed by the Military University of Technology under the university research project No. UGB 819/2023 entitled: Methods of aircraft optimal design in terms of improving their structural, aerodynamic and performance qualities.

The data presented in the article were obtained as a result of the implementation of the Project entitled "Hybrid drive for ultralight aircraft with the possibility of using modules as a range extender and for driving drones" co-financed by the European Union from the European Regional Development Fund under the Smart Growth Programme, Measure 1.1 R&D projects of enterprises, Sub-measure 1.1.1 Industrial research and development works carried out by enterprises.

Project carried out as part of the competition of the National Center for Research and Development: Fast Track. POIR.01.01.01-00-1304/19.

Nomenclature

hb_{temp_C}	inverter temperature	$battery_{Current\_A}$	battery current
i_{q_A}	electric motor current	$battery_{Voltage\_V}$	battery voltage
$power_{\_P}$	inverter input power	$speed_{\_rpm}$	engine speed
t	time		

Bibliography

[1] ATAG, Aviation benefits beyond borders: global summary. Geneva, Switzerland: Air Transport Action Group – ATAG, Tech. rep. 2018. https://aviationbenefits.org/

[2] De Voogt AJ, Van Doorn RR. Sports aviation accidents: fatality and aircraft specificity. Aviation, Space, and Environmental Medicine. 2010;81(11):1033-1036. https://doi.org/10.3357/ASEM.2603.2010

[3] Donateo T, Cavalera D. Increasing safety in ultralight aviation with a wankel-based series/parallel hybrid electric power system. Machines. 2022;10(6):486. https://doi.org/10.3390/machines10060486

[4] Follen GJ, Del Rosario R, Wahls RA, Madavan NK. NASA's fundamental aeronautics subsonic fixed wing project: generation N+3 technology portfolio. SAE Technical Paper 2011-01-2521. 2011. https://doi.org/10.4271/2011-01-2521

[5] Friedrich C, Robertson PA. Hybrid-electric propulsion for aircraft. Journal of Aircraft. 2015;52(1). https://doi.org/10.2514/1.C032660

[6] Friedrich C, Robertson PA. Hybrid-electric propulsion for automotive and aviation applications. CEAS Aeronautical Journal. 2015. https://doi.org/10.1007/S13272-014-0144-X

[7] Gohardani AS. A synergistic glance at the prospects of distributed propulsion technology and the electric aircraft concept for future unmanned air vehicles and commercial/military aviation. Prog Aero Sci. 2013;53:25-70. https://doi.org/10.1016/j.paerosci.2012.08.001

[8] Gohardani AS, Doulgeris G, Singh R. Challenges of future aircraft propulsion: a review of distributed propulsion technology and its potential application for the all electric commercial aircraft. Prog Aero Sci. 2011;47(5):369-391. https://doi.org/10.1016/j.paerosci.2010.09.001

[9] Guynn MD, Berton JJ, Tong MJ, Haller WJ. Advanced single-aisle transport propulsion design options revisited. 13th AIAA Aviation Technology, Integration, and Operations Conference, Los Angeles 2013. https://doi.org/10.2514/6. 2013-4330

[10] Hepperle M. Electric flight – potential and limitations. Tech. Rep, NATO, Braunschweig 2012.

[11] https://www.icao.int/environmental-protection/Pages/climate-change.aspx (accessed on 1.01. 2023).

[12] International Civil Aviation Organization (ICAO), Consolidated Statement of Continuing ICAO Policies and Practices Related to Environmental protection – Global Market-based Measure (MBM) Scheme. 2016.

[13] International Civil Aviation Organization, Technology Standards (2011). http://www.icao.int/environmental-protection/Pages/technology-standards

[14] Matlock JMT. Evaluation of hybrid-electric propulsion systems for unmanned aerial vehicles. 2020. https://dspace.library.uvic.ca/handle/1828/11484 (accessed 23.12.2023).

[15] National Academy of Engineering Committee on Propulsion and Energy Systems to Reduce Commercial Aviation Carbon Emissions, Commercial Aircraft Propulsion and Energy Systems Research: Reducing Global Carbon Emissions, National Academies Press, 2016, https://doi.org/10.17226/23490

[16] Pornet C. Electric drives for propulsion system of transport aircraft. Chromat M. (ed.) New applications of electric drives, InTech, 2015, Chapter 5. https://doi.org/10.5772/61506

[17] Sarlioglu B, Morris CT. More electric aircraft: review, challenges, and opportunities for commercial transport aircraft. IEEE Transactions on Transportation Electrification. 2015;1(1):54-64. https://doi.org/10.1109/TTE.2015.2426499

[18] Thomson R, Sachdeva N, Nazukin M, Martinez N. Aircraft electrical propulsion – the next chapter of aviation? https://www.rolandberger.com/en/Publications/pub_new_trends_in_electric_aircraft.html

[19] U.S. Energy Information Administration. Annual Energy Outlook 2012. DOE/EIA-0383, U.S. Dept. of Energy, Washington 2012.

[20] U.S. Energy Information Administration. U.S. Gulf coast kerosene-type jet fuel spot price FOB. https://www.eia.gov/petroleum/

[21] U.S. Energy Information Administration. Wholesale electricity and natural gas market data. https://www.eia.gov/electricity/wholesale/

Piotr Wróblewski, DEng. – Faculty of Engineering, University of Technology and Economics H. Chodkowska in Warsaw, Poland.
e-mail: *piotr.wroblewski@uth.edu.pl*

Prof. Stanisław Kachel, DSc., DEng. – Faculty of Mechatronics, Armament and Aerospace of the Military University of Technology, Poland.
e-mail: *piotr@swiatek.com.pl*

Piotr Świątek, DEng. – Światek Lech Świątek Companies, Poland.
e-mail: *piotr@swiatek.com.pl*

Tomasz Zyska, DEng. – Lublin University of Technology, Poland.
e-mail: *t.zyska@pollub.pl*

Article citation info:
Michalak P, Urbański P, Jakuszko W, Gallas D., Stobnicki P, Tarnawski P. Technical aspects of the selection of an engine-generator set for a dual-drive locomotive. Combustion Engines. 2024;197(2):97-105. https://doi.org/10.19206/CE-176799

Piotr MICHALAK
Patryk URBAŃSKI
Wojciech JAKUSZKO
Dawid GALLAS
Pawel STOBNICKI
Piotr TARNAWSKI

Combustion Engines
Polish Scientific Society of Combustion Engines

Technical aspects of the selection of an engine-generator set for a dual-drive locomotive

ARTICLE INFO

Received: 17 August 2023
Revised: 2 November 2023
Accepted: 11 December 2023
Available online: 8 January 2024

The use of dual-drive rolling stock is a relatively new solution in the railway market. Vehicles with such type of powertrain are more versatile because it combines the advantages of using diesel vehicles and electric vehicles that consume energy from overhead electric traction. The concept of using such vehicles is highly innovative and has many advantages. However, the design and construction process is more complicated and requires more work than in the case of conventional systems. This article presents the methodology and process of selecting an engine-generator set for a dual-drive locomotive. Indicators and procedures crucial in the process of selecting a dual-drive system for a locomotive, were described and evaluated. All the above mentioned in the work were used during the real design process of a fully Polish locomotive with both diesel and electric drives. The locomotive in Diesel mode was to have an output power of circa 1560 kW for cargo transport. Calculations for the locomotive's power balance are included, showing power losses in the system and for locomotive's own needs. It has been shown that in cargo transport 77% of the maximum engine power is used as tractive power, and in passenger transport 58.6%.

Key words: *dual-drive locomotive, railway, diesel engine, generator set, design process*

1. Introduction

Railway lines can be divided into two types, those with electric traction and those that are not electrified. In the case of Poland, in 2021, the total length of the railway network was 19.3 thousand km, of which 62.8% were electrified standard-gauge lines [11]. Most railway lines have electric traction. However, only vehicles with an independent power source can move on 37.2% of the lines. In practice, this means the use of a vehicle with an internal combustion engine (ICE), mainly Diesel [8, 9]. The use of this type of drive is associated with exhaust emissions, which combined with the average age of diesel rolling stock in Poland, about 40 years old [25], may cause local air pollution [1, 5, 13, 15, 16, 30] and increased fuel consumption [2].

According to the European Environment Agency (EEA), rail transport is responsible for 0.4% of total transport greenhouse gas (GHG) emissions of the European Union (EU) [12]. As a whole, compared to other modes of transport, the emission is negligible. However, the EU policy aimed at reducing exhaust emissions and CO_2 influenced the introduction of strict emission standards also covering rail vehicles. Ambitious zero-emission transport plans [29, 33], led to the development of alternative power sources [4] in the vehicle sector of Non-Road Mobile Machinery (NRMM) [14], which also includes rail vehicles [5, 18, 28]. A particularly discussed issue is the use of hydrogen in rail vehicles [31], mainly using Fuel Cells (FC) [12, 19, 27, 32]. The use of alternative power sources brings benefits, but at the moment, this solution is very expensive and requires huge financial outlays and government subsidies [8].

Therefore, despite their shortcomings, ICEs in railways are widely used and will probably continue to be used for a long time. The reason is the versatility, affordability, and independence of a vehicle with ICE from the railway infrastructure. A diesel vehicle can move on any type of railway line, while an electric vehicle is limited by the availability of electric traction. For this reason, on railway connections that are partly equipped with overhead electric lines, it is common practice to use one electric locomotive on an electrified line and one diesel locomotive on a non-electrified line [24]. However, this solution requires the use of two vehicles, and additional time is required to switch vehicles.

In order to avoid the use of two vehicles for one railway connection, one of the solutions is to use a rail vehicle with two power sources. Combining the most popular drives on the railway – electric and diesel – and installing them on one vehicle brings benefits in the form of using the advantages of both drives. This increases the versatility and flexibility of using such a vehicle on a railway line. Vehicles of this type are not yet so popular a solution on the railway market. However, this solution can be used in any type of railway vehicles, including rail-road vehicles [20, 21, 34], locomotives [22], Multiple Unit (MU) [10], and auxiliary rail vehicles.

The design process of a rail vehicle is characterized by a significant degree of complexity requires experienced design staff in every field, knowledge of railway standards and regulations and a well-thought-out layout of assemblies and subassemblies on the vehicle. In the case of dual-drive vehicles, this is even more challenging due to the two different drivetrains mounted on one vehicle. So far, publications related to the planning, management and implementation of railway projects have been published [17], and related to the selection of the engine-generator set during the locomotive modernization process [23] and auxiliary ICE in special purpose rail vehicle [35]. However, there is still lack of data related to the process and the selection criteria used by designers during the design process of a rail vehicle.

This article presents the most important information regarding the selection process of an engine-generator set for a dual-drive 111DE locomotive from the technical perspective and proceeding scheme of individual stages of the project. The assumptions and requirements for the design of the real locomotive tested on railway lines were also presented. Additionally, in the article, the power balance calculations, which are necessary to determine the energy consumption of the locomotive operating in diesel mode, are also described.

2. Proceeding scheme and assumptions for the selection method of the engine-generator set of a dual-drive locomotive

The design process of a rail vehicle is characterized by a significant degree of complexity and consists of many subsystems and the selection process of devices based on the developed studies and calculations. In the case of selecting an engine-generator set for a dual-drive locomotive, the process is even more complex due to the use and installation of two drive systems on one vehicle. In order to systematize the engine-generator set selection procedure, it was divided into several key stages. In Figure 1, in the form of a block diagram, the sequence of procedure is presented.

The first stage when designing a rail vehicle with two drive systems is to discuss with the ordering party on the detailed technical requirements for the vehicle. These requirements consist primarily of details regarding traction capabilities, i.e. the length and weight of cars that the locomotive will be able to pull, and assumptions regarding the drive systems used. The requirements also include information on maximum speeds depending on operating conditions (dry or wet track, track inclination).

An important element is also specifying the requirements for locomotive equipment. This has a significant impact on the power consumption of the locomotive in diesel mode. An important element is the calculation of a vehicle energy balance. Thanks to this, it is possible to pre-estimate energy consumption, and then based on this information, it is possible to calculate locomotive's traction capacity, both in diesel and electric mode.

If the vehicle is to be built without the participation of the ordering side (e.g. a demonstrator vehicle or in order to expand the company's offer), the process is similar to the one described above, but the requirements are determined on the basis of the experience of the design team and the vehicle manufacturer. During the design process, detailed technical requirements for a dual-drive locomotive were developed in cooperation with the potential user of the locomotive and the manufacturer.

During the process of selecting an engine-generator set, one of the stages is a multi-directional analysis of applicable standards and regulations, in particular regarding the possibility of using ICE and traction generators in railways. The above analyzes are aimed at developing requirements for the engine and generator and starting to call for offers from potential suppliers of these assemblies. Offer analysis and technical consultations require extensive knowledge of the integration of a diesel engine with a generator and, later an engine-generator set with a locomotive.

The next required stage is to carry out analysis regarding the selection of peripheral systems, such as the cooling system or the exhaust aftertreatment system (EAS), which are the subject of commercial offers received from manufacturers. The result of the above activities is the resulting studies and analysis regarding:

- engine and generator life cycle costs, taking into account the load program of the ICE
- exhaust aftertreatment methods and level of exhaust emissions reduction to the assumed/required standard
- mechanical installation of the power unit and determination of permissible loads on the locomotive frame
- mass analysis and its distribution on the vehicle
- service availability
- economic analysis.

Based on the above activities, the final result is the selection of the engine-generator set, along with the necessary systems, as well as the development of the engine-generator set assembly method on the locomotive. Each decision in the design process requires individual analysis and research due to, for example, approval of assembly or approval of using devices in railway vehicles, due to compliance with standards or compliance with the requirements of the project. For this reason, the stages were

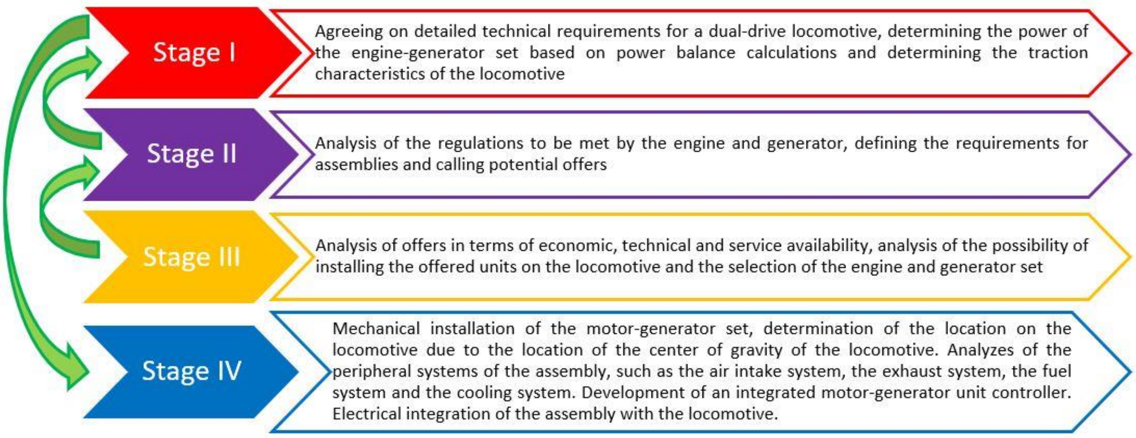

Fig. 1. Block diagram of the stages of selection of the engine-generator set

linked by a "feedback". In the event that the initial element of the layout is adopted, its impact on the rest of the layout must also be traced, which requires "going back" to the previous step.

After completing all the above steps, the last stage consists in the mechanical assembly of the selected engine-generator set. A vehicle with two propulsion systems requires determining the appropriate location of individual units on the locomotive. The even mass distribution of the electrical and diesel systems is a very important factor because it affects the maximum axle loads of the vehicle. These, in turn, are standardized depending on the railway lines and only vehicles with permissible axle load can move on them. During the development process, peripheral circuits and systems were also analyzed. At the same time, analyzes were being carried out to integrate the assembly with the locomotive in electrical and electronic terms. In addition, an integrated controller for the engine-generator set and the control of electric and diesel propulsion systems was being developed.

3. Technical requirements for the vehicle

The project involved designing and building a locomotive with two power sources, where:
– from electric traction line 3 kV DC (Electric mode – E)
– from engine-generator set 3 kV DC (Diesel mode – D).

The dual-drive locomotive was to be a standard-gauge 4-axle locomotive with a power, depending on the mode:
– 2800 kW (E)
– 2000–2200 kW (D).

Table 1. Preliminary detailed design assumptions of a dual-drive locomotive – type 111DE

Parameter	Description
Purpose	passenger/freight
Power supply	3kV DC – railway electric traction and 3 kV DC – diesel power generator – AC-DC-AC transmission
Track gauge	1435 mm
Total length	≤ 20,000 mm
Loading gauge	PN-EN 15273-2 G1
Maximum operating speed	160 km/h
Wheel diameter new/worn	1250 mm/1170 mm
Design mass of the vehicle ready to work	86 t
Load of the wheelset on the track	max. 211 kN
Starting tractive force max.	300 kN adhesion factor (0.3 – dry track)
Locomotive continuous power in cargo transport	electric – 2800 kW diesel engine – c. 1560 kW
Number and arrangement of axles	4, B'o-B'o
Operating speed for passenger trains	Electric traction – 160 km/h Diesel traction – 120 km/h
Operating speed for cargo trains	Electric traction – 110 km/h Diesel traction – 80 km/h
Curve radius of the track	min. 80 m when V ≤ 5 km/h
The longitudinal inclination of the track on which a locomotive can move	max. 40‰
Auxiliary circuit voltage	3×400 V AC; 24 V DC
Control circuit voltage	24 V DC
Multiple traction	up to 2 vehicles

The locomotive's drivetrain was designed to consists of four asynchronous motors powered by traction converters. Electrodynamic, recuperative, and resistive braking was possible. The locomotive was also to be equipped with one or two auxiliary power converters, powered by 3 kV DC, to supply:
– auxiliary voltage network 3×400 V/50 Hz with IT system; some circuits were to be powered by a separate circuit with a voltage of 230 V/50 Hz, powered from a three-phase network by a transformer, and variable-frequency converters controlling the fans operation,
– 24 V DC on-board network, from which the battery was to be charged, and circuits such as control, lighting, railway traffic security, signalling, registration and communication were to be powered.

In passenger traffic, the locomotive was to supply the wagons with 3 kV DC voltage and power up to 400 kW. In power supply mode D, it is provided that the power will be supplied from the power generator, while in mode E, basically from the electric traction. The most important data on design assumptions are presented in Table 1.

One of the two full-fledged power sources in the project was the diesel drive, where the ICE was to drive the electric generator producing a voltage of 3 kV DC. The most important requirements for ICE Diesel are listed in Table 2.

Table 2. Technical requirements for the diesel engine of the 111DE locomotive

Parameter	Requirement
Operating ambient temperature range	–25°C – +40°C
Operating temperature range for electronic devices	–25°C – +70°C
Max. height above sea level	1200 m
Relative humidity of the ambient air	max. 90% at 20°C, annual average 75%
Type of the engine	4-stroke, V-type
Engine power	2000–2200 kW
Rated rotational speed	1800 rpm
Flywheel housing	SAE 00
Adaptation to traction generator drive	Type of the generator construction: single-bearing generator preferred
Electronic engine controller	Yes
Supply voltage of the exciter system's voltage regulator	24 VDC
Exhaust aftertreatment system	Stage IIIB (F cycle) Stage V (for deliveries from 2021)
Design and strength (fastening of accessories and engine to the locomotive)	Acceleration in the: – x axis: ±3 g (longitudinal) – y axis: ±1 g (transverse) – z axis: ±2 g (vertical)
Calculation of engine operating costs – LCC	Post-order delivery required

In the case of the generator, the most important requirements are presented in Table 3. An important indicator in the selection process is the generator power, which in electrical cases is given as apparent power (VA). Apparent power is an electrical indicator where the phase of voltage relative to current (cos φ) for AC must be taken into account. In turn, mechanical power–active power (W), is the real power based on the mechanical efficiency of the generator system and is needed to energy balance calculations. Additionally, for the device that had matching the power of the generator to the power of the engine in the entire rev range, the requirements for the bearings used in the device were specified, the most important of which were:

– possibility of regreasing
– insulated
– temperature measurement required
– bearing design:
  - fixed bearing (no axial displacement of the generator rotor)
  - bearing resistant to micro-vibrations during electric traction (stationary generator)
  - minimum durability of 25,000 hours of operation.

Table 3. Technical requirements for the generator of the 111DE locomotive

Parameter	Requirement
Operating ambient temperature	–30°C – +70°C
Cooling air inlet temperature	–30°C – +40°C
Max. height above sea level	1200 m
Relative humidity of the ambient air	max. 90% at 20°C, annual average 75%
Casing protective level	min. IP 23
Type of work	S9
Type of construction of the generator	synchronous, brushless with built-in generator and rotating rectifier, single-bearing
Diaphragm coupling design	SAE J620
Installation of the generator	claws for mounting flexible supports – two support points
Rated apparent output power	2100–2400 kVA
Rated active output power	~ 1950–2350 kW
Rated generator speed	1800 rpm
Min. generator speed	700 rpm
Rated output voltage (after the rectifier)	3600 V DC
Minimum output voltage (after the rectifier)	2100 V DC
Winding insulation class	H

4. Technical solutions

4.1. Combustion engine

The key stage is the selection of the appropriate drive system, in this case the power generator. On the basis of the previous stages, where technical requirements for the generating set were defined, technical specifications of the sets for suppliers were developed. Based on technical offers, the method of evaluating the selection of a diesel engine and a generator for a dual-drive locomotive project was presented.

In the process of selecting an ICE, potential manufacturers were MTU, Cummins, Liebherr, and CAT. These manufacturers have considerable experience in supplying ICEs for railway applications. In addition, some of the listed companies participated in earlier joint railway vehicle projects.

In the design of the 111DE locomotive, the most important assumptions for the diesel drive were the required power range of the unit 2000–2200 kW and the Stage IIIB or higher emission standard. During the implementation of the project, Liebherr and CAT did not offer engines that meet the requirements in terms of power and the emissions level, which was reflected in the technical assessment.

The remaining offers of the two companies were subjected to technical evaluation, of which the most important factors were:

– emission standard, where Stage IIIB was the highest emission standard available for rail applications
– engine mass – a key element, especially in the aspect of permissible locomotive axles loads
– Exhaust aftertreatment system – assembly possibilities and operating costs
– additional take-off point for driving the hydrostatic pump with a minimum torque of 750 Nm – drive of the hydraulic pump of the hydrostatic fan drive system of the ICE cooling system
– engine overhaul period – ICE durability and life cycle
– availability of the service in Poland and the number of available points in the country for efficient operation.

The process of technical assessment of the available ICEs is presented in Table 4. It was decided to evaluate each of the listed factors individually on a scale from 0 to 5 in terms of benefits for the project. In addition, each factor had its individual degree of significance (rating weight), based on the authors' experience from previous projects, where these factors were assigned from the least to the most significant, respectively: 0.5, 0.7, and 1. The most important for the assessment were: emission standard and mass. Indicators of medium importance were: overhaul period and service availability, and indicators with a low importance were: additional take-off point and development possibilities and EAS operating costs.

Each rating for individual factors was multiplied by the rating weight. The obtained results were marked with the appropriate color depending on the impact factor for the final assessment of the ICE, and then summed up. According to the assessment, with the boundary conditions set by the designers, a more favorable solution for the purposes of the project was the use of the QSK60-L2700 Cummins engine with a rated power of 2013 kW.

Table 4. Technical requirements for the diesel engine of the 111DE locomotive

	Engine manufacturer				Rate		Rating weight	Result		
Parameter	MTU	Cummins	Liebherr	CAT (Eneria)	MTU	Cummins		Max.	MTU	Cummins
Egine type	16V4000R64	QSK60-L2700	Lack of engine with such power and Emission Standard	Lack of engine with such power and Emission Standard	X	X	X	X	X	X
Rated power [kW]	2000	2013			X	X	X	X	X	X
Emission standard	EU IIIB	EU IIIB			5	5	1	5	5	5
Mass [kg]	9159	9046	X	X	4	5	1	5	4	5
EAS (assessment in terms of installing the system on a locomotive and operating costs)	DPF	SCR, AdBlue Tank	X	X	4	4	0.5	2.5	2	2
Additional power take-off point for driving the hydrostatic pump - M = min. 750Nm	Yes (Max. Torque 560 Nm)	Yes (Max. Torque 210 Nm)	X	X	0	0	0.5	2.5	0	0
Engine overhaul period [h]	24000-30000	c. 25000	X	X	4	4	0.7	3.5	2.8	2.8
Service availability in Poland	Yes	Yes	X	X	3	5	0.7	3.5	2.1	3.5
Result								22	**15.9**	**18.3**

Impact					
Zero	Irrelevant	Small	Medium	Relevant	Crucial

4.2. Generator

In diesel rail vehicles, ICE is mainly used to drive a generator that generates electricity to supply traction motors and auxiliary systems. In the case of the 111DE locomotive, an important element was the selection of a generator operating in appropriate conditions with an ICE. In addition, an important assumption of the design was similar electrical parameters during Diesel mode (D) and Electric (E) mode. The reason was the use of power electronic devices in the vehicle, which require appropriate operating conditions. In order to avoid duplication of systems and devices, such an idea was implemented.

On the basis of the requirements set out in the earlier stage, commercial offers for generators were received that could be used in the project. The considered generator manufacturers were: EMIT, Hitzinger, VEM, ABB, Elektroputere, and Jenoptik. The requirements for the generator were quite extensive, but the most important technical indicators presented in the article were:

- generated voltage at generator speed 700 and 1800 rpm
- rated output power 2100–2400 kVA at 1800 rpm
- generator mass
- bearing number
- delivery range.

As in the case of the technical assessment of ICEs, selected parameters of the generators were also assessed on a scale of 0 to 5, and the assessed parameters had a significance weight of 0.5, 0.7, 0.8 or 1. The most important parameters with a weight of 1 were generator operating parameters, i.e. voltage values for the minimum and rated speed, as well as rated output power. The weight of 0.8 was assigned to the mass, which, due to the limitations of the maximum locomotive axles loads, was the second most important factor. Mainly due to the minimization of the size of the system and the characteristics of the operation, it was decided to use one bearing, and the weight of this parameter was set at 0.7. The significance of the delivery range was set at 0.5. The devices considered in delivery range were: generator, voltage regulator, rectifier, connecting gusset and clutch. The evaluation results are presented in Table 5.

Assessing the generated voltage at 700 rpm, Hitzinger, VEM, and Elektroputere generators were the most favorable, where the minimum output voltage was at the required level, i.e. 2100 V. In the case of Emit wyk. I, Jenoptik and ABB the voltage levels were too low. For rated output speed, all generators except Emit – wyk. I met the requirement of 3600 V DC. The rated output power in the requirements was to be in the range of 2100–2400 kVA. However, this requirement was met by three generators. In addition, in the case of Elektroputere, the power was 2108 kVA, which is slightly above the lowest required power. In the remaining cases, three generators had too much power, and in one case, the power generated was insufficient for the requirements of the locomotive.

For non-utility parameters, the following data were assessed: mass, number of bearings and delivery range. The assumption for mass, was the lowest possible mass of the generator. This requirement was the most favorable for EMIT – wyk. I with 3700 kg. For ABB and Hitzinger products, the mass was slightly higher, 4270 kg and 4500 kg, respectively, but in the latter case, this value also included the connecting gusset and clutch. The VEM product was heavier than the Hitzinger by 110 kg, but did not include clutch in the statement. The other products were too heavy for the minimum mass requirement.

In the case of the bearings number, three generators were single-bearing: Hitzinger, ABB, Elektroputere. The remaining solutions contained 2 bearings, therefore they were rated 0. In the case of the delivery range that was to cover the order, the most important elements, due to the

Table 5. Technical requirements for the generator of the 111DE locomotive, where: POS. – possible

Parameter			Generator manufacturer: EMIT - wyk. I Gfp 560S8	EMIT - wyk. II Gfp 560S8	Hitzinger SGE 090B 06T	VEM DREBZ 5012-8	ABB WGx500pb6	ELEKTROPUTERE GST-P	Jenoptik SDV 95.40-10	Rating weight
Voltage [V]	700 [rpm]	AC	1000	1660	1556	1638	1350	no data	no data	1
		DC			2100	2100		2100	1400	
			0	4	5	5	2	5	0	Rate
			0	4	5	5	2	5	0	Total
	1800 [rpm]	AC	2500	2840	2664	2808	2840		2880	1
		DC			3600	3600		3600	3600	
			3	5	5	5	5	5	5	Rate
			3	5	5	5	5	5	5	Total
Apparent power [kVA]	1800 [rpm]		2588	2588	2400	2400	2025	2108	2512	1
			2	2	5	5	1	4	3	Rate
			2	2	5	5	1	4	3	Total
Mass [kg]			3700	6200	4500 (w. connecting gusset and clutch)	4610 (w. connecting gusset)	4270	6300	no data	0.8
			5	0	4	3	4	0	0	Rate
			4	0	3.2	2.4	3.2	0	0	Total
Bearing number			2	2	1	2	1	1	2	0.7
			0	0	5	0	5	5	0	Rate
			0	0	3.5	0	3.5	3.5	0	Total
Delivery range			•generator YES •voltage regulator NO •rectifier NO •connecting gusset YES •clutch NO	•generator YES •voltage regulator NO •rectifier NO •connecting gusset YES •clutch NO	•generator YES •voltage regulator NO •rectifier NO •connecting gusset YES •clutch YES	•generator YES •voltage regulator YES •rectifier NO •connecting gusset YES •clutch NO	•generator YES •voltage regulator POS. •rectifier NO •connecting gusset NO •clutch NO	•generator YES •voltage regulator YES •rectifier YES •connecting gusset YES •clutch NO	• generator YES • voltage regulator YES • rectifier YES • connecting gusset NO • clutch NO	0.5
			2	2	3	3	0	4	2	Rate
			1	1	1.5	1.5	0	2	1	Total
Result			10	12	23.2	18.9	14.7	19.5	9	

Impact					
Zero	Irrelevant	Small	Medium	Relevant	Crucial

later assembly of the engine-generator set, were connecting the gusset and clutch. Due to this, the best offer was made by Elektroputere, where only the clutch was not included in the scope of delivery. The offers from Hitzinger and VEM were rated 3. The other bids were rated 2 or 0.

The rates were multiplied by the rating weight, and then the results for a generator were summed up. The highest score was achieved for the Hitzinger SGE 090B 06T generator – 23.2 points. The second result in the ranking was achieved by Elektroputere – 19.5, and the third by VEM – 18.9. For this reason, the Hitzinger SGE 090B 06T generator was used in the 111DE locomotive.

5. Dual-drive locomotive power balance

5.1. Auxiliary circuits – locomotive own's power demand

Based on the determination of the power balance, it is possible to specify the requirements for ordering devices, subassemblies and apparatuses, as well as to estimate the locomotive's energy demand for selected devices. Mechanism for assessment of energy balance for a 111DE rail vehicle operatingFtable in diesel traction with a maximum power of selected 2013 kW ICE has been shown. Rail vehicles operations in real conditions usually does not take place at maximum engine load, however, the calculations are important to demonstrate, among other things, maximum useful tractive power in different transport modes.

DC circuits

The locomotive consists of a number of devices and assemblies requiring DC power. It is therefore, necessary to estimate the energy consumption of these devices. Table 6 summarizes the most important auxiliary devices or their parts powered by direct current in diesel mode. Non-simultaneity of work resulting from traffic and climatic conditions was taken into account (winter-w and summer-s season).

Table 6. Power demand of DC auxiliary devices (w – winter, s – summer)

24V DC circuit or device	Power in D mode
External lighting – front + rear, solo driving	0.20 kW
Cabin A/C – active in 2 cabins	2 × 0.53 kW
Cabin heaters – active in 1 cabin	0.34 w/0 s kW
Diesel engine and AdBlue tank heaters	2 × 0.59 kW
Battery charging – I10	0.84 kW
Internal lighting (full)	0.15 kW
Control unit	~2 kW
Rest	~5 kW
In total:	10.77 w/10.43 s kW

AC circuits

In the case of AC circuits, the power demand is greater. The circuits or devices operate at 400 or 230 V AC. Figure 2 shows the power demand of AC auxiliary devices. Energy consumption is influenced by climatic aspects, where higher energy consumption is in the winter period. The graph shows that the largest consumers of energy from the AC system are: traction converters cooling (40 kW), main compressors (40 kW), and brake resistor tower fans (37 kW).

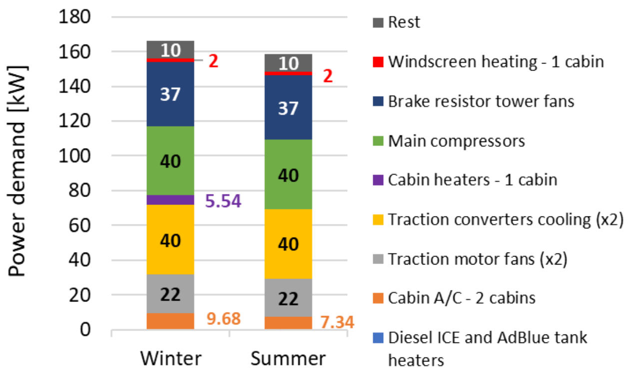

Fig. 2. Power demand of AC auxiliaries in 111DE dual-drive locomotive

High voltage power demand – own needs

The demand for electricity for the locomotive's own needs can therefore be divided into two types: AC circuit and DC circuit. The electricity generated by the power generator to supply both circuits must additionally pass through an auxiliary converter. Assuming the efficiency of the auxiliary converter η_C = 0.83, power demand for the locomotive's own purposes on the supply side 3 kV DC (P_{Ld}) can be calculated from formula (1), where: P_{DC} – DC circuit demand, P_{AC} – AC circuit demand.

$$P_{Ld} = \frac{P_{DC} + P_{AC}}{\eta_C} \tag{1}$$

Based on the formula (1), the maximum energy demand for own purposes of the dual-drive 111DE locomotive in diesel mode, was calculated depending on the season (Fig. 3). By far the largest share of power demand falls on AC circuit. In the case of a DC circuit, this demand is up to 5% of the total power demand for the locomotive's own needs. The diesel locomotive will have the biggest power demand in winter, mainly due to the need to heat the driver's cabins.

In the initial stages of calculation work, a much higher electric energy consumption rate was assumed in order to avoid unplanned energy deficits for traction purposes due to the energy consumption of on-board devices. After energy consumption analyzes of electrical devices selected in later stages, the maximum value of energy consumption for the locomotive's own purposes was adjusted and assumed at the level of 200 kW in diesel mode.

5.2. High voltage circuits

The calculations assumed the maximum power demand for traction purposes. In D mode, the power to the traction purposes is limited. At the assumed maximum power of the ICE P_{ICE} = 2013 kW, the power demand of the ICE's cooling system must be taken into account (P_c) assumed on the 80 kW. This means ICE net power (P_{nICE}):

$$P_{nICE} = P_{ICE} - P_c =$$
$$= 2013\ \text{kW} - 80\ \text{kW} = 1933\ \text{kW} \tag{2}$$

Net ICE power (P_{nICE}) in the form of mechanical energy is then transferred to the generator with a rectifier, where DC electricity is generated (P_G). The efficiency of the traction generator with the rectifier was assumed to η_G = 0.96.

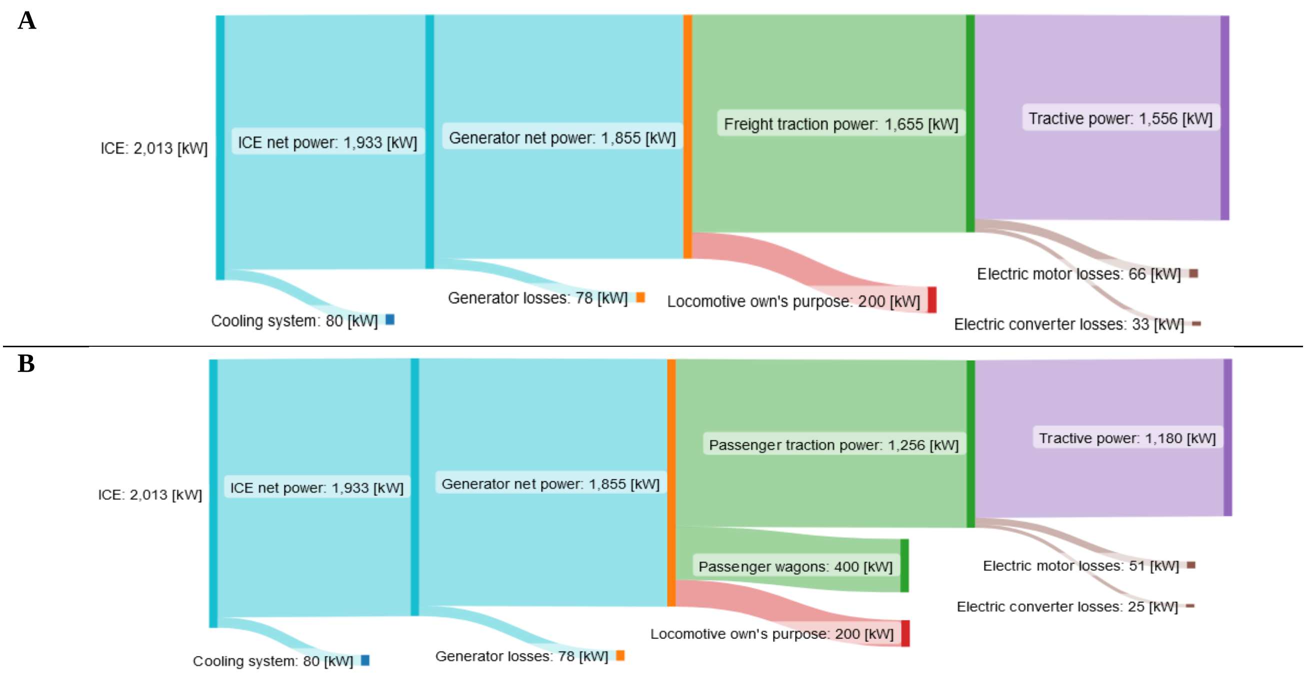

Fig. 4. Energy balance of the dual-drive 111DE locomotive in diesel traction at work: A – freight, B – passenger

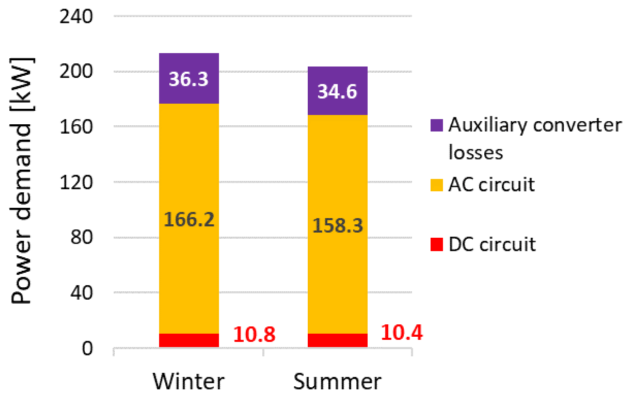

Fig. 3. Calculated total power demand for own purposes of 111DE dual-drive locomotive in Diesel mode

$$P_G = P_{nICE} \cdot \eta_G = 1933\ \text{kW} \cdot 0.96 = 1855\ \text{kW} \quad (3)$$

The locomotive consumes energy for its own purposes (auxiliary circuits) (P_{Ld}), where the demanded power is about 200 kW. This means that the net electric energy behind the generator for other purposes (P_{Gn}) is:

$$P_{Gn} = P_G - P_{Ld} =$$

$$= 1855\ \text{kW} - 200\ \text{kW} = 1655\ \text{kW} \quad (4)$$

In the case of passenger traction, an additional power supply of 400 kW is also required for the passenger wagons (P_{Pd}). This means that the remained available electric power in passenger traction (P_{Gp}) is:

$$P_{Gp} = P_{Gn} - P_{Pd} =$$

$$= 1655\ \text{kW} - 400\ \text{kW} = 1255\ \text{kW} \quad (5)$$

In the power balance for diesel mode, it is also required to take into account the efficiency of traction converters (η_{Tc} = 0.98) and electric traction motors (η_{Te} = 0.96). This means that the maximum tractive power in diesel mode for cargo (P_{Dc}) and passenger (P_{Dp}) purposes is as follow:

$$P_{Dc} = P_{Gn} \cdot \eta_{Tc} \cdot \eta_{Te} =$$

$$= 1655\ \text{kW} \cdot 0.98 \cdot 0.96 = 1556\ \text{kW} \quad (6)$$

$$P_{Dp} = P_{Gp} \cdot \eta_{Tc} \cdot \eta_{Te} =$$

$$= 1255\ \text{kW} \cdot 0.98 \cdot 0.96 = 1180\ \text{kW} \ (7)$$

Figure 4 shows the energy balance of the dual-drive 111DE locomotive in diesel mode, depending on the type of work performed.

6. Summary

The process of selecting the engine-generator set in railway vehicles can be divided into several stages, the most important of which were presented in the article: determining the method and work plan, specifying the requirements for the locomotive and drive system, technical assessment of devices and calculations including, among others, vehicle's energy balance. Based on the mentioned steps, it is possible to select the appropriate engine-generator set for the designed vehicle.

Analyzing the presented process of evaluating the diesel drive system for a dual-drive locomotive, it can be concluded that the mass of the devices plays a very important role both for the engine and the generator. This is due to the very limited possibility of mounting and the permissible axles loads of the vehicle, which has two different sources of drive. Reliable operation of the vehicle is also important, and in the event of an ICE damage, taking the vehicle out of service can be costly [3]. For this reason, the availability of the service is also an important element in the technical assessment of the device.

For the assessment of the generator, the most important elements were the operating parameters of the device that had to work in the required conditions. In addition, the aforementioned mass was also of key importance, as well as the number of bearings used, where their number affected the possibility of installing other devices on the vehicle. The delivery range was not a very important element, but it facilitated the design process and assembly due to the elements properly selected by the manufacturer.

The energy balance of a dual-drive locomotive allows to determine the power demand when operating in Diesel mode. Properly performed calculations based on design assumptions are an important element at the stage of selecting devices and systems in the locomotive, including primarily the drive system, due to the estimation of power demand requirements. In the case of calculations for selected devices, they make it possible to determine the expected performance of the locomotive, e.g. in passenger and freight traction.

It is noteworthy that with the maximum engine power of 2013 kW in freight traction, the vehicle will have a maximum power (on traction motors) of 1556 kW, where about 23% of the power is lost mechanically and thermally or is available for locomotive own's purposes. In the passenger traction, the power of the locomotive in diesel mode is additionally reduced by 400 kW due to the wagon power supply. As a result, the useful power on the traction motors remains about 1180 kW, i.e. 58.6% of the initial power generated by ICE.

Acknowledgements

The article was written in connection with the project POIR. 01.02.00-00-0191/16-00 entitled "Platform of locomotives with advanced diesel-electric (multi-system) drivetrain systems", co-financed by The National Centre for Research and Development.

European Funds Smart Growth | Republic of Poland | The National Centre for Research and Development | European Union European Regional Development Fund

Nomenclature

A/C	air conditioning
AC	alternating current
DC	direct current
DPF	diesel particulate filter
EAS	exhaust aftertreatment system
EEA	European Environment Agency
EU	european union
FC	fuel cell
GHG	green house gases
ICE	internal combustion engine
MU	multiple unit
NRMM	non-road mobile machinery
SCR	selective catalytic reduction

Bibliography

[1] Abbasi S, Jansson A, Sellgren U, Olofsson U. Particle emissions from rail traffic: a literature review. Crit Rev Env Sci Tech. 2013;43:2511-2544. https://doi.org/10.1080/10643389.2012.685348

[2] Andrzejewski M, Daszkiewicz P, Urbański P, Rymaniak Ł, Woch A. Impact of a locomotive engine modernization on fuel consumption. MATEC Web Conf. 2021;338:01001. https://doi.org/10.1051/matecconf/202133801001

[3] Batko M. The concept of balanced maintenance cycle of a railway vehicle. Rail Vehicles/Pojazdy Szynowe. 2019;1:26-38. https://doi.org/10.53502/RAIL-138504

[4] Bielaczyc P, Woodburn J, Joshi A. World-wide trends in powertrain system development in light of emissions legislation, fuels, lubricants, and test methods. Combustion Engines. 2021;184:57-71. https://doi.org/10.19206/CE-134785

[5] Breuer MA, Burgard DA. Bridge-based remote sensing of NO_x emissions from locomotives. Atmos Environ. 2019; 198:77-82. https://doi.org/10.1016/j.atmosenv.2018.10.046

[6] Durzyński Z, Stawecki Ł. Current state and perspectives of non-electrified railway transport in Poland (part 1). Rail Vehicles/Pojazdy Szynowe. 2020;2:12-24. https://doi.org/10.53502/RAIL-138547

[7] Durzyński Z. Current state and perspectives of non-electrified railway transport in Poland (part 2). Rail Vehicles/Pojazdy Szynowe. 2020;2:12-25. https://doi.org/10.53502/RAIL-138558

[8] Durzyński Z. Hydrogen-powered drives of the rail vehicles (part 2). Rail Vehicles/Pojazdy Szynowe. 2021;3:1-11. https://doi.org/10.53502/RAIL-142694

[9] European Environment Agency. Transport and environment report 2021. Decarbonising road transport — the role of vehicles, fuels and transport demand 2022. https://www.eea.europa.eu/publications/transport-and-environment-report-2021 (accessed June 12, 2023).

[10] Far M, Gallas D, Urbański P, Woch A, Mieżowiec K. Modern combustion-electric PowerPack drive system design solutions for a hybrid two-unit rail vehicle. Combustion Engines. 2021;190(3):80-87. https://doi.org/10.19206/CE-144724

[11] GUS. Transport – activity results in 2021. StatGovPl n.d. https://stat.gov.pl/en/topics/transport-and-communications/transport/transport-activity-results-in-2021,6,17.html (accessed June 12, 2023).

[12] Herwartz S, Pagenkopf J, Streuling C. Sector coupling potential of wind-based hydrogen production and fuel cell train operation in regional rail transport in Berlin and Brandenburg. Int J Hydrogen Energ. 2021;46(57):29597-29615. https://doi.org/10.1016/j.ijhydene.2020.11.242

[13] Johnson GR, Jayaratne ER, Lau J, Thomas V, Juwono AM, Kitchen B et al. Remote measurement of diesel locomotive emission factors and particle size distributions. Atmos Environ 2013;81:148-157. https://doi.org/10.1016/j.atmosenv.2013.09.019

[14] Kalociński T. Modern trends in development of alternative powertrain systems for non-road machinery. Combustion Engines. 2022;188:42-54. https://doi.org/10.19206/CE-141358

[15] Kamińska M, Kołodziejek D, Szymlet N, Fuć P, Grzeszczyk R. Measurement of rail vehicles exhaust emissions. Combustion Engines. 2022;189(2):10-17. https://doi.org/10.19206/CE-142526
[16] Krasowsky T, Daher N, Sioutas C, Ban-Weiss G. Measurement of particulate matter emissions from in-use locomotives. Atmos Environ. 2015;113:187-196. https://doi.org/10.1016/j.atmosenv.2015.04.046
[17] Łasińska N. An agile methodology for managing rail transport projects. Rail Vehicles/Pojazdy Szynowe 2021;3: 12-19. https://doi.org/10.53502/RAIL-142230
[18] Ma J, Luo C, Qiu L, Liu X, Xu B, Shou J et al. Recent advances in traction drive technology for rail transit. J Zhejiang Univ-Sc A. 2023;24(3):177-188. https://doi.org/10.1631/jzus.A2200285
[19] Madovi O, Hoffrichter A, Little N, Foster SN, Isaac R. Feasibility of hydrogen fuel cell technology for railway intercity services: a case study for the Piedmont in North Carolina. Railway Engineering Science. 2021;29(3):258-270. https://doi.org/10.1007/s40534-021-00249-8
[20] Medwid M, Daszkiewicz P, Czerwiński J, Jakuszko W, Kazimierczak E. Rail-road tractor with diesel-electric drive. Rail Vehicles/Pojazdy Szynowe. 2019;2019:15-23. https://doi.org/10.53502/RAIL-138536
[21] Merkisz J, Rymaniak Ł, Lijewski P, Kamińska M, Kurc B. Tests of ecological indicators of two-way vehicles meeting Stage IIIB and Stage IV standards in real operating conditions. Rail Vehicles/Pojazdy Szynowe. 2020;1:1-9. https://doi.org/10.53502/RAIL-138495
[22] Michalak P, Jakuszko W. Innowacyjna uniwersalna lokomotywa dwunapędowa. Zeszyty Naukowo-Techniczne Stowarzyszenia Inżynierów i Techników Komunikacji w Krakowie Seria: Materiały Konferencyjne. 2019;2(119).
[23] Michalak P, Merkisz J, Stawecki W, Andrzejewski M, Daszkiewicz P. The selection of the engine unit – main engine generator during the modernization of the 19D/TEM2 locomotive. Combustion Engines. 2020;182:38-46. https://doi.org/10.19206/CE-2020-307
[24] Michalak P, Urbański P, Podziński M, Dobrowolski P. Possibility to use a dual-drive locomotive type 111DE for passenger transport in the territory of Poland. WJTE. 2023; 136:35-47. https://doi.org/10.5604/01.3001.0053.4038
[25] Office of Rail Transport UT. Sprawozdanie z funkcjonowania rynku transportu kolejowego 2021. Urząd Transportu Kolejowego 2022. https://utk.gov.pl/pl/dokumenty-i-formularze/opracowania-urzedu-tran/18979,Sprawozdanie-z-funkcjonowania-rynku-transportu-kolejowego-2021.html (accessed October 10, 2022).
[26] Oldknow K, Mulligan K, McTaggart-Cowan G. The trajectory of hybrid and hydrogen technologies in North American heavy haul operations. Railway Engineering Science. 2021; 29:233-247. https://doi.org/10.1007/s40534-021-00242-1
[27] Peng H, Chen Y, Chen Z, Li J, Deng K, Thul A et al. Co-optimization of total running time, timetables, driving strategies and energy management strategies for fuel cell hybrid trains. eTransportation. 2021;9:100130. https://doi.org/10.1016/j.etran.2021.100130
[28] Pielecha I, Engelmann D, Czerwinski J, Merkisz J. Use of hydrogen fuel in drive systems of rail vehicles. Rail Vehicles/Pojazdy Szynowe. 2022;1-2:10-19. https://doi.org/10.53502/RAIL-147725
[29] Pielecha I, Merkisz J, Andrzejewski M, Daszkiewicz P, Świechowicz R, Nowak M. Ultracapacitors and fuel cells in rail vehicle drive systems. Rail Vehicles/Pojazdy Szynowe. 2019;2:9-19. https://doi.org/10.53502/RAIL-138526
[30] Rymaniak Ł, Wisniewski S, Woźniak K, Frankowski M. Evaluation of pollutant emissions from a railbus in real operating conditions during transport work. Combustion Engines. 2023;194(3):84-88. https://doi.org/10.19206/CE-169138
[31] Sun Y, Anwar M, Hassan NMS, Spiryagin M, Cole C. A review of hydrogen technologies and engineering solutions for railway vehicle design and operations. Railway Engineering Science. 2021;29:212-232. https://doi.org/10.1007/s40534-021-00257-8
[32] Szwajca F, Berger AW, Spalletta R, Pielecha I. Characteristics of fuel cells under static and dynamic conditions. Rail Vehicles/Pojazdy Szynowe. 2022;3-4:44-52. https://doi.org/10.53502/RAIL-157516
[33] Szymanski P, Ciuffo B, Fontaras G, Martini G, Pekar F. The future of road transport in Europe. Environmental implications of automated, connected and low-carbon mobility. Combustion Engines. 2021;186(3):3-10. https://doi.org/10.19206/CE-141605
[34] Tomaszewski S, Medwid M, Andrzejewski M, Cierniewski M, Jakuszko W. New rail-road tractor with a combustion engine and an alternative electric drive. Combustion Engines. 2020;182(3):47-53. https://doi.org/10.19206/CE-2020-308
[35] Urbański P, Gallas D, Stachowicz A, Jakuszko W, Stobnicki P. Analysis of the selection of the auxiliary drive system for a special purpose hybrid rail vehicle. Rail Vehicles/Pojazdy Szynowe. 2022;1-2;30-39. https://doi.org/10.53502/RAIL-149405

Piotr Michalak, DEng. – Center of Rail Vehicles, Łukasiewicz Research Network – Poznan Institute of Technology, Poland.
e-mail: *piotr.michalak@pit.lukasiewicz.gov.pl*

Patryk Urbański., MEng. – Center of Rail Vehicles, Łukasiewicz Research Network – Poznan Institute of Technology, Poland.
e-mail: *patryk.urbanski@pit.lukasiewicz.gov.pl*

Wojciech Jakuszko, MEng. – Center of Rail Vehicles, Łukasiewicz Research Network – Poznan Institute of Technology, Poland.
e-mail: *wojciech.jakuszko@pit.lukasiewicz.gov.pl*

Dawid Gallas, DEng. – Center of Rail Vehicles, Łukasiewicz Research Network – Poznan Institute of Technology, Poland.
e-mail: *dawid.gallas@pit.lukasiewicz.gov.pl*

Paweł Stobnicki, DEng. – Center of Rail Vehicles, Łukasiewicz Research Network – Poznan Institute of Technology, Poland.
e-mail: *pawel.stobnicki@pit.lukasiewicz.gov.pl*

Piotr Tarnawski, MEng. – Center of Rail Vehicles, Łukasiewicz Research Network – Poznan Institute of Technology, Poland.
e-mail: *piotr.tarnawski@pit.lukasiewicz.gov.pl*

Article citation info:
Stoeck T. Diagnostic method for a piezoelectric injector using the Newton-Cotes formula. Combustion Engines. 2024;197(2):106-111. https://doi.org/10.19206/CE-177132

Tomasz STOECK

Combustion Engines
Polish Scientific Society of Combustion Engines

Diagnostic method for a piezoelectric injector using the Newton-Cotes formula

ARTICLE INFO

Received: 26 September 2023
Revised: 9 November 2023
Accepted: 16 December 2023
Available online: 27 December 2023

The article presents a method for regenerating common rail injectors, which involves extending the standard diagnostic procedure with a phase of analytical calculations. The closed-type Newton-Cotes formula (referred to as the trapezoidal rule) was employed to estimate the resulting fuel spray patterns and compare them with the manufacturer's reference. In the discussed example, it was demonstrated that the proposed solution is particularly useful in challenging situations where a definitive assessment of the injector's technical condition remains difficult. Several other advantages were also highlighted, making this method suitable for application in laboratory and workshop conditions.

Key words: *common rail system, piezoelectric fuel injector, Newton-Cotes formula, regeneration process*

1. Introduction

In recent years, there has been an increased demand for the regeneration of common rail fuel injectors, as this process allows for the restoration of factory performance parameters. Consequently, there is a need for precise and reliable monitoring of their technical condition, which is ensured by diagnostic tests on dedicated test benches. In the vast majority of cases, standard procedures are sufficient, primarily based on determining the fuel dosing at selected base points [8, 13, 21]. Unfortunately, problematic situations arise where improper injector operation is observed on the engine, despite meeting rigorous manufacturer criteria during testing. A solution can be extended diagnostics, involving the creation of a fuel delivery characteristic across the full range of working pressures and injection times (nozzle opening) [6, 9, 17]. It is essential to emphasize that this is a significantly more time-consuming process and is only available on advanced test benches, such as STPiW3 [12]. There is also the possibility of employing strictly scientific methods, the use of which is not always feasible in typical workshop conditions [3, 14, 18].

The above reasons led to the proposal of a technique based on the closed Newton-Cotes formula. It is widely known for numerical integration and is used to determine the surface area bounded by a function's graph [4, 25]. However, the mathematical algorithm itself can be easily implemented in the environment of any spreadsheet, allowing for quick calculations, verification of their accuracy, and ultimately the assessment of the technical condition of the injector based on the results of the standard test procedure. Such an approach is practical, as it does not increase the number of measurements in the experimental phase. As a result, costs and labor remain unchanged. As an example, a piezoelectric injector was chosen for which repair technology has been made available, along with a complete set of spare parts (excluding the crystal stack).

2. Methods

2.1. Test beds

The research was conducted on a test bench equipped with a Bosch EPS 205-type table (Fig. 1).

Fig. 1. View of the Bosch EPS 205 test bench

This is a versatile diagnostic device with a single measurement tower, allowing for automatic testing, coding, and internal cleaning of injectors. The results are compared with the manufacturer's database, which is accessible from the control screen and subsequently saved and printed as a final report. The functionality of the tester has been significantly enhanced compared to previous versions (EPS 200/200A), as the manufacturer has installed sets (attachments, adapters, connectors) and software adapted for testing piezoelectric injectors. Due to its compact size and affordable price, the device is very popular in the service market.

During the regeneration process, additional equipment and specialized tools are also used, with the most important ones being:
– Yizhan 13MP HDMI VGA industrial camera
– Bene YesWeCan 3L ultrasonic cleaner

– Facom E.316A200S torque wrench
– clamps, holders, and workshop tools
– PC-class computer.

2.2. Test object

The research was conducted on a piezoelectric injector from Bosch, which was removed from the N47 D20 engine of a BMW X3 vehicle with a mileage of 268,000 kilometers.

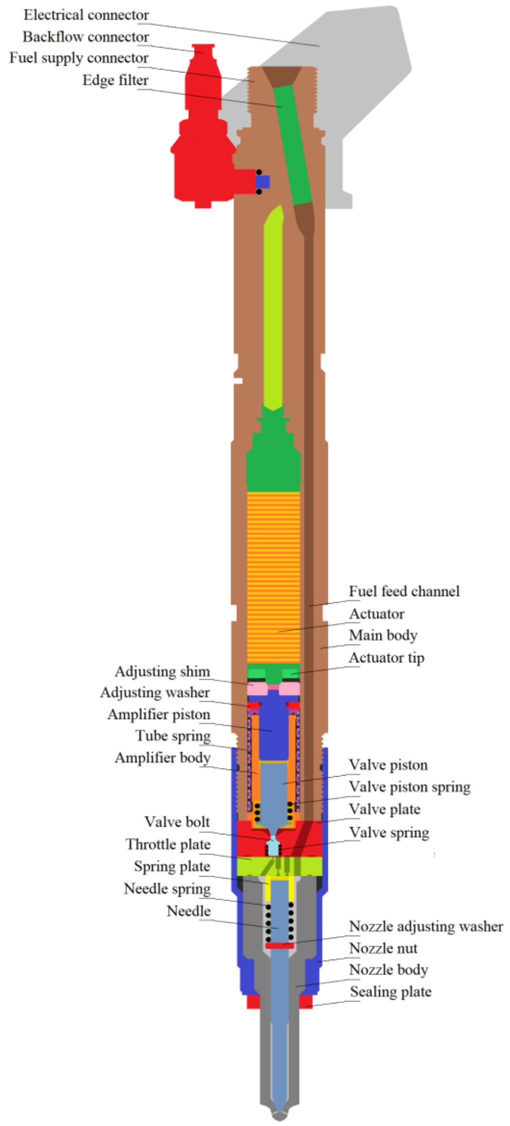

Fig. 2. Structure of the Bosch CRI3-18 injector: a proprietary development based on [16, 19]

Injectors of this type are classified as third-generation systems, operating at maximum pressures up to 180 MPa [15]. Figure 2 illustrates the internal structure, detailing the components of the hydraulic amplifier group, control valve, and nozzle. A characteristic feature is the absence of a lateral fuel supply channel in the nozzle, resulting in the central delivery of fuel in the spaces around the needle. Consequently, this component has a triangular cross-section in the guiding part, which is essentially unique among other manufacturers. The sealing of the tip is achieved solely through the valve assembly [11].

2.3. Research plan

Table 1 presents the research plan, which in the experimental and operational part closely aligned with the manufacturer's procedure [23]. The exception was the additional phase of analytical calculations conducted in a spreadsheet on a workstation with a computer. Typically, it is also used for visualization and recording of images generated from a microscopic industrial camera [24].

Table 1. Research plan with division into stages and workstations

Workplace	Stage I	Stage II
Bosch EPS 205 test bench	Electrical test	Main flow tests
	Leak test	
	Internal cleaning	Injector coding
	Preliminary flow tests	
Tool station (Fig. 3)	Disassembly into parts	Final acceptance
	Ultrasonic washing	
	Part drying	
	Microscopic examination	
	Parts exchange	
	Assembly	
Computer station	Calculation phase	

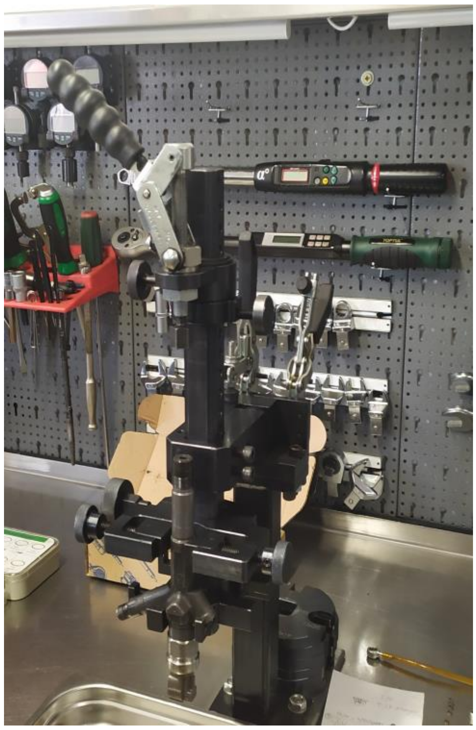

Fig. 3. General view of the tool station

It should be noted that the scope of service-diagnostic activities may change depending on the type of identified malfunctions or the initial condition of the injector. For example, in the case of severe coking of the nozzle (sprayer), the manufacturer recommends performing preliminary cleaning with an ultrasonic cleaner. This process requires placing the injector vertically in the device's basket, eliminating the possibility of damaging its electrical components. Its purpose is to ensure the openness of the outlet holes before conducting a flow test on the test bench.

2.4. Newton-Cotes formula

In the Cartesian coordinate system, points corresponding to the fuel doses of the reference injector were located.

By connecting them, a non-rectangular quadrilateral with vertices 1-2-3-4 was obtained (Fig. 4). Subsequently, trapezoids were extracted, and their surface areas were calculated using the closed Newton-Cotes formula [2]:

$$A_T = (t_{i+1} - t_i)\frac{d_i + d_{i+1}}{2} \tag{1}$$

To simplify the calculations, formula (1) was replicated in spreadsheet cells. The total area of the shape was determined using the relationship [7]:

$$A_{1-2-3-4} = A_{T1} + A_{T2} + A_{T3} - A_{T4} \tag{2}$$

This way, a reference base (a benchmark) for the results was established, which was estimated based on the preliminary and main tests of the regenerated injector.

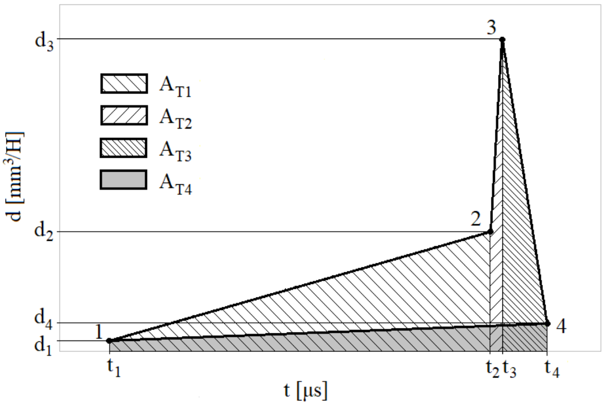

Fig. 4. Graphical interpretation of the trapezoidal method for the discussed example

The Newton-Cotes formula has not been applied in the diagnosis of common rail fuel injectors so far, hence the presented calculations are not reflected in the literature on the subject. However, the presented example indicates that it can be effectively applied in scientific and engineering practice. To automate the computational process, a spreadsheet was used, enabling rapid results at each stage of the conducted operations.

3. Analysis results and discussion

3.1. Preliminary tests

According to the standard procedure, the injector was mounted on the test bench, where it underwent internal cleaning, a leakage test, and testing of basic electrical parameters. In the latter case, crystal stack failure was ruled out, as values consistent with the manufacturer's specifications were obtained, i.e., capacitance C = 2.3 µF (1.5–3.3 µF) and resistance R = 186 kΩ (150–210 kΩ). There was also no evidence of insulation damage between the actuator and the main body ($R_I = \infty$). Similar conclusions were drawn after preliminary flow tests (IVM), as all fuel doses fell within the specified ranges (Table 2). Unfortunately, during the final acceptance on the vehicle's dashboard, the warning light would illuminate, and the engine would enter what is known as 'limp mode'. As a result, the injector was disassembled once again, and the proposed calculation method was implemented.

Table 2. Results of preliminary IVM flow tests

Test name	Point	p_{inj} [MPa]	t_i [µs]	d_i [mm³/H]
Pre-injection	1`	80	190	[1.5 ±1.2] 1.3
Emission point	2`	80	490	[18.9 ±3.6] 15.4
Maximum load	3`	180	500	[49.3 ±5.0] 44.4
Idle	4`	30	535	[4.3 ±2.2] 4.1

3.2. Calculation stage

From the data presented in Tables 3 and 4, it can be observed that the injection process disturbance caused a displacement of the quadrilateral 1`-2`-3`-4`. Although the fuel doses met the requirements of the test procedure, their values were significantly underestimated compared to the reference. This was especially true for points 2` and 3`, which corresponded to engine operating conditions at half and full load. As a result, the surface area for the tested injector was 18.5% smaller (Fig. 5). The cause should be attributed to the improper functioning of the valve group, which should be replaced after disassembly. A similar decision was made regarding the precision pair (nozzle, needle). In this regard, the decisive factor was the relatively high mileage of the vehicle rather than the nature of any dysfunction.

Table 3. Results of surface area calculations for the reference figure

Point	t_i	d_i	A_{T1}	A_{T2}	A_{T3}	A_{T4}
1	190	1.5	3060			
2	490	18.9		341		
3	500	49.3			938	
4	535	4.3				1000.5
1	190	1.5				
$A_{1-2-3-4}$						
3338.5						

Table 4. Results of surface area calculations for the figure 1`-2`-3`-4`

Point	t_i	d_i	$A_{T1`}$	$A_{T2`}$	$A_{T3`}$	$A_{T4`}$
1`	190	1.3	2505			
2`	490	15.4		299		
3`	500	44.4			848.8	
4`	535	4.1				931.5
1`	190	1.3				
$A_{1`-2`-3`-4`}$						
2721.3						

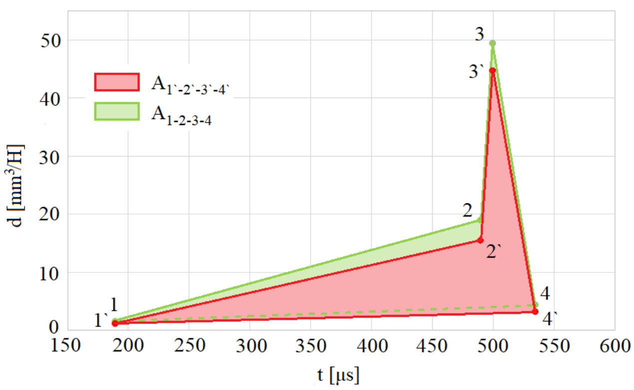

Fig. 5. Graphical interpretation of the results of preliminary tests

3.3. Microscopic examination and injector assembly

The microscopic examination was preceded by disassembling the injector into its components and cleaning them with an ultrasonic cleaner.

During the inspection under high magnification, corrosion was observed on most components that had direct contact with fuel, such as the needle, valve plate, throttle, and the hydraulic amplifier body (Fig. 6). This process had an adverse effect on the dynamics of individual assemblies, and the resulting contaminants further polluted the interior of the injector, leading to accelerated wear of interacting surfaces. It should be noted that corrosion intensification is a commonly encountered phenomenon in injectors operating at such high working pressures. This occurs despite the structural and material modifications employed by manufacturers [1, 5, 10].

Fig. 6. Observation of corrosion on the hydraulic amplifier body

Consequently, it was decided that restoring full functionality would only be possible by replacing all executive and control groups, except the piezoelectric actuator.

During the injector assembly process, it is essential to purge the hydraulic amplifier by assembling its components in diesel oil and then compressing them using a specially dedicated press. This step is of fundamental importance for ensuring accurate fuel delivery during primary investigations, as it eliminates the possibility of result distortion, namely, zero doses. Subsequently, the nozzle assembly (nozzle, needle, spring, washer) is assembled and securely fastened to the main body using a nut. Throughout this operational procedure, strict adherence to the manufacturer's guidelines is crucial, utilizing a torque wrench for this purpose (Fig. 7).

Fig. 7. Tightening the nut with a torque wrench

3.4. Main tests

In Table 5, the results of the main flow tests are presented, while Table 6 compiles the results of calculations conducted after the regeneration process.

Table 5. Results of main IVM flow tests

Test name	Point	p_{inj} [MPa]	t_i [μs]	d_i [mm^3/H]
Pre-injection	1`	80	190	[1.5 ±1.2] 1.5
Emission point	2`	80	490	[18.9 ±3.6] 18.5
Maximum load	3`	180	500	[49.3 ±5.0] 48.6
Idle	4`	30	535	[4.3 ±2.2] 4.4

Table 6. Results of surface area calculations for figures 1``-2``-3``-4``

Point	t_i	d_i	$A_{T1``}$	$A_{T2``}$	$A_{T3``}$	$A_{T4``}$
1``	190	1.5	3000			
2``	490	18.5		335.5		
3``	500	48.6			925.9	
4``	535	4.4				1017.8
1``	190	1.5				
$A_{1``-2``-3``-4``}$						
3245.3						

It can be observed that the replacement of key components yielded favorable results. There was an increase in the values of all fuel doses compared to the preliminary tests. As a result, the surface area of the quadrilateral 1``-2``-3``-4`` almost completely overlapped with the reference, with a difference of only 2.8% (Fig. 8). This suggests that the factory settings of the tested injector have been restored. Of course, new codes were assigned before installation in the engine. This process was carried out automatically on the same test bench where fuel dosing measurements were taken.

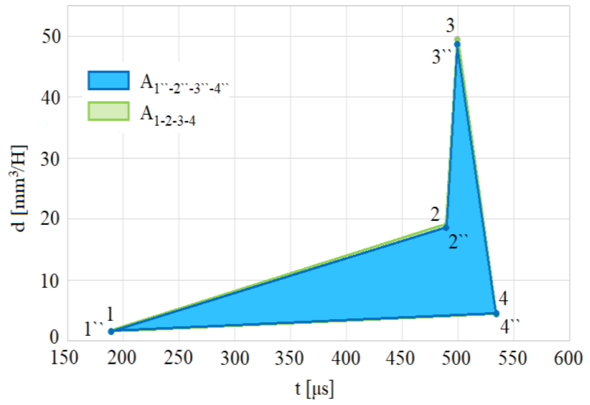

Fig. 8. Graphical interpretation of the results of the main tests

3.5. Validation of calculations

In authorial publications [20, 22], Gauss formulas were employed for the computation of surface areas of polynomials localized in Cartesian coordinate systems. In the context of the considered case, these formulas can be expressed in the following form:

$$A_T = \frac{1}{2}\left|\sum_{i=1}^{n} t_i(d_{i+1} - d_{i-1})\right| \tag{3}$$

and

$$A_T = \frac{1}{2}\left|\sum_{i=1}^{n} d_i(t_{i+1} - t_{i-1})\right| \tag{4}$$

The results presented in Table 7 unequivocally indicate that the formulas (3) and (4) can be successfully applied to verify the accuracy of calculations conducted using the Newton-Cotes method. Their implementation in a spreadsheet environment proceeds in a similar manner and does not pose significant difficulties. Simultaneously, the formulas introduced into the appropriate cells of the program can be reused in their unchanged form, providing the user with a ready computational tool for future research.

Table 7. Example of alternative calculations for figure 1``-2``-3``-4``

Point	t_i	d_i	$t_{i+1} - t_{i-1}$	$d_{i+1} - d_{i-1}$
1	190	1.5	–45	14.1
2	490	18.5	310	47.1
3	500	48.6	45	–14.1
4	535	4.4	–310	–47.1
1	190	1.5	Σ = 0	Σ = 0
$A_{1``-2``-3``-4``}$				
3245.3 = ½|(–45·1.5) + (310·18.5) + (45·48.6) + (–310·4.4)|				
3245.3 = ½|(14.1·190) + (47.1·490) + (–14.1·500) + (–47.1·535)|				

4. Conclusions

The proposed method enables the application of extended diagnostics for common rail injectors that operate incorrectly despite meeting the criteria specified by the manufacturer. Among its most significant advantages are:

1. The use of the standard procedure's baseline points does not require additional measurements in the experimental phase. This eliminates the need to create a complete fuel dosing characteristic, which is only available on selected test benches.
2. There is no need to modify the software used by the tester.
3. Transferring the analytical process to a spreadsheet environment does not increase the regeneration costs. The formulas can be successfully applied in the examination of injectors of various types or generations (including electromagnetic solutions).
4. The position of the vertices of the analyzed figures indicates possible causes of malfunction. However, in laboratory workshop conditions, there is no need for a graphical interpretation of the results. Therefore, the drawings presented in this article are purely illustrative.
5. The accuracy of the conducted calculations can be easily verified using alternative mathematical methods, such as Gauss's formulas. Since these studies were conducted on injectors from different manufacturers and on distinct test benches, the presented conclusions and observations have a more general nature. Simultaneously, the choice of computational technique has no impact on the final results and depends on individual preferences.

It should be emphasized that the resulting dosage areas presented in the form of polygons in the Cartesian coordinate system should be treated purely hypothetically. This is because they do not accurately reflect the actual fuel injection method at intermediate points, i.e., beyond the vertices of the generated figures. Nevertheless, the proposed method allows for the assessment of the technical condition of common rail injectors in problematic situations, as demonstrated in a specific example. In this way, it constitutes an effective solution that has been addressing the needs reported by service companies for years.

Acknowledgments

The research was conducted at the service company AUTO NEXT SERWIS, located in Szczecin, which provided a complete set of measurement equipment and specialized tools necessary for the injector regeneration process.

Nomenclature

A_T	surface area of the component trapezoid
A	surface area of the quadrilateral (indices):
	1-2-3-4 – reference
	1`-2`-3`-4` – in preliminary tests
	1``-2``-3``-4`` – in main tests
d_i	injection dosage
C	piezo actuator capacitance
CRI	common rail injectors
IVM	injector volume metering
p_{inj}	injection pressure
R	piezo actuator resistance
R_I	piezo actuator insulation resistance
t_i	nozzle opening time

Bibliography

[1] Abramek KF, Stoeck T, Osipowicz T. Statistical evaluation of the corrosive wearof fuel injector elements used in common rail systems. Stroj vestn–J Mech E. 2015;61(2):91-98. https://doi.org/10.5545/sv-jme.2014.1687

[2] Billo EJ. Excel® for scientists and engineers. Numerical methods. 1st ed. New Jersey: John Wiley&Sons. Inc. 2007.

[3] Busz W, Walaszyk A. Optimize the testing process common rail fuel injectors. Combustion Engines. 2015;162(3):978-981.

[4] Cheney W, Kincaid D. Numerical mathematics and computing. 7th ed. Pacific Grove: Books/Cole Publishing Company 2012.

[5] Chomik Z, Łagowski P. The analysis of mechanical damage of common rail injectors. Journal of Research and Applications in Agricultural Engineering. 2019;64(1):13-20.

[6] d'Ambrosio S, Ferrari A. Diesel engines equipped with piezoelectric and solenoid injectors: hydraulic performance of the injectors and comparison of the emissions, noise and fuel consumption. Appl Energ. 2018;211:1324-1342. https://doi.org/10.1016/j.apenergy.2017.11.065

[7] Hoffman JD. Numerical methods for engineers and scientists. 2nd ed. New York–Basel: Marcel Dekker Inc. 2001.

[8] Idzior M, Borowczyk T, Karpiuk W, Stobnicki P. The feasibility research of a technical condition of modern injectors for compression ignition engines. Logistics. 2011;3:933-942.

[9] Jocanović MT, Karanović VV, Knežević DM, Orošnjak MD. Diesel fuel filtration problems with modern common rail injection systems. Vojnotehnički glasnik. 2017;65(4):968-993. https://doi.org/10.5937/vojtehg65-11577

[10] Juściński S, Piekarski W, Chomik Z. Analysis of injection systems types used in agricultural machines. Agr Eng. 2017;21(4):37-46. https://doi.org/10.1515/agriceng-2017-0034

[11] Kaczorowski M, Pilewski Z. Piezoelectric injectors – pioneers of high pressures up to 2500 bar. Bosch Autospec. 2017;65(3):7-10.

[12] Karpiuk W, Bor W, Smolec R. Possibilities of analysis of condition and repair of common-rail system injectors. Journal of KONES Powertrain and Transport. 2018;23(4):209-216. https://doi.org/10.5604/12314005.1217208

[13] Kneba Z, Straszak P, Jakóbczyk K. The effectiveness of fault detection in common rail injectors examination methods. Combustion Engines. 2017;170(3):49-56. https://doi.org/10.19206/CE-2017-308

[14] Knefel T. Technical assessment of Common Rail injectors on the ground of overflow bench tests. Eksploat Niezawodn. 2012;14(1):42-53.

[15] Konieczny Ł, Adamczyk B, Adamczyk G. Diagnostics and regeneration of common rail injectors. Scientific Journal of Silesian University of Technology. 2015;86:65-73.

[16] Liu Z, Liu N, Liu J. Study of the influencing factors on the small-quantity fuel injection of piezoelectric injector. Micromachines-Basel. 2022;13(813):1-20. https://doi.org/10.3390/mi13050813

[17] Osipowicz T, Abramek KF. Diagnosing methods common rail fuel injectors. Combustion Engines. 2017;168(1):56-61. https://doi.org/10.19206/CE-2017-109

[18] Osipowicz T, Abramek KF, Mozga Ł. Comparing polynomials and neural network to modelling injection dosages in modern CI engines. Appl Sci-Basel. 2022;12(4):1-17. https://doi.org/10.3390/app12042246

[19] Salvador FJ, Plazas AH, Gimeno J, Carreres M. Complete modelling of a piezo actuator last generation injector for diesel injection systems. Int J Engine Res. 2012;15(1),3-19. https://doi.org/10.1177/1468087412455373

[20] Stoeck T. Analytical methodology for testing common rail fuel injectors in problematic cases. Diagnostyka. 2021;22(3):47-52. https://doi.org/10.29354/diag/135999

[21] Stoeck T. Method for testing modern common rail piezoelectric fuel injectors. Combustion Engines. 2021;186(3):31-36. https://doi.org/10.19206/CE-140246

[22] Stoeck T. Methodology of testing common rail fuel injectors with the use of Gauss's formulas. Combustion Engines. 2021;184(1):11-15. https://doi.org/10.19206/CE-133505

[23] Stoeck T. Problems of regeneration of modern piezoelectric fuel injectors. Combustion Engines. 2022;191(4):3-8. https://doi.org/10.19206/CE-146700

[24] Stoeck T. Repair methodology of a piezoelectric injector utilizing components obtained from selective decomposition. Combustion Engines. 2023;194(3):63-67. https://doi.org/10.19206/CE-167428

[25] Turner PR, Arildsen T, Kavanagh K. Applied scientific computing with Python. Cham: Springer International Publishing AG 2018. https://doi.org/10.1007/978-3-319-89575-8

Tomasz Stoeck, DEng. – Faculty of Mechanical Engineering and Mechatronics, West Pomeranian University of Technology in Szczecin, Poland.

e-mail: *tstoeck@wp.pl*

Article citation info:
Dziubak T. Experimental study of materials for the filtration of the intake air of the internal combustion engine of a motor vehicle. Combustion Engines. 2024;197(2):112-125. https://doi.org/10.19206/CE-178374

Tadeusz DZIUBAK

Combustion Engines
Polish Scientific Society of Combustion Engines

Experimental study of materials for the filtration of the intake air of the internal combustion engine of a motor vehicle

ARTICLE INFO

Received: 4 December 2023
Revised: 27 December 2023
Accepted: 7 January 2024
Available online: 14 February 2024

Fiber composite materials show more favorable filtration properties in terms of filtration efficiency and accuracy, as well as dust absorption. Experimental tests of standard filtration materials based on cellulose, polyester, glass microfiber, cotton and polyester nonwoven fabrics were performed using an original method. Two composite beds consisting of three layers of standard materials were designed using a novel method: K1 (polyester-glass-microfiber-cellulose) and K2 (cellulose-glass-microfiber-cellulose), and determined their effectiveness, the size of dust grains in the cleaned air and the unit dust absorption. It was shown that the K1 composite has high (d_{pmax} = 1.5–3 μm) filtration accuracy, high initial filtration efficiency (99.8%), which shortens the preliminary stage, and extends to 96–98% the duration of the main stage of the filtration process. The K1 composite achieved more than twice the dust mass loading value (k_{dK1} = 148.9 g/m^2), compared to other standard materials. These are parameters that are essential for filter design in automotive technology and can only be obtained through empirical testing. Knowing them will make it possible to make an air filter design with smaller dimensions or to extend vehicle mileage.

Key words: *engine, air filtration, fiber filtration materials, composite materials, air filter characteristics, vehicle mileage*

1. Introduction

Along with the air sucked in by the internal combustion engines of motor vehicles, significant amounts of pollutants are sucked in, which accumulate on the road surface and are carried into the atmosphere as a result of vehicle traffic or wind gusts. The composition of road pollutants is wide and varied. The primary component is mineral dust carried by the wind from the nearby environment, where it was generated by field, road, or construction work. It is also dust that has been carried by the wind from large sandy and desert areas, as well as volcanic ash fallout. Industrial production, the operation of open-pit mines is the cause of emissions of a very large amount of dust [50]. The main components of mineral dust are silica (SiO_2), the mass proportion of which in the dust is in the range of 65–97%, and alumina Al_2O_3, the mass content of which in the dust is 5–18%. Other components are oxides of various metals: F_2O_3, CaO, MgO and organic components [39].

Another component of road dust is plant and tree inflorescence elements, pollen, insect fragments, animal dander and other biological materials [2, 24]. Significant amounts of dust are emitted into the atmosphere during the work of harvesting crops and other crops [20]. The use of motor vehicles is mainly "non-motor" pollutants, i.e. those generated by the abrasion process in friction pairs: brake disc-friction lining, clutch disc-pressure plate [41, 43], as well as by the abrasion of the tire tread against the road surface [19, 22, 36, 47]. The engine's exhaust system is mainly a source of soot, which is a product of incomplete combustion of fuel, as well as products of abrasive wear of the engine's metal surfaces, which form the piston-ring-cylinder or journal-pan associations. During the operation of vehicles in winter conditions, salt and sand, products used for de-icing roads, may be present on the road surface. The accumulation of dirt on the road surface, which is lifted to a considerable height by vehicles or wind, is called road dust in the literature [9, 13, 14].

Passenger car engines operating at rated conditions draw in an air flow of 180–500 kg/h from the environment, depending on the engine's displacement and its speed. Truck engines require 1100–1600 kg/h of air for operation, and vehicle engines require more than 7500 kg/h of ambient air.

In the inlet air stream of an internal combustion engine, there can be significant amounts of impurities, mainly mineral dust, which is the primary component of dust. The presence of hard SiO_2 and Al_2O_3 grains, which are characterized by a hardness of 7 and 9, respectively, on the ten-degree Mohs scale [40], is the main cause of wear of mating parts: piston sealing and scraping rings and cylinder liners, crankshaft and camshaft plain bearings, valve stems and their guides.

The available literature shows that abrasive wear on the surfaces of engine components and, as a result, a reduction in engine performance, durability and reliability is caused largely by the improper quality of air supplied to engine cylinders [1, 30, 45]. Abrasive wear of engine components is determined by the hardness, but also by the size of dust particles, their irregular shape, and sharp edges. It is accepted in the literature that dust particles with sizes in the range of 1–40 μm are the primary cause of wear on the two moving surfaces, but dust grains having a size of 5–20 μm are the most aggressive [4, 6, 7]. The prevailing view is that dust grains between two mating engine components whose diameter d_p is equal to the thickness of the oil film h_{min} at any given time are the cause of wear.

The mass of dust that is in the engine intake air stream depends on the dust concentration in the air, which can take on varying values depending on the conditions of vehicle use. The lowest values of dust concentration in the air (from 0.00045 g/m^3 to 0.1 g/m^3) are found on highways [3], the highest (within 0.001–10 g/m^3) when vehicles are used on sandy roads [16]. During tracked vehicle traffic in desert conditions, dust concentrations in the air reach values of up to about 20 g/m^3 [4, 10, 38].

Not all dust grains that enter the engine cylinders with the air have a destructive effect on engine durability. It is estimated that about 10–20% of the dust that penetrates the engine is retained on the oil-wetted walls of the cylinder liner and comes into contact with the surface of the piston and piston rings, causing their abrasive wear. About 30% of the contaminants that enter the engine can escape with the exhaust in the same form into the exhaust system. Mineral dust grains, whose melting points are much lower than the peak temperature (about 2500°C) in the cylinder during fuel combustion, melt, after which they can enter with the exhaust gas into the exhaust system in the form of droplets and deposit on the walls of the catalytic layer. This creates an additional layer that impedes its operation [5].

Dust grains that enter with the air can retain and deposit on the measuring element (wire or layer thermo anemometer) of the airflow meter, forming an insulating layer that impedes heat dissipation from the measuring element. Deposition is facilitated by moisture and oil mist from the crankcase venting system, which penetrates the measuring element of the flow meter as a result of backflows in the intake system. Isolation of the measuring element, which is incompletely cooled by the flowing air stream, causes: underestimation of the voltage signal U_w of the air flow meter, so that the controller dispenses a lower mass of fuel to create the fuel-air mixture, resulting in lower engine torque and power values. In addition, hard sharp-edged dust grains (SiO_2, Al_2O_3) moving at high speed hit the stationary measuring element (heater wire) causing scratches on its surface, resulting in its weakening or even complete destruction.

Wear and tear on the components of the piston-piston-ring-cylinder association results in an increase in clearance, which is the cause of increased charge blow-off into the crankcase during the compression stroke. The loss of working medium mass from the cylinders caused by this phenomenon results in a decrease in pressure at the end of the compression stroke, resulting in a decrease in engine torque and power and an increase in exhaust emissions [21, 33, 48, 51]. Excessive clearances in the P-PR-C linkage increase the flow of hot exhaust gases through the labyrinth ring spaces into the crankcase. This phenomenon increases the temperature of the lubricating oil and decreases its viscosity, which can lead to excessive wear and seizure of the engine. Exhaust fumes in the crankcase contaminate the oil with soot, increase its temperature and viscosity. This can negatively affect engine life and vehicle reliability [34].

Modern passenger car engines, because that they are used mostly on paved roads with low dust concentrations in the air, are equipped with single-stage filters with a pleated paper insert. In trucks and special vehicles, since their use is mostly on paved roads with a high concentration of dust in the air, it is necessary to use two-stage filters. This is an assembly: an inert filter and a cylindrical filter element arranged in series behind it, shaped from pleated paper or a composite of filter materials, such as: polyester, microglass and cellulose [37].

The placement of an air filter in the engine intake system is a necessity. However, there are negative effects of its presence in the form of a pressure drop, which leads to additional energy losses in the form of reduced torque and a drop in engine power [31, 42]. In addition, in passenger cars, due to the small space around the engine, there are difficulties in placing a filter with a sufficiently large area of filter material. Therefore, it is expedient to use materials with high surface absorption, low flow resistance and high efficiency and accuracy of dust particle filtration. Such possibilities are provided by fibrous composite filter materials, the filtration properties of which will be analyzed in this study.

2. Properties of composite filter beds

Cellulose-based fiber filter media are widely used in the air filtration systems of modern vehicle and machine drive engines and for indoor air filtration [25, 35]. Cellulose filter media, whose structure is formed by fibers with diameters of 10–20 µm, are characterized by high durability compared to some other filter materials. However, their filtration efficiency and accuracy are not always satisfactory, especially during the first (initial) period of filtration, which is characterized by the fact that at the start of the filtration process there is a low-efficiency φ_f and filtration accuracy d_{pmax}, as well as low flow resistance Δp_f [12]. However, as the filtration process proceeds, the mass of dust retained on the filter bed increases. There is an increase in filtration efficiency φ_f, filtration accuracy d_{pmax} and flow resistance Δp_f. According to the research presented in the paper [12], the initial efficiency of the bed made of cellulose is $\varphi_{f0} = 96.3\%$. The criterion for completing the initial filtration period was that the bed achieved a filtration efficiency of $\varphi_f = 99.5\%$. This condition was obtained at a mass loading of dust of $k_d = 110.7$ g/m^2. This is half of the total operating time of the cartridge. During this time, there were maximum dust grains of $d_{pmax} = 10–28$ µm in the air behind the tested cartridge. Under the conditions of actual engine operation, these are the grains that cause the most wear on mating components.

Engine inlet air filter materials are required to have a filtration efficiency of more than 99.5% and a particle filtration accuracy of more than 5 µm over the entire operating range and long service intervals. Because cellulosic filter materials have difficulty meeting these requirements they are modified in various ways.

Improvements in filtration efficiency and accuracy in fiber beds are provided by the use of polymeric nanofibers, i.e. fibers less than 1 µm in diameter. A thin layer of nanofibers (1–5 µm) has low strength, so it is applied over a substrate of filter materials that have greater thickness and strength, for example, cellulose, polyester or microfiber glass. An additional layer applied over standard filter materials significantly improves the efficiency and accuracy of inlet air filtration of motor vehicle engines. A great deal of research has been carried out in this area and a considerable number of studies have been written [8, 15, 17, 18, 26–28, 44, 49]. For example, the paper [8] presents the design of a new bed with a micro/nano-layered structure, and then investigates its application in air filters. The outer layer of the composite bed is a polyester microfiber (PS) layer that has a high electrical resistance. The inner layer is polyacrylonitrile (PAN) nanofibers characterized by high polarization and small pore size. The PS/PAN/PS composite bed was examined and found to have a high filtration efficiency of 99.96% and a low pressure drop of 54 Pa for 0.30 μm particles and at a filtration velocity of 0.053 m/s, as expressed by a quality factor of $q_c = 0.145\ Pa^{-1}$.

The authors of the paper [15] presented the results of testing the filtration properties of four samples made of different materials. It was shown that the filtration efficiency of the material without a layer of nanofibers for dust particles smaller than 2 μm is very low and does not exceed 10%. It was found that a nanofiber layer (even a small one) applied to a conventional filter bed increases the filtration efficiency, the more the thickness of the layer increases. For example, for a nanofiber layer with a surface thickness of $g_m = 0.02\ g/m^2$, a filtration efficiency of more than 60% was obtained for particles smaller than 2 μm. It was shown that the parameters of the filtration process: efficiency and accuracy, as well as the flow resistance of materials with an additional nanofiber layer depend on the type of substrate and the thickness of the nanofiber layer.

Similar test results with a nanofiber layer applied to a standard substrate were presented in the work [17]. A layer of nanofibers with a diameter in the range of 40–800 nm and a bed thickness of 0.3 mm and $g_m = 0.1\ g/m^2$ was applied to a cellulose-based filter medium. The bed made in this way achieved a filtration efficiency of φ_f = 64–99%, with a filtration velocity of $\upsilon_F = 0.03$ m/s and for dust grains in the range of d_p = 0.2–4.5 μm. Increasing the filtration speed seven times to $\upsilon_F = 0.2$ m/s resulted in a slight decrease in filtration efficiency.

The authors of the paper [18] applied a PTFE polytetrafluoroethylene membrane to a standard filter bed. The efficiency of the filter bed made in this way was determined, using nano-$CaCO_3$ powder as a test dust. The efficiency of the bed reached a value significantly higher (more than 99.99% for micron particles) compared to the standard filter material.

The paper [27] studied the effect of nanofiber content of 5%, 10%, 15%, and 20% on the filtration parameters of the cellulose bed. The proportion of 10% nanofibers in the filter bed causes a threefold increase in the flow resistance and filtration efficiency of dust grains with a size of 0.8 μm. Regardless of the content of nanofibers in the bed, an increase in the size of dust grains within 0.03–0.2 μm causes a decrease in filtration efficiency, and within 0.2–2 μm its increase follows. With an increase in the compactness of nanofibers in the bed, the curve of filtration efficiency is shifted almost parallel towards larger values. The particle size at which the filtration efficiency obtained the lowest values (MPPS) on the efficiency curve was around 200 nm for all cases studied.

In [28], a submicrofiber filter medium designed to ensure the purity of engine intake air was made and tested. The filter composite was made by wet bonding two filter layers. The filtration efficiency of the composite so made was 48% and 10% higher than that of the standard bed and the submicrofiber bed, respectively. Field tests of dust loading showed a 45% lower increase in the flow resistance of the submicrofiber bed than that of the standard bed, which was operated in a motor vehicle filter for 10,000 km.

The purpose of the study presented in [26] was to determine the effect of pore size and fiber diameter in a fiber bed and on filtration performance. One polyester bed was subjected to the study of depth filtration phenomena, and surface filtration phenomena were studied on two polyester beds covered with a polytetrafluoroethylene membrane. It was confirmed that the smaller the pore size in the bed, the higher the filtration efficiency and the higher the flow resistance.

The paper [44] presents a study of a two-stage filter constructed of two filter beds (pre-material and main material) placed at a short distance from each other. A synthetic (polypropylene) pleated filter material with low filtration efficiency and accuracy was used as the pre-filter, which was determined by large diameter fibers and high air permeability – 3100 $l/(m^2/s)$. The task of the pre-filter was to remove large dust grains. For the second filtration stage (main material), a PTFE membrane filter material applied to a cellulose substrate was used. Unlike the pre-filter, the main filter is structured with nano-sized fibers and has low permeability. The purpose of the main filter is to remove small-sized particles. This structure of the two-stage filter made it possible to significantly reduce the intensity of the increase in the flow resistance of the main filter, which increased in the correct operating time of the entire filter set, the criterion of which was the achievement of the established permissible value of flow resistance. These findings are consistent with the results of research presented in the work [10].

The authors of the paper [49] performed tests that determined the possibility of separating particulate matter from air using three tubular PTFE membrane filters that varied in diameter and length. The tests were carried out at filtration velocities in the wide range of 0.003–0.15 m/s and with particles of 10–300 nm. Efficiency curves for PTFE membranes showed a typical "V" shape for the particles used and at fixed filtration speeds. Membranes with smaller pore diameters and at flow rates with higher filtration velocities had the lowest MPPS point. It was found that two layers of membranes achieved the lowest pressure drops. Very high filtration efficiency was obtained at 99.98% for 0.3 μm particles and almost 100% efficiency for 2.5 μm particles.

From the above analysis it follows:

- fibrous filter beds of a layered nature show higher filtration efficiency, accuracy and mass dust loading than single layers of which a multilayer bed is made
- multilayer beds, the results of which are available in the literature, cannot be used for engine intake air filtration due to specific operating conditions, including dust concentration in the air and dust particle size. It is necessary to test filter beds that take these conditions into account
- manufacturers of filter materials for motor vehicle air filters provide for the filter manufacturer mainly their structure data such as bed thickness, pore size, grammage, air permeability. Data on filtration efficiency and accuracy, flow resistance and mass loading of dust are

not encountered. Filtration parameters can be determined, but only during experimental testing of the material with the appropriate dust and under established filtration conditions.

The purpose of this study was to evaluate the possibility of increasing engine inlet air filtration efficiency and accuracy, as well as dust absorbency, through the use of multilayer deposits. Obtaining more favorable filtration performance in terms of filtration efficiency and accuracy will increase the life of the engine, and the higher dust absorption capacity of the bed will result in a longer life of the air filter until the permissible resistance is reached.

This is mainly due to their higher dust absorption capacity than single layers. However, it is important whether the filtration efficiency and accuracy of such a bed will obtain the appropriate and required values throughout the filter's service life. This information is not obtainable in the available literature and therefore must be obtained during experimental tests of a given material with test dust on a special stand. For this purpose, two pleated composite filter beds consisting of three standard filter materials with different properties were designed: composite K1 (polyester-glass microfiber-cellulose) and composite K2 (cellulose-glass microfiber-cellulose). In the available literature, one does not encounter studies of multilayer deposits for engine intake air filtration, which were made at the pleating stage. The constituent layers are filtration factory materials with known structure parameters. During the research, original methodology was used, which allows to obtaining of unique parameters of the filtration process of fibrous deposits, such as: initial efficiency, size of maximum grains in the air behind the filter depending on the current unit absorption of dust. The methodology allows ongoing measurement and control of changes in flow resistance as the mass of dust retained by the filter increases. These parameters are essential in the design of air filters used in automotive technology and can be used to predict vehicle mileage. Although such studies are costly and labor-intensive, this is the only way to obtain the most reliable data.

3. Materials and methods

3.1. Subject of the study

In this study, the properties of several types of filter materials were tested, the surface of which was shaped into triangular pleats of 12 mm in height, and then cylindrical filter cartridges of the same design and dimensions and with the same area of filter material $A_c = 0.183$ m^2 were made from them. The cylindrical filter cartridges differed in the filter material used. The filter cartridges before testing are shown in Fig. 1.

Table 1 shows the characteristic parameters and selected properties of the filter materials to be tested. The subject of the study will be three types of filter beds. For ease of analysis of the test results, the name "Filter" is adopted and conventionally designated C, M, P, K1, K2, WP, WB.

- filter materials: C – cellulose, M – microglass, P – polyester
- composite beds K1 and K2 composed at the pleating stage of three filter layers: bed K1 (layers: P+M+C), bed K2 (layers: C+M+C) – Fig. 2–5
- filter materials: WP – non-woven polyester fabric, WB – non-woven cotton fabric.

Fig. 1. Filter cartridges prepared for testing

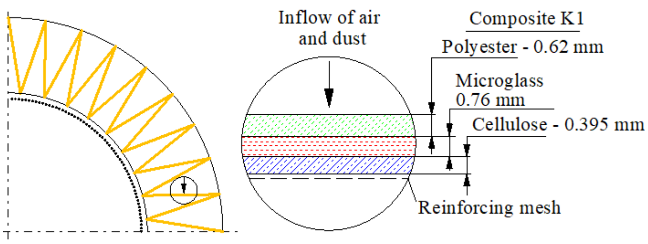

Fig. 2. Arrangement of filter layers in filter bed (composite) K1 (polyester-microglass-cellulose)

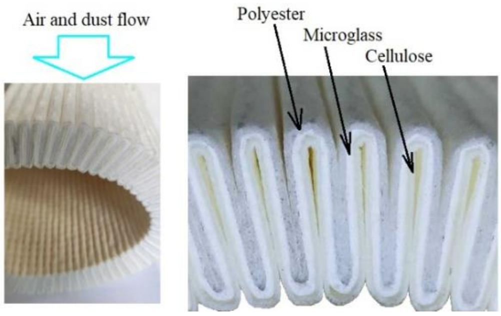

Fig. 3. Design of the K-composite (polyester-microglass-cellulose) filter: a) view of the bed after pleating, b) filter layers in the filter bed

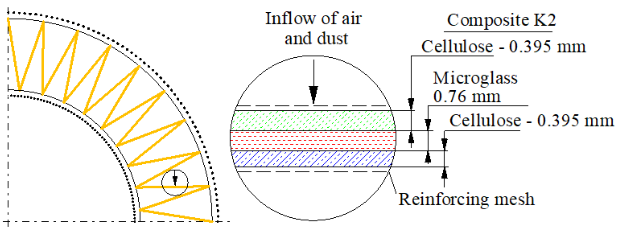

Fig. 4. Arrangement of filter layers in K2 (cellulose-microglass-cellulose) filter bed (composite)

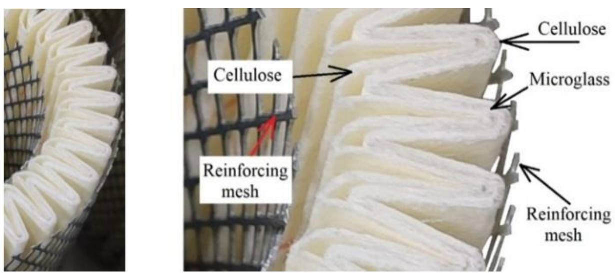

Fig. 5. K2 filter bed (composite: cellulose-microglass-cellulose) after making the pleats

Table 1. Tested filtration materials parameters according to the manufacturer's data

Filter paper identification	Material characteristics	Permeability q_p [$dm^3/m^2/s$]	Grammage g_m [g/m^2]	Thickness g_z [mm]	Max. pore size d_p [µm]
C	Cellulose	255	130	0.395	55
M	Microglass Double layer microglass media is laminated with spounbond scrim on downstream side: microglass leyer 1 microglass leyer 2 polyester spounbond	190	129 50 28 51	0.76	–
P	Polyester High hydrophobic High tensile strengths for longer pulse jet cycles	136	260	0.54	–
K1 (P-M-C)	Polyester-Microglass-Cellulose	–	–	1.775	–
K2 (C-M-C)	Cellulose-Microglass-Cellulose	–	–	1.55	–
WP	Non-woven polyester	540	442	2.5	–
WB	Non-woven cotton				

3.2. Materials and research methods

The purpose of this study was to determine and analyze the comparative filtration properties: filtration efficiency, filtration accuracy and flow resistance of research filters made of different filtration materials: C – cellulose, M – glass microfiber, P – polyester K1 and K2 composite beds composed at the pleating stage of three filter layers (K1 bed – P-M-C layers, K2 bed – C-M-C layers), WP (non-woven polyester), WB (non-woven cotton) filter fabrics, by determining the basic characteristics as a function of mass dust load – k_d:

- particle filtration accuracy $d_{pmax} = f(k_d)$
- particle filtration efficiency $\varphi_f = f(k_d)$
- resistance to flow through the filter material $\Delta p_f = f(k_d)$

and characteristics $\Delta p_f = f(Q_f)$, where: Q_f – the air flow rate through the active surface of the filter under test.

The mass loading of dust k_d was defined by the relation:

$$k_d = \frac{m_z}{A_c}\ [g/m^2] \tag{1}$$

where: m_z – the mass of dust retained on 1 m^2 of the surface of the filter material, assuming its uniform distribution over the entire surface, A_c – the area of the active surface of the filter paper of the tested filter – the area of the filter paper through which the air stream flows.

The filtration velocity is the quotient of the air stream flowing through the filter Q_{fmax} and the area of the active surface A_c:

$$\upsilon_F = \frac{Q_f}{A_c \times 3600}\ [m/s] \tag{2}$$

Filter tests were performed on a bench (Fig. 6) equipped with the necessary equipment and instruments for recording the data necessary for determining filter characteristics. A P_{amas} particle counter was used to record the size and number of particles in the Q_f stream downstream of the filter under test, allowing measurement in i = 32 measurement intervals in the range of 0.7–100 µm. The polluted air stream was drawn to the counter's sensor from the measuring line behind the filter under test, where the tip of the measuring probe was centrally located. The measuring line was terminated with a special filter, which protects the flow meter sensor from dust, and at the same time is a measuring (absolute) filter used to determine the filtration efficiency. To measure the air flow rate Q_f, an FMT430 mass flow meter was used, which has a measuring range of 10–150 m^3/h and an accuracy of 1.2%.

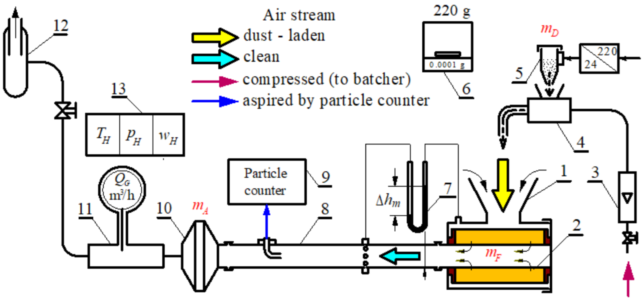

Fig. 6. Schematic of a standard test stand for testing air filters of internal combustion engines of vehicles with air demand up to 350 m^3/h: 1 – dust chamber, 2 – filter cartridge, 3 – rotameter, 4 – dust dispenser, 5 – dust tank, 6 – analytical balance, 7 – U-tube pressure gauge, 8 – measuring tube, 9 – counting device, 10 – measuring (safety) filter, 11 – mass air flow meter, 12 – fan forcing the flow, 13 – instrument for measuring humidity, temperature and ambient pressure

An electromagnetic metering device with an oscillating dust hopper and pneumatic (compressed air) transport of dust to the dust chamber, where it is mixed with the air inlet stream and flows into the filter, was used to supply dust to the test filter. PTC-D test dust was used, which is a substitute for AC fine test dust in Poland [11]. The main components of this dust and its fractional composition are exposed in Fig. 7. The dust contains more than 67% quartz (SiO_2) grains, a mineral characterized by high hardness, causing accelerated wear of engine components.

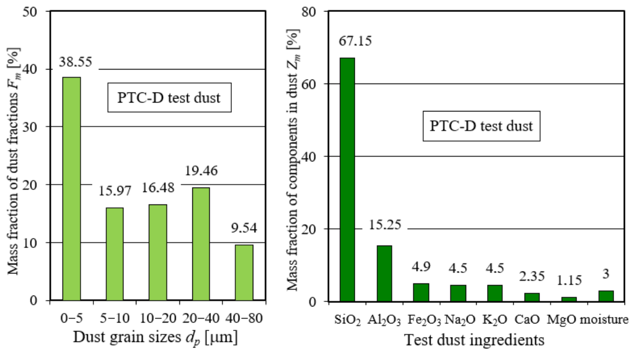

Fig. 7. Characteristics of PTC-D test dust: (a) factual composition of dust, (b) chemical composition of dust. The figure is based on data in [11]

The flow characteristics $\Delta p_f = f(Q_f)$ of filters C, M, P, K1, K2, WP, and WB were determined at 10 measurement points as a function of air flux varying within the limits $Q_f = Q_{fmin}–Q_{fmax}$.

The maximum value of the flux Q_{fmax} was determined from relation (3) assuming the maximum filtration velocity $\upsilon_F = 0.1$ m/s. According to the authors of works [3, 12, 46], for proper operation of passenger car air filters, the maximum filtration velocity should be within the limits $\upsilon_F = 0.06–0.12$ m/s.

$$Q_{fmax} = A_c \cdot v_F \cdot 3600 \text{ [m}^3\text{/h]} \quad (3)$$

Characterizations of the filters: efficiency $\varphi_f = f(k_d)$ and filtration accuracy $d_{pmax} = f(k_d)$, as well as flow resistance $\Delta p_f = f(k_d)$ were performed simultaneously according to the same methodology on the bench (Fig. 6) for one fixed value of air flow $Q_j = 56$ m^3/h, which corresponds to the speed of flow through the filter material $\upsilon_F = 0.085$ m/s. A measurement cycle was established, the duration of which was equivalent to the time of uniform dust dosing at a fixed air flow rate Q_j. The filtration efficiency $\varphi_f = f(k_d)$ was determined by the gravimetric method (measurement of the weight of the filter, the dispenser and the absolute filter before and after the measurement cycle) for a constant air flow and successively repeated j test cycles of fixed duration τ_{pd}. The measurement time (duration of one cycle) was fixed: $\tau_{pd} = 2$ min. in the initial period and $\tau_{pd} = 4–5$ min. in the main period of filter operation. The mass loss of dust from the dispenser m_D (the mass of dust delivered to the filter) and the mass of dust retained on the tested filter m_F and the absolute filter m_A were determined with an analytical balance with a measuring range of 220 g and an accuracy of 0.1 mg. Switching on the particle counter to measure the number and size of dust grains in the air stream behind the filter was set 60 seconds before the scheduled end of the measurement cycle. During one measurement cycle, three particle counts were programmed at the planned measurement intervals ($d_{pimin} – d_{pimax}$), and their average value was used for analysis.

After the measurement cycle j, the parameters of the filtration process were recorded to calculate filtration efficiency, filtration accuracy, flow resistance and mass loading of dust k_d.

1. The efficiency of the filter was calculated as the quotient of the mass of dust m_{Fj} retained and the mass of dust m_{Dj} delivered to the filter during the next j measurement cycle, from the relation:

$$\varphi_j = \frac{m_{Fj}}{m_{Dj}} = \frac{m_{Fj}}{m_{Fj}+m_{Aj}} 100\% \quad (4)$$

2. The mass loading of dust k_{dj} of the filter material used in the filter was calculated from the relationship:

$$k_{dj} = \frac{\sum_{j=1}^{n} m_{Fj}}{A_c} \text{ [g/ m}^2\text{]} \quad (5)$$

3. The number N_{pi} of dust grains in the air stream Q_f downstream of the filter in fixed and diameter-limited ($d_{pimin} – d_{pimax}$) measurement intervals from the particle counter printout.
4. Filtration accuracy as the largest dust grain size $d_{pj} = d_{pmax}$ occurring in the air stream Q_f downstream of the filter and appearing on the particle counter printout.
5. The proportion of the measured N_{pi} number of dust grains in each measurement interval relative to the total number of dust grains passed through the filter for a given test cycle:

$$U_{pi} = \frac{N_{pi}}{Np} = \frac{N_{pi}}{\sum_{i=1}^{32} N_{pi}} 100\% \quad (6)$$

where: $N_p = \sum_{i=1}^{32} N_{pi}$ – the total (from all measurement intervals) number of dust grains present in the airstream downstream of Q_f after the test filter.

6. Flow resistance Δp_{fj} of the filter being the difference in static pressure upstream and downstream of the filter calculated according to the following relationship:

$$\Delta p_{fj} = \frac{\Delta h_{mj}}{1000} \cdot (\rho_m - \rho_H) \cdot g \text{ [Pa]} \quad (7)$$

where: Δh_{mj} – height measured on a U-tube water pressure gauge after dust dosing, ρ_m – density of the manometric liquid [kg/m^{-3}], ρ_H – density of air [kg/m^{-3}], g – earth's attraction [m/s^2].

According to the above methodology, the characteristics of efficiency φ_f and filtration accuracy d_{pmax} and flow resistance $f(k_d)$ of filters C, M, P, K1, K2, WP, WB were determined depending on the mass of dust retained on the filter and defined as "mass loading of dust" k_d [g/m^2]. Two copies of each filter were tested with the same filter material and under the same conditions. Before testing the filters with dust, their $\Delta p_f = f(Q_f)$ characteristics were performed.

4. Research results and their analysis

Figure 8 shows the changes in flow resistance Δp_f of the tested filters with different filter materials as a function of the air flow rate Q_f. Regardless of the filter tested, the increase in air flow rate causes a parabolic increase in flow resistance Δp_f, which is due to the increase in flow velocity through the bed in the second power.

The highest values of flow resistance, over the entire range of air flow Q_f, were recorded for the cartridge, where the filter bed is a K2 composite (C + M + C) of three sequentially arranged layers: cellulose, microglass and cellulose. For $Q_{fmax} = 56$ m^3/h, the flow resistance of the K2 cartridge has a value of $\Delta p_f = 1.304$ kPa (Fig. 8). This value is more than 2.5 times higher than the flow resistance value of material C, which is exclusively a cellulose filter material. Similarly high flow resistance is characterized by composite K1 (P + M + C) of three sequentially arranged layers: polyester, microglass and cellulose. Such significant values of flow resistance are mainly due to the thickness of the composite deposits, which are the sum of the thickness of the three layers of filter material folded together. Composite K2 has a thickness of $g_z = 1.55$ mm, and K1 $g_z = 1.775$ mm. In comparison, the thickness of the cellulose layer is $g_z = 0.395$ mm. The flow resistance of the other filters is at a much lower level in the range $\Delta p_f = 0.471–0.696$ kPa for a flow rate of $Q_f = 56$ m^3/h.

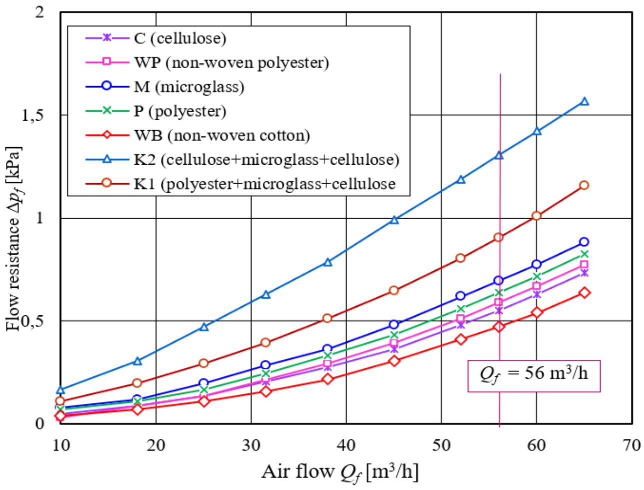

Fig. 8. Flow resistance characteristics $\Delta p_f = f(Q_f)$ of filters with different filter materials

The filtration characteristics: efficiency $\varphi_f = f(k_d)$ and filtration accuracy $d_{pmax} = f(k_d)$ and flow resistance $\Delta p_f = f(k_d)$ of the filter materials C, M, P, WP, WB and composites K1 and K2 made by the author for the study are shown in Fig. 9–19. The characteristics are similar as to the course, but differ as to the obtained values of efficiency, filtration accuracy and flow resistance depending on which filter material they are made of. At the onset of the filtration process, filtration efficiency and flow resistance take on small but varying values, which with the increase in the dust mass on the filter layer (increase in the mass loading of dust k_d) take on increasing values, which is characteristic of fibrous deposits. The increase in filter performance values is due to changes in the structure of the filter bed, which result from the retention of dust grains on the fibers of the filter bed through the action of filtration mechanisms, mainly: inertial, direct retention and diffusion. The first dust particles retained and deposited on the surface of the fibers form a layer on which further dust grains arriving with the air are deposited. Successive layers of dust are superimposed, which form agglomerates that often grow to considerable sizes. In this way, the free spaces between the fibers are filled. The phenomenon of the formation of dust agglomerates on fibers is discussed in detail in the paper [23].

Agglomerates formed on the fibers cause a change in the conditions of air flow and separation of successive dust grains. The distances between the surfaces of dust-laden elements decrease (the porosity of the baffle decreases), which causes an increase in flow velocity, and hence the hydrodynamic flow resistance in the filtration layer must increase as a consequence. Reducing the distance between the dust-laden fibers increases the intensity of the filtration mechanisms, hence the filtration efficiency obtains higher and higher values and gets closer and closer to 100%. From this point on, the filtration efficiency usually remains constant. Therefore, the filtration process of the studied filters was conventionally divided into two stages. It was determined that the first (t_{p1}), the initial stage of each filter's operation, lasts from the beginning of the influx of dust onto the filter until the filtration efficiency reaches φ_f = 99.9%. This efficiency value is required of filter materials intended for motor vehicle engine intake air filters. The following stage of operation is called the main stage and lasts until the filter reaches the set value of flow resistance.

The filtration accuracy, defined as the maximum size of dust grains behind the filter, initially has a small value. In the air behind the filter there are initially dust grains d_{pmax} of large size, after which they decrease with the increase of the mass loading of dust k_d and remain constant for a while, then at the end of the filtration process they generally reach larger and larger values, which is generally associated with a decrease in efficiency and means that the filtering capacity of the filter is exhausted. The direct cause of the appearance of large dust grains in the air behind the filter at the final stage of filtration is the large flow resistance, the value of which increased intensively with the increase in the mass loading of dust k_d of the filter bed. With a large pressure difference and high local flow velocities in the filter bed, dust grains are detached, from the outermost parts of the agglomerates, and migrate towards the outlet. It follows from the above that the operation of the air filter with excessive flow resistance is inadvisable. Therefore, it was assumed that the criterion for completing the testing of filters would be the achievement of a fixed value of resistance, called in the literature the permissible resistance Δp_{fdop}. In the case of the tested filters, the value Δp_{fdop} = 4 kPa was assumed.

Figures 9–11 show the characteristics of filtration efficiency $\varphi_f = f(k_d)$, filtration accuracy $d_{pmax} = f(k_d)$ and flow resistance $\Delta p_f = f(k_d)$ of filters with a filtration bed, respectively: C (cellulose), M (microglass) and P (polyester).

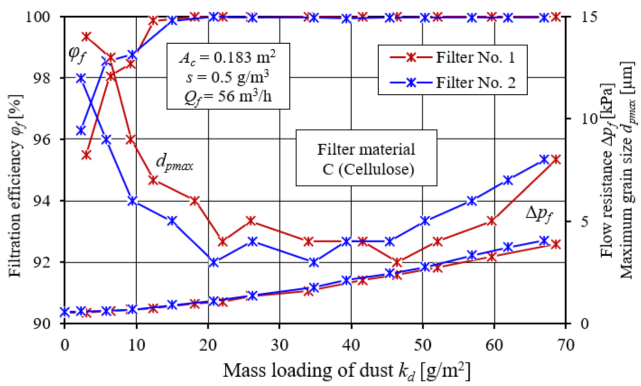

Fig. 9. Changes in efficiency φ_f and filtration accuracy d_{pmax}, as well as flow resistance Δp_f as a function mass loading of dust k_d of the tested filters with filter bed C (cellulose)

Two filters were tested for each filter material. You can notice slight differences in the characteristics and in the obtained values of efficiency, filtration accuracy and flow resistance for two filters made of the same type of filter material.

A comparative analysis in terms of changes in filtration efficiency and accuracy, as well as flow resistance as a function of the mass loading of dust k_d of C, M and P filter beds is shown in Fig. 12.

The characteristics of No. 2 filters of each type of filter material were used. The characteristic curves vary, which is mainly due to the structure of the materials studied.

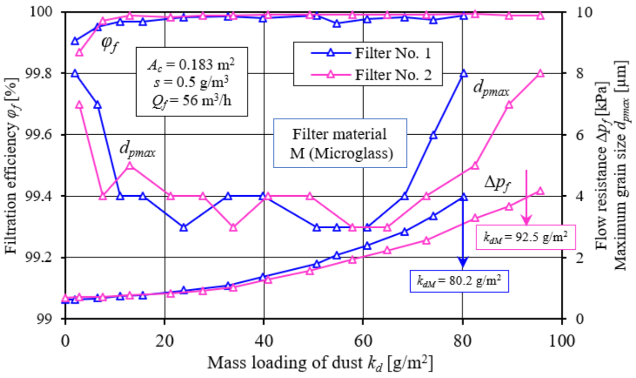

Fig. 10. Changes in efficiency φ_f and filtration accuracy d_{pmax}, as well as flow resistance Δp_f as a function mass loading of dust k_d of the tested filters with filter bed M (microglass)

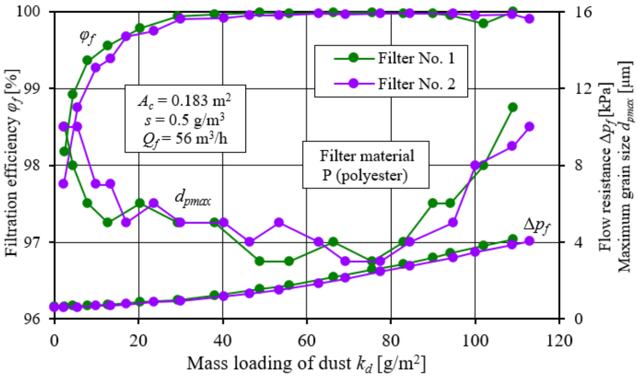

Fig. 11. Changes in efficiency φ_f and filtration accuracy d_{pmax}, as well as flow resistance Δp_f as a function mass loading of dust k_d of the tested filters with material P (polyester)

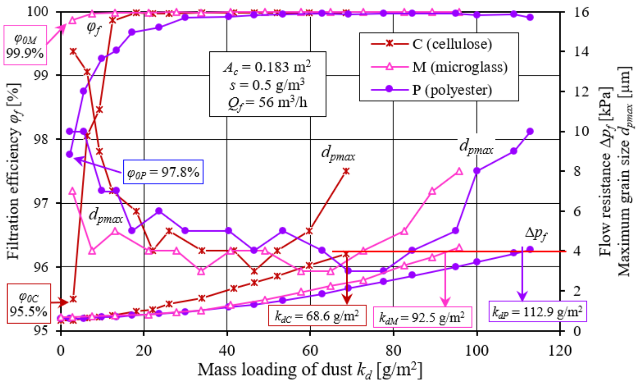

Fig. 12. Comparative analysis of filtration properties in terms of filtration efficiency and accuracy, flow resistance and mass loading of dust of bed filters: C, M and P

Material C, which obtained the lowest (φ_{0C} = 95.5%) filtration efficiency during the initial period, has at the same time the highest permeability (q_p = 255 dm^3/m^2/s) and the smallest (g_m = 130 g/m^2) grammage (Table 1), which means that mainly depth filtration takes place in the bed, which does not guarantee high efficiency of dust grain retention. Material M (microglass), which has a much lower permeability (q_p = 190 dm^3/m^2/s) and a comparable grammage, achieved a very high initial filtration efficiency φ_{0M} = 99.9%). This is due to the fact, this material is constructed of two layers of very thin glass fibers and protected at the outlet by a layer of polyester (Table 1). This guarantees the occurrence of the phenomenon of surface filtration and the retention of dust grains of small size and ensures a high (k_{dM} = 92.5 g/m^2) mass loading of dust (Fig. 12).

Figures 13 and 14 show the characteristics of filtration efficiency $\varphi_f = f(k_d)$, filtration accuracy $d_{pmax} = f(k_d)$ and flow resistance $\Delta p_f = f(k_d)$ of filters with filter bed, respectively: WP (non-woven polyester), WB (non-woven cotton). It can be seen the high reproducibility of the obtained test results for both WB and WP nonwovens.

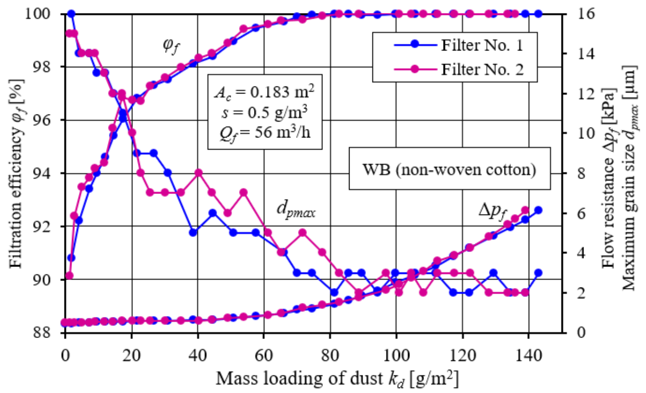

Fig. 13. Changes in efficiency φ_f and filtration accuracy d_{pmax}, as well as flow resistance Δp_f as a function mass loading of dust k_d of the tested filters with WB material (non-woven cotton)

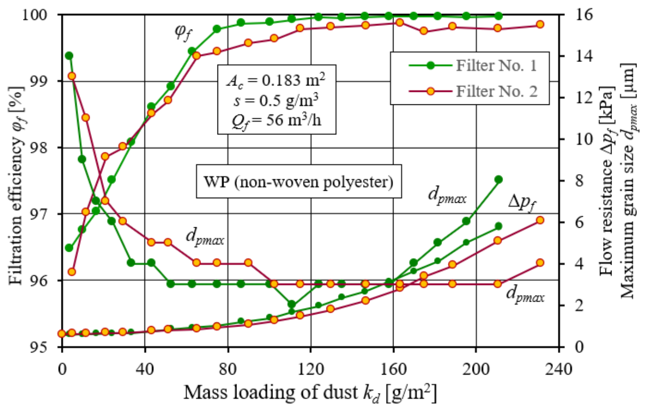

Fig. 14. Changes in efficiency φ_f and filtration accuracy d_{pmax}, as well as flow resistance Δp_f as a function of mass loading of dust k_d of the tested filters with WP (non-woven polyester) material

Figure 15 analyses the changes in filtration efficiency, filtration accuracy and flow resistance as a function of the dust mass loading k_d of the WB and WP filter beds. The results of tests on filter No. 2 of both nonwovens were used for the analysis. Analyzing the slow increase in filtration efficiency and accuracy as a function of dust mass load k_d, it should be noted that the duration of the initial filtration period of both nonwovens is significant. The initial filtration efficiency of the nonwovens obtains small values φ_{0WB} = 90.8% and φ_{0WB} = 96.1%, respectively. In order for the filters to achieve the required filtration efficiency of φ_f = 99.5%, it is necessary to achieve a mass loading of the dust of k_{dWB1} = 65.96 g/m^2 and k_{dWP1} = 115.4 g/m^2, respectively, which is more than 50–70% of the total filter operation time to achieve the established permissible flow resistance Δp_{fdop}

= 4 kPa (Fig. 15). During this time, dust grains of considerable (d_{pmax} = 14–16 µm) size were recorded in the air behind the filter. However, the grain sizes decreased as the mass of dust retained on the filter bed increased, and by the end of the initial period they had stabilized at d_{pmax} = 3–4 µm. Under conditions of actual filter operation, the engine is exposed to dangerous dust. An apparent increase in the flow resistance of the tested filters began when the initial period ended and the main period of filter operation began, during which the filtration efficiency remained high, more than 99.5%. The significant increase in flow resistance was due to the higher intensity of dust accumulation in the bed as a result of the high efficiency. A filter material with such properties cannot be suitable for filtering engine intake air but can be used as a pre-filter in a two-stage filtration system.

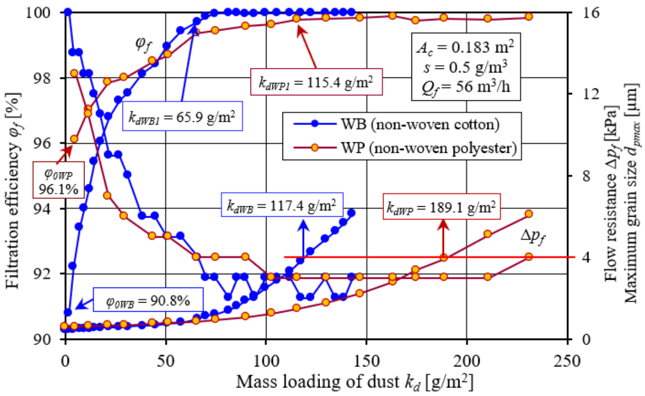

Fig. 15. Comparative analysis of filtration properties in terms of filtration efficiency and accuracy, flow resistance and mass loading of dust of filters with WP (non-woven polyester) and WB (non-woven cotton) material

The characteristics of filtration efficiency $\varphi_f = f(k_d)$, filtration accuracy $d_{pmax} = f(k_d)$ and flow resistance $\Delta p_f = f(k_d)$ of two copies of K1 (P-M-C) composite filter bed filters, presented in Fig. 16, show great similarity as to their course and values. The tested filters achieve a high initial filtration efficiency of φ_{0K1} = 99.8% (for k_{dKp} = 5.95 g/m^2), and the size of maximum dust grains during the initial period does not exceed the value of d_{pmax} = 5–7 µm. After the cartridges reach a mass loading of dust of k_{dK1} = 16.3 g/m^2, the sizes of maximum dust grains stabilize at d_{pmax} = 2–3 µm, which is a very high accuracy for fibrous filter media that can be used in automotive technology. The high filtration efficiency and accuracy of the cartridges was maintained until the flow resistance Δp_f = 6.2 kPa was reached (Fig. 16). The filter elements tested achieved a high mass loading of dust of k_{dK1} = 199.8 g/m^2, which is due to the configuration of the materials used and the considerable (g_m = 1.775 mm) thickness of the composite bed. The first filter layer of the K1 cartridge is a 0.62-mm-thick polyester bed with high permeability, which makes the phenomenon of depth filtration occur, resulting in the retention of dust grains of the largest size. The second filtration layer is M bed (microfiber glass), where the phenomenon of surface filtration occurs, resulting in high efficiency and accuracy of filtration of small-sized dust grains (Fig. 12). The cellulose layer is a reinforcing layer and stabilizes the airflow.

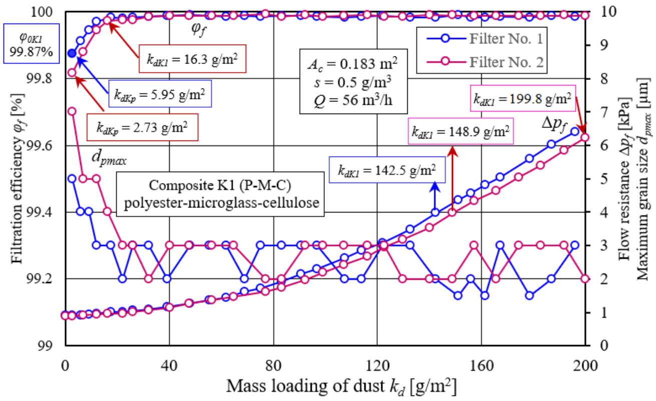

Fig. 16. Variation of efficiency φ_f and filtration accuracy d_{pmax} and flow resistance Δp_f as a function mass loading of dust k_{dK1} of K1 filter with composite bed of three layers: P–M–C

On the other hand, Fig. 17 shows a comparative analysis of the filtration properties of composite K1 (P-M-C) and composite K2 (C-M-C), whose filtration characteristics were performed under the same assumed conditions. It can be clearly seen that the K1 composite, which differs only in the first filtration layer (polyester) from the K2 composite (cellulose), achieves significantly better results in terms of filtration efficiency and accuracy.

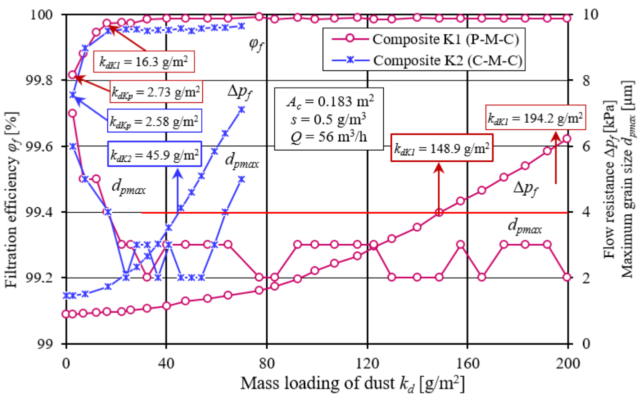

Fig. 17. Characteristics of filtration efficiency $\varphi_f = f(k_d)$, filtration accuracy $d_{pmax} = f(k_d)$ and flow resistance $\Delta p_f = f(k_d)$ of filters with composites: K1 (P-M-C) and K2 (C-M-C)

After the K1 composite reaches a mass loading of dust k_{mK1} = 16.3 g/m^2, the filtration efficiency is at 99.99% and is maintained until the flow resistance Δp_f = 6.2 kPa is reached, which is well beyond the permissible resistance (Fig. 17). It should be noted that at this time there are dust grains of very small size d_{pmax} = 3–4 µm in the exhaust air from the tested filter.

When the flow resistance Δp_{fdop} = 4 kPa is reached, the mass loading of dust of the K1 composite is k_{dK1} = 148.9 g/m^2, which is three times higher than that of the K2 composite, for which k_{dK2} = 45.9 g/m^2. This is due to the increase in flow resistance of the tested materials K1 and K2. As can be seen from Fig. 17, the intensity of the increase in flow resistance of K2 is very high, which may be due to the low efficiency of the C (cellulose) layer and the deposition of most of the dust on the M (fiberglass) filter bed.

From the research presented here, it can be seen that there is a close relationship between the filtration efficiency and flow resistance and the filtration accuracy of the filter material. An increase in filtration efficiency is directly related to an increase in filter accuracy (d_{pmax} decreases) and an increase in flow resistance. Comparing directly the filtration properties of different materials is difficult. Therefore, the "filtration quality factor q_c" is commonly used in the literature, which relates filtration efficiency and flow resistance of the same filter material and, according to [32, 46], is expressed by the relation:

$$q_c = \frac{-\ln(1-\varphi_{f0})}{\Delta p_f}\ [1/kPa] \tag{8}$$

where: φ_{f0} – initial filtration efficiency, Δp_f – flow resistance.

A higher value of q_c means a more favorable relationship between efficiency and flow resistance, which means that the filtration process is more efficient.

In addition, for the purpose of this work, to compare the filtration properties of the tested materials, the filtration efficiency index q_s, was defined, which expresses in (%) the period of correct operation of the filter concerning the total time of its operation:

$$q_s = \left(1 - \frac{k_{d1}}{k_{d2}}\right) 100\% \tag{9}$$

where: k_{d1} – mass loading of dust of the material at the time of obtaining the required filtration efficiency φ_f = 99.5%, k_{d2} – mass loading of dust of the material at the time of obtaining by the filter the established permissible resistance (Δp_{fdop} = 4 kPa).

A smaller value of the q_s index means a shorter duration of the filtration process with the required filtration efficiency and accuracy.

Using the above relationships, the values of q_c and q_s coefficients were calculated for the tested filter materials, and the results are summarized in Fig. 18.

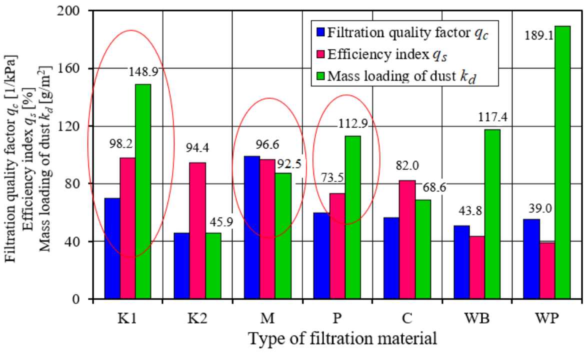

Fig. 18. Filtration quality factor q_c, efficiency index q_s and mass loading of dust k_d of the tested filter materials

5. Vehicle mileage modeling

Determining the duration of proper operation of an air filter is not a straightforward exercise since it depends on many factors that change during vehicle use. The operating time of a filter can be determined experimentally during its use in a vehicle or during tests on a laboratory bench. Depending on the type and size of the air filter, such tests are usually labor-intensive and expensive. The basic criterion for completing the tests is the achievement of a fixed value of the permissible flow resistance Δp_{fdop}. It is also possible to computationally determine the operating time τ_{pf} of an air filter using theoretical relationships, such as that given in [29]:

$$\tau_{pf} = \frac{A_c \cdot k_d \cdot k_c}{Q_{Emax} \cdot s \cdot \varphi_f}\ [h] \tag{10}$$

where: A_c – active surface area of the filter material in the filter [m^2], k_d – mass loading of dust of the filter material [g/m^2] at the permissible value of the flow resistance Δp_{fdop}, k_c – correction factor for the difference between the test dust parameters and the parameters of the real pollution, Q_{Emax} – nominal engine inlet air flow [m^3/h], s – dust concentration in the air entering the filter [g/m^3], φ_f – filtration efficiency of the filter material.

If we assume a constant (average) driving speed V_p (km/h), the distance traveled by the vehicle S_p in time τ_{pf} is described by the formula:

$$S_p = \tau_{pf} \cdot V_p\ [km] \tag{11}$$

If we now consider relation (9), then the distance the vehicle will travel in time τ_{pf} can be described by the relation:

$$S_p = V_p \frac{A_c \cdot k_d \cdot k_c}{Q_{Emax} \cdot s \cdot \varphi_f}\ [km] \tag{12}$$

From the presented relationship, it is clear that for its practical application it is necessary to know several data that describe the filter material, which are: filtration efficiency φ_f, mass loading of dust k_d, and coefficient k_c, which corrects the difference between test and actual parameters under specific operating conditions. Among the most important are the chemical composition of the dust, the type of dust and its concentration, the granularity of the dust, and the speed of the airflow. The k_c, factor is mainly used when the effect of soot on the operating time of a pleated paper cartridge filter must be considered. The k_c factor is usually defined as the ratio of the filter operating time under soot contamination conditions to the operating time when using test dust, which is mineral dust. With higher soot content in the air, the k_c factor takes values less than 1, and the filter's operating time will be correspondingly shorter. This is important in the case of passenger car air filters operated in urban conditions, where soot, as a product of incomplete combustion of fuel in engines, is the predominant pollutant of the air entering the engine, but also of the air inhaled by people.

Filter materials are produced by specialized plants, which describe their structure with characteristic parameters, this is most often: material thickness and grammage, pore dimensions and air permeability at specific flow parameters. Manufacturers also specify the type of filter material or the percentage composition of the component. As can be seen, none of these data is a component of the relationship (11). Previous studies of modern fibrous filter materials applicable in automotive technology report that their filtration efficiency oscillates within narrow limits φ_f = 99.5–99.9% during the main period of filter operation. Such efficiency values were registered during the tests described in this paper.

It follows that the parameter that, in relation (11), significantly determines the course of the S_p vehicle is the mass loading of dust k_d of the filter material used. From the tests carried out in this work, it can be seen that there are significant differences in the achieved values of the mass loading of dust k_d for different filter materials determined at the permissible flow resistance, in this case for Δp_{fdop} = 4 kPa. Using the calculated values of the k_d coefficient for cellulose C and composite K and taking the values of the other parameters in relation (11) as constants, the modeled mileages of a passenger car at which filter servicing – replacement of the filter element – should be carried out were established.

Using relation (11), calculations were carried out based on the data of the Audi A4 engine (CI engine with turbocharging and air cooler): displacement V_{ss} = 2.496 dm^3, filter paper area A_c = 2.09 m^2, engine inlet air flow Q_{Emax} = 554 m^3/h. For the calculations, it was assumed that the test vehicle would be used mainly in non-urban conditions, where dust is the main component of pollution. Therefore, a correction factor of k_c = 1 was assumed. According to [3], the dustiness of air on paved roads and highways can take on values in the wide range of s = 0.0004–0.1 g/m^3. To calculate the vehicle mileage (achieving Δp_{fdop}), the use of the vehicle was assumed at an air dust concentration of s = 0.0005 g/m^3 and a vehicle moving speed of V_p = 60 km/h. Vehicle mileage was estimated for a vehicle equipped with an air filter with composite K1 and materials that are successive layers in this composite: P, M and C. The dust mass load k_d and filtration efficiency φ_f were adopted from filter tests. The results of the calculations are shown in Fig. 19.

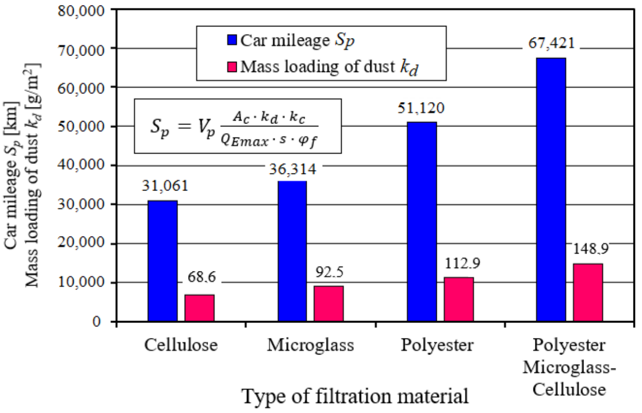

Fig. 19. Modeled car runs for different types of filter beds and corresponding different mass loading of dust k_d

As expected, the higher the mass loading of dust k_d, the higher the vehicle mileage has a higher value (Fig. 19). A filter with a filter material (K-composite made by the author) provides twice the mileage of the other filter materials, which is due to the correspondingly higher mass loading of dust k_d. For the assumptions made, the modeled vehicle mileage has a value of more than 67,000 km. The mileage values are subject to change depending on changes in vehicle operating conditions, such as dust concentration in the air drawn into the engine, driving speed and air flow Q_E, which does not often assume maximum values. The mileage of the vehicle is largely determined by the filter area of the A_c material. Due to the limited space around the engine, where the air filter is most often located, it is difficult to apply a sufficiently large filter paper surface.

Figure 20 shows that an increase in the concentration of dust in the air increases, at the same value of air flow, the mass of dust delivered to, the filter which fills the filter bed with greater intensity. Since the absorptive capacity of the filter bed is limited, the value of the vehicle mileage is shortened accordingly. For filter beds whose dust load k_d the vehicle mileage will be lower. A change in dust concentration within s = 0.0005–0.001 g/m^3 reduces the mileage of the car by 50% regardless of the absorptive capacity of the filter material k_d.

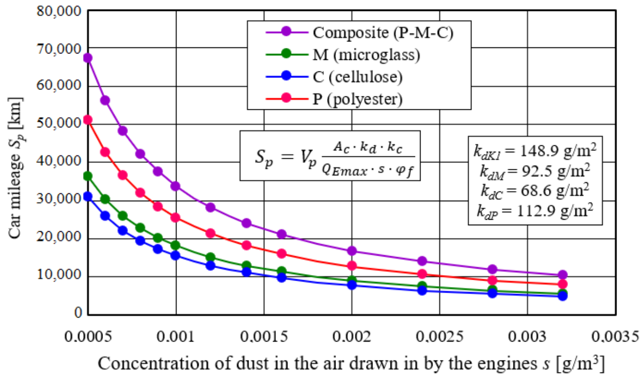

Fig. 20. Modeled car runs depending on the dust concentration in the inlet air for different mass loading of dust k_d of filter beds

6. Summary and final conclusions

The purpose of the study was to experimentally evaluate the properties of filter materials in the context of selecting a filter material with the best parameters for the filtration of air drawn by vehicle internal combustion engines. The evaluation was based on the filtration characteristics determined on the test bench: filtration efficiency and accuracy, as well as flow resistance depending on the mass loading of dust k_d. Filter materials produced by specialized factories were tested: cellulose, polyester, microfiber glass, and a filter bed made of three layers of different materials. A filter bed consisting of three base filter materials (polyester-microglass-cellulose) was designed and fabricated, and the characteristics of the filter bed were determined. A comparative analysis was carried out using the air filtration quality coefficients of the fiber baffles. The results of the study and their analysis led to the following conclusions.

1) Two characteristic stages can be distinguished in the filtration process of the tested filter beds: a preliminary stage showing a low initial, but increasing with the influx of dust on the bed, efficiency φ_f and filtration accuracy d_{pmax}, and a small but slowly increasing flow resistance Δp_f, and a main stage, which starts when a stable efficiency is reached at the conventional minimum level of φ_f = 99.5%.
2) The duration of the pre-stage varies for the filter materials tested and is longer the lower the initial filtration efficiency. For WB and WP nonwovens, this is 96.1% and 90.8%, respectively. This increased the duration of the initial stage and reduced the main stage to 40% of the

total filter operating time with these materials. This has a major impact on the accelerated wear of the engine's tribological associations, due to the large-diameter dust grains (d_{pmax} = 14–16 μm) in the air behind the filter at this time, which are drawn into the engine cylinders.
3) The filter bed (K1 composite) made for the present study, in the form of three composite layers of polyester-glass microfibre-cellulose materials, shows, under the same test conditions as the other materials, a high initial filtration efficiency (99.8%) and thus a short initial filtration period. This resulted in a prolongation of the duration of the main stage involving the filtration process with high efficiency (99.9%) and filtration accuracy (d_{pmax} = 1.5–3 μm) until the set flow resistance value Δp_{fdop} = 4 kPa was reached.
4) Compared to other tested materials, the K1 composite obtained more than twice the value of the mass dust load (k_{dK1} = 148.9 g/m^2), which will allow to extend the operating time of the filter (vehicle mileage in km) until the performance of air filter servicing – filter cartridge replacement.
5) The presented original methodology for experimental testing of filter materials having different chemical composition structure parameters, and thus different filtration properties, partly fills the information gap in the acquisition of basic parameters of filter materials. The results obtained can be used for a more precise design of air filter structures for internal combustion engines of cars and trucks, special vehicles and working machines depending on the expected conditions of use and, in particular, on the concentration of dust in the air.

Fibre filtration materials are characterized by the fact that the three basic parameters of the filtration process: filtration efficiency, filtration accuracy and flow resistance are closely linked. Changing the structure of the filter bed as a result of the retention and accumulation of dust mass results in an increase in filtration efficiency, a reduction in the size of dust grains in the purified air, but also results in an inevitable increase in flow resistance that is detrimental to engine operation. Fibrous materials research is directed towards the construction of a bed that has a high dust absorption capacity with minimal flow resistance, achieves high filtration efficiency and accuracy and maintains these parameters throughout the filter operation until the permissible resistance is reached. In the present work, by investigating a bed consisting of three different filter layers, which is an innovative approach in the field of filter material research, results were obtained that partly meet the above contradictory requirements. Work in this direction, using other composites given their filtration capabilities, should be continued. The results obtained can modernize methods for the design and optimization of air filtration systems in internal combustion engines.

Acknowledgements

This work was financed/co-financed by Military University of Technology under research project UGB 711/2024.

Nomenclature

CI	compression ignition
d_{pmax}	filtration accuracy
k_d	mass loading of dust
q_c	filtration quality factor
q_s	filtration efficiency index
Q_f	air flow
T-PR-C	piston-piston ring-cylinder
Δp_f	flow resistance
φ_f	filtration efficiency

Bibliography

[1] Alfadhli A, Alazemi A, Khorshid E. Numerical minimisation of abrasive-dust wear in internal combustion engines. Int J Surf Sci Eng. 2020;14:68-88. https://doi.org/10.1504/IJSURFSE.2020.105891
[2] Baddocka MC, Zobeck TM, Van Pelt RS, Fredrickson EL. Dust emissions from undisturbed and disturbed, crusted playa surfaces: cattle trampling effects. Aeolian Res. 2011;3: 31-41. https://doi.org/10.1016/j.aeolia.2011.03.007
[3] Barbolini M, Di Pauli F, Traina M. Simulation der Luftfiltration zur Auslegung von Filterelementen. MTZ. 2014; 75:52-57. https://doi.org/10.1007/s35146-014-0556-5
[4] Barris MA. Total filtration™: the influence of filter selection on engine wear, emissions, and performance. SAE Technical Paper 952557. 1995. https://doi.org/10.4271/952557
[5] Bojdo N, Filippone A. A simple model to assess the role of dust composition and size on deposition in rotorcraft engines. Aerospace. 2019;6(44). https://doi.org/10.3390/aerospace6040044
[6] Bojdo N, Filippone A. Effect of desert particulate composition on helicopter engine degradation rate. 40th European Rotorcraft Forum, Southampton. Conference Paper. September 2014. https://doi.org/10.13140/2.1.2959.8086
[7] Bugli N. Automotive engine air cleaners – performance trends. SAE Technical Paper 2001-01-1356. 2001. https://doi.org/10.4271/2001-01-1356
[8] Cai R-R, Li S-Z, Zhang L-Z, Lei Y. Fabrication and performance of a stable micro/nano composite electret filter for effective PM2.5 capture. Sci Total Environ. 2020; 138297. https://doi.org/10.1016/j.scitotenv.2020.138297
[9] Cardozo JIH, Sánchez DFP. An experimental and numerical study of air pollution near unpaved roads. Air Qual Atmos Hlth. 2019;12:471-489. https://doi.org/10.1007/s11869-019-00678-9
[10] Dziubak T. Experimental study of a powercore filter bed operating in a two-stage system for cleaning the inlet air of internal combustion engines. Energies. 2023;16:3802. https://doi.org/10.3390/en16093802
[11] Dziubak T. Properties of material with nanofiber layer used for filtering the inlet air of internal combustion engines. Combustion Engines. 2019;177(2):66-75. https://doi.org/10.19206/CE-2019-212
[12] Dziubak T, Dziubak SD. experimental study of filtration materials used in the car air intake. Materials. 2020;13(16): 3498. https://doi.org/10.3390/ma13163498

[13] Fujiwara F, Rebagliati RJ, Dawidowski L. Gómez D, Polla G, Pereyra V et al. Spatial and chemical patterns of size fractionated road dust collected in a megacitiy. Atmos Environ. 2011;45:1497-1505. https://doi.org/10.1016/j.atmosenv.2010.12.053
[14] Fussell JC, Franklin M, Green MD, Gustafsson M, Harrison RM, Hicks W et al. A review of road traffic-derived non-exhaust particles: emissions, physicochemical characteristics, health risks, and mitigation measures. Environ Sci Technol. 2022;56:6813-6835. https://doi.org/10.1021/acs.est.2c01072
[15] Heikkilä P, Sipilä A, Peltola M, Harlin A. Electrospun PA-66 coating on textile surfaces. Text Res J. 2007;77(11):64-870. https://doi.org/10.1177/0040517507078241
[16] Jaroszczyk T, Pardue BA, Heckel SP, Kallsen KJ. Engine air cleaner filtration performance – theoretical and experimental background of testing. Proceedings of the AFS Fourteenth Annual Technical Conference and Exposition, Tampa, 1 May 2001. Session 16.
[17] Jaroszczyk T, Petrik S, Donahue K. Recent development in heavy duty engine air filtration and the role of nanofiber filter media. Journal of KONES – Powertrain and Transport. 2009;16(4):207-216.
[18] Jiang D, Zhang W, Liu J, Geng W, Ren Z. Filtration and regeneration behavior of polytetrafluoroethylene membrane for dusty gas treatment. Korean J Chem Eng. 2008;25:744-753. https://doi.org/10.1007/s11814-008-0122-2
[19] Jung U, Choi S-S. Classification and characterization of tire-road wear particles in road dust by density. Polymers. 2022; 14:1005. https://doi.org/10.3390/polym14051005
[20] Kanageswari SV, Tabil LG, Sokhansanj S. Dust and particulate matter generated during handling and pelletization of herbaceous biomass: a review. Energies. 2022;15:2634. https://doi.org/10.3390/en15072634
[21] Karczewski M. Evaluation of the diesel engine feed by unified battlefield fuel F-34/F-35 mixed with biocomponents. Combustion Engines. 2019;178(3):240-246. https://doi.org/10.19206/CE-2019-342
[22] Kreider ML, Panko JM, McAtee BL, Sweet LI, Finley BL. Physical and chemical characterization of tire-related particles: comparison of particles generated using different methodologies. Sci Total Environ. 2010;408:652-659. https://doi.org/10.1016/j.scitotenv.2009.10.016
[23] Leung WW-F, Curie Hau CW-Y, Choy H-F. Microfiber-nanofiber composite filter for high-efficiency and low pressure drop under nano-aerosol loading. Sep Purif Technol. 2018; 206:26-38. https://doi.org/10.1016/j.seppur.2018.05.033
[24] Li B, Cao R, He H-D, Peng Z-R, Qin H, Qin Q. Three-dimensional diffusion patterns of traffic-related air pollutants on the roadside based on unmanned aerial vehicles monitoring. Build Environ. 2022;219:109159. https://doi.org/10.1016/j.buildenv.2022.109159
[25] Lippi M, Riva L, Caruso M, Punta C. Cellulose for the production of air-filtering systems: a critical review. Materials. 2022;15:976. https://doi.org/10.3390/ma15030976
[26] Liu X, Shen H, Nie X. Study on the filtration performance of the baghouse filters for ultra-low emission as a function of filter pore size and fiber diameter. Int J Env Res Pub He. 2019;16(2):247. https://doi.org/10.3390/ijerph16020247
[27] Long J, Tang M, Liang Y, Hu J. Preparation of fibrillated cellulose nanofiber from lyocell fiber and its application in air filtration. Materials. 2018;11(8):1313. https://doi.org/10.3390/ma11081313
[28] Long J, Tang M, Sun Z, Liang Y, Hu J. Dust loading performance of a novel submicro-fiber composite filter medium for engine. Materials. 2018;11:2038. https://doi.org/10.3390/ma11102038
[29] Melzer HH, Brox W. Ansauggerauschdampfer und Luftfilter für BMW 524 td. MTZ. 1984;45:223-227.
[30] Michalski J, Woś P. The effect of cylinder liner surface topography on abrasive wear of piston–cylinder assembly in combustion engine. Wear. 2011;271:582-589. https://doi.org/10.1016/j.wear.2010.05.006
[31] Muschelknautz U. Design criteria for multicyclones in a limited space. Powder Technol. 2019;357:2-20. https://doi.org/10.1016/j.powtec.2019.08.057
[32] Nowak B, Bonora M, Winnik M, Gac J. An effect of fibrous filters modification with MTMS aerogel structure on oil mist filtration dynamics. J Aerosol Sci. 2023;170:106147. https://doi.org/10.1016/j.jaerosci.2023.106147
[33] Nyirenda G, Tamaldin N, Zakaria MH. The impact of biodiesel blend variation contamination to engine friction, wear, performance and emission. IJAME. 2021;18(1):8592-8600. https://doi.org/10.15282/ijame.18.1.2021.18.0653
[34] Oszczypała M, Ziółkowski J, Małachowski J. Semi-Markov approach for reliability modelling of light utility vehicles. Eksploat Niezawodn. 2023;25(2):161859. http://doi.org/10.17531/ein/161859
[35] Owens LP, Hubbe MA. Performance factors for filtration of air using cellulosic fiber-based media: a review. BioResources. 2023;18(1):2440-2519. http://doi.org/10.15376/biores.18.1.Owens
[36] Panko J, Kreider M, Unice K. Review of tire wear emissions. Non-exhaust emissions. Chapter 7 – Review of tire wear emissions: a review of tire emission measurement studies: identification of gaps and future needs. 2018;147-160. http://doi.org/10.1016/b978-0-12-811770-5.00007-8
[37] Rieger M, Hettkamp P, Löhl T, Madeira PMP. Efficient engine air filter for tight installation spaces. ATZ Heavy Duty Worldw. 2019;12(2):56-59. https://doi.org/10.1007/s41321-019-0023-9
[38] Schaeffer JW, Olson LM. Air filtration media for transportation applications. Filtr Sep. 1998;35(2):124-129. https://doi.org/10.1016/S0015-1882(97)80292-3
[39] Smialek JL, Archer FA, Garlick RG. Turbine airfoil degradation in the Persian GulfWar. JOM-J Min Met Mat S. 1994;46(12):39-41. https://doi.org/10.1007/BF03222663
[40] Summers CE. The physical characteristics of road and field dust. SAE Technical Paper 250010. 1925. https://doi.org/10.4271/250010
[41] Świderski A, Borucka A, Jacyna-Gołda I, Szczepański E. Wear of brake system components in various operating conditions of vehicle in the transport company. Eksploat Niezawodn. 2019;21(1):1-9. https://doi.org/10.17531/ein.2019.1.1
[42] Thomas J, West B, Huff S. Effect of air filter condition on diesel vehicle fuel economy. SAE Technical Paper 2013-01-0311. 2013. https://doi.org/10.4271/2013-01-0311
[43] Thorpe A, Harrison RH. Sources and properties of non-exhaust particulate matter from road traffic: a review. Sci Total Environ. 2008;400:270-282. https://doi.org/10.1016/j.scitotenv.2008.06.007
[44] Tian X, Ou Q, Liu J, Liang Y, Pui DYH. Particle loading characteristics of a two-stage filtration system. Sep Purif Technol. 2019;215:351-359. https://doi.org/10.1016/j.seppur.2019.01.033
[45] Treuhaft MB. The use of radioactive tracer technology to measure engine ring wear in response to dust ingestion. SAE Technical Paper 930019. 1993. https://doi.org/10.4271/930019
[46] Wang J, Kim SC, Pui DYH. Figure of merit of composite filters with micrometer and nanometer fibers. Aerosol Sci Tech. 2008;42:722-728. https://doi.org/10.1080/02786820802249133

[47] Worek J, Badura X, Białas A, Chwiej J, Kawon K, Styszko K. Pollution from transport: detection of tyre particles in environmental samples. Energies. 2022;15:2816. https://doi.org/10.3390/en15082816

[48] Wróblewski P. Analysis of torque waveforms in two-cylinder engines for ultralight aircraft propulsion operating on 0W-8 and 0W-16 oils at high thermal loads using the diamond-like carbon composite coating. SAE Int J Engines. 2022;15:129-146. https://doi.org/10.4271/03-15-01-0005

[49] Xu H, Jin W, Luo J, Wang F, Zhu H, Liu G et al. Study of the PTFE multi-tube high efficiency air filter for indoor air purification. Process Saf Environ. 2021;151:28-38. https://doi.org/10.1016/j.psep.2021.05.007

[50] Young JM, Kelly TM, Vance L. Determination of size fractions and concentrations of airborne particulate matter generated from construction and demolition waste processing facilities. Air Qual Atmos Hlth. 2008;1:91-100. https://doi.org/10.1007/s11869-008-0015-x

[51] Ziółkowski J, Lęgas A, Szymczyk E, Małachowski J, Oszczypała M, Szkutnik-Rogoż J. Optimization of the delivery time within the distribution network, taking into account fuel consumption and the level of carbon dioxide emissions into the atmosphere. Energies. 2022;15(14):5198. https://doi.org/10.3390/en15145198

Prof. Tadeusz Dziubak, DSc., DEng. – Faculty of Mechanical Engineering, Military University of Technology, Warsaw, Poland.

e-mail: *tadeusz.dziubak@wat.edu.pl*

Article citation info:
Maciorowski D, Ludwiczak A, Kozakiewicz A. Hydrogen, the future of aviation. Combustion Engines. 2024;197(2):126-131. https://doi.org/10.19206/CE-178375

Damian MACIOROWSKI
Aleksandra LUDWICZAK
Adam KOZAKIEWICZ

Combustion Engines
Polish Scientific Society of Combustion Engines

Hydrogen, the future of aviation

ARTICLE INFO

Received: 6 December 2023
Revised: 29 December 2023
Accepted: 7 January 2024
Available online: 27 February 2024

One of the biggest challenges of modern aviation is the development of technologies that reduce or eliminate emissions of harmful combustion components into the atmosphere. European authorities are imposing increasingly stringent emissions regulations. Therefore, new models of combustion chambers, new combustion methods, as well as new types of aviation fuels must be developed.
This article presents the possibilities of using hydrogen propulsion in aviation. The reasons for conducting research on hydrogen propulsion are discussed, as well as the history of the introduction of hydrogen propulsion into aircraft engines. Problems that can be encountered in the production and storage of hydrogen are identified and explained. Proposals for the use of hydrogen combustion or the use of fuel cells to power turbine engines are also presented, and the economic aspect of this type of fuel is discussed.

Key words: *combustion chamber, hydrogen propulsion, aircraft turbine engine, emissions, hydrogen*

1. Introduction

One of the most promising energy sources for aircraft engines is hydrogen. Alongside electric propulsion and batteries, these are two main contenders to achieve zero emission goal. The energy potential of hydrogen, as well as traditional fuels, surpasses that of batteries by a significant margin. In 2020, the costs associated with hydrogen were more than 20 times lower (in €/kWh) compared to Li-Ion batteries. Anticipated cost reductions in the upcoming years are expected to occur much more rapidly for hydrogen than for batteries. This trend may lead to costs reaching approximately 30 times less than the current expenses by 2025, providing hydrogen with an even more substantial advantage [20]. Hydrogen can provide zero carbon dioxide emission. Moreover, the possibility to burn leaner mixtures, significantly reduce emissions of nitrogen oxides, which are responsible for the destruction of the ozone layer, are largely responsible for smog, and have a devastating effect on plants and other living organisms [4]. Depending on the amount of carbon dioxide produced, hydrogen can be divided into gray, blue, and green. The term gray hydrogen refers to the situation when carbon dioxide is created during its extraction or production. In the case of blue hydrogen, pollutants are captured and stored. Green hydrogen is created only through renewable energy sources, when during the electrolysis process and during its combustion, only water is being produced [25]. Looking at the advantages of green hydrogen and the fact that it has a high heating value (2.5 times that of aviation kerosene) it is highly probable that it will become an excellent fuel for turbine engines. The use of hydrogen as aviation fuel, however, is not a new idea. Hydrogen was used as early as 1943 in the United States, during work on the space program, or with the use of hydrogen to power the B-57 bomber in 1956. Besides that, the Russians designed a hydrogen-powered Tu-154 aircraft (named Tu-155 after modifications) [3]. In addition, work on smaller projects was going on all the time. Figure 1 shows some of the most significant designs for the development of hydrogen propulsion, which confirm that hydrogen is still an attractive fuel in various aspects.

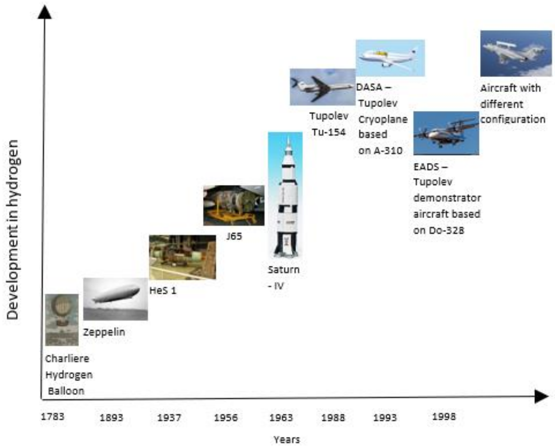

Fig. 1. Development of hydrogen propulsion over the years [15]

One of the most important issues in hydrogen propulsion is how to produce it. Three ways of producing hydrogen are the most popular: thermal dissociation, electrolysis using photonics, and bioenergy. Production can also occur using nuclear energy. Sources of hydrogen, according to 2013 data, are shown in Fig. 2. It can be noticed that: coke oven gases, fossil fuels, oils still play the largest role, but electrolysis is also used.

The properties of hydrogen are shown in the Table 1.

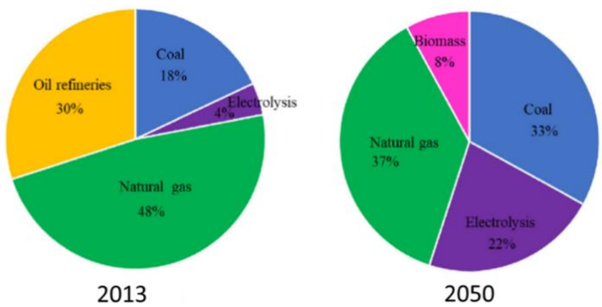

Fig. 2. Sources of hydrogen production with forecast [16]

Table 1. Properties of hydrogen and aviation kerosene [22]

	Hydrogen (LH_2)	Aircraft kerosene (Jet A)
Density [kg/m^3]	71	790
Energy density [MJ/dm^3]	10.03	36.66
Specific energy [MJ/kg]	141.8	46.4
Autoignition point [°C]	500	210
Flame temperature [°C]	2250	2230
LHV [kWh/kg]	33.3	11.9

The most economical way of production is certainly the use of fossil fuels. It uses one of three methods for this: steam reforming, auto-thermal reforming, and partial oxidation.

The most popular of these methods is the Steam Reforming Method (SRM), during which methane and steam, under the influence of an endothermic reaction, are transformed into hydrogen and carbon monoxide, as shown in equations (1)–(3).

$$CH_4 + H_2O + \text{heat} \rightarrow CO + 3H_2 \tag{1}$$

After further conversion, one gets:

$$CO + H_2O \rightarrow CO_2 + H_2 + \text{heat} \tag{2}$$

In the case of a partial oxidation reaction, we have an exothermic reaction and it looks as follows:

$$CH_4 + ½\, O_2 \rightarrow CO + 2H_2 + \text{heat} \tag{3}$$

Another method, ATR (Auto-Thermal Reforming), is a combination of the aforementioned methods. In this process, carbon monoxide is converted to hydrogen according to equation (2).

2. Operating principle of a hydrogen-powered engine

The operating principle of a hydrogen-powered turbine engine is essentially similar to that of an engine powered by traditional aviation fuel. However, there are several differences. First and already mentioned, hydrogen combustion does not contribute to greenhouse gas emissions. However, nitrogen oxides are still produced, as well as water vapor. A hydrogen-burning engine can perform flight operations with a leaner mixture (air-to-fuel ratio), which contributes to lower NO_x, but also results in reduced power output. The amount of nitrogen oxides produced can be further reduced by changes in engine design and by reducing the cruising altitude by about 2 to 3 km compared to that currently used for standard aviation fuels. Hydrogen also has the advantage of being more flammable, which contributes to lower ignition energy compared to aviation kerosene. On the other hand, hydrogen has a higher flame velocity and this can cause flame blow-out and unstable combustion chamber operation. Due to its low density, hydrogen creates also a more uniform mixture in the combustion chamber. In addition, it is also a safer fuel than kerosene, since in aviation accidents deaths are largely due to flames and harmful fumes, while with hydrogen that does not form a vapor cloud.

For engine operation, hydrogen can also be produced from renewable energy sources, through a water electrolysis reaction represented by equation (4).

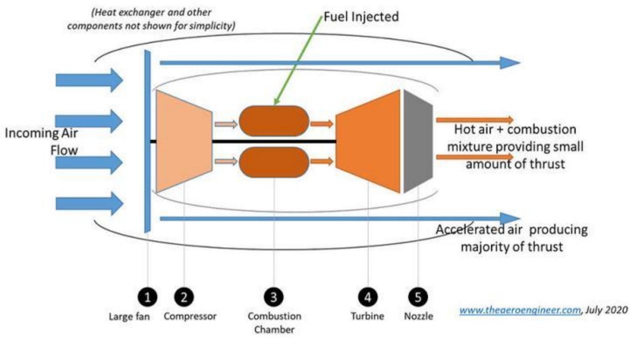

Fig. 3. Schematic of a hydrogen-powered engine [5]

$$H_2O + \text{electricity} \rightarrow H_2 + ½O_2 \tag{4}$$

During alkaline electrolysis, water on the cathode absorbs electrons to form hydrogen. The hydroxide ions move to the anode, where electrons are released. A typical reaction is shown below:

$$\begin{gathered} \text{Cathode: } 2H_2O + 2e^- \rightarrow H_2 + 2OH^- \\ \text{Anode: } 2OH^- \rightarrow ½\, O_2 + H_2O + 2e^- \\ \text{Sum: } H_2O \rightarrow ½\, O_2 + H_2 \end{gathered} \tag{5}$$

Fuel cells can also be used to burn hydrogen in aircraft engines, generating energy through a chemical reaction. The best power-to-weight ratio of the system is characterized by PEM (Proton Exchange Membrane) type fuel cells. In PEM cells, water is created on the cathode and heat is released due to the exothermic reaction. Their disadvantage is the cost of materials for their manufacture, such as carbon composites, platinum, and synthetic polymers.

In the case of PEM-type electrolysis, there is a significant improvement in the conductivity due to the use of a solid polymer membrane as an electrolyte. The reactions occurring in PEM are shown by equation (6).

$$\begin{gathered} \text{Cathode: } 2H^+ + 2e^- \rightarrow H_2 \\ \text{Anode: } H_2O \rightarrow ½\, O_2 + H^+ + 2e^- \\ \text{Sum: } H_2O \rightarrow ½\, O_2 + H_2 \end{gathered} \tag{6}$$

In the case of fuel cells, thermal management is also important. With fuel cell stacks, there is a large accumulation of heat, which can be and impediment for large aircraft.

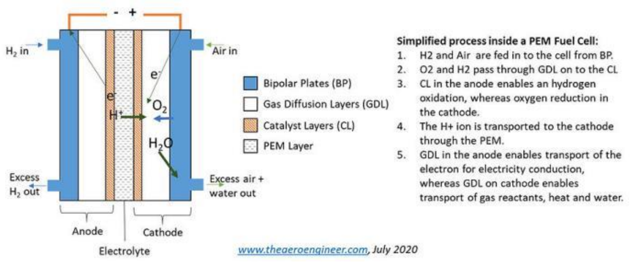

Fig. 4. Fire-fueled PEM [5]

When choosing between the presented methods of using hydrogen in aircraft propulsion, several factors must be taken into account. For long-distance aircraft, hydrogen combustion is more feasible – fuel cells will not yet produce the required energy. For General Aviation, where engines do not require as much power, fuel cells would be more recommended. The literature also suggests that the use of hydrogen combustion can reduce carbon dioxide emissions by 50–75%, while with fuel cells it is as low as 75–90% [11].

In Poland, hydrogen is currently produced from coke oven gas – a thermochemical process. Much better would be producing it by electrolysis, that is, by decomposition of water, under the influence of an electric current, into oxygen and hydrogen – then we are dealing with an electrochemical process. Electricity from hydrogen fuel is obtained through fuel cells during oxidation reactions. In the future, it will also be possible to produce hydrogen by gasifying municipal waste, agricultural waste and biomass. So this would be an additional ecological advantage of this fuel. Figure 5 shows a comparison of the climate impact of synthetic fuel, hydrogen turbines, and hydrogen fuel cells.

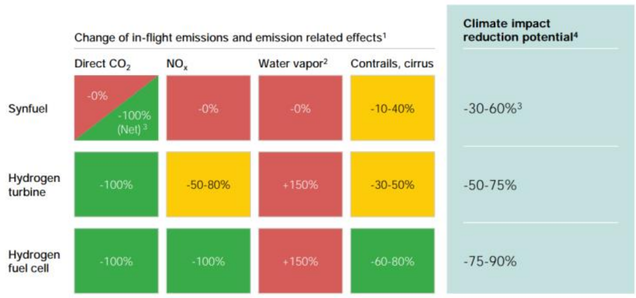

Fig. 5. Comparison of climate impacts between new fuels [11]

3. Distribution and storage

Beneath the surface of this seemingly perfect energy carrier lies a huge challenge: a storage problem. Hydrogen, with its light, gaseous nature, poses unique difficulties when it comes to storage and transportation. Unlike conventional fuels, traditional storage and transportation methods, such as tanks or pipelines, do not work for hydrogen. Instead, hydrogen requires innovative solutions that take into account its special properties and make it a viable energy source.

Hydrogen storage issues are primarily a huge challenge for materials and chemical engineering. The search is on for high-strength materials that, at the same time, do not react with hydrogen or, on the contrary, strong adsorbents that allow to densely accumulate large amounts of hydrogen on their surfaces. The focus is also on elements that form compounds with hydrogen in the form of metal hydrides or complex hydrides. The goal is to concentrate hydrogen elements in the smallest possible volume to achieve the highest volumetric energy density. This can be achieved by: compressing the hydrogen, lowering its temperature and liquefying it, or reducing the intermolecular repulsion force by forming interactions with other materials (metals) [17]. Figure 6 graphically describes the most popular hydrogen storage concepts.

Energy requirements characterize all the previously mentioned forms of increasing hydrogen density. This is an important parameter in evaluating and selecting the best hydrogen storage method. Table 2 summarizes the methods of hydrogen storage, along with information for their initial comparison.

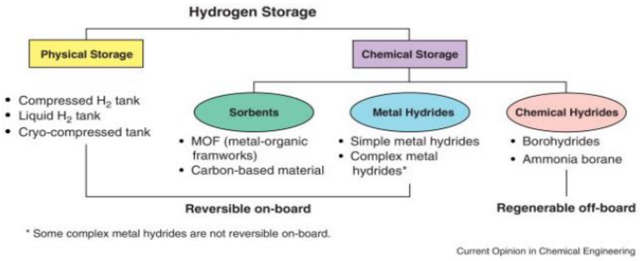

Fig. 6. Ways to store hydrogen [11]

Table 2. The summary of H_2 storage methods with characteristic parameters [26]

Storage method	Volumetric density [$kg \cdot m^{-3}$]	T [ºC]	P [bar]	Energy consumption [%LHV]
Compressed H_2	< 40	25	800	> 7
Liquid H_2	70.8	–252	1	> 45
Physisorption	20	–80	100	No specific data. Relatively low, depends on the host metal
Metal hydrides	14–156	25	1	No specific data. To provide high stability usually moderate temperatures and pressures are used for hydrogenation.
Complex hydrides	150	> 100	1	No specific data. Requires elevated temperatures for hydrogenation and dehydrogenation

4. Problems and directions of development

As mentioned earlier regarding hydrogen, one of the more difficult issues is how to store it. This gas can be stored in compressed or liquid form and in pressure or cryogenic tanks (hydrogen cooled to –252°C and therefore in a liquid state). Pressure tanks maintain a pressure of 35 to 70 MPa. This requires the use of heavy thick-walled tanks such as steel, which is highly uneconomical for aviation. It is also possible to use composite materials, which would significantly reduce the weight of the tank, unfortunately, compressed hydrogen has almost seven times lower volumetric energy density than aviation kerosene. However, when storing hydrogen in a liquid state, cryogenic tanks that maintain a low temperature are necessary. Limiting heat exchange with the environment with very good results is provided by multilayer tanks with a vacuum space between the layers [1, 2, 8, 14, 16, 18, 22]. Due to the low boiling point of hydrogen, heat exchangers also appear to be necessary in the tank itself to prevent vaporization of the hydrogen and, consequently, an uncontrolled increase in tank pressure. A different method of storing hydrogen is to store it inside the crystallographic lattice of metals and form bonds (ionic or covalent) with the metal elements to form hydrides (Fig. 7) [21]. This method is still being developed so that hydrogenation and dehydrogenation of metals can take place under the most applicable conditions (temperatures and pressures close to ambient) [24]. For the time being, however, they are not the best solution for aviation due to their weight. Their application will most likely be limited to large-scale ground storage and transportation. Due to their large surface area and thermal stability, carbon nanotubes are also being considered for hydrogen storage. The large surface area of nanotubes makes them, along with porous materials, appear to be ideal adsorbents for hydrogen storage on their surface based on van der Waals forces. The forces of these bonds, however, are so small that they play a significant role at reduced temperatures of the order of 200 K. Because of their mass and greater potential for hydrogen storage (including the potential for rapid refueling), they represent a promising hydrogen storage method for the aerospace sector [6, 19]. Worth noting are complex metal hydrides of such metals as Lithium, Manganese, Beryllium, and Al. Compared to their simpler counterparts, they often have twice the ratio of hydrogen atoms to metal atoms. The relatively high % hydrogen content by weight of the whole compound is their great advantage [12].

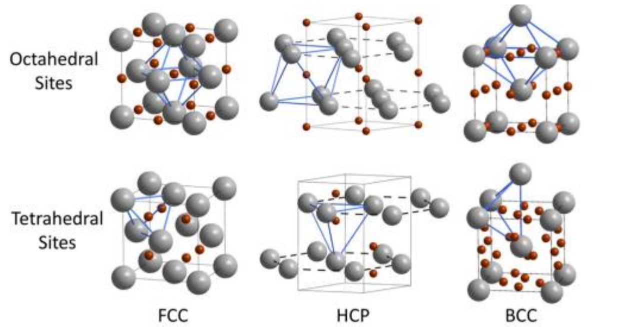

Fig. 7. Hydrogen occupies octahedral or tetrahedral sites in interstitial hydrides. Interstitial sites are marked by brown dots [13]; FCC – face centered cubic, HCP – hexagonal close-packed, BCC – body-centered cubic

Currently, airports do not have infrastructure designed for hydrogen distribution, so this will involve upgrading them. This is an extremely costly challenge, as it requires financial outlays not only for the infrastructure but also for personnel training, legal safeguards or matters related to meeting safety standards. For the moment, however, it is impossible to say that hydrogen is a 100% green solution. The process of production and storage would consume a great deal of energy. Studies also point to problems with fuel pumps and heat exchangers, making it necessary for the engine to be redesigned. In addition, the fuel tanks in the aircraft require a larger volume than the tanks for typical Jet A-1 fuel. Due to the problem of balancing the aircraft, it is suggested that the tanks be located behind the passenger cabin. However, the aircraft's center of gravity would then change. Thus, a second solution could be to place two tanks – one in front of and the other behind the cabin, or to use the space above the passenger cabin for this purpose. An example of liquid hydrogen tank placement is presented in Fig. 8.

Much more of a problem than storing hydrogen can be leaks. Due to the fact that it is a very light gas that can burn explosively by forming a mixture with air. It, therefore requires additional safeguards. Hydrogen also causes an increase in the brittleness of metal materials, which generates damage to fuel tanks and fuel system components.

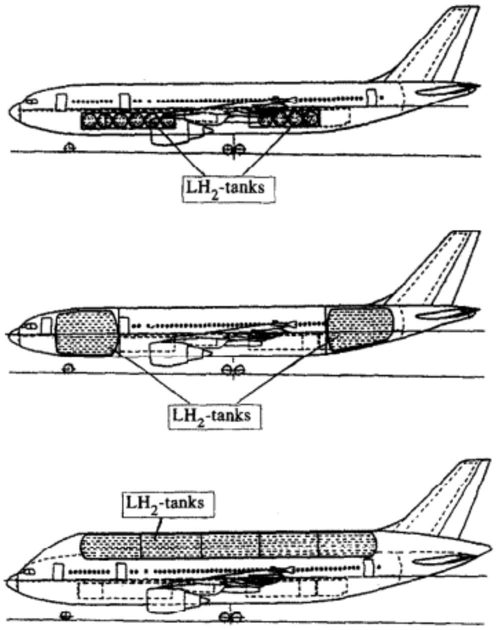

Fig. 8. Conceptual layout of fuel tanks in an aircraft [3]

5. Economic aspect

The cost of traveling on a hydrogen-powered plane will be dictated by the cost of the fuel. The price of an airline ticket includes the cost of producing the fuel but also charges for the pollutants emitted. For the moment, Jet-A fuel is much cheaper than "green solutions". Hydrogen will become profitable for airlines when there is an increase in fees for the emitted carbon footprint for traditional aviation fuels. Fuel costs depending on "carbon compensation" over the years in the European Union and the United States are presented in Fig. 9.

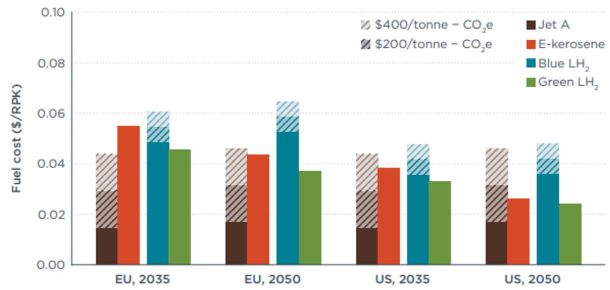

Fig. 9. Comparison of jet fuel costs [15]

The cost of aviation kerosene and "blue" hydrogen is expected to increase over the years. In contrast, the costs of synthetic fuel (E-kerosene) and "green" hydrogen will decrease. The projections are indicative of the emphasis being placed on low emissions. Hydrogen is certainly one of the fuels of the future, as it can provide much more energy than standard aviation kerosene, which would enable high-speed flights, while not contributing to carbon emissions. However, hydrogen is not a 100% environmentally friendly solution due to the condensation plumes produced during combustion, leading to climate warming in large quantities. Nevertheless, it is one of the greenest options for powering aircraft engines. A comparison of the amount of carbon dioxide produced by aviation fuels is presented in Fig. 10.

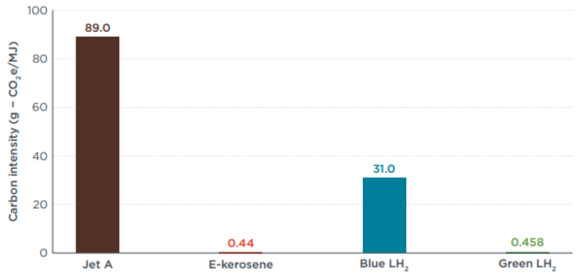

Fig. 10. Comparison of the amount of carbon dioxide produced for different aviation fuels [15]

It can be seen that among the fuel types presented, kerosene and blue hydrogen are responsible for the largest amount of generated CO_2 is accounted for by aviation kerosene and blue hydrogen. A low carbon footprint can be achieved by using synthetic fuel produced from 100% renewable sources or green hydrogen. The predictions shown in Fig. 9 represent the best-case scenario for carbon dioxide production depending on the fuel chosen, but the differences between kerosene and hydrogen are significant enough to recognize the validity of using hydrogen in air transport.

6. Internal combustion engine powered by hydrogen

When assessing the value of hydrogen as a fuel of the future, it is worth paying attention to the industry. An example from the industry can be found in the research of an automotive company that has been going on for nearly a decade. The Japanese manufacturer saw the potential in hydrogen fuel as early as 2014 and developed the technology over the following years. In addition to hydrogen cells, the use of which we can observe today by following one of the corporation's cars, a large amount of effort was put into a hydrogen-powered piston engine. Initially, hydrogen combustion was used in hydrogen-gasoline mixtures. As demonstrated by Karagöz et al. [7], among others, this is not the most efficient, as it contributes to an increase in brake specific fuel consumption (BSFC) (Fig. 11). This is due to a number of factors including: a much higher flame rate, a difference in the mixture equivalence ratio, and a much lower energy required to ignite the hydrogen resulting in a tendency for knocking combustion to occur. This problem was comprehensively overviewed by the Matla [10] indicating the compression ratio and mixture equivalence ratio influence on the knocking combustion and discussing advantages of prechamber implementation as a method of combustion control feature.

This comes to a consequent reduction in engine power of up to 25% for 50% hydrogen content in the mixture. In subsequent steps, further successes were recorded with pure hydrogen fuel stored in a high-pressure tank and then with a liquid hydrogen tank and an intermediate hydrogen gas tank. Research conducted by Longwic et al. [9] indicates however, that diesel fuel/H_2 blends have a significantly beneficial impact on the mean effective pressure. Moreover authors state that in the case of specific diesel engine 62% of carbon dioxide emission reduction was observed (for 46% of hydrogen in the blend) alongside with nearly 76% of soot reduction.

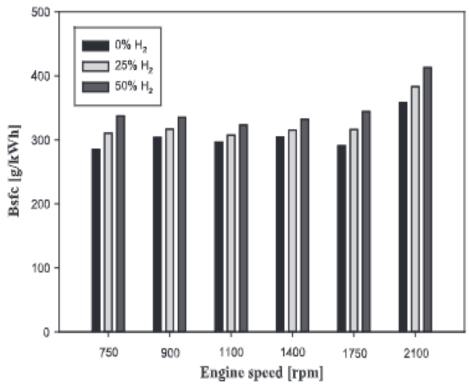

Fig. 11. Piston engine BSFC at range of different rpm for different hydrogen content in a mixture [7]

7. Conclusions

The analysis, done as a part of the research and presented in the article, provides expertise on the directions of aviation development regarding hydrogen propulsion. It needs to overcome economic and ecological difficulties but also address the demand for flights at high speeds (e.g., X-43 A). Authors conduct research on the toxicity of exhaust gases of aircraft propulsion and the possibility of using hydrogen in this type of propulsion systems. The conclusions drawn from the analyses are as follows:

Hydrogen will not fully eliminate nitrogen oxides emissions, yet it will eliminate carbon oxides emission. It is also the main competitor for batteries as a mobile clean energy carrier. The real future of hydrogen depends on efforts to overcome infrastructure limitations and unfavorable chemical properties. The most important issues in hydrogen utilization research at this point are weight issues – tanks must be developed that will reduce the weight by at least half compared to currently proposed solutions and, as always, safety issues.

Storing hydrogen in the solid state is very promising and provides a high volumetric density of hydrogen, higher than that of compressed and liquid hydrogen. However, the energy required to recover hydrogen from the structure of the compound (available at temperatures on the order of 360–500 K) limits the application of this method to above-ground hydrogen storage or large-scale transport. An exception is the storage of hydrogen on the surface of metals based on physical adsorption, but this method appears to be inferior in terms of efficiency compared to liquid hydrogen. The ongoing work and decisions made by the world's largest companies lead to believe that hydrogen has a future in aviation, and it belongs to liquid hydrogen. In favor of hydrogen is the calorific value of this fuel, although due to its low density, the tanks will have to be larger, the mass of hydrogen required for the mission will be almost three times lower than the mass of aviation kerosene while maintaining combustion efficiency.

Acknowledgments

This research was funded by the Military University of Technology, Warsaw, Poland, under research project No. UGB 733/2024.

Bibliography

[1] Ahuwalia RK, Roh H-S, Peng J-K, Papadias D. Liquid hydrogen storage system for heavy duty trucks: configuration, performance, cost, and safety. Int J Hydrogen Energ. 2023;48(35):13308-13323. https://doi.org/10.1016/j.ijhydene.2022.12.152

[2] Choi Y, Kim J, Park S, Park H, Chang D. Design and analysis of liquid hydrogen fuel tank for heavy duty truck. Int J Hydrogen Energ. 2022;47(32):14687-14702. https://doi.org/10.1016/j.ijhydene.2022.02.210

[3] Contreras A. Hydrogen as aviation fuel: a comparison with hydrocarbon fuels. Int J Hydrogen Energ. 1977;22(10/11): 1053-1060. https://doi.org/10.1016/S0360-3199(97)00008-6

[4] Głowacki P, Kalina P, Maciorowski D. Concentration values of PM 2.5 and PM 10 measured in selected locations at an airport and propagation models for NO_x and CO emitted during take-off and landing of airplanes. SAE Technical Paper 2022-01-1029. 2022. https://doi.org/10.4271/2022-01-1029

[5] How hydrogen-powered aircraft work, https://www.theaeroengineer.com/post/hydrogen-powered-aircraft (access on 01.01.2024).

[6] Jepsen LH, Paskevicius M, Jensen TR. Nanostructured and complex hydrides for hydrogen storage. Nanotechnology for Energy Sustainability (eds Raj B, Van de Voorde M, Mahajan Y). 2017. https://doi.org/10.1002/9783527696109.ch18

[7] Karagöz Y, Sandalcı T, Yüksek L, Dalkılıç AS, Wongwises S. Effect of hydrogen–diesel dual-fuel usage on performance, emissions and diesel combustion in diesel engines. Adv Mech Eng. 2016;8(8). https://doi.org/10.1177/1687814016664458

[8] Lee D-H, Kim J-D, Park T, Cho T, Kim T-W, Kim S-K et al. Evaluation of effective thermal conductivity of vacuum insulation system in cryogenic environment for liquid hydrogen vessel application. ISOPE-I-23-499. The 33rd International Ocean and Polar Engineering Conference. Ottawa 2023.

[9] Longwic R, Tatarynow D, Kuszneruk M, Wozniak-Borawska G. Preliminary tests of a Diesel engine powered by diesel and hydrogen. Combustion Engines. 2023;195(4): 35-39. https://doi.org/10.19206/CE-169485

[10] Matla J. Possible applications of prechambers in hydrogen internal combustion engines. Combustion Engines. 2022; 191(4):77-82. https://doi.org/10.19206/CE-148170

[11] McKinsey & Company. Hydrogen-powered aviation. A fact-based study of hydrogen technology, economics, and climate impact by 2050. Publication Office of the European Union. 2020. https://doi.org/10.2843/471510

[12] Milanese C, Jensen TR, Hauback BC, Pistidda C, Dornheim M, Yang H et al. Complex hydrides for energy storage. Int J Hydrogen Energ. 2019;44(15):7860-7874. https://doi.org/10.1016/j.ijhydene.2018.11.208

[13] Møller K, Jensen T, Akiba E, Hai-Wen L. Hydrogen – a sustainable energy carrier. Prog Nat Sci. 2017;27(1):34-40. http://doi.org/10.1016/j.pnsc.2016.12.014

[14] Moreno-Blanco J, Petitpas G, Esponosa-Loza F. The storage performance of automotive cryo-compressed hydrogen vessels. Int J Hydrogen Energ. 2019;44(31):16841-16851. https://doi.org/10.1016/j.ijhydene.2019.04.189

[15] Mukhopadhaya J, Rutherford D. Performance analysis of evolutionary hydrogen-powered aircraft. International Council on Clean Transportation. Washington 2022. https://doi.org/10.13140/RG.2.2.34487.60329

[16] Nayak BB, Jena H, Dey D, Oda BK, Chetia A, Brahma SK et al. Materials selection and design analysis of cryogenic pressure vessel: a review. Mater Today. 2021;47(19):6605-6608. https://doi.org/10.1016/j.matpr.2021.05.095

[17] Otto M, Chagoya KL, Blair RG, Hick SM, Kapat JS. Optimal hydrogen carrier: holistic evaluation of hydrogen storage and transportation concepts for power generation, aviation, and transportation. Journal of Energy Storage. 2022;55: 105714 https://doi.org/10.1016/j.est.2022.105714

[18] Park H, Kim J, Bergan PG, Chang D. Structural design of flexible vacuum insulation system for large-scale LH2 storage. Int J Hydrogen Energ. 2022;47(92):39179-39192. https://doi.org/10.1016/j.ijhydene.2022.09.063

[19] Park J-H, Park S-J. Expansion of effective pore size on hydrogen physisorption of porous carbons at low temperatures with high pressures. Carbon. 2020;158:364-371. https://doi.org/10.1016/j.carbon.2019.10.100

[20] Pielecha I, Engelmann D, Czerwiński J, Merkisz J. Use of hydrogen fuel in drive systems of rail vehicles. Rail Vehicles/Pojazdy Szynowe. 2022;1-2:10-19. https://doi.org/10.53502/RAIL-147725

[21] Rusman NAA, Dahari M. A review on the current progress of metal hydrides material for solid-state hydrogen storage applications. Int J Hydrogen Energ. 2016;41(28):12108-12126. https://doi.org/10.1016/j.ijhydene.2016.05.244

[22] Surer M. State of art of hydrogen usage as a fuel on aviation. European Mechanical Science. 2018;2(1):20-30. https://doi.org/10.26701/ems.364286

[23] Wingerden K, Kluge M, Habib AK, Ustolin F, Paltrinieri N. Medium-scale Tests to Investigate the Possibility and Effects of BLEVEs of storage vessels containing liquefied hydrogen. Chemical Engineering Transactions. 2022;90:547-552. https://doi.org/10.3303/CET2290092

[24] Young K, Metal hydrides. Rreference module in chemistry, molecular sciences and chemical engineering. Elsevier 2018. https://doi.org/10.1016/B978-0-12-409547-2.05894-7

[25] Yusaf T, Sustainable aviation – hydrogen is the future. Sustainability. 2022;14:548. https://doi.org/10.3390/su14010548

[26] Züttel A. Materials for hydrogen storage. Materials Today. 2003;6(9):24-33. https://doi.org/10.1016/S1369-7021(03)00922-2

Prof. Adam Kozakiewicz, DEng. – Faculty of Mechatronics, Armament Aerospace, Military University of Technology (MUT) in Warsaw, Poland.

e-mail: *adam.kozakiewicz@wat.edu.pl*

Damian Maciorowski, MEng. – Faculty of Aviation Engineering, Unmanned Technologies Center, Łukasiewicz Research Network – Institute of Aviation, Poland.

e-mail: *damian.maciorowski@ilot.lukasiewicz.gov.pl*

Aleksandra Ludwiczak, MEng. – Faculty of Mechatronics, Armament Aerospace, Military University of Technology (MUT) in Warsaw, Poland.

e-mail: *aleksandra.ludwiczak@wat.edu.pl*

Article citation info:
Urbański B, Przybyła G, Brodziński Ł, Savitskaya M. Reducing emissions of harmful substances in rally cars. Combustion Engines. 2024;197(2):132-138. https://doi.org/10.19206/CE-181525

Bartłomiej URBAŃSKI
Grzegorz PRZYBYŁA
Łukasz BRODZIŃSKI
Maryia SAVITSKAYA

Combustion Engines
Polish Scientific Society of Combustion Engines

Reducing emissions of harmful substances in rally cars

ARTICLE INFO

Received: 9 November 2023
Revised: 10 January 2024
Accepted: 16 January 2024
Available online: 10 February 2024

This article describes the issue of reducing exhaust emissions in rally cars. The issue of currently used exhaust gas aftertreatment systems is described, as well as the potential possibility of reducing emissions of harmful substances while driving on special sections. Statistical calculations were also carried out regarding the emissions of harmful substances by rally cars during the entire season of the Polish Rally Championship.

Key words: *internal combustion engines, catalytic converters, harmful substances, motorsport, car rallies*

1. Introduction

Motorsport have a history not much shorter than the car itself. Carl Benz patented his first vehicle in 1886, and the first car race took place in France 8 years later in 1894 on the Paris-Rouen route. People's tendency to compete and the desire to achieve the best possible results was the driving force behind the development of motorsports and, consequently, automotive technology. It is important to remember that many of the solutions originally used in performance cars were later adapted for use in their mass-produced counterparts [14]. Features such as double overhead cam timing (DOHC), turbocharging, four-wheel drive, disc brakes, anti-lock braking system (ABS), active suspension and even rear-view mirrors, even if they do not have their roots in motorsport, deserve recognition for their refinement and popularization in mass-produced cars. The extreme nature of competition in motor sports also allows us to obtain answers about the limits of reliability of individual components that would never be operated in such demanding conditions. Motor sports, in addition to providing a development impulse for the automotive industry, have been an object of interest for fans for many years. Both circuit racings, i.e.: FIA Formula One World Championship (F1), FIA World Endurance Championship (WEC), FIA World Touring Car Cup (WTCR) and rallies of various ranks, i.e.: FIA World Rally Championship (WRC), FIA European Rally Championship (ERC) attract the attention of the public both on race tracks and on special stages of rallies. In the case of rallies, the competition covers a much larger area than in the case of circuit racing. At the same time, in the case of rallies, fans can stay much closer to rally cars than in the case of circuit racing, because places such as the start and finish of the rally, regroups, service parks attract interest, and rally cars are within these zones easy to reach for them. In addition to fans, there is also a large group of people from the organizing committee and members of motor sports teams. Both racing and rally cars, like mass-produced cars, emit noise and harmful substances. The least advantageous in this respect is the internal combustion engine drivetrain, hybrid solutions are an intermediate solution, and electric drive systems are the most advantageous. However, these assumptions do not take into account the entire vehicle life cycle, which is increasingly turning out to be much less favourable for electric drive systems. Moreover, currently the Battery Electric Vehicle (BEV) drive system, or more precisely the battery that is the energy source, is so imperfect that this type of drive is unable to enable the car equipped with it to compete with cars equipped with a combustion or hybrid drive. At the same time, electrically powered cars are much more expensive than their combustion counterparts, and safety issues, which are of great importance in motor sport, are much more complicated. Given the above, the internal combustion engine is currently optimal for motorsport and, assuming it continues to be used there, efforts should be made to improve it in terms of noise and emissions. However, it should also be emphasized that reducing noise emissions in motor sport is not always desirable for safety reasons. The noise emitted by a rally car while driving on a special stage makes it easier for fans to recognize an approaching car. Therefore, reducing noise emissions in motor sports is not always desirable for safety reasons and an appropriate compromise must be reached. For this reason, the article will discuss issues related to harmful substances emitted by rally cars. It should be emphasized that the review of the scientific literature indicates gaps in the approaches to the topics discussed in the article. According to the research conducted by the authors, the topic of exhaust gas treatment in cars is the subject of many scientific publications, but not in the case of motor sports. Hence, according to the authors, there is a need to fill this gap, which was the reason for conducting the research described in this article.

2. The impact of harmful substances on human health

Emission of harm substances from passenger cars is a serious problem that negatively affects both human health and the natural environment. A list of harmful substances found in car engine exhaust gases and their negative disease effects is summarized in Table 1.

Table 1. List of harmful substances

Particle	Influence on human health
Particular Matter (PM_{10} and $PM_{2.5}$)	The effect of PM (including black carbon) on the incidence of cardiovascular disease, respiratory disease, lung cancer and mortality due to them as well as total mortality has been shown [8, 19].
Hydrocarbons (HC)	The research indicates a substantial elevation in the risk of Chronic Obstructive Pulmonary Disease (COPD) when individuals are exposed to high levels of environmental Hydrocarbons (HC). Moreover, there is a notable connection to systemic inflammation in this progression. In the context of short-term effects, studies within school populations have identified a decline in lung function, heightened instances of airway inflammation, and an escalated likelihood of developing lung cancer among those consistently exposed to HC over an extended period [10, 17].
Nitrogen oxides (NO_x)	Recent meta-analyses have shown an association between the concentration of NO_2 and mortality from all causes, including lung cancer and respiratory and cardiovascular diseases. Short-term exposure to NO_2 results in an increase in exacerbation of chronic respiratory diseases and bronchial reactivity in people with pre-existing lung disease [1, 4, 5].
Carbon monoxide (CO)	Generally, epidemiological studies revealed that short-term exposure to ambient carbon monoxide is linked to all-cause mortality and cardiovascular diseases [11, 13]. People with heart conditions can be particularly affected by CO causing chest pain and affecting the ability to exercise. Exposure to high concentrations of CO cause vision problems, reduce ability to work, reduced manual dexterity, and difficulty performing difficult tasks. Very high concentrations of CO can cause death [15]. Exposure to ambient CO was associated with the increase in risks for the total number of respiratory diseases such as bronchiectasis, pneumonia, and asthma [18].

All the above-mentioned harmful substances, especially with long-term exposure, have a negative impact on human health. For this reason, just like the automotive industry, motor sports also consistently attach importance to reducing emissions of harmful substances from combustion engines. Various solutions are used, including: the use of exhaust gas treatment systems, or, as mentioned earlier, changing the way the car is propelled. As in the case of mass-produced cars, in motorsport there is no single best answer to the question of what the drive system of the future should look like. Many different drivetrain concepts match those found in mass-produced cars and often go a step further. Hybrid drivetrains are used in various configurations in cars such as Rally1 in rallies, LMP1-Hybrid in long-distance circuit racing, or FIA Formula One World Championship (F1), as well as purely electric drivetrains in Formula E and FIA eTouring Car World Cup (ETCR). Alternative fuels for combustion engines are also used, the main purpose of which is not to reduce emissions of harmful substances, but can be included in activities aimed at making motorsport more environmentally friendly. The topic of the future of drive systems in sports cars is currently also discussed in rallies, where hybrid drivetrains have begun to be implemented in Rally1 cars [7], and in the case of combustion engines, alternative fuels have been introduced. P1 fuel is a synthetic fuel, CO_2 neutral and fossil fuel free. Development work is also underway on hybrid systems for lower groups of rally cars, i.e. Rally2/3/4/5 [16]. It should be emphasized, however, that at the moment, for reasons such as: availability of technology, ability to ensure safety, price-performance ratio, the optimal source of drive in motor sports is still the combustion engine. With this in mind, we should focus on how to clean exhaust gases from such engines.

3. Reducing the emission of harmful substances in rally cars

3.1. On the road sections

Regulations governing use of catalytic converters in motorsport have existed since the 1980s. The overarching document defining the rules of competition in motorsport and the technical regulations of cars is the International Automobile Federation (FIA) International Sporting Code (ISC). In art. 252 App. J 2023 to the FIA ISC stipulates that a rally car must be equipped with an original or homologated catalytic converter indicated in FIA Technical List No. 8, if such are the requirements of the country in which the competition is held [6]. Some of the more technically advanced groups of rally cars must use FIA-approved catalytic converters. This is since in groups such as Rally1, Rally2, Rally3, Rally4 or Rally5 it is permissible to change the engine to an engine other than the original one that has FIA homologation. In such a case, the catalytic converter that a given car model was originally equipped with will most likely no longer meet the requirements, because the parameters of the engine used will be completely different from those of the originally installed one. Modifications to the engine in which a car is equipped, or even replacing it with another one, include the reasons why the FIA provides for the homologation of catalytic converters intended for use in motor sports, including rallies. The catalytic converter homologation process according to the FIA procedure is delegated to the FIA National Sporting Authorities (ASN) [2]. In the case of Poland, ASN is the Polish Automobile and Motorcycle Federation (PZM). The ASN catalytic converter homologation procedure includes the following steps [2]:

– The catalytic converter is approved for a given engine capacity and a group of cars with a specific scope of modifications.
– The cross-section of the catalytic insert must be min. 100 CPSI, and its dimensions depend on the power of the engine with which they are to work.
– The minimum conversion efficiency of individual toxic substances, i.e. CO, HC and NO_x, is specified and must be met during approval tests.
– Approval tests are carried out following the ECE R15 Type I cycle.
– Tests must be performed in an independent testing laboratory.

The analysis of the actual situation shows that the catalytic converter, homologated by the FIA regulations, is not approved for a specific car model, but for the range of engine capacity and modifications of a given group of cars.

This is intended to increase the universality of catalytic converters homologated by the FIA procedure, which is key to ensuring their acceptable selling price in the case of relatively small production series occurring in motorsport. The maximum emission levels of harmful substances were not specified for homologation tests, but the minimum catalytic converter efficiencies for individual harmful substances were provided. This approach results from the need to ensure the already mentioned universality of catalytic reactors in motorsport. When, after passing the above procedure, the catalytic converter is approved, it is entered on the FIA Technical List No. 8, so it can be used in rally cars. It should be installed in a rally car in accordance with the manufacturer's guidelines so that the efficiency of the catalytic converter required by regulations is maintained.

In the discussed case, a catalytic reactor prepared by M-Sport Poland was tested. It was installed in a 2018 Ford Fiesta ST (presented in Fig. 1) test car in accordance with the requirements of the FIA Catalytic Converter Homologation Regulations.

Fig. 1. Ford Fiesta ST

Table 2 presents the basic technical data of the above-mentioned car.

Table 2. Basic technical data of the Ford Fiesta ST

Parameter	Unit	Value
Weight of the car	kg	1262
Engine type	–	Turbocharged, petrol
Number of cylinders	–	3
Displacement	cm^3	1496
Maximum power	kW	147
Maximum torque	Nm	290
Transmission	–	Six speed manual

The tests were carried out on a chassis dynamometer AVL Zoelner 48" 2WD at a BOSMAL Automotive Research and Development Institute Ltd and the emissions of harmful substances were recorded by the exhaust emission analysis system AVL AMA i60 and CVS system AVL i60 LD LE. Exhaust emissions were measured before and after the catalytic converter. The tests were carried out in accordance with the procedure according to the ECE-R15 Type 1 driving cycle, also known as UDC (Urban Driving Cycle). The ECE-R15 Type I cycle is shown in Fig. 2.

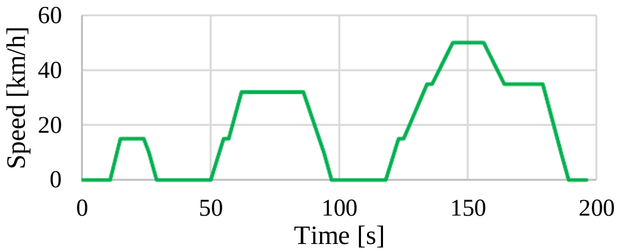

Fig. 2. ECE-R15 Type 1 cycle

The ECE-R15 Type I cycle is an urban driving cycle that was introduced in 1970. Later, after minor modifications, it became part of the EUDC extra-urban driving cycle, the ECE-R101 regulations introduced in 1990, and part of the NEDC cycle used until 2017. It was then replaced by the WLTC cycle [12]. The ECE-R15 type 1 cycle represents low-speed driving in large European cities. The FIA's motivation for choosing this particular driving cycle for testing catalytic converters used in motor sports can be explained by the fact that the main objective in motor rallies is to reduce emissions on the road sections, which constitute approximately 75% of the entire rally route. The average speed on road sections is set so that crews can cover a given section in accordance with road traffic regulations.

The efficiency of the catalytic converter as defined in the FIA regulations can be described (1):

$$K_{(X)} = \frac{Y_{(X)} - Z_{(X)}}{Y_{(X)}} \cdot 100\% \quad (1)$$

where: K(X) – catalytic converter efficiency, X – selected toxic component of exhaust gases, Y – mole fraction of X upstream of the catalytic converter, Z – mole fraction of X after the catalytic converter.

In accordance with the FIA procedure, tests of CO, HC and NO_x mole fractions were carried out both before and after the catalytic converter. The research results were obtained and are presented in Table 3.

Table 3. Results of tests on the efficiency of the catalytic converter

Particle	Pre-cat [g/km]	Post cat [g/km]	$K_{(X)}$	$K_{(X)}$ required by the FIA
CO	6.512	0.198	97.0%	75%
HC	3.288	0.011	99.7%	N/A
NO_x	0.770	0.024	96.9%	N/A
HC + NO_x	4.058	0.035	99.1%	60%

As it can be noted, the catalytic converter met the FIA efficiency requirements. It is interesting to compare the obtained results with the applicable EURO exhaust emission standards [12]. A summary of the maximum emission levels of individual harmful substances is presented in Table 4 below.

Table 4. Maximum emission levels for given Euro standard

	CO [g/km]	THC + NO_x [g/km]	THC [g/km]	NO_x [g/km]
Euro 1	2.72	0.97	–	–
Euro 2	2.2	0.5	–	–
Euro 3	2.3	–	0.2	0.15
Euro 4	1	–	0.1	0.08
Euro 5	1	–	0.1	0.06
Euro 6	1	–	0.1	0.06

Comparing table values from the results presented in Table 3, it can be concluded that the tested car equipped with a catalytic converter approved by the FIA, taking into account the emission of harmful substances, would meet standards up to and including Euro 6. It should be emphasized that these emission values cannot be directly compared. In the case of Euro standards, the homologation testing procedure is different than in the case of the FIA standard, which specifies the test cycle according to ECE R15 Type 1, and not NEDC, WLTP or RDE. However, the ECE-R15 Type 1 Urban Driving Cycle is the least favourable case in terms of emissions (variable engine loads, including stops) [3, 9], it is possible to analyse the amount of harmful substances emitted by rally cars with and without exhaust aftertreatment systems on road sections. It should be emphasized here that the engine maps of modern rally cars are calibrated separately for road sections and separately for special stages. Thanks to this, if full engine operation is not required on the access section, the map can meet the conditions ensuring optimal operating parameters of the catalytic converter. The main such parameter is the excess air coefficient λ. For $\lambda = 1$, the catalyst is characterized by the highest NO_x reduction efficiency and high CO and HC oxidation efficiency.

Taking into account the above results, it was decided to carry out statistical calculations regarding the emissions of harmful substances during the PZM Polish Rally Championship (RSMP) season for two cases. In the first case, the emissions of harmful substances throughout the season were analysed for one car, while in the second case, the average number of crews entered in the rally was analysed. All rallies in the PZM RSMP season were included in the analysis. In the 2023 season, they consisted of rallies with the lengths specified in Table 5. The emissions of individual harmful substances were compared without a catalytic converter and with a catalytic converter installed in the car.

Assuming the above distances, it was possible to estimate the emissions of harmful substances from the entire RSMP season in two versions. In the first case, rally cars are not equipped with a catalytic converter approved by the FIA, while in the second case it is installed in the car. It should be noted that the following analyses assume that all rally cars are the same and are equipped with the same catalytic converters. However, this simplification seems to be good enough for statistical analysis, because the Rally3 group cars are in the middle of rally cars groups in terms of generated power. This should also translate into the average amount of fuel burned and, consequently, the emission of harmful substances for the entire group of rally cars.. The results obtained for one car based on calculations are presented in Fig. 3.

Table 5. Route characteristics in the Polish Rally Championship season 2023

No.	Rally	Road Sections, [km]	Special Stages, [km]	Total, [km]
1.	51. Rajd Świdnicki	261.20	132.60	393.80
2.	79. Rajd Polski	737.41	182.06	919.47
3.	42. Rajd Podlaski	418.48	110.60	529.08
4.	Rajd Małopolski	202.88	118.18	321.06
5.	32. Rajd Rzeszowski	445.12	152.94	598.06
6.	Rajd Śląska	484.78	150.34	635.12
7.	68. Rajd Wisły	364.25	124.36	488.61
Total:		2914.12	971.08	3885.20

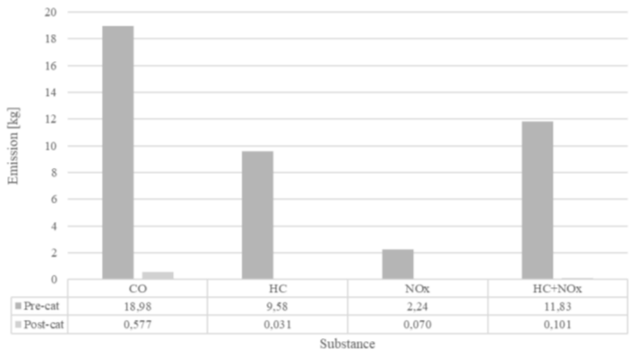

Fig. 3. Results of emissions of harmful substances on road sections for the entire RSMP season for one rally car

Moreover, by assuming the average number of starting cars in the RSMP based on the average number of entries from all rounds, which is 47 crews, it was possible to estimate how many harmful substances the RSMP rallies emits on the road sections throughout the season. The results are presented in Fig. 4.

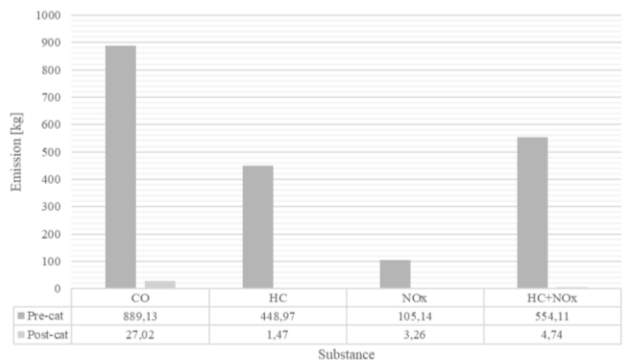

Fig. 4. Results of emissions of harmful substances on approach sections for the entire RSMP season for the average number of rally cars

The graphs show the significant impact of the catalytic reactor on reducing the emission of harmful substances. The difference between a car equipped with a catalytic converter and a car without it is significant, because for each of the harmful substances the reduction in their amount reaches almost 100%, in each case exceeding 97%. The presented data well justify the need to use exhaust gas treatment systems in rally cars. Even taking into account the relatively small number of rally cars that are only on the road temporarily during sporting events. It should be noted that the tested catalytic converter significantly exceeded the standards set by the FIA, which means that it stood out positively from the regulations in force in motorsport. Comparing the obtained analysis results with the situation of all road transport in Poland, in the case of CO the entire emission season of rally cars is given in Table 4. In the case of CO, it is 0.09 ‰ of this emission, and NO_x 0.02 ‰. As it can be noted, rallies constitute a marginal part of road transport in Poland.

3.2. On the special stages

Special stages of a car rally have different characteristics than road sections. Driving on a special stage is a time trial, so the crews try to achieve the shortest possible travel time. In such conditions, the engine of a rally car works almost all the time under full load. The amount of fuel burned in this case is much higher than when driving on the road section. Additionally, rally cars use the Anti-Lag System (ALS), whose task is to maintain a constant, high turbocharger speed when the foot is taken off the throttle pedal by fuel injection at these moments. Apart from the fact that ALS undoubtedly has a positive effect on the performance of a rally car, it also has a negative impact on fuel consumption and an increase in engine operating temperature in engines with an exhaust manifold integrated with the head. Higher fuel consumption directly translates into increased emissions of harmful substances, so it is worth considering replacing the ALS system with another one that will translate into increased fuel consumption to a lesser extent, or preferably none at all.

To show the benefits that can be obtained by replacing the ALS system with another one, tests were carried out during which the Fiesta ST Rally3 (model presented in Fig. 5) built by M-Sport Poland moved along a designated route in 3 modes, i.e.: ALS off, ALS at the highest level of turbocharger support (ALS3) and ALS at an intermediate level of turbocharger support (ALS2). The data was recorded by a data acquisition system installed in the car. Table 6 presents the basic technical data of the above-mentioned car.

Fig. 5. Ford Fiesta ST Rally3

Table 6. Basic technical data of the Ford Fiesta ST Rally3

Parameter	Unit	Value
Weight of the car	kg	1210
Engine type	–	Turbocharged, petrol
Number of cylinders	–	3
Displacement	cm^3	1496
Maximum power	kW	158 (FIA 30 mm restrictor)
Maximum torque	Nm	400
Drivetrain	–	Constant four-wheel drive
Transmission	–	Five-speed sequential gearbox

Based on the tests performed, fuel consumption results were obtained depending on the ALS system used. They are presented in Fig. 6.

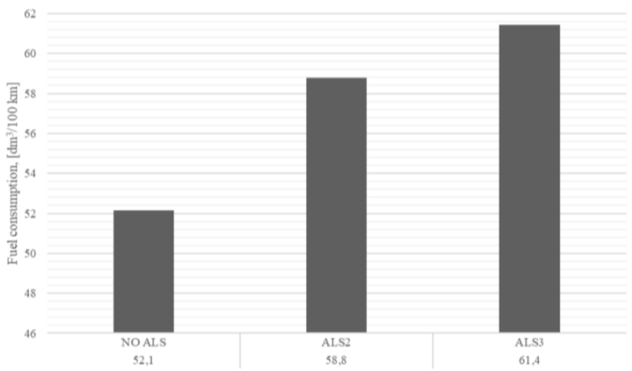

Fig. 6. Comparison of fuel consumption for different levels of ALS operation

As can be seen, the difference in fuel consumption by a rally driver on a special stage with the ALS system on and off can be up to 9.3 dm^3/100 km. Even the intermediate ALS mode increases fuel consumption by 6.6 dm^3/100 km. A comparison of fuel consumption on Special Stages throughout the RSMP season was made, in accordance with Table 5. As a result of the calculations, fuel consumption values per car and the average number of cars entered in the rally were obtained and are presented in Table 7.

Table 7. Calculated fuel consumption for the entire RSMP season for the average number of rally cars (47)

	NO ALS	ALS1	ALS2
Fuel consumption per 1 car, [dm^3]	506.37	570.92	596.53
Fuel consumption per 47 cars, [dm^3]	23,799.58	26,833.26	28,037.12

Analysing the entire RSMP rate in accordance with the adopted assumption, i.e. assuming the average number of registered crews throughout the entire season 47, savings in fuel consumption without the use of the ALS system may amount to approximately 15%. This is an important value, especially since reducing fuel consumption will also reduce emissions of harmful substances from rally cars.

In the article devoted to alternative 48 V drive systems in rally cars, the issue of using an electrically driven compressor was raised [16]. Such a device would allow, to some extent, to provide the required boost pressure in a situation where the turbocharger does not have the required rotational speed. Thus, thanks to the use of such a device, it would be possible to limit the operation of the ALS system, which would result in achieving the assumed goal, i.e. reducing fuel consumption and, consequently, harmful substances consumed by the rally car. while driving on the Special Stage. The next step will be to test a rally car engine equipped with an electrically driven compressor. The conclusions will allow, at least initially, to answer the question to what extent it will be possible to limit the use of the ALS system in a rally car.

4. Summary

Due to the recent change in the Euro 7 standard, combustion engines, also in small cars, which are the basis for building rally cars, will remain available for at least a few more years. Moreover, in the case in question, i.e. rally cars powered solely by electricity with an energy source in the form of batteries, there is a significant difference in the performance of the cars in favour of cars equipped with combustion engines. With this in mind, it seems crucial to improve combustion engines in order to reduce emissions of harmful substances, including fuel consumption, rather than to completely abandon them. On the one hand, there are options regarding exhaust gas treatment systems, which, as presented in this article, allow for:

– reducing emissions of harmful substances such as CO, HC and NO_x by over 96% depending on the substance.
– in the scale of the entire analysed RSMP season, this shows the large scale of this action, which can be counted in hundreds of kilograms when it comes to reducing emissions from the entire rate.

However, it should be borne in mind that exhaust gas treatment systems have a negative impact on engine parameters, which are crucial in car rallies, so this should be taken into account when implementing them.

On the other hand, in addition to exhaust gas treatment systems, the possibilities of using electrical devices can also be used, thus creating hybrid drive systems. Reducing fuel consumption also directly reduces the emission of harmful substances. For this reason, work is being carried out to verify the effect of using a 48V hybrid system consisting of BISG and an electric compressor. The next direction of work should be further tests of the above solutions in conditions similar to those of a real rally.

Acknowledgements

This work was supported by M-Sport Poland sp. z o.o.

Nomenclature

ABS	anti-lock braking system
ALS	turbocharger anti lag system
ASN	national sporting authority
BEV	battery electric vehicle
CPSI	cells per square inch
DOHC	double overhead camshaft
ECE	United Nations Economic Commission for Europe
ERC	FIA European Rally Championship
ETCR	FIA Etouring Car World Cup
F1	FIA Formula One World Championship
FIA	International Automobile Federation
ICE	internal combustion engine
PZM	Polish Automobile and Motorcycle Federation
RDE	real driving emissions
RSMP	Polish Rally Championship
UDC	urban driving cycle
WEC	FIA World Endurance Championship
WLTP	worldwide harmonised light vehicle test procedure
WRC	FIA World Rally Championship
WTCR	FIA World Touring Car Cup

Bibliography

[1] Faustini A, Rapp R, Forastiere F. Nitrogen dioxide and mortality: review and meta-analysis of long-term studies. Eur Respir J. 2014;44(3):744-753. https://doi.org/10.1183/09031936.00114713

[2] FIA Regulations for the homologation of catalytic converters. FIA 2009.

[3] Fontaras G, Franco V, Dilara P, Martini G, Manfredi U. Development and review of Euro 5 passenger car emission factors based on experimental results over various driving cycles. Sci Total Environ. 2014;468-469:1034-1042. https://doi.org/10.1016/j.scitotenv.2013.09.043

[4] Hamra GB, Laden F, Cohen AJ, Raaschou-Nielsen O, Brauer M, Loomis D. Cancer and exposure to nitrogen dioxide and traffic: a systematic review and meta-analysis. Environ Health Perspect. 2015;123(11):1107-1112. https://doi.org/10.1289/ehp.1408882

[5] Hoek G, Krishnan RM, Beelen R, Peters A, Ostro B, Brunekreef B et al. Long-term air pollution exposure and cardio-respiratory mortality: a review. Environ Health. 2013;12(1): 43. https://doi.org/10.1186/1476-069X-12-43

[6] International Sporting Code 2023 Appendix J Art. 252 General Prescriptions for Cars of Group N, A (and Extensions) and R-GT. FIA 2023. https://www.fia.com/sites/default/files/252_2023_wmsc_2023.10.19_pj.pdf (accessed on 07.11.2023).

[7] International Sporting Code 2023 Appendix J Art. 262 Specific Regulations for Rally1 Cars. FIA 2023. https://www.fia.com/sites/default/files/252_2023_wmsc_2023.10.19_pj.pdf (accessed on 07.11.2023).

[8] Janssen NA, Hoek G, Simic-Lawson M, Fischer P, van BreeL, ten Brink H et al. Black carbon as an additional indicator of the adverse health effects of airborne particles compared with PM10 and PM2.5. Environ Health Perspect. 2011;119(12):1691-1699. https://doi.org/10.1289/ehp.1003369

[9] Koszałka A, Szczotka A, Suchecki A. Comparison of fuel consumption and exhaust emissions in WLTP and NEDC procedures. Combustion Engines. 2019;179(4):186-191. https://doi.org/10.19206/CE-2019-431

[10] Letelier P, Saldías R, Loren P, Riquelme I, Guzmán N. MicroRNAs as potential biomarkers of environmental exposure to polycyclic aromatic hydrocarbons and their link with inflammation and lung cancer. Int J Mol Sci. 2023;24(23): 16984. https://doi.org/10.3390/ijms242316984

[11] Liu C, Yin P, Chen R, Meng X, Wang L, Niu Y et al. Ambient carbon monoxide and cardiovascular mortality: a nationwide time-series analysis in 272 cities in China. Lancet Planet Health. 2018;2(1):e12-e18. https://doi.org/10.1016/S2542-5196(17)30181-X

[12] Passenger cars and light duty vehicles emissions standards. BorgWarner 2023. https://www.borgwarner.com/technologies/emissions-standards (accessed on 07.11.2023).

[13] Tian L, Qiu H, Pun VC, Ho K-F, Chan CS Yu I. Carbon monoxide and stroke: a time series study of ambient air pollution and emergency hospitalizations. Int J Cardiol. 2015; 201:4-9. https://doi.org/10.1016/j.ijcard.2015.07.099

[14] Skeete JP. The obscure link between motorsport and energy efficient, low-carbon innovation: evidence from the UK and European Union. J Clean Prod. 2019;214:674-684. https://doi.org/10.1016/j.jclepro.2019.01.048
[15] Townsend CL, Maynard RL. Effects on health of prolonged exposure to low concentrations of carbon monoxide. Occup Environ Med. 2002;59(10):708-711. https://doi.org/10.1136/oem.59.10.708
[16] Urbański B, Przybyła G. Hybrid drivetrain systems 48 V in rally cars. Combustion Engines. 2021;187(4):96-101. https://doi.org/10.19206/CE-141882
[17] Xiao Y, Zhang L, Liu H, Huang W. Systemic inflammation mediates environmental polycyclic aromatic hydrocarbons to increase chronic obstructive pulmonary disease risk in United States adults: a cross-sectional NHANES study. Front Public Health. 2023;11:1248812. https://doi.org/10.3389/fpubh.2023.1248812
[18] Zhao Y, Hu J, Tan Z, Liu T, Zeng W, Li X et al. Ambient carbon monoxide and increased risk of daily hospital outpatient visits for respiratory diseases in Dongguan, China. Sci Total Environ. 2019;668:254-260. https://doi.org/10.1016/j.scitotenv.2019.02.333
[19] Zhu X, Liu B, Guo C, Li Z, Cheng M, Zhu X et al. Short and long-term association of exposure to ambient black carbon with all-cause and cause-specific mortality: a systematic review and meta-analysis. Environ Pollut. 2023;324:121086. https://doi.org/10.1016/j.envpol.2023.121086

Bartłomiej Urbański, MEng. – Faculty of Energy and Environmental Engineering, Silesian University of Technology/M-Sport Poland sp. z o.o., Poland.
e-mail: *bartlomiej.urbanski@polsl.pl*

Łukasz Brodziński, MEng. – M-Sport Poland sp. z o.o., Poland.
e-mail: *lbrodzinski@m-sport.co.uk*

Grzegorz Przybyla, DSc, DEng. – Associate professor at Silesian University of Technology, Institute of Thermal Technology, Poland.
e-mail: *grzegorz.przybyla@polsl.pl*

Maryia Savitskaya, MD. – The Ludwika Rydygiera Specialist Hospital in Kraków, Poland.

Article citation info:
Zimakowska-Laskowska M, Laskowski P. Comparison of pollutant emissions from various types of vehicles. Combustion Engines. 2024;197(2):139-145. https://doi.org/10.19206/CE-181193

Magdalena ZIMAKOWSKA-LASKOWSKA
Piotr LASKOWSKI

Combustion Engines
Polish Scientific Society of Combustion Engines

Comparison of pollutant emissions from various types of vehicles

ARTICLE INFO

Received: 5 September 2023
Revised: 27 October 2023
Accepted: 15 January 2023
Available online: 7 March 2024

This article compares the equivalent emissions from battery electric vehicles (BEVs) with those of internal combustion engines vehicles (ICEVs) and hybrid vehicles (HV). The considerations focused on the dependence of the equivalent emission from electric cars on the official/national Polish energy mix (which is still mainly based on hard coal). The results of mathematical simulations of the impact of the fuel type on pollutants' emissions are presented. The article also focuses on the effects of the fuel used in internal combustion engines vehicles (LPG, CNG, petrol, diesel, hydrogen) and the official/national Polish energy mix for battery electric vehicles on carbon dioxide (CO_2), nitrogen oxides (NO_x), particulate matter (PM), carbon monoxide (CO) and sulphur dioxide (SO_2) emissions.

Key words: *ICEV, BEV, emission, energy mix, air pollution*

1. Introduction

The negative impacts of air pollution on public health and the environment have been a cause of global concern. The Paris Climate Agreement of 2015 [20] outlined a goal to achieve carbon neutrality by 2050 and a target for carbon reduction by 2030, with each country taking up a role in achieving this. The transportation sector is a significant contributor to air pollution, with fossil fuels in internal combustion engines producing carbon dioxide (CO_2).

Road transport is responsible for around one-fifth of the EU's total greenhouse gas emissions, with emissions showing an increasing trend. The case for moving towards zero-emission mobility [4, 17] becomes even more substantial and more apparent in the context of the drive to reduce energy dependence as soon as possible in the EU, given that road transport also accounts for one-third of the EU's total final energy consumption.

The European Green Deal [20] stipulates the goal of attaining climate neutrality by 2050 and an ambitious interim target of reducing net greenhouse gases (GHGs) emissions by at least 55% by 2030 relative to 1990 levels. This is in line with the EU's dedication to global climate action as per the Paris Agreement [17, 20].

The European Green Deal and the goal of achieving climate neutrality are having an impact on the progress of battery electric vehicles (BEVs) [5, 17, 20].

Electric vehicles are often seen as an environmentally-friendly form of transportation, but the emissions produced by them are dependent on the types of fuels used to produce electricity in the country where they are being used. It can refer to vehicles powered mainly from renewable energy sources as being "100% ecological" or "climate-friendly" [18].

According to the latest submission of the national inventory of air pollutant emissions [1, 14, 15], most of the public power in Poland is generated using solid fuels – that's 81% of the total energy mix. Mainly, this means using of hard coal and lignite. The energy sources used in Poland affect the air pollutants generated by electric vehicles, resulting in a transfer of carbon emissions from other sectors into the road transport sector. The effects that electric vehicles have on the environment are largely determined by the energy sources used in the countries where they are produced.

Electric vehicles in Poland can be seen as a source of carbon emissions that have been transferred from the public power and energy sector to the transportation sector. This implies that the environmental impact of electric vehicles is largely dependent on the type of energy that is used to produce electricity in the country. The study [8] shows that the amount of air pollutants created by battery electric vehicles (BEVs) and internal combustion engines vehicles (ICEVs) can be compared based on the energy sources used to produce electricity. This gives researchers a chance to examine the environmental impacts that may come about because of battery electric vehicles and the utilization of energy generated from non-renewable sources [8].

The importance of battery electric vehicles in meeting environmental objectives cannot be overstated, however the extent of their environmental advantages varies based on a variety of factors such as the energy source, the type of air pollutants and greenhouse gases present, and the specific kind of electric vehicle. Undoubtedly, the advantage of battery electric vehicles is shifting the source of transport-related air pollution from roads to power plants [7]. The potential of electric vehicles to cut back on-air pollutants and greenhouse gases may not be fully realized if the electricity used to power them is sourced from non-renewable sources such as coal and oil [18]. In China, research carried out by Huo et al. [6] indicates that electric vehicles can lead to a three to tenfold increase in SO_2 emissions and a doubling of NO_x emissions when compared to internal combustion engine vehicles (ICEVs) [18], given that the majority of electricity is generated from coal.

Electric vehicles do not have the capability to completely reduce all air pollutants and greenhouse gas emissions. Huo et al. [6] demonstrated that battery electric vehicles technology has the potential to reduce greenhouse gas emissions by 20%. However, it may also augment the concentrations of particulate matter (PM both PM10 and

PM2.5), nitrogen oxides (NO_x) and sulphur dioxide (SO_2). According to Nichols et al. [15], battery electric vehicles are capable of decreasing emissions of greenhouse gases, NO_x, and PM10, yet produce substantially higher SO_2 emissions than cars with an internal combustion engine. There is proof that the particulate matter generated beyond exhaust systems varies between battery electric vehicles and internal combustion engine vehicles, as the mass of the vehicle can affect non-exhaust emissions [19, 20]. The amount of wear and tear on tires, brakes, and roads increases significantly for heavy vehicles (50% more than on medium and small cars, which weigh 1600 kg and 1200 kg, respectively) [19]. On average, electric vehicles are about 24% heavier than cars with combustion engines [21, 22].

In addition to energy generation and consumption, the type of electric vehicle is also an essential factor in the environmental benefits of electric mobility. Electric vehicles fall into four categories:

– Hybrid Electric Vehicles (HEV), which run primarily on gasoline with a small battery assisting the internal combustion engine.
– Plug-in Hybrid Electric Vehicles (PHEV), which run on both gasoline and Diesel independently and electricity.
– Battery Electric Vehicles (BEVs) that are powered solely by electricity.
– Fuel Cell Electric Vehicles (FCEVs) which are powered by hydrogen.

Figure 1 compares various types of electric vehicles based on their energy source, consumption, and emissions from exhaust pipes and power plants.

Weiss et al. [23] suggest that battery electric vehicles with high battery capacity can produce between two and three times more greenhouse gases than hybrid electric vehicles, depending on the electricity source and the timing of the battery electric vehicles charging [10].

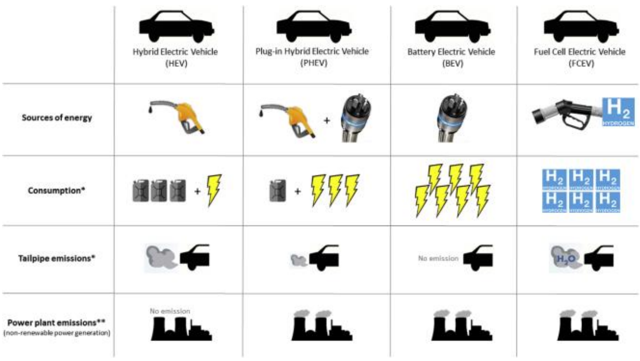

Fig. 1. Comparison of source and energy consumption and tailpipe emissions and energy generation for different types of electric vehicles (EV) [22] (*) The data displayed here is intended to be seen, not analysed. It is not organized or measured in any particular way; **) The technology used by each plant may differ, so we have not supplied numerical data for visualization [22]

The energy mix in Poland is based mainly on fossil fuels. However, a slight increase in the share of renewable sources is noticeable, whereas it is still a small share of the entire energy mix (Fig. 2) [23].

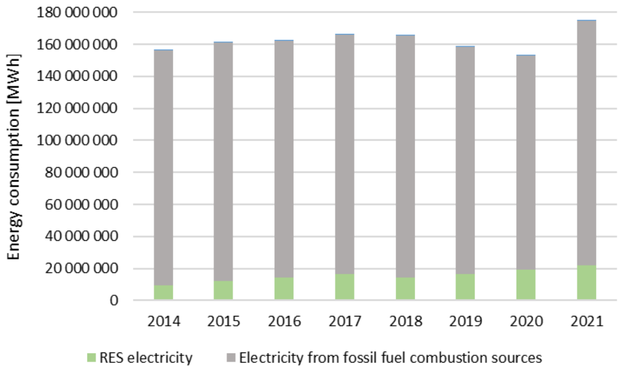

Fig. 2. Polish energy mix (based on [1])

It is apparent that the environmental effects of electric vehicles vary based on the particular circumstances.

Some studies have only concentrated on specific emission chains, including production [11], energy generation [9, 22] and operation [6]. To this end, there is an urgent need for a thorough review of literature studies that can help fully assess the environmental aspects of electric vehicles (EVs), given the issue's complexity and scope. This study is a step in that direction.

2. Materials and Methods

This article examines the emissions of harmful substances given off by different types of vehicles, including conventional internal combustion engine vehicles (ICEV), hybrids, plug-in hybrids, and battery electric vehicles (BEV). It looks at the emissions from different types of passenger cars, such as minis, smalls, mediums and large SUVs and executives, by comparing them in pairs.

The authors employed the COPERT (COmputer Programme to calculate Emissions from Road Transport) software for simulating emissions of internal combustion engines vehicles and energy consumption by battery electric vehicles. The methodology followed the guidelines set out by the 2006 IPCC Guidelines for National Greenhouse Gas Inventories and EMEP/EEA Air Pollutant Emission Inventory Guidebook 2019 [16], which are basic guidelines for inventories of greenhouse gases and air pollutants.

The equivalent emissions from battery electric vehicles were calculated from the formula given below (1):

$$\mathrm{E_i} = \mathrm{E}_c \times \mathrm{EF_i} \times \mathrm{M} \tag{1}$$

where: E_i – emission of pollutant i [g/km], E_c – the amount of electric energy used, measured [Wh], EF_i – emission factor of pollutant i for electricity produced by installations for combustion of fuels [g/Wh] based on [23], M – distance driven by vehicle [km].

Two types of simulations were carried out:

– comparison of emissions for BEV, hybrid, PHEV, and ICE vehicles
– comparison of emission equivalent with BEV for various energy mixes, based on indicators determined in the National Centre for Emissions Management (KOBiZE) studies [1].

Simulations were carried out, assuming that vehicles from each type of passenger cars travelled 10,000 km in each segment of passenger cars (Mini, Small, Medium and Large-SUV-Executive).

3. Results

Figures 3–22 show the influence of the vehicle type on emissions. The dependence is presented for each segment of passenger cars (Mini, Small, Medium and Large-SUV-Executive).

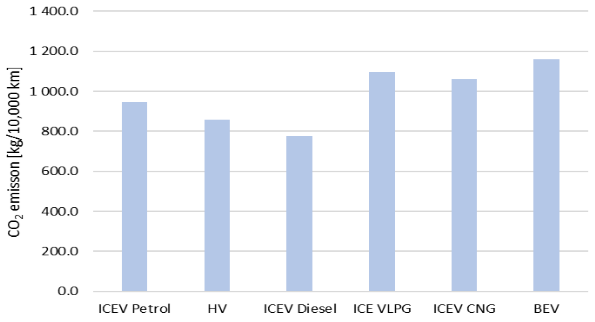

Fig. 3. Comparison of carbon dioxide (CO_2) emissions for the selection of Mini Passenger cars

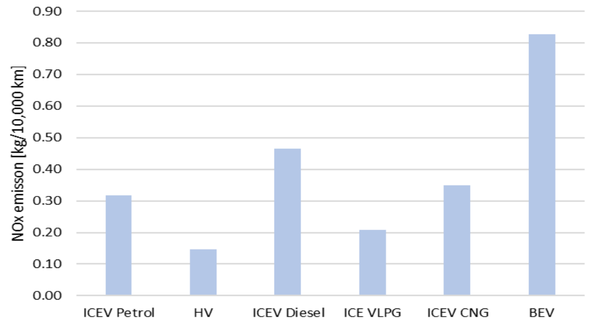

Fig. 4. Comparison of nitrogen oxides (NO_x) emissions for the selection of Mini Passenger cars

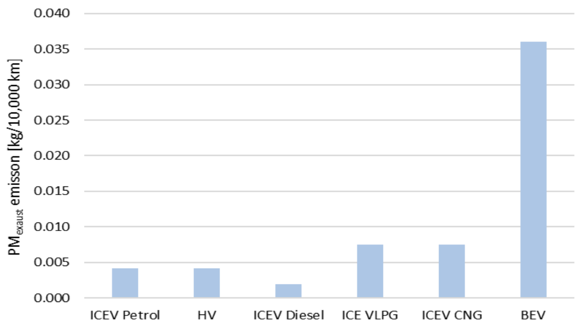

Fig. 5. Comparison of exhaust particulate matter (PM_{exh}) emissions for the selection of Mini Passenger cars

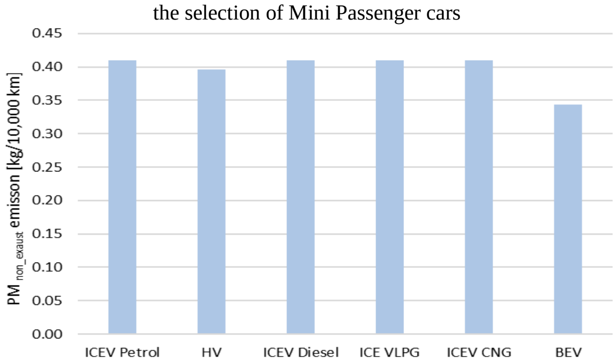

Fig. 6. Comparison of non-exhaust particulate matter ($PM_{non\text{-}exh}$) emissions for the selection of Mini Passenger cars

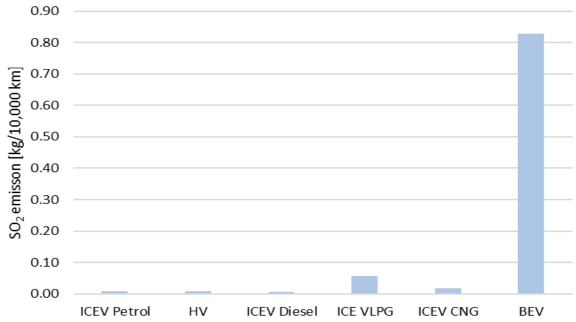

Fig. 7. Comparison of sulphur dioxide (SO_2) emissions for the selection of Mini Passenger cars

The simulation results presented in Fig. 3–22 show that, for the passenger car in the Mini segment, the equivalent emissions of CO_2, NO_x, PM_{exh} (PM emission from the exhaust system) and SO_2 are higher for battery electric vehicles than for internal combustion engines vehicles. The most significant difference can be seen for SO_2, PM_{exh} and NO_x. The simulations also show that in the case of the Mini segment, CO_2 and PM_{exh} emissions are the lowest for diesel internal combustion engines. In the case of NOx emissions, hybrid vehicles (HVs) and internal combustion engines LPG have the lowest emissions.

However, concerning $PM_{non\text{-}exh}$ emissions, it can be seen that the lowest emissions are from battery electric vehicles.

For the passenger car segment in the Small segment, similar to the Mini segment, the equivalent emissions of CO_2, NO_x, $PM_{exh,}$ and SO_2 are higher for battery electric vehicles than for vehicles with internal combustion engines.

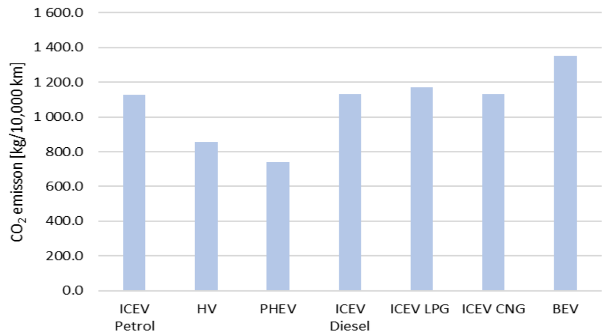

Fig. 8. Comparison of carbon dioxide (CO_2) emissions for the selection of Small Passenger cars

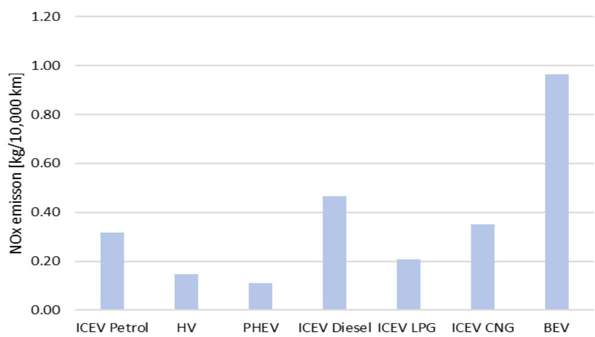

Fig. 9. Comparison of nitrogen oxides (NO_x) emissions for the selection of Small Passenger cars

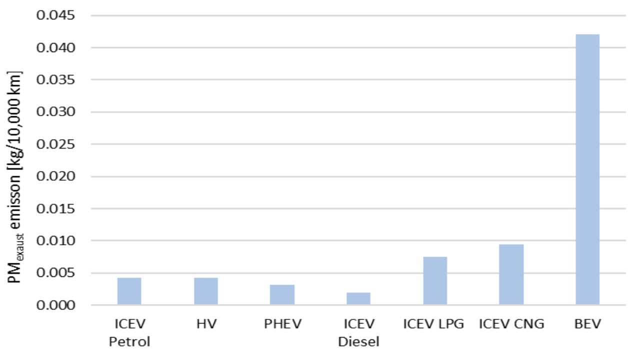

Fig. 10. Comparison of exhaust particulate matter (PM_{exh}) emissions for the selection of Small Passenger cars

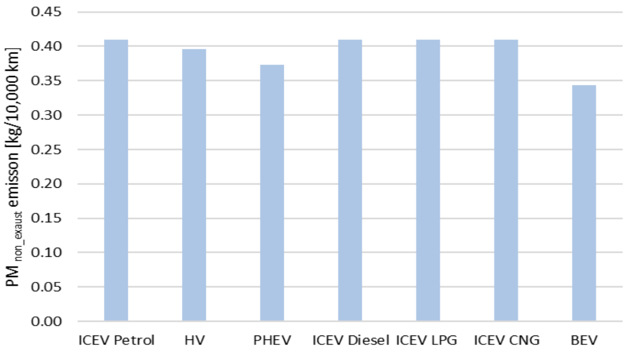

Fig. 11. Comparison of non-exhaust particulate matter ($PM_{non\text{-}exh}$) emissions for the selection of Small Passenger cars

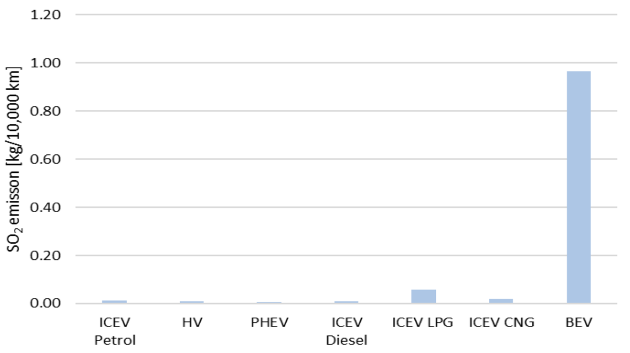

Fig. 12. Comparison of CO_2, NO_x, PM and SO_2 emissions for the selection of Small Passenger cars

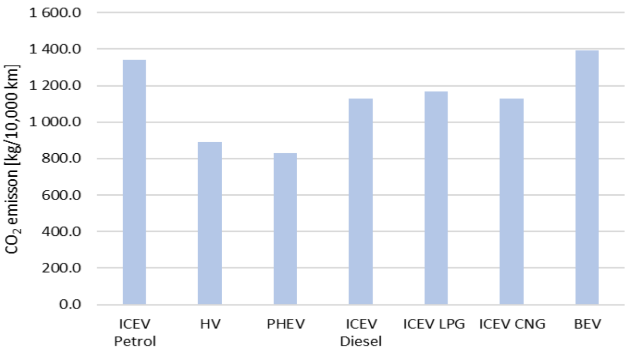

Fig. 13. Comparison of carbon dioxide (CO_2) emissions for the selection of Medium Passenger cars

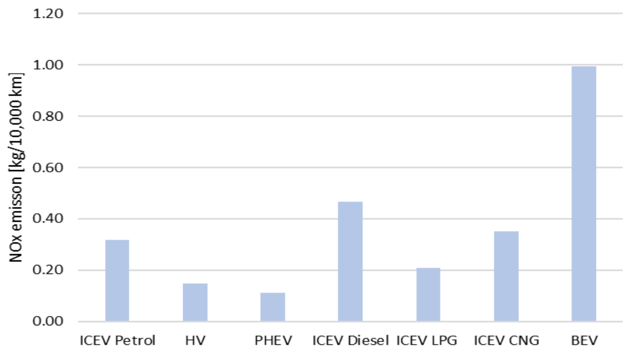

Fig. 14. Comparison of nitrogen oxides (NO_x) emissions for the selection of Medium Passenger cars

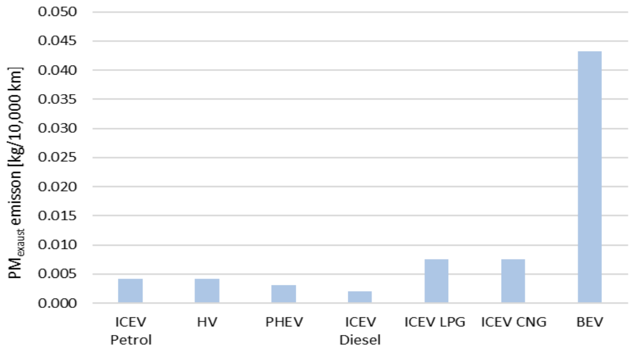

Fig. 15. Comparison of exhaust particulate matter (PM_{exh}) emissions for the selection of Medium Passenger cars

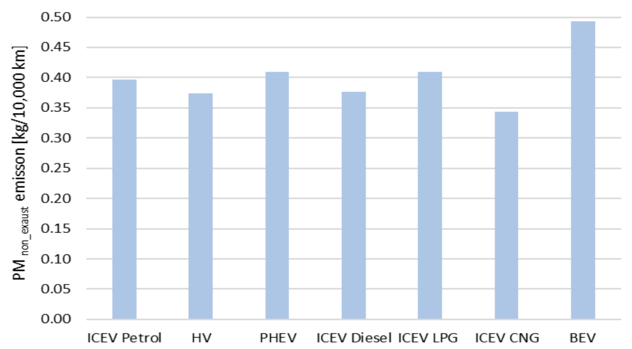

Fig. 16. Comparison of non-exhaust particulate matter ($PM_{non\text{-}exh}$) emissions for the selection of Medium Passenger cars

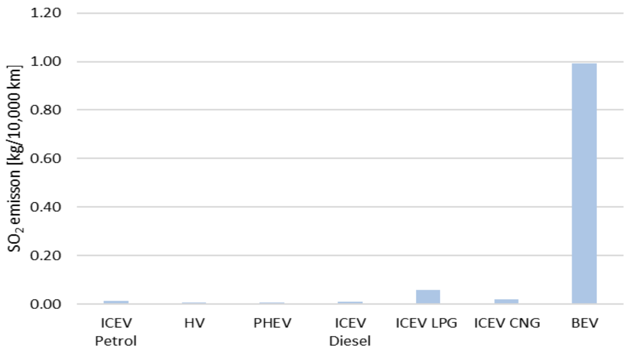

Fig. 17. Comparison of sulphur dioxide (SO_2) emissions for the selection of Medium Passenger cars

The simulations also show that in the Small segment, Plug-in Hybrid Electric Vehicles (PHEV) has the lowest CO_2, PM_{exh}, and NO_x emissions. As in the case of the Mini segment, in the case of PM emissions from abrasion, it can be seen that the lowest emissions are from battery electric vehicles (BEV) and Plug-in Hybrid Electric Vehicles (PHEV).

For the passenger car in the Medium segment, similarly to the previous segments (Mini and Small), the equivalent emissions of CO_2, NO_x, PM_{exh} and $PM_{non\text{-}exh}$ (PM emission from the tribological process) and SO_2 are higher for battery electric vehicles than for internal combustion engines vehicles.

The simulations also show that CO, NO_x and $PM_{non\text{-}exh}$ emissions are the lowest for separate Plug-in Hybrid Electric Vehicles.

In the case of non-exhaust PM emissions, contrary to the Mini and Small segments, the lowest emissions are for CNG internal combustion engines passenger cars.

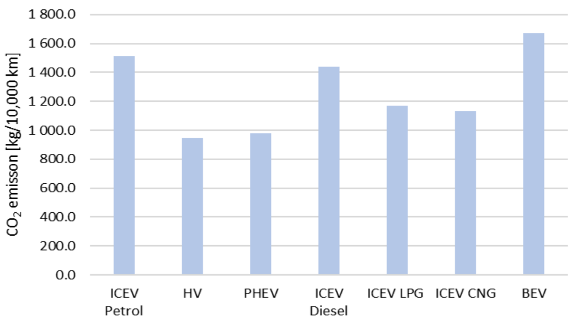

Fig. 18. Comparison of carbon dioxide (CO_2) emissions for the selection of Large-SUV-Executive Passenger cars

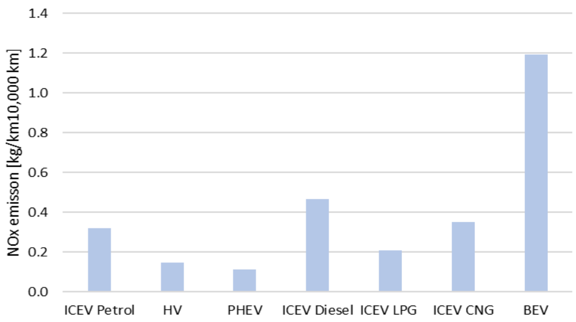

Fig. 19. Comparison of nitrogen oxides (NO_x) emissions for the selection of Large-SUV-Executive Passenger cars

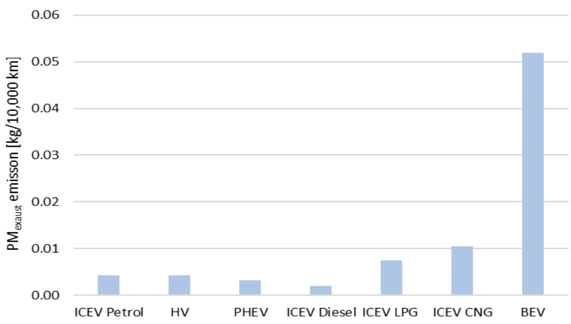

Fig. 20. Comparison of exhaust particulate matter (PM_{exh}) emissions for the selection of Large-SUV-Executive Passenger cars

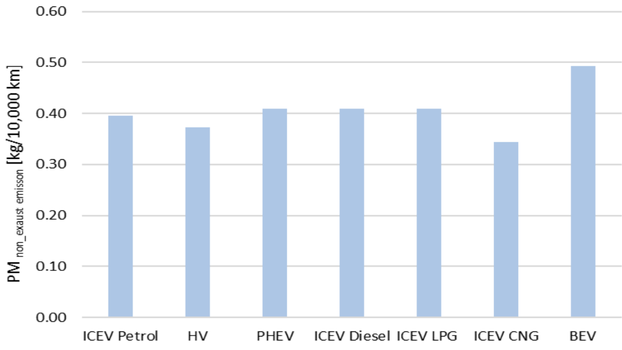

Fig. 21. Comparison of non-exhaust particulate matter ($PM_{non\text{-}exh}$) emissions for the selection of Large-SUV-Executive Passenger cars

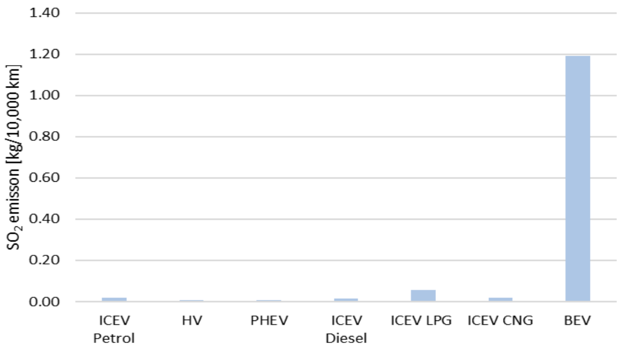

Fig. 22. Comparison of sulphur dioxide (SO_2) emissions for the selection of Large-SUV-Executive Passenger cars

For the passenger car in the Large-SUV-Executive segment, similar to the Medium passenger cars, the equivalent emissions of CO_2, NO_x, PM_{exh} and $PM_{non\text{-}exh}$ and SO_2 are higher for battery electric vehicles than for internal combustion engine vehicles.

The simulations also show that CO_2, NO_x and $PM_{non\text{-}exh}$ emissions are the lowest for separate Plug-in Hybrid Electric Vehicles (PHEV).

In the case of non-exhaust PM emissions, similarly to the Medium segments, the lowest emissions are for CNG internal combustion engines passenger cars.

Figures 23–25 show the influence of energy mix on emissions from battery electric vehicles. The dependence is presented for each segment of battery electric vehicles (Mini, Small, Medium and Large-SUV-Executive).

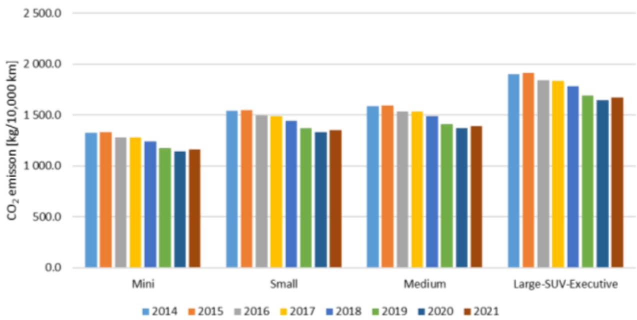

Fig. 23. Comparison of carbon dioxide (CO_2) emissions for BEV depending on polish fuel mix

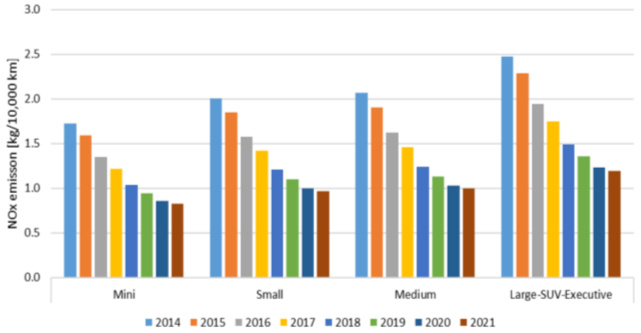

Fig. 24. Comparison of nitrogen oxides (NO_x) emissions for BEV depending on polish fuel mix

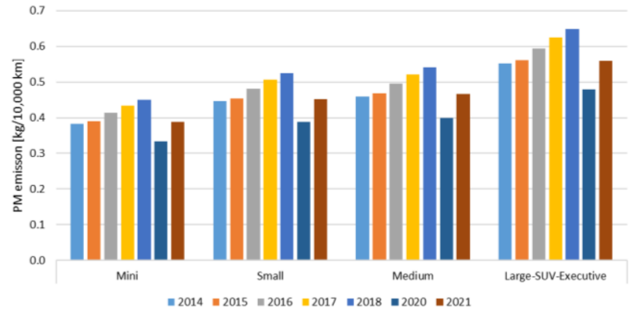

Fig. 25. Comparison of particulate matter (PM) emissions for BEV depending on polish fuel mix

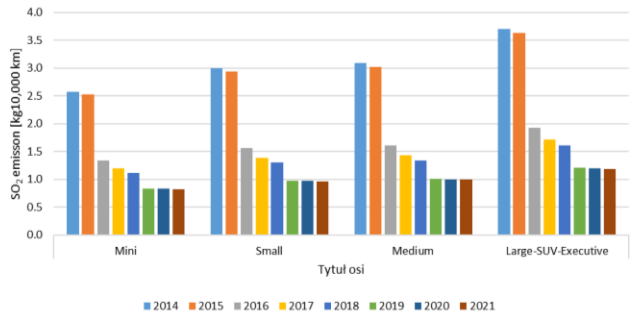

Fig. 26. Comparison of sulphur dioxide (SO_2) emissions for BEV depending on polish fuel mix

Figures 23–25 shows the dependence of equivalent emissions on the energy mix. It can be seen that as Renewable Energy Sources (RES) electricity increases, the equivalent emissions from electric vehicles decrease. For 2020, the share of RES electricity in total electricity production was the highest, almost 12.5%, while for other years, it was approximately 10%.

4. Conclusions

Research conducted and the data presented in the article indicate that the amount of carbon dioxide and pollutants released by cars is largely dependent on the kind of fuel used (in the case of ICEVs) and the energy mix (for BEVs).

Simulation studies conducted in Poland suggest that introducing electric cars to traffic while removing cars with internal combustion engines is not necessarily beneficial.

The simulation results shown in Fig. 3–22 show that the CO_2 emissions of battery electric vehicles are higher than those of internal combustion engine vehicles for all segments (Mini, Small, Medium and Large-SUV-Executive.

The same is true for NO_x, exhaust PM and SO_2 emissions. The SO_2 emissions from battery electric vehicles are significantly higher than those from internal combustion engines because the energy mix is mainly based on coal. Only the non-exhaust emission PM (tire, brake wear and abrasion), is lower for battery electric vehicles, but this difference is negligible.

Figures 23–25 compares CO_2, NO_x, PM and SO_2 emissions for battery electric vehicles depending on the Polish fuel mixture. It shows that the emission depends on the energy mix. Comparing the values in Fig. 2 with the simulation results, it can be seen that the greater the share of renewable sources in the energy mix, the lower the emission of all pollutants under consideration. This relationship clearly shows that if Poland strives for climate neutrality, it should increase the share of renewable sources in the energy mix before decarbonizing transport.

In conclusion, the findings of the research and the evaluation of the sources demonstrate that, with the existing energy mix in Poland, the shift of more cars to electric engines and a decrease in the number of cars with internal combustion engines will not have a beneficial effect on the environment and human health, as the amount of NO_x and SO_2 in the atmosphere will escalate.

This article serves as a benchmark for further exploration into the role of electromobility in the energy mix or electricity industry. The purpose of the study could be to examine the effects of electromobility on the environment and the economy. It is plausible to apply the benchmarking system that is provided to cars powered by alternate fuel sources, such as hydrogen.

Nomenclature

BEV	battery electric vehicles
CO_2	carbon dioxide
EV	electric vehicles
FCEV	fuel cell electric vehicles
GHG	greenhouse gases
HEV	hybrid electric vehicles
ICEV	internal combustion engine vehicles
NO_x	nitrogen oxides
PHEV	plug-in hybrid electric vehicles
PM	particulate matter
RES	renewable energy sources
SO_2	sulphur dioxide

Bibliography

[1] CO_2, SO_2, NO_x, CO and TSP emission indicators for electricity, based on information contained in the National Database on emissions of greenhouse gases and other substances for 2019. KOBiZE IOŚ-PIB, 2020. https://www.kobize.pl/uploads/materialy/materialy_do_pobrania/wskazniki_emisyjnosci/Wskazniki_emisyjnosci_grudzien_2020.pdf

[2] Communication from the Commission to the European Parliament, the Council, the European Economic and Social Committee and the Committee of the Regions. Sustainable and Smart Mobility Strategy – putting European transport on track for the future. https://eur-lex.europa.eu/legal-content/EN/TXT/?uri=CELEX%3A52020DC0789

[3] Fernández RA. A more realistic approach to electric vehicle contribution to greenhouse gas emissions in the city. J Clean Prod. 2018;172:949-959. https://doi.org/10.1016/j.jclepro.2017.10.158

[4] Gis W, Merkisz J. The development status of electric (BEV) and hydrogen (FCEV) passenger cars park in the world and new research possibilities of these cars in real traffic conditions. Combustion Engines. 2019;178(3):144-149. https://doi.org/10.19206/CE-2019-325

[5] Hoekstra A. The underestimated potential of battery electric vehicles to reduce emissions. Joule. 2019;3(6):1412-1414. https://doi.org/10.1016/j.joule.2019.06.002

[6] Huo H, Zhang Q, Liu F, He K. Climate and environmental effects of electric vehicles versus compressed natural gas vehicles in China: a life-cycle analysis at province level. Environ Sci Technol. 2013;47:1711-1718. https://doi.org/10.1021/ es303352x

[7] Ji S, Cherry CR, Bechle MJ, Wu Y, Marshall JD. Electric vehicles in China: emissions and health impacts. Environ Sci Technol. 2012;46:2018-2024. https://doi.org/10.1021/es202347q

[8] Ji S, Cherry CR, Zhou W, Sawhney R, Wu Y, Cai S et al. Environmental justice aspects of exposure to PM2.5 emissions from electric vehicle use in China. Environ Sci Technol. 2015;49:13912-13920. https://doi.org/10.1021/acs. est.5b04927

[9] Laskowski PP, Zimakowska-Laskowska M, Zasina D, Wiatrak M. Comparative analysis of the emissions of carbon dioxide and toxic substances emitted by vehicles with ICE compared to the equivalent emissions of BEV. Combustion Engines. 2021;187(4):102-105. https://doi.org/10.19206/CE-141739

[10] Lee DY, Thomas VM, Brown MA. Electric urban delivery trucks: energy use, greenhouse gas emissions, and cost-effectiveness. Environ Sci Technol. 2013;47:8022-8030. https://doi.org/10.1021/es400179w

[11] Michalek AW. Consequential life cycle air emissions externalities for plug-in electric vehicles in the PJM interconnection. Environ Res Lett. 2016;11:024009. https://doi.org/10.1088/1748-9326/11/2/024009

[12] Michalek JJ, Chester M, Jaramillo P, Samaras C, Shiau CSN, Lave LB. Valuation of plug-in vehicle life-cycle air emissions and oil displacement benefits. Proc Natl Acad Sci. 2011;108:16554-16558. https://doi.org/10.1073/pnas.1104473108

[13] Ministry of Climate and Environment. Poland's Informative Inventory Report. Submission under the UNECE CLRTAP and NEC Directive. 2021. https://cdr.eionet.europa.eu/pl/eu/nec_revised/iir/envyei5sq/.

[14] Ministry of Climate and Environment. Poland's National inventory report 2020 greenhouse gas inventory for 1988-2018. Submission under the United Nations Framework Convention on Climate Change and the Kyoto Protocol. 2021. https://unfccc.int/documents/274762.

[15] Nichols BG, Kockelman KM, Reiter M. Air quality impacts of electric vehicle adoption in Texas. Transport Res D-Tr E. 2015;34:208-218. https://doi.org/10.1016/j.trd.2014.10.016

[16] Ntziachristos L, Samaras Z. Road transport. In: EMEP/EEA air pollutant emission inventory guidebook 2019. 2019. https://doi.org/10.2800/293657

[17] Regulation of the European Parliament and of the Council on establishing the framework for achieving climate neutrality and amending Regulation (EU) 2018/1999 (European Climate Law). https://eur-lex.europa.eu/legal-content/EN/TXT/PDF/?uri=CELEX:52020PC0563&from=EN

[18] Requia WJ, Mohamed M, Higgins CD, Arain A,, Ferguson M. How clean are electric vehicles? Evidence-based review of the effects of electric mobility on air pollutants, greenhouse gas emissions and human health, Atmos Environ. 2018;185:64-77. https://doi.org/10.1016/j.atmosenv.2018.04.040

[19] Simons A. Road transport: new life cycle inventories for fossil-fuelled passenger cars and non-exhaust emissions in Ecoinvent v3. Int J Life Cycle Assess. 2016;21:1299-1313. https://doi.org/10.1007/s11367-013-0642-9

[20] The European Green Deal. 2019. Communication from the Commission to the European Parliament, the Council, the European Economic and Social Committee and the Committee of the Regions. https://eur-lex.europa.eu/legal-content/EN/TXT/PDF/?uri=CELEX:52012DC0673&from=EN

[21] Timmers VRJH, Achten PAJ. Non-exhaust PM emissions from electric vehicles. Atmos Environ. 2016;134:10-17. https://doi.org/10.1016/j.atmosenv.2016.03.017

[22] Van Vliet O, Brouwer AS, Kuramochi T, Van Den Broek M, Faaij A. Energy use, cost and CO_2 emissions of electric cars. J Power Sources. 2011;196:2298-2310. https://doi.org/10.1016/j.jpowsour.2010.09.119

[23] Weiss M, Dekker P, Moro A, Scholz H, Patel MK. On the electrification of road transportation – a review of the environmental, economic, and social performance of electric two-wheelers. Transport Res D-Tr E. 2015;41:348-366. https://doi.org/10.1016/j.trd.2015.09.007

Magdalena Zimakowska-Laskowska, DEng. – Environment Protection Centre, Motor Transport Institute, Poland.
e-mail: *magdalena.zimakowska-laskowska@its.waw.pl*

Piotr Laskowski, DEng. – Faculty of Automotive and Construction Machinery Engineering, Warsaw University of Technology, Poland.
e-mail: *piotr.laskowski@pw.edu.pl*

Article citation info:
Sutkowski M, Mareczek M. Operational experience and new developments for industrial gas engines fuelled with hydrogen fuels. Combustion Engines. 2024;197(2):146-151. https://doi.org/10.19206/CE-183185

Marek SUTKOWSKI
Michał MARECZEK

Combustion Engines
Polish Scientific Society of Combustion Engines

Operational experience and new developments for industrial gas engines fuelled with hydrogen fuels

ARTICLE INFO

Received: 21 May 2023
Revised: 27 January 2024
Accepted: 28 January 2024
Available online: 15 February 2024

Since 2012 Horus-Energia has been developing the technology for the hydrogen fuelled industrial gas engines. The first three units were commissioned in 2014 and, in 2019, reached the forty thousand running hours milestone. The success of the first hydrogen project encouraged Horus-Energia to focus on further developments and improvements of the technology. Several R&D projects have been carried out since 2016 and resulted in two granted patents, and another one is currently being processed. The recent development project focused on hydrogen-hydrocarbon blends is in its final stage. The technology being developed creates a solid base for many new solutions that will cover a wide range of fuels and applications. The paper reports the experience from 40,000 hours of operation of hydrogen-fuelled industrial gas engines and presents the developments carried out by Horus-Energia with its research partners as well as the future development paths for the technology.

Key words: *hydrogen, industrial gas engines, cogeneration, on-site power generation*

1. Introduction

For many decades hydrogen was considered as a fuel of far-future solutions and labelled as too expensive and dangerous for daily use. Even though a lot of research projects were carried out on technologies for safe storage and use, as well as less expensive production, it still remained linked solely to the space industry.

The situation has changed recently, and hydrogen has suddenly become a fuel considered to be within reach for everybody. This, together with more and more hydrogen solutions for daily use already available on the market, is boosting current activities on further developments. Currently, there are available for regular sales: hydrogen fuelled cars, trucks, and buses; hydrogen fuel cells for household power generation; electrolyzers; hydrogen tanks for a wide range of storage pressures and more. Each significant industrial gas engine maker announces developments of its own products to allow the usage of hydrogen as a fuel, at least to some extent. However, most of the technologies presented nowadays are at a very early stage of development, usually at factory tests and improvements. Nevertheless, some OEMs put first prototypes into the initial phase of field testing [1, 7, 8, 10, 13]. Still, most companies working as system integrators do not have either a budget, capabilities, competencies, or facilities to develop engine technology, and thus, they are usually dependent on the technology available from industrial engine manufacturers.

The paper describes over a decade of Horus-Energia experience in development of technologies for industrial gas engines enabling hydrogen usage as a fuel for on-site power generation. The engines were modified inhouse by Horus-Energia and adopted to operate on gas fuels containing hydrogen at various proportions and even for pure hydrogen. Systems were installed on several applications, and the experience from tens of thousands of hours of operation in real conditions will also be present together with the next steps planned for the technology improvements.

2. Solution for low hydrogen content in gas fuel

The basic hydrogen technology available from Horus-Energia is based on the innovative and patented gas-air mixer system called the MUZG. Gas-air mixers are the most common solutions for industrial gas engines on the market due to their simplicity and high reliability, but they have a lot of limitations like slow response to changes in fuel properties, lack of capability to change gas-air mixture composition on demand, or operating range for air/fuel ratio. The MUZG technology, developed together by Horus-Energia and Cracow University of Technology, is much more advanced and sophisticated than typical mixer solutions. In the MUZG system, the gas dosing is additionally regulated by a fast reacting control unit [4, 5, 9, 11]. The MUZG system uses many additional sensors to monitor combustion process inside cylinders, to detect abnormal situations, like knock or misfiring, and to implement necessary correction for engine controls or to mixture composition. Thanks to fast algorithms and fast-response controllers the MUZG system can implement corrective actions within a single engine cycle.

This improves mixer operational flexibility and helps to overcome the main disadvantages of typical mixers i.e. narrow operating window for gas fuel calorific value and slow response when gas fuel calorific value changes – the gas fuel calorific value change causes change in stochiometric gas-air ratio and thus requires correction in stochiometric coefficient (lambda). Additionally, extended sensors and fast processing help to detect many abnormalities at their initial phase, which is very important to implement active knock protection. The operation near the knock limit enables high efficiency, but standard control systems of industrial gas engines create too high a risk of knock. Only effective early knock detection and fast response of the control system allow such engine operation.

The MUZG system was tested in 2017 and 2018 at Horus-Energia premised within R&D project co-financed by the National Centre for Research and Development. During tests, various gas fuels were specially composed to define the real operational limitations of the MUZG system. The tests were focused on wide range of fuel calorific value change, the methane number change and on maximum accepted change rate of these.

The main advantages of the MUZG system over typical mixers are shown in Fig. 1–3.

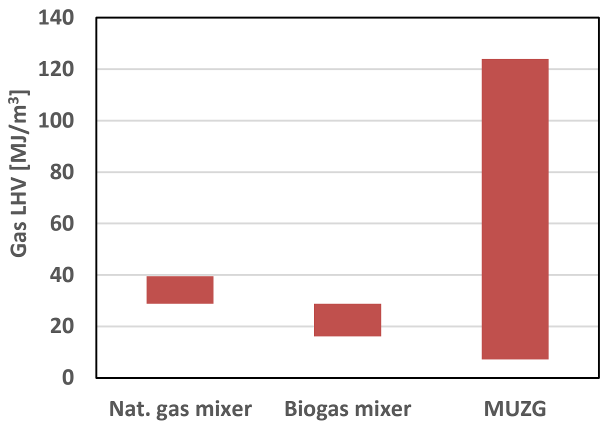

Fig. 1. Comparison of gas-air mixers operation window for gas fuel calorific value

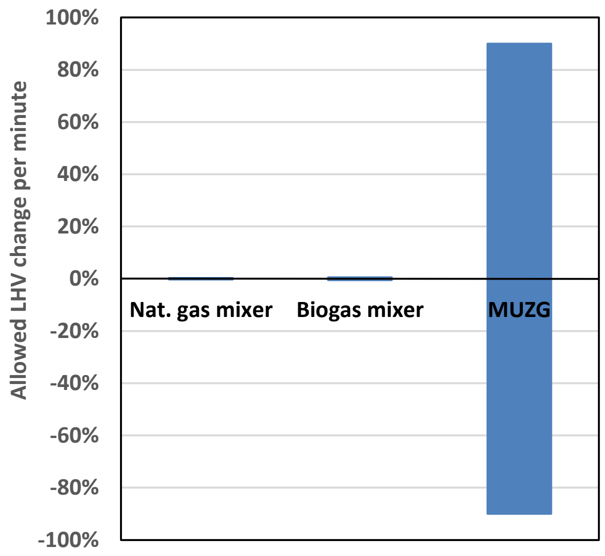

Fig. 2. Comparison of acceptable gas fuel calorific value change speed for stable gas-air mixer operation

The MUZG system tests showed its superiority over standard systems dedicated to industrial. The system allows a significantly wider operating window for gas fuel calorific value change. What is most important, the MUZG system does not require any additional inputs or settings when gas fuel calorific value changes. On the contrary, standard control systems need presetting for particular fuel and quite narrow operating window is than anchored with these initial values giving as a result much narrower operating range in reality than it seems from the theoretical range.

The MUZG system also has unique and incomparable capability in responsiveness to gas fuel properties change. As the tests showed, the MUZG system reaction time is over 100 times shorter than standard systems offer [4, 5].

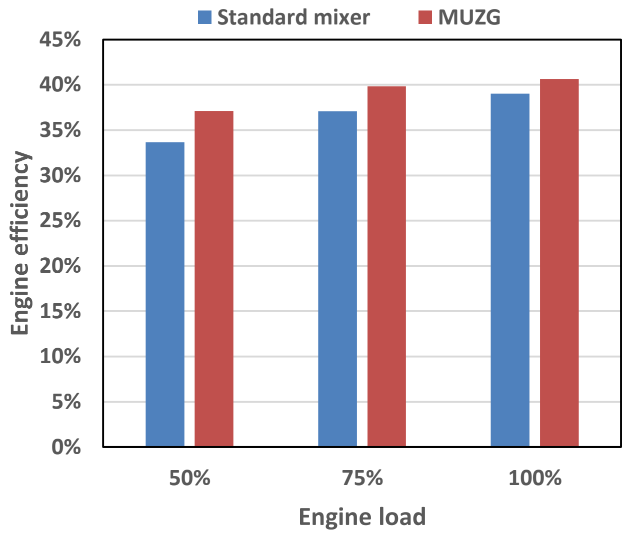

Fig. 3. Comparison of MAN E2876 LE302 gas engine efficiency for various gas-air mixers during operation on methane

The above mentioned advantages are very important when it comes to non-conventional gas fuels but the MUZG system provides significant benefits also for engines fuelled with conventional gas fuels. The visible efficiency improvement achieved during operation on methane results from more accurate fuel dosing linked to measured knock margin and fast processing of controls.

It is important to note that the MUZG system has been designed independently from the engine platform, so it can be installed on any industrial gas engine and will provide extremely flexible, self-adjusting, fast reacting, and efficiently optimized operation of the engine. Horus-Energia has successfully installed the MUZG on many gas engines, like MAN, Perkins or Rolls-Royce MTU.

3. Solution for high hydrogen content in gas fuel

The gas-air mixer solution, where fuel is delivered at the engine air inlet, fills quite a large volume with a flammable mixture and starts to be problematic and hazardous when hydrogen is the dominating gas fuel component. For such cases, the WUZG technology available from Horus-Energia is recommended. The WUZG uses the same control philosophy as the MUZG system, and the main difference is that instead of a gas-air mixer located at the engine air inlet, there is a multipoint injection system with individual injectors for each cylinder located in the intake manifold close to cylinder heads.

The WUZG system was developed in close cooperation between Horus-Energia and Cracow University of Technology already in 2013, and it has the same basic advantages as the MUZG system, but it offers an even faster response when the gas-air mixture composition change is required and enables the possibility to control each cylinder separately [2].

The exact hydrogen content in gas fuel when the WUZG system shall be used instead of the MUZG system is not defined and actually it comes more to gas fuel properties than only hydrogen content in it. Usually fuels with hydrogen content lower than 50% contain significant content of carbon monoxide, nitrogen and also carbon dioxide. Additionally, usually they are some process by-streams or by-products and they are available at low overpressure, typically some millibars, and are seldom cleaned. For such fuels it is more feasible to use the MUZG system. When fuel is clean and hydrogen content is over 50–60% the WUZG system is better and safer solution.

Like the MUZG system, also the WUZG system was developed independently from engine platform, so it can also be installed on any industrial gas engine. Horus-Energia has successfully installed such system on several Perkins (Fig. 4) and MAN engines so far.

Fig. 4. The cogeneration unit with Perkins 4016-61TRS2 industrial gas engine equipped with the WUZG system at customer site in Gaj Oławski

4. Solution for hydrogen-hydrocarbons blend

In 2022, another R&D project started and the aim was to develop a system especially dedicated to gas fuel that is a blend of hydrogen and methane (natural gas). It is meant to be used with future pipeline gas when (probably) hydrogen generated from renewable sources will be injected into the national gas grid and locally its level can change from nearly 0% to even 100% within a short period of time. The methane-hydrogen fuelled industrial gas engines are supposed to be installed in the cogeneration solutions operated locally in a distributed power generation system. For such operation it is crucial to ensure that hydrogen change in the entire range can be done when the engine is operating and without any required change in the engine load during the change. Also, the engine needs to accept quick changes of hydrogen content within the entire range regardless if hydrogen content is being increased or decreased.

The newly developed system is based on the features of the MUZG and the WUZG systems and it benefits from both systems advantages. For the project purpose, the Perkins 4016-61TRS2 industrial gas engine was modified in the autumn of 2022 (Fig. 5), but the system is independent from the engine platform and, as the previously mentioned ones, it also can be used on various industrial gas engines.

The genset was equipped with a heat recovery system providing nominal power of 1 MW electric plus 1 MW thermal power, and the cogeneration unit was tested in 2023 at Horus-Energia premisses (Fig. 6) with the very extended functional and operational test program. During the tests, the unit was fuelled with methane blended with hydrogen in the required proportions.

The test facility at Horus-Energia is equipped with a gas mixing station which allows online blending of fuel gas from its components – in this case, hydrogen was blended with natural gas from the gas distribution network. Hydrogen was delivered in a trailer at a pressure of 200 bar, reduced at the pressure reduction station to a level equal to natural gas pressure. The gas flow was measured simultaneously for each stream separately. During blending, the proportions of natural gas and hydrogen were changed to create the fuel gas blend with the required proportions and also to change them with the required rate. The tests covered the steady-state operation for the efficiency measurements (Fig. 6) and the dynamic tests for fast change of hydrogen content in the fuel at constant load (Fig. 7).

Fig. 5. The Perkins 4016-61TRS2 industrial gas engine is equipped with the specially developed system hydrogen-methane fuel system. The genset arrangement at Horus-Energia test facility

Fig. 6. The containerised cogeneration unit with the Perkins 4016-61TRS2 industrial gas engine at Horus-Energia industrial engines test facility

The functional test showed that the control system developed in the project provides better control and balance for the industrial gas engine than the original control system. Additionally, the addition of hydrogen in the fuel gas improves combustion efficiency and, thus, engine efficiency. The zones with the extremally lean mixture that is non-flammable for methane are usually located close to cylinder walls, which additionally limits flame propagation in these zones due to quenching distance. These zones are sources of methane direct emissions from the exhaust, known as methane slip, and this reduces engine efficiency. When hydrogen is added to the fuel, the situation improves, as hydrogen has much wider flammability limits and a much shorter quenching distance. The non-flammable zones are much smaller, and less unburned fuel is exhausted from the engine.

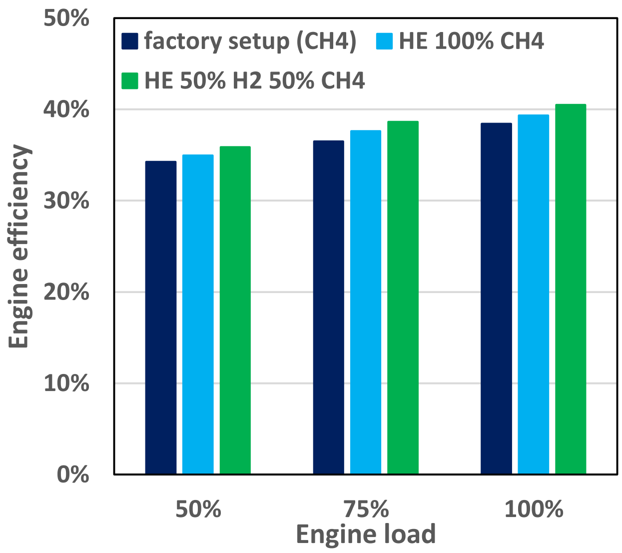

Fig. 7. The efficiency of Perkins 4016-61TRS2 gas engine with standard control system and with the developed one

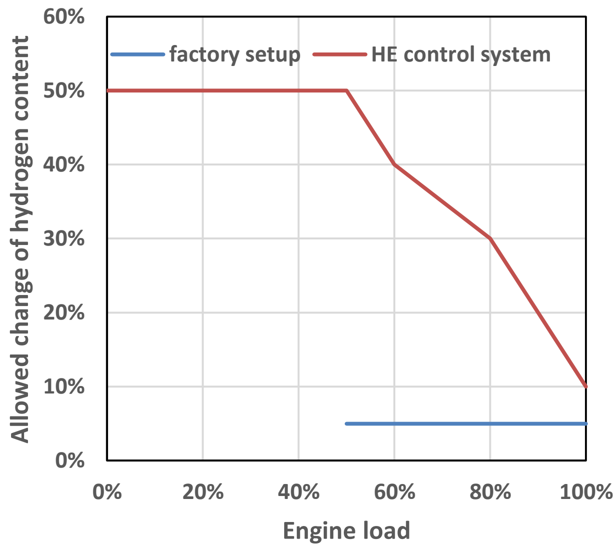

Fig. 8. The maximum allowed sudden change of hydrogen content for Perkins 4016-61TRS2 gas engine with standard control system and with the developed one

The dynamic tests showed that the implemented control system if compared with the standard control system, allows for a much wider range of hydrogen content in the fuel and a much faster change of hydrogen content. It is important to highlight that the engine with its original configuration has two limitations: hydrogen content cannot be higher than 5% (by volume), and the engine shall not be operated for a long time with loads below 50% of the nominal load. The new control system offers better dynamics because of its advanced control philosophy, which includes many more sensors and transducers and a fast data processing controller, which allows to detect even small change in the combustion process, evaluate the cause and react correctively from cycle to cycle. Thanks to such control system ability, the engine operation can be set for more efficiency optimal points but still with a safe distance from the knock margin, especially during fast changes of fuel properties or during fast loading or unloading. Additionally, when a fuel gas injection system is used, the system allows individual control for each cylinder with individually set mixture composition (especially individually set stoichiometric coefficient) and individually set ignition timing.

The observations for tests with hydrogen content over 50% are that further increase of hydrogen in the fuel blend has less influence on the engine efficiency, as the combustion process in the very lean areas is already well stabilised with 50% hydrogen in the fuel blend. Also, charge exchange is already well controlled as the system switches from mixer to injectors, so cylinders are flashed with pure air instead of mixture. Another observation is that due to a lean mixture and lower combustion temperatures NO_x emissions are lower when the share of hydrogen increases (Fig. 9 and Fig. 10).

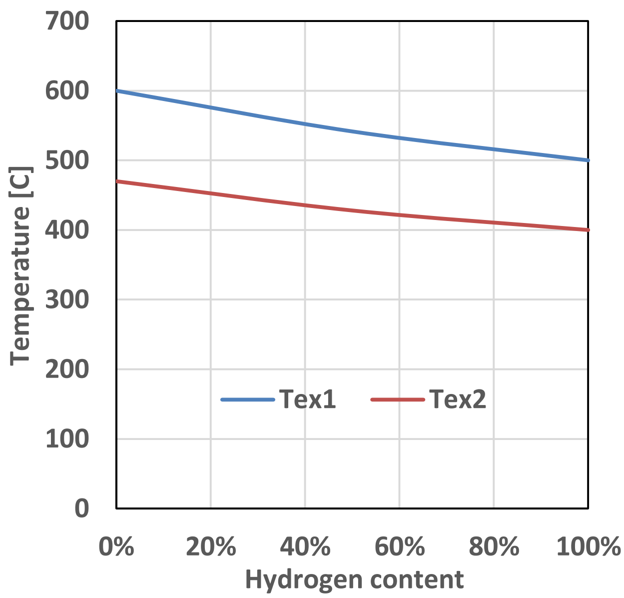

Fig. 9. The exhaust temperatures before turbocharger (Tex1) and after turbocharger (Tex2) for the Perkins 4016-61TRS2 gas engine fuelled with various hydrogen content in the gas fuel

It is important to note that the Perkins 4016-61TRS2 running at a nominal load of 1000 kW consumes about 90 kg of pure hydrogen per hour. Typical hydrogen trailer, as those used during tests at Horus-Energia premisses, contain about 320–400 kg of hydrogen, so one trailer is sufficient for 3.5–4.5 hours of operation only, not enough even to complete one full day of the tests. For that reason, further extensive performance tests are scheduled for 2024 and will be carried out at the location where hydrogen is available locally to avoid frequent hydrogen deliveries and related logistics.

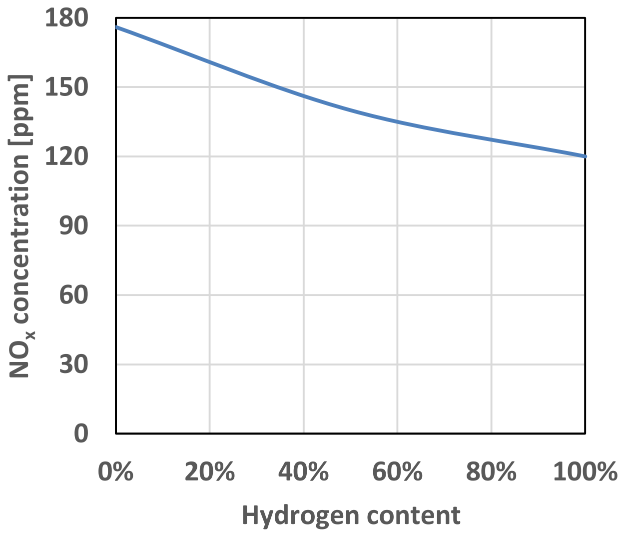

Fig. 10. The NO_x emission from the Perkins 4016-61TRS2 gas engine fuelled with various hydrogen content in the gas fuel

The last part of the test program will be the two years long durability test during normal operation of the cogeneration unit at selected customer.

The final version of the system will enable fuelling the industrial gas engine with a blend of hydrogen and gaseous hydrocarbons at any proportions with the same functionalities as the tested system.

5. Operational experience of the MUZG and WUZG systems

The very first WUZG system was commercially installed on three cogeneration units with MAN industrial gas engines commissioned in 2014 – one MAN E2876 LE302 engine and two MAN E2842 LE322 engines. The units were fuelled with post-processing gas containing 85-95% of hydrogen [2], and in 2019, they gained over forty thousand operating hours, proving very high reliability. Another interesting example of commercial application is the Perkins 4016-61TRS2 engine delivered in March 2022 to operate on pure hydrogen (Fig. 4). The unit is able to generate 1 MW of electric power and 1 MW of heat or 750 kW in chill water to a local factory will also be used as peak shaving solutions for local wind farms. During the overproduction of electricity from the wind farm, the surplus electricity will be used to produce hydrogen using the process of water electrolysis. The hydrogen will be stored in high pressure tanks and can be later used to generate electricity when there is a lack of power in the system or electricity price is attractive enough.

The MUZG system has been installed commercially since 2017 and has also proved its unique flexibility for gas fuels with variable properties. The engines with the MUZG system work well fuelled with syngas (gasified sewage sludge) containing about 40–45% of hydrogen and also other fuels with low quality, like coalmine gas for instance. Those engines also proved their high durability and gained over sixty thousand running hours so far (Fig. 11).

The theoretical average annual availability of industrial gas engines is 8650 hours [4, 9, 12], which is based on ideal operation when all maintenance actions are done as scheduled, with no delays, unexpected stops, and failures. In reality, such number is extremally hard to reach, and typical industrial gas engine has the real average annual availability of about 8000 hours, and well maintained and carefully operated engines with good and stable gas quality can reach 8350–8400 hours of average annual availability.

The engines with the MUZG system reached an average 8100 hours even though the gas quality was low with many impurities and significant fluctuation of gas composition. It is also important to mention that units operating on waste fuels or by-products are treated the same way as fuel, so the owner usually doesn't pay much attention to careful operation or regular maintenance with the required schedule.

The engines equipped with the WUZG system reached even 8600 hours of average annual availability even though the gas composition was not stable and fuel was not purified at all.

These impressive results were possible because both systems have the unique functionality of continuous combustion process monitoring and can react if improper operation is detected to adjust relevant settings (the WUZG system can do it even for each cylinder separately).

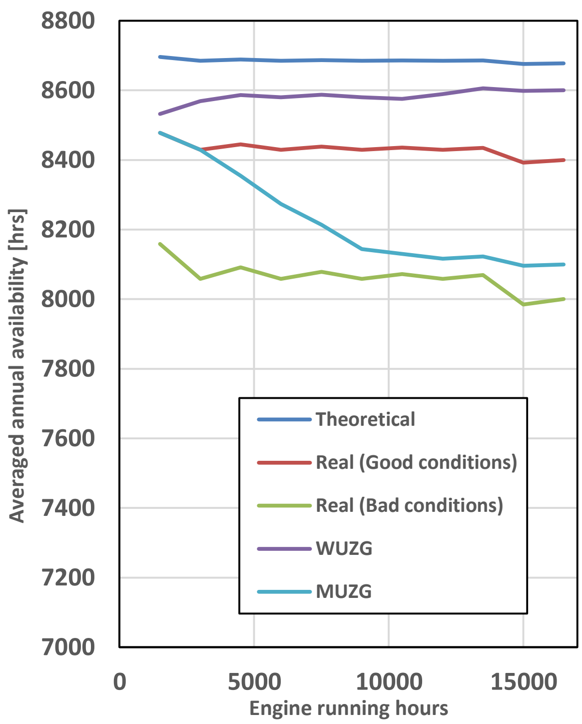

Fig. 11. Comparison of reliability of typical industrial gas engines and the engines with the MUZG and the WUZG

6. Conclusions and future steps

The MUZG and the WUZG systems are universal can be installed on any industrial gas engine and, once installed, they improve engine operation flexibility and performance, even when the engine is operated on conventional fuels. Better performance is achieved mainly due to better detection of knock margin but also thanks to continuous monitoring of engine condition and corrective settings implied for the whole process, from mixture formation to combustion. All additional sensors used to ensure that the gas-air mixture is carefully prepared and the combustion process is well monitored together with fast signal processing help to operate on fuels with variable properties or low quality when the change in control can be applied within one single engine cycle.

The MUZG and the WUZG systems are especially designed to control the combustion of hydrogen based fuels. The functionality of the systems allows the use even pure hydrogen and still to control combustion properly i.e. to prevent from knock, to limit combustion temperatures, to control flame speed etc. All of these are done by early detection of knock or misfiring tendencies, exhaust temperature rise or fall, and once it is detected, counteraction is applied already in the following engine cycle. The WUZG system allows additionally to control of each cylinder separately with the individual mixture composition or with temporary cylinder deactivation if the combustion process is hard to control and leads to potential cylinder failure.

The monitoring also enables save operation of the engine. Even small variations from the desired engine operation can be detected and various corrective actions can applied before the process reaches a serious level or damage occurs. This helps to avoid situations when the engine's available power is limited, or the engine needs to be stopped due to an operation warning or alarm signal. All of these are reflected in the annual average availability of the engines equipped with the MUZG or the WUZG system regardless of fuel type and quality that were used.

The combined MUZG and the WUZG system brings additional operational flexibility, as the engine control system can switch from one fuel supply system to another. The MUZG system gets priority when fuel has low pressure low hydrogen content and the WUZG system is preferred when gas pressure or hydrogen content are relatively high.

As the mentioned systems have high potential for various applications there are many further development projects already ongoing or planned. The combined MUZG-WUZG system will be extended to enable the use of other gaseous hydrocarbons blended with hydrogen. The MUZG system can be used for bi-fuel engines fuelled with oil fuel (biodiesel for instance) and gas fuel (bio-methane for example), which will create a very reliable and carbon dioxide neutral solution for independent power generation with unique operational flexibility and loading performance not observed in typical industrial gas engines. And finally, the WUZG system can also be used for bi-fuel engines combining the combustion of biodiesel with hydrogen or for other fuels, such as alcohols. Basic tests of that system has already been started and the first results are promising, but the solution is still far from final implementation.

Bibliography

[1] Baumann ZCM, Kratz F, Zuschnig A, Schiestl S, Spyra K, INNIO Jenbacher – be prepared for the future with hydrogen. Proceedings of 12th Gas Engines Conference. 2022.

[2] Brzeżański M, Mareczek M, Marek W, Papuga T, Sutkowski M. The realized concept of variable chemical composition fuel gas supply systems for internal combustion engines. Combustion Engines. 2017;170(3):108-114. https://doi.org/10.19206/CE-2017-318

[3] Kovar Z, Scholz C, Beroun S, Nydrle M, Drozda H, Blazek J et al. Hydrogen piston engines: R&D, experiences. Combustion Engines. 2006;125(2):28-36. https://doi.org/10.19206/CE-117350

[4] MAN Gas Engines Handbook, 2023.

[5] Mareczek M, Sutkowski M, Smuga W. Operational tests of an innovative fuel supply system for an industrial 4-stroke gas engines. IOP Conf Ser Mater Sci Eng. 2018;421: 042052. https://doi.org/10.1088/1757-899X/421/4/042052

[6] Matla J. Possible applications of prechambers in hydrogen internal combustion engines. Combustion Engines. 2022; 191(4):77-82. https://doi.org/10.19206/CE-148170

[7] Mattheeuws L. ABC's dual fuel engines running on renewable fuels like methanol and hydrogen. Proceedings of 11th Gas Engines Conference. 2019.

[8] Ohler S, Schultze M. Adaption of a lean-burn gas engine to future hydrogen blending into the natural gas grid. Proceedings of 12th Gas Engines Conference. 2022.

[9] Perkins Service Bulletin. 2022. https://www.perkins.com/en_GB/aftermarket/datasheets-and-bulletins.html

[10] Rösler S, Wahl J, Kunkel C, Bauer M. Investigations on fuel-gas mixtures with a hydrogen content of 25% and more within a prechamber ignited gas engine – the MAN concept for the power application of the future. Proceedings of 12th Gas Engines Conference. 2022.

[11] RR-MTU Fluids and Lubricants Specifications. 2022. https://www.mtu-solutions.com/

[12] RR-MTU Maintenance Schedule. 2022. https://www.mtu-solutions.com/

[13] Schultze M, Drexel C, Kollias-Pityrigkas G. Experimental and numerical investigation of gaseous hydrogen rich fuels in large gas engines. Proceedings of 10th Gas Engines Conference. 2017.

Marek Sutkowski, DEng. – Chief Technology & Innovation Officer, Horus-Energia Sp. z o.o., Poland.

e-mail: *m.sutkowski@horus-energia.pl*

Michał Mareczek, DEng. – Faculty of Mechanical Engineering, Cracow University of Technology, Poland.

e-mail: *mareczek@pk.edu.pl*

Article citation info:
Wesołowski P, Neugebauer M. The influence of the content of phosphates in water on the propagation speed of ultrasonic waves. Combustion Engines. 2024;197(2):152-157. https://doi.org/10.19206/CE-184140

Paweł WESOŁOWSKI
Maciej NEUGEBAUER

Combustion Engines
Polish Scientific Society of Combustion Engines

The influence of the content of phosphates in water on the propagation speed of ultrasonic waves

ARTICLE INFO

Received: 28 November 2023
Revised: 9 February 2024
Accepted: 15 February 2024
Available online: 6 April 2024

The phosphate content of a test sample is one of the indicators of the trophic status of the test water. In this work, an attempt was made to use a non-destructive ultrasonic technique to determine this parameter. For this purpose, a specially prepared measuring station was used to test distilled water samples with different phosphate contents. Specially prepared samples contained 0, 20, 40, 60, 80, and 100 kg/m^3 of phosphates. In addition, tests were carried out on the effect of sample temperature on the values of the characteristic parameter of the wave, in the range from 12 to 30°C. All tests were carried out using two ultrasonic heads with a wave frequency of 2 MHz. The ultrasonic wave parameter analysed in the study was the propagation speed of the ultrasonic wave. The results obtained indicate that the ultrasonic method is useful for non-destructive evaluation of phosphate content in the sample. Additionally, they show a large influence of the sample temperature on the results read.

Key words: *non-destructive ultrasound technique, phosphates, temperature, ultrasonic wave, propagation speed*

1. Introduction

Due to the increasing anthropopressure on the natural environment, their conditions are deteriorating due to the increasing pollution of the surrounding nature. This process applies to all aspects of the natural environment – air, land, water, and the broadly understood biosphere.

In the case of lakes, the influence of anthropopressure is particularly visible. Firstly, because of their relatively small dimensions – the concentration of pollutants is much higher than, for example, in the case of air or seas. Secondly, because of the very diverse purpose of lakes' use. They can be used as a breeding place, and a source of fish for fish farms as tourist attractions – a place for water sports, and their shores are attractive places for the construction of housing estates or hotels. Finally, lakes can serve as drinking water reservoirs. Of course, in practice, all these uses coexist to varying degrees.

The anthropopression exerted on lakes accelerates the natural process of eutrophication (aging of lakes). Excessive inflow of pollutants (first of all – nutrients – nitrogen and phosphorus) causes a number of unfavorable changes in water ecosystems [20]. These changes consist in a decrease in water transparency as a result of the intensification of primary production processes (excessive development of phytoplankton and also bacterioplankton – cyanobacteria), changes in water salinity (increase in electrolytic conductivity), changes in the biological structure of the ecosystem (decrease in biodiversity, disappearance of macrophytes, replacement of valuable fish species by the less valuable) [16, 20]. Excessive production of organic matter causes the consumption of oxygen for the processes of its decomposition, which takes place in the deeper layers of water and causes the development and strengthening of oxygen deficits in the bottom zone.

It may cause an increase in water pollution in lakes and, consequently, the loss of some of their qualities – a ban on bathing due to pollution, or a decline in the fish population. Surface water pollution can be of biological, chemical or physical character. In particular, it may be contamination of water with bacteria, e.g., E. coli, the influx of toxic chemicals into the water, or pollution with heavy metals. Eutrophication is a slow increase in lake pollution caused by the nutrients export from the catchment area, increasing water fertility. The rate of this nutrient alimentation in natural conditions is slow, but human activity has significantly accelerated this process. In the first stage, this leads to the flourishing of life, and after some time – due to the consumption of oxygen resources in the lower layers of water – to a series of unfavorable changes mentioned above.

There are various methods of examining the state of water in terms of physical (temperature, pH, color, smell, Secchi disc visibility, electrolytic conductivity), chemical (determination of the content of various elements and chemical compounds by analytical chemistry methods) [18] or biological (e.g. analysis of species composition, number of organisms, biomass of organisms) [20]. Optical methods are used to measure the phytoplankton content in waters [3].

As a result of the research, it can be proved, that there is a specific relationship between a specific deviation of the parameters of the sound emitted in the water of the tested reservoir depending on its chemical and physical state.

It is known from physics that the speed of sound in liquids depends on the modulus of volumetric elasticity and the density of the liquid – according to the equation (1)

$$v = \sqrt{K \cdot \rho^{-1}} \tag{1}$$

where: K – modulus of volumetric elasticity, ρ – liquid density.

The density of the liquid is primarily influenced by temperature and salinity. It is known from research on physical phenomena that the speed of sound waves in water depends on the temperature and salinity of the water. In turn, the water elasticity coefficient is influenced by pressure, temperature and viscosity [15, 34]. These are relatively old studies – more recent studies in connection with the effect of solution concentration are shown e.g. in the works by Koszela-Marek [22], Koszela et al. [21]. This type of research was conducted especially for sea waters – the basic description of the acoustic properties of sea water is given in the works of Dera [8, 9].

It is known from the literature, that the speed of sound in water is described by the formula (2):

$$c(S,T,P) = 1449.14 + \Delta c_S + \Delta c_T + \Delta c_P + \Delta c_{S,T,P} \quad (2)$$

where 1449.14 m/s = c° (35, 0, 0) is the speed of sound under standard conditions, adopted for ocean water with a salinity of 35‰ at 0°C and atmospheric pressure. The remaining components of this formula expressing corrections for other conditions are given in formulas (2a) [40]:

$$\Delta c_S = 1.3980\,(S-35) + 1.692 \cdot 10^{-3}\,(S-35)^2$$

$$\Delta c_T = 4.5721T - 4.4532 \cdot 10^{-2}\,T^2 - 2.6045 \cdot 10^{-4}\,T^3 + 7.985 \cdot 10^{-6}\,T^4$$

$$\Delta c_p = 1.60272 \cdot 10^{-1}\,P + 1.0268 \cdot 10^{-5}\,P^2 + 3.5216 \cdot 10^{-9}\,P^3 - 3.3603 \cdot 10^{-12}\,P^4 \quad (2a)$$

$$\Delta c_{S,T,P} = (S-35)\,(-1.1244 \cdot 10^{-2}\,T + 7.7711 \cdot 10^{-7}\,T^2 + 7.7016 \cdot 10^{-5}\,P - 1.2943 \cdot 10^{-7}\,P^2 + 3.1580 \cdot 10^{-8}\,PT + 1.5790 \cdot 10^{-9}\,PT^2) + P(-1.8607 \cdot 10^{-4}\,T + 7.4812 \cdot 10^{-6}\,T^2 + 4.5283 \cdot 10^{-8}\,T^3) + P^2(-2.5294 \cdot 10^{-7}\,T + 1.8563 \cdot 10^{-9}\,T^2) + P^3\,(-1.9646 \cdot 10^{-10})T$$

where: T – water temperature, P – water pressure, S – water salinity.

Since this formula does not take into account other factors – e.g. the influence of gas bubbles or the content of organic substances – simpler formulas are used in practice, but also in the form of empirical regression formulas – see, for example, Hamilton [17], Mackenzie [29] or Fine et al. [11].

These formulas describe the relationship between the basic parameters of water (salinity, temperature, pressure) and the speed of sound wave propagation in water.

The phenomenon of absorption of sound waves in water has three main causes: thermal conductivity, molecular viscosity, and molecular relaxation processes. They cause an observable reduction in the acoustic energy carried by the sound wave. For the research hypothesis, the third important reason is relaxing molecular processes [6, 25].

It relies on transforming particles into new structures, caused by an increase in pressure (resulting from the passage of a sound wave). It has been experimentally confirmed that the greatest energy loss (absorption) occurs when the period of the sound wave is equal to the time needed for the particle to transform into a new structure. At present, this phenomenon has been found for three frequencies of the sound wave [12, 30]:

- 1 kHz for boric acid
- 100 and 200 kHz for transformation of $MgSO_4$
- 105 MHz for structural transformation of water.

These phenomena are still being investigated – for example, studies for poly-methylacrylics are described in the work of Ceccorulli and Pizzoli [4].

It implies, that depending on the frequency of the sound wave (ratio of wavelength and particle diameter), it will be possible to notice increased wave scattering in the frequency band corresponding to specific particle diameters [32]. For given phytoplankton components, their diameter is determined by species and stage of development. This should make it possible to find the relationship between the number of organisms (and other particles suspended in water), their type or number of gas particles, and the length (frequency) of the scattered wave [28, 38].

In the literature research, references can be found showing the use of various models of sound wave propagation in water depending on its physical or geometric properties. Primarily for marine waters [1, 24].

In the description of sound propagation phenomena, various mathematical models are used to describe the phenomena occurring in water [7, 26, 27]. The models presented in those works, their mathematical description, and various methods of solving problems related to modeling phenomena occurring during the propagation of the sound wave in the water show that these phenomena are still poorly understood and ambiguous from the point of view of their understanding or mathematical description.

In the case of surface waters – PAM (Passive Acoustic Monitoring) is currently used. In the study by Desjonquères et al. [10], the authors describe the potential application of the PAM method for the assessment of biological phenomena and ecological assessment of surface waters. Putland and Mesinger [36] clearly emphasized that freshwater acoustic monitoring is a field of knowledge that is still more unknown than known. In their research, they focused on monitoring lakes in Minnesota and the impact of sonic anthropopressure on lake waters. However, they also used the PAM method. Similar conclusions can be drawn from the work by Proulx et al. [35].

Also, the work by Rountree et al. [37] focused on "new" sources of sounds in surface waters – from artificial sources (cars, air transport, and others), while confirming that living organisms are the source of a huge sound background in lakes – in practice mostly unrecognized yet.

In turn, Geay et al. [13] analyzed the method of propagation of sounds in shallow mountain streams in their work. In their research, they focused on the use of sound to assess the intensity of gravel and stone erosion in the bottoms of mountain streams. The use of acoustic monitoring methods is not limited to natural reservoirs.

However, there is relatively a lot of work on the propagation of sound waves in sea waters. In these works, the authors discuss the influence of physical parameters (temperature, density) and chemical parameters – salinity) on the propagation speed of the sound wave – pro. For example, works contained in post-conference materials published by Murali et al. [31] or specifically the work by Annalakshmi, and Murugan [2], where the authors devote an entire chapter to measuring the speed of sound in sea waters using the CTD data analysis (conductivity, temperature, depth – pressure). Similar studies are also carried out in

Poland – for example, the work by Opaliński [33] describes a study of the impact of salinity and persistent thermal stratification on the accuracy of bathymetric measurements of water reservoirs with the use of echolocation methods.

To summary the review, the description of physical phenomena related to the propagation of sound waves in water used in the measurement of the position of objects in the water (e.g. submarines, fish schools, underwater obstacles, etc.), i.e., it is well scientifically described, e.g. by Hodges [19]. The available sonic techniques can observe zooplankton clusters [14] – but there is very little research on sound wave propagation and showing the effects of pollution and temperature on sound wave propagation in lake waters [5].

The development of the above-described relationships between the propagation of a sound wave in water and its physicochemical properties will allow for a better understanding and more accurate description of the phenomena occurring in water during the propagation of a sound wave for different frequencies and water conditions. The development of new – more accurate regression formulas for the above-mentioned dependence will not only contribute to the development of science, but may be the basis – in the next step – for the development of new methods of analysis of the state of the water. Currently, such analyses require either measurements made with the use of multi-parameter probes or detailed laboratory analyses (physical, chemical analyses, microscopic analyses of phytoplankton and zooplankton), which are time-consuming and require the work of a team of specialists. These analyses – often tedious and time-consuming from the point of view of current standards, are often based on chemical methods.

2. Research hypothesis

As it was written in paragraph 1 – there are no articles available in the literature that illustrate the relationship between the trophic state of surface waters and physical phenomena related to the propagation of sound waves in water. Conducting the planned research will allow to find mathematical relationships (regression equations) between the mentioned above phenomena of sound wave propagation in water and its chemical, and physical state. Consequently, the scientific goal of the study is to find the relationship between the speed of propagation of sound and the physico-chemical state of surface waters.

The research hypothesis is as follows: a specific water status described by physical-chemical parameters will give characteristic parameters of sound wave propagation.

As a consequence, it is possible to build dependencies that will clearly define the trophic state of water based on the measurements of sound wave propagation.

3. Measuring stand

The ultrasonic measuring stand used in the study consisted of a Panametrics 5800PR ultrasonic wave generator, a Tektronix TDS 1012B digital oscilloscope, a set of M02 2L0o20C INCO measuring heads, and a measuring module that guaranteed a fixed, coaxial position of the heads opposite each other. An Adwa AD1020 laboratory meter with an accuracy of 0.1°C was used for temperature control (Fig. 1).

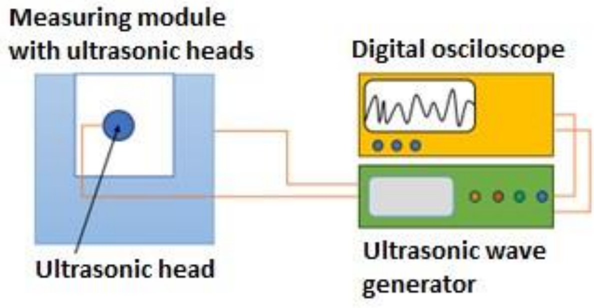

Fig. 1. Measuring stand

Knowing the distance of the heads in the measuring device (s = 48 ±0.05 mm) and measuring the ultrasonic wave transition time between the measuring heads (±0.01 µs), the propagation speed of the ultrasonic wave at a frequency of 2 MHz was calculated based on the relation (3) assuming a constant propagation speed of the ultrasonic waves at a short distance.

$$v = s \cdot t^{-1}\ [ms^{-1}] \tag{3}$$

where: v – ultrasonic wave propagation speed [ms^{-1}], s – distance between measuring heads [m], t – time of ultrasound wave transition through the test medium [s].

4. Material and methods

The research was organised into two stages, the first was to test the effect of phosphates in the sample on the ultrasonic wave propagation velocity, while the second consisted of testing one sample at selected temperatures to determine the effect of temperature on the ultrasonic wave propagation velocity.

In the first stage, laboratory samples based on distilled water with a phosphate content of 0, 20, 40, 60, 80 and 100 $kg \cdot m^{-3}$ were obtained by adding an appropriate amount of di-Potassium hydrogen phosphate 3 ($K_2HPO_4 \times 3H_2O$ – 228.23 $g \cdot mol^{-1}$) to water were used. The substance was then mixed with a mechanical stirrer until the components were dissolved in distilled water. The test consisted in determining changes in the speed of propagation of the ultrasonic wave depending on the phosphate content of the sample. For this purpose, each sample was tested 10 times using a specialised measuring stand described in more detail in section 4, and then the results were compared with each other. Additionally, in order to eliminate the effect of temperature on the measurement results, each of the tested samples was kept at 20 ±0.5°C.

The second stage consisted of using a tap water sample with unknown chemical content. The test was carried out using the same sample at temperatures ranging from 12 to 30°C, changing it every 1°C. Due to technical limitations of the measuring stand, 3 repetitions of the ultrasound propagation time were performed for each temperature value of the sample.

5. Results and discussion

The ultrasonic velocity calculated from the laboratory samples is shown graphically in Fig. 2.

The propagation velocity of the ultrasonic wave for the reference sample with zero phosphate content ranged from

1476.0 to 1476.5 $m \cdot s^{-1}$, and the mean value of the values obtained was 1476.1 ±2.1 $m \cdot s^{-1}$. A difference appeared already in the first sample with 20 $kg \cdot m^{-3}$ phosphate content, for which the calculated velocity ranged from 1502.2 to 1502.3 $m \cdot s^{-1}$ and the mean value was 1502.3 ±2.1 $m \cdot s^{-1}$.

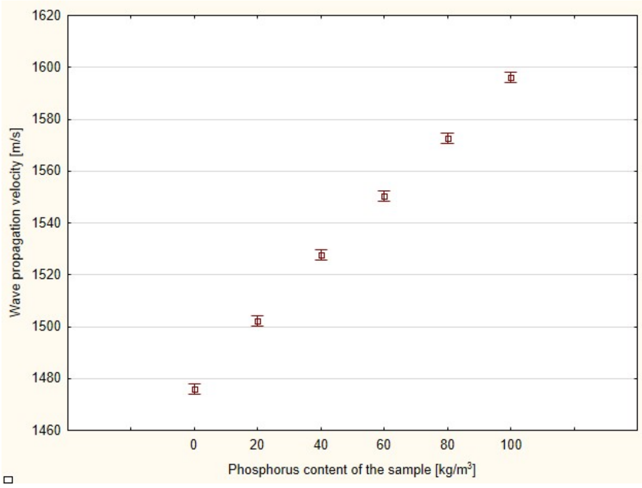

Fig. 2. Ultrasonic velocity calculated from the laboratory samples, phosphorus content

The average wave propagation velocity for the other samples was 1527.7 ±2.2 $m \cdot s^{-1}$ for the 40 $kg \cdot m^{-3}$ sample, 1550.4 ±2.2 $m \cdot s^{-1}$ for the 60 $kg \cdot m^{-3}$ sample, 1572.7 ±2.2 $m \cdot s^{-1}$ for the 80 $kg \cdot m^{-3}$ sample and 1596.3 ±2.3 $m \cdot s^{-1}$ for the 100 $kg \cdot m^{-3}$ sample.

Based on the results obtained, a linear approximating function (Fig. 3) (4) was determined using CurveExpert 1.4 software, whose correlation coefficient was r = 0.9995.

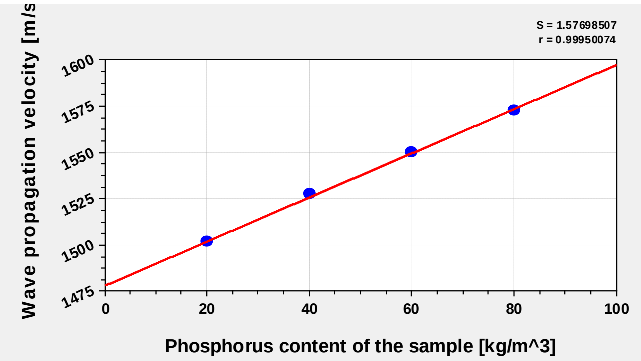

Fig. 3. Linear approximating function, phosphorus content

$$v = 1477.97 + 1.19 \cdot y1 \qquad (4)$$

where: v – ultrasonic wave propagation speed [$m \cdot s^{-1}$], y1 – phosphate content of the test sample [$kg \cdot m^{-3}$].

The second part of the study, testing the sample for changes in the characteristic parameter due to temperature change. Using the same sample continuously, the results were 1469.4 ±2.1 $m \cdot s^{-1}$ for a temperature of 12°C to 1518.5 ±2.1 $m \cdot s^{-1}$ for a temperature of 30°C. Changes in the ultrasonic wave propagation velocity values were observed with each temperature change (Fig. 4).

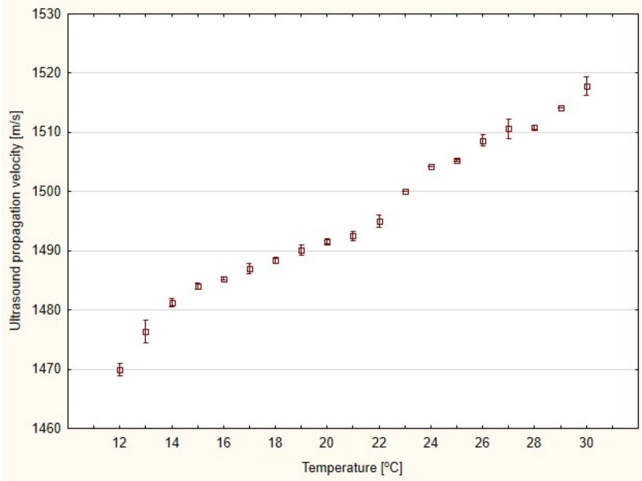

Fig. 4. Ultrasonic wave propagation velocity, temperature

Analogous to the first part, a linear approximating function (Fig. 5) (5) was determined using CurveExpert 1.4 software, whose correlation coefficient was r = 0.9906.

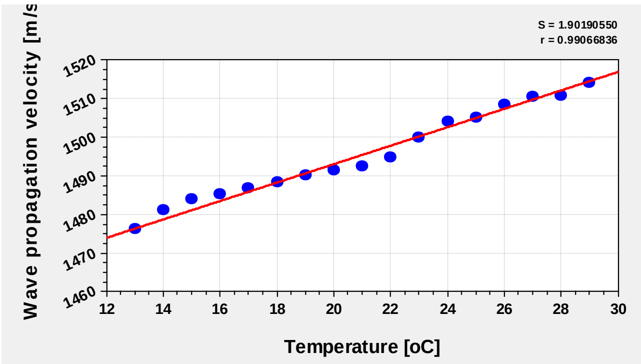

Fig. 5. Linear approximating function, temperature

$$v = 1444.21 + 2.44 \cdot y2 \qquad (5)$$

where: v – ultrasonic wave propagation speed [$m \cdot s^{-1}$], y2 – temperature of the tested sample [^{o}C].

In conclusion, the first part of the study shows that the ultrasonic wave propagation velocity not only increases with increasing phosphate content in the test sample but also this increase is close to linear, as the propagation velocity changed by 25 ±3 $m \cdot s^{-1}$ for each 20 $kg \cdot m^{-3}$ of phosphate content in the samples. This suggests that each 1 kg/m^3 increase in phosphate concentration should increase the wave propagation velocity by approximately 0.25 $m \cdot s^{-1}$.

In the second stage, the significant influence of the test sample temperature on the test results was confirmed. Each change in temperature caused significant differences in the average propagation of the ultrasonic wave in the sample. This shows that in ultrasonic testing, it is necessary to monitor and maintain the temperature of the samples being tested constantly.

6. Conclusions

As a result of the first part of the study, it can be concluded that the proposed method is useful for the measurement of phosphate content in laboratory samples, as the value of the propagation velocity of the ultrasonic wave is dependent on the content of phosphate in the test sample.

The measurements obtained indicate that the propagation speed of the ultrasonic wave not only increases with increasing phosphate concentration, but that this increase is also close to linear, as the propagation speed changes by 25 ±3 $m \cdot s^{-1}$ for every 20 $kg \cdot m^{-3}$ of phosphate concentration in the sample. This shows that each 1 $kg \cdot m^{-3}$ increase in phosphate concentration should increase the wave propagation velocity by approximately 0.125 $m \cdot s^{-1}$.

As a result of the study, it can be concluded that the proposed method is useful for measuring phosphate content in water with an accuracy of ±2.5 $kg \cdot m^{-3}$.

The second part of the study shows how much influence the sample temperature has on the measurement results. A temperature deviation of as little as 0.1 degree causes a significant change in the wave propagation speed. Therefore, it should be kept constant during future tests with the proposed method so that its value can be ignored.

The aim of publishing the paper in an automotive journal is to present the developed method for measuring contaminant content. As is well known, contaminants are also found in engine oils. They contribute to the degradation of the lubricating properties of oils [39]. According to the work [23], soot contamination of the lubricant can damage the power unit, so the rapid detection of its accumulation may be desirable to prevent damage. Adaptation of the presented method in vehicle diagnostics could extend the available methodology to a non-destructive and quick way of determining the properties of engine oils. A pilot study on contaminated engine oils using ultrasound is planned for the near future.

Nomenclature

c	speed of sound in water
c°	speed of sound in water under standard conditions
CTD	conductivity, temperature, depth (pressure) data analysis
K	modulus of volumetric elasticity
P	water pressure
PAM	passive acoustic monitoring
r	correlation coefficient
s	distance between measuring heads
S	water temperature
t	time of ultrasound wave transition through the test medium
T	water salinity
v	ultrasonic wave propagation speed
y1	phosphate content of the test sample
y2	temperature of tested sample
ρ	liquid density

Bibliography

[1] Ainslie MA, Laws RM, Sertlek HÖ. International airgun modeling workshop: validation of source signature and sound propagation models. Dublin, July 16, 2016. Problem Description. IEEE J Oceanic Eng. 2019;44(3):565-574. https://doi.org/10.1109/JOE.2019.2916956

[2] Annalakshmi G, Murugan SS. Analyzing the physical and chemical properties of water column nutrients and sediments along southeast coast of India. Fourth International Conference in Ocean Engineering (ICOE2018). 2019;22:985-996. https://doi.org/10.1007/978-981-13-3119-0_67

[3] Azmi NHBM. Bio-optical properties and seasonal variability of phytoplankton size classes in Peninsular Malaysia. Doctoral Thesis. Universiti Malaysia Terengganu. 2019.

[4] Ceccorulli G. Pizzoli M. Effect of water on the relaxation spectrum of poly (methylmethacrylate). Polym Bull. 2001; 47(3-4):283-289. https://doi.org/10.1007/s289-001-8183-9

[5] Cody R. Acoustic monitoring for leaks in water distribution networks. 2020. http://hdl.handle.net/10012/15773

[6] Davis CM, Jarzynski J. Liquid water – acoustic properties: absorption and relaxation. The Physics and Physical Chemistry of Water. 1972;1:443-461. https://doi.org/10.1007/978-1-4684-8334-5_12

[7] De Francesco A, Scaccia L, Formisano F, Maccarini M, De Luca F, Parmentier A et al. Shaping the terahertz sound propagation in water under highly directional confinement. Phys Rev B. 2020;101(5):054306. https://doi.org/10.1103/PhysRevB.101.054306

[8] Dera J. Fizyka morza (in Polish). PWN, Warsaw 2003.

[9] Dera J. Marine physics. Elsevier. 1992.

[10] Desjonquères C, Gifford T, Linke S. Passive acoustic monitoring as a potential tool to survey animal and ecosystem processes in freshwater environments. Freshwater Biol. 2020; 65(1):7-19. https://doi.org/10.1111/fwb.13356

[11] Fine RA, Wang DP, Millero FJ. The equation of state of water and seawater as determined from sound velocity data. J Acoust Soc Am. 1973;53(1):365-365. https://doi.org/10.1121/1.1982619

[12] Francois RE, Garrison GR. Sound absorption based on ocean measurements: Part I: pure water and magnesium sulfate contributions. J Acoust Soc Am. 1982;72(3):896-907. https://doi.org/10.1121/1.388170

[13] Geay T, Michel L, Zanker S, Rigby JR. Acoustic wave propagation in rivers: an experimental study. Earth Surf Dynam. 2019;7(2):537-548. https://doi.org/10.5194/esurf-7-537-2019

[14] Geraldes P, Barbosa J, Martins A, Dias A, Magalhães C, Ramos S et al. In situ real-time zooplankton detection and classification. Oceans 2019-Marseille IEEE. 2019;1-6. https://doi.org/10.1109/OCEANSE.2019.8867552

[15] Greenwood HJ. The compressibility of gaseous mixtures of carbon dioxide and water between 0 and 500 bars pressure and 450 and 800 centigrade. Amer J Sci. 1969;267:191-208.

[16] Grochowska J, Augustyniak R, Łopata M, Tandyrak R. Is it possible to restore a heavily polluted urban lake? Appl Sci. 2020;10(11):3698. https://doi.org/10.3390/app10113698

[17] Hamilton EL. Sediment sound velocity measurements made in situ from bathyscaph Trieste. J Geophys Res. 1963;68(21): 5991-5998. https://doi.org/10.1029/JZ068i021p05991

[18] Hermanowicz W, Dożańska W, Dojlido J, Koziorowski B, Zerbe J. Physical and chemical analysis of water and sewage. Arkady, Warsaw 1999.

[19] Hodges RP. Underwater acoustics: analysis, design and performance of sonar. John Wiley & Sons. 2011.

[20] Kajak Z. Hydrobiologia-limnologia. Ekosystemy wód śródlądowych (in Polish). PWN, Warsaw 2001.

[21] Koszela J, Koszela-Marek E, Sysak Z. Weryfikacja zmian ściśliwości wody i roztworu soli NaCl pod wpływem wyso-

kich ciśnień (in Polish). Górnictwo i Geoinżynieria. 2008;2:205-211.
[22] Koszela-Marek E. Charakterystyka zmian ściśliwości roztworów soli NaCl pod wpływem wysokich ciśnień hydrostatycznych (in Polish). Górnictwo i Geoinżynieria. 2009;1:361-367.
[23] Kozak M, Siejka P. Soot contamination of engine oil – the case of a small turbocharged spark-ignition engine. Combustion Engines. 2020;182(3):28-32. https://doi.org/10.19206/CE-2020-305
[24] Küsel ET, Siderius M. Comparison of propagation models for the characterization of sound pressure fields. IEEE J Oceanic Eng. 2019;44(3):598-610. https://doi.org/10.1109/JOE.2018.2884107
[25] Leroy CC, Mellen RH, Waton G. Absorption of sound in fresh and sea water. Handbook of Elastic Properties of Solids, Liquids, and Gases. 2001;83-115.
[26] Li C. An efficient multi-layer boundary element method for direct computation of sound propagation in shallow water environments. Doctoral Thesis. Massachusetts Institute of Technology. 2019. https://hdl.handle.net/1721.1/124032
[27] Li C, Campbell BK, Liu Y, Yue DK. A fast multi-layer boundary element method for direct numerical simulation of sound propagation in shallow water environments. J Comput Phys. 2019;392:694-712. https://doi.org/10.1016/j.jcp.2019.04.068
[28] Lunkov AA. Reverberation of wideband signals in shallow water when using sound focusing. Acoust Phys+. 2018; 64(3):347-355. https://doi.org/10.1134/S1063771018030120
[29] Mackenzie KV. Formulas for the computation of sound speed in sea water. J Acoust Soc Am. 1960;32(1):100-104. https://doi.org/10.1121/1.1907859
[30] Mellen RH, Simmons VP, Browning DG. Low-frequency sound absorption in sea water: a borate-complex relaxation. J Acoust Soc Am. 1980; 67(1):341-342. https://doi.org/10.1121/1.384469
[31] Murali K, Sriram V, Samad A, Saha N. Proceedings of the Fourth International Conference in Ocean Engineering (ICOE2018). 2018;1&2. https://doi.org/10.1007/978-981-13-3119-0
[32] Oku T, Hirahara H, Akimoto T. Visualization of deformation and sound emission from bubble in water using VOF method. 18th International Symposium on Flow Visualization, ETH Zurich 2018.
[33] Opaliński P. Wpływ stratyfikacji termicznej i zasolenia na prędkość rozchodzenia się fali akustycznej w wodzie oraz jej wpływ na wynik pomiarów batymetrycznych. Dokonania naukowe doktorantów: nauki inżynieryjne (in Polish). Creativetime, Kraków 2013;151-158.
[34] Pitzer KS, Lippmann DZ, Curl Jr RF, Huggins CM, Petersen DE. The volumetric and thermodynamic properties of fluids. II. Compressibility factor, vapor pressure and entropy of vaporization. J Am Chem Soc. 1955;77(13):3433-3440. https://doi.org/10.1021/ja01618a002
[35] Proulx R, Waldinger J, Koper N. Anthropogenic landscape changes and their impacts on terrestrial and freshwater soundscapes. Current Landscape Ecology Reports. 2019;4(3):41-50. https://doi.org/10.1007/s40823-019-00038-4
[36] Putland RL, Mensinger AF. Exploring the soundscape of small freshwater lakes. Ecol Inform. 2020;55:101018. https://doi.org/10.1016/j.ecoinf.2019.101018
[37] Rountree RA, Juanes F, Bolgan M. Temperate freshwater soundscapes: a cacophony of undescribed biological sounds now threatened by anthropogenic noise. Plos One. 2020; 15(3):0221842. https://doi.org/10.1371/journal.pone.0221842
[38] Shagapov VS, Galimzyanov MN, Vdovenko II, Khabeev NS. Characteristic features of sound propagation in a warm bubble-laden water. Journal of Engineering Physics and Thermophysics. 2018;91(4):854-863. https://doi.org/10.1007/s10891-018-1809-9
[39] Skonieczna D, Szczyglak P, Lemecha M. Modelling lubricating oil wear using fuzzy logic. Combustion Engines. 2024. https://doi.org/10.19206/CE-183186
[40] Wilson WD. Ultrasonic measurement of the velocity of sound in distilled and sea water. US Naval Ordnance Laboratory. 1960;6746.

Paweł Wesołowski, MEng. – Faculty of Technical Sciences, University of Warmia and Mazury in Olsztyn, Poland.
e-mail: *pawel.wesolowski@student.uwm.edu.pl*

Maciej Neugebauer, DSc., DEng. – Faculty of Technical Sciences, University of Warmia and Mazury in Olsztyn, Poland.
e-mail: *mak@uwm.edu.pl*

Article citation info:
Zadrąg R, Socik P, Kniaziewicz T, Zacharewicz M, Bogdanowicz A, Wirkowski P. Analysis of simulated dynamic loads of a ship propulsion system of a non-conventional power system. Combustion Engines. 2024;197(2):158-168. https://doi.org/10.19206/CE-184139

Ryszard ZADRĄG
Paweł SOCIK
Tomasz KNIAZIEWICZ
Marcin ZACHAREWICZ
Artur BOGDANOWICZ
Paweł WIRKOWSKI

Combustion Engines
Polish Scientific Society of Combustion Engines

Analysis of simulated dynamic loads of a ship propulsion system of a non-conventional power system

ARTICLE INFO

Received: 24 November 2023
Revised: 12 February 2024
Accepted: 15 February 2024
Available online: 7 March 2024

Unconventional approaches to propulsion system design are increasingly being explored to meet increasing demands for efficiency, ecology, and reliability. This paper focuses on the analysis of simulated dynamic loads on the propulsion system of ships that feature unconventional power systems – Reformed Methanol Fuel Cell System (RMFC). The analysis is aimed at understanding the performance of these systems under dynamic sea conditions, assessing their performance, and identifying potential challenges and benefits associated with them (including military ones). According to military assumptions, an undeniable benefit is the minimization of the ship's physical fields and its independence from the base (i.e., in the future, obtaining hydrogen from seawater electrolysis).

Key words: *marine diesel combustion engine, RMFC, fuel cell, methanol reforming, hydrogen*

1. Introduction

Today's marine technology is constantly evolving, striving for ever more advanced and efficient solutions. One of the core components of modern vessels is their propulsion system, which plays a key role in ensuring not only efficiency but also the sustainability of the marine environment. Increasingly, unconventional approaches to propulsion system design are being explored to meet the growing demands for efficiency, ecology, and reliability.

In addition to the aforementioned commercial requirements, special – purpose entities – such as the military – focus additionally on logistical aspects (independence from the base), and stealthiness of operations (minimizing the physical ship, including acoustic and thermal). These aspects can be provided by propulsion systems equipped with hydrogen-powered fuel cells.

The conditions of use of marine main propulsion engines are peculiar, resulting from the resistance characteristics of the vessel and the characteristics of the propellers. The movement of the vessel is characterized by significant dynamics resulting from changes in the external conditions of swimming, which significantly affects the course of the resistance characteristics and, thus, changes in the power of the main engines at a given speed of swimming. The dynamic change of loads, during which there is a change in the performance of the propulsion system at a given time, occurs as a result of steering, the interaction of external conditions as well as their correlation. Typical dynamic conditions occur during starting from a standstill, changes in speed, changes in the direction of movement of the vessel, sailing in storm conditions, working on DP, performing special tasks (e.g. fishing, trawling, searching for mines) [17].

Reciprocating internal combustion engines were the traditional solution adopted for most ships of the last century. The emerging sense of environmental responsibility in the early 20th century [15, 35] as the changing climate led to a change of approach in ship propulsion design [1]. The shipbuilding industry focused its efforts on implementing exhaust gas cleaning systems to ensure compliance with MARPOL regulations [3, 16]. The 21st century brought further restrictions on toxic exhaust emissions [16, 22], forcing the introduction of alternatives for energy efficiency as well as emission reduction.

Leo et al. [19] took up the study of PEM fuel cells in terms of exergy loss and exergy efficiency. He performed the analysis for PEM fuel cells powered by hydrogen produced by methanol reforming and direct methanol fuel cells powered by direct liquid methanol [19].

The issue of using hydrogen as an alternative power source at sea was dealt with, among others, by Meryem Gizem Sürer and Hüseyin Turan Arat. They summarized the latest research, hydrogen production, and storage methods and challenges, which allowed them to analyze the development of fuel cell-based marine vehicles [26].

Zuhang et al. [10] in their research present a literature analysis of the economics, feasibility, and primacy of fuel cells and hydrogen for marine applications in four aspects: key technologies for marine fuel cell applications, key technologies for marine hydrogen applications, costs, and standards.

Elammas [7] paper analyzed the environmental benefits of hydrogen fuel cells, including their potential to reduce greenhouse gas emissions and improve energy efficiency. In addition, he addressed the issues of improving energy security and reducing dependence on fossil fuels in maritime transportation.

One variant of the solution is the use of hybrid propulsion systems (HPS), which use electric motors, power generation systems, and power storage systems (Fig. 1). The downside of hybrid solutions is the increased weight of the vessel. However, the benefits of such a solution, including the high efficiency of the electric engine and the reduction of toxic exhaust emissions, outweigh the potential losses.

Satisfactory results obtained for hybrid propulsion systems encourage total propulsion electrification. An issue still being worked out is the optimization of electricity storage in batteries, the efficiency of this process depending on the speed and temperature of battery operation, and the thread of electricity production [2, 25, 32].

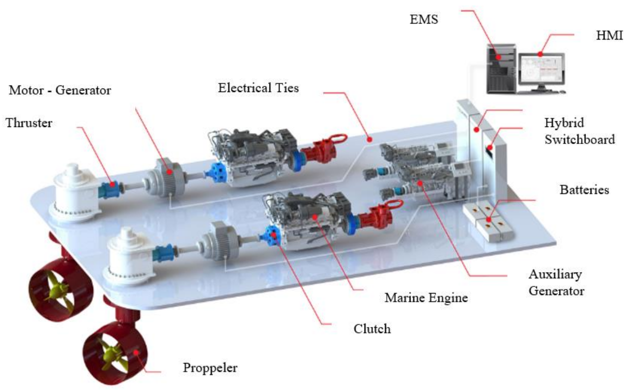

Fig. 1. AKA Hybrid propulsion [36]

A major trend in the development of marine propulsion systems is the use of alternative fuels such as hydrogen and its compounds. The revolution, which is already underway, is being driven by fuel cell (FC) technology and hybrid energy storage systems (HESS). Fuel cells are a quiet and clean energy source. On the plus side, fuel cells have a much higher energy density and high energy efficiency than batteries. Given these advantages, fuel cells themselves as well as hybrid systems have a promising future in marine applications [21, 22, 23]. One example of a hybrid system is the use of a PEMFC cell in a propulsion system in which an electrochemical battery can be recharged from a fuel cell (Fig. 2).

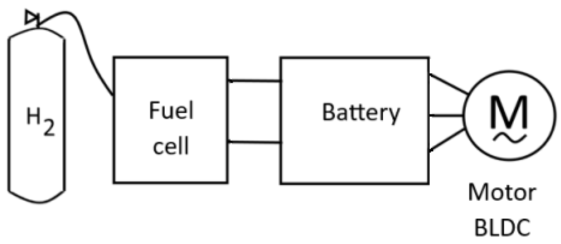

Fig. 2. Schematic of the construction ship propulsion system in which electrochemical battery can be recharged from a PEMFC

Among the 6 main types of fuel cells available (Table 1), which are used commercially, FCs containing a solid electrolyte are the most predisposed for power unit applications.

This group includes proton exchange polymer membrane fuel cells (PEMFCs), which can operate in the temperature range from 20 to 70°C (LT-PEMFC), and solutions operating at temperatures of 120–160°C (HT-PEMFC) [4, 31]. It should be noted that LT-PEMFC polymer cells, with respect to HT-PEMFCs, have already been used commercially in transportation for many years [5, 6, 31].

Despite the main advantage of LT-PEMFCs being low-temperature operation, they have one key disadvantage. In the use of these cells is the need to use high-purity hydrogen H2 (5N), due to the presence of a platinum catalyst. An example of an LT-PEMFC fuel cell stack is shown in Fig. 3. Unfortunately, the cost of the Pt catalyst, accounts for about 50% of the total cost of a PEMFC fuel cell stack. In addition, the Pt catalyst, shows very poor resistance to CO, SO_x (the possibility of catalyst degradation, leading to significant degradation of the electrical performance of the FC stack) [5, 6, 33].

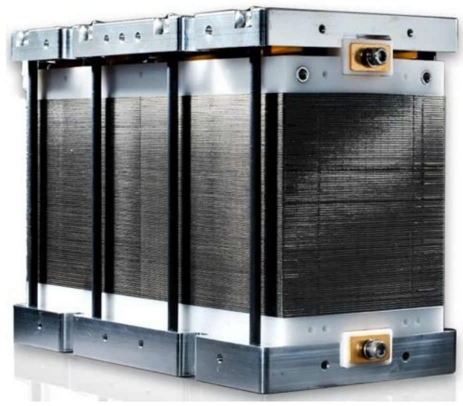

Fig. 3. Example PEM fuel cell stack [11]

LT-PEMFC fuel cells can operate as electricity generators in a wide range of electrical outputs from a few watts to several hundred kW. In turn, these units can be combined in a modular fashion (i.e., series connection of smaller units, parallel connection of more units) or electrically connected in series-parallel to form high-power generators, i.e., the 15–19 MW range [5, 6].

Table 1. Types of fuel cells [9, 31]

Type of cell	Electrolyte	Operating temperature [°C]	Fuel	Efficiency [~%]	Application
PEMFC – polymer membrane fuel cell	solid polymer	20–160	H_2, N_2H_4, CH_4 – fuel and oxidizer devoid of CO_2	53–58	astronautics, military technology
AFC – alkaline fuel cell	solution KOH	50–200	H_2, N_2H_4, CH_4	60	astronautics, military technology
DMFC – methanol fuel cell	solid polymer	20–90	methanol	40	portable
PAFC – phosphoric acid fuel cell	Concentrated H_3PO_4	150–200	H_2, CH_3OH, natural gas, kerosene, biogas	> 40	public facilities
MCFC – molten carbonate fuel cell	fused carbonate (Li, K, Na)	600–700	CH_3OH, natural gas, biogas	45	power generation
SOFC – solid oxide fuel cell	ZrO_2:Y2O_3	500–1000	H_2, CH_4, natural gas, biogas	35–43	power engineering, cogeneration

PEMFC generators have an electrical efficiency of 45–65%,The rest of the energy is lost as heat. In order to remove heat from the fuel cell space, they must have cooling systems. Liquid cooling systems are used at scales above 10 kW. It should be noted that the heat from LT-PEMFC fuel cells can be recovered and used in the system, raising the efficiency of the integrated energy system to 70–80% [8, 28].

As a rule of thumb, LT-PEMFC fuel cells require a supply of 0.8 m^3 of H_2 (at 50% efficiency) to produce 1 kWh. Based on this relationship, it can be assumed that an FC generator (FC stack module of 100 kW, to produce 100 kWh will require the supply of 80 m^3 of H_2 or 7.12 kg of H_2. In the case of FC LT-PEMFC generators, it is necessary to take into account about 2–3% H_2 of hydrogen additionally for the so-called own needs (purification, membranes, over–blowing). Media outlet temperatures from the media cooling system and from the cathode space are in the range of 45–55°C [6, 15, 24, 34].

This article focuses on analyzing the simulated dynamic loads of a ship's propulsion system, which features an unconventional power system (in this case, a power generation module consisting of a 5 kW fuel cell powered by reformer-generated hydrogen (RMFC)). The analysis of such a solution is aimed at understanding their performance under dynamic maritime conditions, assessing their performance, and identifying possible challenges and benefits associated with them.

The conclusions of this analysis may have important implications for the future of marine transportation and vessel operations. By considering unconventional power systems, we are able to chart development paths that will contribute to a more sustainable and efficient use of marine resources, while reducing environmental impact.

In terms of military application, the key is to achieve independence from fossil fuels, which, during a potential conflict, can increase the operational potential of the ships. In addition, which is also part of the research issue, the use of RMFCs allows for minimizing the ship's thermal field by lowering the temperature of the exhaust gases.

2. Research object

In order to carry out the study, it was necessary to obtain the actual load spectra of the marine engine. Data were obtained from a vessel equipped with an MTU 8V2000 M72 propulsion engine (Fig. 4).

Fig. 4. View of the MTU 8V2000 M72 engine [27]

Basic technical engine data is shown below in Table 2.

Table 2. Technical data of the MTU 8V2000 M72 engine [27]

Rated speed	rpm	2250
Rated power	kW	720
Number of cylinders	–	8
Cylinder arrangement and quantity	°	90
Piston stroke	mm	156
Cylinder diameter	mm	135
Cylinder displacement	cm^3	2230
Total engine displacement	cm^3	17840
Number of inlet valves per cylinder	–	2
Number of exhaust valves per cylinder	–	2

The object of laboratory research was a stationary test stand for power generation, which is located at the equipment of the Poznan University of Technology (Fig. 5). The configuration of this station allows simulation studies that faithfully, assuming the scalability of the processes, reflect the nature of load changes in the ship's propulsion system.

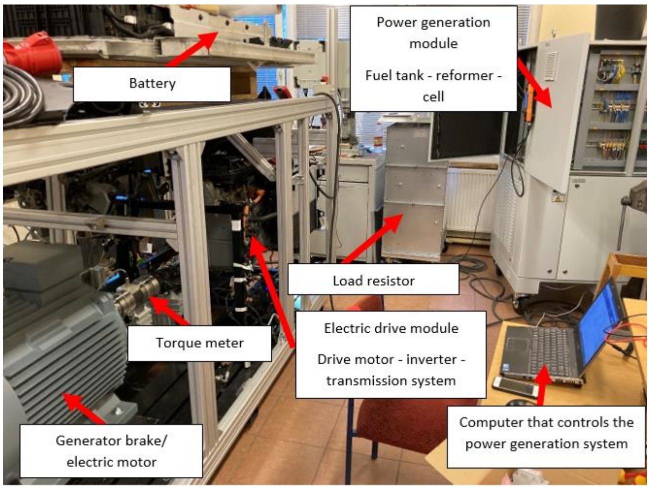

Fig. 5. Reformer test stand including battery, electric motor, power take-off system and data acquisition station

The main components of the stand (Table 3) are a power generation module (H3–5000 is a Reformed Methanol Fuel Cell System (RMFC)) consisting of a 5 kW fuel cell (HTPEM) powered by hydrogen generated in the reformer. The reformer, on the other hand, is powered by an aqueous methanol solution with a methanol–water ratio of 60/40. The stand also includes a battery, an electric motor and a resistor.

The operation of the test stand load system is controlled by software dedicated to the developed test stand design. The reformer feeding the fuel cell operated in automatic mode, selecting the fuel dose according to the charging current. The control interface is shown below (Fig. 6). To test toxic compounds, a TESTO 350 analyzer was used, which was plugged into the reformer's exhaust outlet.

Table 3. Technical specifications test bench [30]

RMFC		
Maximum power output	W	5000
Input/Output voltage	W	42/57
Output current	A	125
Fuel consumption	dm^3/kWh	0.9
Battery		
Total energy capacity	kWh	25.92
Operational energy capacity	kWh	23.30
Number of cells	–	192
Rated voltage of a single cell	V	3.75
Rated capacity of a single cell	Ah	36
Rated voltage	V	395
Electric motor		
Engine power	kW	65 at 3000 rpm
Continuous engine power	kW	43
Maximum torque	Nm	220 in the shaft speed range of 250–2500 rpm

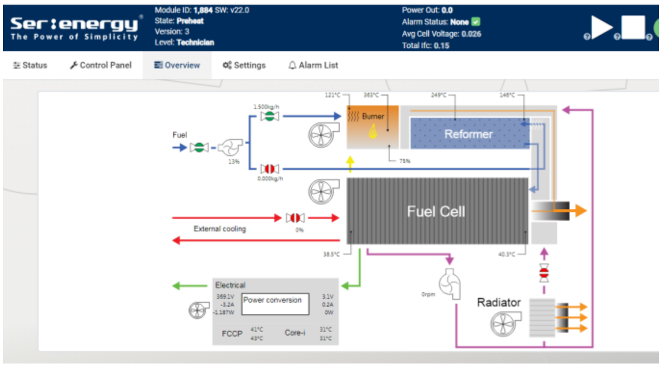

Fig. 6. RMCF data acquisition workstation interface

3. Research plan

In accordance with the research methodology, a research plan was developed, taking into account the research object, the measurement apparatus used and the measured parameters of the research object. Due to the complexity of the processes occurring during the load changes of the marine engine, it was decided to carry out tests for 4 cases determined on the basis of data collected on the vessel according to:

– the experimental plan of PS/DK 3^2
– the propeller characteristics
– the load histogram
– the battery charging plan.

Crankshaft speed, engine torque load, fuel consumption, exhaust toxic content and temperature, battery discharge/charge current, battery voltage, battery charge level were measured for the test object.

3.1. Research according to the experimental plan of PS/DK 3^2

Design of experiment (DoE) is often used to create empirical models. It reduces the number of measurements required, which translates into a reduction in the use of the object under study and, consequently, a reduction in costs. A properly selected research plan gives the possibility of obtaining accurate results, i.e., mathematical relationships describing selected process quantities [12 13, 20].

The study was planned using a static determined complete research plan (PS/DK 3^2), with which the influence of two input factors (crankshaft speed and engine torque load) was analyzed.

One of the steps in planning the experiment is to determine a set of characteristic quantities for the test object (Fig. 7), which were selected by introducing the following simplifications:

1. Constant values, due to their invariable influence on the waveform output values, are not taken into account
2. Interference factors are ignored due to studies conducted under identical environmental conditions
3 The set of input (independent) quantities is defined as follows:
   – shaft speed n = 300–1200 rpm
   – torque set on brake M = 0–60 Nm
4. The output quantities are limited to the quantities:
   – receiver (motor) power P [kW]
   – battery voltage U [V]
   – battery voltage drop dU [V/s]
   – battery current I_{bat} [A]
   – charging current I_{lad} [A]
   – battery charge level [%]
   – exhaust gas temperature t_{sp} [°C]
   – nitrogen oxides concentration in the exhaust gas NO_x [ppm]
   – nitrogen oxide concentration in the exhaust gas NO [ppm]
   – nitrogen dioxide concentration in the exhaust gas NO_2 [ppm]
   – carbon monoxide concentration in the exhaust gas CO [ppm]
   – carbon dioxide concentration in the exhaust gas CO_2 [%].

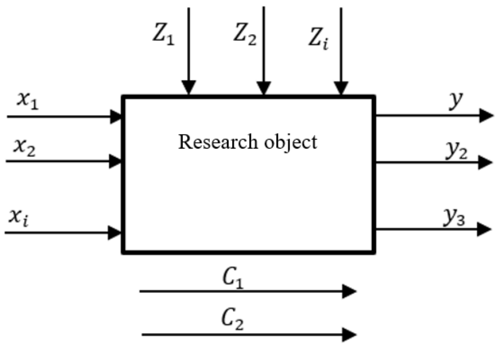

Fig. 7. Research object – structure. x – input quantities, y – output quantities, Z – disturbing quantities, C – constant values [37]

The values of the input parameters (in the number k) in the given intervals took over three levels of variation, which allows us to obtain a mathematical model of the studied process in the form of a polynomial of the second degree [37]:

$$y = b_0 + \sum b_k x_k + \sum b_{kk} x_k^2 + \sum b_{kj} x_k x_j \qquad (1)$$

where: y – dependent output factor, x – j-th independent input factor, b – regression function coefficient.

The experiment was carried out according to the appropriate (for the chosen research plan) set of process input parameter values (Table 4).

Table 4. The experimental plan

Test	A	B	n [rpm]	M [Nm]
1	–1	–1	300	20
2	0	–1	750	20
3	1	–1	1200	20
4	–1	0	300	40
5	0	0	750	40
6	1	0	1200	40
7	–1	1	300	60
8	0	1	750	60
9	1	1	1200	60

The researcher were able to perform as few as nine tests, which made it possible to satisfactorily analyze the results obtained. In this plan:

– A is crankshaft rotational speed
– B is torque set on brake.

Number –1, 0 and 1 means lowest, middle and highest value of parameters A and B.

3.2. Research by propeller characteristics

The analysis by propeller characteristics was performed on the basis of the quantities obtained from the field of the MTU 8V2000 M72 engine (Fig. 8).

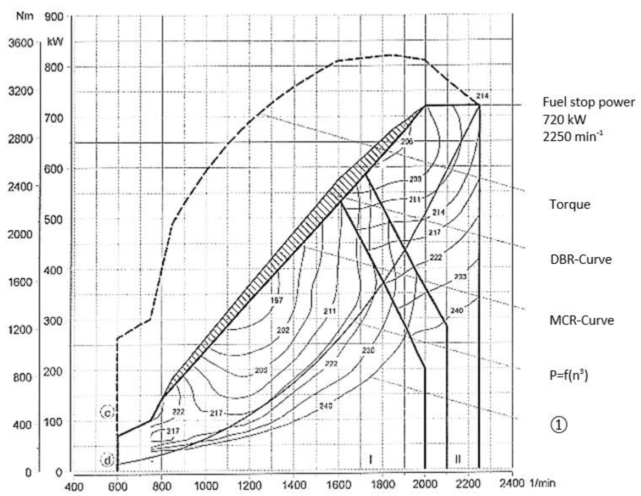

Fig. 8. MTU 8V2000 M72 engine work field. DBR – temporary work curve, WMT – maximum continuous work curve, P = f (n^3) – propeller characteristics, 1 – unit fuel consumption curves [27]

In order to perform the experiment, the assumed values of power and speed obtained from the working field were converted to denominated values to perform the bench test (Table 5).

Table 5. Independent parameter assumptions for the helical characteristics

No.	n [rpm]	M [Nm]	n/n_e	P/P_e	n [rpm]	M [Nm]
1	600	20	0.33	0.03	400	1.8
2	800	40	0.44	0.11	530	6.6
3	1000	60	0.55	0.16	660	9.6
4	1200	110	0.66	0.3	790	18
5	1400	170	0.77	0.46	920	27.6
6	1600	260	0.88	0.7	1050	42
7	1800	370	1	1	1200	60
	SHIP				TEST STAND	

3.3. Research according to the load diagram

Data from the ship's machine log was used to develop the load diagram. In the ship's machine log, load status information is recorded in the form of changes in engine speed. Records are made every hour of continuous operation or when the engine speed changes. Nowadays, this process is done automatically with the help of dedicated ship engine room monitoring programs.

Engine load processes during operation can be treated as a stochastic process (with engine standstill treated as an additional operating state) described by a process state space:

$$\Omega = \{e_1, e_2, e_3, e_4, e_5, e_6\} \qquad (2)$$

where: e_1 – the operating condition of the engine in "loose gear", n = 600 rpm, e_2 – engine running condition on "very slow forward", n = 600 rpm, P_e = 0.03 P_z (20 kW), e_3 – engine running condition on "slow forward", n = 1200 rpm, P_e = 0.15 P_z (110 kW), e_4 – engine running condition at "half ahead", n = 1800 rpm, P_e = 0.51 P_z (370 kW), e_5 – engine running condition at "full ahead", n = 2250 rpm, P_e = P_z (720 kW), e_6 – „stop".

The power values for individual engine loads were determined indicatively for the ship's averaged propeller characteristics and assuming that in the ship's propulsion system the engines reach their rated operating point, i.e. for full displacement at rated speed value n = 2250 rpm the engines reach rated power P_z = 720 kW.

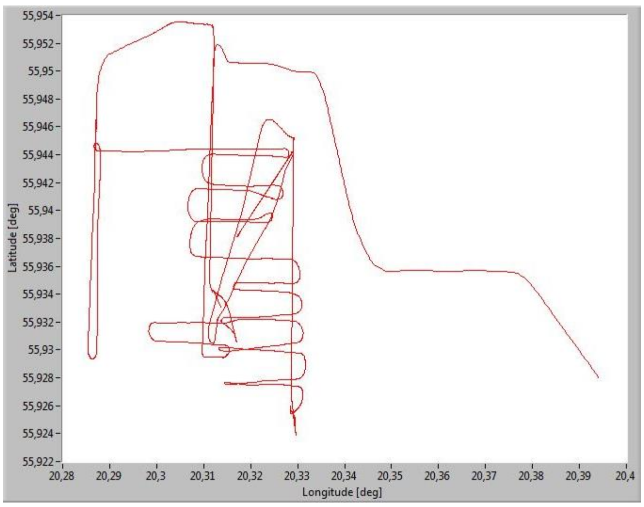

Fig. 9. The recorded path during the task searching by lanes

Also key to the operation of the ship's propulsion system is the type of task being performed, e.g. (minesweeping, patrolling, searching, identification). Each of the tasks requires different engine settings and introduces additional variables (e.g., changes in the direction of swimming, wind influence, making turns). An example of the path of a special–purpose vessel while performing a strip search task is shown in Fig. 9. Data for the chart was obtained from the "Automatic Identification System" AIS system.

Based on the values from the machine log, a histogram was developed for each working conditions (Fig. 10).

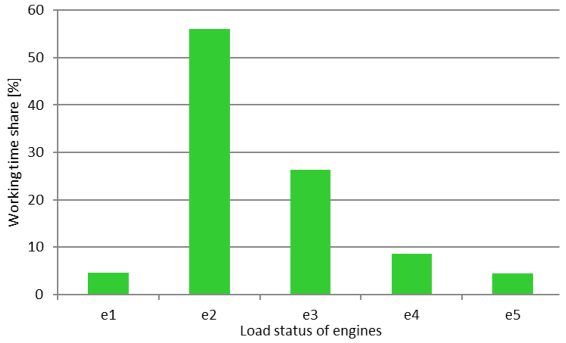

Fig. 10. Histogram of engines running time

In order to perform the experiment, the assumed values of power and speed obtained from the time balance of the motors (load histogram) were converted to denominated values, which allowed to perform the test on the test bench (Table 6).

Table 6. Independent parameter assumptions for the load diagram

Propulsion mode		n [rpm]	Usable power	Power for the propulsion mode [kW]	n [rpm]	M [Nm]
e1	luz	600	0	0	400	0
e2	BWN	600	$P = 0.03\ P_{max}$	20	400	1.8
e3	WN	1200	$P = 0.15\ P_{max}$	110	790	18
e4	PN	1800	$P = 0.51\ P_{max}$	370	1200	60
e5	CN	2250	$P = 1.0\ P_{max}$	720	1400	110
SHIP					TEST STAND	

3.4. Research according to the plan charging the battery

The analysis according to the 'battery charging' plan was carried out during battery charging using the system presented in Chapter 2. During start-up and preheating and cooling of the reformer, the test quantities were not measured due to the lack of measurement capabilities. Attention should be paid to the preparation time of the reformer for operation, i.e. the preheating process, which takes about 36 minutes, and the cooling time – 24 minutes. This accounts for about 33% of the device's operating time. The test plan for battery charging is shown in Table 7.

Table 7. The experimental plan for battery charging

No.	Battery charging current [A]	Measurement time [min]
–	start + preheating	36
–		
1	2	8
2	4	23
3	6	7
4	8	10
5	10	8
6	12	10
7	13	12
8	6	37
–	cooling + stop	24
–		

4. Test results

In accordance with the established test plan, all the mentioned parameters of engine operation were measured and recorded for the set speed, torque, and battery charging current. After the tests were performed, the obtained output values were analyzed in the STATISTICA program.

4.1. Analysis of the results for the experiment plan PS/DK 3^2

The analysis began by determining the significance of the influence of individual input parameters and their interactions were determined using ANOVA analysis of variance. The next step was to determine the quality of fit of the obtained (quadratic) models to the measured values was determined on the basis of coefficients of determination R^2 and standard deviation of the residual component s [12, 18, 29].

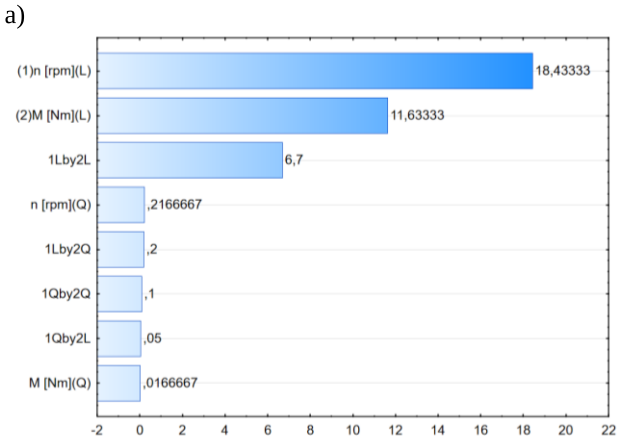

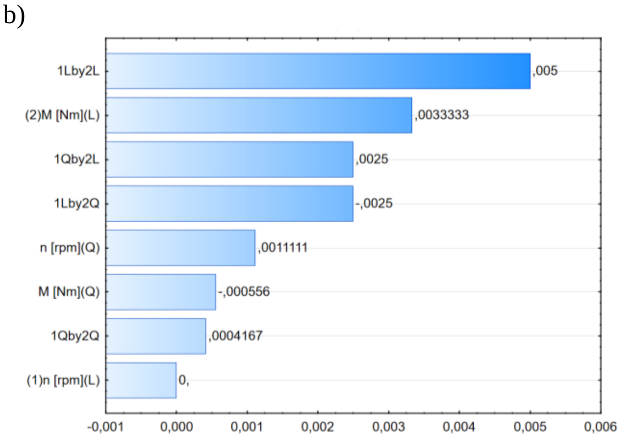

Fig. 11. Pareto charts of concentration of a) battery current I_{bat}, b) battery voltage drop dU

The approximated polynomials (1) allowed the determination of relationships between the variables, including the calculation and evaluation of the effect of loadings on the determination of correlations. Pareto charts were used for preliminary analysis.

Figure 11 shows the effect of individual independent factors and their interactions on battery performance indicators. The input quantities are represented on the vertical axis of the graph. Number 1 is crankshaft rotational speed, 2 – torque on the brake. The designation "L" means that the value of the coefficient is assigned to the linear magnitude of the polynomial, "Q" – to the quadratic magnitude, while "wz" – in relation to. As you can see, the main effect on the studied quantities is directly influenced by the speed as well as the torque, and for changes in battery voltage the relationship between the independent variables.

Based on the data obtained, surface plots were created and the changes in the parameters studied were presented as a function of fuel crankshaft speed and torque set on the brake (Fig. 12).

In the studied range of load and speed, the battery voltage drop was found to be the smallest for high loads and low speeds at the same time, or low loads and high speeds. The other studied parameters, such as power, battery discharge current, and battery charge level, show changes as expected, i.e., as the independent parameters increase, the values of battery current and receiver power increase, while the battery charge level decreases.

4.2. Analysis of results for propeller characteristics

For the results obtained, a slight spike in the battery charge value is visible (Fig. 13). This is due to both the time of measurement, which for technical reasons was limited to two minutes, and the small load variances of the system.

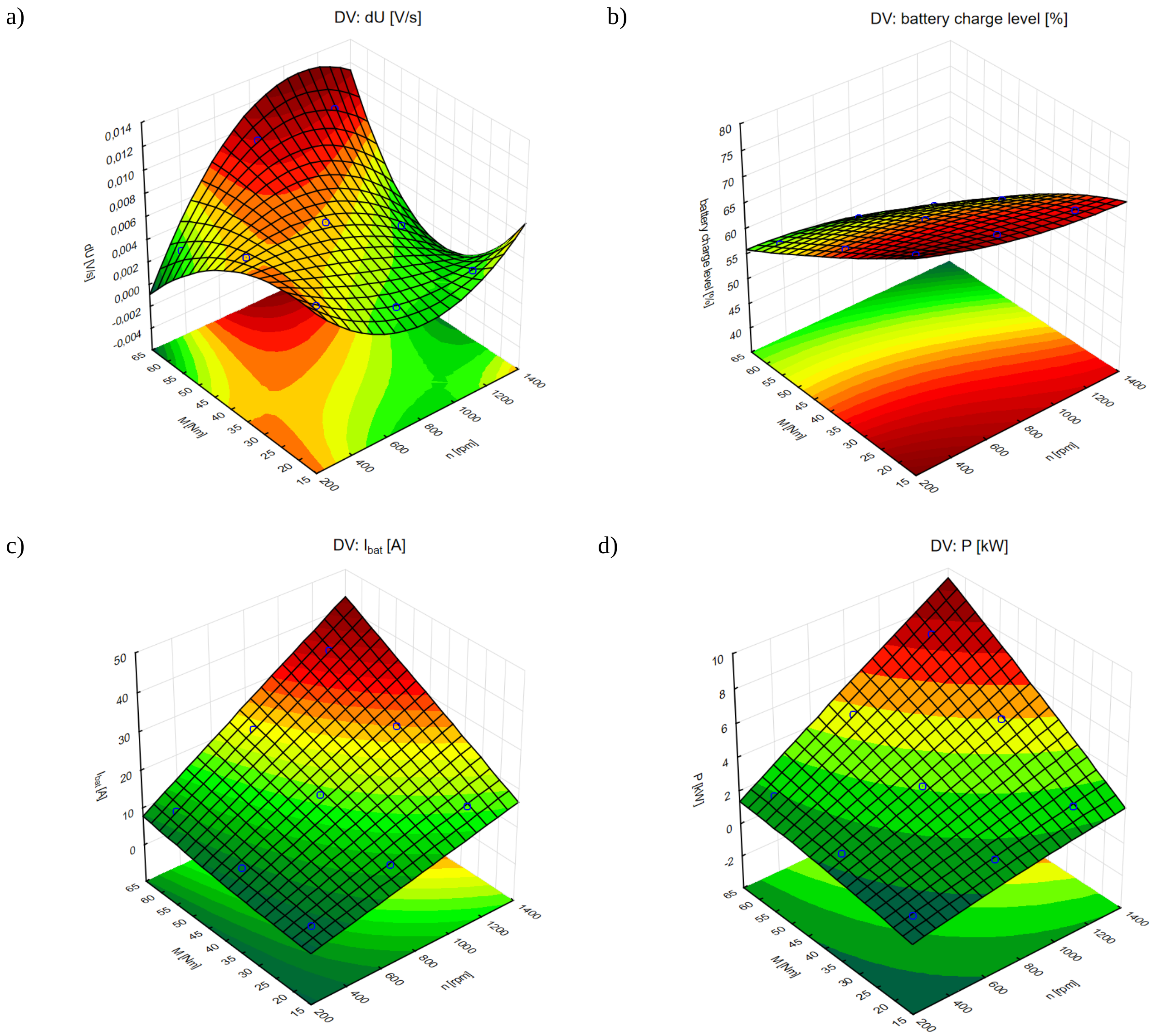

Fig. 12. Dependence of a) battery voltage drop, b) battery charge level, c) battery current, d) receive power

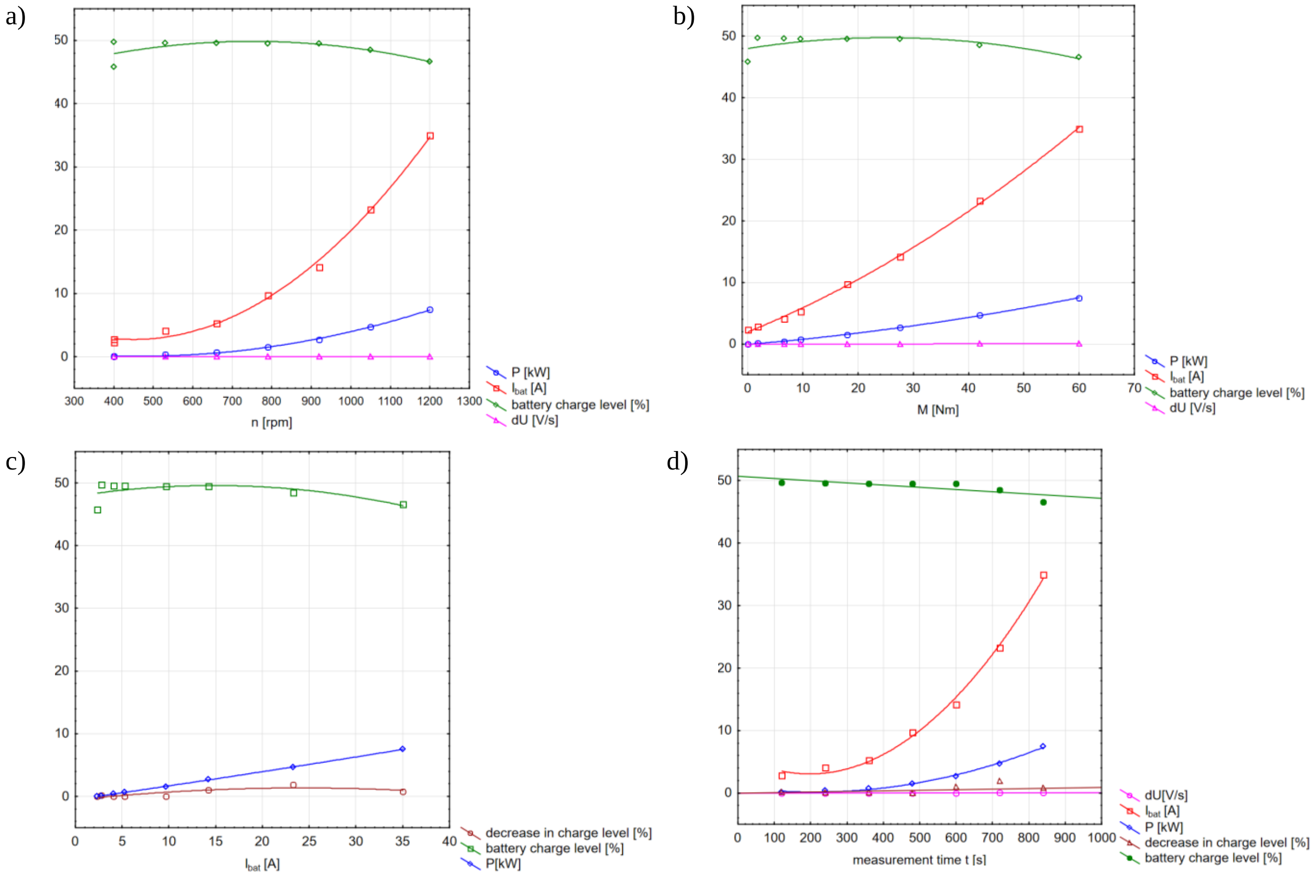

Fig. 13. Scatterplot of multiple variables against a) crankshaft rotational speed n, b) torque on the brake M, c) battery current, d) measurement time

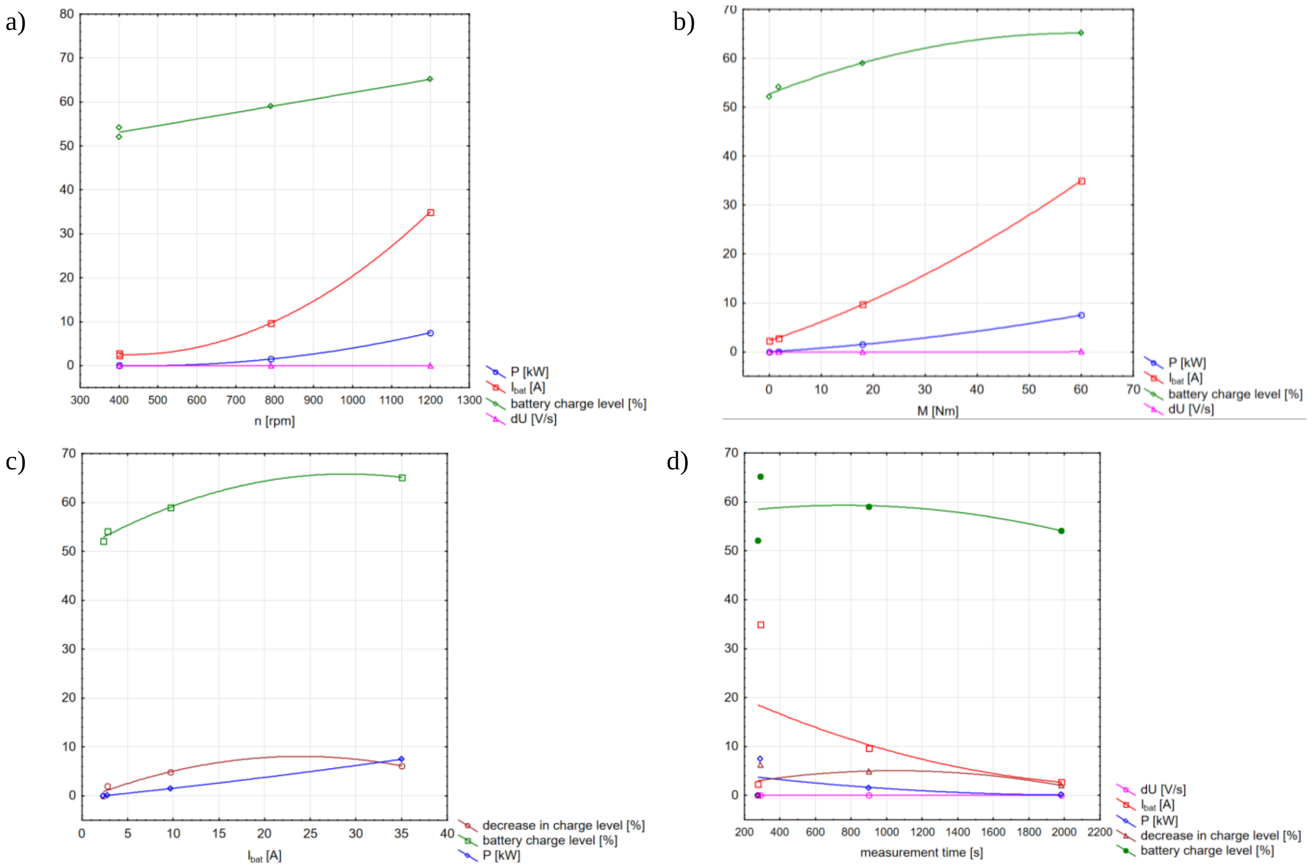

Fig. 14. Scatterplot of multiple variables against a) crankshaft rotational speed n, b) torque on the brake M, c) battery current, d) measurement time

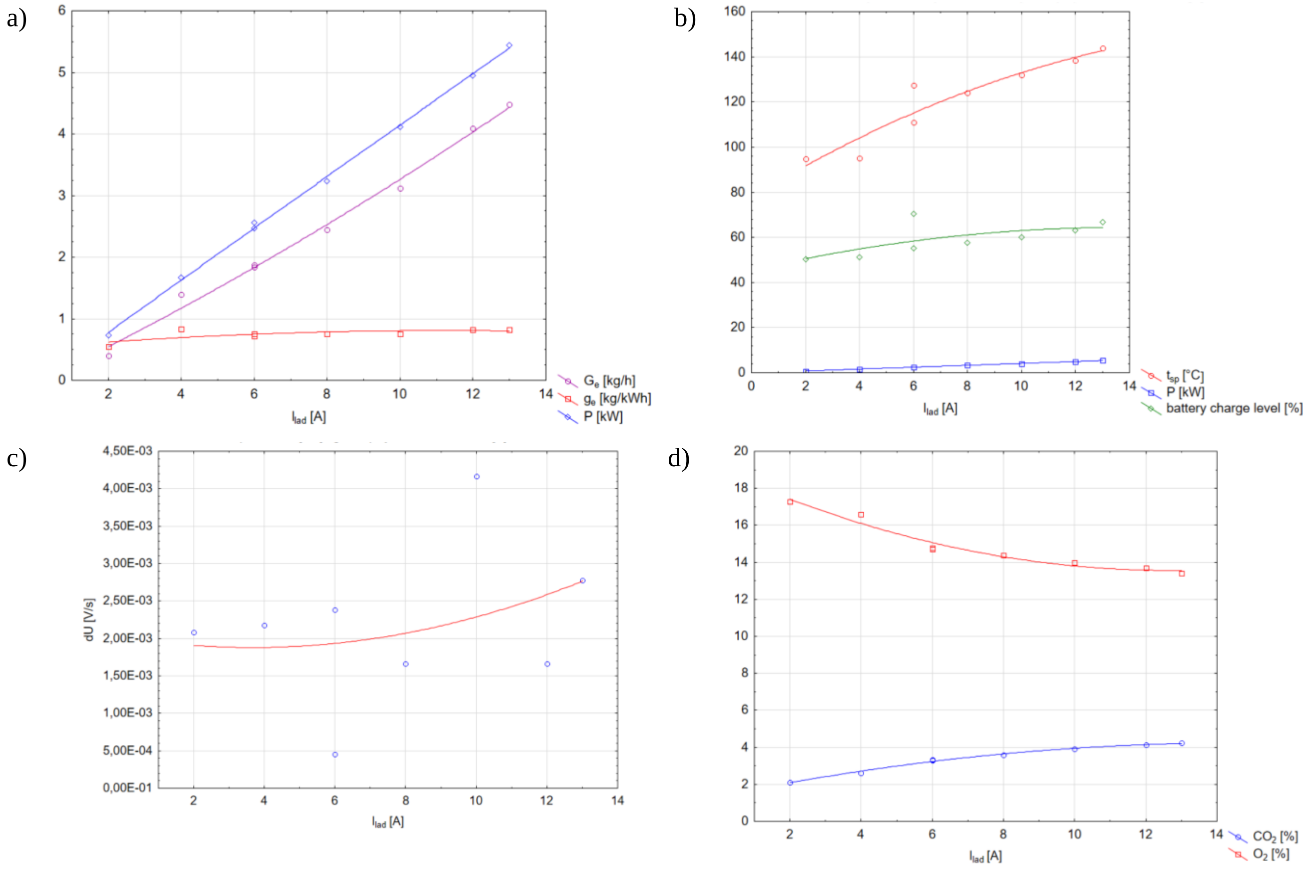

Fig. 15. Scatterplot of multiple variables against charging current I_{lad} a) G_e, g_e, P, b) t_{sp}, P, battery charge level, c) dU, d) CO_2, O_2

Analyzing the data obtained, it can be concluded that both battery currentI_{bat} and battery voltage drop dU show the highest correlations with the other measured quantities.

4.3. Analysis of the results for the load diagram

The analysis according to the load diagram was performed on the basis of the operating time balance of the motors presented in Chapter 3 (Fig. 10, Table 6).

Due to technical limitations of the test stand, measurements were not made for maximum values, i.e. n = 1400 rpm and M = 110 Nm. The tests (Fig. 14) according to the load balance are made for 60 minutes. The operating time for a given float mode was selected proportionally with the actual operating times of the drive.

Comparing the scatter plots for the test according to propeller characteristics (Fig. 13) with the scatter plots for the load diagram (Fig. 14), significant differences in the distribution of variables are apparent. This is due to the measurement times and the actual settings selected for the diagram in Fig. 14. Battery voltage drops over time for high current values are lower, which may allow the battery to run longer at a given load.

4.4. Analysis of results for battery charging

The analysis of the results for battery charging was performed based on the experimental plan shown in Table 7.

During start-up and preheating and cooling of the reformer, the test quantities were not measured due to the lack of measurement possibilities. Note the reformer's own operating time (i.e., the preheating process, which takes about 36 minutes, and the cooling time – 24 minutes). This represents about 33% of the device's operating time. The test results are shown in Fig. 15.

From the above scatter plots, it can be seen that an increase in the charging current affects the increase in the tested quantities. It should be noted that the magnitudes of the measured toxic compounds of the exhaust gas are close to zero. This has a positive effect on environmental protection, including a reduction in the emission of toxic compounds into the atmosphere.

5. Conclusion

The conducted studies, both empirical and model-based, prove that it is reasonable to use unconventional power sources for ship propulsion systems (equipped with fuel cells powered by hydrogen generated in a reformer), especially under specific operating conditions.

The main conclusions of the study are as follows:

1. The test object should be analyzed based on its specific load character.
2. The ship sails more than 50% of the task time in the very slow forward (BWN) mode. The battery voltage drop, for this mode, is the smallest at 1.263 mV/s for the test object.
3. As can be seen from the Pareto plots, speed and torque have the greatest influence on the quantities studied, while their linear and quadratic interactions are much less important.
4. Battery voltage drop is smallest for high loads and low speeds at the same time, or low loads and high speeds.

5. Both battery current $\mathbf{I_{bat}}$ and battery voltage drop **dU** show the highest correlations with the other measured quantities.
6. The magnitudes of the measured values of toxic compounds of exhaust gases are close to zero, and thus close to the values of the measuring resolution of TESTO 350. This is due to the nature of the combustion of methanol and has a beneficial effect on reducing their emission into the atmosphere.

In summary, the use of fuel cells can help improve air quality, reduce greenhouse gas emissions, and create a more efficient and sustainable energy system. However, it is worth noting that the implementation of this technology also requires consideration of aspects related to fuel (hydrogen) production and transportation. According to military assumptions, an undeniable benefit is the minimization of the physical fields of the vessel and its independence from the base (i.e., in the future, obtaining hydrogen from seawater electrolysis).

The promising results of the research will be continued. They will focus on developing a model for optimizing the selection of the battery buffer and placing it on the vessel so that the vessel's stability assumptions are maintained.

Nomenclature

AIS	automatic identification system
ANOVA	analysis of variance
DP	dynamic positioning
DV	dependent variable
FC	fuel cell
HESS	hybrid energy storage system
HPS	hybrid propulsion system
HT	high temperature
LT	low temperature
PEMFC	polymer membrane fuel cell
RMFC	reformed methanol fuel cell system

Bibliography

[1] Acanfora M, Altosole M, Balsamo F, Micoli L, Campora U. Simulation modeling of a ship propulsion system in waves for control purposes. J Mar Sci Eng. 2022;10:36. https://doi.org/10.3390/jmse10010036

[2] Andersson M, Sundèn B. Technology review – solid oxide fuel cell. Report 2017:359, Energiforsk March 2017. www.energiforsk.se

[3] Barelli L, Bidini G, Gallorini F, Iantorno F, Pane N, Ottaviano PA, Trombetti L. Dynamic modeling of a hybrid propulsion system for tourist boat. Energies. 2018;11(10):2592. https://doi.org/10.3390/en11102592

[4] Buchanan F. PEM Fuel Cells: Theory, performance and applications. Nova Science Publisher. Hauppauge 2015.

[5] Dudek M, Lis B, Raźniak A, Krauz M, Kawalec M. Selected aspects of designing modular PEMFC stacks as power sources for unmanned aerial vehicles. Appl Sci. 2021;11(2):675. https://doi.org/10.3390/app11020675

[6] Dudek M, Raźniak A, Rosół M, Siwek T, Dudek P. Design, Development, and Performance of a 10 kW polymer exchange membrane fuel cell stack as part of a hybrid power source designed to supply a motor glider. Energies. 2020; 13(17):4393. https://doi.org/10.3390/en13174393

[7] Elammas T. Hydrogen fuel cells for marine applications: challenges and opportunities. International Journal of Research in Advanced Engineering and Technology. 2023; 9(1):38-43. www.allengineeringjournal.in

[8] Elkafas AG, Rivarolo M, Gadducci E, Magistri L, Massardo AF. Fuel cell systems for maritime: a review of research development, commercial products, applications, and perspectives. Processes. 2023;11(1):97. https://doi.org/10.3390/pr11010097

[9] Fakhreddine O, Gharbia Y, Derakhshandeh JF, Amer AM. Challenges and solutions of hydrogen fuel cells in transportation systems: a review and prospects. World Electr Veh J. 2023;14(6):156. https://doi.org/10.3390/wevj14060156

[10] Fu Z, Lu L, Zhang C, Xu Q, Zhang X, Gao Z et al. Fuel cell and hydrogen in maritime application: a review on aspects of technology, cost and regulations. Sustain Energy Tech Assessments. 2023;57:103181. https://doi.org/10.1016/j.seta.2023.103181.

[11] Fuel cell stack EH-51 15 kW. https://hyfindr.com/marketplace/components/fuel-cell-stacks/pem-stacks/fuel-cell-stack-eh-51-15-kw/

[12] Fuel cell systems for ships. https://new.abb.com/marine/systems-and-solutions/electric-solutions/fuel-cell (accessed on 5.02.2024).

[13] Habrat W, Żółkoś M., Świder J., Socha E. Forces modeling in a surface peripheral grinding process with the use of various design of experiment (DoE). Mechanik. 2018;91(10):929-931. https://doi.org/10.17814/mechanik.2018.10.165

[14] Hydrogen PEM fuel cell. https://hyfindr.com/pem-fuel-cell. Last update 15.02.2023. https://www.imo.org/en/OurWork/Environment/Pages/Default.aspx

[15] International Marine Organization. Regulation 13. http://www.marpoltraining.com/MMSKOREAN/MARPOL/Annex_VI

[16] International Maritime Organization. Regulations for the Prevention of Air Pollution from Ships: Annex VI MARPOL 73/78. 2005. Available online: https://www.epa.gov/sites/production/files/2016-09/documents/marpol-propose-revision-4-05.pdf

[17] Kniaziewicz T, Piaseczny L. Identification of marine internal combustion engine loads in terms of toxic exhaust emissions assessment (in Polish). Scientific Journals of AMW. 2011;187.

[18] Korzyński M. Experimental methodology. Planning, implementation and statistical processing of the results of technical experiments (in Polish). Publishing House of WNT. Warsaw 2017.

[19] Leo TJ, Durango JA, Navarro E. Exergy analysis of PEM fuel cells for marine applications. Energy. 2009;35(2):1164-1171. https://doi.org/10.1016/j.energy.2009.06.010

[20] Leśniewicz T. What is a planned experiment and can almost anything be improved with it?, https://sigmavalue.blog/planowany-eksperyment-doe/

[21] Li S, Gu C, Xu M, Li J, Zhao P, Cheng S. Optimal power system design and energy management for more electric aircrafts. J Power Sources. 2021;512:230473. https://doi.org/10.1016/j.jpowsour.2021.230473

[22] Li S, Gu C, Zhao P, Cheng S. A novel hybrid propulsion system configuration and power distribution strategy for light electric aircraft. Energy Convers Manage. 2021;238:114171. https://doi.org/10.1016/j.enconman.2021.114171
[23] Majka A, Muszyńska-Pałys J. Analysis of the performance of an aircraft powered by hybrid propulsion. Combustion Engines. 2023;193(2):45-51. https://doi.org/10.19206/CE-161107
[24] Marine Power: AKA Hybrid Propulsion. https://www.aka-group.com/marine-power/aka-hybrid-propulsion/
[25] Markowski J, Pielecha I. The potential of fuel cells as a transport drive source. IOP Conf Ser: Earth Environ Sci. 2019;214:012019. https://doi.org/10.1088/1755-1315/214/1/012019
[26] Meryem GS, Hüseyin TA. Advancements and current technologies on hydrogen fuel cell applications for marine vehicles. Int J Hydrogen Energ. 2022;47(45):19865-19875. https://doi.org/10.1016/j.ijhydene.2021.12.251
[27] MTU 8V2000 M72 Documentation.
[28] Nakano A, Shimazaki T, Sekiya M, Shiozawa H, Ohtsuka K, Aoyagi A et al. Research and development of liquid hydrogen (LH_2) temperature monitoring system for marine applications. Int J Hydrogen Energ. 2021;46(29):15649-15659. https://doi.org/10.1016/j.ijhydene.2021.02.052
[29] Online Statistics Handbook. Available online: https://www.statsoft.pl/textbook/stathome_stat.html
[30] User Manual H5-5000 V3 – 48 VDC.
[31] Van Hoecke L, Laffineur L, Campe R, Perreault P, Verbruggen SW, Lenaerts S. Challenges in the use of hydrogen for maritime applications. Energy Environ Sci. 2021;14:815-843. https://doi.org/10.1039/D0EE01545H
[32] Welaya YMA, El Gohary MM, Ammar NR. A comparison between fuel cells and other alternatives for marine electric power generation. Int J Nav Arch Ocean. 2011;3(2):141-149. https://doi.org/10.2478/IJNAOE-2013-0057
[33] Xing H, Stuart C, Spence S, Chen H. Fuel cell power systems for maritime applications: progress and perspectives. Sustainability. 2021;13(3):1213. https://doi.org/10.3390/su13031213
[34] Young Z, Shirong H, Xiaohui J, Yuntao Y, Mu X, Xi Y. Performance study on a large-scale proton exchange membrane fuel cell with cooling, Int J Hydrogen Energ. 2022;47: 10381-10394. https://doi.org/10.1016/j.ijhydene.2022.01.122
[35] Yu W, Zhou P, Wang H. Evaluation on the energy efficiency and emissions reduction of a short-route hybrid sightseeing ship. Ocean Eng. 2018;162:34-42. https://doi.org/10.1016/j.oceaneng.2018.05.016
[36] Yuksel A. Engine emissions regulations for marine applications. Jun 28, 2021. https://www.cummins.com/pl/news/2021/06/28/engine-emission-regulations-marine-applications
[37] Zacharewicz M, Socik P, Wirkowski P, Zadrąg R, Bogdanowicz A. Evaluation of the impact of supplying a marine diesel engine with a mixture of diesel oil and n-butanol on its efficiency and emission of toxic compounds. Combustion Engines. 2023;195(4):40-47. https://doi.org/10.19206/CE-169484

Prof. Ryszard Zadrąg, DSc., DEng. – Faculty of Mechanical and Electrical Engineering, Polish Naval Academy, Poland.
e-mail: *r.zadrag@amw.gdynia.pl*

Paweł Socik, MEng. – Faculty of Mechanical and Electrical Engineering, Polish Naval Academy, Poland.
e-mail: *p.socik@amw.gdynia.pl*

Prof. Tomasz Kniaziewicz, DSc., DEng. – Faculty of Mechanical and Electrical Engineering, Polish Naval Academy, Poland.
e-mail: *t.kniaziewicz@amw.gdynia.pl*

Prof. Marcin Zacharewicz, DSc., DEng. – Faculty of Mechanical and Electrical Engineering, Polish Naval Academy, Poland.
e-mail: *m.zacharewicz@amw.gdynia.pl*

Artur Bogdanowicz, DEng. – Faculty of Mechanical and Electrical Engineering, Polish Naval Academy, Poland.
e-mail: *a.bogdanowicz@amw.gdynia.pl*

Paweł Wirkowski, DEng. – Faculty of Mechanical and Electrical Engineering, Polish Naval Academy, Poland.
e-mail: *p.wirkowski@amw.gdynia.pl*

PTNSS

Silesian University of Technology

XI INTERNATIONAL

CONGRESS ON COMBUSTION ENGINES

POWERTRAINS TECHNOLOGIES AND ALTERNATIVE FUELS

POLISH SCIENTIFIC SOCIETY
OF COMBUSTION ENGINES

23rd-25th June 2025

congress.ptnss.pl

Silesian University of Technology
Faculty of Transport and Aviation Engineering
Zygmunta Krasinskiego str. 8, 40-019 Katowice, Poland

Publisher:

Polish Scientific Society of Combustion Engines

ISSN: 2300-9896
eISSN: 2658-1442

Combustion Engines

Polskie Towarzystwo Naukowe Silników Spalinowych

www.combustion-engines.eu